Journal of Experimental and Theoretical Physics, Vol. 98, No. 6, 2004, pp. 1063–1072.
From Zhurnal Éksperimental'noĭ i Teoreticheskoĭ Fiziki, Vol. 125, No. 6, 2004, pp. 1219–1228.

NUCLEI, PARTICLES, AND THEIR INTERACTION

Quantum Long-Range Interactions in General Relativity¶

I. B. Khriplovich and G. G. Kirilin

Budker Institute of Nuclear Physics, Russian Academy of Sciences, Novosibirsk, 630090 Russia
Novosibirsk State University, Novosibirsk, 630000 Russia
e-mail: khriplovich@inp.nsk.su, g_kirilin@mail.ru

Received February 11, 2004

Abstract—We consider one-loop effects in general relativity that result in quantum long-range corrections to the Newton law, as well as to the gravitational spin-dependent and velocity-dependent interactions. Some contributions to these effects can be interpreted as quantum corrections to the Schwarzschild and Kerr metrics.

1. INTRODUCTION

It was recognized long ago that quantum effects in general relativity can generate long-range corrections to the Newton law. Such corrections due to the photon and massless neutrino contributions to the graviton polarization operator were calculated in [1–4]. The corresponding quantum correction to the Newton potential between two bodies with masses m_1 and m_2 is

$$U_{\gamma\nu} = -\frac{4 + N_\nu}{15\pi}\frac{k^2\hbar m_1 m_2}{c^3 r^3}, \qquad (1)$$

where N_ν is the number of massless two-component neutrinos and k is the Newton gravitational constant.

The reason the problem allows a closed solution is as follows. The Fourier transform of $1/r^3$ is

$$\int d\mathbf{r}\frac{\exp(-i\mathbf{q}\cdot\mathbf{r})}{r^3} = -2\pi\ln q^2. \qquad (2)$$

This singularity in the momentum transfer $\mathbf{q}$ implies that the discussed correction can be generated only by diagrams with two massless particles in the t-channel. The number of such diagrams of the second order in k is finite, and their logarithmic part in q^2 can be calculated unambiguously.

Analogous diagrams with gravitons and ghosts in the loop (Figs. 1a, 1b) were considered in [1, 5–7]. (Here and below, wavy lines refer to quantum fluctuations of metric; double wavy lines denote a background gravitational field; dashed lines here refer to ghosts.) Clearly, other diagrams with two gravitons in the t-channel also contribute to the discussed correction proportional to $1/r^3$. This was pointed out long ago in [8], where all relevant diagrams were explicitly indicated.

The problem of quantum corrections to the Newton law is certainly interesting from the theoretical standpoint. It was addressed later in [9–15]. Unfortunately, as demonstrated in [16], none of these attempts was satisfactory.

The problem was then considered quantitatively in our previous paper [16]. Therein, all relevant diagrams except one (see Fig. 4b below) were calculated correctly. In a recent paper [17], this last diagram has been calculated correctly,[1] and our results for all other contributions are confirmed.

The content of our present work is as follows. Using the background field technique [7], we construct invariant operators that describe quantum power-law corrections in general relativity. In the limit, as one of the interacting particles is heavy, some of the derived corrections can be interpreted as quantum corrections to the Schwarzschild and Kerr metrics. Here, our results differ substantially from those in [18].

We also demonstrate in an elementary way that, to our accuracy, the spin-independent part of the discussed corrections for spinor particles coincides with the corrections for scalar particles. In particular, this implies that the obtained quantum corrections to the Schwarzschild metric are universal, i.e., independent of the spin of the central body. For some loop diagrams relevant to the problem, the mentioned coincidence of the spin-independent contributions of spinor particles with the corresponding results for scalar ones was proved previously in [18] by direct calculation.

With the effective operators constructed, we not only derive the corrections to the Newton law easily, but also obtain quantum corrections to other gravitational effects: spin-dependent and velocity-dependent

¶This article was submitted by the authors in English.

[1] Both previous results for this contribution, by Donoghue [10] and by us [16], were incorrect.

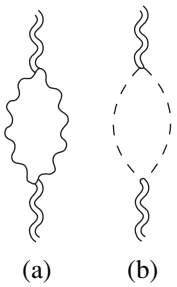

Fig. 1. Graviton loop.

interactions. In the present paper, we mainly consider the case of scalar particles. By spin, we therefore mean the internal angular momentum of a compound particle with scalar constituents.

We also comment on the problem of the classical relativistic corrections to the Newton law. Our conclusions here agree completely with the results in [19–21] (see also the textbook [22, Section 106]), but, on some point, we strongly disagree with the statements in [17].

2. PROPAGATORS AND VERTICES

Below, we use the units where $c = 1$ and $\hbar = 1$. Our metric signature is diag(1, –1, –1, –1).

The graviton operator $h_{\mu\nu}$ describes quantum fluctuations of the metric $g_{\mu\nu}$ in the background metric $g^0_{\mu\nu}$,

$$g_{\mu\nu} = g^0_{\mu\nu} + \kappa h_{\mu\nu}, \quad \kappa^2 = 32\pi k = 32\pi l_p^2. \tag{3}$$

We use the gauge condition

$$h^{\mu}_{\nu;\,\mu} - \frac{1}{2} h^{\mu}_{\mu;\,\nu} = 0 \tag{4}$$

for $h_{\mu\nu}$, where the indices of $h_{\mu\nu}$ are raised with the background metric $g^0_{\mu\nu}$, and the covariant derivatives are taken in the background field $g^0_{\mu\nu}$. The free graviton propagator is

$$D_{\mu\nu,\,\alpha\beta}(q) = i\frac{P_{\mu\nu,\,\alpha\beta}}{q^2 + i0},$$
$$P_{\mu\nu,\,\alpha\beta} = \frac{1}{2}(\delta_{\mu\alpha}\delta_{\nu\beta} + \delta_{\nu\alpha}\delta_{\mu\beta} - \delta_{\mu\nu}\delta_{\alpha\beta}). \tag{5}$$

The tensor $P_{\mu\nu,\,\alpha\beta}$ is conveniently represented as [7]

$$P_{\mu\nu,\,\alpha\beta} = I_{\mu\nu,\,\alpha\beta} - \frac{1}{2}\delta_{\mu\nu}\delta_{\alpha\beta},$$

where

$$I_{\mu\nu,\,\alpha\beta} = \frac{1}{2}(\delta_{\mu\alpha}\delta_{\nu\beta} + \delta_{\nu\alpha}\delta_{\mu\beta})$$

is a sort of unit operator with the property

$$I_{\mu\nu,\,\alpha\beta}t_{\alpha\beta} = t_{\mu\nu}$$

for any symmetric tensor $t_{\alpha\beta}$. We note the useful identity

$$P_{\alpha\beta,\,\kappa\lambda}P_{\kappa\lambda,\,\gamma\delta} = I_{\alpha\beta,\,\gamma\delta}. \tag{6}$$

The propagators of scalar and spinor particles are the usual ones,

$$D(p) = i\frac{1}{p^2 - m^2 + i0} \text{ and } G(p) = i\frac{1}{\hat{p} - m + i0},$$

respectively.

The single-graviton vertex for both scalar and spinor particles (see Fig. 2a) are related to the energy-momentum tensor $T_{\alpha\beta}(p, p')$ of the corresponding particle as

$$V_{\alpha\beta}(p, p') = -i\frac{\kappa}{2}T_{\alpha\beta}(p, p'). \tag{7}$$

The explicit expressions for the scalar and spinor

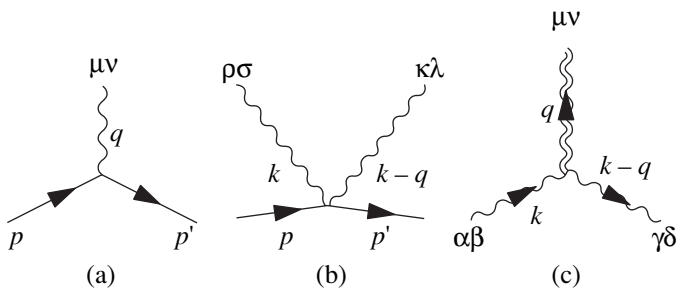

Fig. 2. Gravitational vertices.

particle vertices are

$$V^{(0)}_{\alpha\beta}(p, p') = -i\frac{\kappa}{2}[p_\alpha p'_\beta + p'_\alpha p_\beta - \delta_{\alpha\beta}(pp' - m^2)] \quad (8)$$

and

$$V^{(1/2)}_{\mu\nu} = -\frac{i\kappa}{4}\bar{u}(p')[I_{\mu\nu\alpha\beta}P_\alpha\gamma_\beta - \delta_{\mu\nu}(\hat{P} - 2m)]u(p), \quad (9)$$

respectively; here, $P = p + p'$.

The contact interaction of a scalar particle with two gravitons (see Fig. 2b) is

$$V^{(0)}_{\kappa\lambda,\rho\sigma} = i\kappa^2\Big[I_{\kappa\lambda,\alpha\delta}I_{\delta\beta,\rho\sigma}(p_\alpha p'_\beta + p'_\alpha p_\beta) - \frac{1}{2}\delta_{\kappa\lambda}I_{\rho\sigma,\alpha\beta} + \delta_{\rho\sigma}I_{\kappa\lambda,\alpha\beta}p_\alpha p'_\beta + \frac{(p'-p)^2}{4}\Big(I_{\kappa\lambda,\rho\sigma} - \frac{1}{2}\delta_{\kappa\lambda}\delta_{\rho\sigma}\Big)\Big]. \quad (10)$$

To our accuracy, we can neglect the last term with $(p' - p)^2 = q^2$ in this expression and rewrite the vertex conveniently as

$$V^{(0)}_{\kappa\lambda,\rho\sigma} = i\kappa^2\Big[I_{\kappa\lambda,\alpha\delta}I_{\delta\beta,\rho\sigma}T_{\alpha\beta} - \frac{1}{4}(\delta_{\kappa\lambda}T_{\rho\sigma} + \delta_{\rho\sigma}T_{\kappa\lambda})\Big]. \quad (11)$$

We use the two-graviton vertices on mass shell only. Therefore, the terms with the Kronecker δ entering the energy-momentum tensor in the last expression are also proportional to q^2 and, hence, can be neglected.

The contact two-graviton interaction of a spinor particle (see Fig. 2b) can be written on mass shell as

$$V^{(1/2)}_{\kappa\lambda,\rho\sigma} = i\frac{\kappa^2}{8}\Big[\frac{3}{2}(I_{\kappa\lambda,\mu\beta}I_{\rho\sigma,\beta\alpha} + I_{\rho\sigma,\mu\beta}I_{\kappa\lambda,\beta\alpha})P_\mu - \delta_{\kappa\lambda}I_{\rho\sigma,\mu\alpha}P_\mu - \delta_{\rho\sigma}I_{\kappa\lambda,\mu\alpha}P_\mu\Big]\bar{u}(p')\gamma^\alpha u(p) \quad (12)$$

$$= i\kappa^2\Big[\frac{3}{4}I_{\kappa\lambda,\alpha\delta}I_{\delta\beta,\rho\sigma}T_{\alpha\beta} - \frac{1}{4}(\delta_{\kappa\lambda}T_{\rho\sigma} + \delta_{\rho\sigma}T_{\kappa\lambda})\Big].$$

As regards the 3-graviton vertex (see Fig. 2c), which has the most complicated form, we follow [7, 17] in representing it as

$$V_{\mu\nu,\alpha\beta,\gamma\delta} = -i\frac{\kappa}{2}\sum_i {}^iV_{\mu\nu,\alpha\beta,\gamma\delta},$$

$${}^1V_{\mu\nu,\alpha\beta,\gamma\delta} = P_{\alpha\beta,\gamma\delta}\times\Big[k_\mu k_\nu + (k-q)_\mu(k-q)_\nu + q_\mu q_\nu - \frac{3}{2}\delta_{\mu\nu}q^2\Big],$$

$$\begin{aligned}{}^2V_{\mu\nu,\alpha\beta,\gamma\delta} &= 2q_\kappa q_\lambda[I_{\kappa\lambda,\alpha\beta}I_{\mu\nu,\gamma\delta} + I_{\kappa\lambda,\gamma\delta}I_{\mu\nu,\alpha\beta} - I_{\kappa\mu,\alpha\beta}I_{\lambda\nu,\gamma\delta} - I_{\kappa\nu,\alpha\beta}I_{\lambda\mu,\gamma\delta}],\\ {}^3V_{\mu\nu,\alpha\beta,\gamma\delta} &= q_\kappa q_\mu(\delta_{\alpha\beta}I_{\kappa\nu,\gamma\delta} + \delta_{\gamma\delta}I_{\kappa\nu,\alpha\beta}) + q_\kappa q_\nu(\delta_{\alpha\beta}I_{\kappa\mu,\gamma\delta} + \delta_{\gamma\delta}I_{\kappa\mu,\alpha\beta})\\ &\quad - q^2(\delta_{\alpha\beta}I_{\mu\nu,\gamma\delta} + \delta_{\gamma\delta}I_{\mu\nu,\alpha\beta}) - \delta_{\mu\nu}q_\kappa q_\lambda(\delta_{\alpha\beta}I_{\gamma\delta,\kappa\lambda} + \delta_{\gamma\delta}I_{\alpha\beta,\kappa\lambda}),\end{aligned} \quad (13)$$

$$\begin{aligned}{}^4V_{\mu\nu,\alpha\beta,\gamma\delta} &= 2q_\kappa\times[I_{\kappa\lambda,\alpha\beta}I_{\gamma\delta,\nu\lambda}(k-q)_\mu + I_{\kappa\lambda,\alpha\beta}I_{\gamma\delta,\mu\lambda}(k-q)_\nu - I_{\kappa\lambda,\gamma\delta}I_{\alpha\beta,\nu\lambda}k_\mu - I_{\kappa\lambda,\gamma\delta}I_{\alpha\beta,\mu\lambda}k_\nu]\\ &\quad + q^2(I_{\lambda\mu,\alpha\beta}I_{\gamma\delta,\lambda\nu} + I_{\lambda\nu,\alpha\beta}I_{\gamma\delta,\lambda\mu}) + \delta_{\mu\nu}q_\kappa q_\lambda(I_{\alpha\beta,\kappa\rho}I_{\rho\lambda,\gamma\delta} + I_{\gamma\delta,\kappa\rho}I_{\rho\lambda,\alpha\beta}),\\ {}^5V_{\mu\nu,\alpha\beta,\gamma\delta} &= [k^2 + (k-q)^2]\Big(I_{\lambda\mu,\alpha\beta}I_{\gamma\delta,\lambda\nu} - \frac{1}{2}\delta_{\mu\nu}P_{\alpha\beta,\gamma\delta}\Big)\\ &\quad - k^2\delta_{\gamma\delta}I_{\mu\nu,\alpha\beta} - (k-q)^2\delta_{\alpha\beta}I_{\mu\nu,\gamma\delta}.\end{aligned}$$

In this vertex, we can also neglect the last structure ${}^5V_{\mu\nu,\alpha\beta,\gamma\delta}$ to our accuracy.

3. UNIVERSALITY OF SPIN-INDEPENDENT EFFECTS

We first address the lowest order *s*- and *u*-pole diagrams for graviton scattering, presented in Figs. 3a and 3b.

We start with a scalar particle. The terms with the Kronecker δ in single-graviton vertices (8) then cancel the *s*- and *u*-pole denominators. It can be easily demonstrated that, in the sum of the two diagrams, the arising contact contributions combine into

$$V^{(0)}_{\alpha\beta,\gamma\delta} = i\frac{\kappa^2}{4}[\delta_{\alpha\beta}(p_\gamma p'_\delta + p'_\gamma p_\delta) + \delta_{\gamma\delta}(p_\alpha p'_\beta + p'_\alpha p_\beta)] = i\frac{\kappa^2}{4}(\delta_{\alpha\beta}T^{(0)}_{\gamma\delta} + \delta_{\gamma\delta}T^{(0)}_{\alpha\beta}). \quad (14)$$

In the course of these transformations, we omit the terms with extra powers of the graviton momenta because they do not lead to $\ln q^2$ after subsequent loop

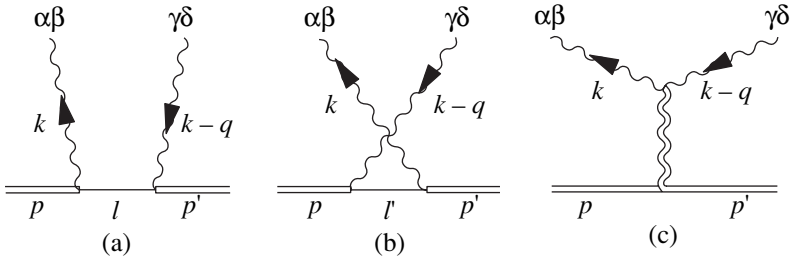

Fig. 3. Pole diagrams.

integration. Combining this induced term with (10), we obtain the total effective two-graviton vertex for a scalar particle,

$$V^{(0)\mathrm{eff}}_{\kappa\lambda,\,\rho\sigma} = i\kappa^2 I_{\kappa\lambda,\,\alpha\delta} I_{\delta\beta,\,\rho\sigma} T^{(0)}_{\alpha\beta} = i\frac{\kappa^2}{2} I_{\kappa\lambda,\,\alpha\delta} I_{\delta\beta,\,\rho\sigma} P_\alpha P_\beta. \quad (15)$$

For spinor particles, the single-graviton vertices (9) also contain terms with the Kronecker δ. Proceeding here with the *s*- and *u*-pole diagrams in the same way as in the scalar case, we obtain the following correction to the two-graviton vertex:

$$V^{(1/2)'}_{\alpha\beta,\,\gamma\delta} = i\frac{\kappa^2}{4}(\delta_{\alpha\beta} T^{(1/2)}_{\gamma\delta} + \delta_{\gamma\delta} T^{1/2}_{\alpha\beta}). \quad (16)$$

The total effective two-graviton vertex for a spinor particle is then given by

$$V^{(1/2)\mathrm{eff}}_{\kappa\lambda,\,\rho\sigma} = i\frac{3}{4}\kappa^2 I_{\kappa\lambda,\,\alpha\delta} I_{\delta\beta,\,\rho\sigma} T^{(1/2)}_{\alpha\beta}. \quad (17)$$

If we are interested in spin-independent effects in the graviton scattering off a spinor particle, one more step is possible. The spinor structure of the numerators in the *s*- and *u*-pole diagrams can be transformed as follows:

$$\bar u(p')\gamma^\sigma(\hat l + m)\gamma^\omega u(p) = \bar u(p')[l^\sigma\gamma^\omega + l^\omega\gamma^\sigma - (\hat l - m)\delta^{\sigma\omega} + i\gamma^5\epsilon^{\sigma\xi\omega\eta} l_\xi\gamma_\eta + m\sigma_{\sigma\omega}]u(p). \quad (18)$$

The term $\bar u(p')(\hat l - m)u(p)$ in this expression, being averaged over spins, transforms to $l^2 - m^2$ (here, we again omit a term proportional to q^2). After cancellation of the denominators, the sum of these terms in the *s*- and *u*-pole diagrams reduces to

$$V^{(1/2)''}_{\kappa\lambda,\,\rho\sigma} = \frac{i\kappa^2}{8} I_{\kappa\lambda,\,\mu\beta} I_{\rho\sigma,\,\beta\alpha} P_\mu P_\alpha. \quad (19)$$

Because the spin-averaged energy-momentum tensor for spinors coincides with the scalar one, which is equal to $P_\mu P_\alpha/2$, the spin-independent term in the sum of (17) and (19) reduces to (15). In other words, from the fermion diagrams, we can single out the sum of structures that coincides with the effective sea-gull for a scalar particle after averaging over spins.

Finally, it can be easily demonstrated that, after averaging over the spins, all the other terms in the numerators of the *s*- and *u*-pole spinor diagrams coincide with the corresponding terms in scalar diagrams with the required accuracy.

For the diagram in Fig. 3c, with the graviton pole in the *t*-channel, the coincidence between the scalar and spin-averaged spinor cases is obvious.

To summarize, the sum of scalar and spin-averaged spinor tree amplitudes, and, hence, the sum of the corresponding loop diagrams coincide with the required accuracy.

4. SPIN-INDEPENDENT EFFECTIVE AMPLITUDES

We start the discussion of loops with the vacuum polarization diagrams (see Fig. 1). The covariant effective Lagrangian corresponding to the sum of these loops was derived in [7] with dimensional regularization. It is given by

$$L_{RR} = -\frac{1}{960\pi^2(4-d)}\sqrt{-g}(42R_{\mu\nu}R^{\mu\nu} + R^2), \quad (20)$$

where, as usual, g is the determinant of the metric tensor, $R_{\mu\nu}$ is the Ricci tensor and $R = R^\nu_\mu$.

For our purpose, Lagrangian (20) can be conveniently rewritten as [9]

$$L_{RR} = -\frac{1}{1920\pi^2}\ln|q^2|(42R_{\mu\nu}R^{\mu\nu} + R^2). \quad (21)$$

We are interested, in particular, in the situation where at least one of the particles is considered in the static limit. In this case, $|q^2| \longrightarrow \mathbf{q}^2$, and, in the coordinate representation, we obtain

$$L_{RR} = \frac{1}{3840\pi^3 r^3}(42R_{\mu\nu}R^{\mu\nu} + R^2). \quad (22)$$

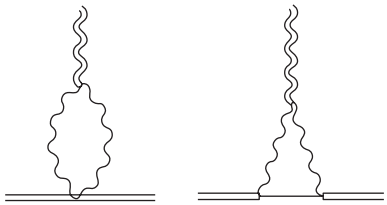

Fig. 4. Vertex diagrams.

The next set of diagrams (Fig. 4) refers to the vertex part. The corresponding effective operator is

$$L_{RT} = -\frac{k}{8\pi^2 r^3}(3R_{\mu\nu}T^{\mu\nu} - 2RT), \quad T = T^{\mu}_{\mu}. \quad (23)$$

Here and below, $T^{\mu\nu}$ is the spin-independent part of the total energy-momentum tensor of matter.

We finally consider the diagrams in Fig. 5. The first two of them, the diagrams in Figs. 5a and 5b, as well as the diagrams in Figs. 1 and 4, depend only on the momentum transfer $t = q^2$. As regards the box diagrams in Figs. 5c and 5d, their contribution is partly reducible to the same structure as that of the diagrams in Figs. 5a and 5b. The sum of all these t-dependent effective operators originating from the diagrams in Fig. 5 is

$$L_{TT} = \frac{k^2}{\pi r^3}T^2. \quad (24)$$

The irreducible contribution of the s-channel box diagram in diagram 5c is

$$M_s = \frac{k^2[(s-m_1^2-m_2^2)^2 - 2m_1^2m_2^2]^2}{m_1^2m_2^2|q^2|}\ln\frac{|q^2|}{\lambda^2} \times \frac{1}{\sqrt{(s-m_-^2)(s-m_+^2)}}\ln\frac{\sqrt{(s-m_-^2)}+\sqrt{(s-m_+^2)}}{\sqrt{(s-m_-^2)}-\sqrt{(s-m_+^2)}}, \quad (25)$$

where m_1 and m_2 are the particle masses,

$$m_\pm = (m_1 \pm m_2), \quad s = (p_1 + p_2)^2,$$

and p_1 and p_2 are the incoming 4-momenta.

The irreducible contribution M_u of the u-channel diagram in Fig. 5d is obtained from formula (25) by the substitution

$$s \longrightarrow u = (p_1 - p_2 - q)^2,$$

with the corresponding analytic continuation.

The expressions for M_s and M_u are convergent in the ultraviolet sense, but diverge in the infrared limit, depending logarithmically on the "graviton mass" λ. As usual, such behavior is directly related to the necessity to cancel the infrared divergence in the bremsstrahlung diagrams (evidently, the gravitational bremsstrahlung in the present case). The box diagrams in Figs. 5c and 5d were considered previously in [23] from a different standpoint.

As regards the three Lagrangians in Eqs. (22)–(24), by virtue of the Einstein equations

$$R_{\mu\nu} = 8\pi k\left(T_{\mu\nu} - \frac{1}{2}g_{\mu\nu}T\right), \quad (26)$$

they can be conveniently combined into

$$L_{\text{tot}} = -\frac{k^2}{60\pi r^3}(138T_{\mu\nu}T^{\mu\nu} - 31T^2). \quad (27)$$

The irreducible amplitudes generated by the box diagrams in Figs. 5c and 5d depend nontrivially on s and u, respectively (in line with their simple dependence on $\ln|q^2|/|q^2|$. Therefore, they cannot be reduced to a product of energy-momentum tensors.

5. QUANTUM CORRECTIONS TO METRIC

The effects due to Lagrangian (27) can be conveniently interpreted as generated by quantum corrections to the metric. To obtain these corrections, we split the total energy-momentum tensor $T_{\mu\nu}$ into those of a static central body and of a light probe particle, $T^0_{\mu\nu}$ and $t_{\mu\nu}$, respectively. Varying the expression resulting in this way from (27) with respect to $t^{\mu\nu}$, we then obtain a ten-

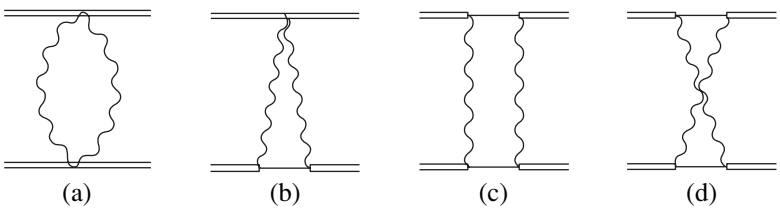

Fig. 5. Scattering diagrams.

sor that can be interpreted as a quantum correction $h^{(q)}_{\mu\nu}$ to the metric created by the central body,

$$h^{(q)}_{\mu\nu} = \frac{k^2}{15\pi r^3}(138T^0_{\mu\nu} - 31\delta_{\mu\nu}T^0). \quad (28)$$

It follows immediately from this expression that

$$h^{(q)}_{00} = \frac{107}{15}\frac{k^2}{\pi r^3}T^0_{00} = \frac{107}{15}\frac{k^2 M}{\pi r^3}, \quad (29)$$

where M is the mass of the central body.

For the space components $h^{(q)}_{mn}$ of the metric created by a heavy body at rest, one might naively expect from formula (28) that they are given by

$$\frac{31}{15}\frac{k^2}{\pi r^3}\delta_{mn}T^0_{00} = \frac{31}{15}\frac{k^2 M}{\pi r^3}\delta_{mn}.$$

However, the calculation of $h^{(q)}_{mn}$ actually requires a modification of formula (28). The point is that we work with gauge condition (4) for the graviton field. It is only natural to require that the resulting effective field $h^{(q)}_{mn}$ should satisfy the same condition, which now simplifies to

$$h^{(q)\mu}_{\nu,\,\mu} - \frac{1}{2}h^{(q)\mu}_{\mu,\,\nu} = 0.$$

The space metric thus obtained is

$$h^{(q)}_{mn} = \frac{k^2 M}{\pi r^3}\left\{\frac{31}{15}\delta_{mn} - \frac{76}{15}\left[\frac{r_m r_n}{r^2} + \ln\left(\frac{r}{r_0}\right)\left(\delta_{mn} - 3\frac{r_m r_n}{r^2}\right)\right]\right\}. \quad (30)$$

Technically, the expression in square brackets in (29) originates from the terms containing structures of the type $\partial_\mu T^{\mu\nu}$. Generally speaking, they arise in calculating Lagrangians (23), (24), and (27), but are omitted there because they vanish on mass shell. These terms are therefore absent in (28). However, they can be restored by rewriting the net result (27), by means of Einstein equations (26), as

$$L_{\rm tot} = -\frac{1}{3840\pi^3 r^3}(138R_{\mu\nu}R^{\mu\nu} - 31R^2), \quad (31)$$

and then attaching energy-momentum tensors to the double wavy lines using graviton propagators (5). The presence of $\ln(r/r_0)$, where r_0 is some normalization point, is quite natural here if we recall $\ln|q^2|$ in the momentum representation. Fortunately, this term in the square brackets does not influence physical effects.

The obtained quantum corrections $h^{(q)}_{00}$ and $h^{(q)}_{mn}$ to the metric are universal, i.e., the same when created by a spinless or spinning heavy pointlike particle.

Our results (29) and (30) differ from the corresponding ones in [18]. The main reason is that the contribution of operator (24) to the metric is absent in [18]. This omission does not appear logical to us: on mass shell, one cannot distinguish this operator from other ones (see (27), (31)). Yet another disagreement is perhaps due to the same inconsistency: the contribution of operator (23) to the metric, as given in [18], is two times smaller than ours.

In addition, the Fourier transformation of $(q_m q_n/\mathbf{q}^2)\ln\mathbf{q}^2$ is performed in [18] incorrectly, which gives a wrong result ($r_m r_n/r^2$ only) for the term in the square brackets in (30).

In concluding this section, we consider the $0n$ component of tensor (28). It is given by

$$h^{(q)}_{0n} = \frac{46}{5}\frac{k^2}{\pi r^3}T^0_{0n} = -\frac{46}{5}\frac{k^2 M\mathbf{v}}{\pi r^3}, \quad (32)$$

where $\mathbf{v}$ is the velocity of the source.

We are interested in the situation corresponding to a compound central body rotating with the angular velocity $\boldsymbol{\omega}$, but with its center of mass being at rest. The velocity of a separate element of the body is then given by $\mathbf{v} = \boldsymbol{\omega}\times\boldsymbol{\rho}$, where $\boldsymbol{\rho}$ is the coordinate of this element. In addition, we must shift $\mathbf{r} \longrightarrow \mathbf{r} + \boldsymbol{\rho}$ in formula (32). Then, following [22, Section 106, Problem 4], we obtain a quantum correction to the Kerr metric,

$$h^{(q)}_{0n} = \frac{69}{5}\frac{k^2}{\pi r^5}[\mathbf{S}\times\mathbf{r}]. \quad (33)$$

We emphasize that the spin $\mathbf{S}$ involved here is in fact the internal angular momentum of a rotating compound central body with spinless constituents. We cannot see any reason why this last quantum correction (33) should be universal (as distinct from $h^{(q)}_{00}$ and $h^{(q)}_{mn}$). If, instead of the compound body discussed here, we deal with a particle of spin 1/2, the general structure of $h^{(q)}_{0n}$ is of course the same, but the numerical coefficient can be quite different.

The last problem, that of a quantum correction to the Kerr metric created by a particle of spin 1/2, was addressed in [18]. However, the treatment of this correction there raises the same objections: the contribution of operator (24) to $h^{(q)}_{0n}$ is missed entirely, and the corresponding effect of operator (23) is not taken into account properly.

6. QUANTUM CORRECTIONS TO GRAVITATIONAL EFFECTS: I

We start with the correction to the Newton law. As usual, it is generated by the 00 component of metric. Here, expression (29) gives

$$U^{qr}(r) = \frac{107}{30}\frac{k^2 Mm}{\pi r^3}. \quad (34)$$

However, in line with (29), we must now take into account the irreducible contribution of the box diagrams in Figs. 5c and 5d, which cannot be reduced to the metric. Having other applications in mind, we write the sum of the two amplitudes, retaining in it the terms of not only the zeroth order in c^{-2}, but also the first order,

$$M_s + M_u = -k^2 m_1 m_2 \ln(\mathbf{q}^2 - \omega^2) \times \frac{2}{3}\left(23 + \frac{524}{5}\frac{p_1 p_2 - m_1 m_2}{m_1 m_2}\right). \quad (35)$$

In the static limit, $\omega \longrightarrow 0$, $p_1 p_2 \longrightarrow m_1 m_2$, expression (35) reduces to

$$M_s + M_u \longrightarrow -\frac{46}{3}k^2 m_1 m_2 \ln \mathbf{q}^2. \quad (36)$$

Changing the sign (in passing from the amplitude to the potential) and performing the Fourier transformation, we obtain [16, 17]

$$U^{qi}(r) = -\frac{23}{3}\frac{k^2 Mm}{\pi r^3}. \quad (37)$$

Thus, the net correction to the Newton law is

$$U^{q}(r) = -\frac{41}{10}\frac{k^2 Mm}{\pi r^3}. \quad (38)$$

This result was also cross-checked and confirmed by independent calculation in the standard harmonic gauge, with the field variables

$$\psi^{\mu\nu} = \sqrt{-g}g^{\mu\nu} - \delta^{\mu\nu}$$

and the gauge condition

$$\partial_\mu \psi^{\mu\nu} = 0.$$

We now consider the quantum correction to the interaction of the orbital momentum **l** of a light particle with its own spin **s**, i.e., to the gravitational spin–orbit interaction. It is most easily obtained with the general expression for the frequency **ω** of the spin precession in a gravitational field derived in [24]. For a nonrelativistic particle in a weak static centrally symmetric field, this expression simplifies to

$$\omega_i = \frac{1}{2}\varepsilon_{imn}(\gamma_{mnk}v_k + \gamma_{0n0}v_m), \quad (39)$$

where

$$\gamma_{mnk} = \frac{1}{2}(\partial_m h_{nk} - \partial_n h_{mk}), \quad \gamma_{0n0} = -\frac{1}{2}\partial_n h_{00}$$

are the Ricci rotation coefficients and **v** is the particle velocity (the present sign convention for **ω** is opposite to that in [24]). A simple calculation results in

$$U^{q}_{ls}(r) = -\frac{169}{20}\frac{k^2}{\pi r^5}\frac{M}{m}(\mathbf{l}\cdot\mathbf{s}). \quad (40)$$

Finally, with formula (33), we easily derive the quantum correction to the interaction of the orbital momentum **l** of a light particle with the internal angular momentum (spin) **S** of a compound central body, i.e., to the Lense–Thirring effect,

$$U^{q,r}_{LT}(r) = -\frac{69}{5}\frac{k^2}{\pi r^5}(\mathbf{l}\cdot\mathbf{S}). \quad (41)$$

7. AN ASIDE ON CLASSICAL RELATIVISTIC CORRECTIONS

In this section, we first consider the classical velocity-dependent correction to the Newton law. On the one hand, this is an introduction to the derivation of quantum velocity-dependent corrections in the next section. On the other hand, this is necessary for the discussion of another, velocity-independent relativistic correction to the Newton law. The derivation of the classical velocity-independent correction via the diagram technique served in [16, 17] as a check of calculations of quantum corrections to the Newton law.

We consider the Born scattering amplitude with the graviton exchange in the harmonic gauge,

$$M_B = 8\pi k\frac{T^1_{\mu\nu}T^2_{\mu\nu} - (1/2)T^1_{\mu\mu}T^2_{\nu\nu}}{\mathbf{q}^2 - \omega^2}, \quad (42)$$

where $T^{1,2}_{\mu\nu}$ are the energy-momentum tensors of particles with the respective masses $m_{1,2}$ and velocities $\mathbf{v}_{1,2}$. To the adopted accuracy, the numerator simplifies to

$$\frac{1}{2}T^1_{00}T^2_{00} - 2T^1_{0n}T^2_{0n} = \frac{m_1 m_2}{2}(1 - 4\mathbf{v}_1\cdot\mathbf{v}_2).$$

We then expand the denominator to the first order

in $\omega^2/\mathbf{q}^2$ and thus arrive at the expression

$$\frac{4\pi k m_1 m_2}{\mathbf{q}^2}\left(1 - 4\mathbf{v}_1\cdot\mathbf{v}_2 + \frac{\omega^2}{\mathbf{q}^2}\right).$$

The term of the zeroth order in c^{-2} in this formula, $4\pi k m_1 m_2/\mathbf{q}^2$, is obviously (after the necessary sign reversal) the Fourier transform of the Newton potential. However, we are interested here in the terms of the first order in c^{-2}. To transform $\omega^2/\mathbf{q}^2$, we note that ω is in fact the energy difference between the initial and final energies of a particle. The particles can now be considered nonrelativistic, and this difference therefore transforms (to the first order in $\mathbf{p}' - \mathbf{p}$) as follows:

$$\varepsilon' - \varepsilon = (\mathbf{p}' - \mathbf{p})\cdot\mathbf{v}.$$

Therefore, the terms of the first order in c^{-2} are rewritten as

$$\frac{4\pi k m_1 m_2}{\mathbf{q}^2}\left[-4\mathbf{v}_1\cdot\mathbf{v}_2 + \frac{(\mathbf{q}\cdot\mathbf{v}_1)(\mathbf{q}\cdot\mathbf{v}_2)}{\mathbf{q}^2}\right].$$

The Fourier transform of this expression, taken with the opposite sign, is the well-known relativistic velocity-dependent correction to the Newton potential [19, 20, 22]

$$U^{cl}_{vv} = \frac{k m_1 m_2}{2r}[7\mathbf{v}_1\cdot\mathbf{v}_2 + (\mathbf{n}\cdot\mathbf{v}_1)(\mathbf{n}\cdot\mathbf{v}_2)], \quad \mathbf{n} = \frac{\mathbf{r}}{r}. \tag{43}$$

We here essentially follow the derivation by Iwasaki [21].

At least equally simple is the derivation of the relativistic velocity-independent correction to the Newton potential. In the harmonic gauge, the metric created by a pointlike mass m_1 is

$$ds^2 = \frac{r - k m_1}{r + k m_1}dt^2 - \frac{r + k m_1}{r - k m_1}dr^2 - (r + k m_1)^2(d\theta^2 + \sin^2\theta d\phi^2). \tag{44}$$

In the expansion in r_g of the classical action $-m_2\int ds$ for a probe particle of mass m_2, the second-order term is $-k^2 m_1^2 m_2/2r^2$. Now, reversing the sign (to pass from a Lagrangian to a potential) and restoring the symmetry between m_1 and m_2, we arrive at the discussed correction

$$U^{cl} = \frac{k^2 m_1 m_2 (m_1 + m_2)}{2r^2}. \tag{45}$$

The classical correction (45) was found long ago in [19, 20] (see also the textbook [22, Section 106]) and was derived later in [21] by calculating the corresponding parts of the diagrams in Figs. 4b and 5b–5d in the harmonic gauge. A subtle point of the last calculation [21] refers to the box diagrams in Figs. 5c and 5d. Obviously, the classical c^{-2} contribution of these diagrams, in particular, contains the result of iteration of the usual Newton interaction and the velocity-dependent interaction (43). Therefore, the result of this iteration should be subtracted from the sum of the contributions of the diagrams in Figs. 4b and 5b–5d. This has been done properly by Iwasaki [21].

However, Bjerrum-Bohr, Donoghue, and Holstein argue (see Section 2.1 in [17]) that, in the scattering problem, as distinct from the bound-state one, this subtraction is unnecessary. They claim that there is a difference between what they call "the lowest order scattering potential" without this subtraction, and the classical correction U^{cl}, which they call the bound state potential. For our part, we do not see any difference of principle between the bound state problem and the scattering one[2] and therefore we believe that it is just (45) that should be considered as a relativistic correction to the Newton law, both in the scattering and bound-state problems.

8. QUANTUM CORRECTIONS TO GRAVITATIONAL EFFECTS: II

We now address the quantum correction to the classical velocity-dependent gravitational interaction (43). We start with the amplitude (27) written in the momentum representation,

$$L_{\rm tot} = \frac{k^2}{30}\ln|q^2|(138T_{\mu\nu}T^{\mu\nu} - 13T^2). \tag{46}$$

Unlike with the previous quantum corrections, we here go beyond the static approximation and, in the spirit of the previous section, expand

$$\ln|q^2| = \ln(\mathbf{q}^2 - \omega^2)$$

to the first order in ω^2. Following the same lines of reasoning further, we easily obtain the quantum velocity-dependent correction

$$U^{q,r}_{vv}(\mathbf{r}) = -\frac{k^2 m_1 m_2}{60\pi r^3} \times [445(\mathbf{v}_1\cdot\mathbf{v}_2) + 321(\mathbf{n}\cdot\mathbf{v}_1)(\mathbf{n}\cdot\mathbf{v}_2)], \quad \mathbf{n} = \frac{\mathbf{r}}{r}. \tag{47}$$

[2] For instance, the second Born approximation is as legitimate a notion to a scattering amplitude as is the second-order correction to a bound state energy.

With formula (47), we can derive (in the spirit of [22, Section 106, Problem 4]) the quantum correction to the spin–spin interaction of compound bodies 1 and 2 rotating with the angular velocities $\boldsymbol{\omega}_1$ and $\boldsymbol{\omega}_2$, but with their centers of masses at rest. The velocity of a separate element of the body i is then given by $\mathbf{v}_i = \boldsymbol{\omega}_i \times \boldsymbol{\rho}_i$, where $\boldsymbol{\rho}_i$ is the coordinate of this element counted off the center of mass of this body. In formula (47), where $\mathbf{r} = \mathbf{r}_1 - \mathbf{r}_2$, we then shift

$$\mathbf{r} \longrightarrow \mathbf{r} + \boldsymbol{\rho}_1 - \boldsymbol{\rho}_2.$$

Again following [22], we thus obtain

$$U_{ss}^{q,r}(\mathbf{r}) = \frac{69}{10}\frac{k^2}{\pi r^5}[3(\mathbf{S}_1\cdot\mathbf{S}_2) - 5(\mathbf{n}\cdot\mathbf{S}_1)(\mathbf{n}\cdot\mathbf{S}_2)], \quad \mathbf{n} = \frac{\mathbf{r}}{r}, \tag{48}$$

where $\mathbf{S}_i$ are the internal angular momenta (spins) of the rotating compound central bodies.

We note that quantum correction (41) to the Lense–Thirring effect can also be derived in the same way.

We finally consider the corresponding corrections induced by irreducible amplitude (35), which is now conveniently rewritten as

$$M_s + M_u = -k^2 m_1 m_2 \ln(\mathbf{q}^2 - \omega^2) \times \frac{2}{3}\left(23 - \frac{524}{5}\mathbf{v}_1\cdot\mathbf{v}_2\right). \tag{49}$$

This amplitude also generates quantum corrections to the velocity-dependent, Lense–Thirring, and spin–spin interactions. The calculations are practically identical with the previous ones, and give the respective corrections

$$U_{vv}^{q,irr}(\mathbf{r}) = \frac{k^2 m_1 m_2}{10\pi r^3}[311(\mathbf{v}_1\cdot\mathbf{v}_2) + 115(\mathbf{n}\cdot\mathbf{v}_1)(\mathbf{n}\cdot\mathbf{v}_2)], \tag{50}$$

$$U_{LT}^{q,irr}(r) = \frac{262}{5}\frac{k^2}{\pi r^5}(\mathbf{l}\cdot\mathbf{S}), \tag{51}$$

$$U_{ss}^{q,irr}(\mathbf{r}) = -\frac{131}{5}\frac{k^2}{\pi r^5}[3(\mathbf{S}_1\cdot\mathbf{S}_2) - 5(\mathbf{n}\cdot\mathbf{S}_1)(\mathbf{n}\cdot\mathbf{S}_2)]. \tag{52}$$

Now, combining these contributions with those originating from quantum corrections to the metric, we finally obtain

$$U_{vv}^{q}(\mathbf{r}) = U_{vv}^{q,r}(\mathbf{r}) + U_{vv}^{q,irr}(\mathbf{r}) = \frac{k^2 m_1 m_2}{60\pi r^3}[1421(\mathbf{v}_1\cdot\mathbf{v}_2) + 369(\mathbf{n}\cdot\mathbf{v}_1)(\mathbf{n}\cdot\mathbf{v}_2)], \tag{53}$$

$$U_{LT}^{q}(r) = U_{LT}^{q,r}(r) + U_{LT}^{q,irr}(r) = \frac{193}{5}\frac{k^2}{\pi r^5}(\mathbf{l}\cdot\mathbf{S}), \tag{54}$$

$$U_{ss}^{q}(\mathbf{r}) = U_{ss}^{q,r}(\mathbf{r}) + U_{ss}^{q,irr}(\mathbf{r}) = -\frac{193}{10}\frac{k^2}{\pi r^5}[3(\mathbf{S}_1\cdot\mathbf{S}_2) - 5(\mathbf{n}\cdot\mathbf{S}_1)(\mathbf{n}\cdot\mathbf{S}_2)]. \tag{55}$$

Note added in proofs. After submitting our manuscript to the journal, we became aware that the problem of long-range quantum corrections in gravity was also addressed by D. Dalvit and F.D. Mazzitelli [Phys. Rev. D **56**, 7779 (1997); E-print archives hep-th/9708102]. In particular, they found the contribution of the vacuum polarization diagrams *1a*, *b* to the metric and to the Newton law.

ACKNOWLEDGMENTS

We are grateful to N.G. Ural'tsev and A.I. Vainshtein for useful discussions. This paper was supported by the Russian Foundation for Basic Research (project no. 03-02-17612).

REFERENCES

1. A. F. Radkowski, Ann. Phys. (N.Y.) **56**, 319 (1970).
2. D. M. Capper, M. J. Duff, and L. Halpern, Phys. Rev. D **10**, 461 (1974).
3. D. M. Capper and M. J. Duff, Nucl. Phys. B **44**, 146 (1974).
4. M. J. Duff and J. T. Liu, Phys. Rev. Lett. **85**, 2052 (2000); hep-th/0003237.
5. D. M. Capper, G. Leibbrandt, and M. Ramon Medrano, Phys. Rev. D **8**, 4320 (1973).
6. M. J. Duff, Phys. Rev. D **9**, 1837 (1973).
7. G. 't Hooft and M. Veltman, Ann. Inst. Henri Poincaré, Sect. A **20**, 69 (1974).
8. D. G. Boulware and S. Deser, Ann. Phys. (N.Y.) **89**, 193 (1975).
9. J. F. Donoghue, Phys. Rev. Lett. **72**, 2996 (1994); gr-qc/9310024.
10. J. F. Donoghue, Phys. Rev. D **50**, 3874 (1994); gr-qc/9405057.
11. J. F. Donoghue, in *Advanced School on Effective Theories*, Ed. by F. Cornet and M. J. Herrero (World Sci., Singapore, 1996); gr-qc/9512024.

12. J. F. Donoghue, in *Proceedings of the Eighth Marcel Grossmann Meeting on General Relativity*, Ed. by Tsvi Piran and Remo Ruffini (World Sci., Singapore, 1999); gr-qc/9712070.

13. I. J. Muzinich and S. Vokos, Phys. Rev. D **52**, 3472 (1995); hep-th/9501083.

14. A. Akhundov, S. Belucci, and A. Shiekh, Phys. Lett. B **395**, 19 (1998); gr-qc/9611018.

15. H. Hamber and S. Liu, Phys. Lett. B **357**, 51 (1995); hep-th/9505182.

16. G. G. Kirilin and I. B. Khriplovich, Zh. Éksp. Teor. Fiz. **122**, 1139 (2002) [JETP **95**, 981 (2002)]; gr-qc/0207118.

17. N. E. J. Bjerrum-Bohr, J. F. Donoghue, and B. R. Holstein, Phys. Rev. D **67**, 084033 (2003); gr-qc/0211072.

18. N. E. J. Bjerrum-Bohr, J. F. Donoghue, and B. R. Holstein, Phys. Rev. D **68**, 084003 (2003); gr-qc/0211071.

19. A. Einstein, L. Infeld, and B. Hoffmann, Ann. Math. **39**, 65 (1938).

20. A. Eddington and G. Clark, Proc. R. Soc. London **166**, 465 (1938).

21. Y. Iwasaki, Prog. Theor. Phys. **46**, 1587 (1971).

22. L. D. Landau and E. M. Lifshitz, *The Classical Theory of Fields*, 5th ed. (Nauka, Moscow, 1967; Pergamon Press, Oxford, 1975), Sect. 106.

23. J. F. Donoghue and T. Torma, Phys. Rev. D **54**, 4963 (1996); hep-th/9602121.

24. I. B. Khriplovich and A. A. Pomeransky, Zh. Éksp. Teor. Fiz. **113**, 1537 (1998) [JETP **86**, 839 (1998)]; gr-qc/9710098.

Journal of Experimental and Theoretical Physics, Vol. 98, No. 6, 2004, pp. 1073–1086.
Translated from Zhurnal Éksperimental'noĭ i Teoreticheskoĭ Fiziki, Vol. 125, No. 6, 2004, pp. 1229–1244.

ATOMS, SPECTRA, RADIATION

Unidirectional Optical Solitons in a Two-Level Medium

A. A. Zabolotskiĭ

Institute of Automation and Electrometry, Siberian Division, Russian Academy of Sciences, Novosibirsk, 630090 Russia

e-mail: zabolotskii@iae.nsk.su

Received July 14, 2003

Abstract—Self-induced transparency is analyzed for optical pulses interacting with a two-level system by solving an integrable system of evolution equations without using the slowly varying envelope approximation. A suitable modification of the inverse scattering method is developed to find soliton solutions. The characteristics of linearly and circularly polarized optical solitons (including those created in a laser) are compared. To assess the scope of the two-level model, the effects due to additional levels are analyzed in the adiabatic approximation. It is shown that these effects violate the integrability of the model and lead to loss of self-induced transparency for pulses with duration comparable to oscillation period. However, self-induced transparency is recovered in the quasi-monochromatic limit. Applications of the results are discussed. © *2004 MAIK "Nauka/Interperiodica".*

1. INTRODUCTION

Generation and evolution of femtosecond pulses with a duration comparable to the oscillation period $2\pi/\omega_0$, where ω_0 is a transition frequency, are the subjects of ongoing research motivated by applications in various branches of physics (e.g., see reviews in [1–4]). The applicability of the two-level model to such pulses requires that the resonant frequency be well separated from other frequencies [5–12]. The applicability conditions are improved if the dipole moment corresponding to the resonant transition is larger than those of the nearest transitions [6].

It was noted in various publications that the theoretical methods developed for analyzing femtosecond optical-pulse propagation do not meet the requirements dictated by experiment. In particular, pulse dynamics are analyzed by using the slowly varying envelope approximation with small corrections allowing for deviations from this approximation [3]. In [13], numerical methods were applied to solve the semiclassical Maxwell–Bloch (MB) equations. In those and other studies, self-induced transparency was analyzed for linearly polarized pulses interacting with a two-level system. However, numerical methods may not provide a sufficiently detailed and reliable characterization of dynamics governed by complicated systems of equations, such as the Maxwell–Bloch system describing femtosecond optical pulse propagation.

The period of a light wave with a wavelength of 780 nm is about 2.6 fs. Currently, the Ti:sapphire laser can be used to generate 7.5-fs pulses [7] and 4.5-fs with the use of a fiber-optic pulse compressor [8]. These pulse durations are only a few times longer than the oscillation period. Therefore, their dynamics cannot be analyzed by using solutions obtained in models with slowly varying amplitudes and phases as zeroth approximations. However, these pulses are not short enough to justify the use of the ultrashort-pulse (USP) approximation, which is applicable if $\tau_p \ll \pi/\omega_0$ (e.g., see [9–12]), and reduce the original Maxwell-Bloch system to simpler equations. Some authors noted that this approximation is not realistic in the optical frequency range [12]. For this reason, simplifying approximations other than the condition $\tau_p \ll \pi/\omega_0$ should be employed. In this paper, the unidirectional approximation is used, in combination with other conditions, to reduce the Maxwell–Bloch equations to an integrable form. Accordingly, appropriate localized solutions to these evolution equations are called unidirectional pulses (UDPs). The concept of UDP was recently developed in [14], where the vector Maxwell equations were solved numerically without using the slowly varying envelope approximation.

It is well known that the most detailed analytic solutions describing pulse evolution can be obtained for integrable models by the inverse scattering method (ISM) [15]. The well-studied integrable models are based on the MB systems describing dynamics of quasi-monochromatic pulse propagation (see [4] for review and [16] for details of ISM as applied to the MB system for a degenerate two-level system). Self-induced transparency for UDPs in a nondegenerate two-level system was analyzed in [17], where the original system was simplified to obtain reduced Maxwell–Bloch (RMB) equations that can be solved by ISM. In [17], the RMB equations were derived for a low-density active medium instead of the slowly varying envelope approximation, which corresponds to unidirectional propagation. However, all of these results correspond to linearly polarized fields and do not apply to

transitions with moments changing by unity and to circularly polarized UDPs. The only exception is the particular soliton solution to the Maxwell–Bloch system found in [11] for a circularly polarized USP interacting with a two-level nondegenerate system. However, analyses of multisoliton propagation and other cases of self-similar dynamics of circularly polarized UDPs based on solutions of the initial–boundary value problems for appropriate systems of equations are by no means less important. It should be emphasized that the applicability conditions imposed in the theory are much less stringent for UDP as compared to USP propagation, which is essential for optical pulses. Moreover, the results presented below can readily be used to show that the theories of USP and quasi-monochromatic pulse propagation are formally subsumed under the UDP propagation theory as its special cases.

The analysis presented in this paper is focused on the dynamics of interaction between a unidirectional femtosecond pulse and a two-level system consisting of atoms with a σ transition, in which the magnetic-moment projection changes by unity ($\Delta m = \pm 1$). The corresponding dipole matrix element is a complex quantity:

$$\mathbf{d} = d_x \mathbf{e}_x - i d_y \mathbf{e}_y$$

(see [18]). Here, $\mathbf{e}_x$ and $\mathbf{e}_y$ are the unit basis vectors of a Cartesian coordinate system. A laser pulse resonant with this transition is circularly polarized [18].

Note that the unidirectional approximation applied in this study to the Maxwell-Bloch equations for circularly polarized field leads to evolution equations having qualitatively different properties, as compared to the equations derived in the slowly varying envelope approximation. As noted in [1], this is an essential distinction between the problems of circularly and linearly polarized pulse propagation. In the latter case, the evolution equations derived by using the slowly varying envelope and unidirectional approximations are related by simple transformations. Accordingly, the ISM apparatus developed for circularly polarized UDPs is substantially different from the technique applied to the MB equations derived in the slowly varying envelope approximation.

The technique is based on an analysis of the dynamics of circularly polarized UDPs interacting with a two-level system described by a new integrable system of equations proposed in [19]. The exact solutions obtained are used to compare the shapes of circularly and linearly polarized UDPs, including those propagating in a two-level laser medium with continuous pumping.

It was mentioned above that the two-level model frequently employed in analyses of the evolution of few-cycle pulses is valid under relatively stringent conditions. In particular, the separation from the nearest level must be at least several times greater than the spectral pulse width. Applicability conditions for the two-level model in this problem were analyzed numerically in [20]. However, the specific results obtained in that study cannot be used to examine UDP dynamics when the influence of additional levels is taken into account. In this paper, an adiabatic approximation is invoked to show that interaction between the field and additional levels leads to violation of integrability for relatively short pulses. Furthermore, the model constructed here provides qualitative explanations for some well-known experimental observations.

The paper is organized as follows. In the next section, the basic system of equations describing the dynamics of a circularly polarized wave in a nondegenerate medium is derived. In Section 3, the most general integrable reduced system is derived from the basic system and an appropriate ISM apparatus for finding soliton solutions is developed. In Section 4, pulse amplification in a laser is analyzed. In Section 5, the contribution due to interaction between pulses and additional levels is examined. Section 6 presents a discussion of the results and their applications.

2. DERIVATION OF THE BASIC SYSTEM OF EQUATIONS

The semiclassical theory of interaction between radiation and a two-level system was developed, in particular, in [21]. The Heisenberg equation for the operator $\hat{S}$ describing a two-level system is written as follows (e.g., see [18]):

$$i\hbar \partial_t \hat{S} = [\hat{S}, \hat{\mathcal{H}}], \tag{1}$$

with

$$\hat{\mathcal{H}} = \frac{1}{2}\omega_0 \hat{\sigma}_3 + (\mathbf{d}_x \cdot \hat{\mathbf{E}})\hat{\sigma}_1 + (\mathbf{d}_y \cdot \hat{\mathbf{E}})\hat{\sigma}_2, \tag{2}$$

where

$$\hat{d} = d_x \hat{\sigma}_1 + d_y \hat{\sigma}_2$$

is the dipole moment operator, $\hat{\sigma}_n$ denotes the Pauli matrices ($n = 1, 2, 3$), and $\hat{\mathbf{E}}$ is the electric field operator. If the electromagnetic wave is elliptically polarized, then $d_{x,y} \neq 0$.

A circularly polarized field stimulates transitions in which the magnetic-moment projection changes by unity. These transitions can be observed in a two-level system with the following optical transition between magnetic sublevels:

$$J_1 = 1/2 \longleftrightarrow J_u = 1/2,$$

where subscripts “l” and “u” correspond to the lower and upper sublevels, respectively. For example, this can

be the $^2S_{1/2}$–$^2P^0_{1/2}$ transition in sodium vapor [18, 22]. When an elliptically polarized field interacts with a two-level system, transitions with $\Delta M = \pm 1$ should be taken into account:

$$\{J_l = 1/2, M_l = -1/2\} \longleftrightarrow \{J_u = 1/2, M_u = 1/2\},$$

$$\{J_l = 1/2, M_l = 1/2\} \longleftrightarrow \{J_u = 1/2, M_u = -1/2\}.$$

Suppose that the initial populations of the $\{J_l = 1/2, M_l = 1/2\}$ and $\{J_l = 1/2, M_u = \pm 1/2\}$ sublevels is zero and the population of the $\{J_l = 1/2, M_l = -1/2\}$ sublevel equals the total population of all sublevels. Then, it can readily be shown that there exists a stable solution corresponding to zero populations of the $\{J_l = 1/2, M_l = 1/2\}$ and $\{J_u = 1/2, M_u = -1/2\}$ sublevels at an arbitrary instant. Therefore, the contribution of the transition

$$\{J_l = 1/2, M_l = 1/2\} \longleftrightarrow \{J_u = 1/2, M_u = -1/2\}$$

can be neglected.

The analysis that follows is restricted to interaction between the transition

$$\{J_l = 1/2, M_l = -1/2\} \longleftrightarrow \{J_u = 1/2, M_u = 1/2\}$$

and an optical pulse of a width comparable or greater than the inverse frequency of this transition. The corresponding Bloch equations for this two-level system is [18]

$$\frac{\partial S_x}{\partial t} = -\omega_0 S_y + \omega_0 f_y \mathscr{E}_y S_z, \tag{3}$$

$$\frac{\partial S_y}{\partial t} = \omega_0 S_x - \omega_0 f_x \mathscr{E}_x S_z, \tag{4}$$

$$\frac{\partial S_z}{\partial t} = \omega_0 (f_x \mathscr{E}_x S_y - f_y \mathscr{E}_y S_x) + W(z), \tag{5}$$

where

$$f_{x(y)} = d_{x(y)} \hbar^{-1} \omega_0^{-1},$$

ω_0 is the transition frequency, and $\mathscr{E}_x$ and $\mathscr{E}_y$ are the projections of the polarization vector. The term W in Eq. (5) represents the pumping of the upper level (see details in Section 4). The components of the Bloch vector **S** can be expressed in terms of the density matrix $\hat{\rho}$ for a two-level system:

$$S_z = \frac{1}{2}(\rho_{11} - \rho_{22}), \quad S_x = \frac{1}{2}(\rho_{12} + \rho_{21}),$$

$$S_y = \frac{i}{2}(\rho_{12} - \rho_{21}).$$

Here,

$$S_z^2 + S_x^2 + S_y^2 = 1;$$

i.e., the total population is normalized to unity:

$$2S_0 = \rho_{11} + \rho_{22} = 1.$$

When $W = 0$, the magnitude of **S** is a conserved quantity:

$$\partial_t S_0 = 0.$$

The Maxwell equations for the field components are obtained as projections on the corresponding axes:

$$\frac{\partial^2 \mathscr{E}_x}{\partial z^2} - \frac{1}{c^2}\frac{\partial^2 \mathscr{E}_x}{\partial t^2} = \frac{4\pi d_x}{c^2}\frac{\partial^2 S_x}{\partial t^2}, \tag{6}$$

$$\frac{\partial^2 \mathscr{E}_y}{\partial z^2} - \frac{1}{c^2}\frac{\partial^2 \mathscr{E}_y}{\partial t^2} = \frac{4\pi d_y}{c^2}\frac{\partial^2 S_y}{\partial t^2}, \tag{7}$$

where c is the speed of light in a medium with density n.

The simplest soliton solution to (3)–(7) was found in [11] under conditions corresponding to USP propagation. The system of equations is simplified in the unidirectional approximation, which is widely used in fluid dynamics. It was applied to obtain reduced Maxwell–Bloch equations in [17]. The approximation is based on the following considerations. Frequently, the density of active atoms or molecules in a real medium is low enough to set

$$\partial_z \approx -c^{-1}\partial_t + O(\epsilon),$$

where ϵ is a small parameter. In other words, the normalized density of two-level atoms is similar in order of magnitude to the derivatives $\partial_z + c^{-1}\partial_t$ of the field polarization. Accordingly, the contribution due to the counterpropagating wave can be neglected. The resulting system of equations describes UDP propagation with a group velocity comparable to the speed of sound in the medium.

The system of equations (3)–(7) describing UDP propagation can be written as

$$\frac{\partial S_x}{\partial \tilde{\tau}} = -S_y + E_y S_z,$$

$$\frac{\partial S_y}{\partial \tilde{\tau}} = S_x - E_x S_z,$$

$$\frac{\partial S_z}{\partial \tilde{\tau}} = E_x S_y - E_y S_x + h(\chi), \tag{8}$$

$$\frac{\partial E_x}{\partial \chi} = \frac{\partial S_x}{\partial \tilde{\tau}},$$

$$\frac{\partial E_y}{\partial \chi} = r^2 \frac{\partial S_y}{\partial \tilde{\tau}},$$

where

$$r = d_y/d_x, \quad E_{x(y)} = f_{x(y)}\mathscr{E}_{x(y)}, \quad \tilde{\tau} = \omega_0(t - c^{-1}z),$$

$$\chi = -z2\pi n d_x^2(c\hbar)^{-1}, \quad h(\chi) = W\omega_0^{-1}.$$

3. INVERSE SCATTERING METHOD

System (8) extends the model proposed in [19] to the case of arbitrary continuous pumping. For an arbitrary real r, is can be written in the Lax representation as

$$\partial_{\tilde{\tau}}\Phi = \frac{1}{2} \times \begin{pmatrix} -i\mathrm{cn}\,\mathrm{dn} & \mathrm{dn}E_x - i\mathrm{cn}E_y \\ -\mathrm{dn}E_x - i\mathrm{cn}E_y & i\mathrm{cn}\,\mathrm{dn} \end{pmatrix}\Phi, \tag{9}$$

$$\partial_{\chi}\Phi = \frac{1}{2\mathrm{sn}^2} \times \begin{pmatrix} -i\mathrm{cn}\,\mathrm{dn}S_z & \mathrm{dn}S_x - i\mathrm{cn}S_y \\ -\mathrm{dn}S_x - i\mathrm{cn}S_y & i\mathrm{cn}\,\mathrm{dn}S_z \end{pmatrix}\Phi, \tag{10}$$

where

$$\mathrm{sn} = \mathrm{sn}(\zeta, r), \quad \mathrm{cn} = \mathrm{cn}(\zeta, r) = \sqrt{1 - \mathrm{sn}^2},$$

$$\mathrm{dn} = \mathrm{dn}(\zeta, r) = \sqrt{1 - r^2\mathrm{sn}^2}$$

are Jacobi ellipsoidal functions, ζ is a spectral parameter, and r is the modulus of a Jacobi function. When pumping is allowed for, the spectral parameter ζ depends on the variable χ defined by the equation

$$\frac{\partial\lambda}{\partial\chi} = \frac{-2r^2h(\chi)\lambda}{1 + r^2 - \sqrt{(1 - r^2)^2 + 4r^2\lambda^2}}, \tag{11}$$

where

$$\lambda = \mathrm{cn}(\zeta, r)\mathrm{dn}(\xi, r)$$

for any real r. It should be noted here that the case of $r = 0$ is described by the limit form of Eq. (11) obtained as $r \longrightarrow 0$.

The algebraically parameterized Lax representation is simpler and, therefore, better suited for application of ISM. It can be found separately for three nonoverlapping subdomains of r: for $r^2 = 1$ (isotropic case), for $r = 0$ (extremely anisotropic case), and for $r^2 \neq 0, 1$.

Note that the case of $r = 0$ and $E_y \equiv 0$ corresponds to propagation of a linearly polarized UDP. If $r = 0$ and $E_y \equiv \mathrm{const} \neq 0$, then Eqs. (8) can be transformed into a set of RMB equations for a linearly polarized field interacting with a two-level system. Indeed, define a new Bloch vector $\mathbf{R} = (R_x, R_y, R_z)$ as follows:

$$R_x = S_x, \quad R_y = \frac{S_y - E_yS_z}{\nu_0}, \quad R_z = \frac{E_yS_y + S_z}{\nu_0}, \tag{12}$$

where

$$\nu_0 = \sqrt{1 + E_y^2}.$$

Then, Eqs. (8) are rewritten as

$$\partial_{\tilde{\tau}}R_x = -R_y\nu_0, \tag{13}$$

$$\partial_{\tilde{\tau}}R_y = R_x\nu_0 - E_xR_z, \tag{14}$$

$$\partial_{\tilde{\tau}}R_z = E_xR_y + h\nu_0, \tag{15}$$

$$\partial_{\chi}E_x = \nu_0R_y, \tag{16}$$

where $h\nu_0$ is the rate of pumping of the upper level for a two-level system with transition frequency ν_0. The Lax representation for Eqs. (13)–(16) with pumping is well known [23, 24]. Hereinafter, it is assumed that $h(\chi) = 0$. The case of $h(\chi) \neq 0$ is considered in Section 4.

In the isotropic case, spectral problem (9) is similar to the Kaup–Newell problem [25] with spectral parameter $\tilde{\lambda} = \mathrm{cn} = \mathrm{dn}$. When $r = 0$, it reduces to the Zakharov–Shabat problem [15] with spectral parameter $\tilde{\lambda} = \mathrm{cn}$ and with $-i\tilde{\lambda}E_y$ added to a real potential $\pm E_x$, where E_y is an arbitrary real function of $\tilde{\tau}$.

Suppose that $r^2 \neq 1$ and $r \neq 0$, in which case the spectral parameter ζ can be replaced by ξ by using the relation

$$\mathrm{cn}(\zeta, r) = \sqrt{1 - r^2}(\xi - \xi^{-1})(2r)^{-1}.$$

As a result, the Lax representation for system (8) becomes

$$\partial_{\tau}\Phi = \begin{pmatrix} -i\left(\xi^2 - \frac{1}{\xi^2}\right) & \xi E^* + \frac{1}{\xi}E \\ -\xi E - \frac{1}{\xi}E^* & i\left(\xi^2 - \frac{1}{\xi^2}\right) \end{pmatrix}\Phi, \tag{17}$$

$$\partial_{\chi}\Phi = \frac{2r^2(1 - r^2)^{3/2}\xi^2}{4r^2 - [(1 - r^2)\xi^2 - 1 - r^2]^2} \times \begin{pmatrix} -i\frac{\kappa}{r}\left(\xi^2 - \frac{1}{\xi^2}\right)S_z & \xi S^* + \frac{1}{\xi}S \\ -\xi S - \frac{1}{\xi}S^* & i\frac{\kappa}{r}\left(\xi^2 - \frac{1}{\xi^2}\right)S_z \end{pmatrix}\Phi \equiv \hat{A}\Phi, \tag{18}$$

where

$$\kappa = \sqrt{1-r^2}/2, \quad E = rE_x/\kappa + iE_y/\kappa,$$

$$S = S_x + iS_y/r, \quad \tau = \kappa^2\tilde{\tau}/(2r).$$

In the limit cases corresponding to the extreme values of ξ and a constant r, problem (17) reduces to the spectral problems mentioned above. In particular, as $\xi \longrightarrow 0$ (or $\xi \longrightarrow \infty$), spectral problem (17) reduces to the Kaup–Newell problem [25] if only the terms proportional to ξ^1 and ξ^2 (or ξ^{-1} and ξ^{-2}, respectively) are retained. When the spectral parameter is represented as $\xi = 1 + \tilde{\xi}$, spectral problem (17) reduces to the Zakharov–Shabat problem [15] with the addition of $-i\tilde{\xi}E_y$ if $\tilde{\xi}^2 \ll \tilde{\xi}$ and only terms of the zeroth and first degrees in $\tilde{\xi}$ are retained.

Since spectral problem (17) contains only the powers ± 1 and ± 2 of the spectral parameter, the ISM associated with this problem must be related to the technique previously developed for related spectral problems for the Thirring equation [26], the nonlinear Schrödinger equation [25], and the Maxwell–Bloch system allowing for the nonlinear Stark effect [27]. Therefore, this presentation is restricted to the basic elements of the ISM for a potential E rapidly decaying toward infinity together with its derivatives.

Solutions to (17) have the following symmetries:

$$\Phi = \hat{M}\Phi(\xi^*)^*\hat{M}^{-1}, \tag{19}$$

where

$$\hat{M} = \begin{pmatrix} 0 & 1 \\ -1 & 0 \end{pmatrix}$$

and

$$\Phi(\xi^*)^* = \Phi(\xi^{-1}). \tag{20}$$

The standard Jost functions $\Phi^{\pm}$ are defined as solutions to (17) having the asymptotic form

$$\Phi^{\pm} = \exp(-i\Lambda\hat{\sigma}_3\tau), \quad \tau \longrightarrow \pm\infty, \tag{21}$$

where

$$\Lambda = \xi^2 - \xi^{-2}.$$

Symmetry (19) entails the following matrix form of the Jost functions:

$$\Phi^{\pm} = \begin{pmatrix} \psi_1^{\pm} & -\psi_2^{\pm *} \\ \psi_2^{\pm} & \psi_1^{\pm *} \end{pmatrix}.$$

These solutions are related by a scattering matrix $\hat{T}$:

$$\Phi^- = \Phi^+\hat{T}, \quad \hat{T} = \begin{pmatrix} a^* & b \\ -b^* & a \end{pmatrix}. \tag{22}$$

Its dependence on χ is determined by the equation

$$\begin{aligned}\partial_\chi\hat{T} = &-\hat{T}\exp(-i\hat{\sigma}_3\Lambda\tau)\hat{A}(\tau=-\infty)\exp(i\hat{\sigma}_3\Lambda\tau) \\ &+ \exp(-i\hat{\sigma}_3\Lambda\tau)\hat{A}(\tau=\infty)\exp(i\hat{\sigma}_3\Lambda\tau)\hat{T}.\end{aligned} \tag{23}$$

The Jost function can be represented as

$$\begin{aligned}\Phi^+(\tau) = &\exp\{-i\hat{\sigma}_3[\Lambda\tau + \mu(\tau)]\} \\ &+ \int_\tau^\infty \begin{pmatrix} [Q_1(\tau,s) + \xi^{-2}Q_2(\tau,s)]\exp(-i\mu(\tau)) & -[\xi K_1(\tau,s) + \xi^{-1}K_2(\tau,s)]\exp(-i\mu(\tau)) \\ [\xi\tilde{K}_1(\tau,s) + \xi^{-1}\tilde{K}_2(\tau,s)]\exp(i\mu(\tau)) & [Q_1^*(\tau,s) + \xi^{-2}Q_2^*(\tau,s)]\exp(i\mu(\tau)) \end{pmatrix}\exp(-i\hat{\sigma}_3\Lambda s)ds,\end{aligned} \tag{24}$$

with a function $\mu(\tau)$ (independent of the spectral parameter) to be specified below. Substituting (24) into (17) and using the symmetries of the Jost functions, one obtains

$$\tilde{K}_{1,2} = K_{1,2}^*.$$

The kernels $K_{1,2}$ and $Q_{1,2}$ must satisfy the conditions

$$\lim_{s\to\infty} K_{1,2}(\tau,s) = 0, \tag{25}$$

$$\lim_{s\to\infty} Q_{1,2}(\tau,s) = 0. \tag{26}$$

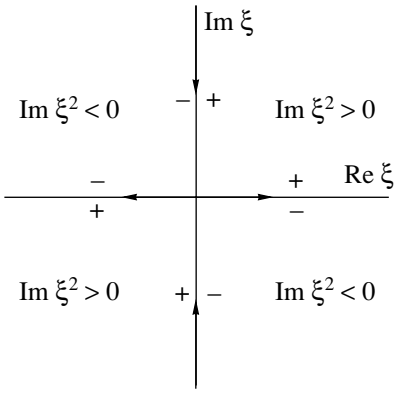

Fig. 1. Contour Γ follows the paths indicated by arrows along the axes and lies above and below the poles in the first and third quadrants, respectively.

By substituting (24) into (17), relations between the potential and the kernels are obtained:

$$E^*(\tau, \chi) = 2K_1(\tau, \tau, \chi)\exp(-2i\mu), \quad (27)$$

$$E(\tau, \chi) = 2K_2(\tau, \tau, \chi)\exp(-2i\mu). \quad (28)$$

Hence,

$$\mu(\chi, \tau) = -\frac{i}{4}\ln\frac{K_1(\tau, \tau, \chi)}{K_2^*(\tau, \tau, \chi)}. \quad (29)$$

Substituting the components of the matrix Φ into (22), integrating the results, with weights $\xi^m\exp(i\Lambda\tau)$ ($m = 0, -1, -2$), along the contour Γ shown in Fig. 1, and using the relations

$$\int_\Gamma \xi^m \exp(i\Lambda\tau)d\xi = 4\pi\delta(\tau), \quad m = 1, -3, \quad (30)$$

$$\int_\Gamma \xi^{2m}\exp(i\Lambda\tau)d\xi = 0, \quad m = -1/2, 0, \pm 1, \pm 2, \quad (31)$$

we obtain the Marchenko equations

$$K_1(\tau, y) = F_0(\tau + y) + \int_\tau^\infty [Q_1(\tau, s)F_0(s + y) + Q_2(\tau, s)F_{-1}(s + y)]ds, \quad (32)$$

$$K_2(\tau, y) = F_{-1}(\tau + y) + \int_\tau^\infty [Q_1(\tau, s)F_{-1}(s + y) + Q_2(\tau, s)F_{-2}(s + y)]ds, \quad (33)$$

$$Q_1(\tau, y) = -\int_r^\infty [K_1(\tau, s)F_1^*(s + y) + K_2(\tau, s)F_0^*(s + y)]ds, \quad (34)$$

$$Q_2(\tau, y) = -\int_r^\infty [K_1(\tau, s)F_0^*(s + y) + K_2(\tau, s)F_{-1}^*(s + y)]ds, \quad (35)$$

where $y \geq \tau$, and the kernel F has the form

$$F_m(y, \chi) = \int_{-\infty}^\infty \frac{b(\chi)}{a(\chi)}\frac{\xi^{2m}\exp(-i\Lambda y)}{2\pi}d\xi - i\sum_k \frac{\xi_k^{2m} b(\chi, \xi_k)\exp(-i\Lambda_k y)}{a'(\chi, \xi_k)}, \quad (36)$$

with

$$\Lambda_k = \xi_k^2 - \xi_k^{-2}, \quad a'(\xi_k, \chi) = \left.\frac{da(\xi, \chi)}{d\xi}\right|_{\xi = \xi_k}.$$

Hereinafter, we consider only the soliton spectrum, which consists of isolated nondegenerate poles ξ_k in the ξ plane. Expression (36) for the kernel is written out without using the symmetries of the problem. Symmetries (19) and (20) can be taken into account by combining the poles ξ_k into pairs in F_m: $\{\xi_k, 1/\xi_k^*\}$. The poles making up a pair obviously coincide on the unit circle. Then, the soliton part $\mathcal{F}_m$ of a kernel F_m is rewritten as

$$\mathcal{F}_m(y) = \sum_k \exp(\eta_k y) \times [\xi_k^{2m+1}C_k(y, \chi, \xi_k) - \xi_k^{*-2m-1}C_k^*(y, \chi, \xi_k)], \quad (37)$$

where

$$C_k(y, \chi, \xi_k) = \frac{-ib_k(\chi, \xi_k)}{\xi_k a'(\chi, \xi_k)}\exp(i\zeta_k y),$$

$$\eta_k = \mathrm{Im}\Lambda_k, \quad \zeta_k = -\mathrm{Re}\Lambda_k.$$

Expression (37) implies that

$$\mathcal{F}_0(y) = -\mathcal{F}_{-1}^*(y), \quad \mathcal{F}_1(y) = -\mathcal{F}_{-2}^*(y). \quad (38)$$

The simplest soliton solution corresponds to the case of a single pole ξ_1 lying in the first or third quadrant. The asymptotic conditions correspond to stable states with

$$E(\pm\infty, \chi) = 0, \quad S_z(\pm\infty, \chi) = -1.$$

By virtue of (20), the single pole ξ_1 is subject to the condition $|\xi_1| = 1$. By setting

$$\xi_1^2 = \exp(i\phi_1), \quad \phi_1 \in \mathbb{R},$$

Eqs. (23), (32)–(36) are solved to find the one-pole solution

$$E(\tau, \chi) = \frac{-2|\sin\phi_1|\exp[i\gamma_1 - i\phi_1/2]}{|\cosh[4\sin\phi_1\theta + \gamma_2 - i\phi_1/2]|}, \qquad (39)$$

where

$$\theta = \tau + \frac{\kappa\chi}{2\sqrt{r^2\cos^2(\phi_1/2) + \sin^2(\phi_1/2)}},$$

$$\gamma_1 = \arg\frac{-ic_1}{2a'(\xi_1)}, \quad \gamma_2 = \ln\left|\frac{c_1}{2a'(\xi_1)}\right|.$$

The relations between kernels that follow from (27) and (28) entail a phase constraint: $\phi_1 = 0, \pi$. The phase dependence of the soliton shape and position is illustrated by Fig. 2.

Note that the two-pole solution corresponding to the pair $\{\xi_1, 1/\xi_1^*\}$ is not subject to any condition for ξ_1. To find this solution, the kernels are represented as

$$K_{1,2}(x, y) = h^+_{1,2}(x)\exp(\eta y + i\zeta y) + h^-_{1,2}(x)\exp(\eta y - i\zeta y), \qquad (40)$$

$$Q_{1,2}(x, y) = g^+_{1,2}(x)\exp(\eta y + i\zeta y) + g^-_{1,2}(x)\exp(\eta y - i\zeta y), \qquad (41)$$

where

$$\eta = \mathrm{Im}\Lambda_1, \quad \zeta = -\mathrm{Re}\Lambda_1,$$

and Eqs. (32)–(35) are solved, with C_1 expressed as a function of χ. The resulting expressions for kernels are

$$K_2(\chi, \chi, \tau) = \frac{c_1\xi_1^{-1}X\exp(\theta + i\theta_1) - c_1^*\xi_1^*X^*\exp(\theta - i\theta_1)}{D}, \qquad (42)$$

$$K_1(\chi, \chi, \tau) = \frac{c_1\xi_1 X\exp(\theta + i\theta_1) - c_1^*\xi_1^{*-1}X^*\exp(\theta - i\theta_1)}{D}, \qquad (43)$$

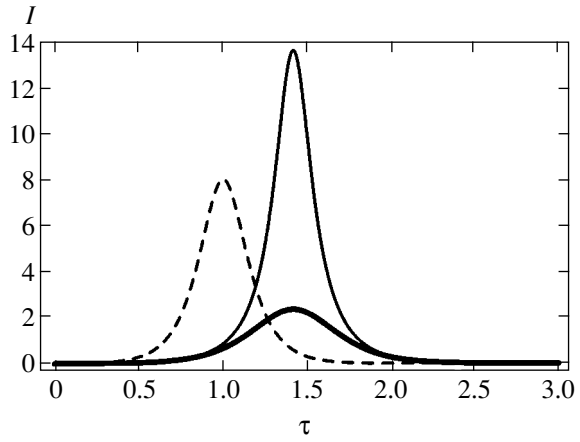

Fig. 2. Soliton intensity $I = |E|^2$ given by (39) versus τ for $\phi_1 = \pi/4$ (thick curve), $\phi_1 = \pi/2$ (dashed curve), and $\phi_1 = 3\pi/4$ (thin curve).

where

$$X(\tau, \chi, \xi_1) = 1 + A - \tilde{Z} + \frac{\tilde{\beta}(|\xi_1|^4 + 1)}{|\xi_1|^4\eta}(\tilde{\beta}\mu^* - \beta\mu),$$

$$D = 1 + A^2 - Z^2 - \tilde{Z}^2, \quad \theta = \eta\tau + \mathrm{Im}\Omega_1\chi,$$

$$\theta_1 = \zeta\tau + \mathrm{Re}\Omega_1\chi,$$

$$A = \frac{\beta(\theta)\tilde{\beta}(\theta)(1 + |\xi_1|^4)^2}{(2\eta|\xi_1|^2)^2}, \quad Z = 2\mu(\theta_1)\beta(\theta),$$

$$\tilde{Z} = 2\mu(\theta_1)\tilde{\beta}(\theta),$$

$$\beta(\theta) = \exp(2\eta\theta)c_1\xi_1^{-1}, \quad \tilde{\beta}(\theta) = \exp(2\eta\theta)c_1^*\xi_1^*,$$

$$C_1(\chi, \xi_1) = c_1(\xi_1)\exp(-2i\Omega_1\chi),$$

$$\mu(\theta_1) = \frac{\exp(2i\theta_1)}{2(\eta + i\zeta)},$$

$$\Omega_1 = \frac{r(1 - r^2)^2(\xi_1^4 - 1)S_3(-\infty, 0)}{4r^2 - [(1 - r^2)\xi_1^2 - 1 - r^2]^2}.$$

Then, (29), (42), and (43) are used to obtain

$$E(\chi, \tau) = -2i \times \frac{c_1\xi_1 X\exp(\theta_1) - c_1^*\xi_1^{*-1}X^*\exp(-\theta_1)}{\sqrt{DD^*}}\exp(\theta). \qquad (44)$$

Soliton solution (44) has an internal degree of freedom manifested in oscillations analogous to the oscilla-

tory behavior of a breather described by the sine-Gordon equation. However, as well as the solution presented above, this solution has an arbitrary amplitude for a finite ξ_1. This is a qualitative distinction of the solution obtained here from solutions to the Maxwell–Bloch equations for a linearly polarized field.

4. THE LIMIT OF ISOTROPIC INTERACTION

As noted above, the isotropic case indicated above corresponds to $\xi \longrightarrow \infty$. Formally, as $r \longrightarrow 1$ and $\xi \longrightarrow \infty$, we have

$$\sqrt{1-r^2}(\xi - \xi^{-1})(2r)^{-1} \longrightarrow \lambda,$$

$$\xi E^* + \xi^{-1}E \longrightarrow \lambda(E_x - iE_y),$$

and

$$\mathrm{dn} \longrightarrow \lambda, \quad \mathrm{cn} \longrightarrow \lambda, \quad \mathrm{sn}^2 \longrightarrow 1 - \lambda^2,$$

in the Lax representation given by (9) and (10), where λ is a spectral parameter. It is clear that symmetry (20) does not hold in this limit. The corresponding Marchenko equations can also be obtained in this limit.

Alternatively, both Lax representation and ISM equations can be found directly for system (8) for an arbitrary value of the spectral parameter by setting $r^2 = 1$. These equations are formally identical to those derived in [25] for the nonlinear Schrödinger equation. However, the difference of the ISM equations for system (8) from those obtained in [25] lies in the scattering matrix as a function of χ and $\lambda = \mathrm{cn}(\zeta, 1)$.

In particular, the Marchenko equations have the form

$$\mathcal{H}_1^*(\tau, y) = \mathcal{F}_0(\tau + y) + \int_\tau^\infty \mathcal{Q}_1(\tau, s)\mathcal{F}_0(s + y)ds, \quad (45)$$

$$\mathcal{Q}_1^*(\tau, y) = -\int_\tau^\infty \mathcal{H}_1(\tau, s)\mathcal{F}_1(s + y)ds, \quad (46)$$

where $y \geq \tau$ and the kernel $\mathcal{F}_m$ has the form

$$\mathcal{F}_m(y, \chi) = \int_{-\infty}^{\infty} \frac{b(\chi)}{a(\chi)} \frac{\lambda^{2m}\exp(-i\xi^2 y)}{2\pi} d\xi - i\sum_k \frac{\lambda_k^{2m} c_k(\chi)\exp(-i\lambda_k^2 y)}{a'(\lambda_k, \chi)}. \quad (47)$$

As the Marchenko equations (32)–(35) are reduced to (45) and (46), the following correspondence between kernels is valid:

$$K_1(r \longrightarrow 1) \longrightarrow \mathcal{H}_1, \quad Q_1(r \longrightarrow 1) \longrightarrow \mathcal{Q}_1, \quad K_2(Q_2)(r \longrightarrow 1) \longrightarrow 0. \quad (48)$$

Relations (27) and (28) reduce to the following relations between the diagonal values of the kernels and the potential $\tilde{E}$:

$$\partial_\tau \mu(\tau, \chi) = 2\left|\mathcal{H}_1(\tau, \tau, \chi)\right|^2, \quad (49)$$

$$\tilde{E}^*(\tau, \chi) = -2\mathcal{H}_1^*(\tau, \tau, \chi)\exp(-2i\mu), \quad (50)$$

where

$$\tilde{E}^* = E_x - iE_y.$$

The one-hump solution to Eqs. (8) with $|r| = 1$ corresponding to a single eigenvalue $\lambda_1 = |\lambda_1|\exp(i\alpha_1)$ lying in the first or third quadrant of the λ plane is

$$\tilde{E}_{\mathrm{circ}}(\tau, \chi) = \frac{-2\mathrm{Im}\lambda_1^2 \exp\{[i(\mathrm{Re}\lambda_1^2\tau - W\chi + \gamma_1 - \alpha_1 - 2\mu)]\}}{|\lambda_1|\cosh[\theta_1 + \beta_1 + i\alpha_1]}, \quad (51)$$

where

$$\theta_1 = \mathrm{Im}\lambda_1^2(\tau + \chi/V), \quad V = (1 - \mathrm{Re}\lambda_1^2)^2 + (\mathrm{Im}\lambda_1^2)^2,$$

$$W = [\mathrm{Re}\lambda_1^2(1 - \mathrm{Re}\lambda_1^2) - (\mathrm{Im}\lambda_1^2)^2]V^{-1},$$

$$\beta_1 = \ln\left|(\lambda_1 c_1)/(4\mathrm{Im}\lambda_1^2 a'(\lambda_1))\right|,$$

$$\mu = -\arctan\left\{\cot\alpha_1 \coth\left[\mathrm{Im}\lambda_1^2\left(\tau - \frac{\chi}{V}\right) + \beta_1\right]\right\} \times \frac{2\mathrm{Im}\lambda_1^2}{\left|\lambda_1^2\right|\sin(2\alpha_1)}.$$

It is of practical interest to compare linearly and circularly polarized pulses in terms of how efficient they are high-power pulsed light sources. For this reason, let us compare solution (51) for a circularly polarized wave with an analogous soliton solution to the RMB equations for a linearly polarized electromagnetic wave interacting with a two-level system (e.g., see [17]):

$$\tilde{E}_{\mathrm{lin}}(\tau, z) = \frac{2\mathrm{Im}\eta_1}{\cosh[\mathrm{Im}\eta_1(\tau - \tau_0 - z/V_0)]}, \quad (52)$$

where $(\mathrm{Im}\eta_1)^{-1}$ is the soliton duration, $(c^{-1} + V_0^{-1})^{-1}$ is its group velocity, and τ_0 is the initial position of the

soliton. For comparison, let us consider solitons (51) and (52) with equal durations and set

$$\eta_1 = \lambda_1^2, \quad |\lambda_1| = 1.$$

An analysis of these solutions shows that the solitons have comparable amplitudes when $\mathrm{Im}\lambda_1^2 \ll \mathrm{Re}\lambda_1^2$, i.e., in the limit of small amplitude ($\propto \mathrm{Im}\lambda_1^2$) and high frequency ($\propto \mathrm{Re}\lambda_1^2$). This corresponds to quasi-monochromatic pulses, i.e., UDPs with slowly varying amplitudes. When $\mathrm{Im}\lambda_1^2 = \mathrm{Re}\lambda_1^2$, the peak intensity I_{circ} of soliton (51) is twice the peak intensity I_{lin} of soliton (52). Figure 3 demonstrates that $I_{\mathrm{circ}} \gg I_{\mathrm{lin}}$ when $\mathrm{Im}\lambda_1^2 \gg \mathrm{Re}\lambda_1^2$, because solution (51) can describe a Lorentzian profile and become singular under specially chosen initial conditions. For example, in the neighborhood of zero, when

$$\lambda_1 = |\lambda_1|\exp(i\alpha_1)$$

$$\theta_1 + \beta_1 = y \ll 1, \quad \alpha_1 = \pi/2 + \phi_1, \quad \phi_1 \ll \pi,$$

the soliton has the form

$$E_{\mathrm{lin}}(y) = \frac{|\lambda_1|\exp(2i\alpha_1)}{y^2 + \phi_1^2}. \qquad (53)$$

Singular behavior implies that the dispersion effects ignored in deriving system (8) should be taken into account to describe a real physical system. Furthermore, the applicability conditions for the two-level approximation also impose a constraint on the normalized field amplitude, $E_{\mathrm{lin}} \lesssim 1$, and restrict the range of initial conditions that can be used in this model.

5. INFLUENCE OF PUMPING ON CHARACTERISTICS OF SOLITONS

A UDP propagating in a single-pass laser can be amplified so that it its amplitude increases while its duration decreases. Effects of this kind were described by deformed integrable models [28] for quasi-monochromatic pulses [28] and for linearly polarized UDPs [24]. Since the MB equations for circularly and linearly polarized UDPs are qualitatively different, they should be expected to exhibit different behavior when propagating a laser medium. In this section, UDP amplification is analyzed by means of an integrable deformation of model (8).

Lasers are frequently modeled by two-level systems with time-independent pumping of the upper level [29]. In model (8), the pumping is represented by an additional term h on the right-hand side of the third equation in (8). It should be noted that pumping modifies the

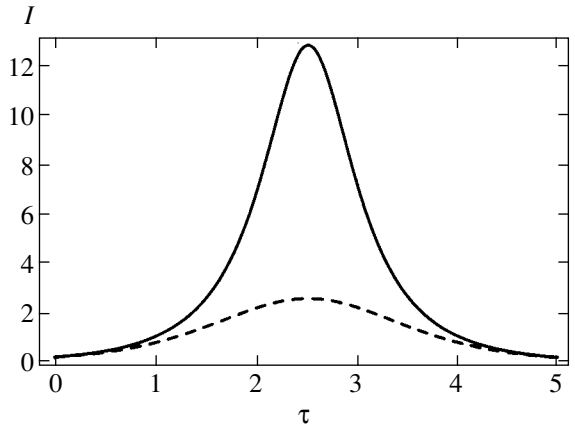

Fig. 3. Soliton intensity $I = |E|^2$ given by (51) (solid curve) and (52) (dashed curve) versus τ for $\lambda_1 = (0.5 + i)/\sqrt{1.25}$.

"reference" solution, because not only solitons are deformed, but also a nontrivial radiation solution corresponding to continuous spectrum is obtained. When the MB equations describe linear polarization, this solution is obtained by solving the Painlevé V equation [30]. The addition of a pumping term proportional to h changes the analytic properties of the Jost functions in the general case, and the ISM apparatus is modified accordingly. A detailed numerical and analytical analysis presented in [24] shows that both changes in the reference solution and the corresponding modifications of the ISM apparatus can be ignored within a certain range of parameters, in particular, when the lower level is the ground state and its initial population is sufficiently high, while the pumping rate h is low, within a short time interval. For this reason, we assume here that the reference solution remains trivial:

$$E_x = E_y = 0.$$

The pumping changes soliton characteristics, since the dependence of λ on χ described by Eq. (11) modifies Lax representation (9), (10). The heights and inverse lengths of solitons are important characteristics of one-humped soliton solutions to (8). It is well known that soliton amplitude (52) increases with χ under positive pumping [23]. However, solutions to (8) may exhibit qualitatively different dynamics induced by pumping. For example, the amplitude of soliton (39) reaches a maximum value of 4 as $r \longrightarrow 0$ for an arbitrary pumping rate. Figure 4 shows its peak intensity versus amplification length. This soliton has no analog corresponding to $r = 1$, whereas the analog of soliton (52) in the case of $r^2 \neq 0, 1$ is a solution with twin poles $\zeta_1^2 = \eta$ and $\zeta_2^2 = \eta^{-1}$, which may have an arbitrary amplitude depending on η.

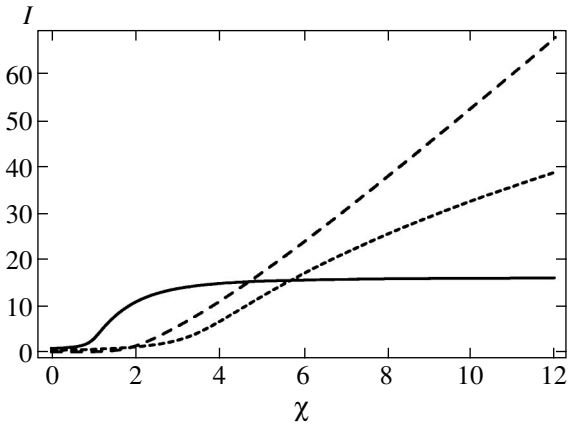

Fig. 4. Peak intensities of solitons in a laser versus χ for $h = 1$ and $r = 0.1$ (dashed curve), $r = 0.5$ (dotted curve), and $r = 0.99$ (solid curve), in arbitrary units.

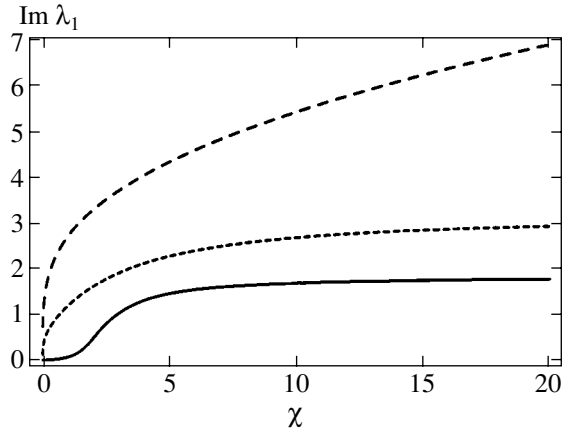

Fig. 5. Inverse soliton duration versus χ for $h = 1$ and $r = 0.1$ (dashed curve), $r = 0.5$ (dotted curve), and $r = 0.99$ (solid curve), in arbitrary units.

Suppose that

$$\xi_1 = \exp(i\phi_0)$$

and

$$\lambda_1 = |\lambda_1|\exp(i\phi_0)$$

for solitons (39) and (51), respectively. Then, the corresponding peak intensities are expressed as

$$A(\chi, r)^2 = 16|\lambda_1(\chi)|\sin^2(\phi_0(\chi)), \qquad (54)$$

where $|\lambda_1| = 1$ for soliton (39). In the case of linear polarization ($r = 0$, $E_y \equiv 0$), the soliton amplitude is

$$A(r = 0) = 2\mathrm{Im}\lambda_1(\chi).$$

Figure 4 shows the peak intensities of small-amplitude solitons versus amplification length for several values of *r*. The figure demonstrates that an almost circularly polarized soliton (with $r^2 = 0.99$) is amplified more strongly when χ is small, whereas a steeper increase in pulse amplitude with χ is predicted in the case of almost linear polarization ($r = 0.1$). Singular solution (53) found above for a circularly polarized USP is not obtained when the soliton amplified in a laser medium has a small initial amplitude.

There also is a substantial difference in the variation of UDP duration between linearly and circularly polarized solitons propagating in a laser medium. Figure 5 shows the curves of inverse soliton duration $\mathrm{Im}\lambda_1$ as a function of χ obtained for several values of *r*. The variation of soliton duration due to increasing amplification length under pumping is qualitatively different for almost linearly and almost circularly polarized waves (with $r = 0.1$ and $r = 0.99$, respectively). In the latter case, the decrease in soliton duration due to increasing pumping is counteracted by increase in nonlinear coupling between field components, i.e., in the phase of the field *E*. This phenomenon is analogous to phase modulation of a pulse in the case of a quasi-monochromatic field.

6. INFLUENCE OF AN ADDITIONAL LEVEL

As a physical example, let us consider a pulse with duration several times greater than the inverse transition frequency. For a real system, a model of such pulses, and especially pulses with a duration $\lesssim \omega_0^{-1}$, interacting with a two-level system must evaluate the contribution of interaction between the pulse and additional levels. This is done here by analyzing the influence of a remote state on the dynamics of circularly and linearly polarized UDPs. Consider a three-level system with $1 \longleftrightarrow 2 \longleftrightarrow 3$ cascade transitions, where levels 2 and 3 lie above levels 1 and 2, respectively, and level 3 is an additional level. Denote by ω_0 and Ω the $1 \longleftrightarrow 2$ and $2 \longleftrightarrow 3$ transition frequencies and assume that $\Omega \gg \omega_0$. It is obvious that the results obtained in this section can be extended to the case of an arbitrary number of transitions between levels 1 and 2 and additional levels without taking into account transitions between the additional levels.

To facilitate adiabatic elimination of the additional level, suppose that the pulse duration for the field

$$\mathscr{E} = \mathscr{E}_x + i\mathscr{E}_y$$

is nearly equal to, or greater than, $\pi\omega_0^{-1}$ and is much greater than $\pi\Omega^{-1}$ (recall that $\mathscr{E}_y \equiv 0$ in the case of linear polarization).

The Schrödinger equations for the population amplitudes ψ_k ($k = 1, 2, 3$) are

$$\partial_t \psi_1 = id_{12}\mathscr{E}\hbar^{-1}\psi_2, \tag{55}$$

$$\partial_t \psi_2 = i\omega_0\psi_2 + id_{12}^*\mathscr{E}^*\hbar^{-1}\psi_1 + id_{23}\mathscr{E}\hbar^{-1}\psi_3, \tag{56}$$

$$\partial_t \psi_3 = i\Omega\psi_3 + id_{23}^*\mathscr{E}^*\hbar^{-1}\psi_2, \tag{57}$$

where d_{1k} denotes the $1 \longleftrightarrow k$ dipole transition moment. Under the conditions for pulse duration imposed above, the following Bloch equations are obtained for the effective two-level medium:

$$\frac{\partial S}{\partial \tilde{\tau}} = iS(1 - gUU^*) - iUS_3,$$
$$\frac{\partial S_3}{\partial \tilde{\tau}} = 2i(US^* - U^*S), \tag{58}$$

where

$$g = \frac{|d_{23}|^2\omega_0}{|d_{12}|^2\Omega}, \quad U = \frac{d_{23}\mathscr{E}}{\omega_0\hbar},$$

$$S = \psi_2\psi_1^*, \quad S_3 = |\psi_2|^2 - |\psi_1|^2,$$

and $\tilde{\tau}$ is defined above. In the unidirectional approximation, Eqs. (6) and (7) reduce to

$$\frac{\partial U}{\partial \chi} = \frac{\partial}{\partial \tilde{\tau}}(S - \nu_0 U - g_1 US_3), \tag{59}$$

where

$$\nu_0 = S_0 g_1, \quad S_0(\chi) = |\psi_2|^2 + |\psi_1|^2, \quad g_1 = \frac{d_{23}\omega_0}{2d_{12}\Omega}.$$

Equations (58) and (59) for a circularly polarized UDP are valid if $r^2 = 1$, i.e., $d_x = d_y = d_{12}$. The last condition is frequently satisfied (see physical examples in [18]). In the case of a linearly polarized UDP, one should formally set $\mathrm{Im}\, U \equiv 0$ in (58) and (59) to discard the Maxwell equation for this component. Since Eqs. (58) and (59) do not admit any Lax representation when $g \neq 0$ and/or $g_1 \neq 0$, they cannot be solved by ISM. Since $\Omega \gg \omega_0$, the terms responsible for the nonintegrability of (58) and (59) can be treated as a perturbation. However, the number of additional levels may be as high as 100. When only transitions between level 2 and additional levels are allowed for, the contributions due to these transitions can be added in the adiabatic approximation. The resultant contribution to UDP dynamics is comparable to the contributions of other terms. In this case, interactions between soliton solutions are not elastic, and the UDP energy is lost by radiation in the course of their evolution. Since the nonlinear perturbation terms increase with soliton amplitude, the pulse amplitude should be expected to decrease under perturbation. Let us show that Eqs. (58) and (59) for UDPs is integrable even if the influence of additional levels is taken into account when the pulse has a small amplitude and a sufficiently large duration (in the quasi-monochromatic limit).

Suppose that the amplitudes of the field components

$$E_{x(y)} = A_{x(y)}\exp(i\omega\tau - ik\chi) + \text{c.c.}$$

are characterized by time and length scales much greater than ω^{-1} and k^{-1}, respectively. Consider the cascade three-level system described above in the case when the transition frequency ω_0 is close to ω and the difference frequency $\nu = \Omega - \omega > 0$ is much greater than the spectral pulse width. In the quasi-monochromatic limit of Eqs. (3)–(7) corresponding to $r^2 = 1$ and allowing for the influence of an additional level, the wave function for the upper level is eliminated analogously to obtain

$$\frac{\partial \tilde{S}}{\partial \tau'} = i\tilde{S}(1 - \tilde{g}\tilde{A}\tilde{A}^*) - i\tilde{A}S_3,$$
$$\frac{\partial S_3}{\partial \tau'} = 2i(\tilde{A}\tilde{S}^* - \tilde{A}^*\tilde{S}), \tag{60}$$

where

$$\tilde{g} = \frac{|d_{23}|^2\nu_0}{|d_{12}|^2\nu}, \quad \nu_0 = \omega_0 - \omega, \quad \tau' = \nu_0(t - c^{-1}z),$$

$$\tilde{A} = \frac{Ad_{12}}{\nu_0\hbar}, \quad S = \tilde{S}\exp(i\omega\tau - ik\chi) + \text{c.c.}$$

Equations (6) and (7) reduce to

$$\frac{\partial A}{\partial \chi} = -2i(\tilde{S} - \tilde{\nu}_0 A - \tilde{g}_1 AS_3), \tag{61}$$

where

$$\nu_0 = S_0\tilde{g}_1, \quad \tilde{g}_1 = \frac{d_{23}\omega_0}{2d_{12}\nu}.$$

Note that similar equations can be obtained (up to a factor of 2 in the Maxwell equation) in the quasi-monochromatic limit by applying this approximation to system (58), (59) and retaining only the nonlinear term ig_1US_z in Eq. (59), which represents the influence of an additional level.

For a quasi-monochromatic field, system (58) and (59) can be reduced, by simple linear transformations, to integrable Maxwell–Bloch (MB) equations describing the interaction between a high-power quasi-

monochromatic electromagnetic field and a two-level system, allowing for the nonlinear Stark effect, and involving a nonlinear term proportional to US_z in the reduced Maxwell equation. The latter nonlinearity is due to the retained first term of the expansion, which is proportional to $\partial_t P/w_0$, where P is polarizability and ω_0 is the transition frequency for the system. The Lax representation was found for this system in [31]. The equations admit elastic interactions between soliton solutions, as well as other attributes of integrable systems [27].

7. CONCLUSIONS AND APPLICATIONS

Self-induced transparency is described for a two-level system interacting with a circularly polarized pulse with a duration nearly equal to, or greater than, the inverse transition frequency. Analysis of the behavior of solutions to the Maxwell–Bloch (MB) equations is important for understanding UDP formation and self-induced transparency in two-level systems. The observability conditions for UDPs formulated in terms of pulse intensity are weaker at least by two orders of magnitude than those required to observe USP dynamics [9–11]. Since UDPs have narrower spectra, the conditions for applicability of the two-level model are also much less restrictive than those imposed on USPs. Formally, model (8) is applicable in the spectral interval between $\tau_1^{-1} \ll \omega_0$ and $\tau_1^{-1} \gg \omega_0$, where τ_1 is the soliton duration. However, the condition $\tau_1^{-1} \lesssim \omega_0$ must be imposed on optical pulses.

The solutions obtained in this study demonstrate that the dynamics of circularly polarized UDPs are qualitatively different from those of linearly polarized UDPs and from the behavior of 2π-pulses in the McCall–Hahn theory [4]. For example, the McCall–Hahn theorem is not applicable to UDPs with durations comparable to the inverse transition frequency. Therefore, the results of the self-induced transparency theory developed for quasi-monochromatic pulses cannot be extended to pulses with $\tau_1 \sim \omega^{-1}$, especially to circularly polarized pulses, for which the nonlinear effects due to interactions between field components are essential. It has been found that σ transitions and circularly polarized electromagnetic pulses can be used to obtain pulses of much higher intensity, as compared to the case of linearly polarized pulses of equal duration. Accordingly, circularly polarized pulses have shorter durations as compared to linearly polarized ones with equal peak amplitudes. To obtain pulses with such characteristics, the initial pulse phase must be close to $\alpha_1 \approx \pi/2$. The required parameters of a pulse injected into a medium can be found by solving problem (17).

An analysis of UDP amplification in a single-pass laser represented by a model with pumping of the upper level shows that linearly polarized pulses are amplified more strongly (see Fig. 4). A comparison of the profiles of amplified pulses shows that the dynamics of amplified circularly and linearly polarized pulses are different because of nonlinear coupling in the reduced Maxwell equations describing the former case.

However, there exists a certain analogy between circularly and linearly polarized unidirectional solitons. One-pole solution (51), with pole η_1 having a zero real part, corresponds to a one-humped pulse-intensity profile. If the pole η_1 has a nonzero real part, then the simplest solution corresponds to the twin poles η_1 and $-\eta_1^*$. It can readily be shown that this solution in the general case corresponds to two-humped profiles of both linearly and circularly polarized solitons when $r = 1$.

The derivation of the Maxwell–Bloch equations for circularly polarized UDPs revealed that these equations are somewhat analogous to the integrable equations for quasi-monochromatic wave found in [31] for a different optical system. These equations describe the interaction between linearly polarized optical pulses and a two-level nondegenerate system, allow for the quadratic Stark effect, and/or contain nonlinear terms associated with the first time derivative of polarizability. This analogy makes it possible to use some results obtained in [27]. Properties specific to the Maxwell–Bloch equations for circularly polarized UDPs must manifest themselves in analyses of optical bistability. In particular, multistable optical solitons can be generated by placing a sufficiently long specimen of a nonlinear material described by Eqs. (8) in a ring cavity with pumping by a field of constant amplitude. The pulse amplitude and duration are many-valued functions of pumping amplitude and initial conditions in certain ranges of the pumping amplitude. It can be shown that multistable linearly polarized UDPs cannot exist under similar conditions.

In the adiabatic limit, interaction with an additional level (or levels) is represented by additional nonlinear terms in the Maxwell–Bloch equations. As a consequence, the integrability of the model is violated in the case of a relatively short pulse, but is retained in the quasi-monochromatic limit. Thus, the degree of violation is determined by deviation from quasi-monochromaticity. Directional pulses with durations comparable to ω_0^{-1} lose energy by radiation under the influence of additional levels, in contrast to quasi-monochromatic pulses. The solutions obtained above can be used to show that adiabatic treatment of additional levels leads to an intensity dependence of the phase for a linearly polarized pulse in the quasi-monochromatic limit and for circularly polarized pulses described by both integrable and nonintegrable systems. This chirp is manifested in the pulse spectrum and shape. The one-hump quasi-monochromatic UDP solution obtained for $r^2 = 1$ by taking into account the chirp is formally identical to (52) up to notation.

The solutions presented in this paper provide a basis for qualitative interpretations of some well-known experimental results. In [32], effects due to an initial phase shift ϕ_0 were studied experimentally for a pulse with a duration of several periods propagating in a nonlinear optical semiconductor, and a two-level approximation was used to analyze the system of levels. The influence of higher energy levels was taken into account in modeling the experiment by modifying the dielectric constant. At the same time, some qualitative disagreement with predictions of the two-level model was found experimentally in [32]. For example, the pulse energy strongly depended on the initial phase ϕ_0, while the effective nonlinear phase of the pulse was a function of its intensity, which could not be explained by the proposed model. The results obtained in the present study can be used to interpret the effects of phase shift ϕ_0 and pulse polarization observed in [32] for a quasi-two-level system without applying perturbation or quasi-monochromatic approximation. The behavior of optical pulses revealed experimentally in [32] is similar to the behavior of circularly or linearly polarized UDPs interacting with a two-level system predicted for a two-level system by taking into account the influence of additional levels analyzed above in the adiabatic approximation. As shown above, the influence of additional levels manifests itself in an intensity dependence of the pulse phase and in a dependence of pulse amplitude on the initial phase α_1.

In [33], the Rabi splitting caused by a pulse with duration corresponding to the transition frequency in an effective two-level system was studied experimentally. The theory based on the approach proposed in [33] predicts an increase in Rabi splitting with pulse intensity. However, the splitting observed experimentally in [33] was substantially weaker than that predicted by the theory. The solutions to Eqs. (58) obtained here can be used to explain the narrow Rabi splitting due to the influence of additional levels. Since the number of additional levels in the optical system examined in [33] was about 50, their influence could be strong. The "instantaneous" Rabi frequency at the instant corresponding to the peak intensity of the pulse, $I_0 = |U|^2$, is found by solving system (58):

$$\Omega_R = \sqrt{(1 - \kappa_0 I_0)^2 + I_0}. \quad (62)$$

The dependence of Ω_R on I_0 reaches a minimum at

$$I_0 = 3/2g,$$

$$\min\Omega_R = \frac{\sqrt{g+6}}{2\sqrt{g}}.$$

With increasing I_0 at $g > 2$, the Rabi splitting decreases, goes through a minimum, and then increases. Since the number of additional levels is large, the value of g can be greater than 2 and their influence can reduce the Rabi splitting, as in the experiment reported in [33]. Note that $\Omega_R(I_0)$ has a minimum when transitions between additional levels and the upper level. When only transitions between additional levels and the lower level are taken into account, it can be shown that $\Omega_R(I_0)$ is a monotonically increasing function.

Integrable model (8) and the ISM apparatus developed above, after some modification, can be used to describe transverse acoustic waves in a paramagnetic crystal doped with ions of spin 1/2, as well as the dynamics of transverse magnetic-field pulses in a magnetic crystal with low spin density and rhombic symmetry.

It would be interesting to apply the results of this study in analyzing polarization effects on circularly polarized ultrashort (pico- and femtosecond) unidirectional pulses propagating in a two-dimensional photonic crystal. It is well known that there exist solitonlike solutions corresponding to forbidden zones of a photonic crystal [34]. The structure of solitonlike pulses in a two-dimensional crystal is much more complicated [35]. Effects of multiple levels and nonlinear coupling between components of a circularly polarized field on UDP propagation must manifest themselves in the structure of pulses propagating in a photonic crystal doped with resonant atoms [36]. One should expect to observe effects due to bistable behavior and compression of circularly polarized pulses in a photonic crystal involving a resonant component. These effects are qualitatively different from the dynamics of linearly polarized pulses with a duration comparable to the inverse transition frequency [37].

ACKNOWLEDGMENTS

I thank H. Steudel for valuable comments concerning some results of this work and J.C. Eilbeck for information about related studies. This work was supported, in part, by the Russian Foundation for Basic Research, project no. 03-02-16297; under the Interdisciplinary Integration for Basic Studies of the Siberian Division of the Russian Academy of Sciences, project no. 84; and under the Program of Basic Research of the Presidium of the Russian Academy of Sciences, grant no. 8-2.

REFERENCES

1. R. K. Bullough, P. M. Jack, P. W. Kitchenside, and R. Saunders, Phys. Scr. **20**, 364 (1979).
2. A. I. Maimistov, A. M. Basharov, S. O. Elyutin, and Yu. S. Sklyarov, Phys. Rep. **191**, 1594 (1990).
3. T. Brabec and F. Krausz, Rev. Mod. Phys. **72**, 545 (2000).
4. A. I. Maĭmistov, Kvantovaya Élektron. (Moscow) **30**, 287 (2000).
5. D. You, D. R. Dykaar, and P. H. Bucksbaum, Opt. Lett. **18**, 290 (1993).

6. M. Wittmann, A. Nazarkin, and G. Korn, Opt. Lett. **26**, 298 (2001).
7. L. Xu, C. Spielmann, and F. Krausz, Opt. Lett. **21**, 1259 (1996).
8. A. Baltuska, Z. Wei, M. S. Pshenichnikov, and D. A. Wiersma, Opt. Lett. **22**, 102 (1997).
9. E. M. Belenov, P. G. Kryukov, A. V. Nazarkin, *et al.*, Pis'ma Zh. Éksp. Teor. Fiz. **47**, 442 (1988) [JETP Lett. **47**, 523 (1988)].
10. E. M. Belenov, A. V. Nazarkin, and V. A. Ushchapovskiĭ, Zh. Éksp. Teor. Fiz. **100**, 762 (1991) [Sov. Phys. JETP **73**, 422 (1991)].
11. S. V. Sazonov and E. V. Trifonov, J. Phys. A: Math. Gen. **27**, L7 (1994).
12. A. Yu. Parkhomenko and S. V. Sazonov, Zh. Éksp. Teor. Fiz. **114**, 1393 (1998) [JETP **87**, 864 (1998)].
13. R. W. Ziolkowski, J. M. Arnold, and D. M. Gogny, Phys. Rev. A **52**, 3082 (1995); S. Hughes, Phys. Rev. Lett. **81**, 3363 (1998); Phys. Rev. A **62**, 055401 (2000).
14. M. Kolesik, J. V. Moloney, and M. Mlejnek, Phys. Rev. Lett. **89**, 283902 (2002).
15. V. E. Zakharov, S. V. Manakov, S. P. Novikov, and L. P. Pitaevskiĭ, *Theory of Solitons: The Inverse Scattering Method* (Nauka, Moscow, 1980; Consultants Bureau, New York, 1984).
16. A. M. Basharov and A. I. Maĭmistov, Zh. Éksp. Teor. Fiz. **87**, 1594 (1984) [Sov. Phys. JETP **60**, 913 (1984)].
17. J. D. Gibbon, P. J. Coudrey, J. K. Eilbeck, and R. K. Bullough, J. Phys. A: Math. Gen. **6**, 1237 (1973).
18. L. Allen and J. H. Eberly, *Optical Resonance and Two-Level Atoms* (Wiley, New York, 1975; Atomizdat, Moscow, 1978).
19. A. A. Zabolotskiĭ, Pis'ma Zh. Éksp. Teor. Fiz. **77**, 558 (2003) [JETP Lett. **77**, 464 (2003)].
20. J. Cheng and J. Zhou, Phys. Rev. A **67**, 041404(R) (2003).
21. R. P. Feynman, F. L. Vernon, and R. W. Hellwarth, J. Appl. Phys. **28**, 49 (1957).
22. R. E. Slusher and H. M. Gibbs, Phys. Rev. **5**, 1656 (1972).
23. S. P. Burtsev and I. R. Gabitov, Phys. Rev. A **49**, 2065 (1994).
24. A. A. Zabolotskiĭ, Zh. Éksp. Teor. Fiz. **121**, 1012 (2002) [JETP **94**, 869 (2002)].
25. D. J. Kaup and A. C. Newell, J. Math. Phys. **19**, 798 (1978).
26. E. A. Kuznetsov and A. V. Mikhaĭlov, Teor. Mat. Fiz. **30**, 303 (1977).
27. A. A. Zabolotskiĭ, Zh. Éksp. Teor. Fiz. **107**, 1100 (1995) [JETP **80**, 614 (1995)].
28. S. P. Burtsev, A. V. Mikhaĭlov, and V. E. Zakharov, Teor. Mat. Fiz. **70**, 323 (1987).
29. O. Svelto, *Principles of Lasers*, 3rd ed. (Plenum, New York, 1989; Mir, Moscow, 1979).
30. *Painlevé Transcendents. Their Asymptotics and Physical Applications*, Ed. by P. Winternitz and D. Levi (Plenum, New York, 1992), NATO ASI Ser., Ser. B: Phys., Vol. 278.
31. A. A. Zabolotskii, Phys. Lett. A **124**, 500 (1987).
32. O. D. Mücke, T. Tritschler, M. Wegener, *et al.*, Phys. Rev. Lett. **89**, 127401 (2002).
33. O. D. Mücke, T. Tritschler, M. Wegener, *et al.*, Phys. Rev. Lett. **87**, 057401 (2001).
34. S. John and N. Aközbek, Phys. Rev. Lett. **71**, 1168 (1993).
35. N. Aközbek and S. John, Phys. Rev. E **57**, 2287 (1998).
36. N. Aközbek and S. John, Phys. Rev. E **58**, 3876 (1998).
37. R. A. Vlasov and A. G. Smirnov, Phys. Rev. E **60**, 5808 (2000).

Translated by A. Betev

Journal of Experimental and Theoretical Physics, Vol. 98, No. 6, 2004, pp. 1087–1097.
Translated from Zhurnal Éksperimental'noĭ i Teoreticheskoĭ Fiziki, Vol. 125, No. 6, 2004, pp. 1245–1257.

ATOMS, SPECTRA, RADIATION

Dynamics of Localized Wave Packets of Rotational States of a Molecule in a Strong Laser Field

O. V. Tikhonova* and M. S. Molodenskiĭ

Skobeltsyn Institute of Nuclear Physics, Moscow State University, Moscow, 119992 Russia

**e-mail: ovt@mics.msu.su*

Received August 4, 2003

Abstract—Numerical simulations are performed to examine the rotational dynamics of a molecule in a strong laser field when the molecular axis is initially oriented in a certain direction. The results obtained by solving the quantum-mechanical problem are compared with those computed in the framework of classical mechanics. It is found that certain characteristics of rotational motion cannot be described by classical theory, particularly for light molecules. It is demonstrated that the axis of a heteronuclear molecule can be reversed by tunneling.

1. INTRODUCTION

Recent progress in the development of high-power pulsed lasers stimulated studies of interaction between coherent radiation and matter, such as interactions between strong laser fields and atomic and molecular systems. Interaction with a strong laser field can excite various electronic, vibrational, and rotational states of a molecule. It is commonly believed that electronic degrees of freedom are excited by interaction with a field at much higher rates, as compared to nuclear ones. For this reason, nuclear degrees of freedom are frequently treated as "frozen" in theoretical analyses. However, this assumption was found to be incorrect. Theoretical [1–7] and experimental [8–13] studies showed that molecular rotations play an important role in the processes in question, leading to alignment of molecules parallel or perpendicular to electric fields [14].

According to a theoretical study, alignment of molecules in a Ti:Sapphire laser field of intensity below 10^{14} W/cm^2 can occur without any significant electronic or vibrational excitation, while 10 to 15 rotational sublevels can be excited [7]. Therefore, substantial rotational dynamics may not be accompanied by dissociation or ionization.

Excitation of a large number of rotational states gives rise to an angular distribution of molecular-axis orientation. In a quantum-mechanical treatment, this state is represented by a wave packet characterized by certain shape and width. Both field-free evolution of this localized wave packet and its dynamics in a "probe" laser field are of great interest. Laser pulses can be used to control the orientation of molecules, align them parallel or perpendicularly to electric fields, and hold molecules in oriented states. Control of the orientation of molecules in space or on solid surfaces offers new opportunities for control of both homogeneous and heterogeneous chemical reactions and other applications. In particular, this effect can be applied to enhance the efficiency of high-order harmonic generation in molecules [15].

Rotational dynamics of molecules interacting with fields can be described by different models. In the approach employed in [11, 16, 17], the effective energy of interaction between the molecule and the field is represented by the classical expression for a field interacting with an induced dipole [18–20]:

$$U = -\frac{(\alpha_\parallel - \alpha_\perp)\varepsilon_0^2(t)}{4}\cos^2\theta. \quad (1)$$

Here, $\varepsilon_0(t)$ is the laser-pulse envelope, $\alpha_\parallel - \alpha_\perp$ is the difference of the longitudinal and transverse molecular polarizabilities, and θ is the angle between the molecular axis and the field polarization. When the envelope is ignored, the potential above is given by a time-independent expression:

$$U = -\frac{1}{4}\varepsilon_0^2(\alpha_\parallel - \alpha_\perp)\cos^2\theta. \quad (2)$$

This expression for potential energy provides a qualitative physical interpretation of alignment of molecules: the minima of the potential correspond to an angle of 0 or π between the molecular axis and the laser field, and its depth is proportional to the laser intensity. Accordingly, the average orientation of the molecular axis is parallel to the field, especially when the field is turned on gradually [3, 4].

Note that (2) is an anharmonic potential. Therefore, it is interesting to explore the feasibility of classical treatment of dynamics of a localized rotational wave packet interacting with a laser field.

Standard classical treatment is based on the assumption that, since the nucleus-to-electron mass ratio is

large, the nuclear wave-packet width is much smaller than both characteristic width of the electron wave function and characteristic range of nuclear motion (several atomic units). Furthermore, the rotational energy quantum is frequently much smaller than the molecule–field interaction energy: $B \ll \alpha\varepsilon^2/4$, where B is the rotational constant and α is the molecular polarizability. For these reasons, the problem is frequently analyzed in the framework of classical mechanics [21, 22]. However, classical description of rotational dynamics of a molecule interacting with a field is not obviously applicable, because the initial rotational state is represented by a relatively wide wave packet or even an uniform angular distribution. Moreover, the interaction is described by an anharmonic potential depending on the field.

In this paper, a quantum-mechanical model is used to simulate the rotational dynamics of a molecule interacting with a laser field in the case when the molecular axis is initially oriented in a certain direction. A comparison of quantum-mechanical calculations with the results obtained within the framework of a classical theory shows that molecular rotation has an essentially quantum nature in the general case. Classical description of rotational dynamics is similar to quantum-mechanical representation only within a narrow range of parameter values. The inherently quantum-mechanical characteristics of rotational dynamics are explained by the substantial width and fast dispersion of rotational wave packets, quantum interference of different parts of the wave function, the anharmonicity of the molecule–field interaction potential, and the possibility of tunneling processes having no analog in classical mechanics.

2. NUMERICAL MODEL

We consider the H_2^+ ion in a plane as a model molecular system. A two-dimensional model is used here because an analysis of rotational dynamics of a molecule must begin with estimation of the range of laser intensity in which both ionization and dissociation of the system are negligible. An analysis of this kind is very difficult to perform for a three-dimensional molecular system. Note that rotational dynamics of a planar molecule are qualitatively similar to rotational motion of a three-dimensional molecule (in a plane defined by the molecular axis and the field polarization) in the case of zero projection of its angular momentum on the z axis.

The rotational dynamics of the model system in a laser field $\boldsymbol{\varepsilon}(t) = \boldsymbol{\varepsilon}_0(t)\cos(\omega t)$ are described by the time-dependent Schrödinger equation

$$i\hbar\frac{\partial\psi}{\partial t} = \hat{H}\psi. \tag{3}$$

In the center-of-mass system, the Hamiltonian is

$$\hat{H} = \frac{\hat{p}_e^2}{2m} + \frac{\hat{p}_N^2}{2\mu} + \frac{e^2}{|\mathbf{R}|} - \frac{e^2}{|\mathbf{r} - \mathbf{R}/2|} - \frac{e^2}{|\mathbf{r} + \mathbf{R}/2|} - \mathbf{d}\cdot\boldsymbol{\varepsilon}(t), \tag{4}$$

where $\hat{p}_e^2/2m$ is the kinetic energy of the electron, $\hat{p}_N^2/2\mu$ is the kinetic-energy operator for the nuclei in the center-of-mass system, $\mathbf{r} = \{x, y\}$ is the electron radius vector and $\mathbf{R}$ is the internuclear radius vector characterized by the angle θ between the vector $\boldsymbol{\varepsilon}$ (x axis) and the molecular axis, $\mu = M/2$ is the reduced mass, and $\mathbf{d}$ is electronic dipole moment of the system (the nuclear dipole moment is zero in the center-of-mass system). The field frequency was set equal to that of the Ti:Sapphire laser ($\hbar\omega = 1.55$ eV), and various field-switching methods were examined.

The problem was solved in the Born–Oppenheimer approximation, and only the lowest two electronic terms of the molecule were taken into account:

$$\Psi = \Phi_1(R, \theta, t)\varphi_1(\mathbf{r}, R) + \Phi_2(R, \theta, t)\varphi_1(\mathbf{r}, R), \tag{5}$$

because the interaction between the molecule and a laser field of intensity not higher than 10^{14} W/cm^2 results in the excitation of only the lowest electronic level, whereas both excitation of all higher states and ionization are negligible [7]. Furthermore, the highest population of the second lowest term during the interaction with a pulse does not exceed several percent.

Both electronic wave functions $\varphi_1(\mathbf{r}, R)$ and $\varphi_2(\mathbf{r}, R)$ and the corresponding electron energies E_1 and E_2 can be found by solving the time-independent Schrödinger equation with the electronic Hamiltonian

$$\hat{H}_e = \frac{\hat{p}_e^2}{2m} - \frac{e^2}{|\mathbf{r} - \mathbf{R}/2|} - \frac{e^2}{|\mathbf{r} + \mathbf{R}/2|} \tag{6}$$

parameterized by R. The functions φ_1 and φ_2 can be used to obtain the transition matrix elements for the electron dipole-moment projections on the internuclear axis and on the perpendicular direction, $d_\parallel = ex_{12} = ex_{21} = e\langle\varphi_1|x|\varphi_2\rangle$ and $d_\perp = ey_{12} = e\langle\varphi_1|y|\varphi_2\rangle$, parameterized by the internuclear distance. A detailed analysis of this parametric dependence can be found in [7]. Note that the symmetry of the wave functions of the lowest two states dictates that $d_\perp \equiv 0$ in the two-dimensional model.

Decomposition (5) was used to derive a system of equations for the nuclear parts $\Phi_{1,2}(R, \theta, t)$ of the wave

function:

$$
\begin{aligned}
i\hbar\frac{\partial\Phi_1(R,\theta,t)}{\partial t} &= \left(\frac{\mathbf{p}_N^2}{2\mu}+V_{\text{eff}}^{(1)}(R)\right)\Phi_1(R,\theta,t)\\
&-e\varepsilon(t)[x_{12}(R)\cos\theta+y_{12}(R)\sin\theta]\Phi_2(R,\theta,t),\\
i\hbar\frac{\partial\Phi_2(R,\theta,t)}{\partial t} &= \left(\frac{\mathbf{p}_N^2}{2\mu}+V_{\text{eff}}^{(2)}(R)\right)\Phi_2(R,\theta,t)\\
&-e\varepsilon(t)[x_{12}(R)\cos\theta+y_{12}(R)\sin\theta]\Phi_1(R,\theta,t),
\end{aligned}
\tag{7}
$$

where

$$V_{\text{eff}}^{(1,2)}(R) = \frac{e^2}{R}+E_{1,2}(R)$$

is the effective potential energy of the nuclei (depending on the electron energy for both electronic terms) as a function of the internuclear distance R.

An analysis of rotational dynamics of molecules taking into account excitation of vibrational levels [7] showed that the population of vibrational states is negligible in the range of laser parameters of interest here. Therefore, the internuclear distance in the molecule is approximately equal to its equilibrium value $R_0 = 1.2$ Å during its interaction with the laser pulse. Thus, the approximation based on a constant internuclear distance is physically correct, the nuclear wave functions in (7) depend only on the angle θ between the field polarization vector and internuclear axis, and all quantities depending on R can be calculated at $R = R_0$.

The expansions of the nuclear wave functions in terms of rotational eigenstates of a planar molecule for $R = R_0$,

$$\Phi_{1,2}(\theta,t) = \sum_m C_m^{(1,2)}(t)\frac{e^{im\theta}}{\sqrt{2\pi}}, \tag{8}$$

were used to derive a system of equations for the population amplitudes of the kth rotational sublevel in both states:

$$
\begin{aligned}
i\hbar\frac{dC_k^{(1)}}{\partial t} &= Bk^2C_k^{(1)}+V_{\text{eff}}^{(1)}(R_0)C_k^{(1)}\\
&-\frac{e\varepsilon(t)}{2}x_{12}(C_{k+1}^{(2)}+C_{k-1}^{(2)}),\\
i\hbar\frac{dC_k^{(2)}}{\partial t} &= Bk^2C_k^{(2)}+V_{\text{eff}}^{(2)}(R_0)C_k^{(2)}\\
&-\frac{e\varepsilon(t)}{2}x_{12}(C_{k+1}^{(1)}+C_{k-1}^{(1)}),
\end{aligned}
\tag{9}
$$

where

$$B = \frac{\hbar^2}{2\mu R_0^2}$$

is the rotational constant.

The initial rotational-sublevel population amplitudes $C_k^{(1,2)}$ were defined so that the initial wave packet was localized in a narrow neighborhood of an angle θ_0. The analysis was performed for several values of the average angular momentum $\langle m\rangle$. In classical mechanics, this initial condition describes a molecule making a certain angle θ_0 with the field polarization and having different initial angular velocities. Since H_2^+ is a homonuclear ion (the nuclei are identical), the initial condition must correspond to localized nuclear wave packets making an angle of π. The initial nuclear angular distribution was described by the function

$$
\Phi_N(\theta,t=0) = \begin{cases}
A\cos^2\dfrac{\theta-\theta_0}{\Delta\theta^*}, & \theta_0-\Delta\theta^*\dfrac{\pi}{2}\le\theta\le\theta_0+\Delta\theta^*\dfrac{\pi}{2},\\
A\cos^2\dfrac{\theta-(\pi+\theta_0)}{\Delta\theta^*}, & \theta_0+\pi-\Delta\theta^*\dfrac{\pi}{2}\le\theta\le\theta_0+\pi+\Delta\theta^*\dfrac{\pi}{2},\\
0, \text{ otherwise } \theta.
\end{cases}
\tag{10}
$$

Here, $\Delta\theta^*$ is the total (base) width of the initial wave packet, and A is a normalization constant. Figure 1a shows the initial angular distribution for $\theta_0 = \pi$ and $\Delta\theta^* = \pi/4$.

Equations (9) were solved numerically. The functions $\Phi_{1,2}(\theta, t)$ were used to determine the probability that the molecule makes an angle θ with a certain direction,

$$\rho_N(\theta,t) = |\Phi_1(\theta,t)|^2+|\Phi_2(\theta,t)|^2, \tag{11}$$

and the time-dependent angle averaged over the nuclear

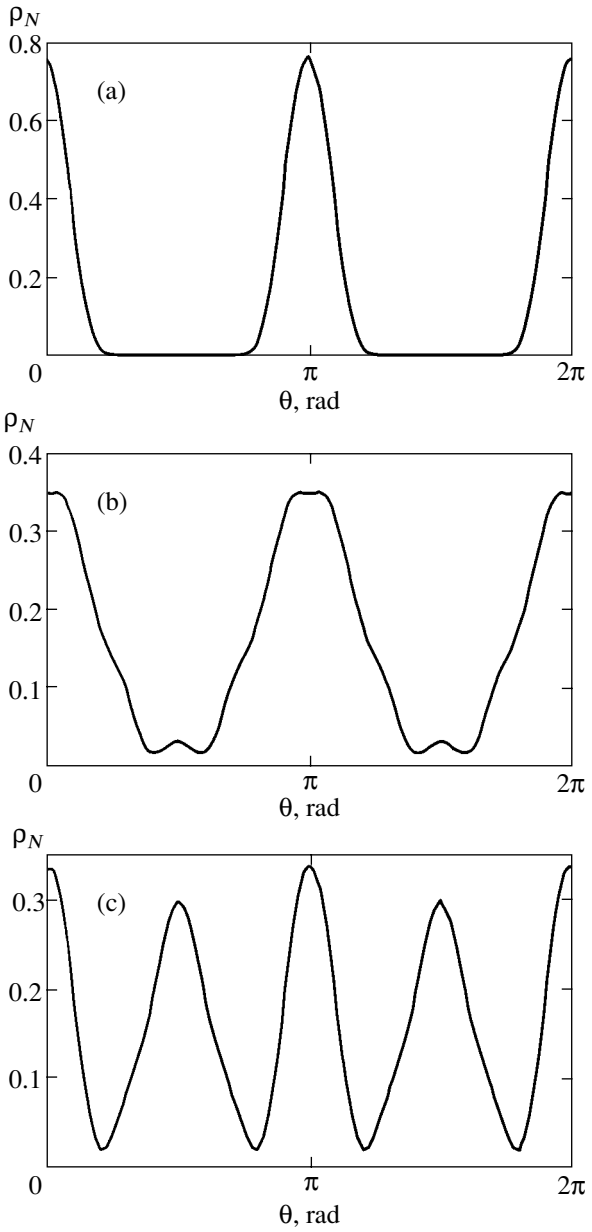

Fig. 1. Angular distribution of nuclear probability density (11) characterizing the field-free dynamics of a homonuclear molecule at (a) $t = 0$, (b) 40, and (c) 140 fs.

wave packet,

$$\langle\theta(t)\rangle = \int_0^{2\pi} \theta[|\Phi_1(\theta, t)|^2 + |\Phi_2(\theta, t)|^2]d\theta. \quad (12)$$

The time-dependent averaged angle was compared with the solution to the equation of motion

$$\ddot{\theta} = -\frac{(\alpha_\parallel - \alpha_\perp)\varepsilon_0^2(t)B}{\hbar^2}\sin(2\theta), \quad (13)$$

which describes a classical rigid rotor driven by molecule–field interaction potential (1).

3. RESULTS AND DISCUSSION

3.1. Field-Free Dynamics of a Molecule

First, we analyze the field-free rotational dynamics of a molecule. It is obvious that a molecule initially at rest will remain at rest in the absence of any interaction and its orientation will be preserved. In a quantum-mechanical treatment, the orientation of a molecule is represented by a wave packet of nonzero width. The field-free dynamics of a molecule predicted by Eqs. (9) are illustrated by the squared amplitudes (11) of the nuclear wave function shown in Fig. 1 for several instants.

Figure 1 demonstrates that both wave packets representing an initially oriented state of a homonuclear molecule tend to spread out and interfere with one another. As a result, several peaks appear in the angular distribution (see Fig. 1c), which means that there is no preferred orientation of the molecular axis. Furthermore, the average angle $\langle\theta\rangle$ given by (12) is a time-dependent quantity. Figure 2 shows details of the evolution of the corresponding nuclear angular distribution. Here, the slice of the distribution taken at any instant is nuclear probability density (11) as a function of θ. Heavier shading corresponds to a higher nuclear probability density. The initial wave packet is localized in the neighborhoods of 0 and π. Figure 2 demonstrates that an early stage of dispersion of the rotational wave packet is similar to the spreading of a free localized wave packet over an infinite axis. After this stage of classical motion of the packet's centroid, wave-packet components interfere with one another and a varying number of peaks appear in the distribution. Accordingly, the quantum average value $\langle\theta\rangle$ of the angular location of the centroid begins to depend on time. This behavior is beyond the scope of classical mechanics. Even in the case of a single initial wave packet (heteronuclear molecule), different parts of the wave function would interfere and the average angle $\langle\theta\rangle$, as well as $\langle\cos\theta\rangle$ and all of its higher order moments, would depend on time.

The interference of different parts of the wave packet is essentially due to the fact that its dynamics are computed on the finite angular interval $[0, 2\pi]$ under periodic boundary conditions and to the quick spreading of the packet over the entire domain of the wave function. Note that any attempt to represent a quantum wave packet as an ensemble of classical particles (rather than a single particle) would not lead to better agreement between quantum-mechanical and classical results. One might expect good agreement if the initial joint distribution of the angular locations and velocities of classical particles were similar to the corresponding quantum distributions before the onset of interference. This could be achieved only if the desired initial distribution were calculated by using a quantum-mechanical uncertainty relation, but the result would be an artificial ensemble rather than a classical one. However, a substantial difference between quantum and classical

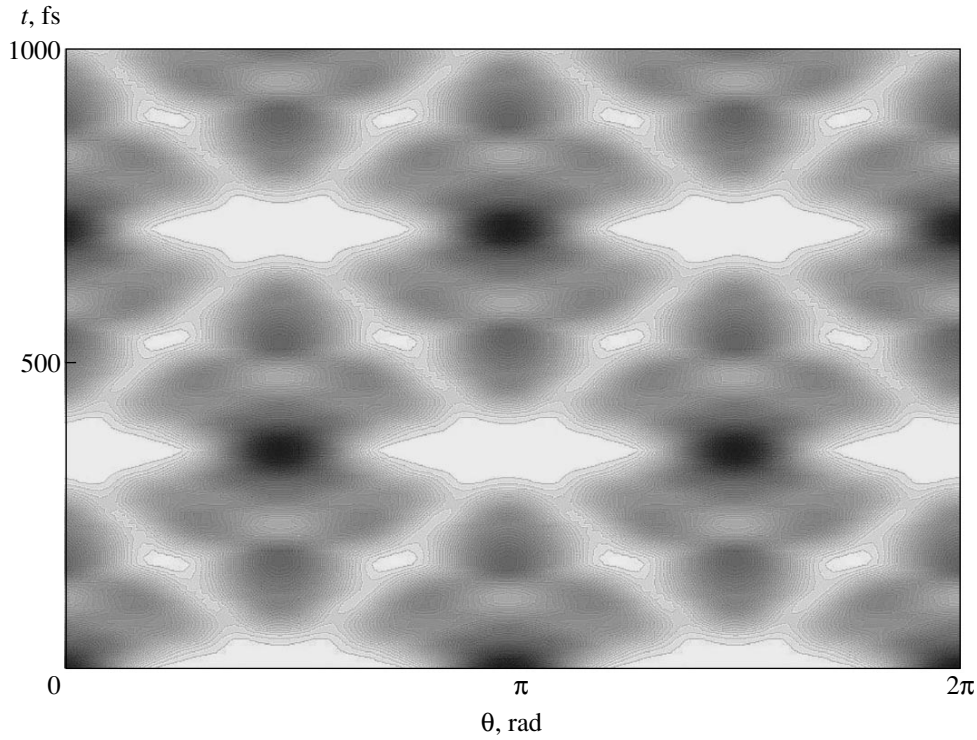

Fig. 2. Field-free evolution of nuclear angular distribution for a nuclear wave packet from initial state (10) with width $\Delta\theta^* = \pi/4$ and deviation angle $\theta_0 = \pi$. Shading varies between 0.1 and 1.0 as a linear function of density.

dynamics would manifest itself by quantum interference even in this hypothetical situation. The quantum probability density would periodically exhibit several peaks corresponding to the most probable orientations of the molecular axis, whereas the angular distribution of particles in the classical ensemble defined above would simply spread and approach a uniform one by virtue of superposition of probabilities in classical mechanics. Of all integral characteristics (in which interference effects are partly smoothed out), higher moments of $\cos\theta$ exhibit the difference most clearly. Note that complete revival of the quantum wave packet would be observed after a certain time interval. In the problem considered here, the revival time is determined by the energy difference between the lowest two states contributing to the superposition. It can be estimated as $T_{\text{rev}} \approx \hbar/B$ (about 700 fs for the system under analysis). The instants at which the distribution consists of several identical peaks correspond to the so-called fractional revivals. This behavior was observed in [23], where the dynamics of a wave packet in an anharmonic potential were analyzed. In the two-dimensional case, the anharmonic spectrum of rotational states of a free molecule is

$$E_m = Bm^2, \quad m = 0, \pm 1, \pm 2, \ldots.$$

Essentially, it is determined by the periodic boundary conditions for the wave function defined on the interval $(0, 2\pi)$.

The breakup of the probability density into several peaks followed by a complete revival explained by the interference that takes place when the system moves within a finite interval under boundary conditions. For example, analogous behavior is characteristic of a wave packet in an infinitely deep potential well [24].

Thus, the quantum field-free evolution considered here is characterized by a quick spreading and subsequent, inherently quantum interference of different parts of the wave packet.

Both self-interference and breakup of the wave packet develop more rapidly in the case of a light molecule. Heavier molecules are characterized by slower spreading and longer time intervals of rotational motion described by classical mechanics.

Molecular dynamics prior to substantial spreading can be analyzed by assuming that the initial average momentum $\langle L\rangle = \hbar\langle m\rangle$ is very large, which corresponds to a high angular velocity of a rotor in classical representation. Curve *1* in Fig. 3 is the quantum average angle $\langle\theta\rangle$ as a function of time given by (12) for a single wave packet with an initial deviation of $\pi + \pi/10$ (in the hypothetical case of a heteronuclear molecule). The initial value of angular momentum was sufficiently large to observe rotation with negligible wave-packet dispersion. The time dependence presented here demonstrates that the molecule executes almost six revolutions during about 10 fs, and the dispersion is exhibited insignificantly (only in the final revolutions). Overall, the rota-

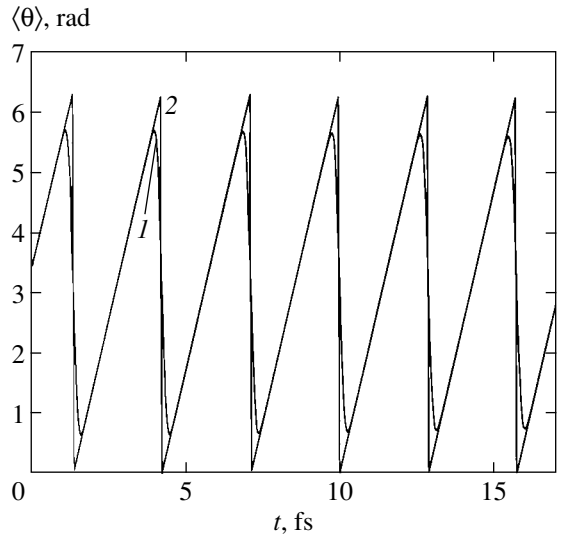

Fig. 3. Trajectory of the centroid of a quantum wave packet (*1*) and a classical particle (*2*) in the case of field-free rotation with initial deviation angle $\pi + \pi/10$ and initial angular momentum $L = 500\hbar$.

tion resembles that of a classical rotor under similar initial conditions (curve *2* in Fig. 3). A difference between quantum and classical dynamics is observed only in the neighborhoods of the extreme points 0 and 2π and is explained by a nonzero packet width and the fact that the evolution is simulated on the finite interval $[0, 2\pi]$ under periodic boundary conditions. These quantum-mechanical predictions should obviously agree with results calculated for a corresponding classical ensemble of particles, because neither interference nor spreading would manifest itself over the time intervals considered here. Note that the packet would execute several revolutions without spreading out to any significant extent if the initial momentum were sufficiently large. For light molecules, the required value must be about $100\hbar$. Such states cannot be implemented for real molecules, because the corresponding energies exceed dissociation thresholds. If the initial angular velocity were lower, then substantial spreading during a "classical" rotation period would lead to interference of different parts of the wave packet, which is beyond the scope of classical mechanics.

Thus, quantum interference due to a nonzero packet width results in a wave-packet centroid dynamics that is different from classical behavior even in the case of field-free rotation of a molecule.

3.2. Dynamics of a Molecule Interacting with Laser Field

Let us now consider the dynamics of a molecule in a laser field. The initial orientation of the molecule is represented by a wave packet localized around a certain direction. It should be expected that the field would impede the dispersion of the wave packet over the entire domain of the wave function. Moreover, the degree of dispersion must strongly depend on the initial packet width. The width corresponding to minimal spreading can be estimated by using effective potential (2) of molecule–field interaction. Using the harmonic potential

$$U_{\text{eff}} \sim \frac{(\alpha_{\parallel} - \alpha_{\perp})\varepsilon_0^2}{4}\theta^2 \tag{14}$$

to approximate (2), we estimate the width minimizing the rate of packet spreading as

$$\Delta\theta = \sqrt[4]{\frac{4B}{(\alpha_{\parallel} - \alpha_{\perp})\varepsilon_0^2}}, \tag{15}$$

which corresponds to the characteristic width of the ground state in this potential. Using (10) to approximate the Gaussian packet with width given by (15), we estimate the total (base) width of the initial wave packet as $\Delta\theta^* \approx \pi/4$ for a laser intensity of 10^{14} W/cm^2.

We consider the dynamics of a molecule in the field of a laser pulse of intensity 10^{14} W/cm^2 for a packet of width $\Delta\theta^* = \pi/4$ deviating by the angle $\theta_0 = \pi/4$ from the field polarization vector. We assume that the pulse is switched on instantly to rule out packet dispersion during the pulse rise time. The evolution of the nuclear wave-packet density in the laser field is depicted in Fig. 4 for one-half of packet (10) only, because the distribution is symmetric. It is clear that the field of a laser pulse restricts the molecule's motion to a bounded angular interval. Furthermore, the packet remains localized and retains its shape during an initial time interval. However, angular oscillation analogous to classical angular oscillation of the molecular axis about the equilibrium point in potential (2) is observed only during one period. After that, the wave packet breaks up and additional peaks appear. Eventually, the packet spreads over the entire domain of admissible classical motion; i.e., a rotational dynamic of an essentially quantum nature is observed.

This behavior of the wave packet is due to the strongly anharmonic form of potential (2) and to the large initial deviation of the packet from the equilibrium point $\theta_0 = \pi/4$. Since the packet moves in an anharmonic potential most of the time under these conditions, its shape is distorted and interference of different parts of the wave function gives rise to "fractional" peaks.

In the steady-state basis corresponding to potential (2), the wave packet is a superposition of the corresponding eigenstates. The energies of these states are sufficiently high to cause deviation from the equidistant spectrum of a harmonic oscillator. On the other hand, these energies are not sufficiently high to justify the use of a quasi-equidistant approximation of the anharmonic

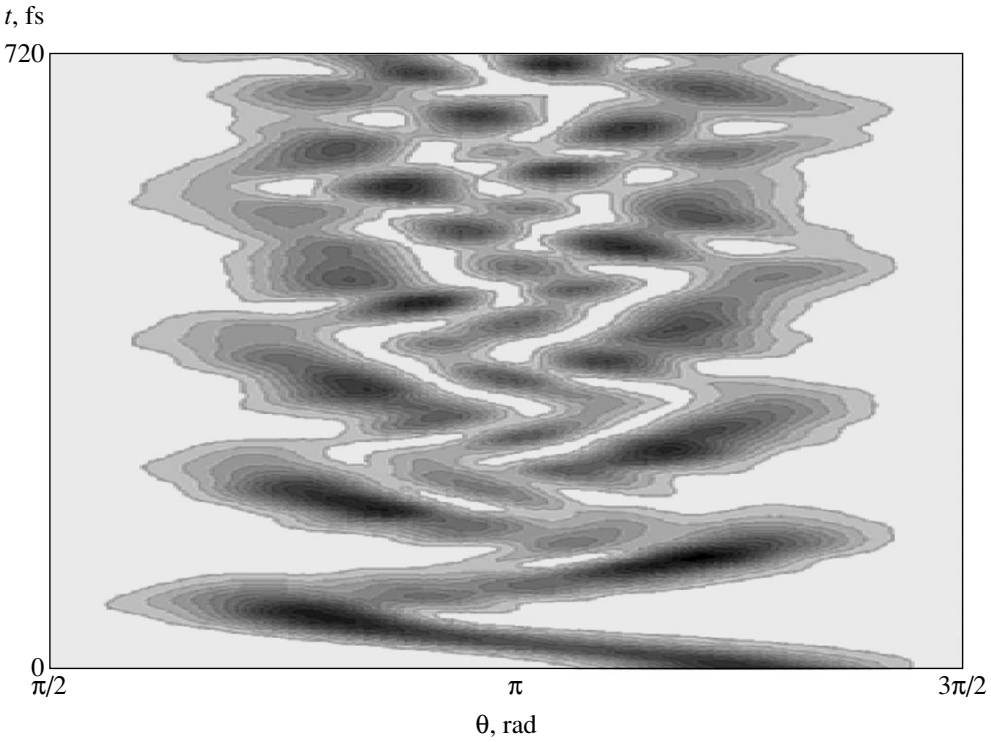

Fig. 4. Evolution of density distribution for a nuclear wave packet with $\theta_0 = \pi/4$ and $\Delta\theta^* = \pi/4$ in laser field of intensity $I = 10^{14}$ W/cm^2 with rectangular envelope.

spectrum corresponding to large quantum numbers, as proposed in [23].

Thus, the essentially nonequidistant energy spectrum of the rotational eigenstates constituting the wave packet in a laser field is responsible for substantial dispersion (without fractional revival after a classical angular-oscillation period) and for reduction of the time interval of nearly classical motion. The packet should be expected to regain its shape characteristic of a superposition of states in an anharmonic potential over "quantum revival" times, which are much longer than the classical oscillation period.

Now, let us analyze the conditions ensuring that quantum rotational dynamics are closest to classical motion over a time interval much larger than the classical rotation period. It is obvious that not only the optimal packet width given by (15) is required, but also the deviation angle must be sufficiently small to remain within the "harmonicity" region of potential (2): $\theta_0 + \Delta\theta \ll 1$. Furthermore, the field must be switched on instantly to rule out dispersion during the pulse rise time. The quantum-mechanical and classical treatments are mutually consistent if the centroid of the wave packet executes classical motion and the packet width is much smaller than its displacement in space. Note that the latter condition is difficult to satisfy for a molecule rotating in a laser field, because the strictly required small initial deviation θ_0 is similar to—or even smaller than—the characteristic packet width given by (15).

Figure 5 illustrates the evolution of one-half of the angular nuclear density for a wave packet characterized by a small initial deviation and optimal width (15). The graphs demonstrate that the H_2^+ molecule executes a nearly classical "angular oscillation" in the field of a laser pulse during several hundreds of femtoseconds. The spreading and distortion of the wave packet are effectively suppressed by virtue of a special choice of initial conditions. Since the packet width is much larger than the oscillation amplitude, the anharmonicity of the potential affects its motion even in this situation, and the rotational dynamic of the molecule can resemble a classical motion only in a qualitative sense.

To perform a more detailed comparison of quantum and classical dynamics of a molecule in a laser field, we analyze the time dependence of the quantum average angle $\langle\theta\rangle$ given by (12) and compare it with the solution to Eq. (13). The dynamics to be analyzed are illustrated by Figs. 6a and 6b, respectively.

The results shown here demonstrate that the "angular-oscillation" amplitude predicted by quantum-mechanical calculations is smaller because of the spreading and distortion of the wave packet. However, the packet shape is almost restored after a time interval $T_{rev} \approx 1.6$ ps, and the initial oscillation amplitude of the packet's centroid is recovered (see Fig. 6a). Note also

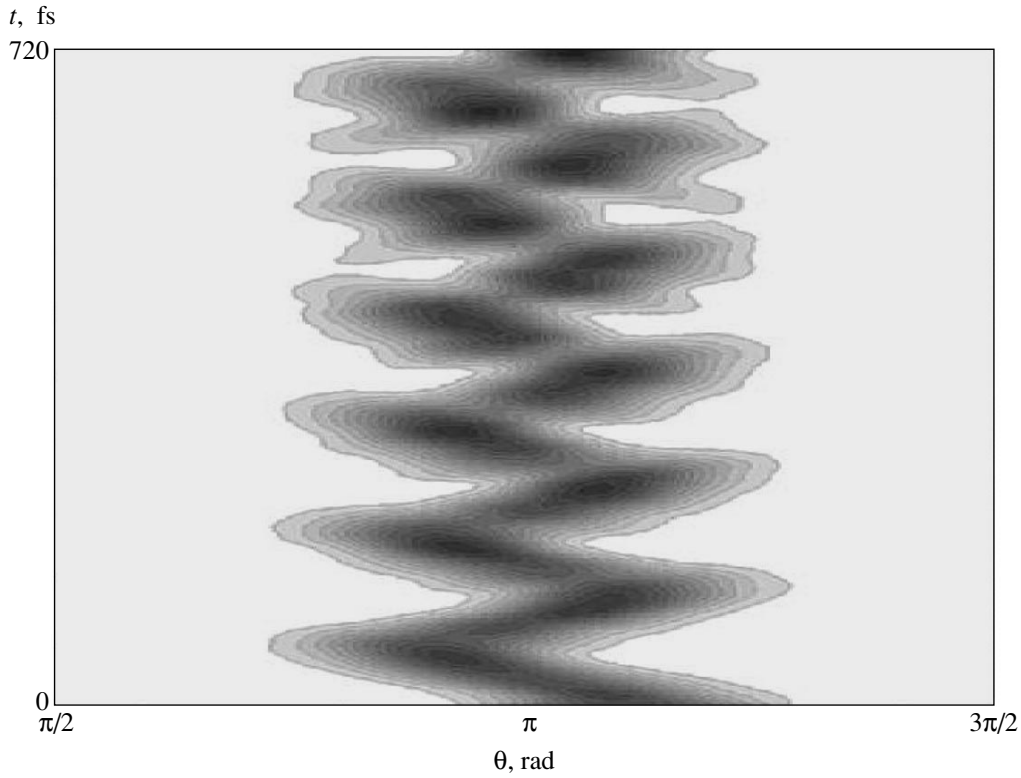

Fig. 5. Evolution of density distribution for a nuclear wave packet with $\theta_0 = \pi/10$, characteristic width given by (15), and other parameters as in Fig. 4.

the difference in frequency between the "quantum" and "classical" angular oscillations. For the parameter values used here, the quantum-to-classical period ratio predicted by numerical calculation is

$$\frac{T_q}{T_{cl}} \approx 1.06. \quad (16)$$

The larger value of the "quantum" period as compared to the classical one is explained by the finite width of the nuclear wave packet, which implies that the force $\langle F(\theta)\rangle$ averaged over a quantum ensemble is weaker than the force $F(\langle\theta\rangle)$ acting at the middle point. The period ratio can be estimated analytically by invoking the Ehrenfest theorem [25]. Assuming that the angular distribution is symmetric about the centroid, we can estimate the difference of the "quantum" and "classical" forces as follows:

$$\langle F(\theta)\rangle - F(\langle\theta\rangle) = -(\alpha_\parallel - \alpha_\perp)\varepsilon_0^2\langle\theta\rangle D_\theta < 0, \quad (17)$$

where D_θ is the variance of the nuclear angular distribution. The difference of these forces increases with angular distribution width and deviation angle. As the wave packet tends to a delta function, the difference between the forces vanishes and the quantum-mechanical description becomes equivalent to the classical treatment. In view of (17), the quantum-to-classical period ratio is

$$\frac{T_q}{T_{cl}} = \frac{1}{\sqrt{1-2D_\theta}} \approx 1.065, \quad (18)$$

which is in good agreement with numerical result (16). It is obvious that the nonzero difference of forces that entails the inequality of the periods characteristic of quantum and classical dynamics is essentially due to the anharmonic potential of interaction between the molecule and the laser field.

Thus, the rotational dynamics of a molecule in a laser field have inherently quantum characteristics, which makes it impossible to reach complete agreement between quantum and classical predictions.

Another essentially nonclassical phenomenon manifests itself in the rotational dynamics of heteronuclear molecules.

It was shown in [6] that problem (7) can be reduced to the motion of a rigid rotor in effective potential (1) if electronic excitations are negligible (in a one-term approximation). Interaction of a heteronuclear molecule with a field contains contributions due both to induced electronic dipole moment and nonzero nuclear dipole moment $\mathbf{d}_0$ parallel to the molecular axis. In the

rigid-rotor approximation, the corresponding potential energy of the molecule is

$$U = -\frac{(\alpha_{\parallel} - \alpha_{\perp})\varepsilon_0^2(t)}{4}\cos^2\theta - d_0\varepsilon(t)\cos\theta. \qquad (19)$$

The latter contribution to (19) has an alternating sign corresponding to a high-frequency deformation of potential well (1). The energy of interaction between the nuclear dipole moment and the field averaged over a time interval much longer than the laser period vanishes, and molecular dynamics in the field of a pulse with rectangular envelope are characterized by potential (2). This is manifested in a much lower efficiency of direct excitation of rotational states in a heteronuclear molecule by high-frequency laser field, as compared to excitation of rotational levels by transitions via an adjacent electronic term.

As noted above, potential (2) has a double-well structure with minima at $\theta = 0$ and $\theta = \pi$ (see Fig. 7). Therefore, a wave packet initially localized in one well can penetrate into the other one by tunneling. In other words, the axis of a heteronuclear molecule initially oriented in a certain direction can reverse via a nonrotational mechanism of an essentially quantum nature. Let us estimate the characteristic time of reversal by tunneling. In the case of a nearly impenetrable barrier, each energy level of both wells splits into two closely-lying levels, which correspond to even and odd states of a particle in a double-well potential. The wave packet representing the lowest eigenstate in either well is the superposition of such "paired" states with energies E_1 and E_2. Then, the characteristic time of packet penetration from one well into the other can be estimated as

$$\tau \approx \frac{\hbar}{|E_2 - E_1|}.$$

Using the semiclassical approximation [26], we estimate the energy difference as follows:

$$E_2 - E_1 = \frac{2\hbar}{T_c}\exp\left\{-\frac{2}{\hbar}\int_{\theta^*}^{\pi/2}|L(\theta)|d\theta\right\}, \qquad (20)$$

where

$$L(\theta) = \sqrt{2\mu R_0^2(U(\theta) - E_0)}$$

is the semiclassical angular momentum of a particle of energy E_0 in the starting well, T_c is the period of its classical motion in the well, and the lower limit of the integral corresponds to a classical turning point. Using har-

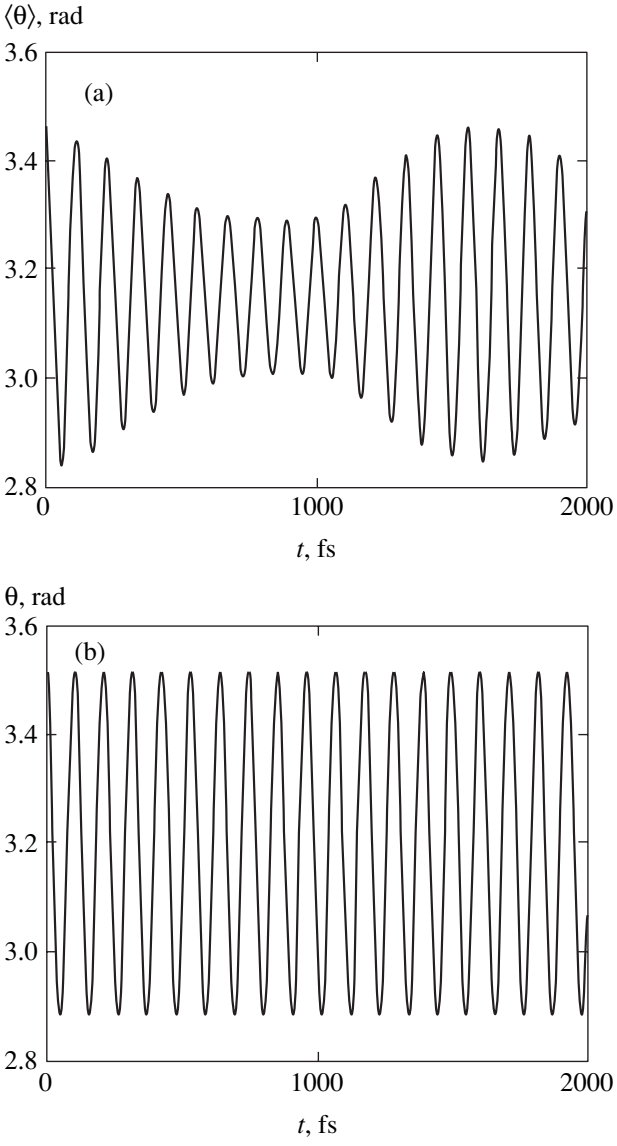

Fig. 6. Quantum average angle $\langle\theta\rangle$ versus time (a) and classical rotational trajectory (b) for a molecule in field of intensity $I = 10^{14}$ W/cm^2, with $\theta_0 = \pi + \pi/10$ and characteristic width given by (15).

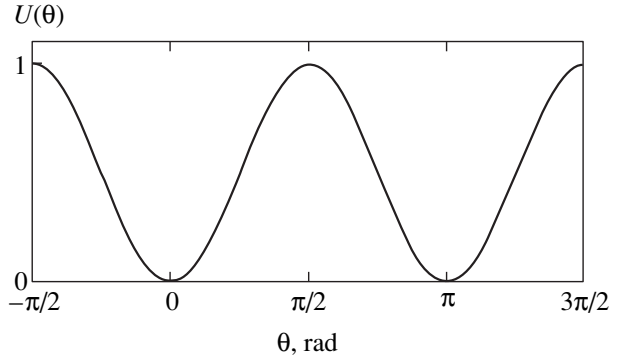

Fig. 7. Effective potential energy (2) versus angle for a planar molecule interacting with laser field.

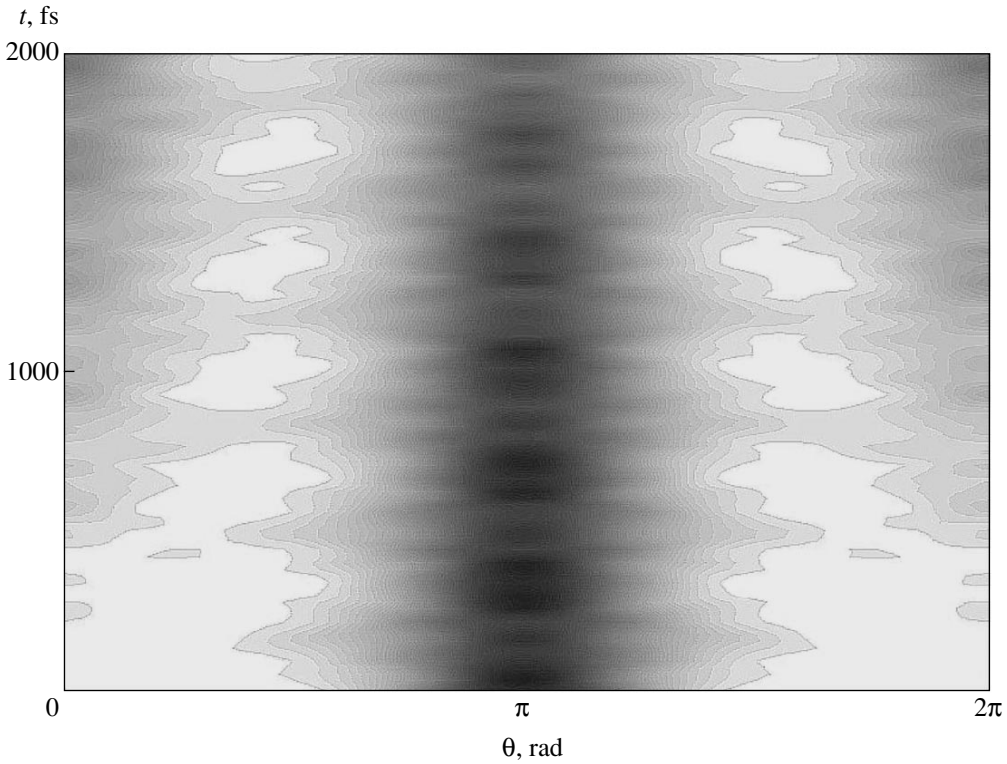

Fig. 8. Evolution of nuclear angular distribution for a molecule with axis reversed by tunneling.

monic approximation (14) for the lowest energy level, we obtain

$$E_2 - E_1 = \frac{2\hbar}{T_c}\exp\left\{-\left(\frac{\pi}{2\Delta\theta}\right)^2\right\}, \qquad (21)$$

where $\Delta\theta$ is equal to vacuum-state width (15) for a harmonic oscillator and

$$T_c = \frac{2\pi\hbar}{\sqrt{\Delta\alpha\varepsilon_0^2 B}}$$

is the classical angular-oscillation period for an individual well.

Expression (21) is valid in the semiclassical approximation. According to (21), the probability of tunneling during a period of classical motion (which depends on the laser intensity) is

$$W \sim \exp\left\{-\frac{\pi}{8}\sqrt{\frac{(\alpha_\parallel - \alpha_\perp)\varepsilon_0^2}{B}}\right\}.$$

In particular, $W \sim 10^{-8}$ if the intensity is 10^{14} W/cm^2, which means that the tunneling probability is 10^{-6} per picosecond. Numerical calculations performed for a stationary wave packet close to an eigenstate in one well resulted in similar values of the probability. Even though the value obtained is small, the exponential dependence of the tunneling probability on field strength implies that the effect will be enhanced in a weaker field, when $(\alpha_\parallel - \alpha_\perp)\varepsilon_0^2 \geq B$. When the barrier penetrability is high, the accuracy of expression (21) is low. However, the numerical results presented in Fig. 8 suggest that the wave packet can penetrate from one well to the other in about 2 ps with a probability of about 50%. Note also that the analytical and numerical results presented here were obtained for a packet initially oriented in the direction corresponding to a minimum of potential energy. When the initial packet deviates from an equilibrium direction, the tunneling probability may increase by several orders of magnitude because of the higher effective energy of the initial state.

4. CONCLUSIONS

Numerical simulations are performed to examine the rotational dynamics of a molecule in a strong laser field when the molecular axis is initially oriented in a certain direction. “Oriented” states of this kind can be created in a physical experiment by irradiating a molecular system with a laser pulse.

It is shown that certain general characteristics of the dynamics of both freely rotating molecule and molecule interacting with a laser field cannot be described by a classical theory. These characteristics are explained by nonzero width and fast spreading of the wave packet

and by quantum interference (particularly when the packet is localized in a region of strongly anharmonic potential).

Because of anharmonicity and "penetration" of a quantum wave packet into the domain where classical motion is forbidden, the difference between quantum and classical dynamics cannot be eliminated even if classical motion is modeled by using an ensemble of particles. The possibility of constructing a classical ensemble of particles that provides an adequate model of quantum state of the system remains an open question.

We have found only a narrow range of laser pulse intensity and initial conditions in which the rotational dynamics obtained in quantum-mechanical and classical representations are mutually consistent. The necessary conditions include an instantly applied field of sufficiently high strength, wave-packet width (15) minimizing the spreading, and an initial deviation of the wave packet from the equilibrium direction that is sufficiently small to ensure its localization in the region of nearly harmonic potential most of the time.

It is found that the axis of a heteronuclear molecule can reverse. This essentially quantum effect is explained by the tunneling of a localized wave packet in the effective molecule–field interaction potential. Estimates for the characteristic times and probability of tunneling obtained in a semiclassical approximation are in good agreement with numerical results. Numerical simulations have shown that the probability of molecular-axis reorientation by tunneling is about 50%. Since this phenomenon is likely to occur in relatively weak fields, it should be easy to observe in experiments. In particular, the HD^+ ion placed in the field of a Ti:Sapphire laser with a pulse intensity of 5×10^{12} to 10^{13} W/cm^2 and a pulse width of about 200 fs must reverse with a probability of 10 to 20%. Note the characteristic time of rotational motion without tunneling in this field substantially exceeds the pulse width.

ACKNOWLEDGMENTS

We thank M.V. Fedorov and A.M. Popov for helpful discussions and attention to this study. This work was supported by the Russian Foundation for Basic Research, project nos. 03-02-16234 and 03-02-06170.

REFERENCES

1. E. Charron, A. Giusti-Suzor, and F. H. Mies, Phys. Rev. Lett. **75**, 2815 (1995).
2. T. Seidemann, J. Chem. Phys. **103**, 7887 (1995).
3. A. I. Andryushin and M. V. Fedorov, Zh. Éksp. Teor. Fiz. **116**, 1551 (1999) [JETP **89**, 837 (1999)].
4. A. I. Andryushin and M. V. Fedorov, Laser Phys. **10**, 226 (2000).
5. T. Seideman, J. Chem. Phys. **115**, 5965 (2001).
6. M. S. Molodenskiy and O. V. Tikhonova, Laser Phys. **13**, 1205 (2003).
7. E. A. Volkova, A. M. Popov, and O. V. Tikhonova, Zh. Éksp. Teor. Fiz. **124**, 781 (2003) [JETP **97**, 702 (2003)].
8. L. J. Frasinski, K. Codling, P. A. Hatherly, *et al.*, Phys. Rev. Lett. **58**, 2424 (1987).
9. J. H. Posthumus, J. Plumridge, L. J. Frasinnski, *et al.*, J. Phys. B **31**, L985 (1998).
10. Ch. Ellert and P. B. Corkum, Phys. Rev. A **59**, R3170 (1999).
11. J. Larsen, K. Hald, N. Bjerre, *et al.*, Phys. Rev. Lett. **85**, 2470 (2000).
12. M. Tsubouchi, B. Whitaker, L. Wang, *et al.*, Phys. Rev. Lett. **86**, 4500 (2001).
13. L. Quaglia, M. Brewczyk, and C. Cornaggia, Phys. Rev. A **65**, 031404(R) (2002).
14. H. Stapelfeldt and T. Seideman, Rev. Mod. Phys. **75**, 543 (2003).
15. M. Yu. Emelin, M. Yu. Ryabikin, A. M. Sergeev, *et al.*, Pis'ma Zh. Éksp. Teor. Fiz. **77**, 254 (2003) [JETP Lett. **77**, 212 (2003)].
16. B. Friedrich and D. Herschbach, Phys. Rev. Lett. **74**, 4623 (1995).
17. L. Cai, J. Marango, and B. Friederich, Phys. Rev. Lett. **86**, 775 (2001).
18. B. A. Zon and B. G. Katsnel'son, Zh. Éksp. Teor. Fiz. **69**, 1166 (1975) [Sov. Phys. JETP **42**, 595 (1975)].
19. V. P. Makarov and M. V. Fedorov, Zh. Éksp. Teor. Fiz. **70**, 1185 (1976) [Sov. Phys. JETP **43**, 615 (1976)].
20. N. B. Delone, V. P. Kraĭnov, and M. E. Sukharev, Tr. Inst. Obshch. Fiz. Ross. Akad. Nauk **57**, 27 (2000).
21. M. E. Sukharev and V. P. Kraĭnov, Zh. Éksp. Teor. Fiz. **113**, 573 (1998) [JETP **86**, 318 (1998)].
22. M. E. Sukharev and V. P. Krainov, J. Opt. Soc. Am. B **15**, 2201 (1998).
23. I. Sh. Averbukh and N. F. Perel'man, Usp. Fiz. Nauk **161** (7), 41 (1991) [Sov. Phys. Usp. **34**, 572 (1991)].
24. I. Marzdi, F. Saif, I. Bialynicki-Birula, *et al.*, Acta Phys. Slov. **48**, 323 (1998).
25. D. I. Blokhintsev, *Principles of Quantum Mechanics* (Gostekhizdat, Moscow, 1949; Allyn and Bacon, Boston, 1964).
26. L. D. Landau and E. M. Lifshitz, *Course of Theoretical Physics*, Vol. 3: *Quantum Mechanics: Non-Relativistic Theory*, 3rd ed. (Nauka, Moscow, 1974; Pergamon Press, Oxford, 1977).

Translated by A. Betev

Journal of Experimental and Theoretical Physics, Vol. 98, No. 6, 2004, pp. 1098–1108.
Translated from Zhurnal Éksperimental'noĭ i Teoreticheskoĭ Fiziki, Vol. 125, No. 6, 2004, pp. 1258–1268.

ATOMS, SPECTRA, RADIATION

Photoabsorption Cross Section of the Thomas–Fermi Atom

S. F. Garanin* and E. M. Palagina

Russian Federal Nuclear Center, All-Russia Research Institute of Experimental Physics, Sarov, Nizhegorodskaya oblast, 607190 Russia

**e-mail: sfgar@vniief.ru*

Received October 8, 2003

Abstract—The photoabsorption cross section $\sigma(\omega)$ and the distribution of oscillator strengths $df/d\omega$ [these values are related as $\sigma = (2\pi^2e^2/mc)(df/d\omega)$] were determined for an atom with a large Z value using the semiclassical approach. These values were found for low frequencies with the use of the Vlasov kinetic equations, which were numerically solved by the method of particles. The asymptotic behavior of the distribution of oscillator strengths at high frequencies was determined by semiclassical equations for the photoabsorption cross section of electron shells in a Coulomb potential. The asymptotic equations were used to suggest an interpolation equation for the distribution of oscillator strengths over the whole Thomas–Fermi frequency range 27 eV $\ll \hbar\omega \ll 27Z^2$ eV. This equation was used to calculate the logarithmic mean excitation energy, which appears in problems of ionization loss of charged particles. The distribution of oscillator strengths in a neutral atom allows the radiative properties of dense matter to be determined. © *2004 MAIK "Nauka/Interperiodica".*

1. INTRODUCTION

Calculations of the photoabsorption cross section as a function of frequency $\sigma(\omega)$ or the distribution of oscillator strengths $df/d\omega$ (these values are related by the equation

$$\sigma = \frac{2\pi^2e^2}{mc}\frac{df}{d\omega} \tag{1}$$

[1]) in multielectron atoms are very complex and often performed in the static approximation; that is, it is assumed that the potential in which each of the electrons moves is constant, and field screening caused by the dynamic polarization of the other electrons is ignored (e.g., see [2]). For frequencies ω lower than or on the order of the characteristic frequency of rotation of most of the electrons in heavy atoms $Zme^4/\hbar^3$ [3] (Z is the atomic number), the error then amounts to a value on the order of one, although the problem contains the small parameter Z^{-1} used in the Thomas–Fermi or Hartree–Fock approximation.

Dynamic polarization was included in calculations of the photoeffect cross section in statistical models of atoms in [4], where polarizability was taken into account using the local electron density in an atom, and in [5] with the use of the Bloch hydrodynamic approach to spatial charge oscillations in the Thomas–Fermi atom.[1] Both these approaches are, however, model in character and lack consistent theoretical substantiation, although they predict reasonable behavior of $\sigma(\omega)$ and satisfy the sum rule. In particular, the applicability of the hydrodynamic approach would require characteristic distances traversed by electrons during spatial charge oscillations (effective range) to be small compared with characteristic distances (distances from the nucleus). The frequency range to which electrons at some distance r from the nucleus contribute is, however, determined by the relation $\omega \sim v/r$ (v is the velocity of electrons). It follows that their path in motion at frequency ω is on the order of the characteristic distance. For this reason, although these approaches determine the power dependences $\sigma(\omega = 0) = \text{const}$ and $\sigma(\omega \longrightarrow \infty) \sim 1/\omega^2$, which are correct for Thomas–Fermi atoms in the limiting cases of low and high (compared with $Zme^4/\hbar^3$) frequencies, the coefficients of these dependences are generally incorrect.

In this work, we use a consistent kinetic approach based on the smallness parameter Z^{-1} to obtain correct asymptotic equations for these limiting cases.

Note that fairly accurate experimental and theoretical data on photoabsorption cross sections taking into account particular electronic structure details are currently available for many elements. Our analysis gives a universal approach to describing cross sections for arbitrary heavy elements; in particular cases, the accuracy of describing cross sections decreases. The results obtained in this work can be helpful for estimating cross sections in the frequency ranges (especially at low frequencies) where polarization effects play an important role, because including these effects in direct quantum-mechanical calculations involves serious difficulties.

Knowledge of the distribution of oscillator strengths for a cold atom allows not only its photoabsorption cross section to be found but also the radiative proper-

[1] Recently, a review of polarization effects on atomic transitions was published [6].

ties of dense matter to be determined. This is shown in Section 6.

The accuracy of the developed approach, which is based on the Thomas–Fermi model, can be estimated as follows. The individual properties of some substance and, accordingly, particular transitions can introduce relative deviations from the statistical Thomas–Fermi description of the cross section on the order of $1/n$, where n is the characteristic quantum number, which is supposed to be large for the semiclassical description of the motion of electrons and photoabsorption to be possible. At low frequencies, $1 < \omega < Z$ (in atomic units), n can be estimated as $n \sim \omega^{1/3}$; therefore, the accuracy of the description is estimated as $\omega^{-1/3}$. At high frequencies, $Z^{1.4} < \omega < Z^2$, we have $n \sim Z/\omega^{1/2}$ (see Section 4), and the accuracy of the description is estimated[2] as $\omega^{1/2}/Z$. For values integral over the spectrum such as the logarithmic mean excitation energy (Section 5) or the intensity of radiation from dense matter (Section 6), details of the electronic structure of elements will be averaged, and we can then expect the usual semiclassical accuracy of about n^{-2}, which corresponds to relative quantum and exchange corrections of $Z^{-2/3}$ [7, 8]. Although the asymptotic behaviors of photoabsorption in the limiting cases of low and high frequencies cannot be used to determine the photoabsorption cross sections of particular elements in these limiting cases, they are necessary for constructing photoabsorption cross sections over the whole Thomas–Fermi frequency range $1 < \omega < Z^2$. In addition, the low- and high-frequency asymptotics can be helpful for estimating cross sections in the intervals $1 \ll \omega \ll Z$ and $Z \ll \omega \ll Z^2$, respectively.

2. EQUATIONS FOR THE DISTRIBUTION FUNCTION OF ATOMIC ELECTRONS IN AN ELECTROMAGNETIC WAVE FIELD

We use the atomic units $e = \hbar = m = 1$.

As the motion of electrons in a heavy atom is semiclassical (with an accuracy to $Z^{-2/3}$), they can be described by the classical distribution function f and the Vlasov equations

$$\frac{\partial f}{\partial t} + \mathbf{v}\cdot\frac{\partial f}{\partial \mathbf{r}} + \nabla\varphi\cdot\frac{\partial f}{\partial \mathbf{p}} = 0,$$

$$\Delta\varphi = -4\pi\rho, \qquad (2)$$

$$\rho = -\int f d^3p,$$

where φ is the electric field potential.

[2] We will not give more complex accuracy estimates for intermediate frequencies $Z < \omega < Z^{1/4}$. Only note that the lowest error of about $Z^{-5/9}$ is obtained at frequencies on the order of $\omega \sim Z^{4/3}$.

The electric field of an incident electromagnetic wave is considered low compared with atomic fields. Let us linearize (2) with respect to the incident wave field **E** and use the equilibrium distribution function of electrons, which, for a neutral atom, is

$$f_0 = \frac{\eta(-\varepsilon)}{4\pi^3}, \qquad (3)$$

where

$$\varepsilon = \frac{p^2}{2} - \varphi_0(r)$$

is the total energy of an electron in the Thomas–Fermi potential $\varphi_0(r)$ and $\eta(-\varepsilon)$ is the Heaviside step function. In (3), it is taken into account that each phase space cell can be occupied by two electrons. As a result, we obtain

$$\frac{\partial f_1}{\partial t} + \mathbf{v}\cdot\frac{\partial f_1}{\partial \mathbf{r}} + \nabla\varphi_0\cdot\frac{\partial f_1}{\partial \mathbf{p}} = -\nabla\varphi_1\cdot\frac{\partial f_0}{\partial \mathbf{p}}, \qquad (4)$$

$$\Delta\varphi_1 = -4\pi\rho_1, \qquad (5)$$

$$\rho_1 = -\int f_1 d^3p, \qquad (6)$$

where index "0" labels equilibrium values, and "1" is for perturbed values. As the wavelength of incident radiation is large compared with the size of an atom, **E** is considered constant at infinity.

To numerically solve kinetic equation (4) by the method of particles, we interpret this equation as follows: its left-hand side describes particle motions in a Thomas–Fermi potential, and the right-hand side corresponds to the creation of particles, electrons if $f_1 > 0$ and holes if $f_1 < 0$. It should be borne in mind that, although holes make a positive contribution to charge density (6), their motion according to (4) occurs in the same potential as the motion of electrons.

Substituting the equilibrium distribution function (3) into the term that describes the creation of particles in (4) yields

$$-\nabla\varphi_1\cdot\frac{\partial f_0}{\partial \mathbf{p}} = \delta(\varepsilon)\frac{\mathbf{p}\cdot\nabla\varphi_1}{4\pi^3}. \qquad (7)$$

This means that electrons and holes are created with zero energy and have a Lambert distribution of exit angles; holes fly out along the field, and electrons, against it. The rate of electron and hole creation in unit volume is

$$\frac{dn}{dt} = \frac{|\nabla\varphi_1|}{4\pi^2}p_F^2 = \frac{|\nabla\varphi_1|}{2\pi^2}\varphi_0, \qquad (8)$$

where p_F is the boundary Fermi distribution momentum.

As the φ_1 potential in our problem can only depend on two vectors, **E** and **r**, and φ_1 should linearly depend on the **E** vector, φ_1 takes the form

$$\varphi_1 = -(\mathbf{E}\cdot\mathbf{r})\psi(r).$$

Here, $\psi(r \longrightarrow \infty) = 1$, because the electric field at infinity is **E**. By virtue of Poisson equation (5), the charge density ρ_1 also has the form

$$\rho_1 = (\mathbf{E}\cdot\mathbf{r})R(r).$$

We can therefore use (5) to obtain a relation between the total dipole moment of particles *P* within a certain radius *r* and ψ', namely,

$$P = \frac{E}{3}\int_0^r 4\pi R r^2 dr = \frac{E}{3}r^4\psi'. \quad (9)$$

The total dipole moment induced on the atom determines the behavior of $\psi(r)$ at infinity,

$$\psi(r \longrightarrow \infty) = 1 - \frac{P}{Er^3}.$$

The photoabsorption cross section that we are interested in can be found as the ratio between the *q* energy absorbed by the atom and the energy flux that passes through the unit area,

$$\sigma = \frac{q}{\int\frac{cE^2}{4\pi}dt}. \quad (10)$$

Here, the time dependence of the electric field at a given frequency has a sinusoidal oscillatory character, and the integral in the denominator and the numerator should generally be considered over an arbitrarily long time interval including an infinite number of oscillation periods.

Let us relate the dipole moment to the energy *q* absorbed by the atom. The *dq* energy absorbed by the atom during a short time interval *dt* comprises two parts [9], namely, the work done on charges

$$dq_J \equiv dt\int -\nabla\varphi_1\cdot\mathbf{j}dV,$$

where **j** is the current density, and the change in the electrostatic energy

$$dq_C = \int\frac{1}{4\pi}\mathbf{E}'\cdot d\mathbf{E}'dV, \quad (11)$$

where $\mathbf{E}' = -\nabla\varphi_1 - \mathbf{E}$ is the field of induced charges and $d\mathbf{E}'$ is the change in this field during time *dt*.

Let us transform dq_J by transferring the sign of ∇ to **j**,

$$dq_J = dt\int\varphi_1 \mathrm{div}\,\mathbf{j}dV,$$

and use first the continuity equation and then the Poisson equation to obtain

$$dq_J = -\int\frac{\varphi_1}{4\pi}\mathrm{div}d\mathbf{E}'dV. \quad (12)$$

Summing (11) and (12) yields the energy absorbed by the atom in time *dt*,

$$dq = \frac{1}{4\pi}\int\mathbf{E}'\cdot d\mathbf{E}'dV - \frac{1}{4\pi}\int\varphi_1\mathrm{div}d\mathbf{E}'dV.$$

Let us represent field **E** in the form $\mathbf{E} = \nabla(Ez)$ (we assume that **E** is directed along the *z* axis) and use the identity $\varphi_1 \equiv \varphi_1 + Ez - Ez$. The last equation can then be rewritten as

$$dq = -\frac{1}{4\pi}\int\nabla(\varphi_1 + Ez)\cdot d\mathbf{E}'dV$$

$$-\frac{1}{4\pi}\int(\varphi_1 + Ez)\mathrm{div}d\mathbf{E}'dV + \frac{E}{4\pi}\int z\mathrm{div}d\mathbf{E}'dV.$$

Combining the first two integrals yields

$$dq = -\frac{1}{4\pi}\int\mathrm{div}((\varphi_1 + Ez)d\mathbf{E}')dV + E\int zd\rho_1 dV.$$

The first integral reduces to the integral over an infinitely distant surface and disappears at infinity. The second integral gives the increment of the dipole moment. We eventually find that $dq = EdP$.

The total energy absorbed by the atom in time *t* is found by the equation

$$q = \int EdP. \quad (13)$$

If we know the time dependence of the dipole moment of the atom, we can use (10) and (13) to calculate the photoabsorption cross section.

3. THE LOW-FREQUENCY LIMIT OF THE DISTRIBUTION OF OSCILLATOR STRENGTHS

3.1. Simplifications in the Low-Frequency Limit

At low frequencies $\omega \ll Z$, the major contribution to oscillator strengths is made by electrons at large distances $r \gg Z^{-1/3}$ from the nucleus. The asymptotic behavior of the Thomas–Fermi function at large dis-

tances has the form $\chi = 144/x^3$, and the asymptotic behavior of the potential is described by the equation

$$\varphi_0 = \frac{81\pi^2}{8r^4}. \quad (14)$$

The motion of zero-energy electrons (and holes) in such a potential is described by simple analytic equations. Their trajectories are circles passing through the center.

The next simplification that can be used in the low-frequency limit is based on the independence of the absorption cross section from frequency in this limit. It follows that the cross section can be found using an electromagnetic wave with an arbitrary time dependence. A wave with a rectangular profile, electric field amplitude E, and time t can conveniently be considered. Equation (13) for the energy q is then written in the form

$$q = EP,$$

and the distribution of oscillator strengths, in the form

$$\frac{df}{d\omega} = \frac{2}{\pi}\frac{P}{Et}. \quad (15)$$

One more simplification follows from (4)–(6); this is the self-similar dependence

$$\psi\left(\frac{r}{t^{1/3}}\right), \quad (16)$$

and, accordingly, a linear time dependence of the dipole moment, as required for calculating the distribution of oscillator strengths by (15).

3.2. The Method for Numerical Calculations

3.2.1. Creation of Particles

Kinetic equation (4) is integrated by the method of particles.

In the language of particles, the right-hand side of (4) corresponds to the creation of pairs of particles, electrons (if the right-hand side is larger than zero) and holes (if the right-hand side is smaller than zero). A random number generator is used to obtain random initial coordinates of holes and electrons and their exit angles. If the created particles are assigned weight wE, then, according to (8), the number of electrons (and holes) created in unit time is

$$\frac{dN}{dt} = \frac{1}{wE}\int\frac{dn}{dt}dV = \frac{81\pi}{4w}\int_0^\infty\frac{\beta(r)}{r^2}dr, \quad (17)$$

where $\beta(r)$ is the angle-average electric field modulus (to simplify equations, we assume that $E = 1$),

$$\beta(r) = \int_0^{\pi/2}|\nabla\varphi_1|\sin\theta d\theta$$

$$= \int_0^{\pi/2}\sqrt{\psi^2 + (2r\psi\psi' + r^2\psi'^2)\cos^2\theta}\sin\theta d\theta.$$

If ψ = const, which corresponds to an electric field constant over space (if polarization-induced screening is absent, the field is constant, and this is so at the initial time moment), then β = const and integral (17) diverges at small radii. For integral (17) to converge, it is necessary that the condition $\psi \propto r^\alpha$, where $\alpha > 1$, be satisfied. Our studies of the behavior of the distribution function at short distances, however, showed that solutions with $\psi \propto r^\alpha$, where $\alpha < 1$, are possible, and numerical calculations (Section 3.3) substantiated that such solutions did exist. For this reason, we had to perform numerical calculations with the integral of the creation of particles that diverged at short distances and cut this integral at some radius $r = r_0$. As the particles created at a small radius made a negligible contribution to the dipole moment [according to (9), $P \propto r_0^{3+\alpha}$], this could not have a noticeable effect on the results. In reality, the r_0 value was successively decreased from one calculation to another during refinement (as calculations with an ever increasing number of particles were performed), which ensured the passage to the $r_0 = 0$ limit. The procedure for cutting off the potential was as follows: the $\psi(r_0)$ potential was determined by solving the Poisson equation, and, at $r < r_0$, it was assumed that

$$\psi(r) = \psi(r_0)\left(\frac{r}{r_0}\right)^2.$$

It was taken that $\psi(r_0) = 1$ at the initial time.

The time step Δt selected for numerical calculations was such that one pair of particles (an electron and a hole) were created during time Δt.

The probability density of the creation of a pair of particles in volume $dV = r^2\sin\theta dr d\theta d\varphi$ is

$$p = \frac{dn}{wdN} = \frac{\sqrt{\psi^2 + (2r\psi\psi' + (r\psi')^2)\cos^2\theta}}{4\pi r^4\int_0^\infty\frac{\beta(r)}{r^2}dr}.$$

As p is independent of φ, the probability of the creation of a pair of particles in the interval of radii from r

to $r + dr$ and in the interval of angles from θ to $\theta + d\theta$ is

$$p(r, \theta)drd\theta = 2\pi r^2 \sin\theta p drd\theta.$$

Hence we obtain the probability distribution of the creation of particles over radii,

$$p_r = \int_0^\pi p(r, \theta)d\theta = \frac{\beta(r)}{r^2\int_0^\infty \frac{\beta(r)}{r^2}dr}, \quad (18)$$

and over angles (at a given radius),

$$p_\theta = \frac{p(r, \theta)}{p_r} = \frac{\sqrt{\psi^2 + (2r\psi\psi' + (r\psi')^2)\cos^2\theta}}{2\beta(r)}\sin\theta. \quad (19)$$

In the calculations, particle creation probabilities were generated by (18) for radii and (19) for angles. The exit angle of a particle with respect to the field was drawn based on the Lambert distribution according to (7).

3.2.2. The Motion of Particles

Let us introduce a polar system of coordinates in the plane of particle motion. The potential energy of a particle has the form $U(r) = -a/r^4$, and the total energy is $\varepsilon = 0$. When a particle moves in a central field, the radius and angle ϕ are related as [10]

$$\phi + C_1 = \int \frac{\frac{M}{r^2}dr}{\sqrt{2[\varepsilon - U(r)] - \frac{M^2}{r^2}}},$$

where $m = 1$ is the mass of the particle, M is the angular momentum, and C_1 = const. This gives the trajectory equation

$$r = \frac{\sqrt{2a}}{M}\cos(\phi + C_1).$$

Let us use the notation $\sqrt{2a}/M = 2R$ and select C_1 in such a way that $r = 2R$ at $\phi = 0$. The last equality can then be rewritten as

$$r = 2R\cos\phi. \quad (20)$$

This is the equation of a circle of radius R that passes through the origin. After a particle falls onto the center because of the Coulomb behavior of the potential at short distances, it flies out of the center in the same direction as it fell, and then again moves in a circle. As a result, its trajectory is two tangent circles that form a figure eight.

Using (20) and the equation that relates the radius and time for motion in a central field [10]

$$t + C_2 = \int \frac{dr}{\sqrt{2[\varepsilon - U(r)] - \frac{M^2}{r^2}}},$$

we obtain the time dependence of the angle for $\varepsilon = 0$,

$$t = \frac{a}{2M^3}(\chi + \sin\chi) \equiv \frac{T}{2\pi}(\chi + \sin\chi), \quad (21)$$

where $\chi = 2\phi$, the angle χ is counted in the direction of hole motion, and the period of particle rotation is

$$T = \frac{a\pi}{M^3}$$

(in reality, the period of a particle that moves along the figure eight is $2T$). As $a = 81\pi^2/8$, the period T expressed at $\varepsilon = 0$ through the circle radius R is written as

$$T = \frac{8R^3}{9}. \quad (22)$$

The initial particle coordinates and exit angles with respect to the field obtained by drawing probabilities can be used to find the trajectory of a particle in the three-dimensional space as a function of the χ parameter. The χ angle itself at arbitrary time t is found from (21). It follows that all particle coordinates can be calculated at arbitrary time t.

3.2.3. The Solution of the Poisson Equation

The potential was numerically calculated using a grid along the radius with step h. The potential cutoff radius r_0 was usually $r_0 = 2h$.

The dipole moment $P(r_i)$ was calculated by summing the contributions of all particles at every grid point. For a particle whose current radius was in the interval $[r_i, r_{i+1}]$ and equaled $r = r_i + \mu h$ $(0 < \mu < 1)$, the zw value of this particle corresponding to its contribution to the dipole moment was projected onto point r_i with the weight $1 - \mu$ and onto point r_{i+1} with the weight μ. All the particles projected onto point r_i created a dipole moment increment at this point. The dipole moment $P(r)$ accumulated for the current radius was obtained by summing all these increments up to this radius.

The integration of (9) with the boundary condition $\psi(r_\infty) = 1$ was performed to find the $\psi(r)$ dependence over the whole space taking into account the interpola-

tion of $\psi(r)$ to the boundary condition $\psi(0) = 0$ (see above).

3.3. Numerical Results

The dependences of P/t and ψ on the self-similar variable $\zeta = r/t^{1/3}$ obtained in the calculations with $w = 0.00001$, $r_0 = 0.016$, and $h = 0.008$ after the creation of 84000 pairs of particles (this corresponded to the total time $t = 1.01 \times 10^{-3}$) are shown in Fig. 1.

According to Fig. 1 and (22), the major contribution to the total dipole moment is made by distances from the nucleus at which the rotation period of particles created in this region is several times larger than time t. The calculations also show that, at small radii, the $\psi(r)$ function behaves irregularly, but decreases fairly slowly as the radius becomes smaller, certainly slower than r^3, as according to the dependence obtained using the polarization of the potential of the static Thomas–Fermi equation. It follows that the kinetics significantly changes the behavior of screening at small radii. The estimate obtained from the dependence of the number of created particles on time $N \propto t^{1-\alpha/3}$, which follows from the self-similar dependence (16) and the behavior of the potential at small radii, namely, $\psi \propto r^\alpha$, gives the exponent $\alpha \approx 0.5$ for the power dependence $\psi \propto r^\alpha$ at small radii. This exponent is within the interval of its admissible values $0 < \alpha < 1$ obtained in our analytical calculations.

The time dependence of the P/t value for the whole atom obtained in our calculations is shown in Fig. 2. The P/t value tends to a constant of 27.11 ± 0.09 as time passes (the oscillations of P/t are explained by fluctuations).

Our calculations show that fluctuations decrease and the results become more accurate as the number of particles increases and we pass to finer grids and simultaneously reduce the smoothing parameters. Some of the results of calculations performed with different particle weights w up to time $t = 0.001$ are summarized in the table.

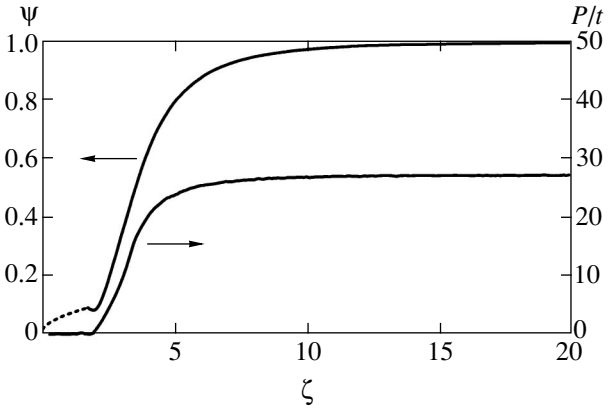

Fig. 1. Dependences of P/t and ψ on self-similar variable $\zeta = r/t^{1/3}$ obtained in numerical calculations.

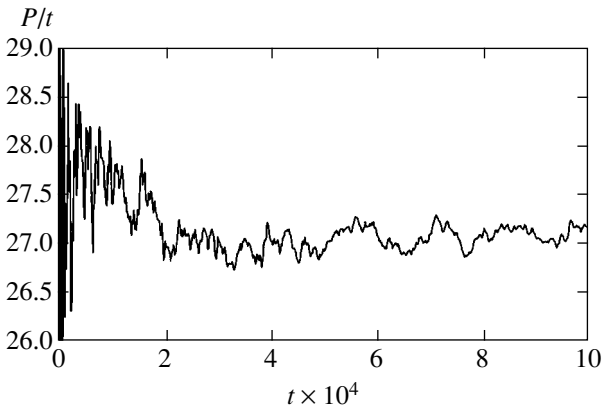

Fig. 2. Time dependence of P/t.

Using the tabulated data on P/t, we can estimate the P/t value taking into account possible errors as

$$\frac{P}{t} = 27.12 \pm 0.09.$$

The low-frequency limit of the distribution of oscil-

Table

Particle weight w	Number of created particles N	r_0	Maximum radius R at which potential ψ fluctuations exceeding 30% are observed	α	P/t
0.00020	14000	0.025	0.275	0.35	29.0 ± 0.6
0.00010	20500	0.025	0.225	0.23	27.3 ± 0.4
0.00005	36000	0.02	0.260	0.05	26.8 ± 0.3
0.00002	46000	0.016	0.208	0.58	27.13 ± 0.09
0.00001	84000	0.016	0.176	0.5	27.11 ± 0.09

lator strengths corresponding to this P/t value is

$$\frac{df}{d\omega} = 17.3. \quad (23)$$

This value is 1.21 times lower than that calculated by us using the hydrodynamic approach developed in [5].[3] It follows that the hydrodynamic approach [5] overestimates the limiting value of the distribution of oscillator strengths. It can be thought that, at nonzero low frequencies, the $df/d\omega$ values in [5] are also exaggerated, although to a lesser extent than at zero frequency, because the sum rule for oscillators, $\int df = Z$, is satisfied in the hydrodynamic approach.

4. THE HIGH-FREQUENCY LIMIT OF THE DISTRIBUTION OF OSCILLATOR STRENGTHS

At high frequencies $\omega \gg Z$, the influence of polarization is insignificant and the potential in which electrons that contribute to oscillator strengths move can be considered Coulomb. This situation can most easily be analyzed using the well-known equations for photoabsorption cross sections in a Coulomb potential [1].

The electron photoionization cross section in a Coulomb field from the level with the principal quantum number n is [1]

$$\sigma_n = \frac{8\pi}{3\sqrt{3}c\omega^3 n^5}\frac{Z^4}{}. \quad (24)$$

Let us multiply (24) by $2n^2$ (the number of electrons in shell n) and integrate it in n from the lowest possible principal quantum number to infinity for

$$\frac{Z^2}{2n^2} = \omega$$

(no transitions from lower n can occur because such transitions would be to discrete levels, which are occupied in a neutral atom). This gives the total photoabsorption cross section

$$\sigma = \frac{16\pi}{3\sqrt{3}c\omega^2}\frac{Z^2}{}$$

and, accordingly, the asymptotic behavior of the distribution of oscillator strengths at high frequencies,

$$\frac{df}{d\omega} = \frac{8}{3\sqrt{3}\omega^2}\frac{Z^2}{}. \quad (25)$$

It should be mentioned that this distribution of oscillator strengths was in essence used earlier [11] to calculate emission from multicharged ions but was obtained by a different method.

The coefficient in dependence (25) is 1.59 times larger than a similar coefficient obtained in [5].[4] As the $df/d\omega$ value decreases compared with the hydrodynamic approximation in the low-frequency limit, we arrive at the conclusion that taking the kinetics of the motion of electrons into account shifts the distribution of oscillator strengths to higher frequencies.

5. THE INTERPOLATION EQUATION FOR THE DISTRIBUTION OF OSCILLATOR STRENGTHS AND THE LOGARITHMIC MEAN EXCITATION ENERGY

The photoabsorption cross sections $\sigma(\Omega)$ for frequencies $\Omega = \omega/Z$ from the interval [0.03, 12] were calculated in [5] using the hydrodynamic approach. The corresponding distribution of oscillator strengths can be found by (1). The low-frequency asymptotic distribution of oscillator strengths $df/d\omega$ obtained in [5] exceeds our value (23), whereas at high frequencies, the coefficient in the asymptotic equation

$$\frac{df}{d\omega} = \frac{0.31}{\Omega^2}$$

is 1.59 times smaller than our coefficient in (25). This leads us to conclude that the hydrodynamic approach underestimates oscillator frequencies. Let us introduce the value

$$F = \frac{1}{Z}\int_0^\omega \frac{df}{d\omega}d\omega,$$

which is the number of oscillators below a given frequency. If exact asymptotic functions differed from the hydrodynamic functions [5] by the same factor k at low and high frequencies, it would be possible to obtain a function with correct asymptotic behavior using cross sections from [5] and transforming the corresponding F

[3] Low-frequency limit calculations in [5] contain an error, which results in the neglect of electron gas polarization and a strong (by a factor of 2.3) exaggeration of the low-frequency limit of $df/d\omega$ compared with correct calculations according to the hydrodynamic approach.

[4] Note that this ratio is close to the ratio between the zero sound velocity [12] in a Fermi gas and the hydrodynamic velocity ($\sqrt{3}$). The elastic properties of the electron gas are determined by the zero sound velocity. Possibly, taking them into account, which appears appropriate for a collisionless gas, would improve the results of the hydrodynamic approach [5]. For instance, the low-frequency limit of $df/d\omega$ would then exceed the exact value given by (23) by as little as 4%.

value as $F(\omega) \longrightarrow F(\omega/k)$. We could even hope to obtain a more accurate description also for intermediate frequencies, because the shortcomings of the hydrodynamic approach in the limiting cases would then be removed. As the oscillator strengths were calculated in [5] for the frequency range far from the low-frequency limit, we will attempt to improve the description of the distribution function of the number of oscillators using the k value obtained at high frequencies.

Thus, if we know the $F(\Omega)$ function from [5], a change in the frequency by the formula $\Omega \longrightarrow 1.59\Omega$ causes the $df/d\omega$ function to transform as

$$\frac{df}{d\omega}(\Omega) \longrightarrow \frac{1}{1.59}\frac{df}{d\omega}\left(\frac{\Omega}{1.59}\right). \quad (26)$$

The new $df/d\omega$ values should satisfy our asymptotic equation at high frequencies (25). The lowest frequency at which the photoabsorption cross section was calculated in [5], $\Omega = 0.03$, is fairly far from the low-frequency limit. We will therefore try to construct an interpolation formula for F using the values from [5] transformed according to (26) and our asymptotic functions at low and high frequencies. We selected the interpolation function

$$F(\Omega) = \frac{17.3\Omega + C_1\Omega^3}{1 + C_2\Omega^{0.4} + C_3\Omega + C_4\Omega^2 + C_1\Omega^3}, \quad (27)$$

where the coefficient 17.3 is determined by the low-frequency asymptotic function (23) and the high-frequency asymptotic function (25) gives the relation $C_1 = 2.04C_4$. The $df/d\omega$ value is then found by the equation

$$\frac{df}{d\omega} = F'(\Omega). \quad (28)$$

The coefficients C_1, C_2, and C_3 in (27) were adjusted by the method of least squares to shift the $df/d\omega = F'(\Omega)$ values toward the $df/d\omega$ values from [5] transformed according to (26). This adjustment gave

$$C_1 = 55.7, \quad C_2 = 11.2, \quad C_3 = 6.6, \quad C_4 = 27.3.$$

The $df/d\omega$ values reported in [5] and calculated by interpolation equation (27) are shown in Fig. 3 (the dashed line shows the asymptotic dependence at low frequencies).

The logarithmic mean excitation energy, which appears in problems of ionization loss of charged particles [3], is calculated by the equation

$$\ln I = \ln Z + \int_0^\infty \frac{df}{d\omega}\ln\Omega d\Omega. \quad (29)$$

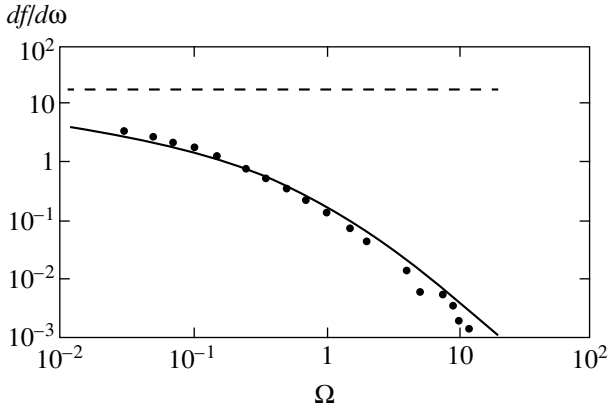

Fig. 3. Distributions of oscillator strengths from [5] (solid circles) and calculated by interpolation equation (27) (solid line); the dashed line is the low-frequency asymptotic obtained in this work.

Substituting $df/d\omega$ from (27) and (28) into (29) yields $I = 8.3Z$ eV, which is closer to the range of experimental values $I/Z = 9.5$–16 eV [13] than the $I/Z = 4.95$ eV value from [5].

6. THE USE OF THE DISTRIBUTION OF OSCILLATOR STRENGTHS IN A NEUTRAL ATOM FOR DETERMINING THE RADIATIVE PROPERTIES OF DENSE MATTER

The degree of ionization of a dense plasma is determined by the Saha equation with multiple ionization [1],

$$I(z + 0.5) = T\ln\left[\frac{2}{zn_Z}\left(\frac{T}{2\pi}\right)^{3/2}\right], \quad (30)$$

where z is the degree of ionization, I is the ionization potential, n_Z is the density of ions, and T is the temperature. In a fairly dense plasma, $I \sim T$. For this reason, in the Thomas–Fermi atom at low temperatures $1 \ll T < Z$, the major contribution to the range of oscillator strengths of interest to us $\omega \sim T$ is made by electrons that fly past at such distances r from the nucleus at which the rotation period is on the order of ω. As we are considering the case $\omega < Z$, the rotation frequency of electrons depends on r as $\omega \sim 1/r^3$ and the major contribution to these frequencies is made by the regions of the atom

$$r_\omega \sim 1/\omega^{1/3} \sim 1/T^{1/3} \ll r_I \sim 1/I^{1/4}. \quad (31)$$

These regions are not involved in ionization, which comes into play at distances $r_I \sim 1/T^{1/4}$. It follows that the distribution of oscillator strengths of a cold Thomas–Fermi atom should be valid at these frequencies.

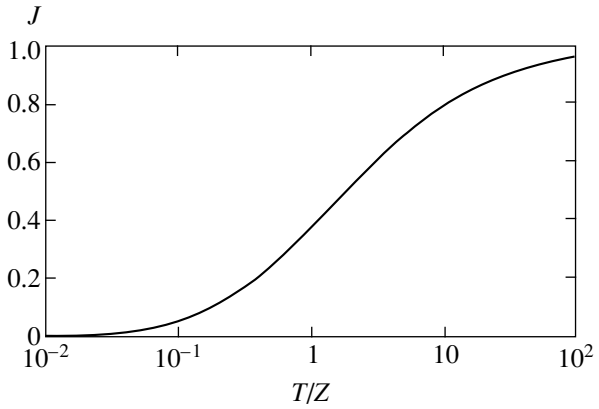

Fig. 4. Intensity of radiation of dense plasma ions as a function of temperature.

At high temperatures $Z \ll T < Z^2$, r_ω and r_I can be estimated by the Coulomb equations

$$\omega \sim \frac{\sqrt{Z}}{r_\omega^{3/2}}, \quad I \sim \frac{Z}{r_I}.$$

The major contribution to the $\omega \sim T$ range of oscillator strengths is then also made by electrons that fly past the nucleus at the distances

$$r_\omega \sim \frac{Z^{1/3}}{T^{2/3}} \ll r_I \sim \frac{Z}{I} \tag{32}$$

not involved in ionization. It follows that, at these frequencies also, the distribution of oscillator strengths of a cold Thomas–Fermi atom should be valid. The distribution of oscillator strengths of a cold Thomas–Fermi atom should therefore determine the true absorption coefficient κ'_ω (the absorption coefficient corrected for stimulated emission) of a fairly dense substance at arbitrary temperatures. Using (1) and passing to the usual units, we can write

$$\kappa'_\omega = n_Z \sigma = \frac{2\pi^2 e^2 n_Z}{mc} \frac{df}{d\omega}. \tag{33}$$

The spectral intensity of radiation of ions J_ω is related to κ'_ω by the equation (in the usual units)

$$J_\omega = \frac{\hbar \omega^3}{\pi^2 c^2 \left(\exp \frac{\hbar \omega}{T} - 1 \right)} \kappa'_\omega \tag{34}$$

and, like κ'_ω (33), is proportional to the density. When using (33) and (34) for calculating the radiative characteristics of substances, it should be borne in mind that, as we use the semiclassical approach, the spectra (33) and (34) are continuous and smoothed over a large number of lines. For this reason, when, for instance, the Rosseland mean free paths are calculated, for which the discrete character of spectra is essential, the use of (33) can only give the lowest mean free paths estimate, because the major contribution to the Rosseland mean free paths is made by regions of maximum transparency.

At high temperatures $T \gg Z$, the distribution of oscillator strengths should be calculated by (25), which allows the radiative plasma characteristics reported in [11] to be obtained. In particular, the intensity of radiation of ions is proportional to T^2 in this limit.

At low temperatures $T \ll Z$, we have $df/d\omega \longrightarrow$ const and the spectral intensity of radiation of ions (34) coincides in form with the spectral intensity of blackbody radiation. Accordingly, the intensity of radiation of ions is proportional to T^4 in this limit. Note that, because the $df/d\omega \longrightarrow$ const limit is only attained at very low frequencies, the transition to the T^4 dependence of radiation intensity also occurs only at exceedingly low temperatures.

The dependence of the total intensity of radiation of ions for $df/d\omega$ from (27) and (28) on the temperature T/Z is shown in Fig. 4. The intensity of radiation of ions J is expressed in the units

$$\frac{8\pi}{9\sqrt{3}} \frac{e^6}{\hbar^4 c^3} Z^2 n_Z T^2.$$

Note that we can actually use (33) with the Thomas–Fermi $df/d\omega$ value to determine the radiative characteristics of substances only at very high densities. This requires that the characteristic distances r_ω for the electrons with the $\omega \sim T$ rotation frequency be small compared with the r_I distances determined by the ionization potential (30). Equations (31) and (32) at low and high temperatures, respectively, Eq. (30), and the relations between I and z at small and large z,

$$I \sim z^{4/3} \quad \text{for} \quad z \ll Z,$$

$$I \sim \frac{Z^2}{(Z-z)^{2/3}} \quad \text{for} \quad Z - z \ll Z,$$

can be used to find the conditions of the applicability of (33) with the Thomas–Fermi $df/d\omega$ value,

$$\text{for} \quad T < Z \quad T \gg \left(\ln \frac{T^{3/4}}{\sqrt{2}\pi^{3/2} n_Z} \right)^3,$$

$$\text{for} \quad T > Z \quad T \ll \frac{Z^2}{\left(\ln \frac{T^{3/2}}{\sqrt{2}\pi^{3/2} Z n_Z} \right)^3}.$$

For instance, for iron at the temperature $T = Z = 0.7$ keV, these conditions are satisfied starting with densities higher than 50 g/cm^3.

At lower densities, ionization decreases oscillator strengths and the "number" of lines in the region of $\omega \sim T$. This makes the discrete character of the spectrum essential, and the intensities of radiation may considerably decrease. A consideration of this situation at high temperatures $T \gg Z$ or $Z - z \ll Z$ (nevertheless, at $T \ll Z^2$) can be found in [14].

The results obtained in [14] can be used to suggest a convenient interpolation equation for the true absorption coefficients of a plasma. This equation gives correct results in the limit of high densities, takes into account the discrete character of the spectrum, and transforms into correct Coulomb formulas at high temperatures [14],

$$\kappa'_\omega = n_Z\sigma = \sum_{k=1}^{\infty} \frac{2\pi^2 e^2 n_Z}{mc}\frac{df}{d\omega}\omega_I \xi_k \delta(\omega - k\omega_I). \quad (35)$$

Here,

$$\xi_k \equiv \pi\sqrt{3}kJ_k(k)J'_k(k) \approx 1 - \frac{0.21775}{k^{2/3}},$$

and ω_I is the electron rotation frequency, which equals $\hbar\omega_I = 2I/n$ in a Coulomb field (I is the ionization potential). Indeed, sum (35) can be replaced by the integral in k in the limit of high densities, when the $\hbar\omega_I = 2I/n \ll I$ value is small compared with the characteristic radiation frequencies $\hbar\omega_I \sim T \sim I$; we then obtain (33). On the other hand, at high degrees of ionization, $df/d\omega$ can be replaced by the high-frequency limit (25) and we obtain the results reported in [14]. For describing a cold substance and/or photoeffect cross sections, the sum in (35) should be taken to k that corresponds to $\hbar\omega = I$ rather than to infinity and then replaced by the integral (on the assumption that $\xi_k = 1$), because these frequencies correspond to the transition to a continuous spectrum.

Assuming that

$$I = \frac{(z+1)^2}{2n^2}\frac{me^4}{\hbar^2},$$

we can obtain an equation for $\hbar\omega_I$ correct at high temperatures and correct in order of magnitude at low temperatures,

$$\hbar\omega_I = \frac{2I}{z+1}\sqrt{\frac{2I}{me^4/\hbar^2}}. \quad (36)$$

Equations (35) and (36) can give incorrect results at low temperatures for a not very dense plasma. However in this region also, a result correct in the order of magnitude can be obtained.

7. CONCLUSIONS

In this work, we suggested a method for calculating the cross section of photoabsorption of complex atoms. This method is based on solving the kinetic equation by the method of particles.

We found that, in the low-frequency limit, the distribution of oscillator strengths of the Thomas–Fermi atom tends to the constant

$$\frac{df}{d\omega} = 17.3\frac{\hbar^3}{me^4}.$$

It was shown that, when an electric field is applied to a neutral atom, field screening at small radii in the kinetic problem is weaker than in the stationary (hydrodynamic) problem.

The asymptotic behavior of the distribution of oscillator strengths at high frequencies is described by the equation

$$\frac{df}{d\omega} = \frac{8}{3\sqrt{3}\pi\omega^2}\frac{Z^2 me^4}{\hbar^3}.$$

We used the results obtained in [5], the sum rule, and asymptotic equations (23) and (25) to suggest an interpolation formula for the distribution of oscillator strengths over the whole frequency range. The logarithmic mean excitation energy, which appears in problems of ionization loss of charged particles, calculated by this equation was $I = 8.3Z$ eV, which was close to the range of experimental values.

We showed that the distribution of oscillator strengths in a neutral atom could be used to determine the radiative properties of dense matter.

ACKNOWLEDGMENTS

The authors thank A.I. Golubev, S.D. Kuznetsov, V.A. Zhmaĭlo, and V.B. Yakubov for useful discussions.

REFERENCES

1. Ya. B. Zel'dovich and Yu. P. Raĭzer, *Physics of Shock Waves and High-Temperature Hydrodynamic Phenomena*, 2nd ed. (Nauka, Moscow, 1966; Academic, New York, 1966 and 1967), Vols. 1 and 2.
2. A. F. Nikiforov, V. G. Novikov, and V. B. Uvarov, *Quantum–Statistic Models of High-Temperature Plasma* (Nauka, Moscow, 2000).
3. L. D. Landau and E. M. Lifshitz, *Course of Theoretical Physics*, Vol. 3: *Quantum Mechanics: Non-Relativistic*

Theory, 2nd ed. (Fizmatgiz, Moscow, 1963; Pergamon, New York, 1977).

4. W. Brandt and S. Lundqvist, Phys. Rev. A **139**, 612 (1965).
5. J. A. Ball, J. A. Wheeler, and E. L. Firemen, Rev. Mod. Phys. **45**, 333 (1973).
6. V. A. Astapenko, L. A. Bureeva, and V. S. Lisitsa, Usp. Fiz. Nauk **172**, 155 (2002) [Phys. Usp. **45**, 149 (2002)].
7. A. S. Kompaneets and E. S. Pavlovskiĭ, Zh. Éksp. Teor. Fiz. **31**, 427 (1956) [Sov. Phys. JETP **4**, 326 (1956)].
8. D. A. Kirzhnits, Zh. Éksp. Teor. Fiz. **32**, 115 (1957) [Sov. Phys. JETP **5**, 64 (1957)].
9. L. D. Landau and E. M. Lifshitz, *The Classical Theory of Fields*, 5th ed. (Nauka, Moscow, 1967; Pergamon Press, Oxford, 1975).
10. L. D. Landau and E. M. Lifshitz, *Course of Theoretical Physics*, Vol. 1: *Mechanics*, 3rd ed. (Nauka, Moscow, 1973; Pergamon Press, Oxford, 1976).
11. S. F. Garanin, in *Proceedings of Russian Federal Nuclear Center–Institute of Experimental Physics* (Sarov, 2001), No. 1, p. 62.
12. E. M. Lifshitz and L. P. Pitaevskiĭ, *Physical Kinetics* (Nauka, Moscow, 1979; Pergamon Press, Oxford, 1981).
13. U. Fano, Annu. Rev. Nucl. Sci. **13**, 1 (1963).
14. S. F. Garanin, Teplofiz. Vys. Temp. **41**, 487 (2003) [High Temp. **41**, 421 (2003)].

Translated by V. Sipachev

Journal of Experimental and Theoretical Physics, Vol. 98, No. 6, 2004, pp. 1109–1115.
Translated from Zhurnal Éksperimental'noĭ i Teoreticheskoĭ Fiziki, Vol. 125, No. 6, 2004, pp. 1269–1275.

ATOMS, SPECTRA, RADIATION

Transition Radiation in a System of Two Cascaded Gratings

B. M. Bolotovskii and A. V. Serov

Lebedev Institute of Physics, Russian Academy of Sciences, Leninskii pr. 53, Moscow, 119991 Russia
e-mail: bolot@lpi.ru; serov@x4u.lebedev.ru

Received December 9, 2003

Abstract—Transition radiation that arises when a charged particle passes through two consecutive plane gratings is considered. The gratings are made up of parallel metal wires. The planes of the gratings are parallel to each other and perpendicular to the direction of motion of the particle. The conductors of one of the gratings are perpendicular to the conductors of the other. It is shown that the generated transition radiation has elliptic polarization; the ellipticity and the sign of rotation depend on the angle of radiation, the distance between the gratings, and the velocity of the charged particle. © *2004 MAIK "Nauka/Interperiodica".*

To diagnose and control a beam of charged particles during their acceleration, one needs continuous acquisition of information about the parameters of the beam: its trajectory, particle energy, etc. A promising method for obtaining such information is the use of transition and diffraction radiation. For this purpose, one places a thin film on the path of particles and records transition radiation generated when fast particles pass through this film. The possibility of using diffraction radiation for the diagnosis of a beam was also discussed. In this case, fast particles generate radiation when they travel near an optical irregularity, without crossing it. This method of recording leads to minimal disturbance of a beam.

It is well known that transition radiation has linear polarization. This fact was established in the first work by Ginzburg and Frank [1]. In most subsequent studies [2, 3], which dealt with various versions of transition radiation, it was also shown that transition radiation has linear polarization (except for the problem of transition radiation in the presence of a gyrotropic medium; see, for example, [4]). In the present paper, we consider the possibility of generating elliptically polarized radiation as a result of two successive processes of transition radiation in each of which linearly polarized waves are emitted. Elliptically polarized radiation is defined by several parameters: the lengths and the disposition of the axes of the polarization ellipse and the sign of rotation. Below, we will show that these parameters carry information about the energy of particles and the direction of a beam. The fact that elliptically polarized radiation depends on a greater number of parameters than linearly polarized radiation provides additional possibilities for diagnosing the parameters of the beam.

Consider a plane diffraction grating situated in the plane *xy* (Fig. 1). The grating consists of metal wires that are parallel to the *x* axis. We assume that the distance between the wires is small compared with the wavelength of the radiated wave. Such a grating can be considered as a conductive plane in which the conductivity along *x* axis is infinite and the conductivity along *y* axis is zero. A charged particle moving along the normal to the grating (along the *z* axis) crosses the grating. This gives rise to transition radiation. This radiation can be considered as radiation due to the currents induced in the wires by the traveling particle. Since all the conductors of the grating are parallel to the *x* axis, the induced currents are also parallel to the *x* axis. Hence, the vector potential describing the radiation of induced currents is also parallel to the *x* axis. Note that the problem of transition radiation in such a grating was consid-

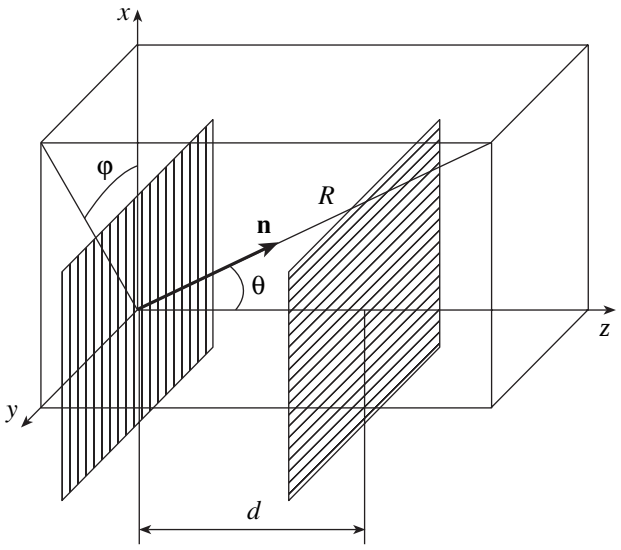

Fig. 1. Geometry of the problem. A charged particle moves along axis *z*.

ered in [5] by Barsukov and Naryshkina. The results obtained by these authors imply, in particular, that the forward small-angle transition radiation is linearly polarized and the polarization vector is indeed parallel to the wires, i.e., to the axis x in our case.

Let us place the second grating at a distance d from the first one. The planes of these gratings are parallel, while the wires of the second grating are perpendicular to those of the first grating, i.e., directed along the y axis. Both the field of the charge and the radiation field of the currents induced in the first grating are incident upon the second grating. Since the electric field radiated by the first grating is perpendicular to the conductors of the second grating, it does not induce any currents in the second grating and freely passes through it. The field of the traveling particle induces currents parallel to the y axis in the second grating, and these currents give rise to radiation in which the electric-field vector is directed along the y axis. Thus, the transmission of a charged particle through two gratings gives rise to two waves. The electric-field vectors of these waves are mutually perpendicular, while their phases differ by a quantity that depends on the distance between the gratings and the flight time. A superposition of two such waves represents an elliptically polarized wave. Below, we will determine the parameters of this wave.

Let us calculate the field generated when a charged particle passes through the first grating. Suppose that the charged particle moves along the z axis at velocity v according to the law

$$z = vt.$$

The field of a uniformly moving particle is determined by a vector potential $\mathbf{A}$ and a scalar potential φ. In the calibration adopted here, the vector potential has only one component, A_z. Let us write out the integral representation of the potentials $\mathbf{A}$ and φ as a plane-wave expansion. If we expand the potentials in time Fourier series,

$$A_z(t) = \int A_{zw}\exp(-i\omega t)d\omega, \tag{1}$$

$$\varphi(t) = \int \varphi_\omega \exp(-i\omega t)d\omega, \tag{2}$$

we then obtain the following expressions for $A_{z\omega}$ and φ_ω:

$$A_{z\omega} = \frac{q}{2\pi^2 c} \times \int \frac{\exp[i(k_x x + k_y y + (\omega/v)z)]}{k_x^2 + k_y^2 + (\omega/v)^2(1-\beta^2)}dk_x dk_y, \tag{3}$$

$$\varphi_\omega = \frac{q}{2\pi^2 v} \times \int \frac{\exp[i(k_x x + k_y y + (\omega/v)z)]}{k_x^2 + k_y^2 + (\omega/v)^2(1-\beta^2)}dk_x dk_y, \tag{4}$$

where q and v are the particle charge and velocity, ω is the radiation frequency, and $\beta = v/c$ is the reduced velocity of the particle. These formulas give an integral representation for A_ω and φ_ω in the form of the expansion in plane waves $\exp[i(k_x x + k_y y + k_z z)]$. Here, k_x, k_y, and k_z are the projections of the wave vector onto the coordinate axes. Note that, for a uniformly moving particle, $k_z = \omega/v$.

The field defined by (3) and (4) is incident upon the first grating and induces currents in its wires. Since these wires are oriented along axis x, the currents are induced only by the E_x component of the field of a uniformly moving particle. Let us write out the component $E_{x\omega}$:

$$E_{x\omega} = -\frac{\partial\varphi}{\partial x} = -\frac{iq}{2\pi^2 v} \times \int \frac{\exp[i(k_x x + k_y y + (\omega/v)z)]}{k_x^2 + k_y^2 + (\omega/v)^2(1-\beta^2)}k_x dk_x dk_y. \tag{5}$$

The field $E_{x\omega}$ induces currents in the wires. We denote the densities of these currents by $j_{x\omega}(x, y)$. Let us represent $j_{x\omega}(x, y)$ also in the form of the Fourier series

$$j_{x\omega}(x, y) = \frac{1}{(2\pi)^3}\int_{-\infty}^{\infty} j_\omega(k_x, k_y) \times \exp[i(k_x x + k_y y)]dk_x dk_y, \tag{6}$$

where $j_{x\omega}(k_x, k_y)$ are to be determined from the boundary conditions on the surface of the grating. Let us calculate the vector potential A'_x of the radiation emitted by the current j_x. The equation for the vector potential A'_x is expressed as

$$\left(\Delta - \frac{1}{c^2}\frac{\partial^2}{\partial t^2}\right)A'_x = \frac{4\pi}{c}j_x = -\frac{2}{c}\int \exp[i(k_x x + k_y y + k_z z - \omega t)] \times j_{x\omega}(k_x, k_y)dk_x dk_y dk_z d\omega. \tag{7}$$

A solution of this equation can be represented as

$$A'_x = \frac{2}{c}\int \frac{\exp[i(k_x x + k_y y + k_z z - \omega t)]}{k_x^2 + k_y^2 + k_z^2 - (\omega/v)^2} \times j_{x\omega}(k_x, k_y)dk_x dk_y dk_z d\omega. \tag{8}$$

Let us integrate with respect to k_z, circumventing the poles of the integrand according to the radiation princi-

ple (i.e., the solution must consist of the waves outgoing from the grating). Then, we obtain

$$A'_{x\omega} = \frac{i2\pi}{c}$$

$$\times \int \exp[i(k_x x + k_y y + \sqrt{(\omega/c)^2 - k_x^2 - k_y^2}|z| - \omega t)] \quad (9)$$

$$\times j_{x\omega}(k_x, k_y)\frac{dk_x dk_y d\omega}{\sqrt{(\omega/c)^2 - k_x^2 - k_y^2}}.$$

The field of the currents induced in the grating is determined by both the vector potential $A'_{x\omega}$ and the scalar potential $\varphi'_\omega = ck_x A'_x/\omega$:

$$\varphi'_\omega = i2\pi$$

$$\times \int \exp[i(k_x x + k_y y + \sqrt{(\omega/c)^2 - k_x^2 - k_y^2}|z| - \omega t)] \quad (10)$$

$$\times j_{x\omega}(k_x, k_y)\frac{k_x dk_x dk_y d\omega}{\omega\sqrt{(\omega/c)^2 - k_x^2 - k_y^2}}.$$

Knowing $A'_{x\omega}$ and φ'_ω, we can determine the component $E'_{x\omega}$ of the electric field generated by the first grating:

$$E'_{x\omega}$$

$$= -2\pi \int \exp[i(k_x x + k_y y + \sqrt{(\omega/c)^2 - k_x^2 - k_y^2}|z|)] \quad (11)$$

$$\times j_\omega(k_x, k_y)\frac{[(\omega/c)^2 - k_x^2]dk_x dk_y}{\omega\sqrt{(\omega/c)^2 - k_x^2 - k_y^2}}.$$

The x component of the total electric field must vanish on the surface of the grating:

$$E'_{x\omega} + E_{x\omega} = 0, \quad z = 0.$$

If we take expression (5) for $E_{x\omega}$ and expression (11) for $E'_{x\omega}$, then we obtain an equation from which one can determine $j_{x\omega}$, the Fourier component of the current induced in the grating,

$$j_{x\omega} = -\frac{iq}{4\pi^3 v}$$

$$\times \frac{k_x \omega\sqrt{(\omega/c)^2 - k_x^2 - k_y^2}}{[k_x^2 + k_y^2 + (\omega/c)^2(1-\beta^2)]((\omega/c)^2 - k_x^2)}. \quad (12)$$

Substituting this expression into formulas (9) and (10), we determine the vector and scalar potentials:

$$A'_{x\omega} = -\frac{q}{2\pi c v}$$

$$\times \int \frac{k_x \omega \exp[i(k_x x + k_y y + \sqrt{(\omega/c)^2 - k_x^2 - k_y^2}|z|)]}{[k_x^2 + k_y^2 + (\omega/v)^2(1-\beta^2)]((\omega/c)^2 - k_x^2)} dk_x dk_y, \quad (13)$$

$$\varphi'_\omega = -\frac{q}{2\pi v}$$

$$\times \int \frac{k_x^2 \exp[i(k_x x + k_y y + \sqrt{(\omega/c)^2 - k_x^2 - k_y^2}|z|)]}{[k_x^2 + k_y^2 + (\omega/v)^2(1-\beta^2)]((\omega/c)^2 - k_x^2)} dk_x dk_y. \quad (14)$$

Formulas (13) and (14) define the radiation emitted when a charged particle passes through the grating situated in the plane $z = 0$. The total field in the region between the first and the second gratings (i.e., between the planes $z = 0$ and $z = d$) is given by the sum of the radiation field $A'_{x\omega}$ (13), φ'_ω (14), and the field of a uniformly moving particle $A_{x\omega}$ (3), φ_ω (4). This total field is incident upon the second grating and induces currents in it. Since the conductivity of the second grating is different from zero only in the y direction, the induced currents have only the y component j_y. In turn, the currents j_y generate a field that can be described by a vector potential A'_y and the corresponding scalar potential φ''.

The y component of the total electric field must vanish on the surface of the second grating. This condition enables one to determine the currents induced in the grating. Indeed, if the currents induced in the second grating have the Fourier component $j_{y\omega}(k_x, k_y)$, then the electric field $E'_{y\omega}$ generated by the grating can be expressed as

$$E'_{y\omega} = -2\pi$$

$$\times \int \exp[i(k_x x + k_y y + \sqrt{(\omega/c)^2 - k_x^2 - k_y^2}|z - d|)] \quad (15)$$

$$\times j_{y\omega}(k_x, k_y)\frac{[(\omega/c)^2 - k_y^2]dk_x dk_y}{\omega\sqrt{(\omega/c)^2 - k_x^2 - k_y^2}}.$$

Recall that the second grating lies in the plane $z = d$. This formula is completely analogous to formula (11) for the field generated by the first grating, with the only difference that, in the first case, the field is generated by the current that flows in the first grating along the x axis, whereas in the second case, it is generated by the cur-

rent flowing in the y direction. Let us also write the y components of the electric fields generated by a uniformly moving charge and by the first grating. The superposition of these fields can be expressed as

$$E_{y\omega} = -\frac{q}{2\pi^2 v}\int\frac{k_y \exp[i(k_x x + k_y y)]dk_x dk_y}{k_x^2 + k_y^2 + (\omega/v)^2(1-\beta^2)} \times\left\{\exp\left[i\frac{\omega}{v}z\right] + \frac{k_x^2}{(\omega/c)^2 - k_x^2} \times \exp[i\sqrt{(\omega/c)^2 - k_x^2 - k_y^2}|z|]\right\}. \quad (16)$$

In this case, the first term in braces refers to the field of a uniformly moving particle, and the second, to the field of the first grating. It is obvious that the sum of (15) and (16) should vanish at $z = d$. From this condition, we determine the currents induced in the second grating:

$$j_{y\omega} = -\frac{q}{4\pi^2 v} \times\frac{ik_y\sqrt{(\omega/c)^2 - k_x^2 - k_y^2}}{[k_x^2 + k_y^2 + (\omega/v)^2(1-\beta^2)]((\omega/c)^2 - k_y^2)} \times\left\{\exp\left[i\frac{\omega}{v}d\right] + \frac{k_x^2}{(\omega/c)^2 - k_x^2} \times \exp[i\sqrt{(\omega/c)^2 - k_x^2 - k_y^2}d]\right\}. \quad (17)$$

Taking into account this formula, we determine the vector potential of the radiation from the second grating:

$$A'_{y\omega} - \frac{q}{2\pi c v} \times\int\frac{k_y\omega\exp[i(k_x x + k_y y + \sqrt{(\omega/c)^2 - k_x^2 - k_y^2}|z-d|)]}{[k_x^2 + k_y^2 + (\omega/v)^2(1-\beta^2)]((\omega/c)^2 - k_x^2)} \times\left\{\exp\left[i\frac{\omega}{v}d\right] + \frac{k_x^2}{(\omega/c)^2 - k_x^2} \times \exp[i\sqrt{(\omega/c)^2 - k_x^2 - k_y^2}d]\right\}dk_x dk_y. \quad (18)$$

Thus, the field in the region behind the second grating consists of three terms: the field of the uniformly moving charged particle, the field described by the vector potential $A'_{x\omega}$ (the radiation of the first grating that freely passes through the second grating), and the field of the second grating, which is described by the vector potential $A'_{y\omega}$.

Consider the field at large distances from the grating ($z \gg d$). Choose such distances at which the proper field of a uniformly moving charged particle does not interfere with the fields of the radiation that are described by the potentials $A'_{x\omega}$ and $A'_{y\omega}$. Calculating these potentials by the method of stationary phase, we obtain

$$A'_{x\omega} = -\frac{iqv}{\omega c}\frac{\sin\theta\cos\theta\cos\varphi}{(1-\beta^2\cos^2\theta)(1-\sin^2\theta\cos^2\varphi)} \times\frac{\exp\left[-i\frac{\omega}{c}R\right]}{R}, \quad (19)$$

$$A'_{y\omega} = -\frac{iqv}{\omega c}C\frac{\sin\theta\cos\theta\sin\varphi}{(1-\beta^2\cos^2\theta)(1-\sin^2\theta\cos^2\varphi)} \times\frac{\exp\left[-i\frac{\omega}{c}R\right]}{R}, \quad (20)$$

where

$$C = \exp\left[i\frac{\omega}{v}d\right](1-\beta\cos\theta) + \frac{\sin^2\theta\cos^2\varphi}{1-\sin^2\theta\cos^2\varphi},$$

R is the distance from the origin to the observation point, $x = R\cos\varphi\sin\theta$, $y = R\sin\varphi\sin\theta$, $z = R\cos\theta$, θ is the angle between the wave vector and the axis z, and φ is the azimuthal angle.

The potentials (19) and (20) represent a spherical vector wave. One can see that the components of this wave are inversely proportional to $(1 - \beta^2\cos^2\theta)$; i.e., for a relativistic velocity of the charged particle, the radiation is concentrated in a narrow range of angles θ of order $1/\gamma$, where $\gamma = 1/\sqrt{1-\beta^2}$. The radiation fields at large distances from the gratings can be obtained from formulas (19) and (20):

$$E_{x\omega} = \frac{q}{c}\frac{\beta\sin\theta\cos\theta}{1-\beta^2\cos^2\theta} \times\left(\cos\varphi - C\frac{\sin^2\theta\sin^2\varphi\cos\varphi}{1-\sin^2\theta\sin^2\varphi}\right)\frac{\exp\left[-i\frac{\omega}{c}R\right]}{R}, \quad (21)$$

$$E_{y\omega} = \frac{q}{c}\frac{\beta\sin\theta\cos\theta}{1-\beta^2\cos^2\theta} \times\left(C\sin\varphi - \frac{\sin^2\theta\cos^2\varphi\sin\varphi}{1-\sin^2\theta\cos^2\varphi}\right)\frac{\exp\left[-i\frac{\omega}{c}R\right]}{R}, \quad (22)$$

$$E_{z\omega} = -\frac{q}{c}\frac{\beta\sin^2\theta\cos^2\theta}{1-\beta^2\cos^2\theta} \times\left(\frac{\cos^2\varphi}{1-\sin^2\theta\cos^2\varphi} + C\frac{\sin^2\varphi}{1-\sin^2\theta\sin^2\varphi}\right)\frac{\exp\left[-i\frac{\omega}{c}R\right]}{R}. \quad (23)$$

In the relativistic case, when $\gamma \gg 1$ (and the angle $\theta \leq 1/\gamma$ is small), the second term in the expression for C is much less than the first one and is therefore negligible. In this case, C gives a phase shift that determines the phase difference between the radiation of the first and the second gratings. For small angles θ, we also neglect the terms proportional to $\sin^2\theta$. In this case, expressions (21)–(23) reduce to

$$E_{x\omega} = \frac{q}{c}\frac{\beta\sin\theta\cos\theta\cos\varphi}{1-\beta^2\cos^2\theta}\frac{\exp\left[-i\frac{\omega}{c}R\right]}{R}, \quad (24)$$

$$E_{y\omega} = \frac{q}{c}\frac{\beta\sin\theta\cos\theta\sin\varphi}{1-\beta^2\cos^2\theta}\frac{\exp\left[-i\frac{\omega}{c}R\right]}{R} \times\exp\left[i\frac{\omega}{c}d\right](1-\beta\cos\theta). \quad (25)$$

These formulas show, in particular, that, for azimuthal angles of $\varphi = 0, \pi$, the electric field of the radiation lies in the *xz* plane, whereas, for $\varphi = \pm\pi/2$, it lies in the *yz* plane. In these cases, the radiation field is linearly polarized for any distance between the gratings. For angles of $\varphi = \pm(\pi/4)$ and $\pm(3\pi/4)$, the fields E_x and E_y are equal in magnitude but differ in phase by

$$\alpha = \frac{\omega}{v}d(1-\beta\cos\theta).$$

Let us introduce unit vectors $\mathbf{e}_x$ and $\mathbf{e}_y$ directed along the coordinates *x* and *y*, respectively. Then, the resulting field can be expressed as

$$\begin{aligned}\mathbf{E} &= \mathbf{e}_x E_0\exp[i(kz-\omega t)] + \mathbf{e}_y E_0\exp[i(kz-\omega t+\alpha)]\\ &= \mathbf{e}_x E_0\exp[i(kz-\omega t)] + \mathbf{e}_y E_0(\cos\alpha + i\sin\alpha)\exp[i(kz-\omega t)].\end{aligned} \quad (26)$$

The wave (26) has a generally elliptic polarization. To determine the parameters of the polarization ellipse and the sign of rotation of the vector **E**, we use the results of [6].

The field (26) can be represented as

$$\mathbf{E} = (\mathbf{A} + i\mathbf{B})\exp[i(kz-\omega t)], \quad (27)$$

where

$$\mathbf{A} = E_0(\mathbf{e}_x + \mathbf{e}_y\cos\alpha), \quad \mathbf{B} = E_0\mathbf{e}_y\sin\alpha. \quad (28)$$

Let us rewrite expression (27) in the following identical form:

$$\begin{aligned}\mathbf{E} &= (\mathbf{A} + i\mathbf{B})\exp[i(kz-\omega t)]\\ &= (\mathbf{A} + i\mathbf{B})\exp[i(kz-\omega t+\psi)]\exp(-i\psi)\\ &= (\mathbf{A} + i\mathbf{B})\exp[i(kz-\omega t+\psi)](\cos\psi - i\sin\psi)\\ &= (\mathbf{C}' + i\mathbf{D}')\exp[i(kz-\omega t+\psi)],\end{aligned} \quad (29)$$

where

$$\mathbf{C}' = (\mathbf{A}\cos\psi + \mathbf{B}\sin\psi), \quad \mathbf{D}' = (\mathbf{B}\cos\psi - \mathbf{A}\sin\psi),$$

and ψ is a certain fitting parameter that will be determined below. Choose ψ so that the scalar product $\mathbf{C}'\mathbf{D}'$ vanishes:

$$(\mathbf{A}\cos\psi + \mathbf{B}\sin\psi)(\mathbf{B}\cos\psi - \mathbf{A}\sin\psi) = 0.$$

After the multiplication, we obtain that ψ must satisfy the equation

$$\tan 2\psi = \frac{2\mathbf{A}\cdot\mathbf{B}}{\mathbf{A}^2 - \mathbf{B}^2}. \quad (30)$$

Substituting (28) into (30), we obtain

$$\tan 2\psi = \frac{2E_0^2\sin\alpha\cos\alpha}{E_0^2(1+\cos^2\alpha - \sin^2\alpha)} = \tan\alpha. \quad (31)$$

Thus, ψ is equal to half the phase difference between the waves E_x and E_y:

$$\psi = \frac{1}{2}\alpha = \frac{1}{2}\frac{\omega}{v}d(1-\beta\cos\theta) = \frac{1}{2}\pi\frac{d}{l_f}, \quad (32)$$

where

$$l_f = \frac{\pi v}{\omega(1-\beta\cos\theta)} \quad (33)$$

is the so-called length of radiation formation. If we consider the radiation at small angles and the velocity v of a charged particle is close to the velocity of light *c*, i.e.,

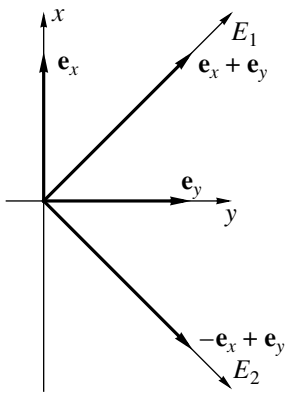

Fig. 2. Disposition of the axes of the polarization ellipse.

if the parameter $\beta = v/c$ is close to unity, then l_f satisfies the approximate equality

$$l_f \approx \lambda\gamma^2$$

to a good accuracy, where λ is the radiation wavelength. The quantity l_f is also called a coherence length.

For a chosen value of ψ, the radiation field can be represented as

$$\mathbf{E} = (\mathbf{E}_1 + i\mathbf{E}_2)\exp[i(kz - \omega t)], \tag{34}$$

where

$$\begin{aligned}\mathbf{E}_1 &= E_0(\mathbf{e}_x + \mathbf{e}_y)\cos\frac{\pi d}{2l_f},\\ \mathbf{E}_2 &= E_0(-\mathbf{e}_x + \mathbf{e}_y)\sin\frac{\pi d}{2l_f}.\end{aligned} \tag{35}$$

The vectors $\mathbf{E}_1$ and $\mathbf{E}_2$ are mutually perpendicular. Their disposition is shown in Fig. 2. The vector $\mathbf{E}_1$ is directed along the bisector of the angle between the positive directions of the axes *x* and *y*. The vector $\mathbf{E}_2$ is directed along the bisector of the angle between the negative direction of axis *x* and the positive direction of axis *y*. The magnitudes of these vectors depend on the ratio d/l_f. The absolute values of $\mathbf{E}_1$ and $\mathbf{E}_2$ represent the semiaxes of the polarization ellipse. One can see from (35) that, for

$$\psi = \alpha/2 = (\pi/4) \pm n\pi, \text{ where } n \text{ is integer},$$

the polarization of the wave is circular. If $\psi = \alpha/2 = (3\pi/4) \pm n\pi$, then the polarization is also circular, but with the opposite sign of rotation. When $\psi = \alpha/2 = \pm n\pi$, the radiation is linearly polarized in the direction of the vector $(\mathbf{e}_x + \mathbf{e}_y)$ (35). If

$$\psi = \alpha/2 = \pm(\pi/2) \pm n\pi,$$

then the polarization is also linear, but is directed along the vector $(-\mathbf{e}_x + \mathbf{e}_y)$ (35). In the remaining cases, the radiation is elliptically polarized.

Note that, according to the derivation of formulas (34) and (35), they apply to small-angle radiation. If we consider the radiation of relativistic particles ($\gamma \gg 1$), the analysis considered above describes the main part of radiation. If a particle is not relativistic or we consider the radiation of a relativistic particle at a large angle ($\theta \gg 1/\gamma$), then formulas (34) and (35) are inapplicable, and one needs additional analysis.

Let us evaluate the radiation intensity. Radiation of frequency ω that passes through a surface element *dS* perpendicular to the radius vector **R** (see Fig. 1) is determined by the formula

$$W_\omega = \frac{c}{2}\int |E_\omega|^2 dS. \tag{36}$$

In this case, $|E_\omega|^2$ is equal to $2|E_0|^2$. The maximal energy is radiated at small angles on the order of $\theta \approx 1/\gamma$; therefore, in formula (24) for $E_{x\omega}$, we can set

$$\theta = 1/\gamma, \quad \sin\theta \approx \theta = 1/\gamma, \quad \cos\theta \approx 1.$$

This approximation yields

$$E_0 = \frac{qv}{c^2}\gamma\cos\varphi\frac{\exp\left(-i\dfrac{\omega}{c}R\right)}{R}. \tag{37}$$

The solid angle into which radiation is emitted is on the order of

$$d\Omega = \sin\theta d\theta d\varphi \approx \frac{1}{\gamma^2}d\varphi.$$

An order-of-magnitude estimate for the spectral intensity yields

$$\begin{aligned}W_\omega &= \frac{c}{2}\int |E_0|^2 d\Omega\\ &= \frac{q^2v^2}{2c^3}\cos^2\varphi\frac{1}{\gamma^2}\gamma^2 d\varphi \approx \frac{\pi q^2 v^2}{2c^3}.\end{aligned} \tag{38}$$

Formula (38) shows that the spectral intensity is independent of frequency. It is also obvious that formula (38) is valid up to a certain frequency at which the wavelength is comparable to the distance between the wires of the gratings.

It follows from the analysis carried out that, to obtain radiation with a pronounced circular or elliptic polarization, the distance between the gratings must be

on the order of the formation length l_f (33). In our case, the formation length is proportional to the wavelength of radiation and to the square of the particle energy. The size of the equipment cannot be too large. This fact imposes certain constraints on the energy of particles. On the other hand, the wavelength of radiation is bounded from below by the distance between the wires of the grating. It might be expected that the waves with elliptic and circular polarization could also be generated in the millimeter and submillimeter wave bands.

ACKNOWLEDGMENTS

We are grateful to professor Y. Shibata, discussions with whom have largely stimulated this paper.

REFERENCES

1. V. L. Ginzburg and I. M. Frank, Zh. Éksp. Teor. Fiz. **16**, 15 (1946).
2. V. L. Ginzburg and V. N. Tsytovich, *Transient Radiation and Transient Scattering* (Nauka, Moscow, 1984).
3. *Bibliography of Scientific Publications on Transient Radiation of Charged Particles (1945–1982)* (Erevan. Fiz. Inst., Erevan, 1983).
4. B. M. Bolotovskiĭ and O. S. Mergelyan, Opt. Spektrosk. **18**, 3 (1965).
5. K. A. Barsukov and L. G. Naryshkina, Izv. Vyssh. Uchebn. Zaved., Radiofiz. **8**, 936 (1965).
6. B. M. Bolotovskiĭ and A. V. Serov, Kratk. Soobshch. Fiz., No. 7, 29 (2003).

Translated by I. Nikitin

Journal of Experimental and Theoretical Physics, Vol. 98, No. 6, 2004, pp. 1116–1122.
Translated from Zhurnal Éksperimental'noĭ i Teoreticheskoĭ Fiziki, Vol. 125, No. 6, 2004, pp. 1276–1282.

ATOMS, SPECTRA, RADIATION

Drastic Deceleration of Light Pulses in Atom Traps: A Semiclassical Theory

N. A. Vasil'ev and A. S. Troshin*

Herzen State Pedagogical University of Russia, St. Petersburg, 191186 Russia

**e-mail: thphys@herzen.spb.ru*

Received January 12, 2004

Abstract—The solution to the Maxwell–Bloch equations describing interaction of two light pulses with a gas of magnetically trapped cold atoms is used to establish fair quantitative agreement between theory and experimental results reported in [5]. The spacetime dependence of the probe- and coupling-pulse fields and nonlinear dynamics of atoms are analyzed. *© 2004 MAIK "Nauka/Interperiodica".*

1. INTRODUCTION

Substantial reduction of the group velocity of light in the interaction between a three-level system and two light waves that are resonant with adjacent transitions (related to electromagnetically induced transparency) was originally hypothesized in [1–3] and supported by experiments [4–7] (e.g., see monograph [8]).

In [5], a drastic reduction of the group velocity of a probe pulse (to 17 m/s) was observed in a gas of magnetically trapped sodium atoms. After laser and evaporative cooling to a temperature of 450 nK, which is close to the Bose–Einstein condensation point (435 nK for a peak density of 5×10^{12} cm^{-3}), the central region of a trapped atom cloud was exposed to two laser beams, a coupling one and a probe one, separated by a short delay. The leading quasi-monochromatic coupling pulse was exactly resonant with the $3 \longleftrightarrow 2$ transition ($\omega_c = \omega_{32}$). The trailing probe pulse was much shorter (by about 40 times), and its central frequency was in resonance with the $1 \longleftrightarrow 3$ transition frequency ($\bar{\omega}_p = \omega_{31}$). In Fig. 1, levels 1 and 2 are the hyperfine sublevels of the ground $3S_{1/2}$ state (with $F = 1$, $M_F = -1$, $F = 2$, and $M_F = -2$), and level 3 is one of the hyperfine sublevels of the $3P_{3/2}$ state (with $F = 2$ and $M_F = -2$).

When a probe pulse enters a medium and excites (even if only very slightly) atoms to a state Ψ_3, the probe and coupling pulses prepare a coherent superposition of the states Ψ_1 and Ψ_2. A narrow transparent region and an extremely steep dispersion curve (refractive index as an increasing function of frequency) are observed in the vicinity of ω_{31}. This leads to reduction of the group velocity of light, which is manifested in an anomalously long residence time of the probe pulse in the trap.

This qualitative explanation of the effect and some estimates can be found in references cited above. Most quantitative theories tend to reduce the explanation to the coherent population trapping outlined above (in the present case, only levels 1 and 2 are substantially populated) and to the mutual compensation of the $1 \longleftrightarrow 3$ and $2 \longleftrightarrow 3$ transition amplitudes (e.g., see [8]).

There is no doubt about the key role played by quantum interference of atomic states in resonant interactions between atoms and radiation. However, zero polarization of an atom exposed to two monochromatic light waves, which means that both absorption coefficient and resonant part of refractive index vanish for a strictly monochromatic wave with frequency $\omega = \omega_{31}$, implies that this wave propagates at the speed of light in free space, but does not explain the deceleration of a probe pulse. As noted above (and, obviously, realized by the authors of papers referenced), this effect must be attributed to a special form of the dispersion curve in the vicinity of the frequency ω_{31} of the so-called dark resonance $1 \longleftrightarrow 3$, as well as to the dark-resonance–to–probe-pulse spectral-width ratio, intensity-dependent effects, and balance of material and wave-energy fluxes. Thus, the dynamics of the system as a whole must be analyzed, and both its spatial extent and induced substantial nonuniformity must be taken into

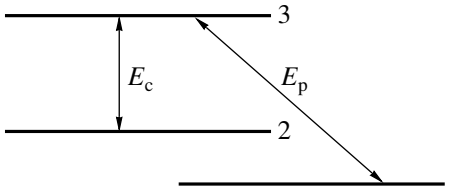

Fig. 1. Schematic diagram of transition in a three-level system.

1063-7761/04/9806-1116$26.00 © 2004 MAIK "Nauka/Interperiodica"

account. Indeed, a probe pulse that has a length of about a kilometer in vacuum is compressed in an atom cloud to a length smaller than the trap size (about 230 μm in [5]).

In what follows, we formulate the problem and present the principal results of a quantitative analysis of the effect, which is motivated primarily by the experimental results reported in [5]. We apply a semiclassical approach, i.e., consider quantum dynamics of atoms interacting with a classical electromagnetic field. We develop a theory describing the nonlinear response of a medium and the propagation of two waves. Under the physical conditions implemented experimentally in [5], the trapped gas may be treated as perfect and secondary quantization may not be applied explicitly. In other words, the density matrix for a system of atoms is factored into single-atom matrices. Sufficient self-consistency (as in most problems in nonlinear optics of gases) is ensured by interaction between atoms and the mean field of two waves, including the secondary field associated with the polarization induced by these waves.

To compare computed results with experiment, we use the parameter values corresponding to a particular measurement in [5] (when the measured group velocity of the probe pulse was $V_g \approx 32.5$ m/s). However, we did not try to achieve complete quantitative agreement between the theoretical results based on the present model and those obtained in [5], because the experiment was complicated by additional factors.

To single out the key effect and simplify computations, we consider the one-dimensional model of parallel propagation of two waves in a homogeneous medium.

We apply the following two approaches.

In one approach, the spectrum of the linear response of an atom due to the $1 \longleftrightarrow 3$ transition is determined, while the effect of a prescribed coupling laser field on the $2 \longleftrightarrow 3$ transition is treated exactly (only the rotating-wave approximation is used). Then, we numerically solve the boundary value problem of probe-pulse propagation in a medium characterized by the complex susceptibility determined in this manner (with linear absorption and dispersion depending on the coupling-field amplitude accordingly).

In the other (much "heavier") approach, we solve the complete Maxwell–Bloch system, i.e., self-consistent equations for density matrix elements of an atom and the wave equations for two waves propagating in a medium. The analysis allows for variation of the complex amplitude of a propagating coupling beam. Thus, we solve a problem that is nonlinear with respect to both waves.

2. EQUATIONS FOR DENSITY MATRIX

The starting system of equations for the density matrix of an atom has a standard form:

$$\begin{aligned}
\dot\rho_{11} &= \gamma_{31}\rho_{33} + \gamma_2\rho_{22} + i[V_p^*\rho_{31} - \text{c.c.}],\\
\dot\rho_{22} &= -\gamma_2\rho_{22} + \gamma_{32}\rho_{33} + i[V_c^*\rho_{22} - \text{c.c.}],\\
\dot\rho_{33} &= -\gamma_3\rho_{33} - i[V_p^*\rho_{31} - \text{c.c.}] - i[V_c^*\rho_{32} - \text{c.c.}],\\
\dot\rho_{31} &= -\frac{\gamma_3}{2}\rho_{31} + i(\omega_p - \omega_{31})\rho_{31}\\
&\quad - iV_p[\rho_{33} - \rho_{11}] + iV_c\rho_{21},\\
\dot\rho_{32} &= -\frac{\gamma_2 + \gamma_3}{2}\rho_{32} + i(\omega_c - \omega_{32})\rho_{32}\\
&\quad - iV_c[\rho_{33} - \rho_{22}] + iV_p\rho_{12},\\
\dot\rho_{21} &= -\frac{\gamma_2}{2}\rho_{21} + i(\omega_p - \omega_{31})\rho_{21}\\
&\quad - iV_p\rho_{23} + iV_c^*\rho_{31},\\
\rho_{13} &= \rho_{31}^*, \quad \rho_{23} = \rho_{32}^*, \quad \rho_{12} = \rho_{21}^*.
\end{aligned} \tag{1}$$

Here,

$$\begin{aligned}
V_c \equiv V_c(t, x) &= \frac{\mathbf{d}_{32}\cdot\mathbf{E}_c(t, x)}{2\hbar},\\
V_p \equiv V_p(t, x) &= \frac{\mathbf{d}_{31}\cdot\mathbf{E}_p(t, x)}{2\hbar},
\end{aligned} \tag{2}$$

$\mathbf{d}_{ik}$ denote the transition dipole moments, and $\mathbf{E}_{c,p}(t, x)$ are the "slow" complex amplitudes of the two waves with $\exp(-i\omega_{c,p}t + ik_{c,p}x)$ factored out (ω_c and ω_p are the central frequencies of the coupling and probe pulses and $k_{c,p}$ are the corresponding wave vectors in vacuum). A similar factorization was performed in the matrix elements $\tilde\rho_{32}(t; x)$ and $\tilde\rho_{31}(t; x)$ (where $\tilde\rho$ denotes the density matrix in the Schrödinger representation), and $\exp[-i(\omega_p - \omega_c)t + i(k_p - k_c)x]$ was factored out in the matrix element $\tilde\rho_{21}(t; x)$. Then, the "fast varying" factors indicated above cancel out. Thus, $\rho_{ik}(t; x)$ ($i \neq k$) are the slowly varying complex amplitudes of the off-diagonal elements of the density matrix of an atom localized in a slab orthogonal to the wave propagation direction, with longitudinal coordinate x.

The relaxation constants γ_{31}, γ_{32}, and γ_{21} are the probabilities of spontaneous emissive $3 \longrightarrow 1$, $3 \longrightarrow 2$, and $2 \longrightarrow 1$ transitions, respectively, and $\gamma_3 \approx 6.3 \times 10^7$ s^{-1} [5, 9] is the inverse lifetime of the state Ψ_3 ($\gamma_3 > \gamma_{31} + \gamma_{32}$, see below). In accordance with the conditions of the experiment described in [5], the nonradiative transverse relaxation is ignored and the constant γ_2 for metastable level 2 is hereinafter set to zero, which implies that the transverse relaxation constants are

$\Gamma_{31} = \Gamma_{32} = \gamma_3/2$ and $\Gamma_{21} = 0$. In view of the actual relations between the rate constants for radiative transitions between hyperfine sublevels of the $3P_{3/2}$ and $3S_{1/2}$ states in the sodium atom [9–11], we set $\gamma_{31} = \gamma_3/2$ and $\gamma_{32} = \gamma_3/3$. Note that the three-level model considered here is not closed with respect to radiative relaxation: normalization is violated by the contribution of the spontaneous $(3P_{3/2}, F = 2, M_F = -2) \longrightarrow (3S_{1/2}, F = 2, M_F = -1)$ transition characterized by the constant $\gamma_0 = \gamma_3/6$. Numerical results confirm that this lack of closure (departure from the subspace spanned by the basis $\{\Psi_i\}$, where $i = 1, 2, 3$) is virtually unobservable because of the extremely low population of level 3 during the probe-pulse propagation time.

3. PROPAGATION OF A WEAK PROBE PULSE

As we already noted, the observed drastic reduction of the group velocity of a probe pulse is primarily due to a special form of dispersion curve in the vicinity of the $1 \longleftrightarrow 3$ resonant transition explained by the effect of the coupling-laser field on the $3 \longleftrightarrow 2$ transition. Therefore, it is reasonable to analyze probe-pulse propagation in the linear approximation with respect to the probe field. In this case, it is sufficient to solve Eqs. (1) in the first approximation with respect to V_p for the matrix elements ρ_{31} and ρ_{13}, which determine the polarization

$$P_p(t, x) = N_0 d_{13} \rho_{31}(t, x) + \text{c.c.}, \quad (3)$$

where N_0 is the concentration of atoms in the zone of their strongest interaction with both pulses. We assume that the coupling laser beam is monochromatic:

$$\omega_c = \omega_{32}, \quad V_c = \text{const}(t, x).$$

We tentatively set $V_p = \text{const}$ and define $\omega = \omega_p$ and $\delta\omega = \omega - \omega_{31}$. In the zeroth approximation with respect to V_p, we have $\rho_{ik} = \delta_{i1}\delta_{k1}$. Therefore, Eqs. (1) can be reduced to

$$\dot{\rho}_{31} = \left[-\frac{\gamma_3}{2} + i\delta\omega\right]\rho_{31} + iV_p + iV_c\rho_{21},$$
$$\dot{\rho}_{21} = i\delta\omega\rho_{21} + iV_c^*\rho_{31}. \quad (4)$$

Equations (4) are solved to find the steady-state value of $\bar{\rho}_{31}$:

$$\bar{\rho}_{31} = \frac{V_p\delta\omega[(|V_c|^2 - \delta\omega^2) + i\delta\omega(\gamma_3/2)]}{(|V_c|^2 - \delta\omega^2)^2 + \delta\omega^2(\gamma_3/2)^2}. \quad (5)$$

Substituting (5) into (3), we obtain an exact expression for the complex linear polarizability in the vicinity of ω_{31},

$$\alpha(\delta\omega) = \frac{N_0 d_{31}^2}{\hbar}\frac{\delta\omega[(|V_c|^2 - \delta\omega^2) + i\delta\omega(\gamma_3/2)]}{(|V_c|^2 - \delta\omega^2)^2 + \delta\omega^2(\gamma_3/2)^2}, \quad (6)$$

and, in a standard approximation, expressions for refractive index and amplitude absorption coefficient $\beta(\delta\omega)$ (see Fig. 2),

$$n(\delta\omega) = 1 + B_p\frac{\delta\omega(\Omega_c^2 - \delta\omega^2)}{(\Omega_c^2 - \delta\omega^2)^2 + \delta\omega^2}, \quad (7)$$

$$\beta(\delta\omega) = \frac{\omega}{c}B_p\frac{\delta\omega^2}{(\Omega_c^2 - \delta\omega^2)^2 + \delta\omega^2}, \quad (8)$$

where

$$B_p = \frac{4\pi N_0 d_{31}^2}{\hbar\gamma_3}, \quad (9)$$

$\delta\omega$ is the detuning normalized to $\gamma_3/2$, and Ω_c is the Rabi frequency in the coupling laser field normalized to γ_3,

$$\Omega_c = \frac{|\mathbf{d}_{32} \cdot \mathbf{E}_c|}{\hbar\gamma_3}. \quad (10)$$

In the calculations based on this approach and the other one (see below), the units of time and length are $(\gamma_3/2)^{-1}$ and $\bar{k}_p^{-1} = 2\pi/\bar{\lambda}_p$, respectively.

In accordance with [5], we set

$$B_p = 0.013, \quad \Omega_c = 0.56.$$

In the present calculations (based on the former approach), the envelope of the input probe-pulse field strength is defined (up to a factor in the linear approximation) as

$$E_{p,0}(t) = (2\pi)^{-1/4}(T_p)^{-1/2}\exp(-t^2/4T_p^2), \quad (11)$$

where $T_p = 34.5$, which corresponds to a probe-pulse full width at half-maximum of 2.5×10^{-6} s [5].

Now, let us consider the propagation of a probe pulse. Let $F_{p,0}(\delta\omega)$ be the Fourier transform of the input probe-pulse envelope. Then, the slow field amplitude at a location x inside the medium can be calculated

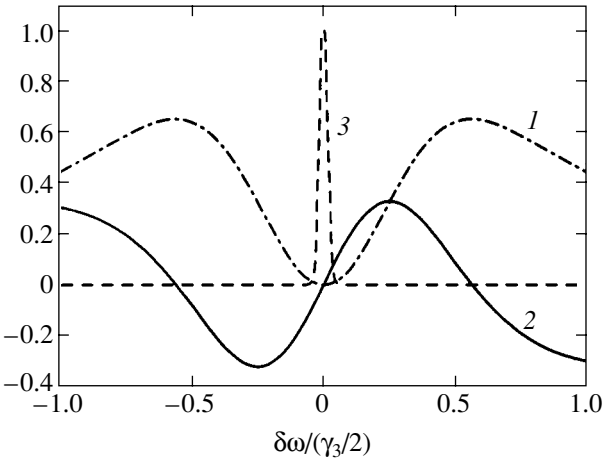

Fig. 2. Spectral characteristics (in arbitrary units): $\beta(\delta\omega) \times 50$ (absorption without the factor ω/c) (*1*); $\Delta n(\delta\omega) \times 50$ (dispersion) (*2*); $|F_{p,0}|^2/25$ (input probe pulse intensity) (*3*).

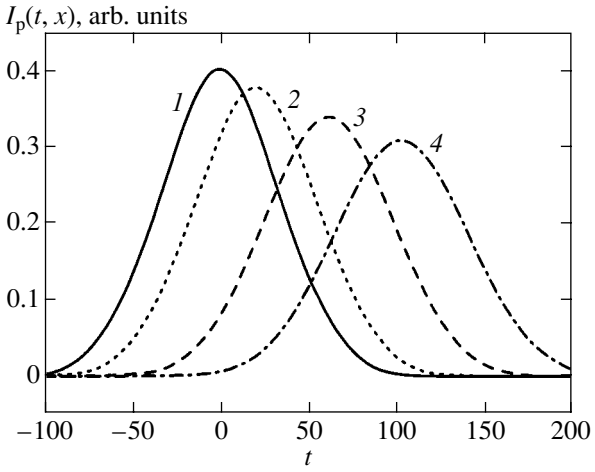

Fig. 3. Temporal profile of the probe pulse at $x = 0$ (*1*), 500 (*2*), 1500 (*3*), and 2440 (output cross section) (*4*). Hereinafter, the units of length and time are $\lambda/2\pi$ and $(\gamma_3/2)^{-1}$, respectively.

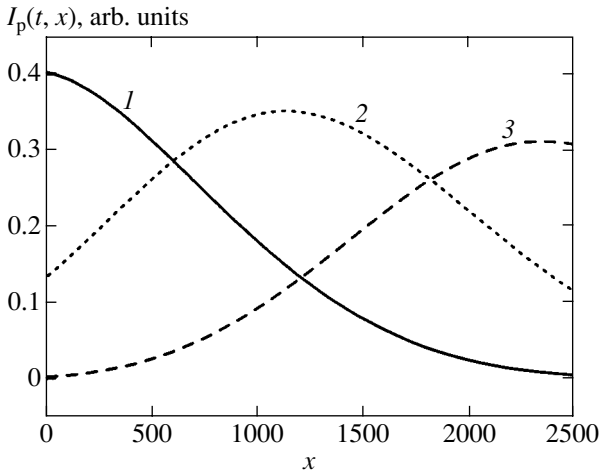

Fig. 4. Spatial profile of the probe pulse at $t = 0$ (*1*), 50 (*2*), and 100 (*3*).

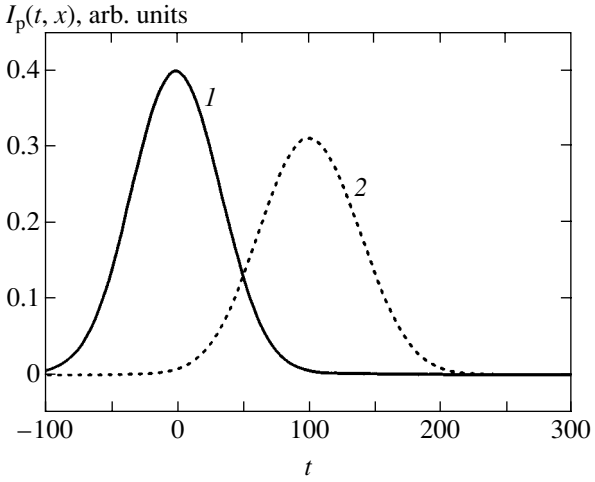

Fig. 5. Input (*1*) and output (*2*) probe pulse profiles.

to sufficient accuracy as a Fourier integral:

$$E_p(t, x) = \frac{1}{\sqrt{2\pi}} \int_{-\infty}^{\infty} \frac{2}{2 + \Delta n(\delta\omega)} F_{p,0}(\delta\omega) \times \exp[-\beta(\delta\omega)x] \cos[\delta\omega t - \Delta n(\delta\omega)x] d(\delta\omega). \quad (12)$$

Figures 3 and 4 show the probe-pulse intensity versus time in several cross sections and the spatial distribution of intensity at several instants, respectively. Figure 5 (which illustrates the key result to be compared with Fig. 3 in [5]) shows the input and output probe pulse intensities. Here, the factor $2/(2 + \Delta n)$ in (12) is replaced with $4(1 + \Delta n)/(2 + \Delta n)^2$; i.e., the changes in field amplitudes at both input and output ends of the specimen are taken into account. However, it should be noted that refractive index is close to unity under the conditions considered here and the boundary of a cloud of atoms can be defined only tentatively.

The results presented in Figs. 3–5 demonstrate good agreement with the experimental results reported in [5]. According to our calculations, the group velocity of the probe pulse is estimated as $V_g \approx 71$ m/s.

4. SOLUTION OF THE COMPLETE MAXWELL–BLOCH SYSTEM

Now, we discard the linear approximation with respect to the probe-pulse field and treat the coupling-pulse field in the medium as unknown. We take into account explicitly the self-induced field of the medium in the vicinity of both ω_{31} and ω_{32}.

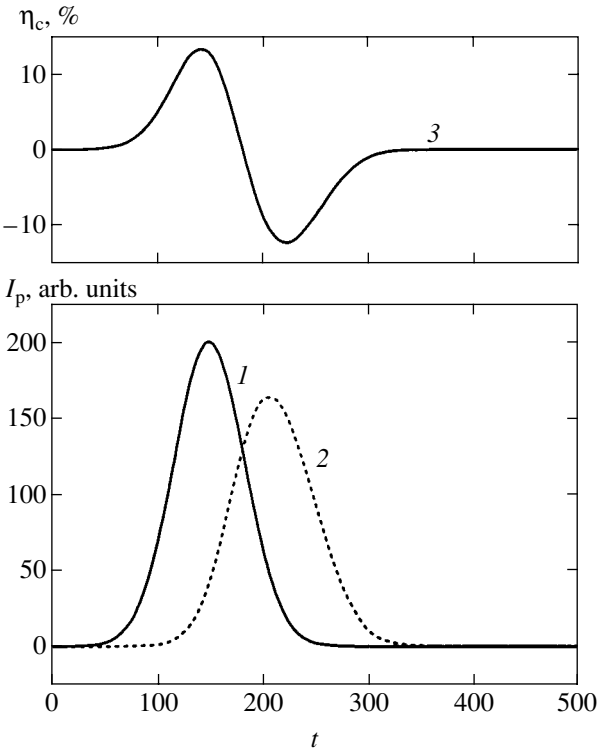

Fig. 6. Solution to the nonlinear problem: input (*1*) and output (*2*) probe pulse profiles and relative variation of the output coupling pulse intensity $\eta_c(t) = I_{c,\,out}(t)/I_{c,\,in}(t) - 1$ (*3*).

Equations (1) relate the evolution of the density matrix of an atom to the variation of the effective mean field of two pulses. These equations must be supplemented by expressions for the secondary fields generated by polarization currents induced in the medium. In one-dimensional problems, these expressions are well known (e.g., see [12]). Neglecting the counterpropagating waves, we write the relations between the positive-frequency amplitudes $E'_{c,\,p}$ and the polarizations $P_{c,\,p}$ as

$$E'_{c,\,p}(t, x) = 4\pi i \int_0^x P_{c,\,p}(t, x')k_{c,\,p}dx'. \qquad (13)$$

Substituting (3) into (13), choosing the units of measure as in the former approach (see above), and rewriting Eqs. (1) and (13) in dimensionless form (under a special choice of input phases in the amplitudes of both waves that does not affect the result), we obtain a closed system of real equations:

$$\begin{aligned}
\dot\rho_{11} &= \rho_{33} + 2E_p\rho_{13},\\
\dot\rho_{22} &= \frac{2}{3}\rho_{33} + 2E_c\rho_{23},\\
\dot\rho_{33} &= -2\rho_{33} - 2E_p\rho_{13} - 2E_c\rho_{23}, \qquad (14)\\
\dot\rho_{12} &= E_p\rho_{23} + E_c\rho_{13},\\
\dot\rho_{13} &= -\rho_{13} + E_p[\rho_{33} - \rho_{11}] - E_c\rho_{12},\\
\dot\rho_{23} &= -\rho_{23} + E_c[\rho_{23} - \rho_{22}] - E_p\rho_{12},\\
E_c(t, x) &= E_{c;\,free}(t, x) + B_c\int_0^x \rho_{23}(t, x')dx',\\
E_p(t, x) &= E_{p;\,free}(t, x) + B_p\int_0^x \rho_{13}(t, x')dx'.
\end{aligned}$$

More precisely, if $\tilde E_{c,\,p}(t, x)$ are the slowly varying local amplitudes of the two waves in the strict sense, then the quantities $E_{c,\,p}$ in (14) are defined as

$$E_{c,\,p}(t, x) = -i\frac{d_{l3}\tilde E_{c,\,p}(t, x)}{\hbar\gamma_3}, \qquad (15)$$

where $l = 2$ and $l = 1$ for E_c and E_p, respectively. The factor B_c is defined by (9) with d_{31} replaced by d_{32}.

System (14) was solved numerically for various combinations of parameters. The results obtained for conditions closest to experiments are presented in Figs. 6 and 7. We used boundary conditions consistent with [5]:

$$E_c(t, 0) = 0.56,$$

$$E_p(t, 0) = E_{p,\,0}\exp\left(-\frac{t^2}{4T_p^2}\right), \quad E_{p,\,0} = 0.2,$$

$$B_c = 0.0086, \quad B_p = 0.013.$$

The calculated group velocity of the probe pulse is $V_g \approx 78$ m/s.

5. DISCUSSION

One expected numerical result obtained by solving the problem that is nonlinear in both waves is that stronger deceleration of the probe pulse corresponds to lower peak intensity of the input pulse. Thus, the lowest V_g is obtained for the linear polarizability given by (6) when the remaining parameters are held constant. Using the definition of group velocity

$$V_g = \frac{d\omega}{dk} = c\left(1 + \omega\frac{dn}{d\omega}\right)^{-1} \qquad (16)$$

and expression (7), we find (dropping the unity in the

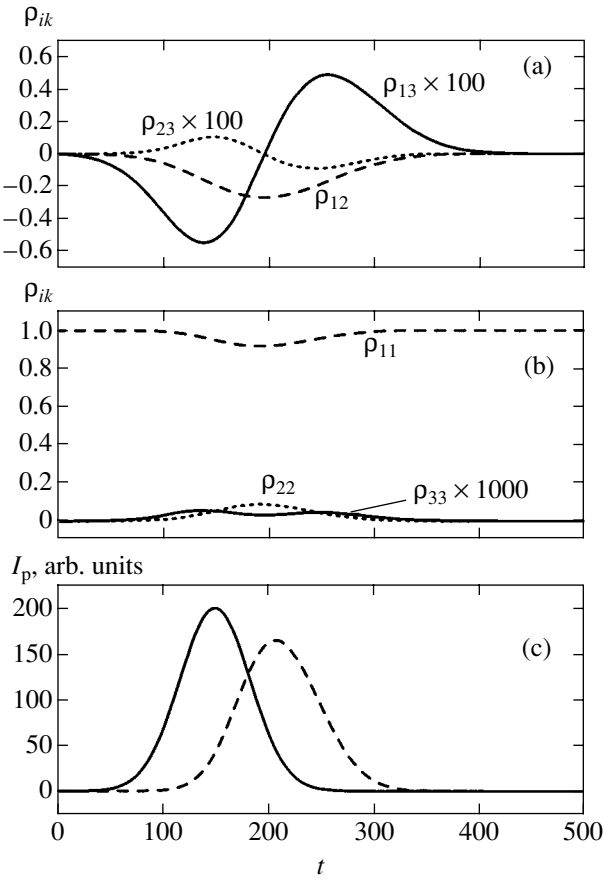

Fig. 7. Average density matrix elements per atom (a, b) and probe pulse (c). Solid and dashed curves correspond to input and output profiles.

denominator)

$$V_g = \frac{\lambda\gamma_3\Omega_c^2}{4\pi B_p}. \quad (17)$$

(This result is obviously equivalent to expression (1) in [5], which was written in SI units.) It should be noted here that the unlimited decrease in V_g as $\Omega_c \longrightarrow 0$ in (17) is an artifact due to the approximation $\gamma_2 = 0$. According to the exact formula for $\alpha(\omega)$ with $\gamma_2 \neq 0$, the Rabi frequency that minimizes V_g is $\gamma_3\Omega_c = \sqrt{\gamma_3\gamma_2}$.

Expression (17) yields $V_g \approx 72$ m/s. This value is nearly equal to our result (determined by the shift of the peak output intensity of the probe pulse in Fig. 5). However, it is more than twice as high as the experimental result (32.5 m/s) obtained for the same values of other parameters. The change in shape and decrease in height observed in the experiment are also much greater than those in Figs. 3–7. As noted above, the experimental conditions in [5] were complicated by additional factors (a nearly resonant fourth sublevel of the upper state, nonuniform concentration of trapped atoms, nonparallel propagation of the probe and coupling pulses, etc.).

The most remarkable result obtained by solving the completely nonlinear problem is the substantial negative correlation between the output intensities of the coupling and probe pulses (see Fig. 6) predicted for a very low, but definitely nonzero, population of level 3 (see Fig. 7). This suggests that the energy of a probe beam propagating in the medium is transferred mainly to the coupling beam and then is partially returned to the probe beam. The density matrix elements ρ_{13} and ρ_{32}, which determine the average induced dipole moment per atom, remain small (Fig. 7). However, they certainly do not vanish as in the "reference" single-atom problem with specially chosen field parameters that leads to the hypothesis of electromagnetically induced transparency (e.g., see [8]).

The average matrix element ρ_{12} per atom (corresponding to a forbidden transition) increases to a considerable extent when the pulses transform substantially. It plays the role of a source of mutual modulation of two waves (as in coherent Raman scattering [13–15], which is analogous to the substantial reduction of speed of light discussed here in terms of nonlinear dynamics).

The main results were published in [16, 17]. A different semiclassical theory of the effect considered here was presented in [16, 18].

ACKNOWLEDGMENTS

We thank E.D. Trifonov for drawing our attention to [5] and for detailed and very helpful discussion of the problem. We also thank the participants of the city seminar on quantum optics held at the Herzen State Pedagogical University of Russia (St. Petersburg), and especially I.M. Sokolov, for their interest in this study and helpful remarks.

This work was supported by INTAS, grant no. 01-855 and by the Ministry of Education of the Russian Federation.

REFERENCES

1. S. P. Tewari and G. S. Agarwal, Phys. Rev. Lett. **56**, 1811 (1986).
2. S. E. Harris, J. E. Field, and A. Imamoglu, Phys. Rev. Lett. **64**, 1107 (1990).
3. S. E. Harris, J. E. Field, and A. Kasapi, Phys. Rev. A **46**, R29 (1992).
4. A. Kasapi, Maneesh Jain, G. Y. Yin, and S. E. Harris, Phys. Rev. Lett. **74**, 2447 (1995).
5. L. V. Hau, S. E. Harris, Z. Dutton, and C. H. Behroozi, Nature **397**, 594 (1999).
6. D. F. Phillips, A. Fleischhauer, A. Mair, *et al.*, Phys. Rev. Lett. **86**, 783 (2001).
7. Chien Liu, Z. Dutton, C. H. Behroozi, and L. V. Hau, Nature **409**, 490 (2001).

8. M. O. Scully and M. S. Zubairy, *Quantum Optics* (Cambridge Univ. Press, Cambridge, 1997).
9. I. I. Sobel'man, *Atomic Spectra and Radiative Transitions* (Nauka, Moscow, 1977; Springer, Berlin, 1979).
10. E. B. Aleksandrov, G. I. Khvostenko, and M. P. Chaĭka, *Interference of Atomic States* (Nauka, Moscow, 1991; Springer, Berlin, 1993).
11. D. A. Steck, *Sodium D Line Data*, http://steck.us/alkalidata.
12. M. G. Benedict, A. M. Ermolaev, V. A. Malyshev, I. V. Sokolov, and E. D. Trifonov, *Super-Radiance: Multiatomic Coherent Emission* (Inst. of Physics, Bristol and Philadelphia, 1996).
13. S. G. Rautian and B. M. Chernobrod, Zh. Éksp. Teor. Fiz. **72**, 1342 (1977) [Sov. Phys. JETP **45**, 705 (1977)].
14. H. Steudel, Ann. Phys. **7**, 34 (1977).
15. E. D. Trifonov, A. S. Troshin, and N. I. Shamrov, Opt. Spektrosk. **48**, 1036 (1980) [Opt. Spectrosc. **48**, 567 (1980)]; Opt. Spektrosk. **54**, 966 (1983) [Opt. Spectrosc. **54**, 573 (1983)].
16. E. D. Trifonov, A. S. Troshin, and N. A. Vasil'ev, in *Technical Digest of International Quantum Electronics Conference, IQEC-2002* (Moscow, 2002), p. 164; in *Proceedings of Conference on Basic Problems of Optics-2002* (St. Petersburg, 2002), p. 112.
17. A. S. Troshin and N. A. Vasil'ev, in *Book of Abstracts of 12th International Laser Physics Workshop* (Hamburg, 2003), p. 387.
18. N. A. Vasil'ev and E. D. Trifonov, Opt. Spektrosk. **96**, 625 (2004) [Opt. Spectrosc. **96**, 556 (2004)].

Translated by A. Betev

Journal of Experimental and Theoretical Physics, Vol. 98, No. 6, 2004, pp. 1123–1132.
Translated from Zhurnal Éksperimental'noĭ i Teoreticheskoĭ Fiziki, Vol. 125, No. 6, 2004, pp. 1283–1294.

PLASMA, GASES

Microdroplet Evolution Induced by a Laser Pulse

M. B. Smirnov[a,b], I. Yu. Skobelev[c], A. I. Magunov[c], A. Ya. Faenov[c], T. A. Pikuz[c], Y. Fukuda[d], K. Yamakawa[d], Y. Akahane[d], M. Aoyama[d], N. Inoue, and H. Ueda[d]

[a]*Russian Research Centre Kurchatov Institute, Moscow, 123182 Russia*
[b]*Moscow Institute of Physics and Technology, Dolgoprudnyĭ, Moscow oblast, 141700 Russia*
[c]*All-Russia Research Institute of Physicotechnical and Radio Engineering Measurements, Mendeleevo, Moscow oblast, 141570 Russia*
[d]*Japan Atomic Energy Research Institute, Kyoto, 619-0215 Japan*
e-mail: smirnov@imp.kiae.ru
Received November 13, 2003

Abstract—Interaction between high-power ultrashort laser pulse and giant clusters (microdroplets) consisting of 10^9 to 10^{10} atoms is considered. The microdroplet size is comparable to the laser wavelength. A model of the evolution of a microdroplet plasma induced by a high-power laser pulse is developed, and the processes taking place after interaction with the pulse are analyzed. It is shown theoretically that the plasma is superheated: its temperature is approximately equal to the ionization potential of an ion having a typical charge. The microdroplet plasma parameters are independent of the pulse shape and duration. The theoretical conclusions are supported by experimental studies of x-ray spectra conducted at JAERI, where a 100-terawatt Ti–sapphire laser system was used to irradiate krypton and xenon microdroplets by laser pulses with pulse widths of 30 to 500 fs and intensities of 6×10^{16} to 2×10^{19} W/cm^2. © *2004 MAIK "Nauka/Interperiodica".*

1. INTRODUCTION

Interaction of a high-power ultrashort laser pulse (with an intensity $I \sim 10^{17}$–10^{20} W/cm^2 and duration $\tau \sim$ 30–300 fs) with a cluster beam differs substantially from its interaction with an isolated atom. In terms of structure, a cluster beam is intermediate between solid and gas targets. It consists of separate atoms or molecules and clusters of size smaller than 10–100 nm, which contain several thousand to several million atoms. The average concentration of atoms in a beam varies between 10^{16} and 10^{19} cm^{-3}, while the local concentration of atoms (in a cluster) is 10^{22} cm^{-3}. The fraction of atoms bound into clusters in a beam varies from 10 to 100% of the total number of particles [1]. A cluster beam irradiated by a high-power laser pulse transforms into a plasma characterized by unique properties. On the one hand, the plasma of highly charged ions created at cluster locations is characterized by a density much higher than critical [2–5] and by electron energies on the order of kiloelectron-volt [6]. On the other hand, since the electron density is lower than critical and the cluster diameter is small, the electromagnetic wave freely propagates and interacts with all target atoms, i.e., penetrates into regions of supercritical electron density instead of being reflected, as in the case of a solid-state target [7]. Thus, a high specific rate of laser-energy absorption can be attained in a cluster beam, which results in a specific excitation rate that is higher than in targets of different types. Accordingly, the results are substantially different from those obtained in experiments on gas and solid targets. First, the laser pulse irradiating a cluster beam is absorbed almost entirely (up to 95%) [8]. Second, the average particle charge in plasmas thus created is higher than in both solid-state and atomic-beam plasmas produced by laser beams with similar parameters [9, 10]. From 10 to 15% of the pulse energy lost via x-ray emission is of a nonthermal nature [11–14]. A substantial neutron yield was obtained by irradiating a jet of deuterium clusters [15].

One disadvantage of a cluster beam, as compared to a solid-state target, is the high sensitivity of the target to the laser-pulse contrast [16–19]. Indeed, when the contrast is low, the prepulse destroys the target and the main pulse interacts with a nearly homogeneous plasma rather than with a cluster beam. Since the rate of cluster decay is primarily determined by the cluster geometry, giant clusters (microdroplets) of a diameter comparable to the pulse wavelength can be used to retain all advantages of a cluster beam, on the one hand, and to reduce the target's sensitivity to contrast, on the other hand. Thus, a wider variety of laser systems can be used in applications and in studies of cluster targets. Even though a droplet target is analogous to a cluster beam, it has some distinctive properties [20, 21]. Since the focal spot of a laser pulse interacting with a cluster beam contains many clusters, the processes taking place both outside and inside individual clusters are of equal importance [22]. In the system considered here, only several tens of microdroplets are in the focal spot,

and an analysis of their interactions and the subsequent plasma evolution can be restricted to a single microdroplet even if the incident intensity is high. This approach is additionally justified by the fact that the fraction of electrons released from a cluster decreases with increasing cluster size, so that the effects due to the processes outside the cluster decrease accordingly. Moreover, an increase in droplet size implies a decrease in the cluster (or microdroplet) breakup rate. Therefore, the increase in cluster (or microdroplet) size over the time of interaction with a laser pulse can be neglected; i.e., the cluster core can be approximately treated as "frozen." In this study, we analyze the evolution of a microdroplet having a size comparable to the laser wavelength consisting of 10^9 to 10^{11} atoms of xenon or krypton excited by a high-power laser pulse ($I \sim 10^{16}$–10^{19} W/cm^2).

2. EVOLUTION OF A MICRODROPLET

2.1. Model

The characteristics of the plasma created by a laser pulse irradiating a droplet and the processes induced by their interaction vary rapidly during and after the interaction. This observation provides a basis for a hierarchy of time scales characteristic of plasma evolution. At the initial stage of irradiation, atoms and ions are ionized, a fraction of electrons is released from the droplet and is distributed uniformly in space, the droplet becomes positively charged, and the remaining electrons are trapped in the self-consistent potential of the droplet. At the next stage, the positive charge and the hydrodynamic pressure of the trapped electrons cause the structure to disintegrate. As the droplet expands, all density gradients tend to zero and the plasma becomes spatially uniform. Simultaneously, the kinetic energy of electrons transforms into x-ray radiation and kinetic energy of ions. The duration of this stage varies from tens to hundreds of picoseconds. Note that the characteristic final ion energy is higher than the electron energy. At the third stage, the resulting uniform plasma decays in several nanoseconds. An analogous model was successfully used to analyze interaction between a cluster beam and a laser pulse [23].

Let us consider the irradiation stage in more detail. A laser pulse ionizes atoms, and the microdroplet transforms into a dense plasma. Driven by the laser field, the electrons trapped in the droplet oscillate, which may lead to droplet deformation and affect both the degree of ionization of the droplet as a whole and the distribution of the trapped electrons. If the oscillation amplitude δ is relatively small as compared to the droplet size, it can be estimated as follows [24]:

$$\delta \approx \frac{F}{\omega_{\mathrm{Mi}e}^2}, \tag{1}$$

where $\omega_{\mathrm{Mi}e}$ is the Mie frequency of electrons in the cloud and F is the external field intensity. (Henceforth, we use the atomic system of units with $\hbar = m_e = e = 1$.) The Mie frequency is related to the electron concentration n_e as

$$\omega_{\mathrm{Mi}e}^2 = \frac{4}{3}\pi n_e = \frac{Z}{r_{\mathrm{W}}^3},$$

where r_{W} is the Wigner–Seitz radius. Comparing the amplitude of electron-cloud oscillation with the droplet radius R, we obtain

$$\frac{\delta}{R} \approx \frac{F}{Z/r_{\mathrm{W}}^2} n_e^{-1/3}. \tag{2}$$

When a xenon droplet consisting of 10^9 ions with charge Z varying between 30 and 40 is exposed to radiation of an intensity of 10^{19} W/cm^2, this ratio does not exceed 10^{-2}; i.e., the droplet retains its spherical symmetry.

The penetration of a laser pulse into a droplet calls for a special analysis. The propagation of an electromagnetic wave into a droplet is impeded by two factors: reflection of the electromagnetic wave from the droplet surface due to skin effect and strong surface absorption due to a high density of electrons in the droplet. If the skin depth exceeds the absorption depth, then a greater part of the radiation incident on the droplet is scattered. In the opposite limit, radiation is absorbed by the droplet and the effective absorption cross section of the droplet is approximately equal to its geometrical cross section. The plasma skin depth l_{skin} is

$$l_{\mathrm{skin}} = \frac{c}{\sqrt{2\pi\sigma\omega}}, \tag{3}$$

where the conductivity σ at an electron temperature T is expressed as

$$\sigma = \frac{4\sqrt{2}}{\pi^{3/2}} \frac{T^{3/2}}{Z\ln\Lambda} \tag{4}$$

if the electron–ion collision frequency ν_{ei} is much higher than the radiation frequency ω ($\ln\Lambda$ is the Coulomb logarithm) [25]. Substituting (4) into expression (3), we estimate the skin depth as

$$l_{\mathrm{skin}} \sim \frac{c}{\omega_{\mathrm{p}}}\sqrt{\frac{\nu_{ei}}{\omega}}, \tag{5}$$

where ω_{p} is plasma frequency. According to [26], the absorption depth l_{abs} for a uniform plasma is

$$l_{\mathrm{abs}} \sim \frac{\nu_{ei} c}{\omega_{\mathrm{p}}^2}. \tag{6}$$

Combining (6) with (5), we have

$$\frac{l_{\text{skin}}}{l_{\text{abs}}} \sim \sqrt{\frac{\omega_p^2}{\nu_{ei}\omega}} \gg 1. \quad (7)$$

Thus, when the plasma density is high, radiation is almost completely absorbed by the droplet and the corresponding effective cross section for a single droplet is equal to its geometrical cross section. Note that the expression for absorption depth used here was obtained in the limit of weak absorption, whereas we consider the opposite limit. However, the use of more complicated models would not lead to qualitatively different results, because the electron mean free path l_{free} in a droplet is much smaller than the droplet radius R. To analyze the heating of electrons, we tacitly assume that absorption by a droplet is due to bremsstrahlung and ignore the Brunel mechanism [27]. This assumption can be justified by simple estimates. When the droplet charge is Q, the concentration of electrons outside the cluster is estimated as Q/R_0^3 (where R_0 is the distance between clusters) and the energy absorbed by the electrons per unit time does not exceed

$$W_{\text{Br}} \sim 4\pi R^2 \nu \frac{Q}{R_0^3}\left(\frac{R}{R_0}\right)^3 \frac{F^2}{\omega^2}. \quad (8)$$

Since the charge Q can be estimated as (10–40)RT and $R/R_0 \sim 0.1$, we compare W_{Br} with the bremsstrahlung absorption rate $cF^2R^2/2$ to obtain

$$\frac{2W_{\text{Br}}}{cF^2R^2} \sim 8\pi \frac{\nu}{c}\frac{Q/R_0}{\omega^2 R_0^2}\left(\frac{R}{R_0}\right)^3 \ll 1. \quad (9)$$

The distribution of electrons in a droplet determines the processes taking place during and after the pulse–droplet interaction. Following [25], we estimate the electron–electron collision time at $T \approx 3$ keV for $Z = 30$ as

$$\tau_{ee} \sim \frac{3T^{3/2}}{4\sqrt{2\pi}n_e \ln\Lambda} \sim 10 \text{ fs}. \quad (10)$$

Therefore, the time of relaxation to the Boltzmann distribution of electron energy is comparable to the laser period (3 fs); i.e., the electron subsystem is in thermal equilibrium even during the interaction with the pulse. In the case of an equilibrium electron energy distribution, the electron concentration in a droplet with charge Q and concentration n_i of ions with charge Z is expressed as

$$n_e(r) \approx Zn_i\left[1 - \frac{2Qe^{-k}}{kTr}\sinh\frac{kr}{R}\right], \quad k = \sqrt{\frac{3N}{RT}}, \quad (11)$$

where N is the number of atoms in the droplet [26]. Thus, the electron concentration is nearly uniform inside the droplet and exponentially decreases at its boundary.

Summarizing the estimates presented above, we come to the following conclusions about the evolution of a microdroplet in a laser field. First, an initially neutral droplet transforms into a dense blob of highly charged ions and electrons and becomes positively charged. Second, a Boltzmann distribution of electron energy is reached during the interaction with a laser pulse, and the electron concentration is nearly uniform inside the droplet, exponentially decreasing toward its boundary. Third, the absorption cross section of a microdroplet is equal to its geometrical cross section, radiation energy is absorbed by the droplet via a bremsstrahlung mechanism and transferred inwards by electrons, the droplet retains its spherical shape in laser field, and the amplitude of its oscillation is small as compared to its radius.

2.2. Results

We used the estimates presented in the preceding subsection to construct a model describing the basic parameters of the resulting plasma at all stages of its evolution. Let us consider the initial stage of plasma formation. The laser pulse ionizes atoms and heats electrons. The first electrons are released via ionization by the laser field, and further ionization is due to inelastic collisions of the droplet electrons with ions. The energy balance equation for these processes is

$$\int_0^t dt I(t)\pi R^2 = N\sum_{Z=0}^{Z_{\max}} J_Z + \frac{Q^2}{2R} + \frac{3}{2}ZNT, \quad (12)$$

where J_Z denotes the ionization potential for an ion with charge $Z - 1$. To obtain a closed system of equations describing the evolution of a droplet, the energy balance equation should be combined with equations describing ionization of ions and droplet as a whole. Ionization of ions is dominated by electron impact ionization, whereas ionization by the laser field is responsible for the creation of highly charged ions (with $Z >$ 8–10) in the course of cluster formation. The concentration of ions with charge Z is found by solving the balance equations

$$\frac{dn_Z}{dt} = S_Z,$$

$$S_Z = W_Z n_{Z-1} + R_{Z+1}n_{Z+1} - (W_{Z+1} + R_Z)n_Z,$$

$$S_0 = R_1 n_1 - W_1 n_0, \quad (13)$$

$$n_i = \sum_{Z=0}^{Z_{\max}} n_Z,$$

$$n_e \approx \sum_{Z=0}^{Z_{\max}} Z n_Z,$$

where W_Z and R_Z are, respectively, the ionization and recombination frequencies for ions with charge Z, and n_i and n_e denote the ion and electron concentrations in the microdroplet, respectively. Straightforward solution of the system of equations requires vast labor and computing resources. To simplify the problem, we make use of the average-ion model [28] and assume that the plasma consists of ions characterized by a continuously varying charge $Z = n_e/n_i$. Neglecting slow relaxation processes (three-body recombination, dielectronic recombination, and photorecombination), we write the following equation for the ion charge:

$$\frac{dZ}{dt} = n_e k(Z) = Z n_i K(Z), \tag{14}$$

with

$$K(Z) = p_Z \sqrt{\frac{8T}{\pi}} \frac{\pi}{J_Z^2} \exp\left(-\frac{J_Z}{T}\right) \equiv K_T \exp\left(-\frac{J_Z}{T}\right),$$

where p_Z is the number of equivalent electrons in a shell. The dominant mechanism of droplet ionization is thermionic emission of electrons from the droplet surface. If the droplet potential Q/R is much lower than the characteristic energy of bound electrons, then the release of electrons does not lead to any significant change in their distribution and its variation is described by the equation

$$\frac{dQ}{dt} = \frac{2}{\pi} T^2 R^2 \exp\left(-\frac{Q}{RT}\right). \tag{15}$$

Thus, we have a complete set of equations describing the evolution of a droplet at the irradiation stage. Let us now find the droplet charge and the contribution of thermionic emission to the energy balance. Ignoring the changes in electron temperature and droplet size, we integrate Eq. (15) with respect to time to obtain

$$Q = TR \ln \frac{2TR\tau}{\pi}, \tag{16}$$

where τ is the laser-pulse duration. According to expression (16), the droplet charge varies within (10–40)TR. Compare the energy E_{ion} required to ionize the droplet with the kinetic energy $E_{\text{kin}} = (3/2)NZT$ of the electron subsystem:

$$\frac{E_{\text{ion}}}{E_{\text{kin}}} = \frac{Q^2}{(3/2)NZTR} \sim 100 \frac{TR}{NZ}. \tag{17}$$

When the electron temperature is $T \approx 1$–3 keV, the ion charge is $Z = 30$–40, and the droplet radius is $R = 500$ nm, this ratio is lower than 10^{-2}; i.e., the contribution due to thermionic emission is insignificant. A fraction of the laser-pulse energy is consumed to ionize atoms in the droplet. The power required to ionize the ions with charge $Z - 1$ reaches a maximum W_{ion} when $T \approx J_Z$:

$$W_{\text{ion}} \approx J_Z \frac{N}{Z} \frac{3}{4\pi r_{\text{W}}^3} \frac{\sqrt{8\pi}}{J_Z^{3/2}} p_Z. \tag{18}$$

The corresponding power consumed to heat the electron subsystem is

$$W_{\text{H}} \approx \frac{3}{2}\left(Z \frac{dJ_Z}{dZ} + \frac{J_Z}{Z}\right). \tag{19}$$

Comparing (18) with (19), we obtain

$$\frac{W_{\text{ion}}}{W_{\text{H}}} \approx \frac{p_Z}{r_{\text{W}}^3 (dJ_Z/dZ)\sqrt{J_Z}} \ll 1. \tag{20}$$

Thus, the energy consumed to ionize both ions and the droplet as a whole is low as compared to that required to heat the electron subsystem, and the rate of ionization of ions is controlled by the electron temperature. The final ion charge Z_{fin} can be found from the relation

$$Z_{\text{fin}} J_{Z_{\text{fin}}} = \frac{r_{\text{W}}^2}{6N^{1/3}} c F^2 \tau = \frac{2\pi r_{\text{W}}^2}{3N^{1/3}} I\tau. \tag{21}$$

If $I\tau = 2 \times 10^{19}$ [W/cm^2] $\cdot$ 30 [fs] and $N = 10^9$, then the xenon and krypton droplet ions are neon- and helium-like, respectively. After interaction with a laser pulse, ionization of droplet ions continues, but at a substantially lower rate, because the droplet breaks up and electrons cool down. Therefore, we can neglect ionization after the interaction with laser pulse in the first approximation.

After the interaction with laser pulse, the droplet begins to decay. A highly charged ion in the cluster is driven by the result of three forces: the electrostatic force F_E exerted by the cluster, the force F_h of electron-gas pressure, and the drag force F_r due to electron scattering. Since the electron density is nearly uniform inside the droplet and rapidly varies only at its bound-

ary, the hydrodynamic pressure is important only at the droplet surface. The hydrodynamic force is comparable to the electrostatic force exerted by the droplet:

$$F_h = -\frac{\nabla P}{n_i} \sim \frac{T}{n_i}\frac{dn_e}{dr} \sim \frac{QZ}{r^2}, \quad (22)$$

where P is the electron-gas pressure. The drag force can strongly affect the motion of ions, being comparable to the electrostatic force:

$$F_r \sim n_e \frac{Z^2}{T^{3/2}} v_i \sim ZN^{1/3}\left(\frac{Z}{r_W T}\right)^2 F_E, \quad (23)$$

where v_i is the ion velocity. The general equation of motion for ions of mass M is

$$\frac{M dv_i}{dt} = -\frac{\nabla P}{n_i} - \frac{Q(r)Z}{r^2 M} - F_r. \quad (24)$$

A solution of this equation can be obtained only by a numerical method that takes into account redistribution of electrons in the self-consistent potential of the droplet, which lies outside the scope of this paper. In this study, we focus on estimating the characteristic droplet breakup time and the effects of both pulse and prepulse on droplet stability. To estimate the cluster expansion time, we retain only the Coulomb term and assume that the droplet expands uniformly (the velocity of each layer is proportional to its distance from the center). Then, the microdroplet breakup time is

$$t_{\exp} \sim \sqrt{\frac{MR_0^3}{QZ}} = \sqrt{\frac{MR_0^2}{TZ}}\sqrt{\frac{TR_0}{Q}}, \quad (25)$$

where R_0 is the initial droplet radius. Suppose that the electron temperature is approximately equal to the ionization potential for an ion with charge Z and energy is consumed to heat and ionize ions. Then, we obtain

$$t_{\exp} \sim \sqrt{\frac{MN}{cF^2}\frac{RT}{Q}}. \quad (26)$$

If time and prepulse intensity are measured in picoseconds and W/cm^2, respectively, then

$$t_{\exp} \sim 10^4 \sqrt{\frac{N}{I_{\rm pr}}}. \quad (27)$$

For $I_{\rm pr} \sim 10^{14}$ W/cm^2, the expansion time is 100 ps; i.e., it exceeds a typical pulse duration by two orders of magnitude. Expression (27) can also be used to estimate the microdroplet breakup time after its interaction with the main pulse. For $I \sim 10^{19}$ W/cm^2, the breakup time is estimated as 100 fs. In the case of a uniformly expanding droplet, this means that an appreciable number of ions accelerate to velocities on the order of 10^9 cm/s. Accordingly, a substantial Doppler broadening must be recorded in experiments, but is not actually observed. This disagreement has an obvious explanation emphasizing the distinction between microdroplets and clusters. Both electron-density gradient and uncompensated droplet charge, which are responsible for the breakup, have relatively large values only on the droplet surface and exponentially decrease toward the center by Eq. (11). In particular, the electrostatic field that accelerates ions is

$$E \sim \frac{Q}{r^2}\exp[-k(R-r_0)],$$

where r_0 is the initial radial location of the ion. Therefore, the forces acting on ions in the droplet are strong only on the surface, and only a small number of ions contained in a layer of thickness about R/k leaves the droplet quickly (recall that $k = \sqrt{3N/RT} \gg 1$), whereas most ions accelerate at later stages. This leads to a higher stability of the droplet.

Let us consider the electron-gas temperature variation due to the expansion of a microdroplet. Droplet breakup is an adiabatic process with respect to the electron subsystem; i.e., the plasma remains in equilibrium at any instant. Indeed, the electron relaxation time (estimated as the electron–electron collision time τ_{ee}) can be used to write

$$\frac{dV}{dt}\frac{\tau_{ee}}{V} \sim \frac{dR}{dt}\frac{\tau_{ee}}{R}. \quad (28)$$

The ion velocity on the droplet surface, $u = dR/dt$, becomes almost constant after the droplet size has increased by a factor of two or three:

$$u = \frac{dR}{dt} \approx \sqrt{\frac{QZ}{2R_0 M}}. \quad (29)$$

Substituting expressions (10) and (29) for electron–electron collision time and expansion velocity into (28), we obtain

$$\frac{dV}{dt}\frac{\tau_{ee}}{V} \sim \left(\frac{T}{Z/\tilde{r}}\right)^2 \frac{Z}{N^{1/3}}\sqrt{\frac{Q}{R_0 T}}\sqrt{\frac{Z}{M}} \ll 1, \quad (30)$$

where $\tilde{r}$ is the average distance between ions. Thus, the electron gas cools down adiabatically:

$$T = T_0\left(\frac{R_{\rm fin}}{R_0}\right)^{9/5}. \quad (31)$$

According to Eq. (31), the electron-gas temperature in a typical target must drop by 100 times (the distance

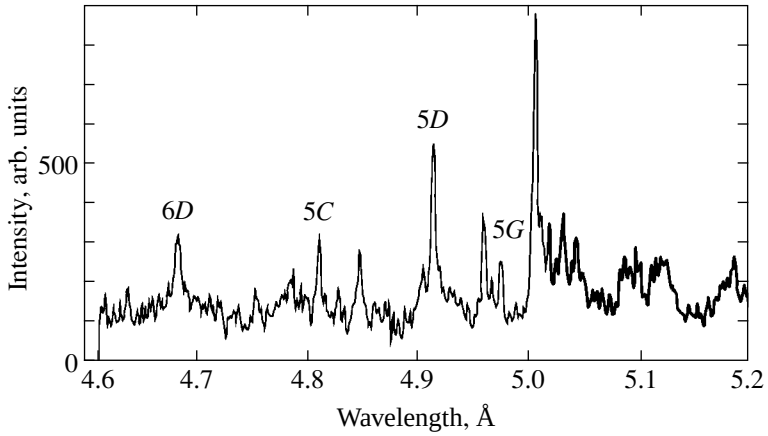

Fig. 1. Example of the x-ray spectrum emitted by krypton microdroplet plasma.

between droplets about ten times larger than the initial droplet size). However, the influence of electrons released from the droplet at earlier stages impedes this process, and the final electron temperature recorded in experiments is higher than the estimated one by an order of magnitude.

We have analyzed the evolution of a microdroplet interacting with a high-power laser pulse and the processes taking place after their interaction. It has been established that the radiation incident on the droplet is entirely absorbed. The plasma thus produced is superheated, and its temperature is comparable to the ionization potential for an ion with a characteristic charge. After interaction with the laser pulse, the electron gas rapidly cools down and its temperature drops by several times, while ion recombination processes are inhibited. A droplet target is totally insensitive to the pulse shape and duration, and even picosecond prepulses of relatively high intensity (about 10^{14} W/cm^2) cannot strongly affect the evolution of a microdroplet. These conclusions are supported by the experimental results presented in the next section.

3. X-RAY SPECTRAL STUDIES OF XENON AND KRYPTON MICRODROPLETS HEATED BY LASER PULSES OF DURATION 30–500 fs

Experiments were performed at JAERI (Kyoto, Japan) by using a 100-terawatt Ti:sapphire laser system with amplification of chirped laser pulses. The system was designed to generate pulses of width 20 fs at a repetition rate of 10 Hz. The pulses could be focused to reach intensities of up to 10^{20} W/cm^2 [29, 30]. The starting pulses (with $\lambda = 800$ nm and $\tau = 10$ fs at a repetition rate of 82.7 MHz) were generated by a Ti:sapphire oscillator. These pulse were stretched to a width of 10 ns, chirped, and then amplified by a regenerative amplifier and two multipass amplifiers. The amplified pulses were compressed to 30 fs by a vacuum pulse compressor with a maximum output energy of 1.9 J. Compressed pulses were directed by two gilded flat mirrors into a vacuum target chamber and focused by an off-axis parabolic mirror with an aperture of *f*/3. The focal-spot diameter measured at the $1/e^2$ level was 11 μm, which is only 10% higher than the diffraction limit. A Gaussian spot of similar diameter would contain about 64% of the total energy. The peak intensity of the laser pulses of width 30 fs and energy 300 mJ used in the experiments was 1.2×10^{19} W/cm^2. The pulses were passed through two Pockels cells to suppress the prepulse. The pulse contrast ratio normalized to a prepulse of similar duration preceding by 1 ns was higher than 10^5.

Microdroplets were created in a supersonic krypton or xenon jet expanding (from 2.8 and 2.0 MPa, respectively) into a vacuum chamber through a specially designed pulsed conical nozzle. The nozzle entrance and exit diameters were 0.5 and 2.0 mm, respectively, and its length was 75 mm. The nozzle geometry was specified by using the results of numerical simulations performed for a two-phase jet to optimize the concentration of clusters of the required diameter ($d_d \approx 1$ μm) [31–33].

In the experiment, a laser pulse was focused on the jet at 1.5 mm downstream of the nozzle exit. The x-ray spectra of the laser plasma were measured with the use of a FSPR-1 focusing spectrometer with spatial resolution [34–37]. The spectrometer was equipped with a mica crystal spherically bent with a radius of 150 mm and a DX420-BN ANDOR vacuum-compatible x-ray camera. When the spectra were recorded near the 4–2 transitions in the neonlike krypton ion, the crystal was placed at 381.2 mm from the plasma radiation source and was oriented at the Bragg angle $\theta = 54.3°$ (with third-order reflection at a wavelength of 0.54 nm). When the Rydberg spectrum of krypton or xenon ions was recorded at 2.7–2.9 Å, the crystal was placed at 360 mm from the plasma and was oriented at a Bragg

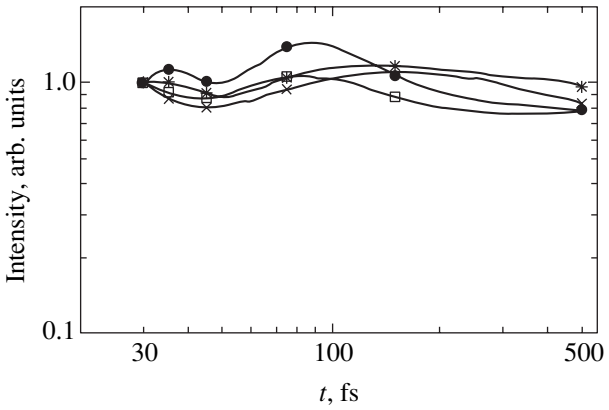

Fig. 2. Spectral line intensity versus laser pulse width for highly charged krypton ions: ●—F-like ion lines; □—4*D* line of Ne-like ion; ∗—Na-like satellites; ×—Mg-like satellites. All intensities are normalized to their respective values at $\tau = 30$ fs.

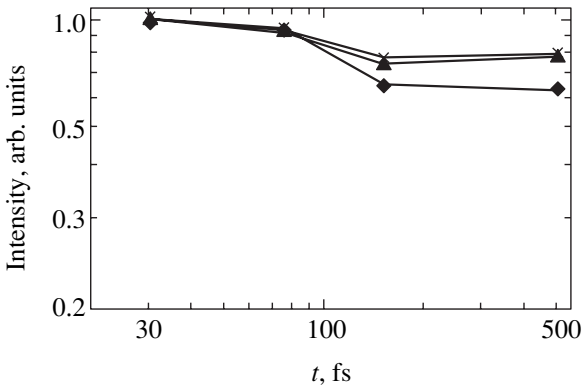

Fig. 3. Rydberg line intensity versus laser pulse width for highly charged krypton ions at $E = 110$ mJ: ▲—5*D* line of Ne-like ion; ◆—6*D* line of Ne-like ion; ×—Na-like satellites. All intensities are normalized to their respective values at $\tau = 30$ fs.

angle of about 45°. In all cases, the reflection plane of the spectrometer was oriented along the laser beam to ensure one-dimensional transverse resolution.

Figure 1 shows the x-ray spectrum emitted by the krypton plasma in the wavelength range of 4.6 to 5.2 Å. Note that the krypton microdroplet spectrum includes lines of the neonlike Kr XXVII ion (in particular, the 6*D*, 5*C*, 5*D*, and 5*G* lines shown in Fig. 1), as well as lines of the fluorine-like Kr XXVIII ion and the dielectronic satellites corresponding to transitions in the sodium-like Kr XXV and magnesium-like Kr XXVI ions. The spectrum emitted by xenon microdroplet plasma includes resonant lines of the neonlike Xe XLV ion and their dielectronic satellites in the wavelength range of 2.75 to 2.95 Å.

One principal prediction of the model of microdroplet evolution considered above is that droplet-target plasmas are insensitive to the width of laser pulses of constant energy. Figure 2 demonstrates that this conclusion is fully consistent with experimental results. Indeed, as the pulse width varies from 30 to 500 fs, the intensities of the spectral lines corresponding to transitions between the shells with the principal quantum numbers 4 and 2 in F-, Ne-, Na-, and Mg-like krypton ions are equal within 20%, whereas the heating-radiation flux density changes by 25 times. A similar variation of the laser-pulse width leads to a 30% drop in the intensities of transitions from Rydberg states of Ne- and Na-like krypton ions (see Fig. 3). This can be explained by the drop in concentration of generated

Table 1. Numerical results for krypton (focal-spot diameter = 10.8 μm)

N	*E*, J	*R*, nm	*T*, eV	*Z*
10^9	0.035	255	850	18
10^{10}	0.035	550	500	14
10^{11}	0.035	1200	330	10
10^9	0.07	255	1200	25
10^{10}	0.07	550	790	18
10^{11}	0.07	1200	470	14
10^9	0.11	255	1800	26
10^{10}	0.11	550	1000	22
10^{11}	0.11	1200	640	16
10^9	0.305	255	4010	33
10^{10}	0.305	550	2370	26
10^{11}	0.305	1200	1190	24

Table 2. Numerical results for xenon (focal-spot diameter = 10.8 μm)

N	*E*, J	*R*, nm	*T*, eV	*Z*
10^9	0.035	260	845	18
10^{10}	0.035	570	504	14
10^{11}	0.035	1200	328	10
10^9	0.07	260	1216	25
10^{10}	0.07	570	784	18
10^{11}	0.07	1200	468	14
10^9	0.13	260	2000	32
10^{10}	0.13	570	1150	26
10^{11}	0.13	1200	650	21
10^9	0.3	260	3400	43
10^{10}	0.3	570	2050	33
10^{11}	0.3	1200	1200	26

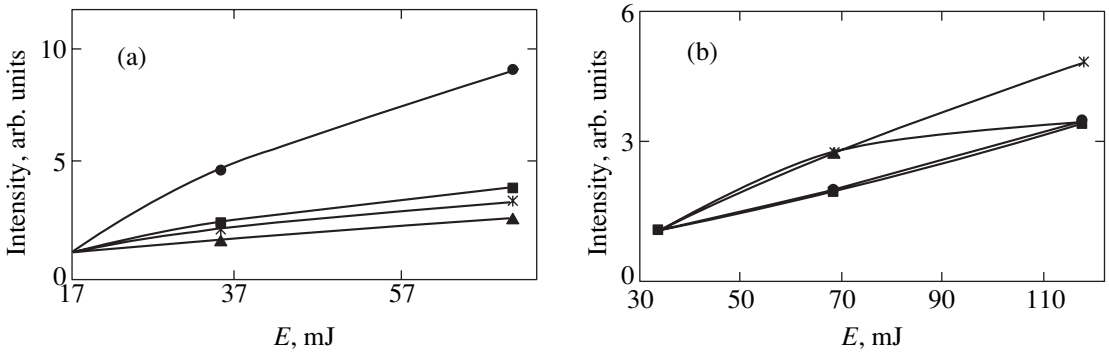

Fig. 4. Spectral line intensity versus laser pulse energy for highly charged krypton ions at $\tau = 45$ fs (a) and $\tau = 500$ fs (b): ●—F-like ion lines; ■—4*D* line of Ne-like ion; ∗— Na-like satellites; ▲—Mg-like satellites. All intensities are normalized to their respective values at minimal energies.

superthermal electrons when the pulse duration exceeds 100 fs (i.e., the flux density is below 10^{18} W/cm^2). Note that these electrons are ignored in the simple model presented above, but they may contribute substantially to the populations of high-lying excited states. According to Fig. 3, superthermal electrons play an insignificant role in the case of ions with L shells in the ground states: when the flux density is below 6×10^{18} W/cm^2, their contribution to Rydberg line intensities does not exceed 30%.

The numerical results listed in Tables 1 and 2 demonstrate that the parameters of droplet-target plasmas mainly depend on the total pulse energy. Figures 4a and 4b show line intensities measured for highly charged krypton ions as functions of pulse energy at $\tau = 45$ fs and $\tau = 500$ fs, respectively. It is clear that the x-ray emission by the plasma does increase with pulse energy. Note (see Fig. 4b) that the line intensities increase almost similarly for all krypton ions considered when the flux density is relatively low ($I \approx 2 \times 10^{17}$ W/cm^2), whereas the line intensities for the F-like Kr XXVIII ion increase to much higher values when $I > 5 \times 10^{17}$ W/cm^2. This result can also be explained by generation of superthermal electrons, which shifts the ionization balance in the plasma. As a consequence, the increase in F-like transition line intensity is determined not only by an increase in the rate of excitation by electron impact, but also by an increase in the concentration of higher charged (F-like) ions.

Figure 5 shows Rydberg line intensities versus pulse energy measured for Ne- and Na-like krypton ions. The laser pulse width was 30 fs, and the flux density was as high as 2×10^{19} W/cm^2. The figure demonstrates that the spectral line intensities are nonmonotonic functions of pulse energy decreasing as the energy increases to 380 mJ, with maxima at $E \approx 160$ mJ. According to Table 1, the ionized states corresponding to the highest energies in this interval are shifted toward higher charged ions (even to heliumlike ones), which explains the decrease in the Ne- and Na-like ion line intensities.

Analogous results were obtained for xenon droplets. As an example, Fig. 6 shows the intensities of three spectral lines (with wavelengths of 2.77, 2.90, and 2.96 Å) versus pulse width and energy. These lines correspond to resonant transitions in the neonlike xenon ion and their electron satellites. As in the case of krypton, these line intensities are virtually independent of pulse width when the pulse energy is constant (see Fig. 6b) and increase as the pulse energy is increased to 300 mJ while the pulse width is held constant (see Fig. 6a). In contrast to krypton plasmas, the concentrations of the neonlike Xe XLV reach maximum values at energies up to 300 mJ (see Table 2), and the curves shown in Fig. 6a do not exhibit explicitly nonmonotonic behavior.

In addition to x-ray spectrometry of plasma radiation, we also used a time-of-flight detector, which also recorded the total vacuum UV and x-ray emission by ions leaving the plasma. Figure 7 shows examples of oscilloscopic traces obtained for heated krypton droplets. They also demonstrate that the time-of-flight detector output remains invariant as the pulse width is increased from 30 to 500 fs while the pulse energy is

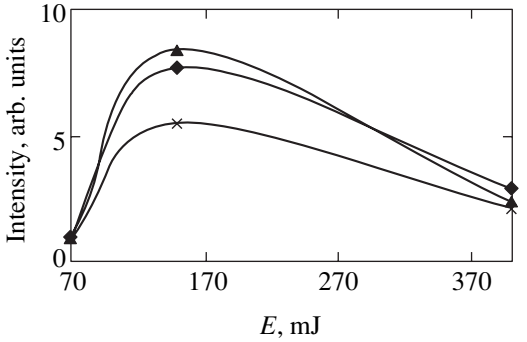

Fig. 5. Rydberg line intensity versus laser pulse energy for highly charged krypton ions at $\tau = 30$ mJ: ▲—5*D* line of Ne-like ion; ◆—6*D* line of Ne-like ion; ×—Na-like satellites. All intensities are normalized to their respective values at $E = 70$ mJ.

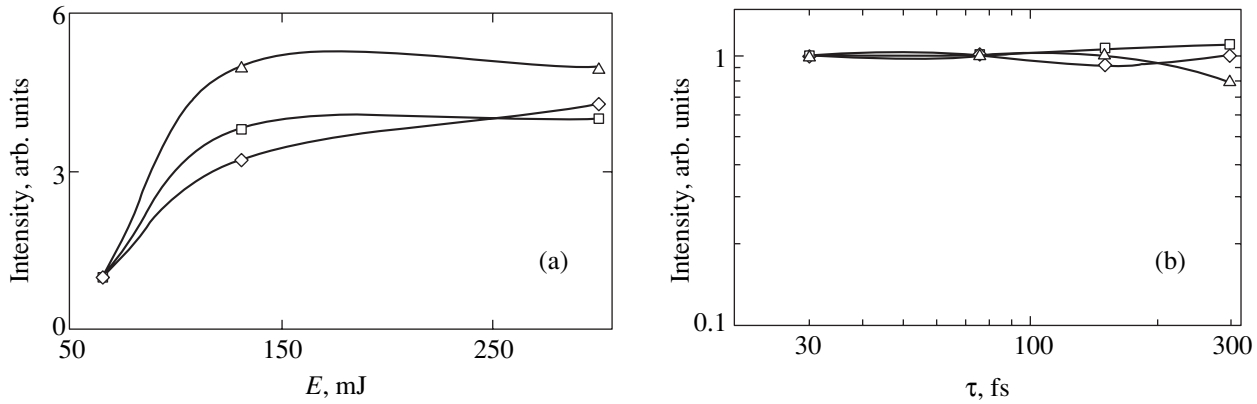

Fig. 6. Spectral line intensity versus laser pulse energy at $\tau = 30$ fs (a) and width at $E = 300$ mJ (b) for highly charged xenon ions: □—2.77 Å; Δ—2.90 Å; ◇—2.96 Å. All line intensities are normalized to their values at $E = 70$ mJ.

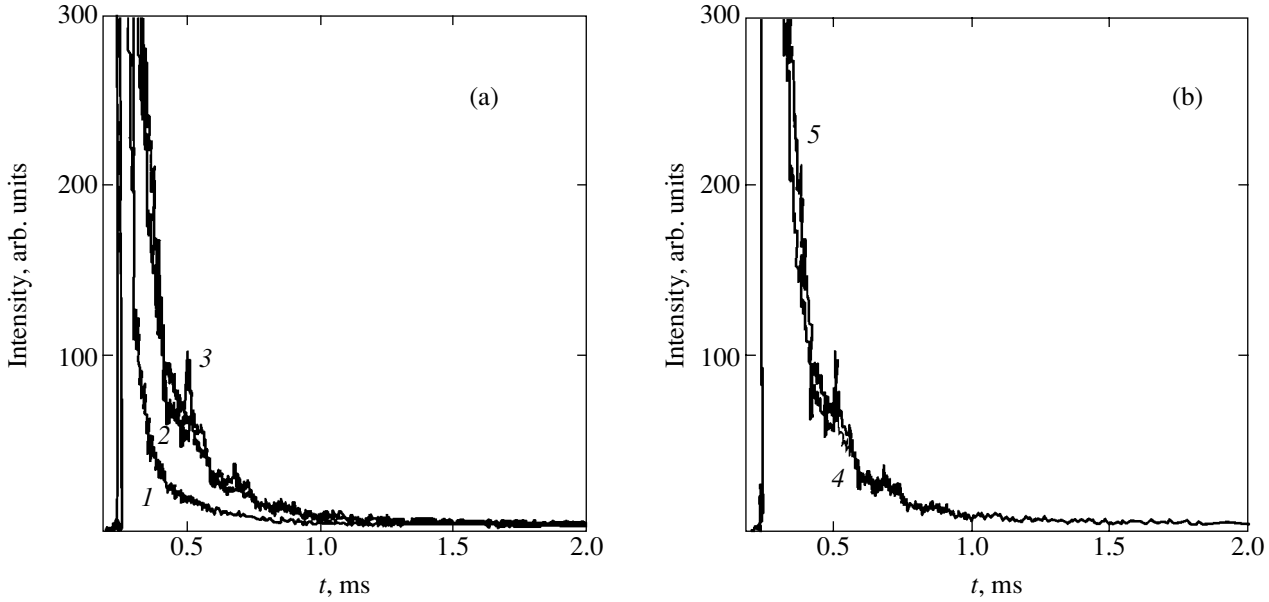

Fig. 7. Time-of-flight detector output signals obtained in experiments on krypton microdroplets at constant pulse width (a) and energy (b): *1*—$E = 57$ mJ, $\tau = 30$ fs; *2*—$E = 123$ mJ, $\tau = 30$ fs; *3*—$E = 326$ mJ, $\tau = 30$ fs; *4*—$E = 320$ mJ, $\tau = 500$ fs; *5*—$E = 320$ mJ, $\tau = 30$ fs.

held constant (curves *4* and *5*), whereas an increase in the energy of pulses of equal width leads to a substantial increase in output at short times of flight, where the detector signal is due to high-energy ions and photons (curves *1–3*).

4. CONCLUSIONS

We propose a simple model of microdroplet evolution induced by a high-power ultrashort laser pulse. It is shown theoretically that the droplet target is insensitive to the pulse shape and duration and the characteristics of the resulting laser plasma are almost entirely determined by the pulse energy. Theoretical predictions are supported by x-ray spectral studies performed with laser pulses of widths varying from 30 to 500 fs, energies between 10 and 400 mJ, and flux densities of 6×10^{16} to 2×10^{19} Wt/cm^2.

ACKNOWLEDGMENTS

This work was supported by INTAS, project no. 01-0233; the Russian Foundation for Basic Research, project no. 02-01-00708; and the CRDF, grant no. RPI-2328-ME-02. One of the authors (M.B.S.) is grateful for support provided by the Russian Foundation for Basic Research, project no. 01-02-16506, and the CRDF, grant no. MO-011-0.

REFERENCES

1. B. M. Smirnov, *Clusters and Small Particles in Gases and Plasmas* (Springer, New York, 2000).

2. T. Ditmire, T. Donnelly, A. M. Rubenchik, *et al.*, Phys. Rev. A **53**, 3379 (1996).
3. V. P. Krainov and M. B. Smirnov, Phys. Rep. **370**, 237 (2002).
4. G. C. Junkel-Vives, J. Abdallah, Jr., F. Blasco, *et al.*, Phys. Rev. A **66**, 033204 (2002).
5. A. I. Magunov, T. A. Pikuz, I. Yu. Skobelev, *et al.*, Pis'ma Zh. Éksp. Teor. Fiz. **74**, 412 (2001) [JETP Lett. **74**, 375 (2001)].
6. Y. L. Shao, T. Ditmire, J. W. G. Tisch, *et al.*, Phys. Rev. Lett. **77**, 3343 (1996).
7. B. N. Chichkov, Y. Kato, H. Ruhl, and S. A. Uryupin, Phys. Rev. A **50**, 2691 (1994).
8. T. Ditmire, R. A. Smith, J. W. G. Tisch, and M. H. R. Hutchinson, Phys. Rev. Lett. **78**, 3121 (1997).
9. S. Dobosz, M. Schmidt, M. Perdrix, *et al.*, Zh. Éksp. Teor. Fiz. **115**, 2051 (1999) [JETP **88**, 1122 (1999)].
10. M. B. Smirnov and V. P. Krainov, Phys. Rep. A (in press).
11. T. Ditmire, T. Donnelly, R. W. Falcone, and M. D. Peny, Phys. Rev. Lett. **75**, 3122 (1995).
12. T. Mocek, C. M. Kim, H. J. Shin, *et al.*, Appl. Phys. Lett. **76**, 1819 (2000).
13. M. Mori, T. Shiraishi, E. Takahashi, *et al.*, J. Appl. Phys. **90**, 3595 (2001).
14. M. Schnurer, S. Ter-Avetisyan, H. Stiel, *et al.*, Eur. Phys. J. D **14**, 331 (2001).
15. J. Zweiback, R. A. Smith, T. E. Cowan, *et al.*, Phys. Rep. Lett. **84**, 2634 (2000).
16. T. Auguste, P. D'Oliveĭra, S. Hulin, *et al.*, Pis'ma Zh. Éksp. Teor. Fiz. **72**, 54 (2000) [JETP Lett. **72**, 38 (2000)].
17. I. Yu. Skobelev, A. Ya. Faenov, A. I. Magunov, *et al.*, Zh. Éksp. Teor. Fiz. **121**, 1124 (2002) [JETP **94**, 966 (2002)].
18. G. C. Junkel-Vives, J. Abdallah, Jr., T. Auguste, *et al.*, Phys. Rev. E **65**, 036410 (2002).
19. J. Abdallah, Jr., A. Ya. Faenov, I. Yu. Skobelev, *et al.*, Phys. Rev. A **63**, 032706 (2001).
20. K. Y. Kim, I. Alexeev, E. Parra, and H. M. Milchberg, Phys. Rev. Lett. **90**, 023401 (2003).
21. E. Parra, I. Alexeev, J. Y. Fan, *et al.*, J. Opt. Soc. Am. B **20**, 118 (2003).
22. M. B. Smirnov and V. P. Krainov, Phys. Plasmas **10**, 443 (2003).
23. M. B. Smirnov, Zh. Éksp. Teor. Fiz. **124**, 48 (2003) [JETP **97**, 42 (2003)].
24. P. B. Parks, T. E. Cowan, R. B. Stephens, and E. M. Campbell, Phys. Rev. A **63**, 063203 (2001).
25. E. M. Lifshitz and L. P. Pitaevskiĭ, *Physical Kinetics* (Nauka, Moscow, 1979; Pergamon Press, Oxford, 1981).
26. V. P. Kraĭnov and M. B. Smirnov, Usp. Fiz. Nauk **170**, 969 (2000) [Phys. Usp. **43**, 901 (2000)].
27. F. Brunel, Phys. Rev. Lett. **59**, 52 (1987).
28. N. E. Andreev, I. L. Beĭgman, M. E. Veĭsman, *et al.*, Preprint No. 59, FIAN (Physical Inst., USSR Academy of Sciences, Moscow, 1988).
29. K. Yamakawa, M. Aoyama, S. Matsuoka, *et al.*, Opt. Lett. **23**, 1468 (1998).
30. K. Yamakawa and C. P. J. Barty, IEEE J. Sel. Top. Quantum Electron. **6**, 658 (2000).
31. A. S. Boldarev, V. A. Gasilov, F. Blasko, *et al.*, Pis'ma Zh. Éksp. Teor. Fiz. **73**, 583 (2001) [JETP Lett. **73**, 514 (2001)].
32. G. C. Junkel-Vives, J. Abdallah, Jr., T. Auguste, *et al.*, Phys. Rev. E **65**, 036410 (2002).
33. Y. Fukuda, K. Yamakava, Y. Akahane, *et al.*, Pis'ma Zh. Éksp. Teor. Fiz. **78**, 146 (2003) [JETP Lett. **78**, 115 (2003)].
34. A. Ya. Faenov, S. A. Pikuz, A. I. Erko, *et al.*, Phys. Scr. **50**, 333 (1994).
35. T. A. Pikuz, A. Ya. Faenov, S. A. Pikuz, *et al.*, J. X-Ray Sci. Technol. **5**, 323 (1995).
36. I. Yu. Skobelev, A. Ya. Faenov, B. A. Bryunetkin, *et al.*, Zh. Éksp. Teor. Fiz. **108**, 1263 (1995) [JETP **81**, 692 (1995)].
37. B. K. Young, A. L. Osterheld, D. F. Price, *et al.*, Rev. Sci. Instrum. **69**, 4049 (1998).

Translated by A. Betev

Journal of Experimental and Theoretical Physics, Vol. 98, No. 6, 2004, pp. 1133–1137.
Translated from Zhurnal Éksperimental'noĭ i Teoreticheskoĭ Fiziki, Vol. 125, No. 6, 2004, pp. 1295–1301.

PLASMA, GASES

Neutron Production in a Picosecond Laser Plasma at a Radiation Intensity of 3×10^{17} W/cm^2

V. S. Belyaev[a], V. I. Vinogradov[a], A. S. Kurilov[a], A. P. Matafonov[a], V. P. Andrianov[b], G. N. Ignat'ev[b], A. Ya. Faenov[c], T. A. Pikuz[c], I. Yu. Skobelev[c], A. I. Magunov[c], S. A. Pikuz, Jr.[d], and B. Yu. Sharkov[e]

[a]*Central Research Institute of Machine Building, Korolev, Moscow oblast, 141070 Russia*
[b]*Research Institute of Pulsed Technology, Moscow, 115304 Russia*
[c]*Multicharged Ions Spectra Data Center, VNIIFTRI, Mendeleevo, Moscow oblast, 141570 Russia*
[d]*Moscow State University, Vorob'evy gory, Moscow, 119992 Russia*
[e]*Institute of Theoretical and Experimental Physics, Moscow, 117218 Russia*
e-mail: VadimBelyaev@mtu-net.ru
Received November 5, 2003

Abstract—Neutron production as a result of the reaction ^{2}H(d, n)^{3}He in a picosecond laser plasma is reported. A considerable neutron yield of 5×10^4 per pulse is obtained for the first time in a picosecond laser plasma on the surface of a solid deuterated target at laser radiation intensity of 3×10^{17} W/cm^2. © *2004 MAIK "Nauka/Interperiodica".*

1. INTRODUCTION

Considerable advances in laser technology made in recent years in designing high-power lasers with ultrashort pulses (50 fs–1.5 ps) have created unique opportunities for solving new problems in such fields as nuclear physics, physical kinetics, and physics of atomic and radiative processes in plasma [1]. Such laser systems make it possible to attain powers of up to 10^{15} W and radiation intensities of 10^{17}–10^{21} W/cm^2 for radiation focused at a target. The laser plasma formed in this case is a source of X rays and γ radiation, as well as beams of charged particle (electrons, protons, ions, and α particles) and neutrons [2]. Analysis of the characteristics of these types of radiation serves as a tool for studying the atomic and nuclear processes occurring in such laser plasmas. Neutrons produced as a result of the reaction ^{2}H(d, n)^{3}He in a laser plasma were detected for the first time in [3], where the possibility of nuclear fusion reactions in a dense laser plasma was studied.

A number of recent publications have been devoted to the production of neutrons in a laser plasma with the help of laser radiation with an ultrashort pulse duration of τ = 35 fs–1.3 ps. Solid deuterated targets of CD_2, TiD_2, SiD_2, and PdD_2 [4–8], D_2 cluster targets [9–11], and gaseous D_2 targets [12] were used in these studies.

Almost all experiments on studying the neutron yield from a laser plasma on solid deuterated targets were performed with relativistic intensities exceeding 10^{18} W/cm^2. The reported neutron yield varied from 140 [7] to 10^9 [4]. Neutron production on a TiD_2 target with a subrelativistic intensity of 2×10^{16} W/cm^2 and with a yield of five neutrons per pulse has been reported so far only in one publication [8]. Nevertheless, the problem of obtaining an appreciable neutron yield for subrelativistic intensities is of considerable importance since its solution will make it possible to use relatively small terrawatt laser devices for the production and practical application of pulsed sources of nuclear radiation and for studying nuclear processes in a laser plasma.

2. EXPERIMENTAL SETUP

Experiments were made on a Neodim terrawatt laser system [13]. The laser setup has the following laser pulse parameters: energy up to 1.5 J, wavelength 1.055 μm, and duration 1.5 ps. The focusing system ensures a concentration of at least 50% of the laser beam energy at a spot 15 μm in diameter and, accordingly, an intensity on the target at a level of 3×10^{17} W/cm^2.

Laser radiation generated by the Neodim system is characterized by the presence of two types of prepulses, viz., picosecond and nanosecond prepulses. The first type is associated with the multipass nature of amplification in the regenerative amplifier and a finite transmission of the Pockels cell in such an amplifier [14]. A prepulse emerges 13 ns prior to the main pulse and has a duration of 1.5 ps. The energy of this prepulse does not exceed 100 μJ after its passage through the amplification path, which determines a laser radiation

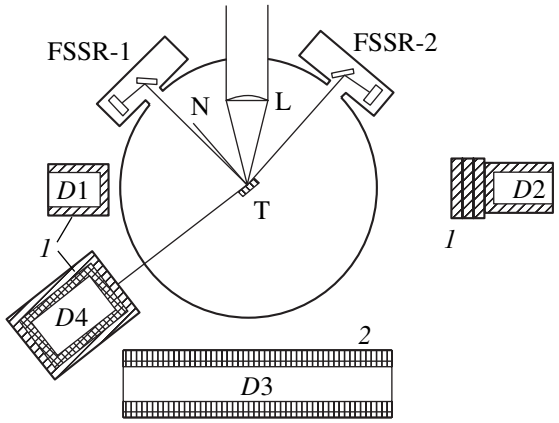

Fig. 1. Block diagram of experiment: *T*—flat target, *L*—focusing lens, *N*–normal to the target surface, FSSR-1 and FSSR-2—X-ray spectrographs, *D*1—scintillation detector based on a stilbene crystal ($C_{14}H_{12}$), *D*2—detector based on a plastic scintillator, *D*3—neutron detector with helium counters, *D*4—high-sensitivity activation neutron detector, *1*—lead, *2*—polyethylene.

intensity contrast of not worse than 10^4. The second prepulse is the result of amplified spontaneous emission in the regenerative amplifier. The duration of this pulse at half-height was 4 ns. The prepulse energy of an amplified spontaneous emission after its passage through the amplification path does not exceed 150 μJ, which determines a laser radiation intensity contrast of not worse than 10^7 relative to the amplified spontaneous emission pulse.

Unless special measures are taken, picosecond prepulses may appear tens of picoseconds prior to the main pulse. The reasons for the emergence of such prepulses are given in [15], where the method of chirped pulsed spectral interferometry is also described. This method can also be used for detecting such prepulses, for determining the reason for their emergence, and for eliminating these prepulses by suppressing their action (this was done using the Neodim laser system).

The block diagram of the setup is shown in Fig. 1. The laser beam was focused by an aspherical lens with a focal length of 14 cm to the surface of solid target *T* at an angle of 40° to the target normal. The targets were 150-, 250-, and 350-μm-thick flat plates of deuterated polyethylene $(CD_2)_n$, 200-μm-thick fluoroplastic plates, and 2-mm-thick beryllium plates. The target was placed at the center of a vacuum chamber 30 cm in diameter and 30 cm in height. The residual gas pressure in the vacuum chamber was not higher than 10^{-3} Torr. The laser radiation intensity at the target was controlled by measuring hard X-ray radiation with an energy of quanta of above 100 keV with the help of detector *D*1 mounted at a distance of 17 cm from the target. Detector *D*1 is a scintillation counter based on a stilbene crystal ($C_{14}H_{12}$) 5 cm in diameter and 5 cm in height. A 1.5-cm-thick lead shield was installed in front of detector *D*1; the thickness of the shield remained unchanged during the entire series of experiments. The lateral surfaces of detector *D*1 were covered by 1.5-cm-thick protecting lead plates.

The maximal energy of hard X-ray radiation and the number of hard γ quanta were estimated using scintillation detector *D*2 located at a distance of 35 cm from the target. The detector sensor was in the form of a plastic scintillator of diameter 5.0 cm and length 10.0 cm. Lead shields having a thickness up to 5 cm were installed in front of detector *D*2. The lateral surfaces of detector *D*2 were also covered by a 1.5-cm-thick protective lead layer.

Neutron radiation emitted by the laser plasma was monitored by neutron detector *D*3 operating on helium counters mounted at a distance of 25 cm from the target. Detector *D*3 consists of the following parts: a block of neutron counters based on three SNM-18 helium counters, a voltage transducer, a signal takeout device, and a power amplifier. Detector *D*3 was 45 cm in width, 20 cm in height, and 10 cm in thickness. The lateral surfaces of the detector are encased in a polyethylene covering 2 cm thick. Neutrons produced during a short (~1.5 ps) laser pulse are slowed down in polyethylene to the thermal energy over different time intervals and are detected by helium counters at different instants. In this way, a delay (stretching) in the time of detection of instantaneous neutron fluence is carried out. The efficiency of neutron detection for a steady-state neutron flow from a ^{252}Cf source was approximately 50%. Since the time resolution of detector *D*3 is on the order of 1 μs, it can be used only for neutron radiation monitoring.

Signals from detectors *D*1 and *D*2 are fed to the input of a TEKTRONIX TDS-3032 digital oscilloscope, while the signal from detector *D*3 is supplied to the input of a TEKTRONIX TDS-3014 digital oscilloscope. The neutron yield is determined with the help of a high-sensitivity activation-type neutron detector *D*4 mounted at a distance of 20 cm from the target. The detector is 9 cm in diameter and 5 cm in length. The sensitive element in detector *D*4 is an indium sleeve with a wall thickness of 0.8 mm, covering a 1.5-mm-thick scintillator.

The performance of the detector is based on the nuclear reaction $^{115}In(n, \gamma)^{116}In$, accompanied by the formation of radioactive nuclei with a half-life of 14.2 s. Figure 2 shows the variation of the total neutron capture cross section in indium in the thermal range of neutron energy [16]. A sharp resonance at 1.46 eV is clearly seen. The capture cross section in this energy range amounts to about 30000 barn.

The detector contains a polyethylene moderator for improving the sensitivity at the expense of resonance and thermal neutrons. The detector is protected from background radiation by a 1-cm-thick external lead shield.

The scintillator in the detector registers β particles with a threshold energy of 3.3 MeV, emitted during the decay of ^{116}In, over a period of 30 s. Weak light pulses

from the scintillator are amplified by a photomultiplier. The apparatus spectra of pulses have the shape of a clearly manifested peak formed during detection of β particles. Figure 3 shows an example of the recorded spectrum. The channel number of the spectrometric amplitude-to-digital converter is laid on the *x* axis and the relative count in the channels is plotted along the *y* axis.

The number of pulses recorded over 30 s are counted by summing the counts in channels from 110 to 330 with the help of a spectrometric transducer board. The sensitivity of detector *D*4 for a pulsed neutron beam with an energy of 2.5 MeV amounts to 0.5 counts/(neutrons/cm^2).

X-ray radiation emitted by the plasma produced as a result of the interaction of a laser pulse with the target was detected with the help of FSSR spectrographs [17] with spherically bent quartz or mica crystals (the radius of curvature of the crystal surface was 150 mm). In all experiments, the angle of observation was 5° to the normal to the target surface for spectrometer no. 1, and 85° for spectrometer no. 2 (see Fig. 1). Kodak-2492 X-ray film was used to detect radiation reflected from the crystal. The input window of the film was protected from visible radiation by a double-layer filter in the form of a 1-μm-thick polypropylene film with an Al layer of a total thickness of 0.2 μm deposited on both sides of the film. The emission spectra of the plasma were analyzed in the spectral range containing the Ly_α line of the H-like ion F IX. The spectral resolution $\lambda/\Delta\lambda$ ensured by the spectrographs under the experimental conditions was not worse than 5000.

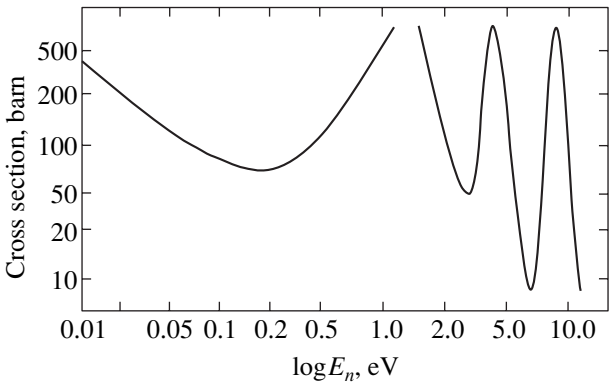

Fig. 2. Energy dependence of indium cross section.

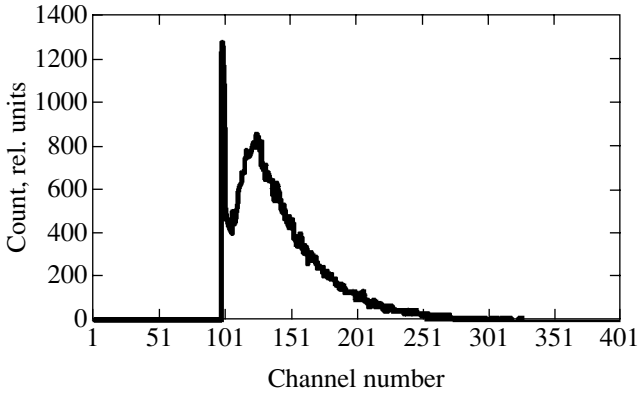

Fig. 3. An example of the recorded β-particle spectrum. The channel number of the amplitude-to-digital converter is laid on *x* axis and the relative count in the channel is plotted along the *y* axis.

3. EXPERIMENTAL RESULTS: DISCUSSION

Investigating the neutron yield from a laser plasma with an intensity of 3×10^{17} W/cm^2, we carried out in 8 series (10 experiments in each) using three different targets of deuterated polyethylene $(CD_2)_n$ of thickness 150, 250, and 350 μm. A neutron yield was detected from each target, but the best results were obtained with the 350-μm-thick $(CD_2)_n$ target. Figure 4a shows oscillograms of signals from neutron detector *D*3 operating on helium counters, which were obtained during the recording of neutron radiation from the laser plasma at the 350-μm-thick $(CD_2)_n$ target. The upper oscillogram shown in Fig. 4a was obtained from the digital output of detector *D*3, while the lower oscillogram was obtained from the analog output. Pulses from neutrons were detected only during the first 200 μs. No neutrons were detected from Be and fluoroplastic targets. The oscillograms of signals from the *D*3 detector (Fig. 4b) display a single pulse due to the action of γ radiation from the laser plasma and electromagnetic noise of the laser system. The neutron yield from the laser plasma on $(CD_2)_n$ targets was determined using activation detector *D*4. Taking into account the solid angle 0.16 sr of neutron detection and the detector sensitivity and assuming that the neutron distribution is isotropic, we determined the neutron yield per laser pulse. The maximal neutron yield per laser pulse amounted to 5×10^4. Considerable fluctuations in the value of neutron yield, amounting to a factor of several units, were observed from pulse to pulse.

Using scintillation detector *D*2 with a set of lead shields, we performed experiments on determining the maximal energy of γ quanta in a laser plasma on $(CD_2)_n$ as a function of the lead shield thickness. The attenuation of the γ-quantum flux was measured as a function of the lead shield thickness. The measured dependence was used for estimating the maximal energy of γ quanta, which amounted to 650 keV, the number of such quanta being equal to 10^6.

The presence of a considerable number of high-energy ions in the plasma is confirmed by the experimental observation of spectral profiles of X-ray lines. For this purpose, we performed a series of experiments with a fluoroplastic target for the same values of the laser pulse parameters, in which the spectral profiles of the Ly_α line of the H-like ion F IX were recorded.

Figure 5 shows the recorded profile of the 2*p*–1*s* line of the H-like ion F IX. It can be seen that the profile has

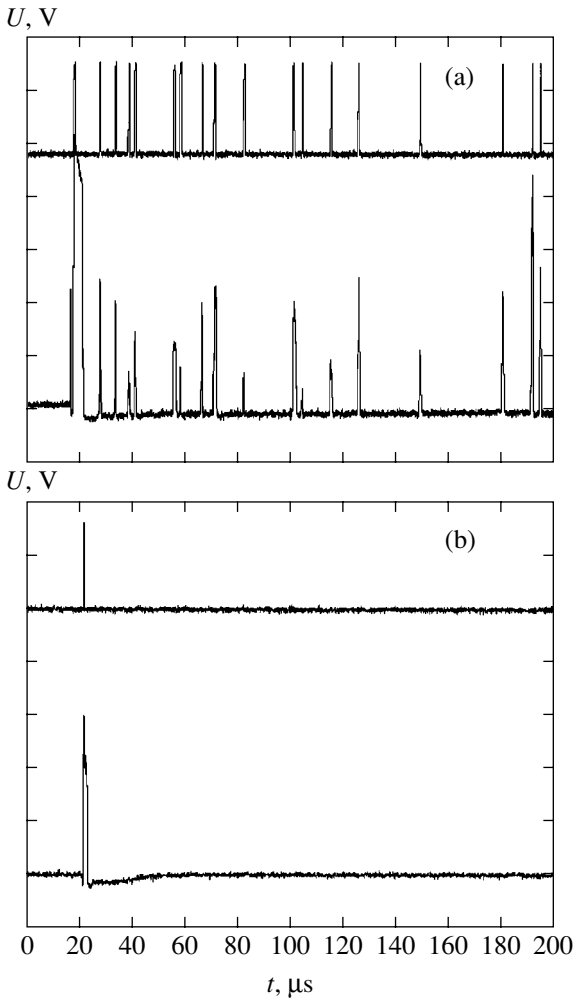

Fig. 4. Oscillograms of pulses from neutron detector *D*3 on helium counters (the upper oscillogram is obtained from the digital output of the detector and the lower, from the analog output): (a) $(CD_2)_n$ target, 350 μm in thickness; (b) Be target, 2 mm).

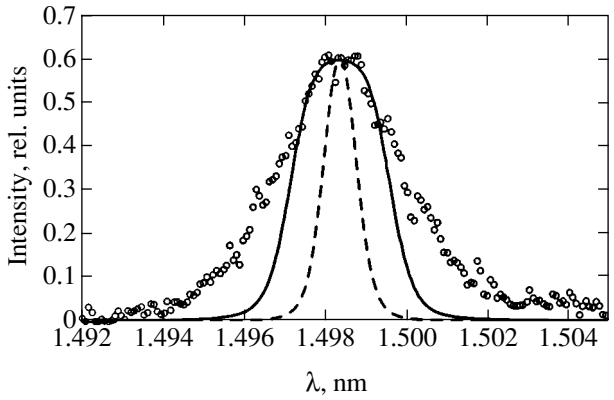

Fig. 5. Profile of the Ly_α line of the F IX ion: experimental result (circles) and calculation for an optically thin plasma with $N_e = 10^{21}$ cm^{-3} and $T_i = 1$ keV (dashed curve) and an optically thick plasma with $N_e = 10^{21}$ cm^{-3}, $T_i = 3$ keV, and $\tau = 3.7$ (solid curve).

an essentially non-Gaussian shape corresponding to a distribution at a certain temperature. To demonstrate this difference, Fig. 5 shows the Doppler profiles of the lines corresponding to ion temperatures T_i = 1 and 3 keV. It can be seen that the observed emission spectrum contains high-intensity "tails" corresponding to the presence of fast ions with an energy considerably higher than the thermal energy. It follows from the symmetry of the Doppler profile of the lines that the distribution of such ions is isotropic to a considerable extent.

A considerable fraction of fast ions, which follows from the presence of intense wings of the Doppler-broadened line in Fig. 5, is worth noting. To determine the fraction of fast ions in their total energy spectrum from the experimentally measured Doppler profile of the Ly_α line, the energy distribution of fast ions was determined (Fig. 6). Analysis of the results presented in Figs. 5 and 6 shows that the fraction of fast ions with an energy exceeding 10 keV is appreciable (20%). An important feature of the energy distribution is also a comparatively slow decay with increasing energy, which makes it possible to detect ions having an energy higher than 100 keV. Thus, the results of measurement of X-ray spectra indicate the presence of a considerable number of fast ions in the plasma.

It would be interesting to compare the obtained experimental data on the neutron yield with the estimate based on the familiar formula for the number of neutrons produced in a laser plasma [18]:

$$N_n \approx 0.25 n_D^2 \langle \sigma v \rangle_{DD} \tau V,$$

where τ is the lifetime of a dense plasma and/or the time of its cooling, V is the plasma volume, and $\langle \sigma v \rangle_{DD}$ is the rate of the thermonuclear reaction averaged over the ion distribution. The energy distribution of deuterons was not measured in the experiment. The neutron yield can be estimated assuming that the deuteron energy distribution corresponds to the energy distribution for fluorine ions, which is obtained under the same experimental conditions and shown in Fig. 6. In this case, we find that the total number of neutrons produced in a laser plasma is $N_n \approx 10^4$ for $n_D \approx 3 \times 10^{22}$ cm^{-3}, $\tau \approx 1.5$ ps, and $V \approx 3 \times 10^{-10}$ cm^{-3}, which is in reasonable agreement with the experimentally measured neutron yield.

It should be emphasized that a considerable neutron yield (5×10^4 neutrons per pulse) was detected here for the first time for a solid $(CD_2)_n$ target for a moderate laser radiation intensity at a level of 3×10^{17} W/cm^2. Such neutron yields were detected earlier with $(CD_2)_n$ targets using only laser pulses of a relativistic intensity $I \geq 10^{18}$ W/cm^2 [4–7].

Figure 7 shows the data on experimental measurement of the neutron yield from a laser plasma on the surface of solid deuterated $(CD_2)_n$ targets for various laser radiation intensities and various laser pulse durations (triangles correspond to femtosecond lasers in the range of 50–300 fs, while circles correspond to pico-

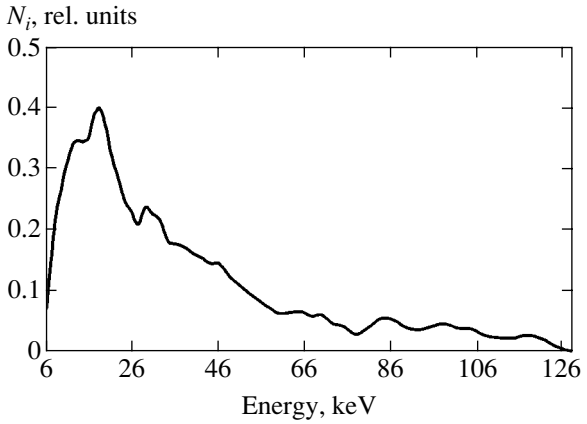

Fig. 6. Distribution of fast F IX ions obtained from analysis of the Ly_α line profile.

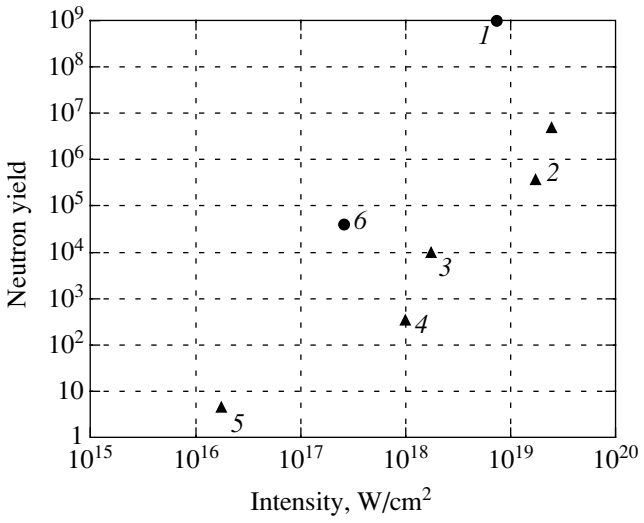

Fig. 7. Neutron yield obtained in a laser plasma on the surface of solid deuterated $(CD_2)_n$ targets: *1*—VULCAN: 20 J, 1.3 ps, 1.06 μm [4]; *2*—France: 7 J, 300 fs, 0.53 μm [5]; *3*—MBI, Berlin: 0.3 J, 50 fs, 0.8 μm [6]; *4*—ATLAS: 0.2 J, 160 fs, 0.79 μm [7]; *5*—Moscow State University: 1 mJ, 200 fs, 0.8 μm [8]: *6*—NEODIM: 1.5 J, 1.5 ps, 1.06 μm.

second lasers with a pulse duration of 1.3–1.5 ps). The figure clearly demonstrates that picosecond lasers are preferable for obtaining the maximum neutron yield from the laser plasma on the surface of the solid deuterated $(CD_2)_n$ target; the threshold intensity of laser radiation for obtaining an appreciable neutron yield on the order of 10^4 per pulse is higher than 10^{18} W/cm^2 for femtosecond lasers and 10^{17} W/cm^2 for picosecond lasers.

4. CONCLUSIONS

It has been shown for the first time that a considerable neutron yield of up to 5×10^4 per pulse can be obtained using a picosecond laser plasma at the surface of a solid deuterated $(CD_2)_n$ target with a laser radiation intensity of 3×10^{17} W/cm^2. Consequently, relatively small laser devices with a terrawatt power can be used for obtaining and practical application of pulsed sources of nuclear radiation and for studying nuclear processes in a laser plasma.

ACKNOWLEDGMENTS

This study was financed by the International Science and Technology Center (project no. 2155) and INTAS (grant no. 01-0233).

REFERENCES

1. P. G. Kryukov, Kvantovaya Élektron. (Moscow) **31**, 95 (2001).
2. A. V. Andreev, V. M. Gordienko, and A. B. Savel'ev, Kvantovaya Élektron. (Moscow) **31**, 941 (2001).
3. N. E. Basov, S. D. Zakharov, P. G. Kryukov, *et al.*, Pis'ma Zh. Éksp. Teor. Fiz. **8**, 26 (1968) [JETP Lett. **8**, 14 (1968)].
4. P. A. Norreys, A. P. Fews, F. N. Beg, *et al.*, Plasma Phys. Controlled Fusion **40**, 175 (1998).
5. L. Disdier, J.-P. Garconnet, G. Malka, and J.-L. Miquel, Phys. Rev. Lett. **82**, 1454 (1999).
6. D. Hilsher, O. Berndt, M. Enke, *et al.*, Phys. Rev. E **64**, 016414 (2001).
7. G. Pretzler, A. Saeman, A. Pukhov, *et al.*, Phys. Rev. E **58**, 1165 (1998).
8. R. V. Volkov, D. M. Golishenkov, V. M. Gordienko, *et al.*, Pis'ma Zh. Éksp. Teor. Fiz. **72**, 577 (2000) [JETP Lett. **72**, 401 (2000)].
9. J. Zweiback, R. A. Smith, T. E. Cowan, *et al.*, Phys. Rev. Lett. **84**, 2634 (2000).
10. G. Grillon, Ph. Balcon, J.-P. Chambaret, *et al.*, Phys. Rev. Lett. **89**, 065005 (2002).
11. K. W. Madison, P. K. Patel, M. Allen, *et al.*, J. Opt. Soc. Am. B **20**, 113 (2003).
12. S. Fritzler, Z. Najmudin, V. Malka, *et al.*, Phys. Rev. Lett. **89**, 165004 (2002).
13. V. S. Belyaev, V. I. Vinogradov, A. S. Kurilov, *et al.*, in *Collected Scientific Papers* (Tsentr. Nauchno–Issled. Inst. Mashinostr., Korolev, 2002), p. 34.
14. V. S. Belyaev, V. I. Vinogradov, A. S. Kurilov, *et al.*, in *Collected Scientific Papers* (Tsentr. Nauchno–Issled. Inst. Mashinostr., Korolev, 2002), p. 47.
15. V. S. Belyaev, V. I. Vinogradov, A. S. Kurilov, *et al.*, Kvantovaya Élektron. (Moscow) **30**, 229 (2000).
16. W. D. Allen, *Neutron Detection* (George Newnes, London, 1960; Gos. Izd. Lit. Oblasti At. Nauki Tekh., Moscow, 1962).
17. T. A. Pikuz, A. Ya. Faenov, S. A. Pikuz, *et al.*, J. X-Ray Sci. Technol. **5**, 323 (1995).
18. K. A. Brueckner and S. Jorna, *Laser Driven Fusion, KMS Fusion* (Ann Arbor, Michigan, 1973; Atomizdat, Moscow, 1977).

Translated by N. Wadhwa

Journal of Experimental and Theoretical Physics, Vol. 98, No. 6, 2004, pp. 1138–1145.
Translated from Zhurnal Éksperimental'noĭ i Teoreticheskoĭ Fiziki, Vol. 125, No. 6, 2004, pp. 1302–1310.

FLUIDS

Focusing of an Oscillating Shock Wave Emitted by a Toroidal Bubble Cloud

V. K. Kedrinskiĭ, V. A. Vshivkov, G. I. Dudnikova, Yu. I. Shokin, and G. G. Lazareva

Lavrent'ev Institute of Hydrodynamics, Siberian Division, Russian Academy of Sciences, Novosibirsk, 630090 Russia

Institute of Computational Technologies, Siberian Division, Russian Academy of Sciences, Novosibirsk, 630090 Russia

e-mail: kedr@hydro.nsc.ru

Received July 28, 2003

Abstract—An analysis of pressure-field dynamics is performed for an axially symmetric problem of interaction between a shock wave and a "free" bubble system (toroidal cluster) giving rise to a steady oscillating shock wave. The results of a numerical study of near-axis wave structure are presented for a focusing shock wave emitted by a bubble cluster. It is shown that the wave reflected from the axis has irregular structure. The Mach disk developing on the axis has a core of finite thickness with a nonuniform radial pressure distribution. The evolution of the Mach-disk core is analyzed, and the maximum pressure in the core is computed as a function of the gas volume fraction in the cluster. The effect of geometric parameters of the toroidal bubble cloud on the cumulative effect is examined. © *2004 MAIK "Nauka/Interperiodica".*

1. INTRODUCTION

Generation of pressure pulses in liquids and gases has been the subject of ongoing research for many years. This work resulted in the development of various pressure generators and shock-wave cumulation methods. Research efforts were focused on the exploration of media in which the energy transferred by relatively weak pulsed loading can be absorbed, concentrated in a local region, and reemitted in a pulse of substantially higher amplitude. Frequently, it is required not only to cumulate energy, but also to emit it in a certain direction. From a wide variety of relevant publications, we single out experimental and theoretical studies of axially symmetric shock waves related to annular shock-wave generators and conical flows. In particular, an experimental investigation of the focusing of a pressure wave generated on the surface of a toroidal high-voltage discharge source was reported in [1]. Theoretical studies based on the model developed by Chester, Chisnell, and Whitham for a gas [2–4] have shown that unlimited cumulation can also be achieved by focusing annular and conic shock waves [5–7]. According to [7] the Mach-wave velocity increases by a factor of α^{-1} (if dissipative processes are neglected), where α is the cone half-angle.

The topological changes in a curved shock front associated with its cumulation and the resulting flow patterns were analyzed experimentally and theoretically in [8]. Experimental investigations of irregular reflection of annular shock waves propagating in gases from symmetry axes and rigid walls were conducted in [9–11]. It was found that a quasi-spherical convergent shock enhanced the cumulative effect in a local region [11]. Irregular reflection of axially symmetric shock waves generated in the atmosphere from liquid surfaces was observed in experimental simulations of surface point explosions (see [12]). The wave pattern associated with the toroidal shock generated in water by an underwater high-voltage explosion of a ring-shaped conductor, the focusing of the shock wave, its subsequent interaction with the expanding toroidal cavity containing the explosion products, the focusing of the accompanying rarefaction wave, and the development of bubble cavitation at the center of the torus were also examined in [12]. Underwater explosions of spiral coils of detonating cords and spiral three-dimensional charges were studied in [12, 13]. The focusing of the shock wave generated in air by a detonation wave propagating along a ring and the structure of the pressure fields created by explosions of ring-shaped and spiral charges in air were investigated in [14, 15]. The results of a numerical analysis of the focusing of toroidal shock waves obtained for different Mach numbers and geometric parameters were reported in [16].

In the 1990s, the first publications appeared on the basic principles of hydroacoustic analogues of laser systems, such as SASER (shock amplification by systems with energy release) or SABSER (shock amplification by bubbly systems with energy release). In [17], the model developed by Iordanskii, Kogarko, and van

1063-7761/04/9806-1138$26.00

Wijngaarden [18–21] was used in numerical studies to show that interaction between a plane shock wave and a bubble cluster gives rise to a shock wave with a pressure gradient tangent to its curved front. By focusing such a wave, its amplitude can be increased by one or two orders of magnitude. As another example of waves focusing in an axially symmetric geometry, processes taking place in a shock tube with abruptly changing cross section filled with a chemically active bubbly medium were analyzed numerically in [22]. It was shown that the focusing of a bubbly detonation wave on the axis results in a Mach configuration; i.e., the possibility of irregular Mach reflection was demonstrated for media of this kind.

Thus, bubbly media are of great interest as sources of high-energy emission in fluids. In this study, the focusing of the steady oscillating shock wave generated by a toroidal bubble cluster and the wave pattern in the near-field zone of the cluster are analyzed numerically. The pressure fields are analyzed for liquids described by the Tait equation of state (see Eqs. (1)). The gas phase is air (with ratio of specific heats 1.4), and the liquid is water (characterized by viscosity, surface tension, and ratio of specific heats).

2. STATEMENT OF THE PROBLEM AND GOVERNING EQUATIONS

We consider the shock wave generated by piston motion at the end of a shock tube of radius r_{st} filled with a liquid at the moment $t = 0$. The shock tube contains a toroidal bubble cluster whose center is located on the shock-tube axis (denoted by z) at a distance l_{cl} from its left boundary. The plane of the base circle of the torus (hereinafter called the toric plane), which has a radius R_{tor} ($R_{tor} < r_{st}$), is perpendicular to the shock-tube axis. The cross-sectional radius of the torus is R_{circ} (see Fig. 1). The initial volume fraction of the gas phase in the cluster is denoted by k_0. All gas bubbles have equal radii R_b, and their distribution over a cluster is uniform. At $t > 0$, the shock wave propagates along the positive z axis, interacts with the toroidal bubble cloud, bypasses around it, and is refracted as it encounters the cluster. The interaction between the refracted wave and the bubble cloud results in its focusing inside the cluster, and its intensity increases to an extent determined by the cluster parameters and the cross-sectional radius R_{circ} of the torus. The shock wave amplified by interaction with the cluster propagates further into the ambient liquid.

The focusing of the refracted wave by the cluster was computed by using a modified Iordanskii–Kogarko–van Wijngaarden model [17], based on the continuity and momentum equations written for the average pressure p, density ρ, and velocity $\mathbf{u}$:

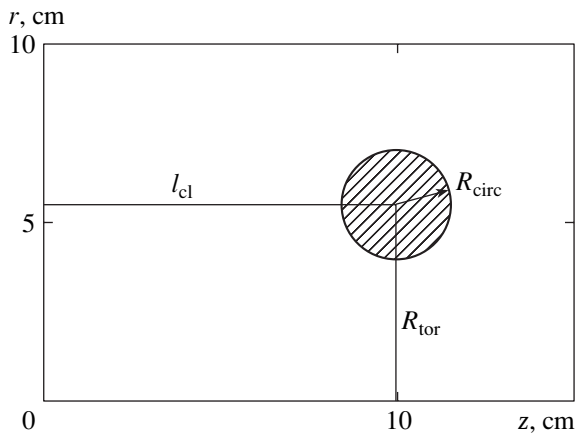

Fig. 1. Toroidal bubble cluster: the hatched area is the toric section; z is the symmetry axis.

$$\frac{\partial \rho}{\partial t} + \operatorname{div}(\rho \mathbf{u}) = 0, \quad \frac{\partial \mathbf{u}}{\partial t} + \mathbf{u}(\nabla \mathbf{u}) = -\frac{1}{\rho}\nabla p,$$

$$p = p(\rho) = 1 + \frac{\rho_0 c_0^2}{n p_0}\left[\left(\frac{\rho}{1-k}\right)^n - 1\right], \qquad (1)$$

$$k = \frac{k_0}{1-k_0}\rho\beta^3,$$

where ρ_0 is the unperturbed liquid density, c_0 is the speed of sound in the liquid, and ρ is the density of the bubbly liquid normalized to ρ_0. It is obvious that system (1) is not closed: the Tait equation of state for the liquid phase contains the volume fraction k of gas in the cluster, which is expressed in terms of the dynamic variable $\beta = R/R_0$ (relative bubble radius).

In the Iordanskii–Kogarko–van Wijngaarden model, a physically heterogeneous medium is treated as homogeneous, and the Rayleigh equation for β

$$\frac{\partial S}{\partial t} = -\frac{3}{2\beta}S^2 - \frac{C_1}{\beta^2} - C_2\frac{S}{\beta^2} - \frac{p}{\beta} + \beta^{-3\gamma-1}, \qquad (2)$$

where

$$S = \frac{\partial \beta}{\partial t}, \quad C_1 = \frac{2\sigma}{R_0 p_0}, \quad C_2 = \frac{4\mu}{R_0\sqrt{p_0\rho_0}},$$

is used as a closure for system (1). Here, σ is surface tension; μ is viscosity; $n = 7.15$; and p_0, ρ_0, R_0, $\sqrt{p_0/\rho_0}$, and $R_0\sqrt{\rho_0/p_0}$ are the reference parameters used to obtain a dimensionless system of equations.

Starting from papers published in 1968 (see references in [12]), both one- and two-dimensional versions of the model were applied to describe cavitation, liquid strength, structure of shock and rarefaction waves, and their interactions in both inert [17, 23] and chemically active [22] bubbly media. The numerical results concerning shock waves and the dynamics and structure of bubbly media were compared with experiments, and it was shown that the Iordanskii–Kogarko–van Wijngaarden model and its modifications provide correct descriptions of various processes in both inert and chemically active bubbly media.

In cylindrical coordinates, the flow domain is a rectangle with $0 \le z \le z_{max}$ and $0 \le r \le r_{st}$. The boundary conditions set at $z = 0$ correspond to a steady shock wave of amplitude P_{sh} with prescribed axial velocity and zero radial velocity. Symmetry conditions are set at $r = 0$. The computations were performed for $k_0 = 0.001$–0.1, $R_0 = 0.01$–0.4 cm, and $P_{sh} = 3$–10 MPa. The boundary condition set at $r = r_{max}$ rules out reflection of the shock wave from the shock-tube wall. For the wave emerging from the flow domain at $z = z_{max}$, the second axial derivatives of all variables are set to zero. To solve system (1), we adapted the upwind explicit and splitting schemes described in [24] to the present problem. At the first stage, we applied the scheme proposed in [25]. Subsystem (2) was computed by using the Runge–Kutta–Merson fourth-order implicit scheme.

Table

k_0	p	α	R_{Mach}, cm	Z_{Mach}, cm
0.001	47.6	37.45	1.4	4.6
		40.6	1.5	5.1
		54.8	2.2	8.5
		59.8	2.5	10.3
		63.43	3.3	12.0
		66.35	6.0	13.7
0.010	99.4	40.9	2.4	5.2
		45.2	2.5	6.1
		56.0	2.7	8.9
		60.5	3.1	10.6
		63.8	3.6	12.2
		66.5	4.1	13.8
		68.7	6.0	15.4
0.050	199.2	23.4		2.6
		48.6	3.2	6.8
		55.1	3.6	8.6
		59.5	3.8	10.2
		63.2	6.0	11.9
0.100	231	17.6		1.9
		42.5	2.2	5.5
		51.34	3.2	7.5
		56.9	3.8	9.2
		63.0	5.0	11.8

The results presented below were validated as follows:

(i) the mathematical technique was tested against a known analytical solution;

(ii) the results obtained by means of the first-order accurate upwind explicit scheme and the second-order accurate splitting scheme adapted to flows with strongly nonlinear equations of state were compared;

(iii) the convergence of numerical methods was verified by performing computations on a sequence of progressively refined grids;

(iv) the results were checked for self-consistency and agreement with available experimental observations.

3. RESULTS

Figure 2 shows contour maps of constant pressure in a focusing shock wave generated by the toroidal bubble cloud at several instants. The pressure is quantified (in units of the hydrostatic pressure $p_0 = 0.1$ MPa) by the gray scale shown in Fig. 2c. Each instant is illustrated by two panels: an overall map (right column) and an enlarged view of the region bounded by the toric plane $z = 10$ cm, the toric radius R_{tor}, and the shock front incident on the torus (left column). The maps were computed for $P_{sh} = 3$ MPa, $r_{st} = 20$ cm, $z_{max} = 40$ cm, $l_{cl} = 10$ cm, $R_{tor} = 6$ cm, $R_{circ} = 1$ cm, $k_0 = 0.01$, and $R_b = 0.1$ cm.

Figure 2a shows the pressure field before the wave emitted by the torus focuses on the axis. Note that the pressure distribution over the shock front is highly nonuniform and the reflection of the precursors propagating ahead of the wave from the axis is already irregular. It is natural that reflection of the toroidal wave from the axis is irregular even at the initial stage, as illustrated by Fig. 2b (see the leading-edge isobar of the incident wave). This map demonstrates the second maximum of the oscillating shock wave generated by the cluster. The maps in Fig. 2c illustrate the development of two Mach disks on the axis. The intricate wave structure (including rarefaction waves, precursors, and a decaying sequence of pressure peaks in the oscillating shock wave) somewhat obscures the detailed pattern in the zone of irregular reflection.

Figure 3 illustrates the onset of irregular reflection of the shock waves emitted by the toroidal bubble cluster. These results were computed with a finer resolution

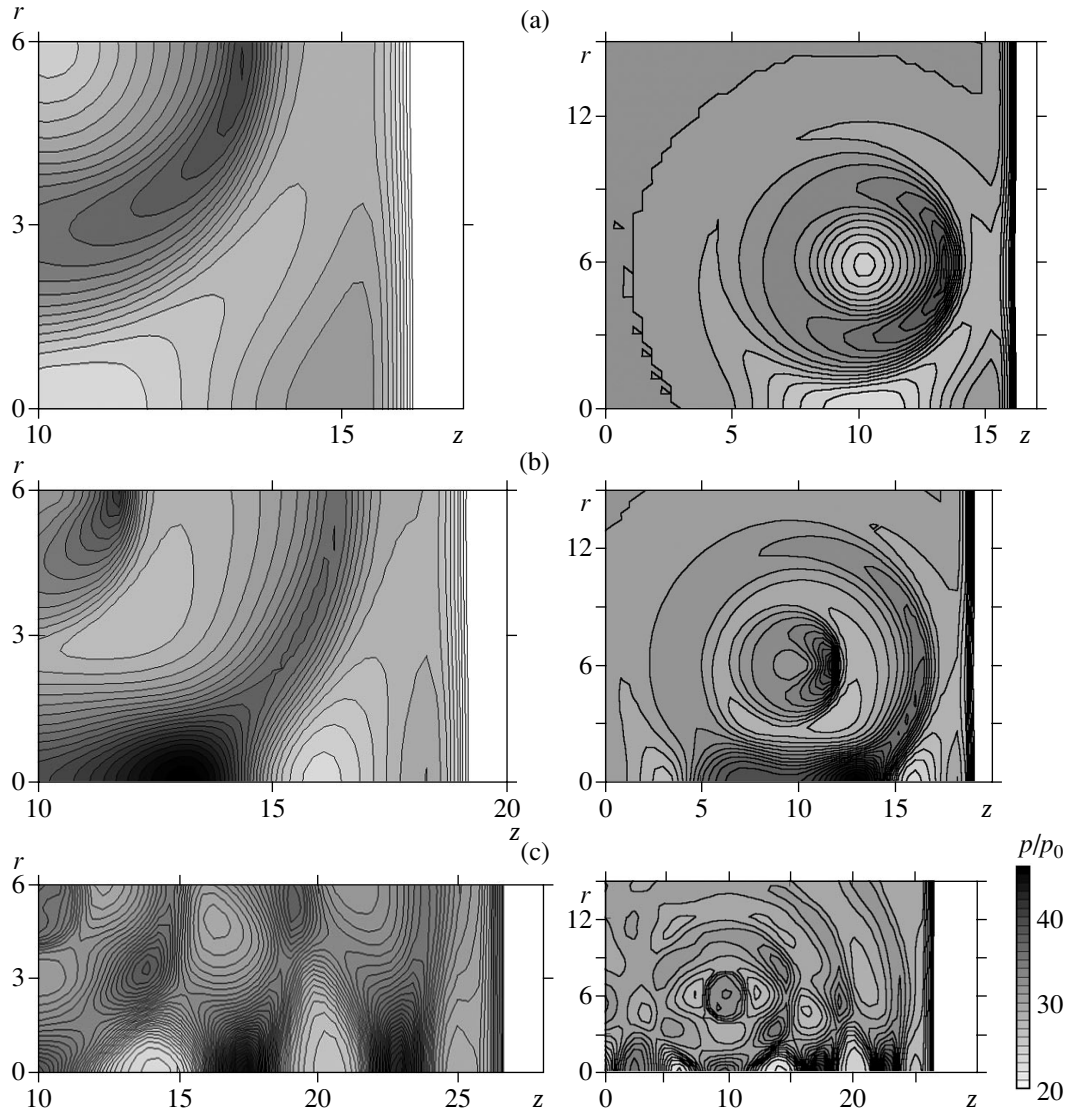

Fig. 2. Pressure fields: (a) $t = 110$ μs; (b) $t = 130$ μs; (c) $t = 180$ μs. Panels in the left column are enlarged maps of the reflection zone.

for four values of the volume fraction of gas in the torus (other parameters are as specified above). It is clear that the zone of axially symmetric irregular reflection (the Mach disk) has a finite thickness of 4 to 5 cm. The disk contains a well-defined zone of high pressure (bounded by closed isobars), which can be identified as the core of the Mach disk. In Figs. 3a–3c, the centroid of the core is shifted slightly to the right of the point z = 15 cm. In Fig. 3d, the core occupies the interval between z = 12 and 15 cm. The isobars ahead of the core belong to the leading front associated with a maximum pressure in the focusing shock wave; those behind it, to the reflected-wave pattern. In the process of reflection illustrated here, the consecutive peaks of the focusing oscillating wave are characterized by progressively increasing pressures, and the reflected wave interacting with them is "bent" toward the axis. This phenomenon gives rise to a zone of relatively rarefied flow behind the Mach disk (see Fig. 2c).

The table lists the results of a numerical analysis of the Mach-disk core radius R_{Mach} as a function of the distance Z_{Mach} between the disk and the toric plane. It demonstrates that R_{Mach} monotonically increases with Z_{Mach} and the angle α of shock incidence on the axis in the entire range of k_0. The choice of the range of k_0 is dictated by its substantial influence on shock-wave amplification and acoustic wave generation in bubbly media [23]. For each value of k_0 shown in the table, a pressure value in the core is given to illustrate the degree of shock amplification.

At first glance, unexpected effects are observed when R_{circ} is varied while R_{tor} is held constant. They are illustrated by Fig. 4, which shows results obtained for

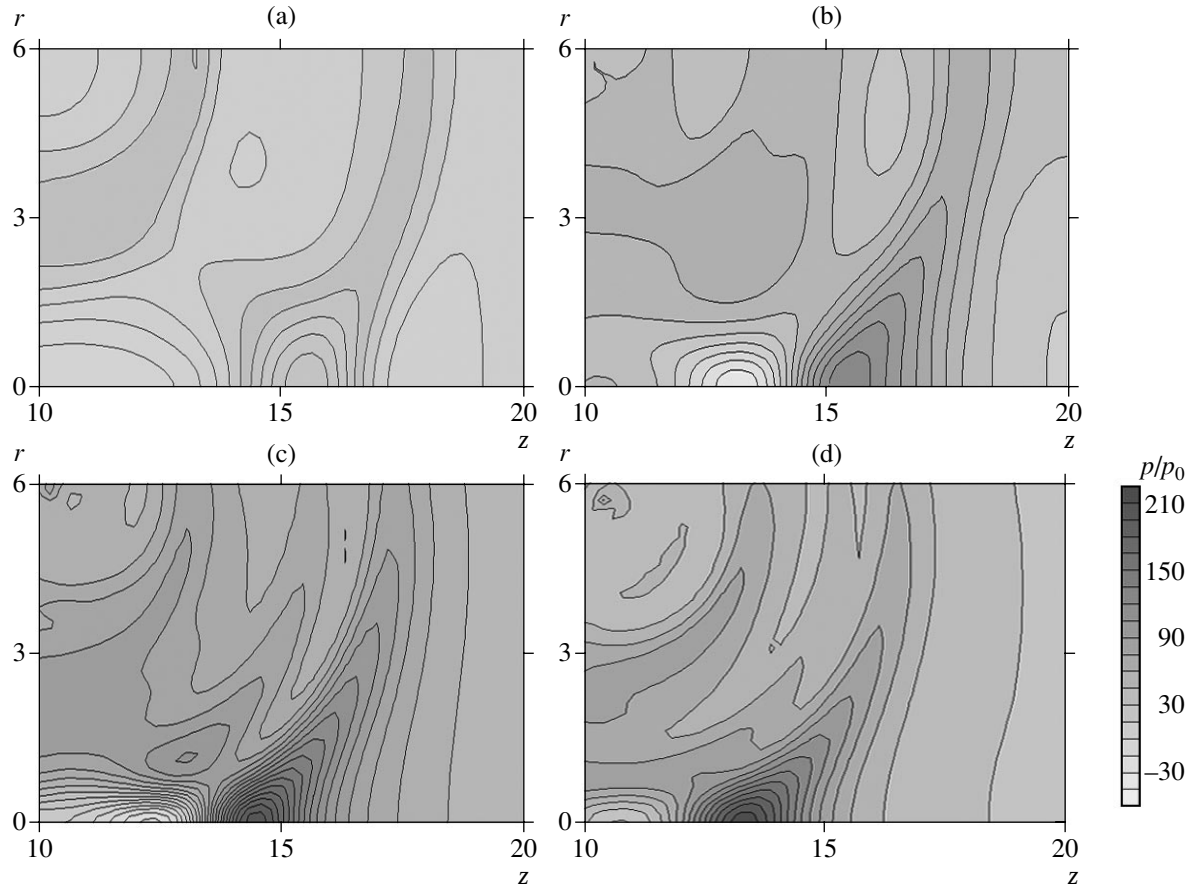

Fig. 3. Contour maps of constant pressure in Mach disks: (a) $k_0 = 0.001$; (b) $k_0 = 0.01$; (c) $k_0 = 0.05$; (d) $k_0 = 0.1$.

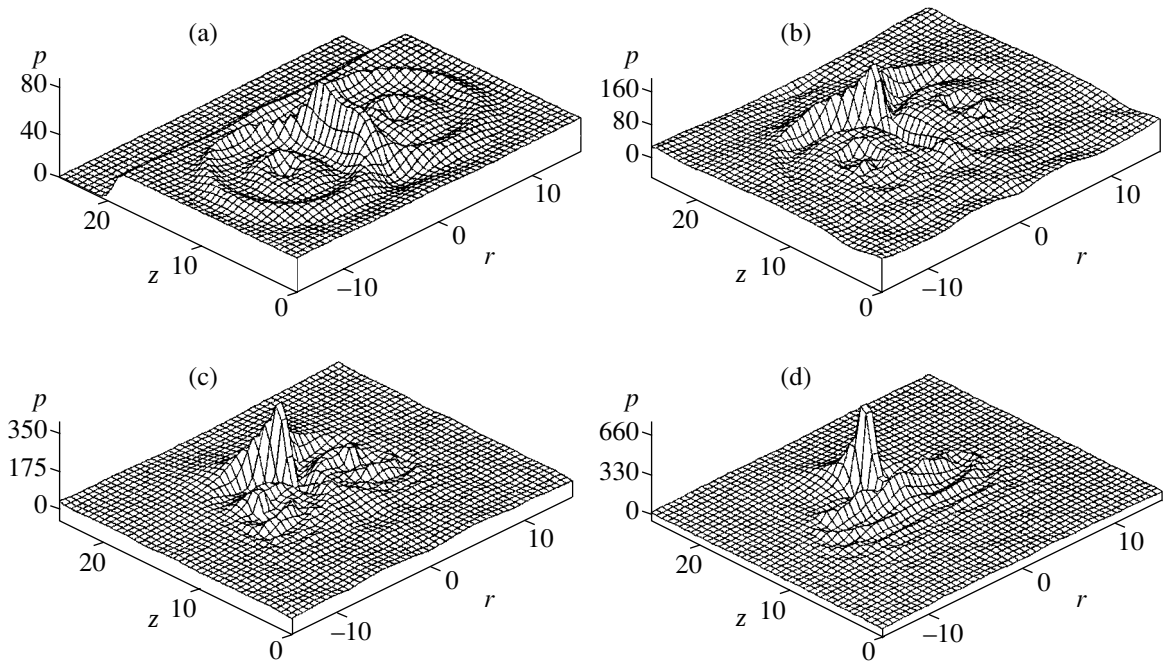

Fig. 4. Effect of the toric section of the bubble cluster on the structure of the first solitary shock wave generated in the fluid: (a) $R_{circ} = 0.5$ cm; (b) $R_{circ} = 2.0$ cm; (c) $R_{circ} = 4.0$ cm; (d) $R_{circ} = 6.0$ cm.

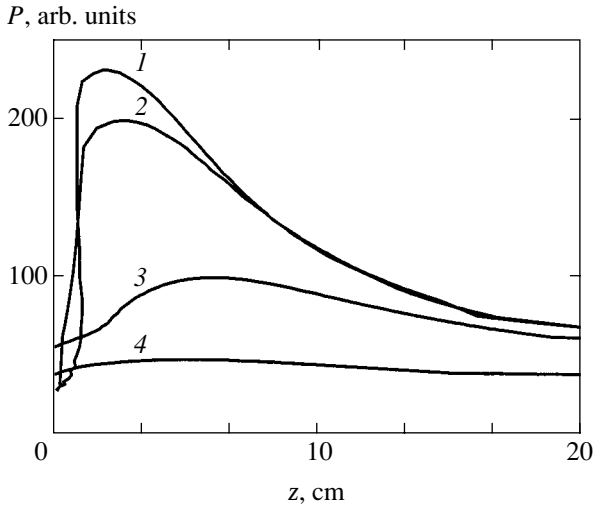

Fig. 5. Peak pressure in the core of the Mach disk versus distance from the toric plane for R_{circ} = 1 cm and R_{tor} = 6 cm: *1*—k_0 = 0.1; *2*—k_0 = 0.05; *3*—k_0= 0.01; *4*—k_0 = 0.001.

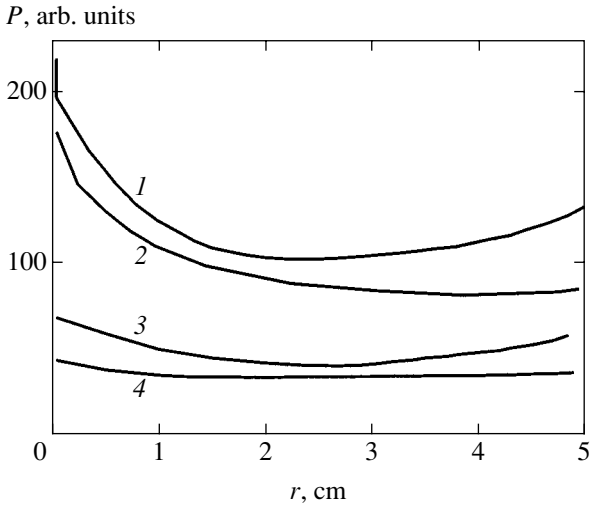

Fig. 6. Pressure distribution in the converging shock wave: *1*—k_0 = 0.1; *2*—k_0 = 0.05; *3*—k_0 = 0.01; *4*—k_0 = 0.001.

R_{circ} = 0.5, 2.0, 4.0, and 6.0 cm; P_{sh} = 3 MPa; R_{tor} = 6 cm; k_0 = 0.01; and R_b = 0.1 cm. The flows corresponding to the first three values of R_{circ} are topologically equivalent. Computations show that the wave amplitude in the Mach-disk core substantially increases with R_{circ}: P = 81.7 for R_{circ} = 0.5 cm, P = 99.4 for R_{circ} = 1.0 cm, P = 166 for R_{circ} = 2.0 cm, P = 258 for R_{circ} = 3.0 cm, P = 386 for R_{circ} = 4.0 cm, P = 568 for R_{circ} = 5.0 cm, and P = 859 for R_{circ} = 6.0 cm.

When R_{circ} = 6.0 cm, the inner boundary of the torus contracts to a point on the axis and the pressure field exhibits substantially different dynamics. The shock front converging to the axis is a concave surface with an outward pressure gradient. Even though the pressure on the converging front is minimal in the vicinity of the axis, cumulation eventually gives rise to a high-intensity shock wave with an amplitude higher than that of the wave interacting with the torus by a factor of 30 (see Fig. 4d).

An analysis of the shock-wave structure shows that the peak pressure in the Mach disk moving along the axis is a nonmonotonic function of the distance between the disk and the torus (see Fig. 5). When the torus geometry and initial bubble radius are held constant, the pressure reaches a distinct maximum, which increases with the gas volume fraction. The pressure in the Mach-disk core rapidly grows with distance from the torus in the near-field zone around it, and the wave amplitude increases by six to seven times. For k_0 = 0.01–0.1, the core pressure levels off at a distance of 20 cm from the torus, remaining higher than the amplitude of the wave interacting with the torus (by a factor of 2.0 to 2.5).

According to our computations, the cumulation of the toroidal wave inside the torus follows a classical scenario: an initial pressure decrease near the torus' surface is followed by its increase as the wave approaches the axis, and a maximum is reached when at the focal point (see Fig. 6). Note that cumulation can be interpreted as the second stage of wave amplification. The initial stage (which is no less important) involves processes taking place inside the toroidal cluster, in which the refracted incident shock wave is absorbed, transformed, amplified by focusing, and reemitted into the ambient liquid. We define the focal spot as the intersection of the focal region with a plane parallel to the toric plane. The location of the spot inside the torus and the degree of wave amplification

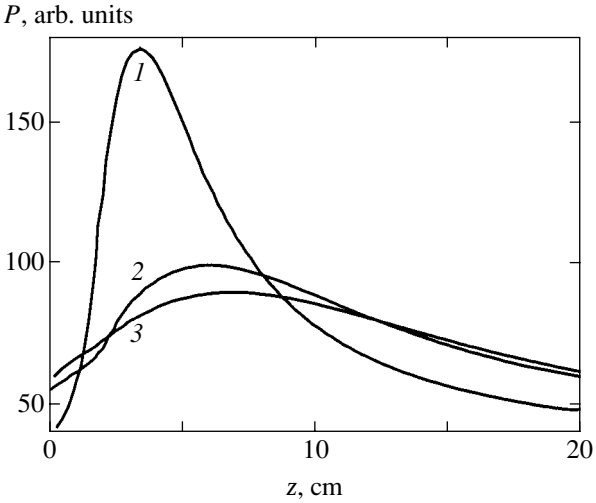

Fig. 7. Axial pressure distribution in the core of the Mach disk for tori of equal volume: *1*—R_{circ} = 1.414 cm, R_{tor} = 3 cm; *2*—R_{circ} = 1 cm, R_{tor} = 6 cm; *3*—R_{circ} = 0.866 cm, R_{tor} = 8 cm.

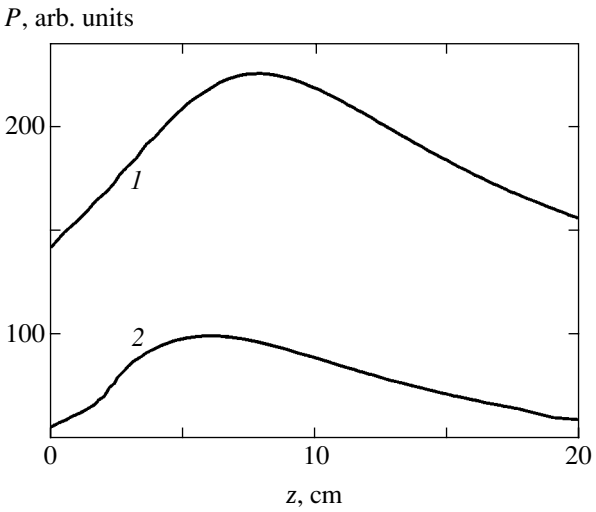

Fig. 8. Axial pressure distribution in the core of the Mach disk for identical tori and different incident-wave amplitudes P_{sh}: *1*—P_{sh} = 120; *2*—P_{sh} = 30.

depend on the value of k_0, which determines the velocity of wave propagation in the cluster and, therefore, both the curvature of the converging shock front and pressure distribution over the front.

It is shown above that the torus volume (determined by its radius) has a strong effect on the pressure in the Mach-disk core. According to our computations, an analogous effect can be obtained by varying the geometry of the torus while its volume is held constant. Figure 7 shows the core pressure as a function of the axial coordinate for three pairs of torus parameters: R_{tor} = 3 cm and R_{circ} = 1.414 cm (curve *1*), R_{tor} = 6 cm and R_{circ} = 1 cm (curve *2*), and R_{tor} = 8 cm and R_{circ} = 0.866 cm (curve *3*). The pressure curves are similar to those presented in Fig. 5. Figure 7 demonstrates that the degree of wave amplification is the highest for the smallest value of the toric radius combined with the largest cross-sectional radius (curve *1*). As the toric radius is reduced by half (from 8 to 4 cm), the normalized pressure increases by 40, and a further reduction (from 4 to 2 cm) results in an increase by 200. When the characteristic radii are equal, the generated wave has the largest amplitude.

The variation of the core pressure amplitude with increasing distance from the toric plane is analogous for different incident wave amplitudes P_{sh} (see Fig. 8).

4. CONCLUSIONS

We present the results obtained by using an axially symmetric numerical model of pressure-field dynamics developed and implemented for a shock wave interacting with a toroidal bubble cluster in a hydrodynamic shock tube.

The problem is formulated and analyzed for the first time here. This is done in order to find out if this method can be effectively used to generate strong shock waves emitted in a certain direction before starting an experimental study of the problem. As a result, we found that the incident shock wave is substantially amplified via the formation of Mach disks as it propagates along the axis.

A numerical simulation of the interaction between a shock wave and a “free” bubble system has shown that

(1) the convergence of the toroidal shock wave reemitted by the bubble cluster is a classical cumulative process;

(2) the wave reflection from the symmetry axis is irregular, and the Mach disk of finite thickness developing on the axis has a core in which pressure reaches a maximum;

(3) the shock wave generated by the torus in the liquid is characterized by a decaying sequence of pressure peaks generated by the bubble system;

(4) the focusing of the wave results in successive formation of a sequence of Mach disks on the axis.

ACKNOWLEDGMENTS

This work was supported by the Siberian Division of the Russian Academy of Sciences, Integration project no. 22 and Leading Scientific School grant 2073.2003.1.

REFERENCES

1. N. K. Berezhetskaya, E. F. Bol’shakov, S. K. Golubev, *et al.*, Zh. Éksp. Teor. Fiz. **87**, 1926 (1984) [Sov. Phys. JETP **60**, 1108 (1984)].
2. G. B. Whitham, J. Fluid Mech. **2**, 146 (1957).
3. W. Chester, Philos. Mag. **45**, 1293 (1954).
4. R. F. Chisnell, J. Fluid Mech. **2**, 286 (1957).
5. I. V. Sokolov, Zh. Éksp. Teor. Fiz. **91**, 1331 (1986) [Sov. Phys. JETP **64**, 784 (1986)].
6. I. V. Sokolov, Teplofiz. Vys. Temp. **26**, 560 (1988).
7. I. V. Sokolov, Izv. Akad. Nauk SSSR, Ser. Mekh. Zhidk. Gaza, No. 4, 148 (1989).
8. É. M. Barkhudarov, I. A. Kossyĭ, M. O. Mdivnishvili, *et al.*, Izv. Akad. Nauk SSSR, Ser. Mekh. Zhidk. Gaza, No. 2, 164 (1988).
9. É. M. Barkhudarov, M. O. Mdivnishvili, I. V. Sokolov, *et al.*, Pis’ma Zh. Éksp. Teor. Fiz. **52**, 990 (1990) [JETP Lett. **52**, 379 (1990)].
10. É. M. Barkhudarov, M. O. Mdivnishvili, I. V. Sokolov, *et al.*, Izv. Akad. Nauk SSSR, Ser. Mekh. Zhidk. Gaza, No. 5, 183 (1990).
11. E. M. Barhudarov, M. O. Mdivnishvili, I. V. Sokolov, *et al.*, Shock Waves **3**, 273 (1994).

12. V. K. Kedrinskiĭ, *Hydrodynamics of Explosion: Experiment and Models* (Sib. Otd. Ross. Akad. Nauk, Novosibirsk, 2000).
13. V. K. Kedrinskiĭ, Prikl. Mekh. Tekh. Fiz., No. 5, 51 (1980).
14. A. V. Pinaev, V. K. Kedrinskiĭ, and V. T. Kuzavov, Fiz. Goreniya Vzryva **37**, 106 (2001).
15. A. V. Pinaev, V. K. Kedrinskiĭ, and V. T. Kuzavov, Prikl. Mekh. Tekh. Fiz. **41** (5), 81 (2000).
16. Z. Jiang and K. Takayama, Comput. Fluids **27**, 553 (1998).
17. V. K. Kedrinskiĭ, Yu. I. Shokin, V. A. Vshivkov, *et al.*, Dokl. Akad. Nauk **381**, 773 (2001) [Dokl. Phys. **46**, 856 (2001)].
18. S. V. Iordanskiĭ, Prikl. Mekh. Tekh. Fiz., No. 3, 102 (1960).
19. B. S. Kogarko, Dokl. Akad. Nauk SSSR **137**, 1331 (1961).
20. B. S. Kogarko, Dokl. Akad. Nauk SSSR **155**, 779 (1964).
21. L. van Vijngaarden, J. Fluid Mech. **33**, 465 (1968).
22. V. K. Kedrinskiĭ, I. V. Maslov, and S. P. Taratuta, Prikl. Mekh. Tekh. Fiz. **43** (2), 101 (2002).
23. V. K. Kedrinskiĭ, V. A. Vshivkov, G. I. Dudnikova, and Yu. I. Shokin, Dokl. Akad. Nauk **361**, 41 (1998) [Dokl. Phys. **43**, 400 (1998)].
24. V. M. Kovenya and A. S. Lebedev, Zh. Vychisl. Mat. Mat. Fiz. **34**, 886 (1994).
25. V. M. Kovenya, Vychisl. Tekhnol. **7**, 59 (1992).

Translated by A. Betev

Journal of Experimental and Theoretical Physics, Vol. 98, No. 6, 2004, pp. 1146–1151.
Translated from Zhurnal Éksperimental'noĭ i Teoreticheskoĭ Fiziki, Vol. 125, No. 6, 2004, pp. 1311–1316.

FLUIDS

Manifestations of the Higher Moments of the Orientation Distribution Function of Molecules in the Spectral Properties of an Impurity Nematic

E. M. Aver'yanov[a] and V. G. Rumyantsev[b]

[a]*Kirenskiĭ Institute of Physics, Siberian Division, Russian Academy of Sciences, Akademgorodok, Krasnoyarsk, 660036 Russia*

[b]*Research Institute of Organic Intermediates and Dyes, Dolgoprudnyĭ, Moscow oblast, 141700 Russia*

e-mail: aver@iph.krasn.ru

Received December 29, 2003

Abstract—The polarized electronic absorption spectra, orientation ordering, and the special local field features were studied for push-pull linear dye molecules with strong donor–acceptor electronic conjugation of terminal fragments in the matrix of a nematic liquid crystal. The temperature-induced inversion of the sign of the splitting of polarized impurity absorption bands was observed. This effect was shown to be caused by the statistical character of orientation ordering of impurity molecules and manifestation of the higher moments of the orientation distribution function. The dependence of local field parameters (Lorentz tensor components) of impurity molecules on their orientation ordering was established. This dependence was used to reproduce the temperature dependence of the orientation order parameter of the matrix. *© 2004 MAIK "Nauka/Interperiodica".*

1. INTRODUCTION

Orientation ordering of uniaxial molecules in a nematic liquid crystal with respect to director **n** is statistical in character and is characterized by the moments $\langle P_n(\cos\theta)\rangle$ of the orientation distribution function $f(\theta)$. Here, θ is the angle between the longitudinal molecular axis **l** and **n**, $P_n(\cos\theta)$ represents even Legendre polynomials, and angle brackets denote statistical averaging. The degree of molecular ordering is determined by the $\langle P_2\rangle = S$ parameter, and the $\langle P_n\rangle$ values with $n \geq 4$ characterize inhomogeneity of the orientation distribution of molecules, which is described by the variances $\Delta_{mq} = \langle P_m P_q\rangle - \langle P_m\rangle\langle P_q\rangle$. The influence of the $\langle P_n\rangle$ parameters on the physical properties of liquid crystals is of great interest for understanding the nature of the liquid crystalline state, development of molecular-statistical theory, and practical applications. For instance, the ratio between S and $\langle P_4\rangle$ determines the anisotropy of elastic deformation moduli of nematics K_{ii} [1] and the volt–contrast characteristics of liquid crystalline displays, the thresholds and periods of distortions of the director **n**(**r**) field in nematics under field actions [2], the anisotropy of Leslie viscosity coefficients α_i [3], the time characteristics of Freedericksz transitions [2], the amplification coefficients and threshold characteristics of lasers with dyes in nematic matrices as active media [4], the intensity of polarized Raman bands [5], the dichroism of two-photon absorption [6], the splitting of polarized absorption bands of impurity molecules in a nematic phase [7], and other properties of liquid crystals. This has stimulated many works concerned with measuring $\langle P_{2,4}\rangle$ by various methods and theoretical interpretation of the observed dependences of $\langle P_4\rangle$ on S.

Much less is known about the physical effects in liquid crystals caused by the $\langle P_n\rangle$ moments with $n \geq 6$. The $\langle P_{2–6}\rangle$ values determine the saturation parameters and the output generation power of lasers with dyes in nematic matrices as active media [4] and also the splitting of polarized Raman bands in nematic liquid crystals [8]. Apart from the physics of liquid crystals, manifestations of the $\langle P_n\rangle$ moments with $n \geq 6$ in anisotropic statistically ordered molecular media are of interest because the $\Delta_{mq}(S)$ dependences at high S values are sensitive indicators of fine structural distinctions related to the appearance of medium structure anisotropy under external actions or as a result of molecular self-organization [9]. Recently, the first neutron diffraction measurements of $\langle P_{2–6}\rangle$ in various liquid crystalline phases were performed [10]. The first physical effect caused by $\langle P_{2–8}\rangle$ moment manifestations, the temperature inversion of the sign of the splitting of polarized electronic absorption bands of impurity dye molecules in a nematic phase, was reported in [11]. The present work is a complete study of this system taking into account the special features of orientation ordering of matrix and impurity molecules, the local field anisotropy for impurity molecules, and other aspects that had not been considered earlier.

1063-7761/04/9806-1146$26.00

2. OBJECTS OF STUDY AND EXPERIMENTAL PROCEDURE

The effects caused by $\langle P_n \rangle$ moments with $n \geq 4$ can be observed if we select a liquid crystal property that fully depends on the variances Δ_{2n} with $n \geq 2$, because the Δ_{2n} value contains contributions of the $\sim\langle P_n \rangle$ and $\langle P_{n\pm2} \rangle$ terms. Such a property is the difference $\Delta\nu = \nu_\parallel - \nu_\perp$ between the ν_j maxima (splitting) of the $D_j(\nu)$ electronic absorption bands of uniaxial impurity molecules in a nematic matrix when the light wave is polarized parallel ($j = \parallel$) and normally ($j = \perp$) to **n** [12]. The ν_j value for impurity absorption bands with the transition dipole moment **d** $\parallel$ **l** is given by the equation [12]

$$\nu_j = \nu_i - S_m \sum_{n \geq 2} A_n(S_m) \left[\langle P_n \rangle + \frac{C_j \Delta_{2n}}{1 + C_j S} \right], \qquad (1)$$

where the summation is over even n, $C_\parallel = 2$, $C_\perp = -1$, ν_i is the $D_i(\nu)$ band maximum of impurity absorption in the isotropic liquid crystalline phase, and S_m is the orientation order parameter of matrix molecules. The $A_n(S_m) = A_{n0} + A_{n1}S_m$ coefficients [7] characterize changes in the impurity–matrix anisotropic interaction energy under electronic excitation of the impurity, and magnitudes and signs of the $A_{n0,1}$ parameters are determined by intermolecular interaction contributions of various types.

The splitting $\Delta\nu$ is determined by the statistical character of orientation ordering of molecules in the nematic phase, and its value

$$\Delta\nu = -\frac{3S_m}{(1-S)(1+2S)} \sum_{n \geq 2} A_n(S_m) \Delta_{2n} \qquad (2)$$

depends on the balance of the contributions of the variances Δ_{2n} and the $\langle P_q \rangle$ values with $q \geq 4$. The Δ_{2n} parameters change as the temperature of the mesophase varies and are characterized by different dependences on S [9], which must manifest itself in the character of temperature variations of ν_j. One of the possible effects is the temperature-induced inversion of the sign of $\Delta\nu$ caused by mutual balancing of the Δ_{2n} contributions to $\Delta\nu$, which is only possible if at least $n = 2$, 4 and $\langle P_{2-6} \rangle$ are taken into account. At the inversion point, the condition $\nu_\parallel = \nu_\perp \neq \nu_i$ should be satisfied. This effect of the manifestation of the $\langle P_n \rangle$ moments with $n \geq 6$ is easy to distinguish from the temperature-induced inversion of the sign of $\Delta\nu$ when only one term with $n = q$ is included in (2) and A_q vanishes at this point, because the equality $\nu_j = \nu_i$ is then satisfied.

It follows from (2) that the impurity molecules and nematic matrix should satisfy several requirements for the contribution of Δ_{2n} with various n to $\Delta\nu$ to be noticeable. For $A_{n0,1}$ values to be large, the electronic excitation of molecules should be accompanied by strong changes in quite a number of their properties, namely, the dipole moment and the anisotropy of linear and nonlinear polarizabilities. Impurity molecules should also have high S values in the nematic matrix for the Δ_{2n} values with $n \geq 4$ to be large. Such objects are long linear push-pull-type molecules with a system of π conjugated fragments that have terminal π electron–donor and acceptor substituents bound by polar conjugation through a system of molecular fragments. We used the K-6 dye [13],

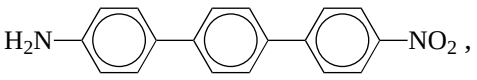

which satisfied the above requirements. The nematic matrix should have high S_m values for the $A_n(S_m)$ and $\Delta\nu$ values to be maximum and broad nematic phase and S_m variation ranges. These requirements are satisfied by 4-butoxyphenyl 4'-hexyloxybenzoate liquid crystals (BEHA [13]),

with the crystal–nematic–isotropic liquid (Cr–N–I) phase transition temperatures of 50 and 102.5°C, respectively.

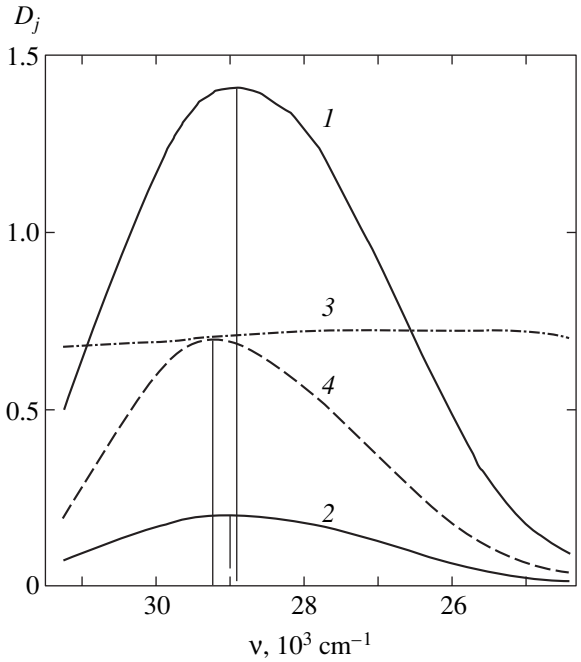

Fig. 1. Spectral dependences of the sample optical density components (*1*) $D_\parallel(\nu)$ and (*2*) $D_\perp(\nu)$ and (*3*) the dichroic ratio $0.1D_\parallel(\nu)/D_\perp(\nu)$ in the nematic phase at $\Delta T = -21.5$ K and (*4*) $D_i(\nu)$ in the isotropic phase at $\Delta T = 6$ K.

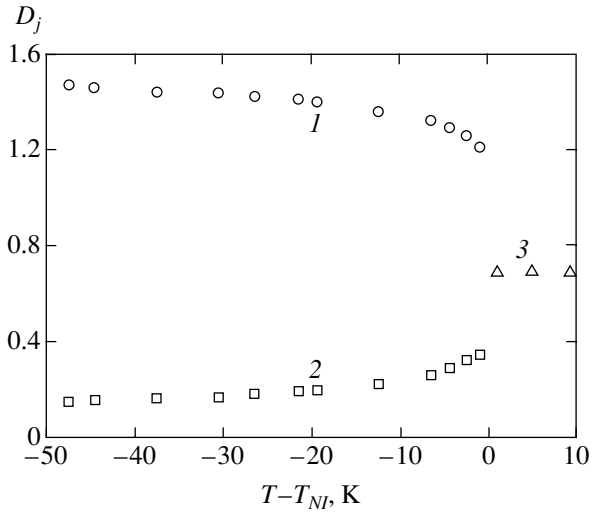

Fig. 2. Temperature dependences of the optical densities (*1*) $D_\parallel$, (*2*) $D_\perp$, and (*3*) D_i for dye K-6 in the BEHA matrix.

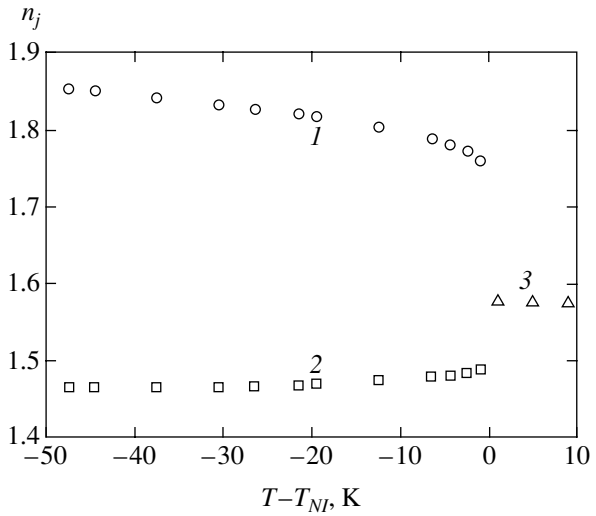

Fig. 3. Temperature dependences of the refractive indices (*1*) $n_\parallel$, (*2*) $n_\perp$, and (*3*) n_i of the BEHA matrix at λ = 345 nm.

The spectra of the $D_j(\nu)$ polarized optical density components of the sample in the region of the electronic absorption of K-6 were measured in a plane-parallel cell of thickness d = 40 μm with a uniform planar director orientation at a 0.3 wt % dye concentration, which had no noticeable effect on the T_{NI} value, sample birefringence, and the degree of matrix ordering. The spectra were recorded and automatically processed on a PU-8800 spectrophotometer. Weak background absorption of the pure matrix in the high-frequency wing of the impurity band was subtracted from the absorption of impurity liquid crystals at equal d and reduced temperature $\Delta T = T - T_{NI}$ values for each spectrum component. The resulting $D_j(\nu)$ spectra were used to determine $D_j(\nu_j)$ and ν_j for the nematic and isotropic phases. Such $D_j(\nu)$ spectra obtained at ΔT = –21.5 K and the $D_j(\nu)$ spectra at ΔT = 6 K are shown in Fig. 1. The isolated nondegenerate long-wave transition in K-6 is polarized along the long molecular axis, and the dichroism $N_1(\nu) = D_\parallel(\nu)/D_\perp(\nu)$ is virtually independent of ν within the absorption band, which is evidence of its uniform polarization in the absence of latent unresolved vibronic transitions.

3. ORIENTATION ORDERING OF IMPURITY MOLECULES AND LOCAL FIELD ANISOTROPY

The temperature dependences of the $D_j = D_j(\nu_j)$ and $D_i = D_i(\nu_i)$ parameters are shown in Fig. 2. At every ΔT value, the dichroic ratios $N_1 = D_\parallel/D_\perp$ and $N_2 = D_\perp/D_i$ were used to consistently determine S and the Lorentz tensor L_j components by the procedure described in [14]. The S value is given by the equation

$$S = \frac{N_1 g_1 - 1}{N_1 g_1 + 2}, \tag{3}$$

and the L_j components, by the system of equations

$$N_2 g_2 (N_1 g_1 + 2) = 3, \quad \mathrm{Sp}\mathbf{L} = 1. \tag{4}$$

The correction factors have the form

$$g_1 = \frac{n_{b\parallel} f_{b\perp}^2}{n_{b\perp} f_{b\parallel}^2}, \quad g_2 = \frac{n_{b\perp} \rho_i f_{bi}^2}{n_{bi} \rho f_{b\perp}^2}. \tag{5}$$

Here, $n_{bj} = n_j(\nu_j)$ is the background refractive indices in the impurity absorption band, which coincide with the refractive indices of the matrix because of the low concentration of impurity molecules, $f_{bj} = 1 + L_j(n_{bj}^2 - 1)$ is the background components of the light wave local field for impurity molecules in their absorption band, and $f_{bi} = (n_{bi}^2 + 2)/3$. The n_j values at a λ = 345 nm wavelength (the mean wavelength of the maxima of the $D_{i,j}(\lambda)$ bands) obtained as in [7] are shown in Fig. 3. The densities ρ and ρ_i for the nematic and isotropic BEHA phases were taken from [13].

The $S(\Delta T)$ dependence shown in Fig. 4 is well approximated by the equation

$$S = S_0(1 - T/T_1)^\beta \tag{6}$$

with the parameters S_0 = 1.047, β = 0.127, and $T_1 - T_{NI}$ = 0.18 K. Figure 4 shows that the experimental $L_\perp$ values in the nematic matrix phase are substantially different from L_i = 1/3 for the isotropic phase, and the $L_\perp(S)$ dependence is well approximated by the equation

$$L_\perp = a + bS \tag{7}$$

with the parameters $a = 0.343$ and $b = 0.056$. The $f_{b\perp} > f_{b\parallel}$ components differ weakly from each other at $\lambda = 345$ nm over the whole nematic phase interval because of the mutual balancing of the contributions of the tensor **L** anisotropy and matrix birefringence to the anisotropy of the tensor $\mathbf{f}_b$. For the K-6 dye, the inclusion of the local field anisotropy insignificantly increases S compared with the value obtained in [11] by (3) in the isotropic approximation $f_{b\parallel} = f_{b\perp}$.

The $S_m(\Delta T)$ dependence is not known for the BEHA matrix. In [11, 13], it was identified with the $S(\Delta T)$ dependence for impurity molecules of dye K-2 (4-dimethylamino-4'-nitroazobenzene, $\lambda_{max} = 490$ nm) obtained from the dichroism N_1 of its absorption band without taking the tensor $\mathbf{f}_b$ anisotropy into account. Let us show that the experimental $S(\Delta T)$ and (7) dependences can be used to determine the $S_m(\Delta T)$ function for the nematic matrix. The dependence [14]

$$L_\perp = 1/3 + CS_m \tag{8}$$

and the universal relation [15]

$$S(\Delta T) = AS_m(\Delta T) + B, \tag{9}$$

which is valid for all impurity nematics studied thus far, lead to empirical formula (7) with the parameters $a = 1/3 - bB$ and $b = C/A$. Substituting $B = (1 - 3a)/3b$ into (9) yields the dependence $AS_m(\Delta T)$. Approximating this dependence by (6) allows the AS_{m0} product and A parameter to be determined (in the natural limit $S_{m0} = 1$). Applying this procedure to BEHA yields $B = 0.116$, $AS_{m0} = 1.191$, $\beta = 0.118$, and $T_1 - T_{NI} = 0.6$ K. At $S_{m0} = 1$ and $A = 1.191$, the $S_m(\Delta T)$ values insignificantly differ from $S(\Delta T)$ for K-6 molecules over the whole range of the existence of the nematic phase and are somewhat underestimated at $\Delta T > 35$ K, whereas the S values for K-2 molecules [11, 13] are slightly higher than those for K-6 in this temperature range.

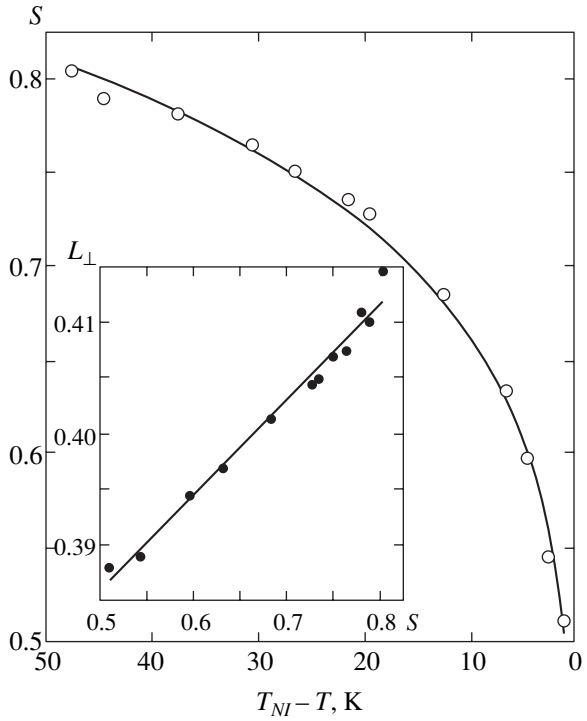

Fig. 4. Dependences $S(\Delta T)$ and $L_\perp(S)$ for K-6 molecules in the BEHA matrix (open and solid circles) and their approximations by (6) and (7) (lines).

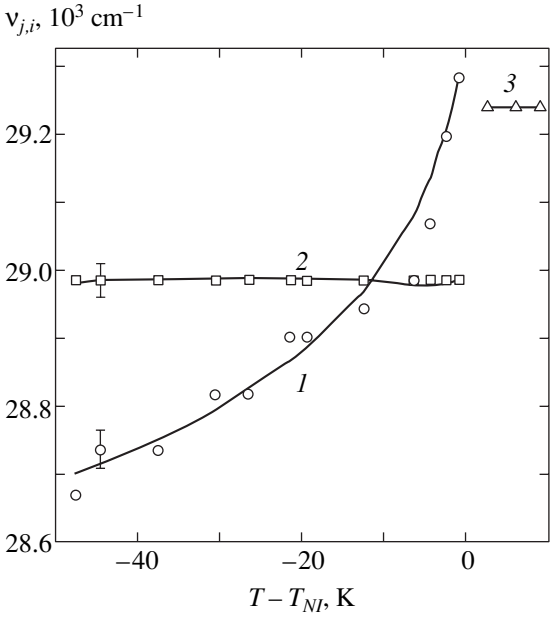

Fig. 5. Temperature dependences of the maxima (*1*) $\nu_\parallel$, (*2*) $\nu_\perp$, and (*3*) ν_i of $D_{j,i}(\nu)$ absorption bands of dye K-6 in the BEHA matrix. Solid lines were obtained by interpolating the ν_j values calculated by (1) with the parameters given in text.

4. THE SPECIAL FEATURES OF CHANGES IN $\nu_j(\Delta T)$ AND THEIR INTERPRETATION

The $\nu_j(\Delta T)$ dependences shown in Fig. 5 are characterized by certain features that have not been observed earlier for transitions with $\mathbf{d} \parallel \mathbf{l}$ [7, 12]. The temperature inversion of the sign of $\Delta\nu$ is observed at $\Delta T = \Delta T^* = -6.5$ K, while the $\nu_\perp$ value is constant over the whole mesophase interval, and a strong $\nu_\parallel(\Delta T)$ dependence is observed with a change in the ratio between ν_j and $\nu_\parallel$ close to T_{NI}. The $D_\parallel(\nu)$ and $D_\perp(\nu)$ bands correspond to the absorption of orthogonally polarized normal light waves in the liquid crystal that do not interact with each other. As a result, exact degeneracy $\nu_\parallel = \nu_\perp$ is observed at ΔT^*. The difference $\nu_i > \nu_j$ at ΔT^* is evidence of the presence in (2) of contributions of variances Δ_{2n} with several values of $n \geq 2$ and mutual balancing of these contributions to $\Delta\nu$ at this point. Figures 2–4 show that the $S(\Delta T)$ dependence and the ensuing temperature dependences of the D_j, n_j, and $L_\perp$ parameters do not have singularities in the neighborhood of the ΔT^* point,

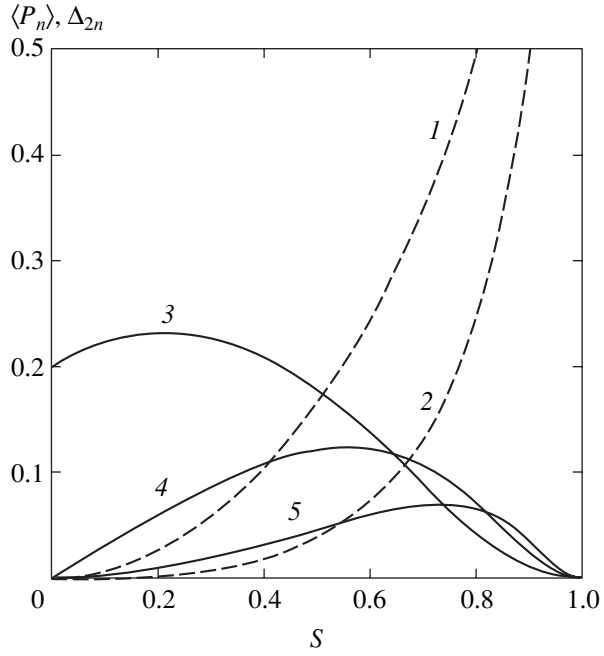

Fig. 6. Dependences of (*1*) $\langle P_4\rangle$, (*2*) $\langle P_6\rangle$, (*3*) Δ_{22}, (*4*) Δ_{24}, and (*5*) Δ_{26} on $\langle P_2\rangle = S$ for distribution function (10).

which is also evidence of contributions of moments $\langle P_n\rangle$ with $n \geq 4$ to $\Delta\nu$ sign change. Note that, for many impurity systems studied thus far, taking into account terms with $n = 2$ in (1) was sufficient for describing $\nu_j(S)$ dependences (see [7, 12] and the references therein).

The $\langle P_n\rangle$ parameters and Δ_{2n} variances in (1) were calculated using the distribution function

$$f(\theta) = \frac{1}{Z}\exp[\lambda_2(S)P_2(\cos\theta)],$$
$$Z = \int_{-1}^{1}\exp[\lambda_2(S)P_2(\cos\theta)]d\cos\theta, \quad (10)$$

which corresponds to experimental distributions when S values are high and native and impurity molecules are fairly long and do not contain terminal alkyl chains [7, 10, 12]. The $\lambda_2(S)$ parameters were found by the equation $S = \partial\ln Z/\partial\lambda_2$ and then used to calculate the $\langle P_n\rangle(S)$ and $\Delta_{2n}(S)$ dependences shown in Fig. 6. Because of the closeness of the S and S_m values at equal ΔT values (see above), it was assumed that $S_m = S$ in (1).

An analysis showed that including terms with $n = 2$ and 4 in (1) and the determination of the $A_{n0,1}$ adjustment parameters from two pairs of $\nu_{\|,\perp}$ values at two ΔT points or from $\nu_\perp$ values at four ΔT points gave a linear $\nu_\|(\Delta T)$ dependence with $\Delta\nu$ sign change at ΔT close to the middle of the mesophase temperature interval. Including terms with n = 2–6 into (1) substantially improved agreement between theory and experiment. The $\nu_j(\Delta T)$ dependences corresponding to the smallest mean-square deviation of the calculated $\nu_j(\Delta T)$ values from experimental ones with the parameters A_{20} = 1855, A_{21} = 2348, A_{40} = –20123, A_{41} = 13867, A_{60} = 36773, and A_{61} = –35260 cm^{-1} are shown in Fig. 5. Agreement between theory and experiment is evidence of mutual consistency of all special features of changes in $\nu_j(\Delta T)$ and the ratios between them and ν_i mentioned above. Even an insignificant deviation of the calculated $\nu_\perp$ values at ΔT = –6.5 and –4.5 K toward lower values compared with experiment corresponds to substantial exaggeration of calculated $\nu_\|$ values at the same temperatures. On the whole, agreement between the calculated and experimental $\nu_j(\Delta T)$ dependences obtained in this work is similar to that reported [11], where S values for dye K-2 were used as S_m [13] and the local field anisotropy was ignored in determining S. The $A_{n0,1}$ parameters given above are also close to those obtained earlier [11]. These observations are evidence of a weak influence of the characteristics of changes in $S_m(\Delta T)$ and $S(\Delta T)$ on $\Delta\nu$ sign change for impurity molecules.

The largest discrepancy between the theoretical and experimental $\nu_j(\Delta T)$ values is observed at the inversion point ΔT^*; the discrepancy rapidly decreases as the system departs from this point. Figure 6 shows that, in the interval S = 0.5–0.8, $\Delta_{22}(S)$ monotonically decreases as S increases, whereas the $\Delta_{24}(S)$ and $\Delta_{26}(S)$ dependences are nonmonotonic and pass maxima at S = 0.55 and 0.74, respectively. As the experimental $S(\Delta T^*) = 0.633$ value coincides with the value 0.638 at which the $\Delta_{22}(S) - \Delta_{24}(S)$ difference changes sign from positive to negative as S increases, the discrepancy between theory and experiment in the vicinity of ΔT^* can be related to a small difference between the real distribution function and model (10). Such differences have been reported for low S values [5, 7, 14].

To summarize, the temperature-induced inversion of the sign of $\Delta\nu$ and the other observed characteristics of changes in $\nu_j(\Delta T)$ are caused by the statistical character of orientation ordering of impurity molecules and manifestations of the $\langle P_n\rangle$ moments of the orientation distribution function with n = 2–8. Distribution function (10) can serve as a good approximation for theoretically modeling the physical properties of nematics in the region of high S values. The spectral characteristics of polarized impurity absorption and luminescence [9] are effective and are the only indicators of fine structural features of anisotropic statistically ordered molecular media known thus far.

REFERENCES

1. D. A. Dunmur and K. Toriyama, in *Physical Properties of Liquid Crystals*, Ed. by D. Demus, J. Goodby, G. W. Gray, H. W. Spiess, and V. Vill (Wiley–WCH, Weinheim, 1999), Chap. 5, p. 151.

2. L. M. Blinov, in *Physical Properties of Liquid Crystals*, Ed. by D. Demus, J. Goodby, G. W. Gray, H. W. Spiess, and V. Vill (Wiley–WCH, Weinheim, 1999), Chap. 9, p. 375.
3. F. Schneider and H. Kneppe, in *Physical Properties of Liquid Crystals*, Ed. by D. Demus, J. Goodby, G. W. Gray, H. W. Spiess, and V. Vill (Wiley–WCH, Weinheim, 1999), Chap. 8, p. 352.
4. G. A. Lyakhov and Yu. P. Svirko, Kvantovaya Élektron. (Moscow) **6**, 2490 (1979).
5. S. Jen, N. A. Clark, P. S. Pershan, and E. B. Priestley, J. Chem. Phys. **66**, 4635 (1977).
6. S. D. Durbin and Y. R. Shen, Phys. Rev. A **30**, 1419 (1984).
7. E. M. Aver'yanov, V. M. Muratov, and V. G. Rumyantsev, Opt. Spektrosk. **67**, 603 (1989) [Opt. Spectrosc. **67**, 354 (1989)].
8. E. M. Aver'yanov, Opt. Spektrosk. **65**, 868 (1988) [Opt. Spectrosc. **65**, 513 (1988)].
9. E. M. Aver'yanov, Mol. Mater. **14**, 233 (2001).
10. I. W. Hamley, G. R. Luckhurst, R. M. Richardson, and F. Santos, J. Chem. Phys. **116**, 3887 (2002).
11. E. M. Aver'yanov and V. G. Rumyantsev, Pis'ma Zh. Éksp. Teor. Fiz. **76**, 47 (2002) [JETP Lett. **76**, 40 (2002)].
12. E. M. Aver'yanov, Opt. Spektrosk. **63**, 790 (1987) [Opt. Spectrosc. **63**, 469 (1987)].
13. L. M. Blinov, V. A. Kizel, V. G. Rumyantsev, and V. V. Titov, J. Phys. Colloq. C1 **36**, C1-69 (1975).
14. E. M. Aver'yanov, *Local Field Effects in Optics of Liquid Crystals* (Nauka, Novosibirsk, 1999).
15. E. M. Aver'yanov, Nuovo Cimento D **12**, 1281 (1990).

Translated by V. Sipachev

Journal of Experimental and Theoretical Physics, Vol. 98, No. 6, 2004, pp. 1152–1163.
Translated from Zhurnal Éksperimental'noĭ i Teoreticheskoĭ Fiziki, Vol. 125, No. 6, 2004, pp. 1317–1328.

SOLIDS
Structure

Behavior of the Dynamic Magnetic Susceptibility under Spontaneous Phase Transitions in Quasi-Uniaxial Ferromagnetic Films

I. E. Dikshteĭn†, F. V. Lisovskiĭ*, and E. G. Mansvetova

Institute of Radio Engineering and Electronics, Russian Academy of Sciences, Fryazino, Moscow oblast, 141120 Russia

**e-mail: lisf@dataforce.net*

Received November 18, 2003

Abstract—Behavior of the magnetic susceptibility of quasi-uniaxial ferromagnetic films in the vicinity of the Curie point was studied with allowance for a periodic spatial inhomogeneity in the distribution of the magnetization vector for an arbitrary frequency ω of an external magnetic field. In the presence of a constant bias magnetic field $\mathbf{H}_0$, the temperature dependence of the real and imaginary parts of the magnetic susceptibility exhibits, in the general case, both frequency-independent extrema and numerous additional extrema having shapes and positions dependent on frequency. © *2004 MAIK "Nauka/Interperiodica".*

1. INTRODUCTION

The first investigations of anomalies in the magnetic susceptibility of magnetically ordered media under orientational and spontaneous phase transitions were performed more than half a century ago (see, e.g., monographs [1, 2] and references therein). Despite long and extensive research, there is still considerable interest in these problems. Theoretical analysis is usually performed using the approximation of an infinite medium (or a massive sample), which makes it possible to ignore the domain structure. However, real samples always have finite dimensions and, hence, the absence of domains is a rare exception rather than the rule. For this reason, attempts to interpret the results of experiments in terms of the theoretical calculations performed in a monodomain approximation often do not provide acceptable results. In recent years, limitations of the traditional approach, which ignores the influence of the long-range dipole–dipole interaction on the behavior of the magnetic susceptibility in the vicinity of phase transitions, are being more thoroughly recognized by theorists (see, e.g., [3–5]) because the existence of a domain structure in magnets occurring in the critical state not only leads to trivial consequences (such as a shift of the susceptibility extrema relative to their positions theoretically predicted for the infinite medium), but gives rise to some qualitatively new phenomena [4, 6].

For second kind phase transitions in magnetically uniaxial films, the Landau theory [7] provides for a sufficiently exhaustive analysis of behavior of the magnetic susceptibility with allowance for the fluctuations, domain structure, and its possible amorphization caused by the formation of magnetic dislocations and disclinations. Previously [8], we have used this approach for description of the static differential ($\omega = 0$) magnetic susceptibility under spontaneous and orientational second kind phase transitions. It was established that a shift of the point of a second kind phase transition and the contribution to the magnetic susceptibility related to the formation of a domain structure in finite samples hinder determination of the critical indices using the traditional method.

Below we present the results of investigation of the magnetic susceptibility of quasi-uniaxial ferromagnetic films in the vicinity of the Curie point T_C with allowance for a periodic spatial inhomogeneity in the distribution of the magnetization vector $\mathbf{M}$ for an arbitrary frequency ω of an external magnetic field.

2. GENERAL THEORY

The results of theoretical calculations presented below refer, strictly speaking, to ferromagnetic films with a rhombic anisotropy and the energy density described by the expression

$$f_a = -\beta_u(\mathbf{M}\cdot\mathbf{n}_u)^2 + \beta_p(\mathbf{M}\cdot\mathbf{n}_p)^2, \qquad (1)$$

where $\beta_u > 0$ and β_p (of any sign) are the anisotropy constants satisfying the condition $\beta_u \gg |\beta_p|$; $\mathbf{n}_u$ and $\mathbf{n}_p$ are the unit vectors of the mutually perpendicular axes of anisotropy ($\mathbf{n}_u \perp \mathbf{n}_p$). The introduction of a weak "rhombic" anisotropy component was shown [9] to remove the manifold degeneracy of states at the point of a spontaneous transition in the absence of a bias mag-

† Deceased.

netic field ($H_0 = 0$). This is achieved due to splitting of the multicritical point on the phase diagram in the coordinates (T, H_0) into two tricritical points connected by the line (a critical parabola) of second kind phase transitions from the paramagnetic state to that with a stripe domain structure. This line separates second-order transitions in weak bias fields ($|\mathbf{H}_0| < H_{cr}$) from the first-order phase transitions for $|\mathbf{H}_0| > H_{cr}$ [9].

Considering a Cartesian coordinate system with the unit vectors $\{\mathbf{e}_x, \mathbf{e}_y, \mathbf{e}_z\} = \{\mathbf{n}_p, \mathbf{n}_u \times \mathbf{n}_p, \mathbf{n}_u\}$ and assuming that the easy magnetization axis (collinear with $\mathbf{n}_u$) is oriented along the normal $\mathbf{n}$ to the film surface, the free energy of the system in the presence of an external magnetic field $\mathbf{H} = H\mathbf{e}_z$ directed along the normal can be presented as

$$F = \frac{M_s^2}{2}\int dV\Big[\alpha(\nabla_i m_k)^2 - \xi m^2 + \frac{1}{2}\delta m^4 + \beta_u m_\perp^2 + \beta_p m_x^2 + -2\mathbf{h}\cdot\mathbf{m} - \mathbf{h}_x\cdot\mathbf{m}\Big], \quad (2)$$

where

$$\mathbf{m} = \frac{\mathbf{M}}{M_s} = \mathbf{m}_\perp + m_z\mathbf{e}_z, \quad \mathbf{h} = \frac{\mathbf{H}}{M_s}, \quad \mathbf{h}_m = \frac{\mathbf{H}_m}{M_s},$$

δ and $\alpha \sim \delta a^2$ are the uniform and nonuniform exchange constants, respectively; a is the lattice parameter; $\mathbf{M}$ is the magnetization vector; $M_s = M$ ($T = 0$); $\mathbf{H}_m$, is the magnetostatic field; and $\xi(T) \le 4\pi$ is a function determining the temperature dependence of the absolute value of the magnetization vector. In the region of temperatures T close to the Curie temperature T_0 of the infinite medium (in the absence of the bias field), we can use for function $\xi(T)$ a linear approximation $\xi(T) = c_0(T_0 - T)$, where $c_0 = -\partial\xi/\partial T|_{T=T_0}$ is a positive constant [10]; the value $\xi = 4\pi$ corresponds to the Curie temperature T_f of a monodomain ferromagnetic film ($H_0 = 0$), that is, $T_f = T_0 - 4\pi/c_0$.

The spatial and temporal variation of the magnetization vector are described by the Landau–Khalatnikov equation

$$\eta_1\frac{d^2\mathbf{M}}{dt^2} + \eta_2\frac{d\mathbf{M}}{dt} = -\frac{\delta F}{\delta\mathbf{M}}, \quad (3)$$

where η_1 and η_2 are the kinetic coefficients, and by the equations of magnetostatics

$$\mathrm{rot}\mathbf{H}_m = 0, \quad \mathrm{div}(\mathbf{H}_m + 4\pi\mathbf{M}) = 0. \quad (4)$$

Equations (3) and (4) have to be solved with the corresponding boundary conditions on the film surfaces $z = \pm L/2$ (L is the film thickness),

$$\nabla_z\mathbf{M} = 0, \quad \mathbf{H}_{m\perp}^{(i)} = \mathbf{H}_{m\perp}^{(e)}, \quad H_{mz}^{(i)} + 4\pi M_z = H_{mz}^{(e)}, \quad (5)$$

where $\mathbf{H}_{m\perp} = H_{mx}\mathbf{e}_x + H_{my}\mathbf{e}_y$, $\mathbf{H}_m^{(i)}$ is the magnetostatic field inside the film (demagnetizing field), and $\mathbf{H}_m^{(e)}$ is the external magnetic field in the free space (stray field).

The consideration below is restricted to the static and dynamic properties of the possible distributions of the magnetization vector in sufficiently thick films ($L \gg \sqrt{\alpha}$) with a strong ($\beta_u \gg 4\pi$) uniaxial anisotropy in a small vicinity of the Curie point, which corresponds to $|\xi| \ll \beta_u$.[1]

Let the film be exposed to a uniform harmonic magnetic field

$$\tilde{\mathbf{H}}(t) = \tilde{H}(t)\mathbf{e}_z = (\tilde{H}e^{-i\omega t} + \tilde{H}^* e^{i\omega t})\mathbf{e}_z \quad (6)$$

with a small amplitude $\tilde{H}$ as compared to the absolute value of the bias field $\mathbf{H}_0 = \mathbf{H}_\parallel = H_\parallel\mathbf{e}_z = H_0\mathbf{e}_z$ (i.e. $|\tilde{h}| = |\tilde{H}|/M_s \ll |h_0| = |H_0|/M_s \ll \beta u$).[2] In the general case, a distribution of the magnetization vector in the film can be described by the formula

$$\mathbf{m}(\mathbf{r}, t) = \mathbf{m}(\mathbf{r}) + \tilde{\mathbf{m}}(\mathbf{r}, t), \quad (7)$$

where $\mathbf{m}(\mathbf{r})$ is the static magnetization component and

$$\tilde{\mathbf{m}}(\mathbf{r}, t) = \tilde{\mathbf{m}}(\mathbf{r})e^{-i\omega t} + \tilde{\mathbf{m}}^*(\mathbf{r})e^{i\omega t}$$

is the dynamic component induced by the alternating magnetic field. In the small amplitude approximation adopted in this study, the dynamic response of the system is harmonic and is a linear function of the external force, while the dynamic magnetic susceptibility of the system at a frequency ω is a tensor

$$\chi_{ij}(\omega) = \chi'_{ij}(\omega) + \chi''_{ij}(\omega) = \tilde{m}_i(\omega)/\tilde{h}_j, \quad (8)$$

where $\tilde{\mathbf{m}}(\omega)$ is the complex amplitude of the harmonic component of the magnetization vector averaged over the volume of the magnet. In what follows, we will consider only one component of the susceptibility tensor,

[1] The first limitation allows us to ignore the contribution of the surface modes to the free energy of the film; the second and third limitations (together with the conditions introduced above) allow us to construct the theory using the method of expansion with respect to small parameters ξ/β_u, $4\pi/\beta_u$, and β_p/β_u.

[2] The alternative notation $H_\parallel$ for the component of the external constant bias field along the normal to the film surface is introduced for convenience of comparison to the results reported in [8].

$\chi_{zz}(\omega)$, because m_z the dominating component of the magnetization vector in the approximation adopted in this study (see also [11, 12]).

According to Eq. (3), the behavior of $m_z(\mathbf{r}, t)$ in the general case is described by the equation

$$\eta_1\frac{d^2m_z(\mathbf{r},t)}{dt^2}+\eta_2\frac{dm_z(\mathbf{r},t)}{dt} = h_0+\tilde{h}+h_{mz}^{(i)}(\mathbf{r},t) + \alpha\frac{\partial^2 m_z(\mathbf{r},t)}{\partial x^2}+\alpha\frac{\partial^2 m_z(\mathbf{r},t)}{\partial z^2} + \xi m_z(\mathbf{r},t)-\delta m_z^3(\mathbf{r},t), \quad (9)$$

where $h_{mz}^{(i)} = H_{mz}^{(i)}/M_s$ is the normalized z-component of the demagnetizing field.

3. DYNAMIC SUSCEPTIBILITY OF A UNIFORM FILM

For a film without domain structure in the absence of an alternating magnetic field, we have $m_z(\mathbf{r}, t) = m_0 =$ const and $h_{mz}^{(i)} = -4\pi$. Then, Eq. (9) yields

$$(4\pi-\xi+\delta m_0^2)m_0 = h_0, \quad (10)$$

and

$$m_0 = 2\sqrt{p}\sinh\left(\frac{1}{3}\operatorname{arcsinh}\frac{h_0}{2\delta p\sqrt{p}}\right), \quad (11)$$

where $p = (4\pi - \xi)/3\delta$. It should be noted that, in the region where the adopted theory is valid, $\partial m_0/\partial T < 0$ and $\partial^2 m_0/\partial T^2 > 0$.

In the presence of a weak alternating magnetic field, we have

$$m_z(t) = m_0 + \tilde{m}_0(t),$$

where $|\tilde{m}_0(t)| \ll m_0$, and Eq. (9) can be reduced, to within the terms of the first order of smallness, to

$$\eta_1\frac{d^2\tilde{m}_0}{dt^2}+\eta_2\frac{d\tilde{m}_0}{dt}+(4\pi-\xi+3\delta m_0^2)\tilde{m}_0 = \tilde{h}. \quad (12)$$

According to this, the real and imaginary parts of the complex magnetic susceptibility

$$\chi_{zz}^{(0)}(\omega) = \chi_{zz}^{(0)\prime}(\omega)+i\chi_{zz}^{(0)\prime\prime}(\omega) = \tilde{m}_0(\omega)/\tilde{h}$$

are given by the expressions

$$\chi_{zz}^{(0)\prime}(\omega) = \frac{\omega_0^2-\omega^2}{\eta_1[(\omega_0^2-\omega^2)^2+\omega_\eta^2\omega^2]}, \quad (13)$$

$$\chi_{zz}^{(0)\prime\prime}(\omega) = \frac{\omega\omega_\eta}{\eta_1[(\omega_0^2-\omega^2)^2+\omega_\eta^2\omega^2]}, \quad (14)$$

where $\omega_0^2 = (4\pi - \xi + 3\delta m_0^2)\eta_1^{-1}$ is the frequency of the "soft" mode and $\omega_\eta = \eta_2/\eta_1$ is the relaxation frequency.[3] An explicit expression for the temperature dependence of the "soft" mode frequency is as follows:

$$\omega_0 = \sqrt{\frac{p\delta}{\eta_1}\left\{2\cosh\left[\frac{1}{3}\operatorname{arccosh}\left(1+\frac{27h^2}{2\delta^2p^3}\right)\right]-1\right\}}. \quad (15)$$

In deriving expressions (13) and (14), we took into account that, in magnets with a large uniaxial anisotropy, the transverse component of the magnetization vector is small in absolute value as compared to the longitudinal component:

$$|\mathbf{m}_\perp| = |m_x\mathbf{e}_x+m_y\mathbf{e}_y| \sim |m_z|\beta_u^{-1} \ll |m_z|.$$

It should be noted that, in the case under consideration, the magnetic susceptibility depends not only on the frequency, but on the temperature and the bias field as well, so that $\chi_{zz}^{(0)} = f(\omega, T, h_0)$. The frequency dependences of the susceptibility at T = const and h_0 = const, having a shape typical of the resonant dispersive media, are not considered here in detail. The temperature dependences of $\chi_{zz}^{(0)\prime}$ and $\chi_{zz}^{(0)\prime\prime}$ exhibit some special features, which will be discussed below. For better presentation, the main theoretical conclusions will be illustrated by the curves calculated for a physical model of a ferromagnet with the following parameters (changes will be stipulated in each case):

$$\delta = 4\times10^5, \quad \eta_1 = 10^{-11}, \quad \eta_2 = 2\times10^{-8}, \quad \omega_\eta = 2\times10^3.$$

These values are typical of some ferromagnets, for example, for alloys of the permalloy type ($M_s \approx 100$ G, $T_0 \approx 600$ K) [1, 13].

Application of the standard procedure for determining the temperatures of extrema in the real and imagi-

[3] Quotation marks in the term "soft" mode emphasize that a uniform mode (with a wavevector $\mathbf{k} = 0$) in the case under consideration is actually not soft: as the temperature decreases from the region of $T > T_0$, the nonuniform mode (with $\mathbf{k} \neq 0$) exhibits softening and freezing much earlier, thus leading to the formation of a domain structure (see below).

nary parts of the susceptibility for $\omega = \text{const}$ and $h_0 = \text{const}$ and the signs of the second derivatives $\partial^2\chi_{zz}^{(0)\prime}/\partial T^2$ and $\partial^2\chi_{zz}^{(0)\prime\prime}/\partial T^2$ at these points showed that, in the general case, the susceptibility components exhibit the main and additional extrema. For the main extremum, existing for any frequency ω, the position of an mapping point on the (h_0, T) plane is independent of the frequency and is determined by the equation

$$\frac{\partial(\omega_0^2)}{\partial T} = \frac{1}{\eta_1}\frac{\partial}{\partial T}(4\pi - \xi + 3\delta m_0^2) = 0. \qquad (16)$$

This equation can be rewritten as

$$T^{(m)} = T_\mathrm{f} + \frac{3}{2c_0}\left(\frac{\delta H_0^2}{2M_\mathrm{s}^2}\right)^{1/3} \qquad (17)$$

or

$$4\pi - \xi^{(m)} = \frac{3}{2}\left(\frac{\delta h_0^2}{2}\right)^{1/3}, \qquad (18)$$

where $T^{(m)} = T_0 - \xi^{(m)}/c_0$ is the temperature corresponding to the main extremum; $\xi^{(m)}$ is the value of function $\xi(T)$ at this temperature. As the bias field increases, the main extrema shift toward higher temperatures.

Equation (16) shows that the temperature of the main extremum corresponds to a minimum of the frequency $\omega_0^{(m)}$ of the "soft" mode; therefore, this minimum also corresponds to $\xi = \xi^{(m)}$. The temperature dependence of the "soft" mode frequency in a model film for $h_0 = 0.002$ is presented by the curve $\omega_0^{(m)}$ in Fig. 1 (negative values of ξ are selected to provide that the positive direction of the abscissa axis would correspond to increasing temperature). At the point of minimum (point A in Fig. 1), the absolute value of the magnetization vector and the "soft" mode frequency are given by the formulas

$$m_0^{(m)} = \left(\frac{h_0}{4\delta}\right)^{1/3}, \quad \omega_0^{(m)} = \sqrt{\frac{3}{\eta_1}}\left(\frac{\delta h_0^2}{2}\right)^{1/6},$$

while the real and imaginary parts of the susceptibility are determined by formulas (12) and (13) for $\omega_0 = \omega_0^{(m)}$. For the selected parameters of the film, the "soft" mode frequency is $\omega_0^{(m)} = \omega(A) = 5.27727 \times 10^5\ \mathrm{s}^{-1}$ and is attained at $\xi^{(m)} = 11.1739$. For $\omega \longrightarrow 0$, the imaginary part of the susceptibility at the point of extremum tends to zero, while the real part tends to $(1/3)(2/\delta h_0^2)^{1/3}$; for $\omega \longrightarrow \infty$, both components become negligibly small.

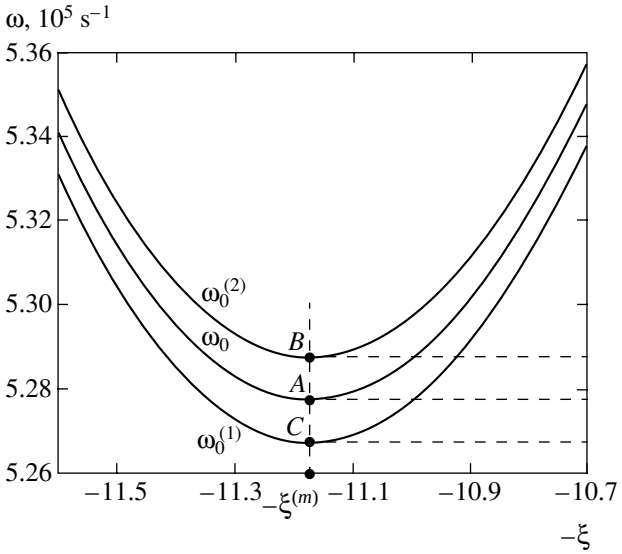

Fig. 1. Temperature dependences of the characteristic frequencies for a uniformly magnetized ferromagnetic film (for parameters, see text).

For the real part, the main extremum corresponds to a minimum for $\omega_0^{(1)} < \omega < \omega_0^{(2)}$, where

$$\omega_0^{(1,2)} = \sqrt{\omega_0^2 + \frac{\omega_\eta^2}{4}} \mp \frac{\omega_\eta}{2}, \qquad (19)$$

and to a maximum for the frequencies outside the above interval. The imaginary part of the susceptibility at the point of the main extremum reaches maximum for $\omega < \omega_0$ and minimum for $\omega > \omega_0$. The absolute maximum and minimum of $\chi_{zz}^{(0)\prime}$ (equal to $(2\omega_0^{(1m)}\eta_2)^{-1}$ and $-(2\omega_0^{(2m)}\eta_2)^{-1}$, respectively) are observed for the frequencies $\omega = \omega_0^{(1m)}$ and $\omega = \omega_0^{(2m)}$ given by the formula

$$\omega_0^{(1m,2m)} = \sqrt{\omega_0^{(m)2} + \frac{\omega_\eta^2}{4}} \mp \frac{\omega_\eta}{2}.$$

These quantities are the minimum possible values of the characteristic frequencies $\omega_0^{(1)}$ and $\omega_0^{(2)}$ reached for $\xi = \xi^{(m)}$ (see formula (18)). The absolute maximum of $\chi_{zz}^{(0)\prime\prime}$ (equal to $(\omega_0^{(m)}\eta_2)^{-1}$) is observed for the frequency $\omega_0 = \omega_0^{(m)}$. The temperature dependences of the boundary frequencies $\omega_0^{(1)}$ and $\omega_0^{(2)}$ are presented in Fig. 1, where points C and B correspond to the minimum values of these frequencies:

$$\omega_0^{(1m)} = \omega(C) = 5.26727 \times 10^5\ \mathrm{s}^{-1},$$

$$\omega_0^{(2m)} = \omega(B) = 5.28727 \times 10^5\ \mathrm{s}^{-1}.$$

Now let us turn to analysis of the additional extrema of the susceptibility, which exist for $\chi_{zz}^{(0)\prime}$ only under

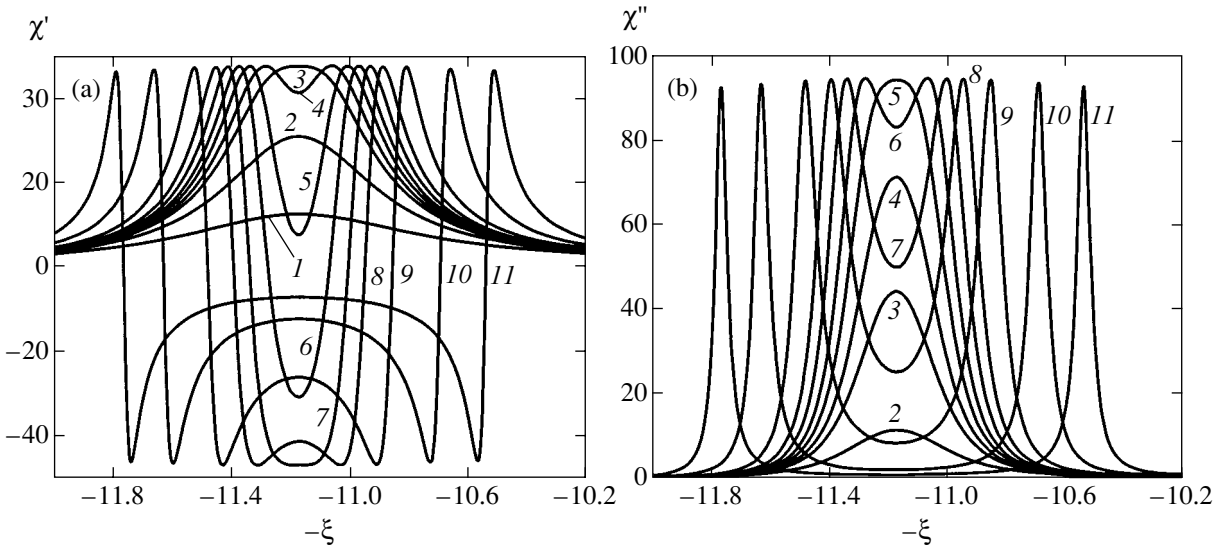

Fig. 2. Temperature dependences of the (a) real and (b) imaginary parts of the susceptibility for a ferromagnetic film uniformly magnetized at various frequencies (see text for the values of frequencies for curves *1–11*).

the condition that $(\omega_0^2 - \omega^2)^2 = \omega_\eta^2 \omega^2$ (i.e., at $\omega = \omega_0^{(1)}$ or $\omega = \omega_0^{(2)}$), and for $\chi_{zz}^{(0)\prime\prime}$ only provided that $\omega = \omega_0$. At these points, the imaginary part of the susceptibility always exhibits a maximum. For the real part, a maximum takes place for $\omega < \omega_0$, while the reverse inequality corresponds to a minimum. At the points of maximum and minimum, the values of $\chi_{zz}^{(0)\prime}$ equal to $(2\omega\eta_2)^{-1}$ and $-(2\omega\eta_2)^{-1}$, respectively; the absolute maximum and minimum are observed at $\omega = \omega_0^{(1m)}$ and $\omega = \omega_0^{(2m)}$. The imaginary part of the susceptibility at the points of maximum equals to $(\omega\eta_2)^{-1}$; at the point of absolute maximum ($\xi = \xi^{(m)}$, $\omega = \omega_0^{(m)}$), this corresponds to $(\omega_0^{(m)}\eta_2)^{-1}$.

Thus, at low frequencies (whereby the line $\omega = \text{const}$ in Fig. 1 passes below point *C*), both susceptibility components exhibit only the main maxima. At frequencies above the first critical value (point *C* in Fig. 1), $\chi_{zz}^{(0)\prime}$ acquires two additional maxima, while the main extremum becomes a minimum. For the imaginary part of susceptibility, the same conversion is observed at higher frequencies (for $\omega = \omega_0^{(m)}$, that is, above the point *A* in Fig. 1). Further increase in the frequency leads neither to the appearance of new extrema, nor to a change in the character of the existing extrema. For the real part of the susceptibility, there exists a second critical frequency (point *B* in Fig. 1). For frequencies above this critical value, the main extremum becomes a maximum again and two additional minima appear between this and the additional maxima. As the frequency increases, both "right" and "left" additional extrema move away from the main extremum (Fig. 1).

Modification of the shape of the temperature dependences of extrema in the real and imaginary parts of the susceptibility in response to the frequency variation is illustrated by the families of curves in Fig. 2. The values of $\omega \times 10^{-5}$ for curves *1–11* are 5.2, 5.25, 5.2665, 5.2715, 5.2765, 5.281, 5.2868, 5.294, 5.31, 5.35, and 5.4 s^{-1}, respectively (in Fig. 2b, curve *1* is not depicted because it virtually coincides with the abscissa axis). These curves clearly illustrate the process of appearance and development of various extrema in the susceptibility. Note that such dramatic variations in the temperature dependence of the susceptibility take place over a very narrow (about 2%) relative change in the frequency.

For determining the shapes of curves reflecting the positions of additional extrema in the (T, H_0) or $(-\xi, h_0)$ planes for $\omega = \text{const}$, we can use a relationship between the characteristic frequency ω_0 and the normalized bias field h_0 following from the equation of state (10):

$$h_0 = \frac{1}{3}\sqrt{\frac{1}{3\delta}(C_\omega^3 + 3\Delta C_\omega^2 - 4\Delta^3)}. \qquad (20)$$

Here, $C_\omega = \eta_1\omega_0^2$ and $\Delta = 4\pi - \xi$. Substituting the condition $\omega_0 = \omega$ into Eq. (20), we obtain an expression describing the positions of mapping points on the (T, H_0) plane for an additional maximum in the imaginary part of the susceptibility. By the same token, substituting the conditions $\omega_0^2 = \omega^2 + \omega\omega_\eta$ and $\omega_0^2 = \omega^2 - \omega\omega_\eta$ into Eq. (20), we obtain analogous expressions for the additional maximum and minimum in the real part

of the susceptibility. The resulting curves $h_{0i} = f_i(-\xi_i)$ (i = 1, 2, 3) exhibit temperature-dependent maxima at the points $-\xi_t = C_{\omega i}/2 - 4\pi$, where

$$\mathbf{C}_\omega = \eta_1(\omega^2;\ \omega^2 + \omega\omega_\eta;\ \omega^2 - \omega\omega_\eta),$$

and the corresponding values of the normalized bias field equal to $h_{0i} = \sqrt{2C_{\omega i}^3/27\delta}$.

Thus, additional extrema in the temperature dependence of the magnetic susceptibility can be observed only provided that the bias magnetic field strength does not exceed a certain frequency-dependent value. The regions of determination of the functions $h_{0i} = f_i(-\xi_i)$ bounding the interval of existence of the additional extrema in the absence of the bias field (H_0 = 0) fall within the limits

$$-4\pi < -\xi < C_{\omega i}/2 - 4\pi.$$

It should be recalled that $\xi = 0$ and $\xi = 4\pi$ correspond to the Curie temperatures T_0 and T_f for the infinite medium and the monodomain film at H_0 = 0, respectively. The existence of a low-temperature limit in the above sequence of inequalities is related only to the linear approximation of the function $\xi(T)$ used in this study. More accurate estimates can be obtained by using an alternative, for example, the Brillouin function, for approximating the temperature dependence of the magnetization. The possibility to observe additional extrema in the susceptibility increases with the frequency of the alternating magnetic field; for $\omega \longrightarrow 0$, the region of existence of the additional extrema on the (H, T) plane degenerates into a point.

The character of field-induced variations in positions of the temperature peaks of susceptibility is clearly illustrated in Figs. 3 and 4. Figure 3 shows the $h(-\xi)$ curves for the main (frequency-independent) extremum (curve *0*) and the additional extrema in the imaginary part of the susceptibility for the frequencies $\omega \times 10^{-6}$ = 1.4, 1.05, and 0.545 s^{-1} (curves *1–3*, respectively). Analogous curves for the additional extrema in the real part of the susceptibility for the selected film parameters virtually coincide with the $\chi_{zz}^{(0)''}(-\xi)$ curves; for this reason, the upper part of Fig. 3 is depicted in a different scale in Fig. 4, where curves *1'* and *1"* refer to the additional maxima in $\chi_{zz}^{(0)'}(-\xi)$ and minima in $\chi_{zz}^{(0)''}(-\xi)$, while curve *0* refers (as in Fig. 3) to the main (frequency-independent) extremum. Figures 3 and 4 show only the first quadrant of the Cartesian coordinate system because the analogous curves for the negative values of h_0 are obtained as mirror reflections relative to the abscissa axis. The dashed line in Fig. 3 corresponds to the loss of stability of the uniform state with respect to the domain structure formation (see Section 4) for a 2-μm-thick film. The above analysis is inapplicable to the region of bias fields and temperatures inside the area confined between this curve and the abscissa axis. At low frequencies (determined by curve *3* in Fig. 3), only the main extremum (in

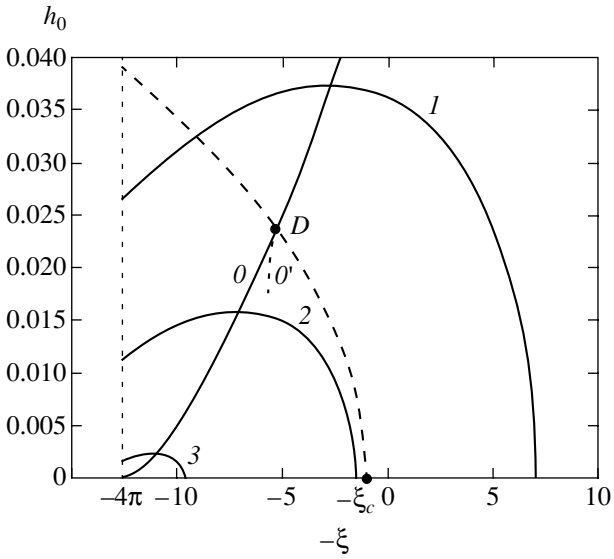

Fig. 3. The plots of $h_0(-\xi)$ for the main extremum (curve *0*) and additional maxima in the imaginary part of the susceptibility (curves *1–3*) for a ferromagnetic film uniformly magnetized at various frequencies (see text for the values of frequencies for curves *1–3*). The dashed line indicates the position of the curve describing the loss of stability of a uniform state with respect to the domain structure formation in a 2-μm-thick film.

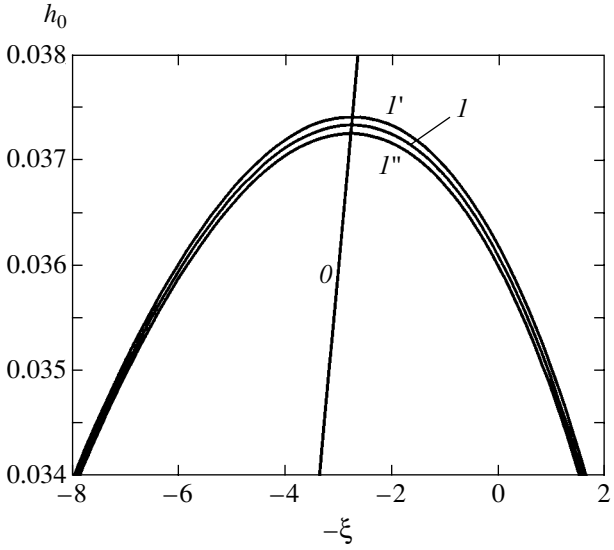

Fig. 4. The plots of $h_0(-\xi)$ for the main extremum (curve *0*), additional maxima in the imaginary part (curve *1*), and additional maxima (curve *1'*) and minima (curve *1"*) in the real part of the susceptibility for a uniformly magnetized ferromagnetic film measured at a frequency of $\omega = 1.4 \times 10^6$ s^{-1}.

the region above the point of intersection of curve *0* and the dashed line corresponding to the loss of stability of the uniform state) has to be (and usually is) observed in experiment (see, e.g., [8]).

4. DYNAMIC SUSCEPTIBILITY OF A FILM WITH DOMAINS

It is known that, as the temperature decreases from the region $T > T_0$ in the presence of a bias field, the uniform state of the film (paraphase) loses stability with respect to the formation of a stripe domain structure with a wavevector $k_c = 2\pi(4\pi\mu\alpha L^2)^{-1/4}$ at T and H_0 (or ξ and h_0) obeying the relation (see, e.g., [8])

$$T^{(ud)}(H_0) = T_C - \frac{3\delta}{c_0}\left(\frac{H_0}{4\pi M_0}\right)^2, \quad (21)$$

or

$$\xi^{(ud)}(h_0) = \xi_c + 3\delta(h_0/4\pi)^2, \quad (22)$$

where $\xi_c = (4\pi/L)\sqrt{\pi\alpha/\mu}$, $T_C = T_0 - \xi_c/c_0$ is the Curie temperature (for the domain structure formation at $H_0 = 0$) in the film, and

$$\mu = \begin{cases} 1 + 4\pi\beta_u^{-1} \text{ at } \beta_p < 0, \\ 1 + 4\pi(\beta_u + \beta_p)^{-1} \text{ at } \beta_p > 0. \end{cases}$$

The sign of β_p determines orientation of the wavevector $\mathbf{k}_c$ for the nucleating stripe domain structure ($\mathbf{k}_c \parallel \mathbf{e}_x$ for $\beta_p > 0$ and $\mathbf{k}_c \parallel \mathbf{e}_y$ for $\beta_p < 0$); in both cases, the difference of μ from unity for $\beta_u \gg 4\pi$ can be ignored.

According to Eq. (9), the normal magnetization component

$$m_z(\mathbf{r}) = m_d(\mathbf{r}) = m_{d0} + m_{dr}(\mathbf{r})$$

in the film with a domain structure in the absence of an alternating magnetic field is described (within the framework of the adopted approximation) by the equation

$$h_0 + h_{md}^{(i)} + \alpha\frac{\partial^2 m_d}{\partial x^2} + \alpha\frac{\partial^2 m_d}{\partial z^2} + \xi m_d - \delta m_d^3 = 0. \quad (23)$$

Following [14], let us seek a solution to Eq. (23) in the vicinity of the phase transition line with allowance for the boundary conditions (5) in the form of a two-dimensional series

$$m_d(\mathbf{r}) = m_{d0} + (A_{11}^{(0)}\cos qz + A_{13}^{(0)}\cos 3qz)\cos kx + (A_{20}^{(0)} + A_{22}^{(0)}\cos 2qz)\cos 2kx + (A_{31}^{(0)}\cos sqz + A_{33}^{(0)}\cos 3qz)\cos 3kx, \quad (24)$$

where m_{d0} is the (spatially-uniform) constant of the z-component of magnetization and $q = \pi/L$. Coefficients $A_{ij}^{(0)}$ can be expressed as

$$A_{11}^{(0)} = (\lambda_0), \quad A_{13}^{(0)} = \delta a_3(\lambda a)^3,$$
$$A_{20}^{(0)} = \delta b_0 m_{0d}(\lambda a)^2, \quad A_{22}^{(0)} = \delta b_2 m_{0d}(\lambda a)^2, \quad (25)$$
$$A_{31}^{(0)} = \delta c_1(\lambda a)^3, \quad A_{33}^{(0)} = \delta c_3(\lambda a)^3,$$

where (λa) is a formal small parameter characterizing the degree of proximity to the line of phase transitions. Explicit expressions for the coefficients a_3, b_0, b_2, c_1, and c_3 can be found in [14] (these quantities are not used below).

Substituting expansion (24) into Eq. (23) and selecting terms with the same dependence on the spatial coordinates, we obtain a recurrent system of equations (not presented here for brevity) relating m_{d0} to the coefficients A_{ij}^0. An analysis of this system shows that, to within terms of the second order of smallness with respect to (λa), we have

$$\left[4\pi - \xi + \delta m_{d0}^2 + \frac{3}{4}\delta(A_{11}^{(0)})^2\right]m_{d0} = h_0. \quad (26)$$

The effect of a weak alternating magnetic field on a film with domains is manifested by the appearance of small corrections to each term in expansion (24):

$$m_z(\mathbf{r}, t) = m_d(\mathbf{r}) + \tilde{m}_d(\mathbf{r}, t) = m_{d0} + \tilde{m}_{d0}(t) + m_{dr}(\mathbf{r}) + \tilde{m}_{dr}(\mathbf{r}, t), \quad (27)$$

where

$$\tilde{m}_{dr}(\mathbf{r}, t) = (\tilde{A}_{11}(t)\cos qz + \tilde{A}_{13}(t)\cos 3qz)\cos kx + (\tilde{A}_{20}(t) + \tilde{A}_{22}(t)\cos 2qz)\cos 2kx + (\tilde{A}_{31}(t)\cos qz + \tilde{A}_{33}(t)\cos 3qz)\cos 3kx, \quad (28)$$

and $|\tilde{A}_{ij}| \ll |\tilde{m}_{d0}| \ll |m_{d0}|$. Substituting expression (27) into Eq. (9) and taking into account that the static part $m_d(\mathbf{r})$ of the magnetization satisfies Eq. (23), we obtain an equation describing the dynamic response $\tilde{m}_d(\mathbf{r}, t)$:

$$\eta_1\frac{d^2\tilde{m}_d}{dt^2} + \eta_2\frac{d\tilde{m}_d}{dt} - \alpha\frac{\partial^2\tilde{m}_d}{\partial x^2} - \alpha\frac{\partial^2\tilde{m}_d}{\partial z^2} + (4\pi - \xi + 3\delta m_d^2)\tilde{m}_d = \tilde{h}. \quad (29)$$

Using this equation and expressions (24) and (28), we obtain an equation describing the uniform part of the dynamic response of the film with domains to the uniform alternating magnetic field. To within terms of the second order of smallness with respect to $(\lambda a)^2$, this equation appears as

$$\eta_1\frac{d^2\tilde{m}_{d0}}{dt^2}+\eta_2\frac{d\tilde{m}_{d0}}{dt}+\left[4\pi-\xi+3\delta m_{d0}^2+\frac{3}{4}\delta(A_{11}^{(0)})^2\right]\tilde{m}_{d0}=\tilde{h}. \quad (30)$$

A comparison of Eqs. (10) and (12) for a uniformly magnetized film with the analogous Eqs. (26) and (30) for the film with domains shows that the former equations convert into the latter upon substitutions

$$m_0 \longrightarrow m_{d0},\quad \tilde{m}_0 \longrightarrow \tilde{m}_{d0},\quad \xi \longrightarrow \xi^*,$$

where

$$\xi^* = \xi-\frac{3}{4}\delta(A_{11}^{(0)})^2 = \xi-\frac{3}{4}\delta(\lambda a)^2. \quad (31)$$

This analogy allows us to use the results obtained in the preceding section for the uniformly magnetized state and perform the above substitutions instead of considering once again behavior of the susceptibility in the domain phase. It should be taken into account that, in contrast to parameter ξ depending only on the temperature, the quantity ξ^* also depends on the amplitude of magnetization variation (λa) in the domains. Since $(\lambda a) = f(h_0)$, the new parameter depends on both the temperature and the bias field: $\xi^* = f(T, h_0)$.

The form of the function $(\lambda a) = f(h_0)$ for thermodynamically stable stripe domain structures (with $k = k_c$) in the vicinity of a phase transition with the critical point

$$h_{\rm cr} = \pi\sqrt{3\xi_c/\delta},\quad \xi_{\rm cr} = \xi^{(ud)}(h_{\rm cr})$$

was determined by Tarasenko [14]. In particular, it was established that the form of this function for second kind phase transitions ($|h_0| < h_{\rm cr}$) depends on the interval of ξ. For $\xi_d \ll \xi_c|1-h_0^2/h_{\rm cr}^2|$, where $\xi_d = \xi - \xi^{(ud)}(h_0)$, we have the relationship

$$(\lambda a) = \frac{4}{3}\sqrt{\frac{\xi_d}{\delta\left|1-h_0^2/h_{\rm cr}^2\right|}}, \quad (32)$$

while for $\xi_c|1-h_0^2/h_{\rm cr}^2| \ll \xi_d \ll \xi_c$ the function changes to

$$(\lambda a) = \frac{5}{4}\xi_d^{1/4}\left(\frac{\xi_c}{\delta}\right)^{1/2}. \quad (33)$$

The consideration below is restricted to the former relationship, since the latter case is simple and adds no new qualitative features to the behavior of magnetic susceptibility.

Using expressions (31) and (32), we obtain the formula

$$\xi^* = \frac{-\xi(1+3h_0^2/h_{\rm cr}^2)+4(\xi_c+3\delta h_0^2/16\pi^2)}{3\left|1-h_0^2/h_{\rm cr}^2\right|}, \quad (34)$$

which shows that the sign of the derivative $\partial\xi^*/\partial T$ in the domain phase is opposite that of $\partial\xi/\partial T$. For this reason, the derivative $\partial m_{d0}/\partial T$ is positive, which can be readily checked by direct differentiation of relation (26). This implies that the uniform magnetization component m_{d0} decreases when the mapping point leaves the line corresponding to the loss of stability of the uniform state and moves toward lower temperatures.[4] Since both derivatives ($\partial\xi^*/\partial T$ and $\partial m_{d0}/\partial T$) change sign in the domain phase, this does not affect the character of extrema in the magnetic susceptibility,

$$\chi_{zz}^{(d0)}(\omega) = \chi_{zz}^{(d0)\prime}(\omega) + i\chi_{zz}^{(d0)\prime\prime}(\omega) = \tilde{m}_{d0}(\omega)/\tilde{h}.$$

In accordance with the above considerations, the imaginary and real parts of this susceptibility are determined by the formulas

$$\chi_{zz}^{(d0)\prime}(\omega) = \frac{\omega_{d0}^2-\omega^2}{\eta_1[(\omega_{d0}^2-\omega^2)^2+\omega_\eta^2\omega^2]}, \quad (35)$$

$$\chi_{zz}^{(d0)\prime\prime}(\omega) = \frac{\omega\omega_\eta}{\eta_1[(\omega_{d0}^2-\omega^2)^2+\omega_\eta^2\omega^2]}, \quad (36)$$

where $\omega_{d0}^2 = (4\pi - \xi^* + 3\delta m_{d0}^2/\eta_1)$ and m_{d0} satisfies Eq. (26), which can be rewritten as

$$(4\pi-\xi^*+\delta m_{d0}^2)m_{d0} = h_0. \quad (37)$$

Similarly to the case of uniform magnetization, the type of the main (frequency-independent) extremum, as well as the types and positions of additional extrema in the domain phase at a fixed bias field depend on the relationship between the frequency of the variable mag-

[4] This result is a consequence of making allowance for the correction quadratic in (λa) in Eq. (26) for m_{d0}. In [14], this correction was ignored and the constant magnetization component was calculated using Eq. (10), which was quite expedient for the purposes of that investigation. In our case, this approximation cannot be used because all special features in the behavior of magnetic susceptibility in the domain state are determined entirely by the corrections proportional to $(\lambda a)^2$ in the equation of motion of the magnetization vector.

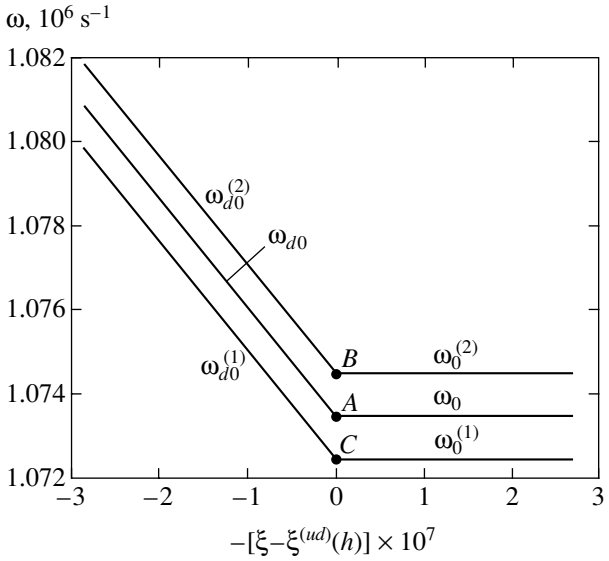

Fig. 5. Temperature dependences of the characteristic frequencies determining the types and positions of extrema in the real and imaginary parts of the magnetic susceptibility of a 2-μm-thick model film.

netic field and three characteristic frequencies: ω_{d0}, $\omega_{d0}^{(1)}$, and $\omega_{d0}^{(2)}$, where

$$\omega_{d0}^{(1,2)} = \sqrt{\omega_{d0}^2 + \frac{\omega_\eta^2}{4}} \mp \frac{\omega_\eta}{2}. \quad (38)$$

Figure 5 shows the temperature dependence of the frequencies ω_0, $\omega_0^{(1,2)}$ and ω_{d0}, $\omega_{d0}^{(1,2)}$ at $h_0 = 0.002$ for a model film with the parameters

$$\delta = 4 \times 10^5, \quad \eta_1 = 10^{-11},$$
$$\eta_2 = 2 \times 10^{-8}, \quad \omega_\eta = 2 \times 10^3,$$
$$L = 10^{-3}\ \text{cm}, \quad \beta_u = 100, \quad \beta_p \ll \beta_u.$$

The temperatures are measured from the point $\xi^{(ud)}(0.002) = 1.008006$ corresponding to the domain structure nucleation for the given bias field. At this point on the phase transition line, the minimum characteristic temperatures are

$$\omega_{0\min} = \omega_{d0\min} = \omega_A = 1.073434 \times 10^6\ \text{s}^{-1},$$
$$\omega_{0\min}^{(1)} = \omega_{d0\min}^{(1)} = \omega_C = 1.072435 \times 10^6\ \text{s}^{-1},$$
$$\omega_{0\min}^{(2)} = \omega_{d0\min}^{(2)} = \omega_B = 1.074434 \times 10^6\ \text{s}^{-1},$$

and the corresponding critical point on the (ξ, h_0) plane as the coordinates

$$\xi_{cr} = 1.04966, \quad h_{cr} = 0.008815.$$

Since the Intersection of the line corresponding to the main (frequency-independent) extremum (curve *0* in Fig. 3) with the line of phase transitions (dashed line in Fig. 3) takes place at $\xi^{(cp)} = 5.3248$, $h_0^{(cp)} = 0.02372$ (point *D* in Fig. 3), this extremum is not observed (see considerations at the end of this section).[5]

Figure 5 shows a considerable difference between the rates of variation of the characteristic frequencies in the uniform and domain phases depending on the temperature (in the selected scale, the branches corresponding to the uniform phase appear as almost horizontal, but in fact they possess a significant negative slope). This implies that the extrema of the magnetic susceptibility in these phases must exhibit significantly different temperature sensitivity. For $\xi - \xi^{(ud)} = 0$ (phase transition point), all three curves in Fig. 5 exhibit minima, which implies the appearance of a localized (frequency-independent) extremum (referred to below as additional frequency-independent extremum).[6]

Behavior of the additional extrema in the temperature dependence of the real and imaginary parts of the susceptibility for $h_0 = \text{const}$ and variable frequency can be readily traced using Fig. 5 (by analogy with the analysis in Section 3), Fig. 6 (for the real part of the susceptibility), and Fig. 7 (for the imaginary part of the susceptibility). Note that Figs. 6 and 7 employ different temperature scales, since the behavior of extrema in the susceptibility of the uniform and domain phases cannot be depicted in the same scale. Below, the consideration refers to the case of $h_0 = 0.002$ (the analysis for other h_0 values encounters no difficulties). The values of the frequency $\omega \times 10^{-6}$ for curves *1–10* in Figs. 6 and 7 are 1.06, 1.07, 1.0725, 1.07305, 1.0735, 1.0745, 1.078, 1.082, 1.094, and 1.13 s^{-1}, respectively.

The simplest behavior is observed for the imaginary part of the susceptibility: for $\omega < \omega_A$, this part exhibits only an additional frequency-independent maximum (at the phase transition point) with the amplitude smoothly increasing with the frequency (Fig. 7, curves *2–4*). When

[5] The abscissa $\xi^{(cp)}$ of this intersection point is a real root of the equation $\xi^3 - 12\pi\xi^2 + 57\pi^2 - (9\xi_c + 64\pi)\pi^2 = 0$, while the ordinate is given by the formula $h_0^{(cp)} = 4\pi\sqrt{(\xi^{(cp)} - \xi_c)/3\delta}$.

[6] Note that quantitative results obtained for the additional frequency-independent extremum should be treated with care, because the line of the second kind phase transition occurs at the center of the fluctuational interval, where the Landau theory is inapplicable [15]. Our analysis [8] of behavior of the differential magnetic susceptibility showed that allowance for fluctuations leads to the appearance of an additional fluctuational maximum in the susceptibility on the phase transition line, so that a total response is observed in experiment.

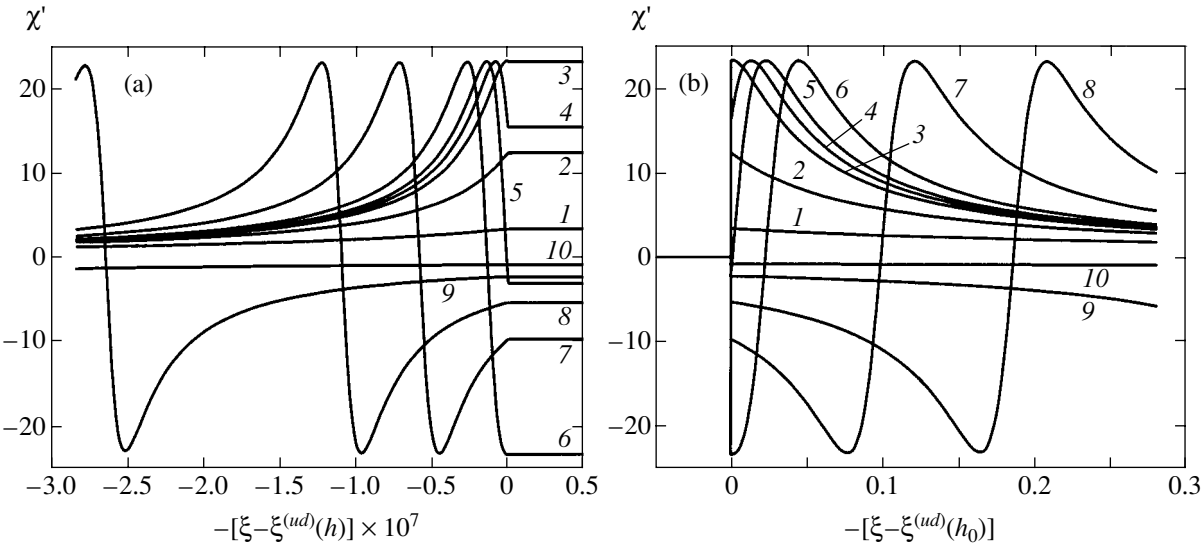

Fig. 6. Temperature dependences of the real part of the magnetic susceptibility of a ferromagnetic film in the uniform and domain magnetization states; the temperature scale is (a) expanded and (b) not expanded (the values of frequencies for curves *1–10* are given in the text).

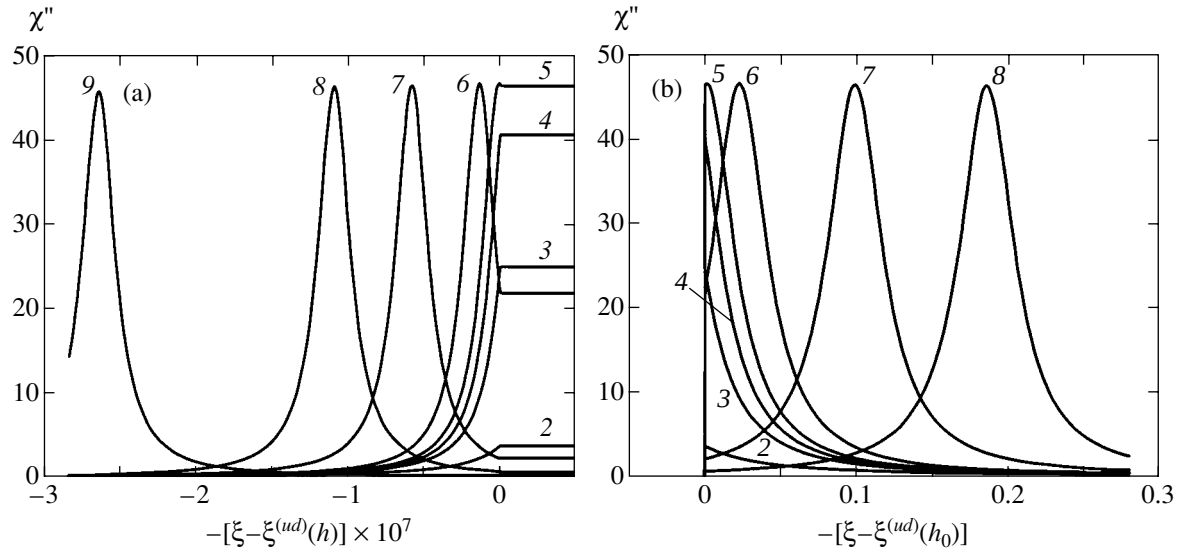

Fig. 7. Temperature dependences of the imaginary part of the magnetic susceptibility of a ferromagnetic film in the uniform and domain magnetization states; the temperature scale is (a) expanded and (b) not expanded (the values of frequencies for curves *1–10* are given in the text) (curve *1* is not shown since it virtually coincides with the abscissa axis).

the frequency exceeds the value ω_A (see Fig. 5) at which the imaginary part of the susceptibility reaches absolute maximum, the additional frequency-independent extremum converts into a minimum and there appear two frequency-dependent maxima (one in the uniform phase and another, in the domain phase). As the frequency grows further, these maxima move away in opposite directions from the phase transition point (Fig. 7, curves *5–9*).

For $\omega < \omega_C$, the real part of the susceptibility exhibits only an additional frequency-independent maximum (at the phase transition point). The χ' value smoothly increases with frequency and reaches a maximum (positive) at $\omega = \omega_A$ (Fig 6, curves *1* and *2*). When the frequency grows further in the interval $\omega_B > \omega > \omega_A$, this extremum converts into a minimum and there appear two frequency-dependent maxima (in the uniform and domain phases, see Fig 6, curves *3–5*). As the frequency ω keeps increasing, the χ' value at the point of the additional frequency-independent minimum monotonically decreases, becomes negative, and exhibits a minimum (negative) at $\omega = \omega_B$. Then (for $\omega > \omega_B$), the additional frequency-independent extremum again converts into a maximum and acquires (besides the two additional fre-

quency-independent maxima) two additional frequency-independent minima (in the uniform and domain phases, see Fig. 6, curves *6–10*).

It should be noted that the existence of the main (frequency-independent) extremum at the line of the phase transition from the uniformly magnetized state to a state with domain structure is also possible for other parameters of the film and/or for other values of the bias magnetic field. For calculating the temperature of this extremum in the region of existence of the domain structure, it is necessary to replace in expression (18) $\xi^{(m)}$ by $\xi^{(m)} - (3/4)(\lambda a)^2$ in accordance with formula (31) and use the analytical relationship $(\lambda a) = f(h_0)$ valid in the selected interval of the bias fields for the given parameters of the film. For example, formally assuming that the function $(\lambda a) = f(h_0)$ at the line of phase transitions is described by formula (32), the curve of $\xi^{(m)}(h_0)$ in the region of existence of the domain phase on the (ξ, h_0) plane will have the shape depicted by dashed line *0'* in Fig. 3.

The degree of deviation of this line from line *0* (corresponding to the calculation for the uniformly magnetized state) will depend on the particular form of the function $(\lambda a) = f(h_0)$, but qualitative behavior will be generally the same. Indeed, in the vicinity of the phase transition, the value of (λa) (i.e., the amplitude of variation of the *z*-component of magnetization in the domain phase) monotonically increases with distance from the phase transitions line. For this reason, the position of the main (frequency-independent) extremum (which is frequently the only experimentally observed feature) on the (H_0, T) plane cannot be described by the same function. This circumstance most probably accounts for the discrepancies between theoretical and experimental vales of the critical indices for the magnetic susceptibility in the vicinity of the Curie point (see, e.g., [8]).

5. CONCLUSIONS

The above analysis showed that an analysis of the temperature dependence of the magnetic susceptibility of ferromagnetic films in the vicinity of the Curie temperature in the general case is a quite complicated problem. The theory predicts, in particular, the possible existence of multiple extrema in the real (χ') and imaginary (χ'') parts of the susceptibility and the different functional relationships describing the positions of these extrema in the phase plane (T, H) for the uniform and domain phases.

Since the behavior of the magnetic susceptibility in the vicinity of the Curie temperature was performed within the framework of the Landau theory, the quantitative results obtained are, formally speaking, inapplicable in the region of temperatures inside the fluctuational interval $(\Delta\xi)_f$. For real ferromagnets, the width of this temperature interval is comparable to the value of ξ_c determining the temperature interval of applicability of the Landau theory ($\xi \ll \xi_c$). However, this circumstance does not deprive the results obtained above of practical significance, because the main qualitative conclusions from the Landau theory—the existence of a temperature minimum for the uniform modes of oscillations of the magnetic moment (ω_0 and ω_{d0}) near the Curie point and the difference between the functions $\omega_0(\xi)$ and $\omega_{d0}(\xi)$ for the uniform and domain phases, respectively—remain valid for $\xi > \max\{\xi_c, (\Delta\xi)_f\}$.

This statement is confirmed by the fact that many features in the behavior of the magnetic susceptibility near T_C predicted by the Landau theory (in, particular, the existence of the main frequency-independent extremum, the presence of a jump in the susceptibility at the line of the phase transition from the uniform state to the domain phase, etc.) were repeatedly observed in experiment (see, e.g., [2, 8, 16–18]. Moreover, some ferroelectrics (e.g., $RbHSO_4$) whose behavior near the Curie point is described by analogous equations (see, e.g., [19]) exhibit (besides the main frequency-independent extremum) two additional extrema in the real part of the permittivity at frequencies above 455 MHz, which shift in opposite directions from T_C when the frequency of the external alternating electric field increases to 9.5 GHz (see [20] and the monograph [19], where this paper is cited). It should be noted that the observation of such effects in ferromagnets (in contrast to ferroelectrics) requires conducting the experiments in an extremely narrow frequency interval and using frequency-stabilized sources of the alternating magnetic field (see Sections 3 and 4).

REFERENCES

1. K. P. Belov, *Magnetic Transitions* (Fizmatgiz, Moscow, 1959; Consultants Bureau, New York, 1961).
2. K. P. Belov, *Ferrites in Strong Magnetic Fields* (Nauka, Moscow, 1972).
3. E. Frey and F. Schwabl, Z. Phys. B: Condens. Matter **71**, 355 (1988).
4. A. Berger, A. W. Pang, and H. Hopster, J. Magn. Magn. Mater. **137**, L1 (1994).
5. R. Arias and H. Suhl, Phys. Rev. B **51**, 979 (1995).
6. N. Vukadinovic, A. Serraj, H. Le Gall, and J. Ben Youssef, Phys. Rev. B **58**, 385 (1998).
7. L. D. Landau, Zh. Éksp. Teor. Fiz. **7**, 819 (1937).
8. I. E. Dikshteĭn, F. V. Lisovskiĭ, E. G. Mansvetova, and E. S. Chizhik, Zh. Éksp. Teor. Fiz. **90**, 614 (1986) [Sov. Phys. JETP **63**, 357 (1986)].
9. I. E. Dikshteĭn, F. V. Lisovskiĭ, E. G. Mansvetova, and V. V. Tarasenko, Zh. Éksp. Teor. Fiz. **86**, 1473 (1984) [Sov. Phys. JETP **59**, 863 (1984)].
10. V. V. Tarasenko, E. V. Chenskiĭ, and I. E. Dikshteĭn, Zh. Éksp. Teor. Fiz. **70**, 2178 (1976) [Sov. Phys. JETP **43**, 1136 (1976)].

11. L. N. Bulaevskiĭ and V. L. Ginzburg, Zh. Éksp. Teor. Fiz. **45**, 772 (1963) [Sov. Phys. JETP **18**, 530 (1963)].

12. V. G. Bar'yakhtar and V. F. Klepikov, Pis'ma Zh. Éksp. Teor. Fiz. **15**, 411 (1972) [JETP Lett. **15**, 289 (1972)].

13. S. V. Vonsovskiĭ, *Magnetism: Magnetic Properties of Dia-, Para-, Ferro-, Antiferro-, and Ferrimagnets* (Nauka, Moscow, 1971), Vols. 1 and 2.

14. V. V. Tarasenko, Fiz. Tverd. Tela (Leningrad) **22**, 504 (1980) [Sov. Phys. Solid State **22**, 294 (1980)].

15. V. L. Ginzburg, Fiz. Tverd. Tela (Leningrad) **2**, 1031 (1960) [Sov. Phys. Solid State **2**, 1824 (1960)].

16. K. P. Belov and N. V. Shebaldin, Pis'ma Zh. Éksp. Teor. Fiz. **7**, 268 (1968) [JETP Lett. **7**, 208 (1968)].

17. S. A. Poltinnikov, Fiz. Tverd. Tela (Leningrad) **10**, 3687 (1968) [Sov. Phys. Solid State **10**, 2928 (1968)].

18. I. D. Luzyanin and V. P. Khavronin, Zh. Éksp. Teor. Fiz. **87**, 2129 (1984) [Sov. Phys. JETP **60**, 1229 (1984)].

19. B. A. Strukov and A. P. Livanyuk, *Physical Principles of Ferroelectric Phenomena in Crystals* (Nauka, Moscow, 1995).

20. T. Ozaki, J. Phys. Soc. Jpn. **49**, 234 (1980).

Translated by P. Pozdeev

Journal of Experimental and Theoretical Physics, Vol. 98, No. 6, 2004, pp. 1164–1173.
Translated from Zhurnal Éksperimental'noĭ i Teoreticheskoĭ Fiziki, Vol. 125, No. 6, 2004, pp. 1329–1339.

SOLIDS
Structure

Magnetic Properties of Nonmagnetic Metals with Randomly Distributed Paramagnetic Impurities

E. Z. Meĭlikhov

Russian Research Centre Kurchatov Institute, Moscow, 123182 Russia
Moscow Institute of Physics and Technology, Dolgoprudnyĭ, Moscow oblast, 141700 Russia
e-mail: meilikhov@imp.kiae.ru

Received December 3, 2003

Abstract—A generalized mean field theory for disordered systems with the RKKY interaction is constructed on the basis of calculation and analysis of distribution functions for random magnetic fields produced by magnetic moments with an irregularly spatial distribution. These distribution functions are determined by two methods: (i) analytically and (ii) numerically by statistical processing of the results of calculation of random fields in a model system. For metals diluted by magnetic impurities, it is shown that the ground state of the system becomes magnetically ordered when the impurity concentration exceeds a certain critical value depending on the type of crystal lattice of the metal and the sample shape. The magnetic phase diagram of the system is determined and the temperature dependence of its magnetic susceptibility, the concentration dependence of the Curie temperature, and the temperature and concentration dependences of the magnetization and magnetic part of the heat capacity of the system are established. © *2004 MAIK "Nauka/Interperiodica".*

1. INTRODUCTION

The introduction of magnetic impurities into a nonmagnetic matrix is known to change the physical properties of the composite (its magnetic susceptibility, specific heat, etc.). Systems of this type can be classified according to the type of the matrix: (i) magnetic impurities in a diamagnetic metal, (ii) magnetic impurities in a semiconductor, and (iii) magnetic impurities in an insulator. An example of the first-type systems are metal alloys $Cu_{1-x}(Mn, Fe)_x$ and $Au_{1-x}Fe_x$, which have been studied for a long time [1] and in which the interaction between magnetic moments μ of introduced impurities is effected by free charge carriers of the metallic matrix (the concentration of these carriers virtually does not change upon the introduction of impurities). Second-type systems can be represented by magnetic semiconductors such as $Ca_{1-x}Mn_xAs$ [2] or $Cd_{1-x}Mn_xTe$ [3], which have been studied extensively due to their properties, which are of interest for new trends in electronics and especially spintronics. Free charge carriers in such systems not only carry out the interaction between magnetic impurities, but are also supplied by these impurities. Systems of the third type remain insulators even after the introduction of impurities; for this reason, the magnetic interaction in such systems is of the dipole–dipole type. An example of such a dielectric system is $LiY_{1-x}Ho_xF_4$. The properties of this system were studied in [4] and will not be considered here.

A common property of all these systems is random distribution of impurities among the lattice sites of the matrix. It is well known, however, that the traditional mean field theory does not provide an adequate description for such a disordered (random) system of magnetic moments [5]. This study aims at generalization of the mean field theory for systems with an indirect interaction of magnetic impurities (via conduction electrons) allowing for the random nature of their spatial distribution. We confine our analysis to the Ising approximation and assume that the indirect interaction between the magnetic moments of impurity atoms is effected with the help of the RKKY interaction via the polarization of free charge carriers [2, 3, 6–8]. The magnetic properties of the system are described using the distribution function for random effective local magnetic fields. The latter is determined analytically (for strongly dilute systems) or using numerical calculations for a model random system of Ising magnetic moments arranged at the lattice sites of the matrix. In real systems, the spread in these fields is so strong that the RKKY interaction overcomes this spread "with difficulty" and can ensure a magnetic ordering at considerably lower temperatures (as compared to the predictions of the traditional mean field theory). The dependence of magnetic properties of such systems on the impurity concentration is also peculiar.

This approach was proposed and used for the first time in the well-known publication by Klein and Brout [7].[1] However, the analysis carried out in [7] pertained only to the properties of the magnetically disordered state. According to Klein and Brout, the correlation of the magnetic moments of impurity atoms must

[1] A similar approach for calculating random fields in the RKKY interaction was proposed in [9].

be taken into account in this case. According to the ideas formulated by these authors, these moments are completely or partly correlated if the distance between atoms is smaller than a certain correlation radius $R_c = 0.51x^{-1/3}a$, where a is the parameter of the cubic lattice of the crystal. The number of impurity atoms in a sphere of radius R_c is independent of their concentration x and is equal to $(4\pi/3)R_c^3 x \approx 2.3$ (except for the atom located at the center of the sphere.). The magnetic field at each atom is the sum of two independent contributions, viz., the "near" field of the atoms of the correlation sphere and the "far" field of the remaining atoms. Each of these fields is characterized by its own distribution function. According to this scheme, a body consists of small clusters of atoms with correlated magnetic moments, which are coupled via the RKKY interaction (the average number of atoms in a cluster is approximately equal to 3.3).

Further, it was assumed that the distribution function for the fields produced by the atoms of the external region ($R > R_c$) is a Gaussian function with the peak at $H = 0$ and with variance $\sigma \propto x$. The distribution function for the fields produced by the atoms of the correlation sphere was described by a certain implicit relation, which is used for numerical calculations. The total distribution function for random magnetic fields in a face-centered cubic (fcc) lattice, which was determined for $x = 0.18$, was found to be the function with the maximal value (for $H = 0$) equal to one-fourth (!) of its value in the absence of correlations.

Using this approach, the authors of [7] drew the conclusion that the systems in question cannot be magnetically ordered for impurity concentrations $x < 0.5$. This contradicts the experiments with Pd(Co) [10], Pd(Fe) [11], and Au(Fe) [12], in which a ferromagnetic ordering was observed for $x_c < 0.01$. It was also predicted in [7] that the magnetic part C_m of the specific heat capacity of such systems must be independent of the impurity concentration, which is in contradiction to the results of experiments with Cu(Co) [13] and Au(Co) [14], according to which $C_m \propto x^2$.

In our opinion, the reason for the noted discrepancy lies in the fact that role of correlations was grossly overestimated in [7]. In order to verify this, it is sufficient to compare the results of the model numerical calculations of the field distribution functions in magnetically disordered systems of two types: (i) with complete correlation of the moments within a sphere of radius R_c and (ii) in the absence of any correlation of these moments (see below). As a result, the maximal values of the corresponding functions differ by less than 5%. In addition, the methods for taking into account correlations used in [7] obviously becomes less and less applicable upon an increase of the magnetic order parameter of the system. In this connection, we can state that it is possible to obtain a qualitatively adequate description of the properties of the systems in question without taking into account the correlation between magnetic moments, but (in contrast to [7]) the method should be extended to systems with nonzero magnetization. This leads to the results that are in better agreement with the experimental data.

It should also be noted that we will disregard the Kondo effect (antiferromagnetic interaction of conduction electrons with magnetic impurities, leading to compensation of impurity magnetic moments) everywhere in the subsequent analysis; in other words, we assume that the indirect RKKY interaction of impurities is predominant. Such a situation is obviously realized [1] in some nonmagnetic metals with 3*d* impurities of the Fe and Co type (e.g., in Au(Fe)).

2. DISTRIBUTION FUNCTIONS OF RANDOM FIELDS

We write the energy w_{RKKY} of the indirect (via free charge carriers) exchange RKKY interaction between two parallel spins of magnetic ions separated by a distance r from each other in the form [6]

$$w_{RKKY}(r) = -W\phi(2k_F r), \quad W = \frac{9\pi}{2}\frac{(nVJ)^2}{\varepsilon_F},$$
$$\phi(y) = \frac{y\cos y - \sin y}{y^4}\exp\left(-\frac{y}{2k_F l}\right), \tag{1}$$

where J is the energy of exchange interaction between the spin and a free charge carrier; ε_F and k_F are the Fermi energy and the Fermi wave number of free charge carriers with number density n and mass m; in the standard band model, these quantities are defined as

$$\varepsilon_F = (\hbar^2/2m)(3\pi^2 n)^{2/3}, \quad k_F = (3\pi^2 n)^{1/3},$$

and V is the unit cell volume of the matrix. The exponential function in the expression for $\phi(y)$ reflects the finite value of the mean free path l of free charge carriers. Energy w_{RKKY} can be represented as the result of the interaction of the spin with the effective local magnetic field equal to

$$h(r) = h_J\phi(2k_F r), \quad h_J = W/\mu, \tag{2}$$

where μ is the magnetic moment.

Let us suppose that a system consisting of randomly located Ising magnetic moments (spins) is in the state characterized by the average magnetization I. The local effective fields H_3 produced by randomly distributed spins at various points and the random value H of the sum of all such fields can be characterized by the distribution function $F_x(j; H_3)$ depending on the relative concentration x of magnetic ions and on the relative magnetization $j \equiv I/\mu N_\mu$ of the system. Here, $N_\mu = xN$ is the magnetic impurity concentration and N is the concentration of the matrix atoms replaced by impurities.

Magnetization j determines the average fraction $\eta = (1 + j)/2$ of spins oriented along its direction ($F_x(1; H_3)$ is the distribution function in the case when all spins are parallel to one another).

The random nature of the impurity distribution is limited by the fact that they are "forced" to be localized only at definite places (sites) of the matrix lattice. For strongly dilute systems, this limitation is insignificant and the distribution function for random local fields can be determined with the help of the Markov method [13], according to which

$$F(j; H) = \frac{1}{2\pi}\int_{-\infty}^{\infty} A(q)\exp(-iqH_3)dq, \qquad (3)$$

where

$$A(q) = \lim_{N_{\max}\to\infty}\left[\sum_{\zeta=\pm1}\int_0^{r_{\max}}\exp[iqh_\zeta(r,\zeta)]\tau(r,\zeta)dr\right]^{N_{\max}};$$

here, $h_\zeta(r, \zeta) = \zeta h(r) = \zeta w_{RKKY}/\mu$ is the effective magnetic field produced at the origin by the spin separated from it by a random distance r. Random parameter ζ assumes values of ±1 (with probability η and $(1 - \eta)$, respectively) and determines the direction of the spin; $\tau(r, \zeta)$ is the continuous distribution function of random values of distance r and parameter ζ; and $N_{\max} = 4\pi r_{\max}^3 N_\mu/3$ is the number of impurities in a sphere of radius $r_{\max}$ (integration is carried out over the volume of this sphere). If we now assume that the distributions of r and ζ are uniform and disregard the correlation of magnetic moments, we can write

$$\tau(r,\zeta)d\rho d\zeta = \begin{cases}[3r^2/(r_{\max}^3 - r_{\min}^3)]dr[(1-\eta)\delta(\zeta+1)] \\ +\eta\delta(\zeta-1)]d\zeta, \quad r > r_{\min}, \\ 0, \quad r < r_{\min},\end{cases} \qquad (4)$$

where we have taken into account the existence of the minimal possible distance $r_{\min} \approx N^{-1/3}$ between magnetic ions (for the alignment of impurity atoms into a cubic sublattice).

Substituting expressions (4) into (3), we obtain

$$A(q) = \exp[-4\pi xNC(q)],$$
$$C(q) = \int_{r_{\min}}^{\infty}\{1 - \cos[qh(r)] - ij\sin[qh(r)]\}r^2dr. \qquad (5)$$

Among other things, this expression shows that, in the absence of magnetization ($j = 0$), distribution function $F_x(0; H_3)$ for local fields is even, i.e., symmetric relative to $H_3 = 0$ (as assumed in [7]).

Relations (5) do not lead to a simple analytic expression for distribution function $F_x(j; H)$. To determine the latter function, we used two mutually supplementing methods: (i) the "small q approximation" based on the fact that the range of large q's in inverse Fourier transformation (3) is insignificant and (ii) numerical calculations for the model random system of Ising moments.

In the framework of the first approach, functions $\cos[qh(r)]$ and $\sin[qh(r)]$ subjected to integration in Eq. (5) are replaced by their approximate power expansions in small argument qh (up to the first nonvanishing term in qh). In this approximation, we have

$$C(q) = Pq^2 - ijSq, \qquad (6)$$

where

$$P = \int_{r_{\min}}^{\infty} h^2(r)r^2dr = \frac{3}{8}W\frac{W}{\mu^2k_F^3}\phi_P(2k_Fr_{\min}),$$
$$\phi_P(2k_Fr_{\min}) = \int_{2k_Fr_{\min}}^{\infty} y^2\phi^2(y)dy,$$
$$S = \int_{r_{\min}}^{\infty} h(r)r^2dr = \frac{3}{4}\mu\frac{W}{\mu^2k_F^3}\phi_S(2k_Fr_{\min}), \qquad (7)$$
$$\phi_S(2k_Fr_{\min}) = \int_{2k_Fr_{\min}}^{\infty} y^2\phi(y)dy.$$

For $l = \infty$, we have

$$\phi_S(y) = -\frac{\sin y}{y}, \quad \phi_P(y) = \frac{1}{5}\left[\frac{2}{3}\left(\frac{\pi}{2} - \mathrm{Si}2y\right)\right.$$
$$+\frac{(y\cos y - \sin y)^2}{y^5} + \frac{1 - \cos 2y - y\sin 2y}{3y^3} \qquad (8)$$
$$\left.+\frac{\sin 2y - 2y\cos 2y}{6y^2}\right],$$

where $\mathrm{Si}2y = \int_0^{2y}(\sin t/t)\,dt$.

The values of the functions $\phi_P(2k_Fr_{\min})$ and $\phi_S(2k_Fr_{\min})$ for $l = \infty$ are shown in Fig. 1. Among other things, it follows from this figure that the average direction of the random effective field (the position of the peak of distribution function $F_x(j; H)$) determined by the sign of parameter $\phi_S(2k_Fr_{\min})$ depends on the lattice type: for body-centered cubic (bcc) and face-centered

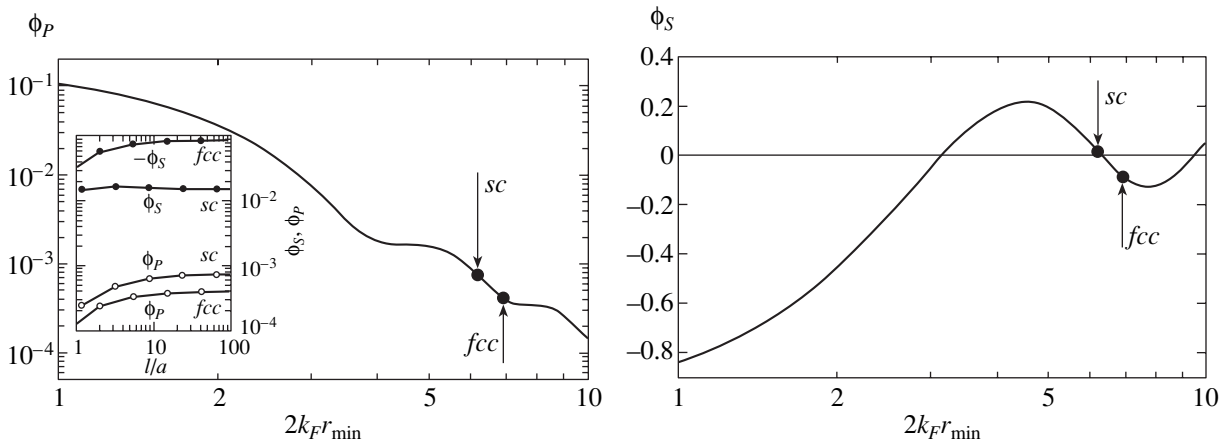

Fig. 1. Functions $\phi_P(2k_F r_{\min})$ and $\phi_S(2k_F r_{\min})$ for cubic metals ($l = \infty$). The inset shows the dependence of these functions on the mean free path of charge carriers.

cubic (fcc) lattices, it coincides with the direction of average magnetization ($H_j > 0$), while for a simple cubic (sc) lattice, it is opposite to this direction ($H_j < 0$).

Functions $\phi_P(2k_F r_{\min})$ and $\phi_S(2k_F r_{\min})$ considerably depend on the mean free path of charge carriers only for $l/a \lesssim 10$ (see the inset to Fig. 1). Consequently, in a "good" metal (in which $l/a \gg 1$), this dependence can be disregarded.

Substituting Eq. (5) into (3), we see that distribution $F_x(j; H_3)$ in this approximation is described by a Gaussian function displaced relative to $H = 0$:

$$F_x(j; H_3) = \frac{1}{\sqrt{2\pi}\sigma}\exp\left[-\frac{(H_3 - jH_j)^2}{2\sigma^2}\right],$$

$$H_j = -4\pi x N S \propto x, \tag{9}$$

$$\sigma = (4\pi x N P)^{1/2} \propto x^{1/2}.$$

The width σ of this distribution is proportional to $\sqrt{x}$ and is determined by parameter P, while the position of the peak ($H = jH_j$) is determined by parameter S. With decreasing magnetization, the peak in distribution $F_x(j; H)$ is linearly displaced towards smaller (in absolute value) fields, while its width remains unchanged. The exponentially descending wings of the Gaussian distribution function correspond to a low probability of the emergence of strong local fields for which $qh \gtrsim 1$. This approximation holds well when the concentration x of magnetic ions is low (see below). The value of parameter $2k_F r_{\min}$ depends on the lattice type. For systems of the first type (nonmagnetic metals with impurities), the corresponding value of characteristic parameters for monovalent metals with a cubic lattice of period a are given in the table.

For metals with an fcc lattice (Cu, Ag, Au, and Pd), relations (9) for shift H_j of distribution function $F_x(j; H_3)$ and its width σ can be written in the form

$$H_j = \left|x\frac{\phi_S(2k_F r_{\min})}{\pi}\right| h_J,$$
$$\sigma = \left|x\frac{\phi_P(2k_F r_{\min})}{2\pi}\right|^{1/2} h_J. \tag{10}$$

The corresponding dependences $H_j(x)$ and $\sigma(x)$ for a monovalent metal with an fcc lattice are shown in Fig. 2 (dashed lines).

The model system was constructed via a uniformly random distribution of spins with the ratio of "up" and "down" moments determined by a selected value of relative magnetization $0 \le j \le 1$ among the sites of the cubic lattice (with a total number of sites varying from 10^4 to 10^5). Then the magnetic field H_3 at the central lat-

Vital parameters determining the properties of monovalent metals with a cubic lattice

Parameters	Lattice type		
	sc	*bcc*	*fcc*
$r_{\min}/a$	1	$\sqrt{3}/2$	$1/\sqrt{2}$
Na^3	1	2	4
$Nr_{\min}^3$	1	1.30	1.41
$2k_F a$	6.19	7.79	9.80
$2k_F r_{\min}$	6.19	6.75	6.94
$\phi_S(2k_F r_{\min})$, $l = \infty$	–0.0150	0.0667	0.0880
$\phi_P(2k_F r_{\min})$, $l = \infty$	7.43×10^{-4}	4.54×10^{-4}	4.23×10^{-4}

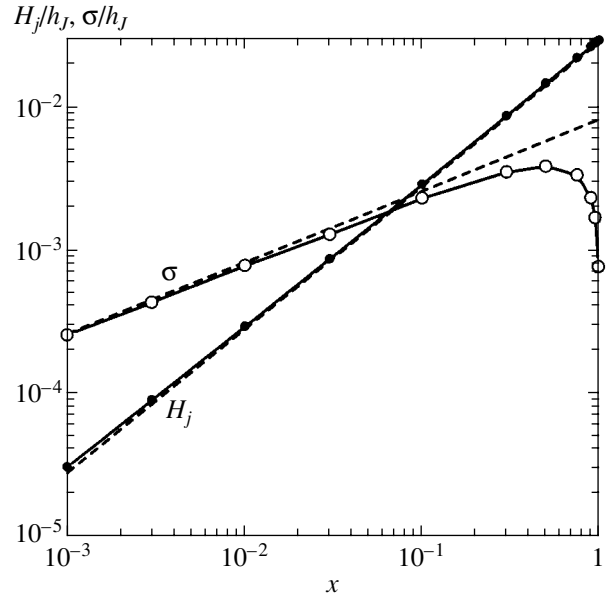

Fig. 2. Concentration dependences of parameters H_j and σ of the Gaussian distribution function $F(1; H_3)$ for effective magnetic fields, resulting from RKKY interaction between magnetic ions located at the sites of the fcc lattice of a monovalent metal. Symbols correspond to numerical calculations and the dashed straight lines describe the analytic approximation for small q at $l = \infty$.

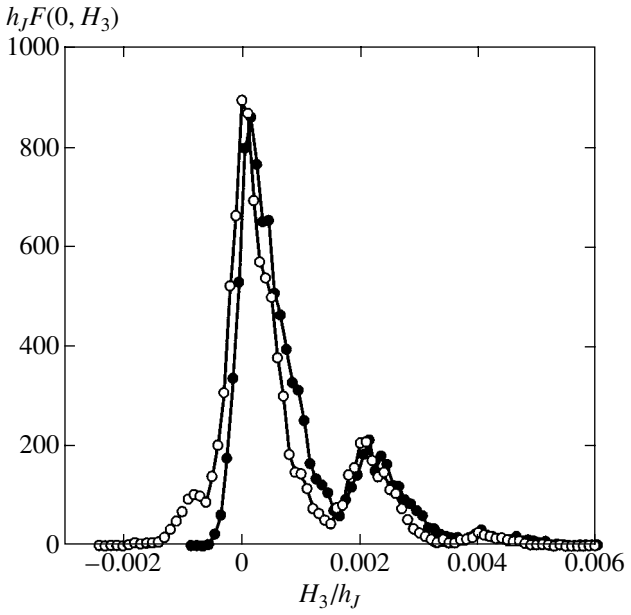

Fig. 3. Distribution function $F(0; H_3)$ for systems with correlated (●) and noncorrelated (○) magnetic moments of impurities with concentration $x = 0.02$ located at sites of the fcc lattice of a monovalent metal ($l = \infty$). The results are obtained by numerical simulation.

tice site was calculated with the help of formula (1) and functions $F_x(j; H_3)$ were determined by sampling from a large number (about 10^4) of realizations of such a system.

The procedure for verifying the results obtained in [7] was slightly different: a quasi-spherical domain surrounding the central site and containing the required number of sites,[2] in which all impurities produced a magnetic field coinciding in direction with the moment of impurity at the central site, was singled out in a system with zero magnetization. In this way, the correlation of magnetic moments predicted in [7] was imitated.[3] Figure 3 shows the result of one of such calculations. It can be seen that, although the magnetic field distribution functions "perceives" the presence of correlations, its general form is preserved and the maximal value changes insignificantly (for $x = 0.02$, by less than 5%). This means that the role of correlations in [7] is considerably overestimated and can be disregarded when the distribution function $F_x(j; H_3)$ is calculated.

The evolution of the distribution function $F_x(1; H_3)$ determined in this way upon a change in the concentration x of magnetic ions in a metallic fcc lattice is depicted in Fig. 4. Approximating such functions by the Gaussian functions, we can find the corresponding values of parameters H_j and σ; the concentration dependences of these parameters are shown in Fig. 2 (circles). It can be seen that the small q approximation gives correct values of H_j for any concentrations x; however, this approximation can be used for calculating σ only for low concentrations $x \lesssim 0.1$. By the way, practically any actual system satisfies this condition.

3. GENERALIZED MEAN FIELD THEORY FOR SYSTEMS WITH RKKY INTERACTION

The traditional mean field theory for a regular system corresponds to a δ-shaped distribution function

$$F_x(j; H_3) = \delta[H_3 - H_0(x, j)]$$

for any value of magnetization j. Clearly, the broadening of this distribution in the case of a random system is a factor "hampering" ferromagnetism. The magnetization of such a disordered system must be calculated taking into account the spread in local fields H_3 via direct generalization of the equation $I/\mu N_\mu = \tanh(\mu H_0/kT)$ corresponding to the regular system:

$$\frac{I}{\mu N_\mu} = \int_{-\infty}^{\infty} \tanh\left(\frac{\mu H}{kT}\right) F_x(j; H)\, dH, \qquad (11)$$

or

$$j = \int_{-\infty}^{\infty} \tanh\left(\frac{H/h_J}{\Theta}\right) F_x(j; H)\, dH, \qquad (12)$$

[2] According to [7], this number is independent of the impurity concentration and amounts to $2.3/x \sim 100$.

[3] It is not necessary to take such a correlation into account for the lattice sites located outside the selected sphere in view of the large distances separating these sites from the central one.

where $H = (4\pi/3)I + H_d + H_3$ is the total field consisting of the field $(4\pi/3)I$ of the magnetic moments on the surface of the Lorentz sphere, the demagnetizing field $H_d = -\eta I$ (η is the demagnetizing factor), and the random field H_3; $\Theta = kT/W$ is the reduced temperature (equal to the ratio of the thermal energy to the characteristic energy of RKKY interaction).

Using expression (9) for distribution function $F(j; H)$, we obtain the following equation generalizing the standard mean field equation:

$$j = \frac{1}{\sqrt{2\pi}\sigma/h_J}\int_{-\infty}^{\infty}\tanh\left[\frac{(4\pi/3-\eta)(x\mu N/h_J)j+u}{\Theta}\right] \times \exp\left[-\frac{(u-jH_j/h_J)^2}{2(\sigma/h_J)^2}\right]du. \quad (13)$$

This equation defines the phase diagram of the system, the temperature dependences of its magnetization (in the ferromagnetic phase) and susceptibility (in the paramagnetic phase), and the dependence of the Curie temperature Θ_C of the system on the concentration of magnetic ions.

To determine the conditions under which this equation has a solution corresponding to the magnetically ordered state ($j > 0$), we note that for $\Theta \longrightarrow 0$ this equation is transformed to

$$j = \Phi(z_0 j), \quad (14)$$

where

$$z_0 = \frac{1}{\sqrt{2}\sigma}\left[H_j + \left(\frac{4\pi}{3}-\eta\right)x\mu N h_J\right]$$

and

$$\Phi(x) = \frac{2}{\sqrt{\pi}}\int_0^x \exp(-x^2)dx$$

is the probability integral. Equation (14) has a solution $j > 0$ if $z_0 > \sqrt{\pi}/2$, i.e., for

$$\frac{H_j}{h_J} + \frac{4\pi}{3}\frac{x\mu N}{h_J} > \sqrt{\frac{\pi}{2}}\frac{\sigma}{h_J} + \eta\frac{x\mu N}{h_J}. \quad (15)$$

The meaning of the last condition is that the effective RKKY field H_j and the field $(4\pi/3)x\mu N$ produced by magnetic moments on the surface of the Lorentz sphere must together "overcome" the spread in local fields (on the order of σ) and the demagnetizing field (proportional to η). The most favorable conditions for the emergence of magnetic ordering are naturally created for $\eta = 0$ (a long cylindrical sample).

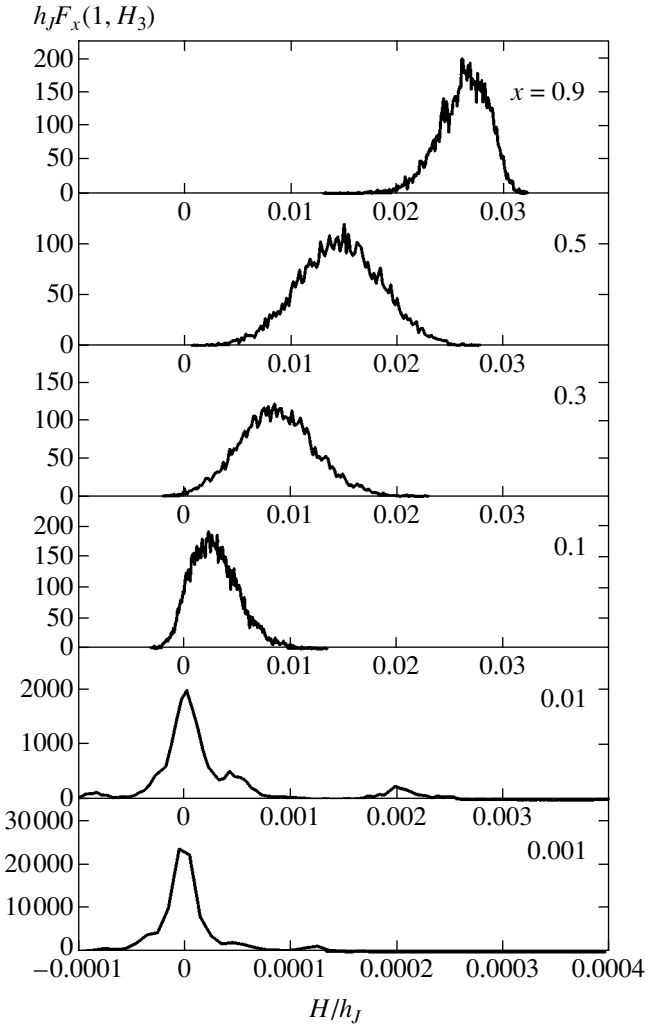

Fig. 4. Evolution of distribution function $F(1; H_3)$ upon a change in concentration x of magnetic ions located at sites of the fcc lattice of a monovalent metal for $l = \infty$. The results are obtained by numerical simulation.

The ground state will be magnetically ordered for $x > x_c$, where the critical concentration x_c of magnetic ions is determined by the equation

$$\sqrt{\frac{\pi}{2}}\frac{\sigma(x_c)}{h_J} - \frac{H_j(x_c)}{h_J} = Z_0 x_c, \quad (16)$$

where

$$Z_0 = \frac{\mu N}{h_J}\left(\frac{4\pi}{3}-\eta\right),$$

parameter Z_0 being a function of the magnetic moment of the impurity and the intensity of RKKY interaction. Using the functional dependences $\sigma(x)$ and $H_j(x)$ determined earlier by numerical simulation (see Fig. 2), we can find the dependence $x_c(Z_0)$ for a monovalent metal with an fcc lattice, represented by dark circles in Fig. 5.

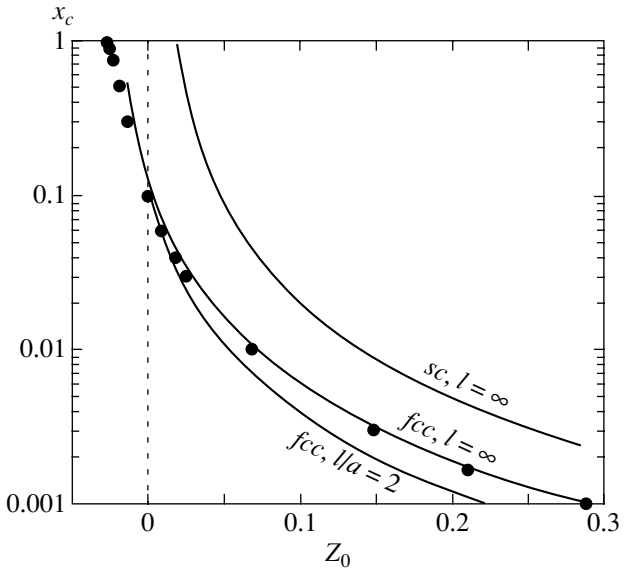

Fig. 5. Dependence of the critical concentration x_c of magnetic ions located at sites of the cubic lattice of a monovalent metal on parameter Z_0. Circles correspond to numerical calculations, while the curves describe the analytic approximation of small q. Sample shape: oblong ellipsoid ($Z_0 > 0$), prolate ellipsoid ($Z_0 < 0$), and sphere ($Z_0 = 0$).

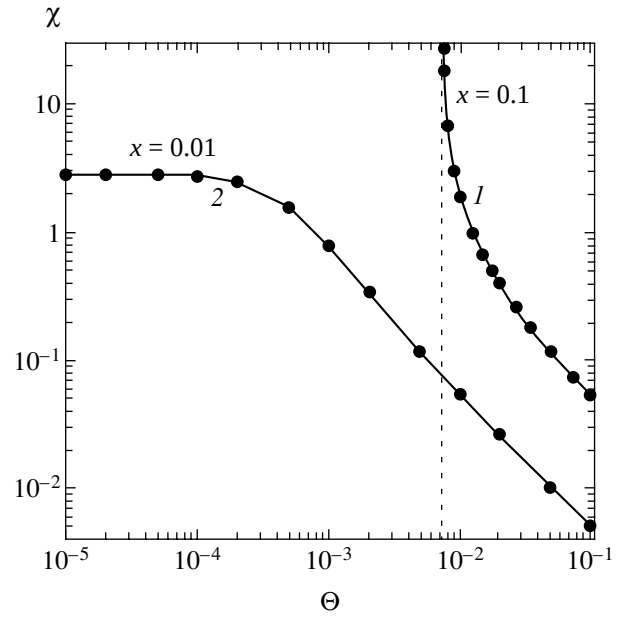

Fig. 6. Temperature dependences of magnetic susceptibility χ of a system of magnetic ions with concentrations $x > x_c$ (curve *1*) and $x < x_c$ (curve *2*), located at sites of the fcc lattice of a monovalent metal ($Z_0 = 0.05$, $l = \infty$).

For a spherical sample ($\eta = 4\pi/3$), the critical concentration x_c is equal to 0.10 irrespective of the value of parameter Z_0.

For a sample in the form of an oblong ellipsoid ($\eta < 4\pi/3$), the critical concentration of magnetic impurities rapidly decreases upon an increase in this parameter. For $\eta = 0$ (long cylinder), for typical values of $W \sim 0.01$ eV and $\mu \approx 5\mu_B$, we obtain $Z_0 \sim 0.05$, which corresponds to $x_c \sim 0.01$. It is also interesting to note that the critical concentration in a "poor" metal ($l/a = 2$) in this case is smaller than in a "good" metal (see Fig. 5).

For a sample in the form of a prolate ellipsoid ($\eta > 4\pi/3$), the critical concentration of magnetic impurities increases with the absolute value of parameter Z_0 and attains the value $x_c = 1$ for $Z_0 \approx -0.025$. This in fact indicates the absence of a magnetic order under real conditions.

The same dependence $x_c(Z_0)$ can be determined proceeding from analytic expressions (10) for parameters σ and H_j:

$$x_c = \frac{\phi_P(2k_F r_{\min})}{4[(\phi_S(2k_F r_{\min})/\pi + Z_0]^2}. \qquad (17)$$

It can be seen from Fig. 5, in which this dependence corresponds to the middle curve, that it correctly determines the critical concentration x_c for $Z_0 > 0$; however, this is not surprising since the small q approximation is quite accurate in this range (see above).

The same figure shows an analogous dependence for a metal with an sc lattice, for which the critical concentration is much higher.

Equation (14) also defines the low-temperature magnetization $j_0 \equiv j(T \longrightarrow 0)$ of the system, which naturally differs from zero only for $x > x_c$. The concentration dependence $j_0(x)$ shown in Fig. 7 indicates that $j_0 < 1$ in all cases; however, the equilibrium magnetization j_0 of the system approaches unity even when the impurity concentration x slightly exceeds the threshold value x_c. Thus, the system is formally an unsaturated ferromagnet. In fact, this phase with random direction and frustration of magnetic moments of impurities is a magnetic (spin) glass.[4]

In the range of low concentrations ($x < x_c$) or high temperatures, the system is paramagnetic. To describe the properties of such a system in an external magnetic field H_e, it is sufficient to carry out the substitution $H_3 \longrightarrow H_3 + H_e$ in the argument of the hyperbolic tangent in Eq. (13). In a weak external field ($H_e/h_J \ll 1$), the magnetization of the paramagnetic system is small

[4] The equality of spontaneous magnetization to zero is a generally accepted, but not a necessary property of the spin glass state. For example, a state with a nonzero magnetization can exist in systems with a nonzero average value of the random exchange integral [14]. In our case, an analog of the latter state is a random RKKY field for which the distribution functions is such that its mean value (equal to jH_j) differs from zero.

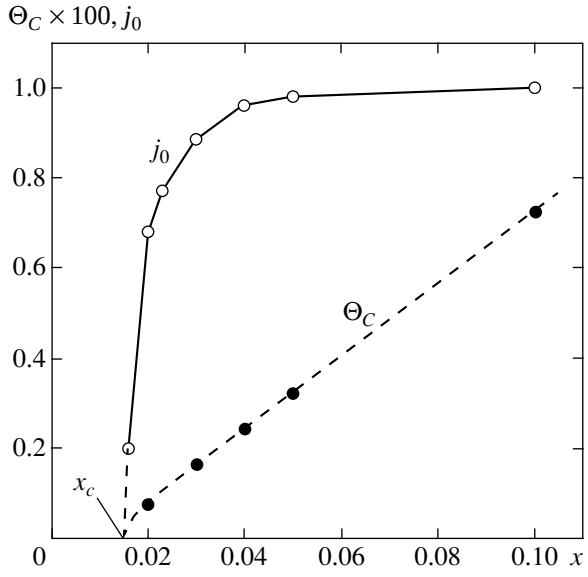

Fig. 7. Concentration dependences of low-temperature magnetization j_0 and Curie temperature Θ_C for a system of magnetic ions located at sites of the fcc lattice of a monovalent metal ($Z_0 = 0.05$, $l = \infty$).

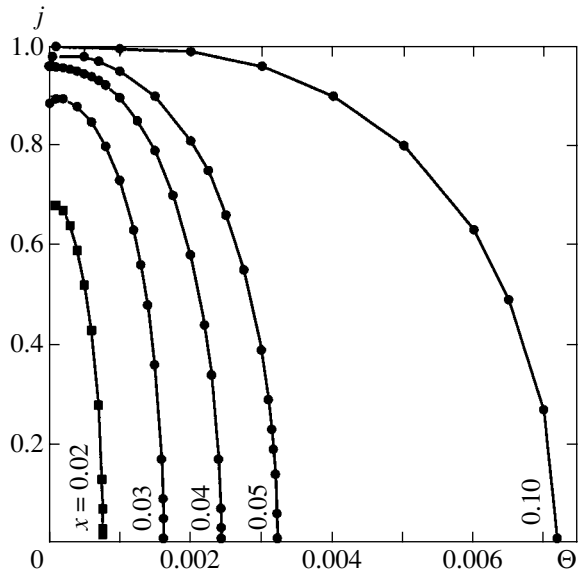

Fig. 8. Temperature dependences of magnetization j of a system of magnetic ions with various concentration $x > x_c$, located at sites of the fcc lattice of a monovalent metal ($Z_0 = 0.05$, $l = \infty$).

($j \ll 1$); expanding the functions appearing in Eq. (13) in H_e and j, we obtain

$$j = \frac{(H_e/h_J)I_0}{1-(Z_0x + H_j/h_J)I_0},$$
$$I_0(x,\Theta) = \frac{1}{\Theta\sqrt{2\pi}}\int_{-\infty}^{\infty}\frac{\exp(-u^2/2)}{\cosh^2[(\sigma/h_J\Theta)u]}du. \quad (18)$$

Relation (18) makes it possible to determine the low-field magnetic susceptibility of the system,

$$\chi = \frac{I}{H_e} = \frac{jZ_0x}{H_e/h_J},$$

and its temperature dependence (see Fig. 6) as well as the Curie temperature and its concentration dependence (see Fig. 7).

At low temperatures ($\Theta \ll \sigma/h_J$), we have $I_0 = \sqrt{2/\pi}\,h_J/\sigma$, which gives $\chi_0 \equiv \chi(\Theta \ll 1) = x/(x_c - x)$, i.e., a temperature-independent susceptibility. In the vicinity of the ferromagnetic transition (with the boundary determined by condition (16)), the susceptibility increases indefinitely.

At high temperatures ($\Theta \ll \sigma/h_J$), we have $I_0 \longrightarrow 1/\Theta$ and relation (18) leads to $\chi(\Theta \gg 1) = 1/\Theta$, or $I = x\mu N(\mu H_e/kT)$, i.e., the ordinary Curie law for noninteracting Ising dipoles with magnetic moment μ.

Vanishing of the denominator in expression (18) corresponds to a transition to the ferromagnetic state. The corresponding condition

$$I_0(Z_0x + H_j/h_J) = 1 \quad (19)$$

for $T = 0$ coincides with Eq. (16) determining the critical concentration x_c of magnetic impurities; for $x > x_c$, this condition makes it possible to determine the Curie temperature Θ_C. Figure 7 shows the dependence of $\Theta_C(x > x_c)$ on the impurity concentration. The characteristic value of $\Theta_C \approx 5 \times 10^{-3}$ corresponds (for $W \sim 0.01$ eV) to the actual temperature $T_C \approx 0.5$ K.

The temperature dependence of the system magnetization at temperatures $\Theta \le \Theta_C$ is defined by Eq. (13). Figure 8 shows a series of similar dependences for various impurity concentration $x > x_c$.

In the framework of the generalized mean field theory used above, we can determine not only magnetization, but also any other quantity depending on the magnetic field. For example, we can calculate the magnetic component C_m of the heat capacity of the system under investigation; for noninteracting Ising magnetic moments in a uniform magnetic field H, this component is defined as

$$C_m = kNx\left[\frac{\mu H/kT}{\cosh(\mu H/kT)}\right]^2. \quad (20)$$

This relation predicts a linear concentration dependence $C_m \propto x$; the violation of this dependence in an experiment would indicate the uselessness of such a

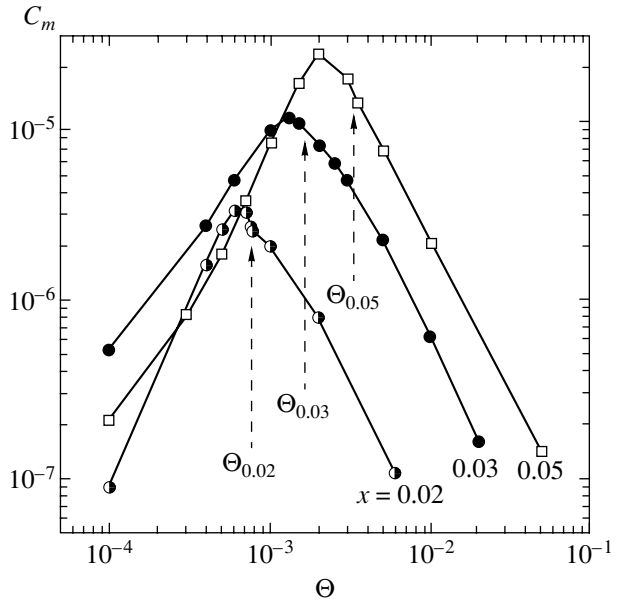

Fig. 9. Temperature dependences of magnetic part of heat capacity $C_m(\Theta, x)$ of a system of magnetic ions with various concentration x, located at sites of the fcc lattice of a monovalent metal ($Z_0 = 0.05$, $l = \infty$). Arrows indicate the corresponding values of the Curie temperature.

simple model and would necessitate the inclusion of the interaction between magnetic moments.

Generalizing this relation to random local fields described by distribution function (9), we obtain, analogously to Eq. (13),

$$C_m(x, \Theta) = kNI_1,$$

$$I_1(x, \Theta) = \frac{x}{\sqrt{2\pi}\sigma/h_J} \times \int_{-\infty}^{\infty} \left\{ \frac{(Z_0 xj + u)/\Theta}{\cosh[(Z_0 xj + u)/\Theta]} \right\}^2 \exp\left[-\frac{(u - jH_j/h_J)^2}{2(\sigma/h_J)^2} \right] du, \quad (21)$$

where $j = j(x, \Theta)$ is the equilibrium magnetization of the system defined above and $\sigma(x)$ and $H_j(x)$ are the parameters of distribution (9).

It follows from Eq. (21) that, as a result of the interaction between magnetic moments, the heat capacity is not proportional to the impurity concentration even in the paramagnetic state ($j = 0$). Indeed, in this case, relation (21) leads to

$$I_1 = x\sqrt{\frac{2}{\pi}}\frac{\Theta}{\sigma/h_J} I_2,$$

where

$$I_2 = \int_0^{\infty} \frac{z^2}{\cosh^2 z} \exp\left[-\frac{\Theta^2 z}{2(\sigma/h_J)^2} \right] dz.$$

At high temperatures, when $\Theta^2/2(\sigma/h_J)^2 \gtrsim 1$, we have $I_2 \approx \sqrt{\pi/2}\,(\sigma/\Theta h_J)^3$ and, hence,

$$C_m(x, \Theta > \Theta_C) \approx kNx\left(\frac{\sigma/h_J}{\Theta}\right)^2. \quad (22)$$

Considering that $\sigma/h_J \propto \sqrt{x}$ (see relation (10)), we obtain $C_m \propto x^2/\Theta^2$. This quadratic concentration dependence of the magnetic component of heat capacity was repeatedly observed for metals with magnetic impurities (see, for example, the results obtained in [15, 16] for the alloys Cu(Co) and Au(Co), respectively. Numerical calculations show, however (see Fig. 2), that the dependence $\sigma(x) \propto \sqrt{x}$ is typical only for comparatively low impurity concentrations $x \lesssim 0.1$ and then becomes "flatter," which must decelerate the increase in heat capacity with increasing concentration. Precisely this tendency was observed in experiment [15]. It should also be noted that, in accordance with relation (22), $C_m \propto 1/T^2$ in the paramagnetic region. Unfortunately, the accuracy of the corresponding measurements is too low to verify the correctness of this dependence.[5]

To determine the concentration and temperature dependences of heat capacity C_m in the low-temperature region, we observe that

$$I_1 = x\sqrt{\frac{2}{\pi}}\frac{\Theta}{\sigma/h_J} I_3,$$

where

$$I_3 = \frac{1}{\Theta^2}\int_{-\infty}^{\infty} \left[\frac{z}{\cosh(z/\Theta)} \right]^2 \times \exp\left[-\frac{(z - jZ_0 x - jH_j/h_J)^2}{2(\sigma/h_J)^2} \right] dz.$$

For $\Theta \lesssim \sigma/h_J$, we have

$$I_3 \approx \frac{\pi^2}{6}\Theta \exp\left[-\frac{j^2(Z_0 x + H_J/h_J)^2}{2(\sigma/h_J)^2} \right],$$

[5] The low accuracy of measurements is due to the fact that the magnetic component of specific heat is small as compared to the total specific heat of the metal (see discussion in [17] and the references therein).

taking into account dependences (10), we obtain

$$I_3 \approx \frac{\pi^2}{6}\Theta \exp\left[-\frac{xj^2(Z_0 + |\phi_S|/\pi)^2}{\phi_P/\pi}\right].$$

For ordinary impurity concentrations $x \ll 1$ and for typical values of Z_0, ϕ_S, and ϕ_P (see table), the exponent in the last exponential is comparable to unity; i.e., the value of I_3 depends on x. Thus, in the low-temperature range, the magnetic component of specific heat is not a monotonic function of the impurity concentration. This explains the ambiguity of the conclusions concerning the presence or absence of such a dependence [17]. The obtained conclusions are illustrated by the temperature dependences $C_m(T, x)$ derived with the help of expressions (21) and depicted in Fig. 9.

4. CONCLUSIONS

A description of disordered systems with RKKY interaction (such as nonmagnetic metals diluted with magnetic impurities) calls for a generalization of the mean field theory with allowance for nonequivalence of individual magnetic moments in such a system. We have considered a version of such a theory, based on the calculation and analysis of the distribution function for random magnetic fields produced by magnetic moments irregularly distributed in space. These distribution functions were obtained by two methods, i.e., analytically and numerically (from statistical processing of the results of calculation of random fields in a model system). The former method makes it possible to find only approximate analytic expressions for distribution functions in a limited range of impurity concentrations; however, this enables one to obtain reliable qualitative estimates of the form of these functions and, hence, about the properties of the system being studied.

In the framework of the generalized mean field theory, it is shown that the ground state of the system becomes magnetically ordered when the magnetic impurity concentration exceeds a certain critical value determined by the type of the crystal lattice of the metal and the sample shape. The magnetic phase diagram of the system is constructed and the temperature dependence of its magnetic susceptibility of the system, the concentration dependence of the Curie temperature, as well as the temperature and concentration dependences of the magnetization and the magnetic component of the heat capacity of the system. All these dependences are in qualitative agreement with the experimental results.

ACKNOWLEDGMENTS

This study was supported by the Russian Foundation for Basic Research (project no. 03-02-17029).

REFERENCES

1. S. V. Vonsovskiĭ, *Magnetism: Magnetic Properties of Dia-, Para-, Ferro-, Antiferro-, and Ferrimagnets* (Nauka, Moscow, 1971; Wiley, New York, 1974), Vols. 1 and 2.
2. H. Ohno, J. Magn. Magn. Mater. **200**, 110 (1999).
3. T. Dietl, A. Haury, and Y. Merle d'Aubigné, Phys. Rev. B **55**, R3347 (1997).
4. E. Z. Meĭlikhov, Pis'ma Zh. Éksp. Teor. Fiz. **77**, 675 (2003) [JETP Lett. **77**, 571 (2003)].
5. E. Z. Meĭlikhov, Zh. Éksp. Teor. Fiz. **124**, 650 (2003) [JETP **97**, 587 (2003)].
6. K. Yosida, Phys. Rev. **106**, 893 (1957).
7. M. W. Klein and R. Brout, Phys. Rev. **132**, 2412 (1963).
8. M. W. Klein, Phys. Rev. **173**, 552 (1968); **188**, 933 (1969).
9. V. I. Belokon' and K. V. Nefedev, Zh. Éksp. Teor. Fiz. **120**, 156 (2001) [JETP **93**, 136 (2001)]; Fiz. Tverd. Tela (St. Petersburg) **44**, 1632 (2002) [Phys. Solid State **44**, 1708 (2002)].
10. A. Pilipovicz and H. Claus, Phys. Rev. B **36**, 773 (1987).
11. G. Griffith, F. A. Volkening, and H. Claus, J. Appl. Phys. **57**, 3392 (1985).
12. J. Crangle and W. R. Scott, Phys. Rev. Lett. **12**, 126 (1964).
13. S. Chandrasekhar, Rev. Mod. Phys. **15**, 1 (1943).
14. S. L. Ginzburg, *Irreversible Processes in Spin Glasses* (Nauka, Moscow, 1989).
15. L. T. Crane and J. E. Zimmerman, Phys. Rev. **123**, 113 (1961).
16. L. T. Crane, Phys. Rev. **125**, 1902 (1962).
17. D. L. Martin, Phys. Rev. B **36**, 2147 (1987).

Translated by N. Wadhwa

Journal of Experimental and Theoretical Physics, Vol. 98, No. 6, 2004, pp. 1174–1182.
Translated from Zhurnal Éksperimental'noĭ i Teoreticheskoĭ Fiziki, Vol. 125, No. 6, 2004, pp. 1340–1348.

SOLIDS
Structure

Impurity Absorption of Light Involving Resonant States of Shallow Donors in Quantum Wells

V. Ya. Aleshkin and L. V. Gavrilenko

Institute of Physics of Microstructures, Russian Academy of Sciences, Nizhni Novgorod, 603950 Russia
e-mail: aleshkin@ipm.sci-nnov.ru

Received November 27, 2003

Abstract—The energy spectrum of localized and resonant states of shallow donors in heterostructures GaAs/$Al_xGa_{1-x}As$ with quantum wells is calculated. The widths of the resonant states belonging to the second size quantization subband are determined. It is shown that the width of a resonance level is mainly determined by the interaction with optical phonons. The spectrum of impurity absorption of light due to electron transitions from the ground state of the donor to the resonant states belonging to the second size quantization subband is calculated. © *2004 MAIK "Nauka/Interperiodica".*

1. INTRODUCTION

The growing interest in resonant states of shallow impurity centers in semiconductors is due to the possibility of employing the resonant states of a shallow impurity for lasing in the long-wave IR range. This possibility was demonstrated for an axially compressed *p*-Ge placed in a strong electric field [1]. Naturally, the possibility of resonant states of other bulk semiconductors and heterostructures being used for obtaining stimulated radiation, and the optimization of parameters of available sources of stimulated radiation, has been explored. However, it is quite difficult to change the parameters of resonant states in bulk semiconductors. The parameters of impurity states may vary over a wide range in semiconductors with quantum wells (QWs). Indeed, owing to the presence of an impurity in a QW or in a neighboring barrier, discrete impurity levels with parameters depending both on the position of the impurity and on the characteristics of QWs appear in addition to the continuous parabolic spectrum of size quantization subbands. The impurity levels "associated" with the second, third, etc., size quantization subbands may fall in the continuous energy spectrum of lower-lying subbands. In this case, the electron lifetime in these states is finite and such states are referred to as quasi-stationary or resonant. The resonant states of shallow donors in QWs have been studied insufficiently. The ionization energies and level widths were calculated by the variation method in [2]. It should be noted that resonant states of donors in barriers were investigated in [3] in the approximation of configuration interaction and zero radius. However, the scattering at phonons, which mainly determines the resonance level width, has not been taken into account. The absorption coefficients for radiation induced by electron transitions to resonant states have not been calculated either. The lack of calculations of the observed properties of such states is probably the reason for the absence of systematic experimental studies.

In this study, we report on the results of theoretical analysis of resonant states of shallow donors in QWs in heterostructures $Al_xGa_{1-x}As$/GaAs. The dependence of the resonance level width and the ionization energy of resonant states on the impurity position in a QW is analyzed. The absorption coefficient is calculated for the radiation induced by electron optical dipole transitions from the donor ground state belonging to the first subband to the donor states and to the continuous spectrum of the second subband. It is shown that the resonance level width and the spectrum of impurity absorption of the radiation stimulated by transitions to resonant states are mainly determined by scattering from optical phonons (unless it is forbidden by the conservation laws).

2. MODEL FOR CALCULATING THE STATES OF A SHALLOW DONOR

To describe electron states, we use the effective mass approximation. The dispersion relation for the electron was assumed to be isotropic and quadratic in the QW plane. The polarization of the heteroboundary associated with charges was discarded in view of the small difference between the permittivities of the materials of the QW and the barrier (in the following analysis, we will consider the GaAs/$Al_{0.2}Ga_{0.8}As$ system). The difference between the effective electron masses in GaAs and $Al_{0.2}Ga_{0.8}As$ was disregarded.

To calculate the energy spectrum of the states of shallow donors in a QW, we used the method of expansion in "plane waves," which was proposed in [4] and developed in [5]. The wave functions of resonant states

and the states in the continuum were expanded into a series in the eigenfunctions of the Hamiltonian $\hat{H}_0$ for an electron in the QW (disregarding the impurity potential),

$$\hat{H}_0 = \hat{\mathbf{p}}^2/2\mu + U(z), \tag{1}$$

where μ is the electron effective mass and potential $U(z)$ defines the QW profile and depends on the aluminum concentration in the solid solution $Al_xGa_{1-x}As$ [6]. Since the dispersion relation for electrons is assumed to be isotropic in the QW plane, the system possesses axial symmetry and the angular momentum projection $L_z = \hbar m$ onto the normal to the QW (z axis) is conserved. The wave function corresponding to quantum number m can be written in the form [5]

$$\Psi^m(\rho, \varphi, z) = \exp(im\varphi)\sum_{n,k}\int_0^{2\pi}\frac{\sqrt{2}a_n^m(k)}{\sqrt{k}\pi^{1/4}S^{3/4}} \times \exp(ik\rho\cos\theta + im\theta)\psi_n(z)d\theta, \tag{2}$$

where S is the area of the QW, ρ and φ are the polar coordinates in the QW plane, k is the modulus of the 2D wave vector in the same QW plane, n is the size quantization subband number, and $\psi_n(z)$ is the normalized wave function describing the motion of the electron along the z axis and satisfying the Schrödinger equation with Hamiltonian (1),

$$\hat{H}_0\psi_n(z)\exp(i\mathbf{k}\cdot\boldsymbol{\rho}) = \left(E_n + \frac{\hbar^2k^2}{2\mu}\right)\psi_n(z)\exp(i\mathbf{k}\cdot\boldsymbol{\rho}), \tag{3}$$

energy E_n corresponding to the bottom of the nth subband. It should be noted that we have omitted the term corresponding to the contribution from the continuous spectrum in expansion (2). This assumption is justified in the case when the binding energy of the donor states being described is much smaller than the QW depth and the states are localized in the QW.

To find the expansion coefficients $a_n^m(k)$, we substitute the wave function in form (2) into the Schrödinger equation with the total Hamiltonian

$$\hat{H} = \hat{H}_0 + F, \quad F = -\frac{e^2}{\kappa\sqrt{\rho^2 + (z - z_{\text{im}})^2}}, \tag{4}$$

where κ is the permittivity of the material, e is the electron charge, and z_{im} is the z coordinate of the donor. The integral equation for the expansion coefficients has the form

$$\left(E_n + \frac{\hbar^2k^2}{2\mu}\right)a_n^m(k) - \sum_{n'}\int_0^\infty dk' a_{n'}^m(k')I_{n,n'}^m(k,k') = \varepsilon a_n^m(k), \tag{5}$$

where ε is the electron energy; the kernel of the integral operator is defined by the relation

$$I_{n,n'}^m(k,k') = \frac{q^2}{2\pi\kappa}\int_0^{2\pi}d\theta\frac{\sqrt{kk'}\cos m\theta}{\sqrt{k^2 + k'^2 - 2kk'\cos\theta}} \times\int_{-\infty}^{\infty}dz\exp\left\{-|z - z_{\text{im}}|\sqrt{k^2 + k'^2 - 2kk'\cos\theta}\right\}\psi_n^*(z)\psi_{n'}(z).$$

Integral equation (5) can be solved by the finite difference method, in which the integral with respect to k' is replaced by the sum. Each term of this sum corresponds to the integral with respect to k' in a certain interval. If this interval is smaller than the characteristic scale of variation of the integrand, the integral over each interval can be replaced by the product of the length of the interval and the value of the integrand in this interval. We will use an equidistant partition in k' with a step of Δk.

If we choose the step in k' much smaller than the reciprocal Bohr radius ($\Delta k \ll 1/r_B$), the integrand in Eq. (5) varies insignificantly over a step. In addition, functions $a_n^m(k)$ in expansion (2) for localized and resonant states decrease quite rapidly for large values of k' (such that $1/k'_{\max} \ll r_B$); consequently, the sum over k' can be truncated. For the chosen partition in k', Eq. (5) can be written in the form

$$\sum_{n',j}a_{n'}^m(k_j)\left(\left(E_{n'} + \frac{\hbar^2k^2}{2\mu}\right)\delta_{n',n}\delta_{i,j} - \Delta kI_{n,n'}^m(k_i,k_j)\right) = \varepsilon a_n^m(k_i). \tag{6}$$

This equation shows that the problem is reduced to determining the eigenvalues of quantity ε and eigenvectors $a_n^m(k)$ of the symmetric real-valued matrix

$$A_{n,i;n',j}^m = \left(\varepsilon_n + \frac{\hbar^2k_i^2}{2\mu}\right)\delta_{n',n}\delta_{i,j} - \Delta kI_{n,n'}^m(k_i,k_j). \tag{7}$$

The eigenvalues and eigenvectors of matrix A^m define the energy spectrum and the wave functions for local-

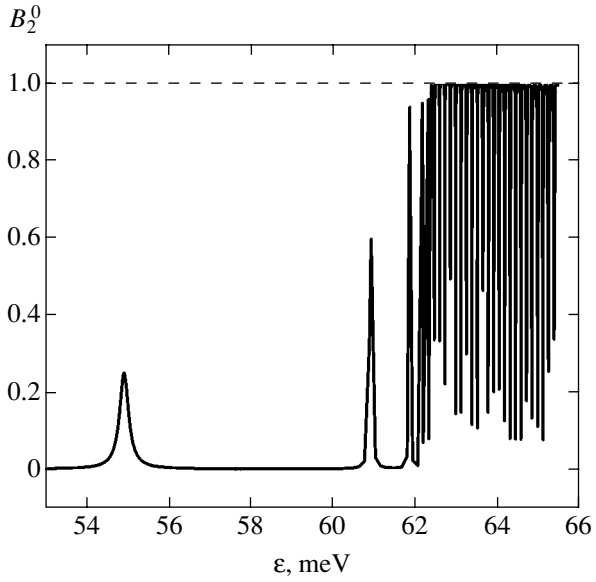

Fig. 1. Electron energy dependence of the probability of finding an electron in the second subband ($m = 0$). The peaks in the range of energies smaller than 62.5 meV correspond to donor resonant states of the electron. For energies $\varepsilon > 62.5$ meV, the continuous spectrum of the second size quantization subband begins.

ized and delocalized states. The expansion coefficients of the wave function satisfy the normalization relation

$$\sum_{n,\,j} \left|a_n^m(k_i)\right|^2 = 1.$$

It should be noted that kernel $I^m_{n,\,n'}(k, k')$ has a singularity for $k = k'$. A method for overcoming this difficulty was proposed in [4]. In this method, while replacing an integral by a sum, allowance should be made for the finiteness of the integral in any interval in spite of the tendency of the integrand to infinity. For this reason, we must take the value of $I^m_{n,\,n'}(k, k')$ averaged over Δk in such a replacement. In this case, matrix A^m can be written in the form

$$A^m_{n,\,i;\,n',\,i} = \delta_{n,\,n'}\left\{\varepsilon_n(k_i) - \frac{q^2\Delta k}{\pi\kappa}\sqrt{\pi}\right\}$$

$$-\frac{q^2\Delta k}{\pi\kappa}\int\limits_{\Delta k/2k_i}^{\pi} d\theta\,\frac{\cos m\theta}{\sqrt{2(1-\cos\theta)}}\int\limits_{-\infty}^{\infty} dz \qquad (8)$$

$$\times\exp\left\{-|z-z_i|\,k_i\,\sqrt{2(1-\cos\theta)}\right\}\psi^*_{n'}(z)\psi_n(z),$$

and matrix elements $A^m_{n,\,i;\,n',\,i}$ are finite.

3. RESULTS OF CALCULATION OF THE ELECTRON SPECTRUM AND THE LIFETIME OF RESONANT STATES

The parameters of resonant states were calculated for the $Al_{0.2}Ga_{0.8}As/GaAs$ heterostructure with a QW of width $d_{QW} = 150$ Å. The QW contains three energy levels (size quantization subbands) with energies of $E_1 = 15.8$ meV, $E_2 = 62.5$ meV, and $E_3 = 136.8$ meV, measured from the bottom of the conduction band of GaAs. To find the resonance levels of a shallow donor, we diagonalized the 3000×3000 matrix (three subbands, 1000 points in k) with $\Delta k = 4 \times 10^{-5}$ Å$^{-1} = 4 \times 10^3$ cm^{-1}; in the course of the diagonalization, the eigenvectors and eigenvalues were determined. The results given below will be qualitatively valid for QWs of width below 200 Å. For broader QWs, the interaction of electrons with optical phonons does not affect the width of resonance levels.

The resonant states belonging to the nth subband can be easily found from analysis of the electron energy dependence of the probability of finding an electron in the given subband (for a given m):

$$B^m_n(\varepsilon) = \sum_i \left|a^m_n(k_i)\right|^2/k_i. \qquad (9)$$

Figure 1 shows the $B^0_2(\varepsilon)$ dependence corresponding to the position $z_{im} = 0.3d_{QW}$ of the donor ($z_{im} = d_{QW}$ and $z_{im} = 0$ correspond to the QW boundaries). Four peaks with energies lower than $E_2 = 62.5$ meV can be clearly seen on this dependence. The peaks correspond to resonant states belonging to the second size quantization subband. For energies higher than E_2, we can see the states of continuous spectrum of the first and second subbands, which are mixed by the Coulomb potential of the impurity. The fraction of the third subband in the wave functions of these resonant states is on the order of 10^{-5}. Consequently, the share of states from the continuous spectrum must also be small. It should be noted that the model used for calculations is not suitable for describing strongly excited resonant and localized states with a characteristic size of the orbit exceeding $1/\Delta k$. To improve the accuracy of calculations, the number of resonant states being calculated should be increased. The values of k_i used in the calculations make it possible to resolve four resonant states. It will be shown below, however, that the resonance width amounts to about 2 meV due to the interaction with optical phonons. For this reason, all resonant states except the first are poorly resolved since the binding energy for these states is smaller than their width. The $B^m_2(\varepsilon)$ dependence in the vicinity of the peak is Lorentzian [7],

$$B^{(m)}_2(\varepsilon) = \frac{A}{(\varepsilon - \varepsilon^m_{2,\,s})^2 + (\Gamma^m_{2,\,s})^2/4}, \qquad (10)$$

where $\varepsilon^m_{2,s}$ is the energy of the sth resonance level of the second subband, $\Gamma^m_{2,s}$ is its width determined by the interaction of the states of the subbands in the presence of the donor ("Coulomb" width), and A is the normalization constant depending on the number of points in k. The values of $\Gamma^m_{2,s}$ can be found from the dependence $B^m_2(\varepsilon)$ in the vicinity of the peak by determining, for example, the values of A, $\varepsilon^m_{2,s}$, and $\Gamma^m_{2,s}$ from three points. To determine the values of $\varepsilon^m_{2,s}$ and $\Gamma^m_{2,s}$, we can also use the method described by Fano [7]. For this purpose, we must solve the Schrödinger equation disregarding the intersubband elements of the Coulomb interaction (setting $A^m_{n,i;n',i} = 0$ for $n \neq n'$) and then make use of the expressions [7]

$$\varepsilon^m_{2,s} = E^m_{2,s} + P\int dE \frac{\left|F^m_{2,s;1}(E)\right|^2}{E^m_{2,s} - E'} G_1(E), \qquad (11)$$

$$\Gamma^m_{2,s} = 2\pi \int dE \left|F^m_{2,s;1}(E)\right|^2 \delta(E - E^m_{2,s}) G_1(E), \qquad (12)$$

where $E^m_{2,s}$ is the energy of the sth localized state of the second subband from which a resonant state originates; $F^m_{2,s;1}(E)$ is the interband matrix element of operator F, calculated for the sth localized state of the second subband and the delocalized state of the first subband, corresponding to energy E; and $G_1(E)$ is the 1D density of states of the first subband with the z component of the angular momentum equal to $\hbar m$. Symbol $P\int$ indicates the principal value of the integral. It should be borne in mind that the uniform partition in k is almost equivalent to zero boundary conditions for $\rho = R = \pi/\Delta k$. The equivalence would be complete if the roots of the Bessel function $J_m(kR)$ were taken as points in k. However, the roots with larger numbers are spaced almost equidistantly; if the characteristic Bohr radius is smaller than Δk^{-1}, the error associated with a uniform partition in k is small. In this case, the following expression holds for the 1D density of states:

$$G_1(E) = \sqrt{2\mu}/\hbar\Delta k\sqrt{E - E_1}.$$

Energy $E^m_{2,s}$ can be determined from the solution of the Schrödinger equation disregarding the intersubband elements of the Coulomb interaction. While deriving expressions (11) and (12) from the results obtained in [7], we assumed that the matrix element $F^m_{2,s;1}(E)$ varied insignificantly on the scale of energies $\Gamma^m_{2,s}$. It should be noted that equality (11) corresponds to the formula for determining the energy in the second order of perturbation in F, while expression (12) corresponds to the golden rule of quantum mechanics for determining the probability of a transition induced by perturbation F.

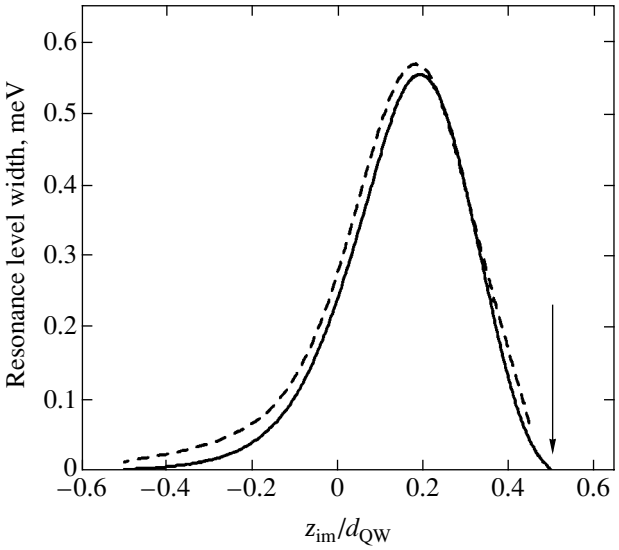

Fig. 2. Comparison of the widths of the lower resonance level, calculated by using perturbation theory (solid curve) and by approximating the probability density peak by the Lorentzian function (dashed curve). The relative position z_{im}/d_{QW} of the impurity (d_{QW} is the QW width) is laid along the abscissa axis.

Figure 2 shows the Coulomb width of the lower resonant donor state ($m = 0$) belonging to the second subband calculated by the two methods described above vs. the relative position of the impurity. It can be seen that the results obtained for a level width exceeding 0.1 meV almost coincide. For smaller values of this quantity, the first method is characterized by a considerable error for the given value of Δk since the level width becomes comparable to the separation between the energy levels obtained in calculations for the states of the continuous spectrum. For example, for an impurity located at the center of the QW, the resonance level width tends to zero and the steady-state method of expansion in plane waves yield incorrect results (this point is marked by the arrow in Fig. 2). For this reason, the widths of excited donor resonance levels were calculated using the second method.

The dependences of the ionization energy and the Coulomb width of resonance levels on the position z_{im} of the impurity are shown in Fig. 3. Negative values of z_{im}/d_{QW} correspond to the donor position in the barrier. It can be seen from the figure that the ionization energies of resonant states associated with the second subband have a local minimum for $z_{im} = 0.5d_{QW}$. This is due to the fact that the wave function of the second subband vanishes at the center of the QW. For this reason, an electron located in the second subband weakly "per-

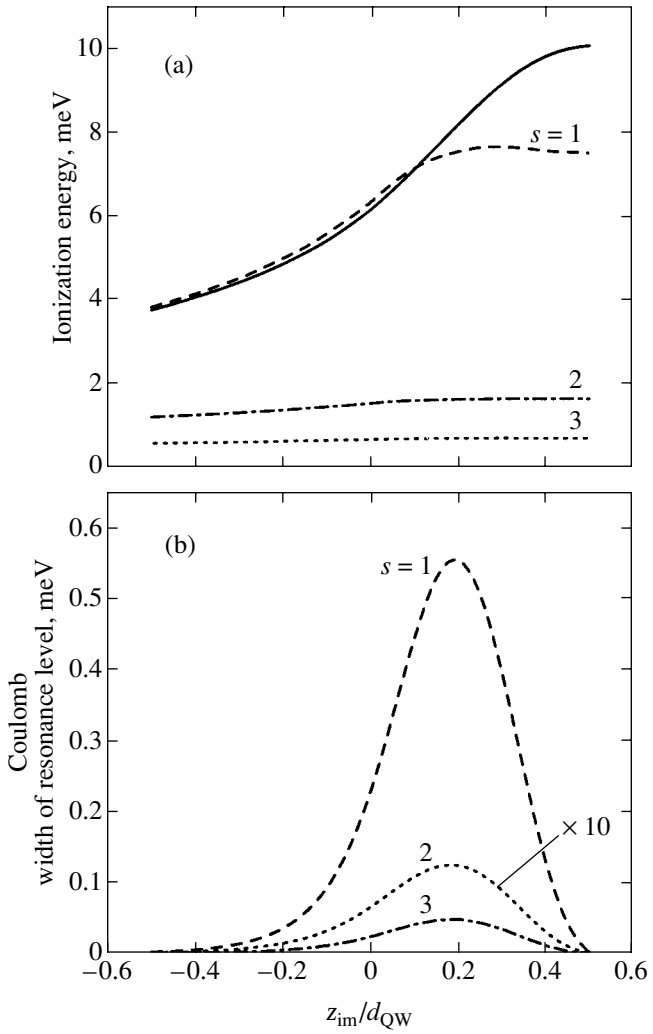

Fig. 3. (a) Dependence of the ionization energy on the position of the impurity in the QW. The donor ground state (solid curve) and the resonant states belonging to the second subband: the first state (dashed curve), the second state (dot-and-dash curve), and the third state (dotted curve). (b) the Coulomb width of resonance levels as a function of the position of the impurity in the QW. For better visualization, the width of the third resonance level is increased tenfold.

ceives" the attractive potential of the impurity located at the center of the QW.

The Coulomb width of the resonance level belonging to the second subband vanishes when the impurity is at the center of the QW; i.e., the states become localized. The impurity located at the center of the QW does not break the symmetry of the potential; this means that parity is preserved and transitions between the first and second subbands are ruled out. For small displacements of the donor from the center of the QW, the resonance level width is a quadratic function of the displacement since matrix elements $A^m_{n,i;n',i}$, which are off-diagonal in the subbands, are linear functions of the displacement. It should be noted that the Coulomb width of the lower resonance level calculated for the same structure using the variational method [2] is approximately 20% larger than the value obtained here.

To verify the accuracy of calculations, we calculated the parameters of resonance levels for $z_{im} = 0.3d_{QW}$ using 1500 points in each band with $\Delta k = 2.7 \times 10^{-5}$ Å$^{-1} = 2.7 \times 10^3$ cm^{-1}. The results differ from those obtained with 1000 points in each subband by less than 2–3% for the ionization energies and by less than 10% for the resonance level widths.

4. SCATTERING FROM POLAR OPTICAL PHONONS

The total resonance level width is determined not only by the departure of an electron from the resonant state due to the interaction of subbands via the Coulomb potential of the impurity. Another important mechanism of resonance level broadening for donors is the interaction with phonons. We are interested in the case of low temperatures, when scattering is mainly determined by the spontaneous emission of phonons. For not very broad quantum wells in which the energy gap between the lower resonance level belonging to the second subband and the bottom of the first subband exceeds the energy of the optical phonon, emission of optical phonons is the main scattering mechanism. The interaction between electrons and acoustic phonons is much weaker. For this reason, we will consider the scattering only from optical phonons. Like the Coulomb interaction between the states of the subbands, scattering causes resonance level broadening.

It is well known that the scattering of electrons by deformation-induced optical phonons in the Γ valley in GaAs cannot take place in view of the high symmetry of this valley [8]; for this reason, we take into account only the interaction of electrons with polar optical (PO) phonons. We assume that optical phonons correspond to bulk GaAs. As a result of the emission of a PO phonon, the electron in a resonant state may pass to the continuous spectrum of the first subband. It will be proved later that the resonance level width determined by the interaction with PO phonons considerably exceeds the Coulomb width.

The matrix element of the operator of spontaneous emission of a polar phonon in our description is a function of quantum numbers m_i and m_f characterizing the wave functions of the initial and final states, respectively,

$$V_{m_i m_f}(q) = \left(\frac{2\pi e^2}{\bar{\kappa} V}\hbar\omega_{LO}\right)^{1/2} \times \int (\Psi^{m_i}(\mathbf{r}))^* \frac{\exp(i\mathbf{q}\cdot\mathbf{r})}{q}\Psi^{m_f}(\mathbf{r})d^3r, \quad (13)$$

where V is the crystal volume, $\hbar\omega_{LO}$ is the energy of a longitudinal optical phonon, q is the wave vector of the

phonon, and $1/\bar{\kappa}$ is the difference between reciprocal permittivities of the material at low and high frequencies,

$$\frac{1}{\bar{\kappa}} = \frac{1}{\kappa_0} - \frac{1}{\kappa_\infty}. \tag{14}$$

For the wave functions of the initial and final states, we can use the wave functions calculated disregarding the possibility of the electron departure from the resonant state due to the Coulomb interaction. Since the processes of scattering from PO phonons are taken into account in perturbation theory, the total frequency of transitions (taking into account scattering and resonance transitions) is equal (in the linear approximation) to the sum of the corresponding frequencies.

Taking into account the above simplifying assumptions and integrating with respect to angle φ in the r space, we can write expression (13) in the form

$$V_{m_i, m_f}(q) = \left(\frac{2\pi e^2}{\bar{\kappa} V}\hbar\omega_{LO}\right)^{1/2} 2\pi (i)^{m_i - m_f}$$
$$\times \int \phi_2^{m_i}(\rho)\frac{J_{m_f - m_i}(q_\perp \rho)}{\sqrt{q_\perp^2 + q_z^2}}\phi_1^{m_f}(\rho)\rho d\rho \tag{15}$$
$$\times \int \psi_1(z)\exp(iq_z z)\psi_2(z)dz,$$

where $\phi_n^m(\rho)$ is the radial part of the wave function (the subscript specifies the subband number and the superscript is the quantum number m) and $q_\perp$ and q_z are the components of the phonon wave vector perpendicular and parallel to the z axis.

It should be noted that the z component of the phonon angular momentum is equal to the difference between the electron angular momentum components of the final and the initial state since the total angular momentum component of the entire electron–phonon system along the z axis is conserved in the course of scattering. The electron angular momentum component ($L_z = \hbar m$) may change during such scattering. Consequently, calculating the probability of the electron departure from state i accompanied by the emission of a phonon, we must carry out summation over all quantum number of final states (including m_f) and over q. In the subsequent calculations, we assume that the quantum number m_i of the initial state is equal to zero and omit the corresponding index. This particular case is interesting in connection with possible application of the obtained results for calculating the spectrum of the absorption coefficient.

The frequency of transitions from the sth resonant state under the second subband to the continuous spectrum of the first subband is described by the formula

$$\nu_{sc}^s = \frac{2\pi}{\hbar}G_1(\varepsilon_{res}^{2,s} - \hbar\omega_{LO})$$
$$\times \sum_{m_f}\frac{V}{(2\pi)^3}\int \left|V_{m_f}^s(q)\right|^2 d^3q. \tag{16}$$

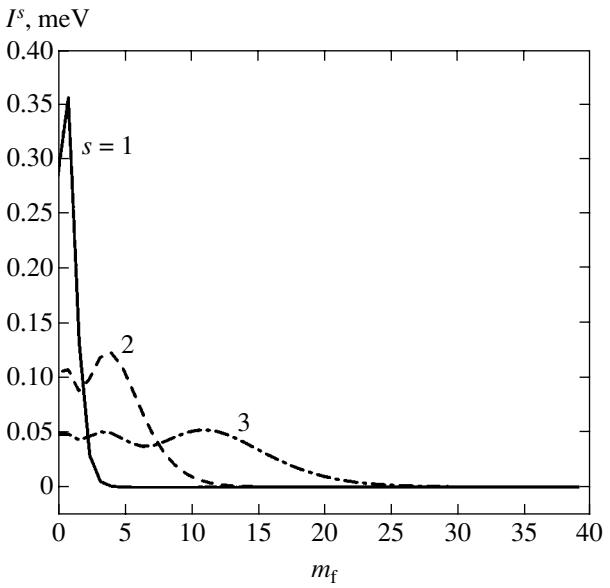

Fig. 4. Dependence $I^s(m_f)$ for $z_{im} = 0.35d_{QW}$. Physical meaning can be attached only to integral values of the angular momentum projection m_f. The resonant states belonging to the second subband: the first state (solid curve), the second state (dashed curve), and the third state (dot-and-dash curve).

It is convenient to evaluate the integral of the squared matrix element over d^3q numerically. For the "phonon" level width, we obtain the expression

$$\hbar\nu_{sc}^s = \sum_{m_f = -\infty}^{\infty} I^s(m_f), \tag{17}$$

where

$$I^s(m_f) = G_1(\varepsilon_{res}^{2,s} - \hbar\omega_{LO})\frac{V}{(2\pi)^2}\int \left|V_{m_f}^s(q)\right|^2 d^3q.$$

In addition, $I^s(m_f) = I^s(-m_f)$, which allows us to write

$$\hbar\nu_{sc}^s = I^s(0) + 2\sum_{m_f = 1}^{\infty} I^s(m_f). \tag{18}$$

Figure 4 shows the dependences of integral $I^s(m_f)$ on m_f for various values of s for $z_{im} = 0.35d_{QW}$.

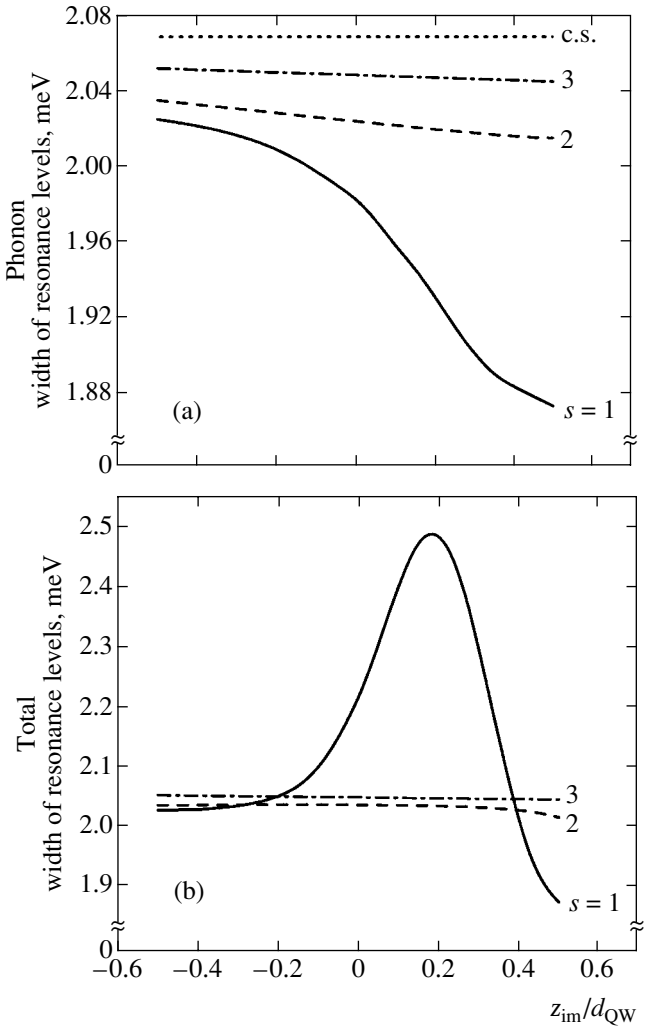

Fig. 5. (a) Dependence of the "phonon" width of resonance levels on the position of the impurity in the QW. Notation: s = 1, 2, and 3 are respectively the widths of the first (belonging to the second subband), second, and third resonance levels; c.s. stands for the broadening of the states of the continuous spectrum at the bottom of the second subband. (b) Total width of resonance levels as a function of the position of the impurity in the QW.

It can be seen from Fig. 4 that, first, function $I^s(m_f)$ for $s = 1$ decreases the most rapidly; second, the number of peaks of this function corresponds to number s. The energy of ionization of the sth resonant state decreases with increasing s ($E_{ion} \propto 1/s^2$ for the hydrogen atom), while the localization radius increases. With increasing localization radius of the wave function, the dependence of I^s on m_f becomes smoother. It is hence clear that the $I^s(m_f)$ dependence also becomes weaker as the impurity is displaced from the center of the QW since the localization radius increases in this case. As the impurity passes to the barrier, the total scattering probability tends to the value corresponding to a free electron; this is illustrated in Fig. 5, which shows the dependences of the phonon and total widths of resonance levels on the position of the donor. It should be noted that the $I^s(m_f)$ dependence for free electrons in a size quantization subband is absent altogether for all possible values of m_f.

A comparison of Figs. 3b and 5a shows that the main contribution to resonance line broadening comes from the scattering by PO phonons.

Estimates of resonance level broadening associated with the interaction with acoustic phonons give values of 0.002 meV for scattering by the deformation acoustic potential and 0.0004 meV for scattering by the piezoelectric acoustic potential. These values are much smaller than the "Coulomb" width of the resonance level and will be disregarded in subsequent analysis.

5. DIPOLE TRANSITIONS OF ELECTRONS

Since resonant states are often observed in experiments by measuring the impurity absorption spectra, it would be interesting to calculate the absorption coefficient for dipole optical transitions of electrons from the donor ground state to the second subband (including resonant states). Uniform and nonuniform broadening of the transition line play an important role in absorption spectra. If the initial state of the electron coincides with the ground state of the donor, while its final state after the absorption of a photon is a resonant state, uniform broadening is determined by the total width of the resonance level. Nonuniform broadening is determined by the coordinate distribution of the impurity. For the given structure, the uniform broadening of the absorption line amounts to about 1 meV (half the resonance level width). It can be seen from Fig. 3 that, to ensure such a linewidth due to nonuniform broadening in the case when the average coordinate of the impurity corresponds to the QW center, the variance in the position of the impurity must be approximately 30 Å. We will assume that the variance in the position of the impurity is smaller than this value, which allows us to disregard nonuniform broadening.

The wave function of the impurity state is formed to a considerable extent by states from the subband that is the closest on the energy scale. Consequently, the selection rules for the dipole transitions of electrons between the ground donor state and the resonant states are almost the same as for transitions from the first subband to the subband forming the given resonant states. Thus, the probability of electron transitions to the resonant states belonging to the second subband assumes the highest values for transitions induced by radiation polarized along the z axis. However, transitions induced by radiation polarized in the QW (xy) plane are not completely forbidden since the wave functions of the resonant states contain small contributions from far subbands as well. In addition, x- and y-polarized radiation induces transitions between states belonging to the same subband. At the same time, intrasubband transitions under the action of z-polarized radiation are for-

bidden for an electron with a parabolic isotropic dispersion relation. We will henceforth consider only the transitions induced by the *z*-polarized radiation since the probability of such transitions is many times higher than the probability of transitions with the *x* and *y* polarization.

An electric field directed along the *z* axis does not break the axial symmetry; consequently, the angular momentum component along the *z* axis is conserved in dipole optical transitions. The probability of such transitions between the ground donor state and the states of the second subband is described by the formula

$$W(\hbar\omega) = \frac{2\pi}{\hbar} q^2 E^2 |z_{if}|^2 G_1(\hbar\omega - \varepsilon_{gs}), \qquad (19)$$

where z_{if} is the matrix element of operator *z* between the initial and final states, *E* is the electric field amplitude, $\hbar\omega$ is the photon energy, and ε_{gs} is the energy of the donor ground state. The dimensionless absorption coefficient is proportional to the probability of dipole transitions,

$$\beta(\hbar\omega) = \frac{2\pi W(\hbar\omega)\hbar\omega N}{cE^2 n}, \qquad (20)$$

where *c* is the velocity of light; *N* is the planar impurity concentration; which is assumed to be equal to 3×10^{10} cm^{-2} (even D^- centers are observed [9] in the QW for such an impurity concentration); and *n* is the refractive index. The ordinary dimensional absorption coefficient for radiation propagating along the QW can be derived from relation (20) by dividing it by the QW thickness.

Figure 6 shows for comparison the spectra of the dimensionless absorption coefficient $\beta(\hbar\omega)$ for dipole optical transitions of electrons taking into account and disregarding scattering (for the impurity position $z_{im} = 0.35d_{QW}$).

It can be seen that scattering considerably reduces the amplitude of the main peak corresponding to the electron transition from the ground state belonging to the first subband to the lowest resonant state belonging to the second subband. Since the density of states determining the peak of the Lorentz line is $G_{max} = 2/\pi\Gamma$, the absorption peak amplitude is inversely proportional to the width of the level to which the transition takes place. Auxiliary peaks and the plateaus of the continuous spectrum are hardly distinguishable on the "tail" of the main peak.

It should be noted that the shape of the absorption line for the electron transition from the donor ground state to the lower resonant state, which is induced by a field with the *z* polarization, is Lorentzian. This is a consequence of the fact that the matrix element of the *z* operator for transitions from the donor ground state to the states of the first subband is equal to zero. Otherwise, the absorption spectrum would have zero value in the vicinity of the resonance [7].

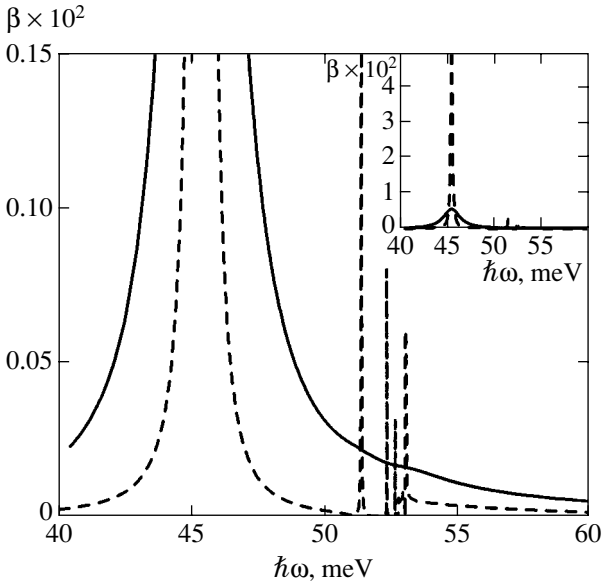

Fig. 6. Absorption coefficient spectrum (solid curve is plotted taking into account scattering by PO phonons and the dashed curve, disregarding scattering). The inset shows the ratio of the amplitudes of the main peaks.

It can be seen from Fig. 6 that the absorption amounts to about half a percent. This means that such an effect can easily be observed for a structure containing 5–10 such QWs by using the experimental geometry of total internal reflection, which is conventionally used for observing the intersubband absorption [10].

6. CONCLUSIONS

Summarizing the results of calculations, we can formulate the following conclusions. The electron transition from the donor ground state to the lower resonant state belonging to the second subband determines the impurity absorption of light with the photon energy corresponding to intersubband transitions under the conditions of freezing out of electrons in $GaAs/Al_xGa_{1-x}As$ heterostructures. The absorption line corresponding to this transition has a Lorentzian shape. The absorption linewidth is mainly determined by the interaction of electrons with optical phonons. The value of the dimensionless absorption coefficient at the peak for a planar donor concentration of 3×10^{10} cm^{-2} amounts to about 0.5%.

ACKNOWLEDGMENTS

The authors are grateful to A.M. Satanin for fruitful discussions.

This study was financed by the Russian Foundation for Basic Research (grant nos. 01-02-16106 and

04-02-17178), the International Center of Science and Technology (grant no. 2293), the program Russian Universities (grant no. UR.01.01.057), and the Ministry of Industry, Science and Technology of the Russian Federation (contract nos. 40.072.1.1.1173 and 40.031.1.1.1187).

REFERENCES

1. I. V. Altukhov, M. S. Kagan, K. A. Korolev, *et al.*, Zh. Éksp. Teor. Fiz. **115**, 89 (1999) [JETP **88**, 51 (1999)].
2. S. T. Yen, Phys. Rev. B **66**, 075340 (2002).
3. A. Blom, M. A. Odnoblyudov, I. N. Yassievich, *et al.*, Phys. Rev. B **65**, 155302 (2002).
4. J. P. Loehr and J. Singh, Phys. Rev. B **41**, 3695 (1990).
5. V. Ya. Aleshkin, B. A. Andreev, V. I. Gavrilenko, *et al.*, Fiz. Tekh. Poluprovodn. (St. Petersburg) **34**, 582 (2000) [Semiconductors **34**, 563 (2000)].
6. E. H. Li, Physica E (Amsterdam) **5**, 215 (2000).
7. U. Fano, Phys. Rev. **124**, 1866 (1961).
8. V. F. Gantmakher and I. B. Levinson, *Scattering of Carriers in Metals and Semiconductors* (Nauka, Moscow, 1984).
9. S. R. Ryu, Z. X. Jiang, W. J. Li, *et al.*, Phys. Rev. B **54**, R11086 (1996).
10. B. F. Levine, J. Appl. Phys. **74**, R1 (1993).

Translated by N. Wadhwa

Journal of Experimental and Theoretical Physics, Vol. 98, No. 6, 2004, pp. 1183–1197.
Translated from Zhurnal Éksperimental'noĭ i Teoreticheskoĭ Fiziki, Vol. 125, No. 6, 2004, pp. 1349–1366.

SOLIDS
Structure

Lower and Upper Bounds on the Critical Temperature for Anisotropic Three-Dimensional Ising Model

M. A. Yurishchev

Institute of Problems of Chemical Physics, Russian Academy of Sciences, Chernogolovka, Moscow oblast, 142432 Russia

e-mail: yur@icp.ac.ru

Received December 4, 2003

Abstract—The Ising model is considered on a simple cubic lattice, with a coupling constant J along one axis and coupling constants J' along the remaining two axes. The transfer-matrix technique and an extended phenomenological renormalization group theory [18, 19] are applied to obtain two-sided bounds on the critical temperature for the model with $J'/J \le 1$. The bounds monotonically converge with decreasing J'/J and provide improved estimates for the phase-transition temperature in anisotropic three-dimensional Ising model, as compared with those available from the literature. © *2004 MAIK "Nauka/Interperiodica".*

1. INTRODUCTION

Unlike the two-dimensional Ising model, the three-dimensional one is not solved exactly. Current studies of the model rely on various approximate methods. Permanent interest in the model is dictated by the fact that it admits a phase transition whose universal properties can be used to describe critical behavior of a broad class of materials, including easy-axis magnets, binary alloys, simple liquids and their mixtures, polymer solutions, subnuclear matter, etc. [1–3].

An analysis of a phase transition begins with the definition of the corresponding critical point. To date, the most reliable estimates for the phase-transition temperature T_c in the isotropic three-dimensional Ising model were obtained by using high-temperature series [4] and Monte Carlo RG methods [5]. The best estimates rely on finite-size scaling of Monte Carlo simulations on $L \times L \times L$ cubes [6, 7]:

$$K_c = 0.22165459(10),$$

i.e.,

$$k_B T_c/J = 1/K_c = 4.5115240(21).$$

Thus, numerical studies have provided, at least, the first five or six digits in the critical temperature for the simple cubic Ising lattice:

$$k_B T_c/J = 4.51152\ldots. \quad (1)$$

Note that rigorous bounds have been found for the critical temperature in the isotropic model [8], but they are too rough as compared to numerical result (1).

In the case of an anisotropic Ising model, an asymptotically exact formula was found for the phase-transition temperature [9]:

$$\frac{k_B T_c}{J} = 2\left[\ln\left(\frac{J}{2J'}\right) - \ln\ln\left(\frac{J}{2J'}\right) + O(1)\right]^{-1}, \quad J'/J \longrightarrow 0. \quad (2)$$

This expression predicts logarithmic decrease in the critical temperature with increasing lattice anisotropy. However, the accuracy of (2) is relatively low in the interval of highest importance for applications, $10^{-3} \le J'/J \le 1$ (see Section 6).

Numerical estimates for $k_B T_c/J$ in an anisotropic Ising model were also obtained by using high-temperature series [10]. However, since series of this kind contain a finite number of terms, the estimation error increases with decreasing J'/J and degrades even the results obtained for $J'/J \le 10^{-2}$.

Similar difficulties arise in every approach based on the use of strictly finite subsystems. In particular, Monte Carlo simulations on $L \times L \times pL$ parallelepipeds reported in [11] were not sufficient to calculate $k_B T_c/J$ for $J'/J < 3 \times 10^{-3}$. Moreover, substantial errors were obtained starting from $J'/J < 10^{-1}$. This is explained primarily by insufficiently large relative lengths of the parallelepipeds ($p \le 6$).

On the other hand, the accuracy of results obtained by methods based on the use of subsystems that are infinite along the axis corresponding to the dominant interaction increases with lattice anisotropy. In particular, even the simplest approximation of the original lattice by a set of linear chains embedded in a molecular field [12] leads to asymptotically correct expression (2)

for the critical temperature. (In this approximation, the dominant interaction represented by J is treated exactly, whereas the weak bonding between chains responsible for J' is described by a mean-field theory.) The success is obviously explained by the fact that chain clusters reflect the physics of an anisotropic system.

The accuracy of estimates for the critical temperature improves when a method that is more reliable than molecular field theory is applied or the transverse dimensions of an infinitely long system subsystem are increased in a systematic manner [13–17]. A detailed discussion of these results is presented below.

In this paper, the phase-transition temperature in an anisotropic Ising model is calculated by applying recently improved versions of the phenomenological renormalization group theory proposed in recent publications [18, 19]. The variety of available versions makes it possible to select those yielding both upper and lower bounds. These methods were applied to $L \times L \times \infty$ chain clusters with transverse dimensions $L \leq 4$. Group-theoretic reduction is performed to determine the eigenvalues and eigenvectors of full transfer matrices with dimensions up to 65536×65536, which can be done by virtue of symmetry of the subsystems.

The paper is organized as follows. The equations of an extended phenomenological renormalization group theory are presented in Section 2. Section 3 presents formulas that can be used directly to compute the susceptibilities and the derivative of the inverse correlation length contained in the renormalization group equations. In Section 4, the methods developed here are tested by applying them to the two-dimensional anisotropic Ising model, which admits an exact solution. The calculation of critical temperature in the three-dimensional Ising model is presented in Section 5. In Section 6, the results obtained by different methods are discussed. Section 7 summarizes the results of this work and outlines guidelines for future studies. A basic description of group-theoretic reduction of transfer matrices is given in the Appendix.

2. EXTENDED PHENOMENOLOGICAL RENORMALIZATION GROUP AND EQUATIONS FOR T_c

According to the theory of finite-size scaling [20–22] (see also reviews in [23, 24]), the singular part f_s of the dimensionless Helmholtz free energy and the inverse correlation length κ in the vicinity of a phase-transition point satisfy the functional equations

$$f_s(t, h, 1/L) = l^{-d} f_s(tl^{y_t}, hl^{y_h}, l/L), \quad (3)$$

$$\kappa(t, h, 1/L) = l^{-1}\kappa(tl^{y_t}, hl^{y_h}, l/L). \quad (4)$$

Here, d is the space dimension, $t = (T - T_c)/T_c$ is the reduced temperature, h is the normalized external magnetic field, L is the characteristic length of a strictly or partly finite system, y_t is the thermal critical exponent, y_h is the magnetic critical exponent, and l is the Kadanoff scaling parameter.

Relations (3) and (4) are generalized homogeneous equations [25]. They can be solved by substituting standard expressions for l to find various characteristics of the system as functions of deviations from the critical point $t = h = 1/L = 0$ along different directions. In particular, if $l = L$, then Eq. (4) yields the inverse correlation length for a finite subsystem of an infinite system at the phase-transition point $t = h = 0$:

$$\kappa_L(T_c) \equiv \kappa(0, 0, 1/L) = L^{-1}\kappa(0, 0, 1). \quad (5)$$

Applying Eq. (5) to two subsystems with characteristic sizes L and L', i.e., to the cluster pair (L, L'), one has

$$L\kappa_L(T_c) = L'\kappa_{L'}(T_c), \quad (6)$$

which is used to estimate critical temperature in the conventional phenomenological renormalization group theory [26–29].

The mth derivatives of (3) and (4) with respect to h,

$$f_s^{(m)}(t, h, 1/L) = l^{my_h - d} f_s^{(m)}(tl^{y_t}, hl^{y_h}, l/L), \quad (7)$$

$$\kappa^{(m)}(t, h, 1/L) = l^{my_h - 1}\kappa^{(m)}(tl^{y_t}, hl^{y_h}, l/L), \quad (8)$$

can be combined to obtain alternative equations for T_c, which correspond to extended versions of the phenomenological renormalization group theory.

By using isotropic lattice models as test examples, it was found that the renormalization-group equation

$$L^{1-d}\kappa_L''/\chi_L\big|_{T_c} = (L')^{1-d}\kappa_{L'}''/\chi_{L'}\big|_{T_c} \quad (9)$$

yields lower bounds for critical temperatures [18, 19]. On the other hand, the equation

$$L^{-d}\chi_L^{(4)}/\chi_L^2\big|_{T_c} = (L')^{-d}\chi_{L'}^{(4)}/\chi_{L'}^2\big|_{T_c}, \quad (10)$$

as well as (6), provides upper bounds. However, the bounds obtained by using (10) are more accurate.

In (9) and (10),

$$\chi_L(T) \equiv \partial^2 f_L/\partial h^2\big|_{h=0} = f_s^{(2)}(t, 0, 1/L) \quad (11)$$

is the initial linear susceptibility of a subsystem,

$$\chi_L^{(4)}(T) \equiv \partial^4 f_L/\partial h^4\big|_{h=0} = f_s^{(4)}(t, 0, 1/L) \quad (12)$$

is its initial nonlinear susceptibility, and

$$\kappa_L''(T) = \partial^2\kappa/\partial h^2\big|_{h=0} = \kappa^2(t, 0, 1/L). \quad (13)$$

In these expressions, f_L is the total Helmholtz free energy per site in a subsystem:

$$f_L = f_0 + f_s, \tag{14}$$

where f_0 is the regular (background) part of the Helmholtz free-energy density for a system with $L = \infty$.

To solve Eqs. (9) and (10), they should be supplemented with expressions for the susceptibilities and the second derivative of the inverse correlation length with respect to the external field at $h = 0$. This problem is addressed in the next section.

3. CALCULATIONS OF χ_L, $\chi_L^{(4)}$, AND κ_L''

In the anisotropic Ising model, the Hamiltonian is written as

$$\mathcal{H} = -J\sum_{\langle i,j\rangle} S_iS_j - J'\sum_{[i,j]} S_iS_j - H\sum_i S_i, \tag{15}$$

where the spin variables S_i are localized at the lattice sites and are equal to +1 or –1, and H is magnetic field. The sums with $\langle i, j\rangle$ and $[i, j]$ are taken over the nearest-neighbor pairs along the directions with the coupling constants J and J', respectively.

To calculate the thermodynamic characteristics of the subsystem defined on an $L^{d-1}\times\infty$ lattice (which is infinite along the J direction), consider the transfer matrix V with elements

$$\langle S_1, \ldots, S_n|V|S_1', \ldots, S_n'\rangle = \exp\left[K\sum_{i=1}^{n} S_iS_i' + \frac{1}{2}K'\sum_{[i,j]}(S_iS_j + S_i'S_j') + \frac{1}{2}h\sum_{i=1}^{n}(S_i + S_i')\right]. \tag{16}$$

Here, $n = L^{d-1}$ is the number of chains in the subsystem, $K = J/k_BT$, $K' = J'/k_BT$, $h = H/k_BT$, and S_i and S_i' denote the spin variables at sites in adjacent layers of the $L^{d-1}\times\infty$ lattice. To eliminate undesirable surface effects, consider a subsystem subject to a periodic boundary condition in the transverse direction. The transfer matrix V is a real, symmetric, full matrix with positive elements.

Note that the transfer matrix defined by (16) can be expressed as

$$V = U^{1/2}V_0U^{1/2}, \tag{17}$$

where $V_0 = V|_{h=0}$ is the transfer matrix corresponding to zero external field and

$$U = e^{hM} = 1 + Mh + \frac{1}{2}M^2h^2 + \ldots \tag{18}$$

is a diagonal matrix with a magnetic moment

$$M = \sigma_1 + \sigma_2 + \ldots + \sigma_n, \tag{19}$$

where

$$\sigma_i = 1\times 1\times\ldots\times\sigma^z\times\ldots\times 1. \tag{20}$$

In this product, the Pauli matrix σ^z is the ith multiplicand and the remaining ones are two-dimensional identity matrices.

According to [26–29] (see also earlier publications cited therein), the dimensionless Helmholtz free-energy density can be expressed in terms of the largest eigenvalue Λ_1 of the transfer matrix as

$$f_L = L^{1-d}\ln\Lambda_1, \tag{21}$$

and the longitudinal inverse correlation length for an $L^{d-1}\times\infty$ subsystem is

$$\kappa_L = \ln(\Lambda_1/|\Lambda_2|), \tag{22}$$

where Λ_2 is the second largest eigenvalue of V. Analogous formulas are valid for the model with zero external field, with Λ_i replaced with λ_i, where λ_i denote eigenvalues of V_0. Thus, to determine the critical temperature in the conventional phenomenological renormalization group theory (i.e., by solving Eq. (6)), only certain eigenvalues of V_0 must be found.

A transfer matrix (V or V_0) is an $N\times N$ matrix with positive elements, where $N = 2^n$. By the Perron–Frobenius theorem [30], its largest eigenvalue is not degenerate and positive.

In the Ising model, the second largest eigenvalue λ_2 is not degenerate either. In particular, this follows from the fact that the second largest eigenvalue in the q-state Potts model is degenerate with multiplicity $q - 1$ (e.g., see [31, p. 441]), and $q = 2$ in the Ising model.

Exact formulas for χ_L, $\chi_L^{(4)}$, and κ_L'' in zero external field are obtained by applying perturbation theory to nondegenerate λ_1 and λ_2 as follows. The transfer matrix V for a nonzero external field is represented as a power series in h up to the fourth-order terms inclusive:

$$V = V_0 + hV_1 + h^2V_2 + h^3V_3 + h^4V_4 + O(h^5). \tag{23}$$

The expressions for V_s can be derived from (16) and written as

$$V_1 = \frac{1}{2}(MV_0 + V_0M), \tag{24}$$

$$V_2 = \frac{1}{2!2^2}(M^2V_0 + 2MV_0M + V_0M^2), \tag{25}$$

etc. In the analysis that follows, it should be kept in mind that the matrices V_s with even and odd s consist of

terms containing even and odd numbers of operators M, respectively.

Denote by Ψ_i the eigenvectors of V_0 corresponding to $\lambda_1 < |\lambda_2| < \ldots$. With second-order corrections calculated by using the perturbation theory, it holds that

$$\Lambda_1 = \lambda_1 + \left[(V_2)_{11} + \sum_k{}' \frac{(V_1)_{2k}^2}{\lambda_1 - \lambda_k}\right] h^2 + O(h^4), \quad (26)$$

where $(V_s)_{ij} = \Psi_i^+ V_s \Psi_j$. In the primed sum, the singular term (with $k = 1$) is skipped. Recalling definition (11) and using expressions (21) and (26), one finds an exact formula for the initial linear susceptibility:

$$\chi_L = \frac{2}{L^{d-1}\lambda_1}\left[(V_2)_{11} + \sum_k{}' \frac{(V_1)_{1k}^2}{\lambda_1 - \lambda_k}\right]. \quad (27)$$

Similarly, the following expression is obtained by collecting the fourth-order terms in the perturbation series for Λ_1:

$$\chi_L^{(4)} = \frac{24}{L^{d-1}\lambda_1}\left\{(V_4)_{11} + \sum_k{}' \frac{(V_2)_{1k}^2}{\lambda_1 - \lambda_k}\right.$$

$$+ 2\sum_k{}' \frac{(V_1)_{1k}(V_3)_{1k}}{\lambda_1 - \lambda_k} + 2\sum_{k,l}{}' \frac{(V_1)_{1k}(V_1)_{kl}(V_2)_{l1}}{(\lambda_1 - \lambda_k)(\lambda_1 - \lambda_l)}$$

$$+ \sum_{k,l}{}' \frac{(V_1)_{1k}(V_2)_{kl}(V_1)_{l1}}{(\lambda_1 - \lambda_k)(\lambda_1 - \lambda_l)} - (V_2)_{11}\sum_k{}' \frac{(V_1)_{1k}^2}{(\lambda_1 - \lambda_k)^2} \quad (28)$$

$$+ \sum_{k,l,m}{}' \frac{(V_1)_{1k}(V_1)_{kl}(V_1)_{lm}(V_1)_{m1}}{(\lambda_1 - \lambda_k)(\lambda_1 - \lambda_l)(\lambda_1 - \lambda_m)}$$

$$\left. - \sum_{k,l}{}' \frac{(V_1)_{1k}^2(V_2)_{l1}^2}{(\lambda_1 - \lambda_k)^2(\lambda_1 - \lambda_l)} - \frac{1}{2\lambda_1}\left[(V_2)_{11} + \sum_k{}' \frac{(V_1)_{1k}^2}{\lambda_1 - \lambda_k}\right]^2\right\}.$$

Finally, the inverse correlation length in zero external field is obtained by perturbative calculation of corrections to λ_1 and λ_2:

$$\kappa_L'' = 2\left\{\frac{1}{\lambda_1}\left[(V_2)_{11} + \sum_k{}' \frac{(V_1)_{1k}^2}{\lambda_1 - \lambda_k}\right]\right.$$
$$\left. - \frac{1}{\lambda_2}\left[(V_2)_{22} + \sum_k{}' \frac{(V_1)_{2k}^2}{\lambda_2 - \lambda_k}\right]\right\}. \quad (29)$$

Thus, to determine the critical temperature in the extended phenomenological renormalization group theory (based on Eqs. (9) and (10)), one has to find all eigenvalues and eigenvectors of V_0 or its submatrices. On the one hand, this requires tedious calculations. On the other hand, since Eqs. (9) and (10) carry more information about the system, the resulting estimates are expected to be more accurate as compared to those based on the conventional phenomenological renormalization group theory.

Expressions (27)–(29) were used in a program written in C, while the eigenvalues and eigenvectors of relatively small transfer matrices V_0 were found by direct diagonalization with the use of the library functions *tred2* and *tqli* [32].

4. HEURISTIC EXAMPLE: TWO-DIMENSIONAL ISING LATTICE

Before new results were obtained for the three-dimensional Ising model, Eqs. (9) and (10) were tested by applying them to its exactly solvable analog defined on an anisotropic square lattice.

In the two-dimensional Ising model [33], critical temperature satisfies the transcendental equation

$$\sinh\frac{2J}{k_B T_c}\sinh\frac{2J'}{k_B T_c} = 1. \quad (30)$$

In in the isotropic limit ($J' = J$),

$$\frac{k_B T_c}{J} = \frac{2}{\ln(1+\sqrt{2})} = 2.269185\ldots. \quad (31)$$

According to (30), the critical temperature for a slightly anisotropic lattice is calculated in the linear approximation as

$$\frac{T_c(J'/J)}{T_c(1)} \approx 1 - \frac{1}{2}\left(1 - \frac{J'}{J}\right), \quad J' \longrightarrow J. \quad (32)$$

In the model with strong interaction, iterative solution of Eq. (30) provides an asymptotically exact expression [34]:

$$\frac{k_B T_c}{J} \approx \frac{2}{\ln(2J/J')}, \quad \frac{J'}{J} \longrightarrow 0. \quad (33)$$

The critical temperatures for intermediate values of J'/J can be found by solving Eq. (30) numerically.

Table 1 shows the lower and upper bounds for critical temperature, $T_<^{(L,L')}$ and $T_>^{(L,L')}$, obtained by solving Eqs. (9) and (10) for cluster pairs (L, L') with $L' = L \pm 1$, respectively. The calculations were performed for $L \times \infty$ strips with periodic boundary conditions in the transverse direction. Since the strip width was varied between 2 and 5, the transfer matrices were not larger than 32×32. For these relatively small dimensions, the eigenvalues and eigenvectors of V_0 were found by

Table 1. Lower and upper bounds for critical temperature and its exact values in the two-dimensional anisotropic Ising model ($k_B = J = 1$)

J'/J	$T_<^{(2,3)}$	$T_<^{(3,4)}$	$T_<^{(4,5)}$	Exact	$T_>^{(5,4)}$	$T_>^{(4,3)}$	$T_>^{(3,2)}$
1.0	2.1088	2.2147	2.2409	2.26919	2.2898	2.3126	2.3478
0.5	1.5660	1.6134	1.6266	1.64102	1.6484	1.6587	1.6894
0.1	0.8788	0.8962	0.9011	0.90588	0.9076	0.9097	0.9180
0.05	0.7219	0.7345	0.7380	0.74131	0.7425	0.7439	0.7492
0.01	0.4988	0.5054	0.5072	0.50893	0.5095	0.5102	0.5128
0.005	0.4375	0.4427	0.4441	0.44546	0.4459	0.4465	0.4485
0.001	0.3378	0.3409	0.3418	0.34266	0.3429	0.3433	0.3445

direct numerical diagonalization and $\chi_L(T)$, $\chi_L^{(4)}(T)$, and $\kappa_L''(T)$ were calculated by using formulas given in Section 3. The roots of Eqs. (9) and (10) were obtained numerically by the bisection method. The exact values of the critical temperature determined by Eq. (30) are also listed in Table 1 for comparison.

In Table 1, the lower bounds determined from renormalization group equation (9) are denoted by subscript "<." The estimation accuracy improves with increasing strip width. Moreover, Table 1 demonstrates that the estimation accuracy improves with increasing degree of lattice anisotropy as well. This result is also dictated by physical considerations, since the strip geometry provides an increasingly better model of quasi-one-dimensional coupling with decreasing parameter J'/J.

According to Table 1, the accuracy of the upper bounds $T_>^{(L,L-1)}$ determined from Eq. (10) also uniformly increases with strip width and coupling anisotropy.

The analogy between the two- and three-dimensional models suggests that the bounds predicted by Eqs. (9) and (10) will be uniformly convergent in the case of an anisotropic Ising lattice, when no exact solution is available.

5. THREE-DIMENSIONAL ISING LATTICE

This section presents the calculations performed to solve Eqs. (9) and (10) in the three-dimensional case.

Since Eqs. (9) and (10) are transcendental, they should be solved by applying an iterative procedure. The bisection method was used again in this study. At each iteration step, two problems must be solved: both eigenvalues and eigenvectors of the transfer matrix V_0 must be found, and the susceptibilities and κ_L'' given by (27)–(29) must be calculated. It is well known [35] that solution of the spectral problem for an $N \times N$ full matrix requires $O(N^3)$ operations [35] (*tred2* includes three nested cycles of length N each). Calculation of χ_L, κ_L'', and especially $\chi_L^{(4)}$ must also include nested cycles, which entail even higher computational costs than solution of the spectral problem. (The program used in this study to calculate $\chi_L^{(4)}$ contained five 3-cycles of length N for each inner cycle.)

For $L \times L \times \infty$ parallelepipeds used as subsystems, the transfer-matrix dimension increases as $N = 2^{L^2}$, whereas $N = 2^L$ in two dimensions. In particular, 16×16, 512×512, and 65536×65536 transfer matrices are to be analyzed when $L = 2$, 3, and 4, respectively.

5.1. Quasidiagonalized Transfer Matrices and Reduced Formulas for $\chi_L(T)$, $\chi_L^{(4)}(T)$, and $\kappa_L''(T)$

To find the eigenvalues and eigenvectors of a large transfer matrix, it was represented in block diagonal form by using symmetries of Ising subsystems. Note that this transformation also facilitates calculations of (27)–(29) involving nested cycles, because the lengths of all cycles reduce to subblock dimensions. Moreover, it is shown below that only two submatrices of a quasidiagonalized transfer matrix V_0 are actually required.

In the case of zero external field, the Hamiltonian of the Ising model defined on an $L \times L \times \infty$ cyclic parallelepiped and, therefore, the transfer matrix V_0 are invariant under the group $\mathbf{Z}_2 \times (\mathbf{T}_L \wedge \mathbf{C}_{4v})$, where $\mathbf{Z}_2$ is the group of spin inversions, $\mathbf{T}_L$ is the group of transverse translations relative to $L \times L \times \infty$, and $\mathbf{C}_{4v}$ is the point group consisting of rotations about the infinite axis of the parallelepiped and reflections in the planes containing the axis. The symbols $\times$ and $\wedge$ correspond to direct and semidirect products, respectively.

The largest eigenvalue of a quasidiagonalized transfer matrix (V or V_0) must belong to the subblock corresponding to the totally symmetric representation of the group. This follows from the Perron–Frobenius theorem, the invariance of eigenvalues under changes of

matrix elements and model parameters, and the positivity of all elements in the subblock.

Generally, the second largest eigenvalue may belong to different subblocks depending on model parameters (see [27, 36]). However, a numerical analysis shows that the second largest eigenvalue Λ_2 for Ising models defined on a square or simple cubic lattice with nearest-neighbor interactions is localized in the subblock associated with the totally symmetric representation of the subgroup of spatial transformations (i.e., the subgroup $\mathbf{T}_L \wedge \mathbf{C}_{4v}$ in three dimensions). In the case of zero external field, the internal symmetry under $\mathbf{Z}_2$ holds and this block can be represented as a direct product of two subblocks. The largest eigenvalue λ_1 is associated with the subblock spanned by the totally symmetric basis functions of $\mathbf{Z}_2 \times (\mathbf{T}_L \wedge \mathbf{C}_{4v})$. The second largest eigenvalue λ_2 lies in the subblock spanned by the basis functions that are symmetric under the spatial transformations and antisymmetric under transformations involving spin inversion.

Thus, the present analysis of the quasidiagonalized transfer matrix V can be restricted to the subblock associated with the totally symmetric representation of the subgroup of spatial transformations. The series expansion of this subblock in powers of h is similar to (23). By using the basis in which the representation of $\mathbf{Z}_2$ is totally reduced and taking into account the symmetry and antisymmetry of V_s with even and odd s, respectively, with respect to spin inversion (which can be derived from (19), (24), and (25)), the subblock in question is written as

$$V' = \left(\begin{array}{c|c} V_0^{(1)} & 0 \\ \hline 0 & V_0^{(2)} \end{array}\right) + h\left(\begin{array}{c|c} 0 & V_1^{(12)} \\ \hline V_1^{(21)} & 0 \end{array}\right) + h^2\left(\begin{array}{c|c} V_2^{(1)} & 0 \\ \hline 0 & V_2^{(2)} \end{array}\right) + h^3\left(\begin{array}{c|c} 0 & V_3^{(12)} \\ \hline V_3^{(21)} & 0 \end{array}\right) + h^4\left(\begin{array}{c|c} V_4^{(1)} & 0 \\ \hline 0 & V_4^{(2)} \end{array}\right) + O(h^5). \quad (34)$$

The sequence of alternate diagonal and antidiagonal blocks in this expansion is ordered so that $V_0^{(1)}$ and $V_0^{(2)}$ correspond to symmetric and antisymmetric irreducible representations of $\mathbf{Z}_2$, respectively.

Let λ_k and ψ_k be the eigenvalues and eigenvectors of $V_0^{(1)}$, and denote its dimension by N_1. Let ξ_k, φ_k, and N_2 be the eigenvalues, eigenvectors of $V_0^{(2)}$, and dimension of $V_0^{(2)}$. Then (27) reduces to the following expression:

$$\chi_L(T) = \frac{2}{L^2\lambda_1}\left[\psi_1^+ V_2^{(1)}\psi_1 + \sum_{k=1}^{N_2}\frac{(\psi_1^+ V_1^{(12)}\varphi_k)^2}{\lambda_1 - \xi_k}\right]. \quad (35)$$

Similarly, (28) yields the expression

$$\chi_L^{(4)}(T) = \frac{12}{L^2\lambda_1} \times \left[\frac{1}{\lambda_1}Q^2 - 2(Q_1 + Q_2 + Q_3 + Q_4 + Q_5 - Q_6 + Q_7 - Q_8)\right], \quad (36)$$

where

$$Q = \psi_1^+ V_2^{(1)}\psi_1 + \sum_{k=1}^{N_2}\frac{(\psi_1^+ V_1^{(12)}\varphi_k)^2}{\lambda_1 - \xi_k},$$

$$Q_1 = \psi_1^+ V_4^{(1)}\psi_1, \quad Q_2 = \sum_{k=2}^{N_2}\frac{(\psi_1^+ V_2^{(1)}\psi_k)^2}{\lambda_1 - \lambda_k},$$

$$Q_3 = 2\sum_{k=1}^{N_2}\frac{(\psi_1^+ V_1^{(12)}\varphi_k)(\psi_1^+ V_3^{(12)}\varphi_k)}{\lambda_1 - \xi_k},$$

$$Q_4 = 2\sum_{k=1}^{N_2}\sum_{l=2}^{N_1}\frac{(\psi_1^+ V_1^{(12)}\varphi_k)(\varphi_k^+ V_1^{(21)}\psi_l)(\psi_l^+ V_2^{(1)}\psi_1)}{(\lambda_1 - \xi_k)(\lambda_1 - \lambda_l)}, \quad (37)$$

$$Q_5 = \sum_{k=1}^{N_2}\sum_{l=1}^{N_2}\frac{(\psi_1^+ V_1^{(12)}\varphi_k)(\varphi_k^+ V_2^{(2)}\varphi_l)(\varphi_l^+ V_1^{(21)}\psi_1)}{(\lambda_1 - \xi_k)(\lambda_1 - \xi_l)},$$

$$Q_6 = \psi_1^+ V_2^{(1)}\psi_1 \sum_{k=1}^{N_2}\frac{(\psi_1^+ V_1^{(12)}\varphi_k)^2}{(\lambda_1 - \xi_k)^2},$$

$$Q_7 = \sum_{k=1}^{N_2}\sum_{l=2}^{N_1}\sum_{m=1}^{N_2}\frac{(\psi_1^+ V_1^{(12)}\varphi_k)(\varphi_k^+ V_1^{(21)}\psi_l)(\psi_l^+ V_1^{(12)}\varphi_m)(\varphi_m^+ V_1^{(21)}\psi_1)}{(\lambda_1 - \xi_k)(\lambda_1 - \lambda_l)(\lambda_1 - \xi_m)},$$

$$Q_8 = \sum_{k=1}^{N_2}\frac{(\psi_1^+ V_1^{(12)}\varphi_k)^2}{(\lambda_1 - \xi_k)^2}\sum_{l=1}^{N_2}\frac{(\psi_1^+ V_1^{(12)}\varphi_l)^2}{\lambda_1 - \xi_l}.$$

It was noted above that the Λ_2 is also localized in V'. The required expression for the second derivative of the inverse correlation length is found from (29) by taking into account the structure of the terms that

constitute V':

$$\kappa_L''(T) = L^2\chi_L(T) - \frac{2}{\xi_1}\left[\varphi_1^+ V_2^{(2)}\varphi_1 + \sum_{k=1}^{N_1}\frac{(\psi_k^+ V_1^{(12)}\varphi_1)^2}{\xi_1 - \lambda_k}\right], \quad (38)$$

where $\chi_L(T)$ is given by (35).

Before using the expressions for χ_L, $\chi_L^{(4)}$, and κ_L'', the transfer matrix V_0 must be partially quasidiagonalized by isolating two subblocks, and the terms V_1–V_4 must be rewritten in a different basis. Technically, this is the most difficult part of the present study. The key details of this procedure are given in the Appendix.

Table 2 lists the dimensions of the subblocks contained in expansion (34). The values of N_1 and N_2 are obtained by performing a group-theoretic analysis, which is also developed in the Appendix for $L = 2$, 3, and 4. The subblock dimensions for $L = 5$ and 6 are also presented in Table 2, but their calculations are omitted.

5.2. Intervals of Localization for Critical Point and Estimates for Critical Temperature

The block quasidiagonalization was used to perform calculations for $L \times L \times \infty$ subsystems with $L \le 4$, i.e., for transfer matrices with dimensions up to $2^{16} \times 2^{16}$. The results are listed in Table 3.

The bounds $T_<^{(2,3)}$ and $T_<^{(3,4)}$ were obtained by solving Eq. (9) for the cluster pairs (2,3) and (3,4) respectively; $T_>^{(3,2)}$ and $T_>^{(4,3)}$, by solving Eq. (10) for the same pairs of subsystems. An analysis of the tabular data shows that the highly accurate value of critical temperature given by (1) for $J' = J$ lies between $k_B T_<^{(3,4)}/J$ and $k_B T_<^{(4,3)}/J$ (the factor k_B/J is omitted in tables). Therefore, the temperatures denoted by "<" and ">" (at least, in the first row) are the lower and upper bounds, respectively.

Furthermore, Table 3 demonstrates that the values of $T_<^{(2,3)}$ and $T_<^{(3,4)}$ and those of $T_>^{(3,2)}$ and $T_>^{(4,3)}$, respectively, converge with decreasing J'/J, but never meet. By analogy with the two-dimensional model considered in Section 4, it should be expected that exact critical temperature for anisotropic Ising lattice lies between the values $T_<^{(3,4)}$ and $T_>^{(4,3)}$. These are the best lower and upper bounds obtained in the present study.

The analysis above suggests that the mean value

$$T_c = (T_<^{(3,4)} + T_>^{(4,3)})/2 \quad (39)$$

Table 2. Dimensions of the leading-order subblocks of the transfer matrices for $L \times L \times \infty$ Ising lattices with $\mathbf{Z}_2 \times (\mathbf{T}_L \wedge \mathbf{C}_{4v})$ group symmetries

	L				
	2	3	4	5	6
N_1	4	13	433	86056	119583470
N_2	2	13	372	86056	119539680

provides the most reliable estimate for critical temperature. The corresponding absolute error does not exceed

$$\Delta T_c = (T_>^{(4,3)} - T_<^{(3,4)})/2. \quad (40)$$

These estimates and errors are listed in the last column of Table 3. As J'/J decreases from 1 to 10^{-3}, the relative error of these estimates for the critical temperature monotonically decreases from 0.7 to 0.14%; i.e., the accuracy is higher than that achieved for the two-dimensional model (see Table 1).

Note that, as in the case of planar lattice, the deviations of the upper and lower bounds from the exact critical temperature in the three-dimensional model are approximately equal. Therefore, the actual errors must be even smaller than those listed in the last column of Table 3. In particular, the actual error of the estimate for the critical temperature given by (1) in the case of isotropic lattice is as small as 0.01%, rather than 0.7%. This error is even smaller than that of the estimate $k_B T_c/J = 4.53371$ obtained in [37] by solving conventional renormalization group equation (6) for the isotropic cluster pair (4,5) (see also [38]).

The data listed in the last column of Table 3 can be used to quantify the behavior of critical temperature for a quasi-isotropic lattice:

$$\frac{T_c(J'/J)}{T_c(1)} \approx 1 - 0.075\left(1 - \frac{J'}{J}\right), \quad J' \longrightarrow J. \quad (41)$$

Thus, the slope at $J' = J$ is lower than that in the two-dimensional Ising model by almost an order of magnitude (cf. (32)).

6. COMPARISON WITH RESULTS OBTAINED BY VARIOUS METHODS

To compare the bounds for critical temperature in the anisotropic three-dimensional Ising model found in the preceding section with those obtained by different methods, consider Table 4. Its rows are arranged so that accuracy improves as the *Exact* row is approached from above or below.

In the linear-chain (LC) approximation considered in [12], three-dimensional Ising lattice is represented as

Table 3. Lower and upper bounds for critical temperature in the three-dimensional anisotropic Ising model and the corresponding estimates for T_c calculated as the arithmetic means of $T_<^{(3,4)}$ and $T_>^{(4,3)}$, with errors ΔT_c given in parentheses ($k_B = J = 1$)

J'/J	$T_<^{(2,3)}$	$T_<^{(3,4)}$	$T_>^{(4,3)}$	$T_>^{(3,2)}$	T_c
1.0	4.413461	4.479658	4.544243	4.582331	4.512(32)
0.9	4.121298	4.178933	4.237039	4.275470	4.208(29)
0.8	3.823165	3.872973	3.924647	3.962271	3.899(26)
0.7	3.517969	3.560676	3.605985	3.641676	3.583(23)
0.6	3.204178	3.240483	3.279517	3.312201	3.260(20)
0.5	2.879539	2.910087	2.942957	2.971640	2.927(16)
0.4	2.540487	2.565829	2.592660	2.616479	2.579(13)
0.3	2.180792	2.201317	2.222236	2.240527	2.212(10)
0.2	1.787702	1.803508	1.818607	1.831006	1.8110(76)
0.1	1.325918	1.336496	1.345701	1.352289	1.3411(46)
0.09	1.272257	1.282236	1.290826	1.296859	1.2865(43)
0.08	1.216271	1.225625	1.233592	1.239075	1.2296(40)
0.07	1.157454	1.166154	1.173484	1.178424	1.1698(37)
0.06	1.095101	1.103112	1.109789	1.114190	1.1065(33)
0.05	1.028172	1.035449	1.041449	1.045316	1.0385(30)
0.04	0.955023	0.961509	0.966800	0.970133	0.9642(27)
0.03	0.872788	0.878403	0.882937	0.885728	0.8807(23)
0.02	0.775604	0.780225	0.783922	0.786148	0.7821(19)
0.01	0.647148	0.650541	0.653231	0.654821	0.6519(14)
0.009	0.630851	0.634096	0.636669	0.638185	0.6354(13)
0.008	0.613470	0.616560	0.619008	0.620449	0.6178(12)
0.007	0.594762	0.597689	0.600005	0.601367	0.5989(12)
0.006	0.574388	0.577140	0.579317	0.580595	0.5782(11)
0.005	0.551841	0.554405	0.556431	0.557619	0.5554(10)
0.004	0.526316	0.528672	0.530533	0.531622	0.52960(93)
0.003	0.496386	0.498507	0.500181	0.501160	0.49934(84)
0.002	0.459088	0.460929	0.462382	0.463231	0.46166(73)
0.001	0.405958	0.407430	0.408590	0.409267	0.40801(58)

an array of one-dimensional chains parallel to the J (dominant interaction) direction. The coupling in chains is treated exactly; the coupling between chains, by invoking molecular field theory. The critical temperature predicted in the LC approximation satisfies the equation

$$k_B T_c = zJ' \exp(2J/k_B T_c), \qquad (42)$$

where z is the number of the nearest chains ($z = 2$ and 4 for two- and three-dimensional lattices, respectively). The numerical results obtained by solving Eq. (42) with $z = 4$ are listed the *LCA* row of Table 4.

It is well known (see [39]) that iterative solution of the equation $xe^x = t$ yields

$$x = \ln t + O(\ln\ln t),$$

$$x = \ln t - \ln\ln t + O(\ln\ln t/\ln t), \ \ldots,$$

and the series for x is absolutely and uniformly conver-

Table 4. Estimates for critical temperature in the three-dimensional Ising model obtained by different methods

	J'/J						
	1.0	0.5	0.1	0.05	0.01	0.005	0.001
(2)	–	–	1.7644	1.3619	0.7849	0.6498	0.4558
(45)	–	–	1.6215	1.2831	0.7740	0.6452	0.4552
LCA	5.6861	3.5264	1.5075	1.1458	0.6991	0.5907	0.4280
ECA	4.9326	3.2061	1.4647	1.1277	0.6965	0.5896	0.4278
ELCA	4.8815	3.1251	1.4009	1.0776	0.6694	0.5686	0.4155
EBPA	4.8106	3.0906	1.3918	1.0718	0.6669	0.5667	0.4144
(46)	–	–	1.3619	1.0534	0.6498	0.5508	0.4020
CPRGT	–	–	1.3473	1.0428	0.6540	0.5574	0.4089
UB	4.5442	2.9430	1.3457	1.0414	0.6532	0.5564	0.4086
Exact	4.51152…						
Series	4.5106	2.9286	1.343	1.041	0.65	–	–
LB	4.4797	2.9101	1.3365	1.0354	0.6505	0.5544	0.4074

gent if t is sufficiently large. Therefore, the solution to Eq. (42) with $J'/J \longrightarrow 0$ is

$$\frac{k_B T_c}{J} \approx 2\left[\ln\left(\frac{2J}{zJ'}\right) - \ln\ln\left(\frac{2J}{zJ'}\right)\right]^{-1}. \quad (43)$$

In the three-dimensional case ($z = 4$), this result is equivalent to asymptotic expression (2). However, its accuracy is very low (see the top row in Table 4).

The extended chain approximation (ECA) developed in [17] is listed next to LCA in Table 4. In this approximation, an Ising chain with offshoots is embedded in a molecular field and the equation for critical temperature is

$$\left[z\exp\left(\frac{2J}{k_B T_c}\right) - 2\right]\left[\exp\left(\frac{2J'}{k_B T_c}\right) - 1\right] = 2. \quad (44)$$

Iterative solution of this equation for a three-dimensional lattice with $J'/J \longrightarrow 0$ yields

$$\frac{k_B T_c}{J} \approx 2\left\{\ln\left[\frac{J}{2J'} + \frac{1}{2}\ln\left(\frac{J}{2J'} + \frac{1}{2}\right)\right] - \ln\ln\left(\frac{J}{2J'} + \frac{1}{2}\right)\right\}^{-1}. \quad (45)$$

According to Table 4, this expression leads to better results as compared to those predicted by (2).

The extended linear-chain approximation (ELCA) [13, 14] deals with a simple Ising chain similar to that used in LCA. However, the use of a variational approach in the ELCA leads to results that are better than the ECA estimates, even though a more realistic cluster is used in the latter approximation, as demonstrated by the numerical results listed in Table 4.

The accuracy is substantially improved by increasing the number of chains in the approximating subsystems and treating exactly all interactions within chains and part of interactions between chains (coupling within clusters). In Table 4, this is demonstrated by the numerical results obtained in the extended Bethe–Peierls approximation (EBPA) [15] and in the framework of the conventional phenomenological renormalization group theory (CPRGT) [16]. In the former, an Ising cluster consisting of five chains (central one and four nearest neighbors) is embedded in a molecular field, i.e., not only coupling within a chain, but also interaction within a cylinder, is treated exactly. In CPRGT, phase-transition temperatures were calculated by solving Eq. (6) for the pairs (1,2), (2,3), and (3,4) and extrapolating the results to the thermodynamic limit $L = \infty$. (However, because of certain anomalies due to the $1 \times 1 \times \infty$ cluster, the extrapolation could be performed only for relatively high degree of anisotropy [16].)

The approaches enumerated above lead to upper bounds for critical temperature that are less accurate than the upper bounds $T_>^{(4,3)}$, which are shown in the UB row of Table 4. The lower bounds $T_<^{(3,4)}$ obtained in this study are listed in the LB row of the table.

An analysis of high-temperature expansions [10] leads to intermediate estimates between those listed in the LB and UB rows (see the *Series* row in Table 4). The only exception is the value corresponding to $J'/J = 10^{-2}$,

which falls outside the lower bound for critical temperature ($0.65 < 0.6505$). This is obviously explained by the loss of accuracy due to a finite number of terms (≤ 11) retained in the high-temperature expansions for anisotropic lattices.

In [11], asymptotic expression (2) for the critical temperature in the anisotropic Ising model was replaced with

$$\frac{k_B T_c}{J} \approx 2\left[\ln\left(\frac{J}{J'}\right) - \ln\ln\left(\frac{J}{J'}\right)\right]^{-1}, \quad (46)$$

which is equivalent to replacing z with $z/2$ in (43). In the two-dimensional case ($z = 2$), this yields the asymptotically correct behavior predicted by (33). It was claimed in [11] that asymptotic expression (46) is correct in an unexpectedly wide interval of J'/J. According to Fig. 14 in [11], the results obtained by a Monte Carlo method are in good agreement with (46) for J'/J between 0.3 and 3×10^{-3}.

The numerical results obtained in the present study can be used to evaluate the actual errors associated with expression (46). Table 4 shows that the values predicted by (46) for $J'/J = 0.1$ and 0.05 lie above the interval of critical temperatures found here, while those predicted for $J'/J \leq 0.01$ fall below the lower bounds. Thus, (46) should actually be interpreted only as an approximate interpolation; moreover, it is not monotonically convergent.

7. CONCLUSIONS

The main results of this study are numerical bounds for critical temperature in anisotropic three-dimensional Ising model. The interval found here is monotonically narrowing with increasing degree of anisotropy, and the average values corresponding to its centerline provide the best estimates obtained to date for phase-transition temperatures in the anisotropic model.

These results are obtained by performing extensive transfer-matrix computations based on two unconventional phenomenological renormalization schemes for statistical models. One scheme (using the universal quantity $Y = L^{1-d}\kappa_L''/\chi_L$) leads to lower bounds for critical points. The other strategy (associated with an equation for $L^{1-2d}\chi_L^{(4)}/\chi_L^2$) leads to upper bounds. These assertions are supported, on the one hand, by a qualitative comparison with analogous computations performed for the exactly solvable two-dimensional Ising model. On the other hand, detailed comparisons with available quantitative results for the three-dimensional Ising model show that the upper and lower bounds for critical temperature found here are correct.

The bounds obtained for critical temperature are used to specify, in terms of J'/J, limits for correct predictions of $k_B T_c/J$ based on high-temperature expansions [10]. Moreover, the high accuracy attained here in computing the interval of critical points makes it possible to elucidate the actual behavior of the function defined by (46).

The highly accurate relation between T_c and the coupling constants J and J' can be used to interpret experimental results concerning quasi-one-dimensional Ising magnets.

The accuracy of bounds for the critical point can be further improved by the size of an $L \times L \times \infty$ subsystem to $L = 5$. An additional estimate could also be used to perform three-point interpolations, which would further improve the accuracy of results. (Unfortunately, the pair (1,2) cannot be used in the versions of the extended phenomenological renormalization group considered here.) According to Table 2, all of the problems discussed above must be solved for 86056×86056 subblocks if $5 \times 5 \times \infty$ subsystems are employed. Currently, this task can be accomplished only by using the best supercomputing facilities. In particular, recent computations [40, 41] performed on the MVS-1000M supercomputer at the Joint Supercomputing Center [42], which is rated as one of the world top 100 [43], advanced the solution of the complete spectral problem only to $2^{15} \times 2^{15}$ Hamiltonian matrices.

APPENDIX

The procedure used to reduce an $L \times L \times \infty$ unperturbed transfer matrix V_0 to block diagonal form relies on group theory and includes three stages: (1) a group-theoretic analysis performed to determine subblock dimensions in advance, (2) determination of the basis vectors of irreducible representations by finding a similarity transformation of the transfer matrix into block diagonal form, and (3) actual calculations of submatrix elements. Despite its outward simplicity, the last stage is the most labor-consuming.

The group $\mathbf{Z}_2 \times (\mathbf{T}_L \wedge \mathbf{C}_{4v})$ is on the order of $g = 16L^2$. It can be generated by spin inversion R, translations t_1 and t_2 by one step in both transverse directions for a cyclic $L \times L \times \infty$ parallelepiped, rotation C_4 to an angle of $\pi/2$ about the longitudinal axis of the parallelepiped, and reflections in the symmetry planes σ_v and σ_v' containing the axis. In the initial representation defined by the basis vectors

$$|S_{11}, S_{12}, \ldots, S_{LL}\rangle \equiv \left|\begin{array}{cccc} S_{11} & S_{12} & \ldots & S_{1L} \\ S_{21} & S_{22} & \ldots & S_{2L} \\ \ldots & \ldots & \ldots & \ldots \\ S_{L1} & S_{L2} & \ldots & S_{LL} \end{array}\right\rangle \quad (A.1)$$

(spin variables S_{ij} are now denoted by double sub-

Table 5. Characters of the initial and two irreducible representations of the transfer-matrix symmetry group for the $2 \times 2 \times \infty$ Ising subsystem

$\mathbf{Z}_2 \times \mathbf{C}_{4v}$	E	C_2	$2C_4$	$2\sigma_v$	$2\sigma'_v$	R	RC_2	$2RC_4$	$2R\sigma_v$	$2R\sigma'_v$
$\Gamma^{(1)}$	1	1	1	1	1	1	1	1	1	1
$\Gamma^{(2)}$	1	1	1	1	1	–1	–1	–1	–1	–1
Γ	16	4	2	4	8	0	4	2	4	0

scripts), the group generators are

$$R|S_{11}, S_{12}, \ldots, S_{LL}\rangle = |-S_{11}, -S_{12}, \ldots, -S_{LL}\rangle, \quad \text{(A.2)}$$

$$t_1\left|\begin{array}{cccc} S_{11} & S_{12} & \ldots & S_{1L} \\ \ldots & \ldots & \ldots & \ldots \\ S_{L1} & S_{L2} & \ldots & S_{LL} \end{array}\right\rangle = \left|\begin{array}{cccc} S_{1L} & S_{11} & \ldots & S_{1,L-1} \\ \ldots & \ldots & \ldots & \ldots \\ S_{LL} & S_{L1} & \ldots & S_{L,L-1} \end{array}\right\rangle, \quad \text{(A.3)}$$

$$t_2\left|\begin{array}{ccc} S_{11} & \ldots & S_{1L} \\ S_{21} & \ldots & S_{2L} \\ \ldots & \ldots & \ldots \\ S_{L1} & \ldots & S_{LL} \end{array}\right\rangle = \left|\begin{array}{ccc} S_{21} & \ldots & S_{2L} \\ \ldots & \ldots & \ldots \\ S_{L1} & \ldots & S_{LL} \\ S_{11} & \ldots & S_{1L} \end{array}\right\rangle, \quad \text{(A.4)}$$

$$C_4\left|\begin{array}{ccc} S_{11} & \ldots & S_{1L} \\ \ldots & \ldots & \ldots \\ S_{L1} & \ldots & S_{LL} \end{array}\right\rangle = \left|\begin{array}{ccc} S_{1L} & \ldots & S_{LL} \\ \ldots & \ldots & \ldots \\ S_{11} & \ldots & S_{L1} \end{array}\right\rangle, \quad \text{(A.5)}$$

$$\sigma_v\left|\begin{array}{ccc} S_{11} & \ldots & S_{1L} \\ S_{21} & \ldots & S_{2L} \\ \ldots & \ldots & \ldots \\ S_{L1} & \ldots & S_{LL} \end{array}\right\rangle = \left|\begin{array}{ccc} S_{L1} & \ldots & S_{LL} \\ S_{L-1,1} & \ldots & S_{L-1,L} \\ \ldots & \ldots & \ldots \\ S_{11} & \ldots & S_{1L} \end{array}\right\rangle, \quad \text{(A.6)}$$

$$\sigma'_v\left|\begin{array}{ccc} S_{11} & \ldots & S_{1L} \\ \ldots & \ldots & \ldots \\ S_{L1} & \ldots & S_{LL} \end{array}\right\rangle = \left|\begin{array}{ccc} S_{LL} & \ldots & S_{1L} \\ \ldots & \ldots & \ldots \\ S_{L1} & \ldots & S_{11} \end{array}\right\rangle. \quad \text{(A.7)}$$

Every group transformation is a combination of these operators.

Multiplying (A.2)–(A.7) on the left by the conjugate vectors and using the normalization condition

$$\langle S_{11}, S_{12}, \ldots, S_{LL}|S'_{11}, S'_{12}, \ldots, S'_{LL}\rangle = \prod_{i,j=1}^{L} \delta_{S_{ij}S'_{ij}}, \quad \text{(A.8)}$$

one obtains the matrices of the initial representation Γ of $\mathbf{Z}_2 \times (\mathbf{T}_L \wedge \mathbf{C}_{4v})$. To analyze the structure of Γ, the characters (traces of the constructed matrices) are calculated by using definitions (A.2)–(A.7) and relations (A.8) and summing over all repeated indices in S:

$$\chi(E) = \langle S_{11}, S_{12}, \ldots, S_{LL}|S_{11}, S_{12}, \ldots, S_{LL}\rangle = \prod_{i,j=1}^{L} \delta_{S_{ij}S_{ij}} = 2^{L^2}, \quad \text{(A.9)}$$

$$\chi(R) = \langle S_{11}, S_{12}, \ldots, S_{LL}|R|S_{11}, S_{12}, \ldots, S_{LL}\rangle = \prod_{i,j=1}^{L} \delta_{S_{ij},-S_{ij}} = 0, \quad \text{(A.10)}$$

and so on. This procedure was programmed in integer arithmetic, and the characters of all elements in the group were computed.

The multiplicity a_μ of each irreducible representation $\Gamma^{(\mu)}$ in Γ is calculated as

$$a_\mu = \frac{1}{g}\sum_i g_i \chi_i \chi_i^{(\mu)*}, \quad \text{(A.11)}$$

where g_i is the number of elements in the ith class of the group, χ_i is the character of an element of the ith class in the initial representation Γ, and $\chi_i^{(\mu)}$ is the character of an element of the ith class in the μth irreducible representation; the sum is taken over all classes i of the group (e.g., see [44]). The dimensions of the subblocks corresponding to the one-dimensional irreducible representations are equal to the multiplicities thus defined.

Table 5 shows the characters of the symmetry group $\mathbf{Z}_2 \times \mathbf{C}_{4v}$ associated with the $2 \times 2 \times \infty$ Ising cluster. (In this case, there is actually no transverse translation, and periodic boundary conditions imply mere doubling of the constants of interactions between chains.)

The tabular data and formula (A.11) are used to determine the structure of the initial representation of the group:

$$\Gamma = 4\Gamma^{(1)} + 2\Gamma^{(2)} + \ldots. \quad \text{(A.12)}$$

According to group theory, after a similarity transformation into a totally reduced representation, the transfer matrix of the system has a block diagonal structure, with 4×4 and 2×2 subblocks $V_0^{(1)}$ and $V_0^{(2)}$, respectively ($N_1 = 4$ and $N_2 = 2$).

Table 6. Characters of the initial representation of the group $\mathbf{T}_3 \wedge \mathbf{C}_{4v}$, which has nine classes of conjugate elements

E	$6\sigma_v$	$6\sigma'$	$9C_2$	$4t_1$	$4t_1t_2$	$18C_4$	$12t_1\sigma_v$	$12t_1\sigma'_v$
512	64	64	32	8	8	8	4	4

The characters of the representation Γ of the spatial group $\mathbf{T}_3 \wedge \mathbf{C}_{4v}$ are shown in Table 6. It is easy to see (or verify by calculations) that the odd number of chains in the system, combined with the fact that spatial transformations can only move a spin configuration S_{11}, S_{12}, …, S_{LL} on an $L \times L$ lattice by, implies that the characters of the elements involving spin inversions R are zeros. When the set of characters is known, the structure of the representation Γ can be found for $L = 3$:

$$\Gamma = 13(\Gamma^{(1)} + \Gamma^{(2)}) + \ldots . \qquad \text{(A.13)}$$

Thus, the dimensions of the required subblocks are $N_1 = N_2 = 13$. Therefore, the calculation of the eigenvalues and eigenvectors of a full 512×512 matrix can be reduced to an analogous calculation performed for two matrices of dimension as low as 13. The characters of $\mathbf{Z}_2 \times (\mathbf{T}_4 \wedge \mathbf{C}_{4v})$ listed in Table 7 are used to expand the initial representation in terms of the irreducible representations in question:

$$\Gamma = 433\Gamma^{(1)} + 372\Gamma^{(2)} + \ldots . \qquad \text{(A.14)}$$

This result implies that the eigenvalues and eigenvectors of the 65536×65536 transfer matrix can be found by solving spectral problems for matrices with dimensions 433 and 372 on a PC instead of solving the complete spectral problem on a supercomputer.

These procedures were also used to find N_1 and N_2 for Ising parallelepipeds with $L > 4$. The results of the group-theoretic analyses performed for the $5 \times 5 \times \infty$ and $6 \times 6 \times \infty$ systems are shown in Table 2.

The basis vectors of irreducible representations are obtained by symmetrizing linear combinations of the original basis vectors given by (A.1) or by applying projection operators [44]. In particular, the basis vectors of the irreducible representations $\Gamma^{(1)}$ and $\Gamma^{(2)}$ for the $2 \times 2 \times \infty$ chain are

$$f_1^{(1,2)} = \frac{1}{\sqrt{2}}\left(\left|\begin{matrix}\cdot & \cdot\\ \cdot & \cdot\end{matrix}\right\rangle \pm \left|\begin{matrix}\times & \times\\ \times & \times\end{matrix}\right\rangle\right),$$

$$f_2^{(1,2)} = \frac{1}{2\sqrt{2}}\left[\left|\begin{matrix}\cdot & \cdot\\ \cdot & \times\end{matrix}\right\rangle + \left|\begin{matrix}\cdot & \cdot\\ \times & \cdot\end{matrix}\right\rangle + \left|\begin{matrix}\cdot & \times\\ \cdot & \cdot\end{matrix}\right\rangle + \left|\begin{matrix}\times & \cdot\\ \cdot & \cdot\end{matrix}\right\rangle \pm \left(\left|\begin{matrix}\cdot & \times\\ \times & \times\end{matrix}\right\rangle + \left|\begin{matrix}\times & \cdot\\ \times & \times\end{matrix}\right\rangle + \left|\begin{matrix}\times & \times\\ \cdot & \times\end{matrix}\right\rangle + \left|\begin{matrix}\times & \times\\ \times & \cdot\end{matrix}\right\rangle\right)\right], \qquad \text{(A.15)}$$

$$f_3^{(1)} = \frac{1}{\sqrt{2}}\left(\left|\begin{matrix}\cdot & \cdot\\ \times & \times\end{matrix}\right\rangle + \left|\begin{matrix}\times & \times\\ \cdot & \cdot\end{matrix}\right\rangle\right),$$

$$f_4^{(1)} = \frac{1}{\sqrt{2}}\left(\left|\begin{matrix}\cdot & \times\\ \cdot & \times\end{matrix}\right\rangle + \left|\begin{matrix}\times & \cdot\\ \times & \cdot\end{matrix}\right\rangle\right),$$

$$f_5^{(1)} = \frac{1}{\sqrt{2}}\left(\left|\begin{matrix}\cdot & \times\\ \times & \cdot\end{matrix}\right\rangle + \left|\begin{matrix}\times & \cdot\\ \cdot & \times\end{matrix}\right\rangle\right),$$

where dots and crosses correspond to +1 and –1, respectively. The basis vectors are then used to find the sets of coefficients in matrix elements $f_i^{(\mu)+} V_s f_j^{(\nu)}$.

Table 7. Characters of the group $\mathbf{Z}_2 \times \mathbf{T}_4 \wedge \mathbf{C}_{4v}$

	I (1)	II (4)	III (12)	IV (27)	V (16)	VI (52)	VII (16)	VIII (27)	IX (52)	X (16)	XI (33)
$\Gamma^{(1)}$	1	1	1	1	1	1	1	1	1	1	1
$\Gamma^{(2)}$	1	1	1	1	1	1	1	–1	–1	–1	–1
Γ	2^{16}	2^{12}	2^{10}	2^8	2^6	2^4	2^2	2^8	2^4	2^2	0

Note: To minimize the table size, 40 classes are combined into 11 unified classes for which characters are equal in the representations $\Gamma^{(1)}$, $\Gamma^{(2)}$, and Γ simultaneously. The number of elements in each unified class is shown in parentheses. The unified classes are I$\{E\}$, II$\{4t_1\sigma_v\}$, III$\{4t_1t_2C_2,\ 8\sigma'_v\}$, IV$\{2t_1^2,\ t_1^2t_2^2,\ 4C_2,\ 8t_1C_2,\ 4\sigma_v,\ 4t_1^2\sigma_v,\ 4t_1^2t_2\sigma_v\}$, V$\{16t_1C_4\}$, VI$\{4t_1,\ 4t_1t_2,\ 4t_1^2t_2,\ 16C_4,\ 8t_1\sigma_v,\ 8t_1t_2\sigma_v,\ 8t_1^2\sigma'_v\}$, VII$\{16t_1\sigma'_v\}$, VIII$\{2Rt_1^2,\ 2Rt_1^2t_2^2,\ 4RC_2,\ 8Rt_1C_2,\ 4R\sigma_v,\ 4Rt_1^2\sigma_v,\ 4Rt_1^2t_2\}$, IX$\{4Rt_1,\ 4Rt_1t_2,\ 4Rt_1^2t_2,\ 16RC_4,\ 8Rt_1\sigma_v,\ 8Rt_1t_2\sigma_v,\ 8Rt_1^2\sigma'_v\}$, X$\{16Rt_1\sigma'_v\}$, and XI$\{R,\ 4Rt_2\sigma_v,\ 4Rt_1t_2C_2,\ 8R\sigma'_v,\ 16Rt_1C_4\}$.

These sets consist of integers, which are calculated once and for all, stored on a disk, and retrieved to construct the matrices $V_0^{(1)}$, $V_0^{(2)}$, $V_1^{(12)}$, …, $V_4^{(2)}$ corresponding to given T, J, and J'. For example, the matrix elements in the subblocks $V_0^{(1,2)}$ of the $3\times3\times\infty$ system are

$$(V_0^{(1)})_{ij} = \frac{2}{\sqrt{n_i n_j}}\left[\sum_{s=1}^{5}\left|g_s^{(ij)}\right|\cosh(Kn_s^a)\right] \times \exp\left[\frac{K'(m_i^b + m_j^b)}{2}\right], \tag{A.16}$$

$$(V_0^{(2)})_{ij} = \frac{2}{\sqrt{n_i n_j}} \times\left[\sum_{s=1}^{5} g_s^{(ij)}\sinh(Kn_s^a)\right]\exp\left[\frac{K'(m_i^b + m_j^b)}{2}\right], \tag{A.17}$$

with $i, j = 1, 2, \ldots, 13$ and

$$n_i = \{2, 18, 36, 12, 36, 72, 72, 72, 18, 72, 18, 12, 72\}, \tag{A.18}$$

$$m_i^b = \{18, 10, 6, 6, 2, 2, -2, 2, 2, -2, -6, -6, -6\}, \tag{A.19}$$

$$n_s^a = \{9, 7, 5, 3, 1\}. \tag{A.20}$$

Since $V_0^{(1)}$ and $V_0^{(2)}$ are symmetric matrices, the coefficients $g_s^{(ij)}$ may be calculated only for their upper triangular parts. Overall, 91 sets of five numbers are required. After ordering the sets of indices i and j column-by-column into a one-dimensional sequence so that $i, j \longrightarrow l = i + j(j-1)/2$, the coefficients g are written as

1) 2 0 0 0 0, 2) 0 18 0 0 0,

3) 18 0 144 0 0, 4) 0 0 36 0 0,

5) 0 72 0 252 0, 6) 36 0 216 0 396,

7) 0 0 0 12 0, 8) 0 0 36 0 72,

9) 0 36 0 72 –108, 10) 12 0 0 –24 36,

11) 0 0 36 0 0, 12) 0 72 0 252 0,

13) 0 0 288 0 360, 14) 0 0 0 144 –72,

15) 36 0 216 0 396, 16) 0 0 0 72 0,

17) 0 0 216 0 432, 18) 0 144 0 576 –576,

19) 0 0 144 –144 144, 20) 0 72 0 720 –504,

21) 72 0 504 –648 1368, 22) 0 0 0 72 0,

23) 0 0 216 0 432, 24) 0 72 0 720 –504,

25) 0 0 72 –72 288, 26) 0 144 0 576 –576,

27) 0 0 576 –576 1440, 28) 72 0 504 –648 1368,

29) 0 0 0 0 72, 30) 0 0 0 288 –360,

31) 0 0 288 –432 576, 32) 0 72 –72 72 –216,

33) 0 0 144 –288 864,

34) 0 144 –432 1008 –1008,

35) 0 72 –216 936 –1368,

36) 72 –144 504 –936 936,

37) 0 0 0 0 18, 38) 0 0 0 72 –90,

39) 0 0 72 –108 144, 40) 0 0 –36 72 0,

41) 0 0 36 –72 216, 42) 0 72 –72 144 –360,

43) 0 0 –72 288 –288,

44) 0 –72 144 –144 288,

45) 18 0 0 –72 72, 46) 0 0 0 0 72,

47) 0 0 0 288 –360, 48) 0 0 216 –360 720,

49) 0 0 –72 216 –144, 50) 0 0 216 –360 720,

51) 0 144 –288 864 –1296,

52) 0 144 –288 864 –1296,

53) 0 –144 432 –720 1296,

54) 0 0 144 –288 216,

55) 72 –72 288 –864 1296, 56) 0 0 0 0 18,

57) 0 0 0 72 –90, 58) 0 0 36 –72 216,

59) 0 0 0 36 –72, 60) 0 0 72 –108 144,

61) 0 0 –72 288 –288, 62) 0 72 –72 144 –360,

63) 0 0 72 –216 360, 64) 0 –18 0 0 144,

65) 0 0 144 –288 216, 66) 18 0 0 –72 72,

67) 0 0 0 12 0, 68) 0 0 36 0 72,

69) 0 0 0 144 –72, 70) 0 0 0 0 72,

71) 0 36 0 72 –108, 72) 0 0 72 –72 288,

73) 0 0 144 –144 144,

74) 0 0 0 144 –288, 75) 0 0 0 36 –72,

76) 0 0 –72 216 –144, 77) 0 0 –36 72 0,

78) 12 0 0 –24 36, 79) 0 0 0 0 72,

80) 0 0 0 288 –360, 81) 0 0 144 –288 864,

82) 0 0 0 144 –288, 83) 0 0 288 –432 576,

84) 0 72 –216 936 –1368,

85) 0 144 –432 1008 –1008,

86) 0 0 288 –864 1440, 87) 0 0 72 –216 360,

88) 0 –144 432 –720 1296,

89) 0 –72 144 –144 288,

90) 0 72 –72 72 –216,

91) 72 –144 504 –936 936.

The coefficients $g_s^{(ij)}$ were calculated by using a special program and stored in a file on a hard disk. The sets of coefficients $\{n_i\}$, $\{m_i^b\}$, $\{n_s^a\}$, and $\{g_s^{(ij)}\}$ are used in (A.16) and (A.17) to calculate the matrix elements of subblocks. In particular,

$$(V_0^{(1)})_{11} = 2\cosh(9K)\exp(18K'),$$

$$(V_0^{(1)})_{34} = 2\sqrt{3}[\cosh(7K)$$

$$+ 2\cosh(3K) + 3\cosh K]\exp(6K'), \qquad \text{(A.21)}$$

$$(V_0^{(2)})_{13,13} = 2\{\sinh(9K) - 2\sinh(7K)$$

$$+ 7\sinh(5K) - 13[\sinh(3K) - \sinh K]\}\exp(-6K').$$

Similar operations are executed for the $4 \times 4 \times \infty$ system. Since the amount of numerical data that determine g is huge, they cannot be written out here.

ACKNOWLEDGMENTS

I highly appreciate the support provided by É.B. Fel'dman in this study. This work was also supported by the Russian Foundation for Basic Research, project no. 03-02-16909.

REFERENCES

1. A. Z. Patashinskiĭ and V. L. Pokrovski, *Fluctuation Theory of Phase Transitions*, 2nd ed. (Nauka, Moscow, 1982; Pergamon Press, Oxford, 1979).
2. J. Cardy, *Scaling and Renormalization in Statistical Physics* (Cambridge Univ. Press, Cambridge, 1997).
3. A. Pelissetto and E. Vicari, Phys. Rep. **368**, 549 (2002); cond-mat/0012164.
4. P. Butera and M. Comi, Phys. Rev. B **62**, 14837 (2000).
5. R. Gupta and P. Tamayo, Int. J. Mod. Phys. C **7**, 305 (1996).
6. M. Hasenbusch, K. Pinn, and S. Viniti, Phys. Rev. B **59**, 11471 (1999).
7. H. W. J. Blöte, L. N. Shchur, and A. L. Talapov, Int. J. Mod. Phys. C **10**, 1137 (1999).
8. J. O. Vigfusson, J. Phys. A **18**, 3417 (1985).
9. C.-Y. Weng, R. B. Griffiths, and M. E. Fisher, Phys. Rev. **162**, 475 (1967); M. E. Fisher, Phys. Rev. **162**, 480 (1967).
10. R. Navarro and L. J. de Jongh, Physica B (Amsterdam) **94**, 67 (1978).
11. T. Graim and D. P. Landau, Phys. Rev. B **24**, 5156 (1981).
12. J. W. Stout and R. C. Chisholm, J. Chem. Phys. **36**, 979 (1962).
13. J. R. Faleiro Ferreira and N. P. Silva, Phys. Status Solidi B **114**, 47 (1982).
14. J. R. Faleiro Ferreira, Phys. Status Solidi B **148**, 709 (1988).
15. M. A. Yurishchev, Phys. Status Solidi B **128**, 537 (1985).
16. M. Yurishchev and A. Sterlin, J. Phys.: Condens. Matter **3**, 2373 (1991).
17. Y. Muraoka and T. Idogaki, Phys. Status Solidi B **195**, 553 (1996).
18. M. A. Yurishchev, Nucl. Phys. B (Proc. Suppl.) **83**/**84**, 727 (2000).
19. M. A. Yurishchev, Zh. Éksp. Teor. Fiz. **118**, 380 (2000) [JETP **91**, 332 (2000)].
20. M. E. Fisher, in *Proceedings of the 1970 E. Fermi International School of Physics on Critical Phenomena*, Ed. by M. S. Green (Academic, New York, 1971), Vol. 51, p. 1 [*Stability and Phase Transitions* (Mir, Moscow, 1973), p. 245].
21. M. E. Fisher and M. N. Barber, Phys. Rev. Lett. **28**, 1516 (1972).
22. M. Suzuki, Prog. Theor. Phys. **58**, 1142 (1974).
23. M. N. Barber, in *Phase Transitions and Critical Phenomena*, Ed. by C. Domb and J. L. Lebowitz (Academic, London, 1983), Vol. 8, p. 145.
24. V. Privman, in *Finite Size Scaling and Numerical Simulation of Statistical Systems*, Ed. by V. Privman (World Sci., Singapore, 1990), p. 1.

25. H. E. Stanley, *Introduction to Phase Transitions and Critical Phenomena* (Clarendon Press, Oxford, 1971; Mir, Moscow, 1973).
26. M. P. Nightingale, Physica A (Amsterdam) **83**, 561 (1976).
27. M. P. Nightingale, Proc. K. Ned. Akad. Wet., Ser. B **82**, 235 (1979).
28. P. Nightingale, J. Appl. Phys. **53**, 7927 (1982).
29. M. P. Nightingale, in *Finite Size Scaling and Numerical Simulation of Statistical Systems*, Ed. by V. Privman (World Sci., Singapore, 1990), p. 287.
30. F. R. Gantmakher, *The Theory of Matrices*, 4th ed. (Fizmatgiz, Moscow, 1988; Chelsea, New York, 1959).
31. H. W. J. Blöte and M. P. Nightingale, Physica A (Amsterdam) **112**, 405 (1982).
32. W. H. Press, S. A. Teukolsky, W. T. Vetterling, and B. P. Flannery, *Numerical Recipes in C: The Art of Scientific Computing*, 2nd ed. (Cambridge Univ. Press, Cambridge, 1992).
33. L. Onsager, Phys. Rev. **65**, 117 (1944).
34. D. J. Scalapino, Y. Imry, and P. Pincus, Phys. Rev. B **11**, 2042 (1975).
35. B. N. Parlett, *The Symmetric Eigenvalue Problem* (Prentice Hall, Englewood Cliffs, N.J., 1980; Mir, Moscow, 1983).
36. T. Yokota, Phys. Rev. B **39**, 12312 (1989).
37. M. A. Novotny, Nucl. Phys. B (Proc. Suppl.) **20**, 122 (1991).
38. C. F. Baillie, R. Gupta, K. A. Hawick, and G. S. Pawley, Phys. Rev. B **45**, 10438 (1992).
39. N. G. de Bruijn, *Asymptotic Methods in Analysis* (North-Holland, Amsterdam, 1958; Inostrannaya Literatura, Moscow, 1961).
40. S. I. Doronin, E. B. Fel'dman, I. Ya. Guinzbourg, and I. I. Maximov, Chem. Phys. Lett. **341**, 144 (2001).
41. I. Ya. Ginzburg, S. I. Doronin, and I. I. Maksimov, Mat. Model. **14**, 3 (2002).
42. http://www.jscc.ru
43. http://www.top500.org
44. M. Hamermesh, *Group Theory and Its Applications to Physical Problems* (Addison-Wesley, Reading, Mass., 1962; Mir, Moscow, 1966).

Translated by A. Betev

Journal of Experimental and Theoretical Physics, Vol. 98, No. 6, 2004, pp. 1198–1204.
Translated from Zhurnal Éksperimental'noĭ i Teoreticheskoĭ Fiziki, Vol. 125, No. 6, 2004, pp. 1367–1374.

SOLIDS
Structure

Magnetic Relaxation in a Random System of Interacting Rodlike Nanoparticles

E. Z. Meĭlikhov* and R. M. Farzetdinova

Russian Research Centre Kurchatov Institute, pr. Kurchatova 1, Moscow, 123182 Russia
**e-mail: meilikhov@kiae.ru*

Received December 15, 2003

Abstract—It is shown in the framework of the generalized mean-field approximation taking into account spatial fluctuations of the local magnetic field that the collective effect of dipole interaction in a random 3D system of identical (rodlike) magnetic nanoparticles with parallel easy magnetization axes shifts the relaxation magnetization curves towards shorter times (i.e., accelerates the relaxation process). In addition, the course of this process depends (via the demagnetizing field) on the sample shape. The interaction between nanograins affects the magnetization relaxation of a random 2D system only when the magnetic moments of the grains are perpendicular to the plane of the system. *© 2004 MAIK "Nauka/Interperiodica".*

1. INTRODUCTION

The relaxation of the magnetization of a system of magnetic nanoparticles is a process determined by a large number of factors, such as the spread in the geometrical parameters (volume and shape) of such particles in real systems, the spread in the directions of their easy magnetization axes and anisotropy fields, and the (dipole–dipole) interaction between particles. The description of this process is a difficult problem; it is therefore not surprising that various approximate methods for solving this problem lead to contradictory results (see [1] and the literature cited therein). One of the basic questions is whether the above factors decelerate or accelerate the relaxation process. The experimentally observed long-term relaxation processes in such magnetic systems are often associated with a strong spread in the values of at least one of the parameters influencing the relaxation [2]. For example, the considerable spread in the sizes and shapes of magnetic grains, which is typical of such systems, is chosen in [3, 4] as a reason for such relaxation of magnetization of magnetic nanocomposites. Another reason for prolonged relaxation may be the long-range interaction between individual relaxing elements of the system, which accelerates relaxation. In this case, a negative feedback appears: the reason for this acceleration is simultaneously eliminated in the course of relaxation process (i.e., when a relaxing integrated quantity approaches its equilibrium value). In [5], for example, the relaxation of magnetization of a 2D system of Ising magnetic moments with the easy axis perpendicular to the plane is considered in the mean field approximation. The factor accelerating the relaxation of individual elements in such a system is the demagnetizing field proportional to the relaxing quantity itself (total magnetization of the system). In [6, 7], an attempt was made to transgress the frames of the mean field approximation due to the inclusion of a part of the local field fluctuating with time. Such fluctuations elevate the effective temperature of the system and, hence, change the relaxation rate. The feedback mechanism operates in this case so that, along with the suppression of fluctuations, the effective temperature decreases (approaching the actual temperature) as the system attains equilibrium, which slows down the relaxation.

In this study, it will be shown that long-term relaxation of magnetization may occur in the ensemble of interacting magnetic nanoparticles even in the absence of all the three sources listed above (the spread in parameters, the demagnetizing field, and time fluctuations) if the arrangement of individual elements of the system is not regular (i.e., if spatial disorder leading to spatial field fluctuations takes place).

We will consider the systems consisting of monodomain nanograins with uniaxial magnetic anisotropy (geometrical or crystallographic). The magnetic energy E of such a grain in a magnetic field H directed along the easy axis can be written in the form

$$E = -K_u V\cos^2\theta + \mu H\cos\theta, \qquad (1)$$

where θ is the angle between the magnetic moment of the grain and its easy axis, K_u is the anisotropy energy per unit volume, and $\mu = I_s V$ is the magnetic moment of a grain, I_s being the saturation magnetization of the grain material and V its volume. The angular dependence of energy (1) corresponds to two potential wells of different (for $H \neq 0$) depth, corresponding to angles

$\theta = 0$ and $\theta = \pi$ and separated by an asymmetric barrier. Different heights of this barrier,

$$\Delta_{\pm} = K_u V\left(1 \pm \frac{H}{H_A}\right)^2, \tag{2}$$

are measured from the bottom of the corresponding well ($H_A = 2K_u/I_s$ and the plus and minus signs correspond to the "deep" and "shallow" wells, respectively; for $H > H_A$, the shallow well disappears and we must set $\Delta_- = 0$.[1]

Thermal fluctuations lead to "jumps" of the magnetic moment of a grain from well to well, the rate of such jumps being determined by the height of the corresponding barrier. Let n_+ and n_- be the grain concentration in the states corresponding to the lower and higher values of energy (1) (i.e., in the states corresponding to the deep and shallow wells). Then the change in the concentration can be written in the form

$$\begin{aligned}\frac{dn_+}{dt} &= -\Omega\left[n_+\exp\left(-\frac{\Delta_+}{kT}\right) - n_-\exp\left(-\frac{\Delta_-}{kT}\right)\right],\\ \frac{dn_-}{dt} &= -\Omega\left[n_-\exp\left(-\frac{\Delta_-}{kT}\right) - n_+\exp\left(-\frac{\Delta_+}{kT}\right)\right],\end{aligned} \tag{3}$$

where $\Omega \sim 10^9$–10^{10} s^{-1} is the frequency of the magnetic moment's "attempts to escape" from the well [10]. The magnetization of the system is $I = \mu(n_+ - n_-)$; if we introduce the relative magnetization $j = (n_+ - n_-)/n$, where $n = n_+ + n_-$ is the total concentration of the grains, it follows from Eqs. (3) that

$$\begin{aligned}\frac{dj}{dt} = -\Omega\Bigg[&(1 + j)\exp\left(-\frac{\Delta_+}{kT}\right)\\ &-(1 - j)\exp\left(-\frac{\Delta_-}{kT}\right)\Bigg],\end{aligned} \tag{4}$$

or

$$dj/dt = -\Omega\Phi(j, H), \tag{5}$$

where

$$\Phi(j, H) = \Bigg\{(1 + j)\exp\left[-\frac{K_u V}{kT}\left(1 + \frac{I_s H}{2K_u}\right)^2\right] - (1 - j)\exp\left[-\frac{K_u V}{kT}\left(1 - \frac{I_s H}{2K_u}\right)^2\right]\Bigg\}.$$

For a 3D system, the magnetic field

$$H = H_e + H_3 + H_d + 4\pi I/3 \tag{6}$$

appearing in expressions (1), (2), and (5) is a function of magnetization I and is the sum of (i) external field H_e, (ii) field H_3 produced by all the grains located in the Lorentz sphere, (iii) field $4\pi I/3$ produced in the bulk of a given grain by the magnetic moments of the grains located on the surface of the Lorentz sphere surrounding the grain, and (iv) demagnetizing field $H_d = -NI$ (N is the demagnetizing factor) [11].

For a 2D system (monolayer of magnetic grains), the expression for field H depends on the direction of the easy axis of the grains. If this axis lies in the plane of the system, the last two terms in expression (6) are missing; if, however, this axis is perpendicular to the plane of the system, $H_d = -4\pi I$ and the last term is absent.

As regards field H_3, it is determined by the spatial configuration and the directions (signs) of the magnetic moments of the grains neighboring with the given grain and varies from grain to grain. In the mean field model, this difference is neglected and H_3 is replaced by the average (averaged over all grains) field $\langle H_3\rangle$ proportional to magnetization I: $\langle H_3\rangle = \alpha I$. Moreover, since $\alpha = 0$ for a cubic lattice of the grains [11], the mean field $\langle H_3\rangle$ is usually also discarded (although $\alpha \neq 0$, for example, for tetragonal and hexagonal lattices [12, 13]); the same applies to a 2D square lattice of moments [14]. It will be shown below that the generalized mean field approximation in which the spread in local fields H_3 is taken into account qualitatively changes the results obtained in the traditional model in which field H_3 is disregarded. In this model, it is assumed that in zero external field (typical conditions for observing the relaxation of magnetization), the mean magnetic field at grains is given by

$$\langle H\rangle = \begin{cases}(4\pi/3 - N)I,\\ -NI,\\ 0,\end{cases} \tag{7}$$

respectively, for a 3D system, a quasi-two-dimensional system with the moments perpendicular to the planes, and a quasi-two-dimensional system with the moments parallel to the plane. Field $\langle H_3\rangle$ proportional to the magnetization of the system ensures the feedback between

[1] In actual practice, magnetization reversal of rodlike particles occurs not via the rotation of the uniform magnetization, but via the formation and subsequent growth of a critical "nucleus" with a turned magnetization, i.e., an activation-type process [8]. Naturally, the activation barrier height changes in this case. However, according to the results of calculations [8], the field dependence of the barrier height functionally differs from that in the Néel–Braun theory only slightly. In accordance with experiment [9] (elongated nanograins with an aspect ratio of about 10), the angular dependence of the remagnetization field also remains virtually the same as in the Stoner–Wohlfahrt theory. Consequently, formulas (2) following from this model can be used as before. The change in the activation barrier height in this case is equivalent only to renormalization of anisotropy energy K_u.

the magnetization relaxation rate and its instantaneous value. In the traditional approach, substitution $H \longrightarrow \langle H \rangle$ is performed in Eq. (5) (using relations (7)). Precisely this method was used for deriving the equation for relaxation of the magnetization in a 2D system of moments perpendicular to the planes, which was studied in [5]. It can be seen from relations (7) that in this case the feedback leading to long-term relaxation is ensured by a nonzero demagnetizing factor. We will prove that such a relaxation is possible for $N = 0$ as well.

2. RELAXATION OF MAGNETIZATION IN THE GENERALIZED MEAN FIELD MODEL

The generalization of the mean field approximation lies in averaging Eq. (5) with the help of the distribution function $F(j, H_3)$ of local fields H_3 instead of the substitution $H \longrightarrow \langle H \rangle$:

$$\frac{dj}{dt} = -\Omega \int_{-\infty}^{\infty} \Phi\left[j, H = H_e + H_3 + H_d + \frac{4\pi}{3}\mu n j \right] \times F(j, H_3) dH_3; \quad (8)$$

this equation defines the relaxation of magnetization.

In this approximation, the problem is reduced to defining distribution function $F(j, H_3)$, which was determined earlier [15, 16] for a number of systems with disorder. In studying the effect of the interaction between grains on the relaxation process, it is usually assumed that the grains are pointlike magnetic dipoles [1, 6, 7]; this assumption is valid only for spherical grains.[2] However, the "defect" of fundamental importance in the mean field theory, i.e., the disregard of spatial correlations, becomes significant in this case. As a matter of fact, the distribution function $F(j, H_3)$ for a system consisting of spherical grains (of diameter $2a$) is a Lorentzian function (independent of magnetization j and even in H_3) with wings truncated due to finite size of the grains[3] [15]:

$$F(j, H_3) = \begin{cases} \left[2 \arctan \frac{\mu}{h_0 a^3} \right]^{-1} \frac{h_0}{h_0^2 + H_3^2}, & |H_3| \le \mu/a^3, \\ 0, & |H_3| > \mu/a^3, \end{cases} \quad (9)$$

where $h_0 = (8\pi^2/9\sqrt{3})\mu n$.

[2] The interaction of uniformly magnetized spheres is equivalent to the interaction of pointlike magnetic dipoles [17].

[3] For $a \longrightarrow 0$, the distribution function is transformed into the Lorentzian function: $F(j, H_3) \longrightarrow h_0/[\pi(h_0^2 + H_3^2)]$. The type of the ground state of such a system depends on the grain concentration: it is paramagnetic for $na^3 < 0.183$; otherwise, the ground state is ferromagnetic with a Curie temperature $T_C \sim \mu^2 n/k$.

The initial stage of relaxation in this case is associated with a change in the magnetic state of the grains which at the initial instant were in a field $H_3 \sim H_A$ that virtually eliminated the barrier Δ_+ (see relation (2)). It is well known, however [15], that strong local fields $H_3 \gtrsim h_0$ corresponding to the wings of the (Lorentzian) distribution $F(j, H_3)$) in a random system of spherical dipoles cannot be regarded as a collective effect of a large number of magnetic dipoles (as is assumed in the mean field model), but are produced by the nearest neighbors. It is these grains (forming only a small fraction of the system) that determine the initial stage of relaxation. We cannot expect that the "collective" mean field approximation will provide a correct description for such a "local" relaxation.

A completely different situation is observed in a 3D system of randomly arranged rodlike grains, which ensures the uniaxial form of magnetic anisotropy of the grains ($K_u \approx \pi I_s^2$). For such a system (thin rodlike grains of length $2a$), the form of distribution function $F(j, H_3)$ depends on the grain concentration n determined by the value of parameter na^3. However, in a wide concentration range $0.3 \lesssim na^3 \lesssim 300$, in which the ground state of the system is paramagnetic, this function is of a Gaussian shape (Fig. 1) with a peak linearly displaced towards negative fields H_3 (directed opposite to the magnetization) upon an increase in the magnetization [16]:

$$F(j, H_3) = \frac{1}{\sqrt{2\pi}\sigma} \exp\left[-\frac{(H_3 + jH_j)^2}{2\sigma^2} \right]. \quad (10)$$

The parameters of this distribution (the position of the peak and the width) are determined by the grain concentration:

$$H_j = \frac{4\pi}{3}\mu n, \quad \sigma = \frac{\sqrt{\pi}}{2}\sqrt{\frac{1}{na^3}}\mu n. \quad (11)$$

It is important to note that actual fields H_3 in this case are a collective result of composition of the fields produced by a large number of grains, which corresponds to the spirit of the mean field approximation and raises hopes that this method provides a correct description of relaxation of the magnetization in such a system.

The correlation of interacting magnetic moments is of considerable importance for analysis of magnetic relaxation. Unfortunately, analytic methods for calculating such correlations in the case of the long-range anisotropic interaction (which is the case in our system) have not been developed. Nevertheless, the following two arguments can be put forth, which allow us to disregard correlations in the present case.

1. Since only long-wave correlations can exist in a system with long-range interaction, these correlations can be accounted for in the framework of the Ginzburg–Landau theory (it is well known [18] that the results of this theory differ from the results of the mean field theory only in a range of temperatures close to the critical temperature).

2. We have estimated the possible effect of correlations by calculating the distribution function for local magnetic fields in the case when all magnetic moments in a sphere with the diameter equal to the length of the rodlike grains completely correlate (the field produced by each magnetic moment is parallel to the magnetic moment at the center of the sphere). The allowance for such a correlation only leads to a shift in the distribution function (which is the smaller, the higher the integrated magnetization of the system), the width of the function remaining unchanged. Since the increase in the effective temperature of the system, which determines the change in the magnetic relaxation rate, depends precisely on the width of the distribution function (see formula (13)), we can assume that the inclusion of correlations will not change the final conclusions.

We will study the relaxation of magnetization in zero external field ($H_e = 0$); to reveal the role of disorder in pure form, we will first consider a spherical sample for which $N_d = 4\pi/3$. It follows from relation (6) that the contribution of the magnetization to local field H in this case is associated with random field H_3 alone ($H \equiv H_3$). If local fields H_3 were to be identical for all grains and proportional to the magnetization ($H_3 = jH_j$, H_j = const), Eq. (5) would not require any averaging and would be transformed, after the substitution $H_3 \longrightarrow jH_j$, into a relaxation equation similar to that analyzed in [5]. However, in our case, this equation has a completely different meaning: local field $H_3 = jH_j$ is not a demagnetizing field (as in [5]), but a random field of magnetic moments in the Lorentzian sphere.

Substituting distribution function (10) into relation (8) and integrating the result, we obtain the equation describing the relaxation of magnetization in a random system of rodlike grains:

$$\frac{dj}{dt} = -\Omega\sqrt{\frac{\Theta}{\Theta_{\text{eff}}}}\left\{(1+j)\exp\left[-\frac{(1-jH_j/H_A)^2}{\Theta_{\text{eff}}}\right] - (1-j)\exp\left[-\frac{(1+jH_j/H_A)^2}{\Theta_{\text{eff}}}\right]\right\}, \quad (12)$$

where $\Theta = kT/K_uV$ is the reduced temperature and

$$\Theta_{\text{eff}} = \Theta + \Delta\Theta, \quad \Delta\Theta = \frac{2\sigma^2}{H_A^2}. \quad (13)$$

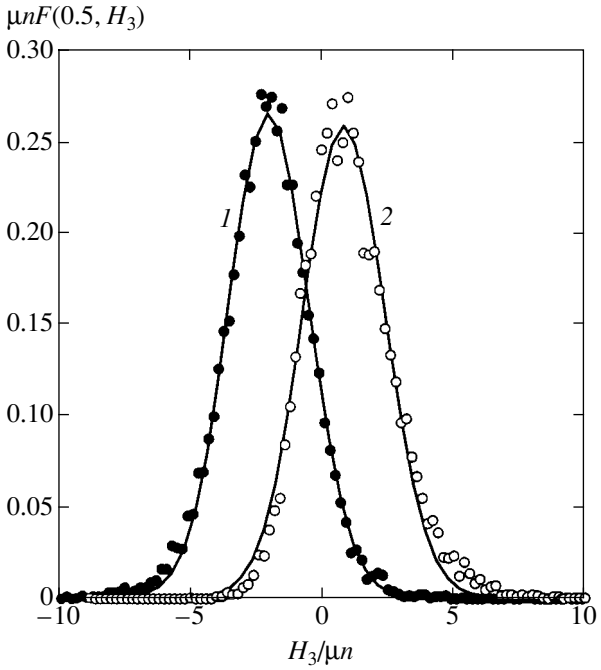

Fig. 1. Distribution functions $F(0.5, H_3)$ of local fields for the model system of randomly arranged rodlike Ising dipoles with $na^3 = 1$. The solid curves are approximating Gaussian functions: uncorrelated magnetic moments (*1*) and correlated magnetic moments (*2*) (see text).

Here, Θ_{eff} is the effective relaxation temperature exceeding the actual temperature Θ by the quantity $\Delta\Theta$ proportional to variance σ^2 of the distribution of random local fields H_3. Formally, Eq. (12) coincides with the magnetization relaxation equation [15]; however, as noted above, this equation has a completely different meaning. Analogously, the excess of the effective relaxation temperature over the real temperature resembles the result obtained in [6] where temporal field fluctuations were taken into account. However, in the present case, we are dealing with the result of spatial field fluctuations.

Using the definitions of various parameters introduced above, we can write the average local field and the effective excess of temperature in the form

$$H_j/H_A = \frac{2}{3}nV \ll 1, \quad \Delta\Theta = \frac{\pi}{4}\left(\frac{D}{2a}\right)^2 nV \ll 1$$

(since the relative fraction nV of the volume occupied by the grains and the ratio of the grain diameter D to the grain length $2a$ are always smaller than unity). Although it follows from Eqs. (12) and (13) that local field fluctuations can affect the relaxation process only for $\Theta \lesssim \Delta\Theta \ll 1$, this does not mean that the corresponding temperatures are very low. Indeed, for grains of a material with $I_s \approx 10^3$ Oe, having a length of $2a$ = 100 nm, a ratio of $D/2a = 0.1$, and a concentration of

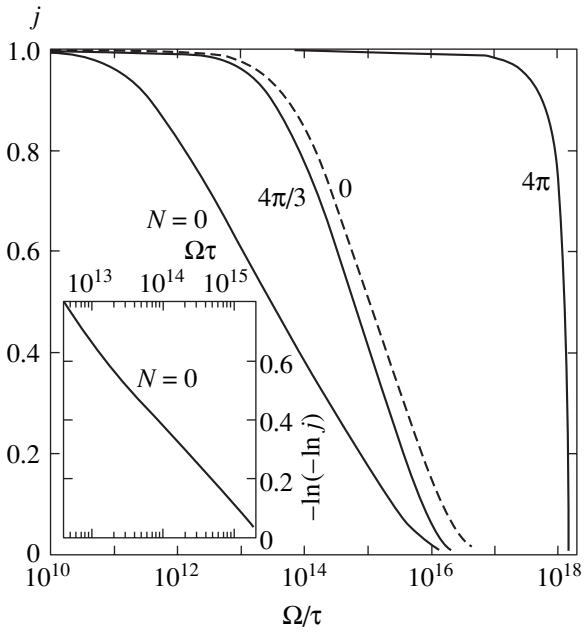

Fig. 2. Magnetization relaxation in a random system of rodlike grains for samples in the form of a long cylinder ($N = 0$), a sphere ($N = 4\pi/3$), and a thin disk ($N = 4\pi$) at a temperature $\Theta = 0.025$ and for a grain concentration $nV = 0.1$ (solid curves). The inset illustrates that the magnetization relaxation in a cylinder can be described by an "extended" exponential (with exponent $\gamma \approx 0.3$). The dashed curve describes the magnetization relaxation in a cylinder at the same temperature, but with $nV = 0.05$.

$nV = 0.1$, the latter inequality is satisfied even at $T \lesssim 100$ K.

Let us now consider the relaxation of magnetization in the given system, which was preliminarily magnetized to saturation ($j = 1$) with the help of a strong external field. In accordance with Eq. (12), after the removal of the field (at instant $t = 0$), the relaxation process obeys the law

$$\left(1 + \frac{\Delta\Theta}{\Theta}\right)^{1/2} \int_j^1 \frac{dj}{\Psi(j, \Theta, nV)} = \Omega t, \qquad (14)$$

where

$$\Psi(j, \Theta, nV) = (1 + j)\exp\left[-\frac{(1 - \beta jnV)^2}{\Theta_{\text{eff}}}\right] - (1 - j)\exp\left[-\frac{(1 + \beta jnV)^2}{\Theta_{\text{eff}}}\right], \quad \beta = \frac{2}{3}. \qquad (15)$$

The nature of this process is determined by two parameters: temperature Θ and its effective increment $\Delta\Theta$ proportional to interaction parameter σ^2 (see above). If we disregard the terms proportional to j in the arguments of the exponential functions in relation (15) (for a low grain concentration or a low magnetization of the system), the solution to Eq. (14) has the form

$$j(t) = \exp\left(-\frac{t}{\tau}\right), \qquad (16)$$

where

$$\tau = \frac{1}{2\Omega}\left(1 + \frac{\Delta\Theta}{\Theta}\right)^{1/2} \exp\left[\frac{1}{\Theta(1 + \Delta\Theta/\Theta)}\right].$$

In accordance with this equation, the magnetization relaxation in the present case follows a simple exponential law, but relaxation time τ depends to a considerable extent on the interaction of magnetic moments. In systems where this interaction is strong, the relaxation time at low temperatures can decrease by several orders of magnitude. However, this can hardly be observed in experiments since this time itself is very long at low temperatures.

In nonspherical samples, local field H is determined not only by the random field H_3 produced by the dipoles in the Lorentzian sphere, but, in accordance with relation (6), has an additional component

$$H_d + 4\pi I/3 = (4\pi/3 - N) j I_s nV.$$

In this case, the procedure for deriving the relaxation equation leads to the familiar equation (14) with a modified integrand:

$$\Psi(j, \Theta, nV) = (1 + j)\exp\left[-\frac{(1 + \beta_1 jnV)^2}{\Theta_{\text{eff}}}\right] - (1 - j)\exp\left[-\frac{(1 + \beta_2 jnV)^2}{\Theta_{\text{eff}}}\right], \qquad (17)$$

where $\beta_1 = N/2\pi - 4/3$ and $\beta_2 = N/2\pi$ (for a spherical sample, $N = 4\pi/3$ and, hence, $-\beta_1 = \beta_2 = 2/3$; see relations (15)).

At the initial stage of the relaxation process (as long as $j \approx 1$), the first term of function (17) prevails. The effect of the demagnetizing field on the relaxation process is determined by the sign of parameter β_1: magnetization relaxation is slowed down for $\beta_1 > 0$ (i.e., for $N > 8\pi/3$) and accelerated for $\beta_1 < 0$. The final relaxation stage ($j \longrightarrow 0$), as well as the magnetization relaxation in a "dilute" system with a small volume fraction of grains, always occurs in accordance with an exponential law with the time constant τ defined by relation (16).

The results of calculations (based on Eq. (14) with the integrand (17)) are presented in Fig. 2, which shows the relaxation (solid) curves for samples in the form of a long cylinder ($N = 0$), a sphere ($N = 4\pi/3$), and a thin disk ($N = 4\pi$), which were magnetized along their rotational axes. The dashed curve describing the magnetization relaxation in a cylindrical sample with a lower

concentration of magnetic grains demonstrates the effect of the grain concentration on the relaxation process (in the present case, a twofold decrease in the concentration increases the characteristic relaxation times by more than two orders of magnitude).

It can be seen that the most prolonged magnetization relaxation occurs in the cylindrical sample, In this case, it is close to a logarithmic relaxation (i.e., described by the law $j = \text{const} - \ln t$) over the third–fourth decade (on the time axis). The inset to Fig. 2 shows that the magnetization relaxation law for a long cylinder ($N = 0$) over a time interval of 2–3 decades can also be described by the "extended" exponential

$$j = j_0 \exp[-(t/t_0)^\gamma], \quad 0 < \gamma < 1,$$

which is often employed for describing relaxation processes [19].

The model described here is also applicable for analysis of a 2D random system of rodlike nanoparticles. For moderate grain concentrations ($0.1 \lesssim na^3 \lesssim 100$), distribution function $F(j, H_3)$ for random fields in this case is close to the Gaussian function, but the values of parameters σ and H_j of this distribution are different [12]:

$$H_j/h_0 = na^2 I_1, \quad (\sigma/h_0)^2 = 2na^2 I_2, \tag{18}$$

where $h_0 = \mu/a^3 \equiv I_s V/a^3$ and n is the 2D (surface) concentration of grains. Numerical parameters I_1 and I_2 are determined by the spatial dependence of energy $W(\rho, \alpha) = -(\mu^2/4a^3)h(\rho, \alpha)$ of interaction between two uniformly magnetized rodlike grains on the distance $r \equiv \rho a$ between the grains and on the angle α formed by the straight line connecting these grains and the direction of the magnetic moment [16]:

$$I_1 = -\int_0^{\pi/2} d\alpha \int_0^\infty h(\rho, \alpha)\rho\, d\rho,$$
$$I_2 = \frac{1}{8}\int_0^{\pi/2} d\alpha \int_0^\infty h^2(\rho, \alpha)\rho\, d\rho, \tag{19}$$

where

$$h(\rho, \alpha) = -\frac{2}{\rho} + \frac{1}{\sqrt{\rho^2 + 4 + 4\rho\cos\alpha}} + \frac{1}{\sqrt{\rho^2 + 4 - 4\rho\cos\alpha}}. \tag{20}$$

For the system in question, both the demagnetizing field and the field of the Lorentzian 2D sphere (circle) are equal to zero. For this reason, in zero external field, the magnetization relaxation equation for a 2D system coincides with Eq. (12) for a 3D system of a spherical shape, in which we now have

$$\frac{H_j}{H_A} = \frac{I_1}{2\pi} na^2 \frac{V}{a^3},$$
$$\Delta\Theta = \frac{2\sigma^2}{H_A^2} = \frac{I_2}{\pi^2} na^2 \left(\frac{V}{a^3}\right)^2. \tag{21}$$

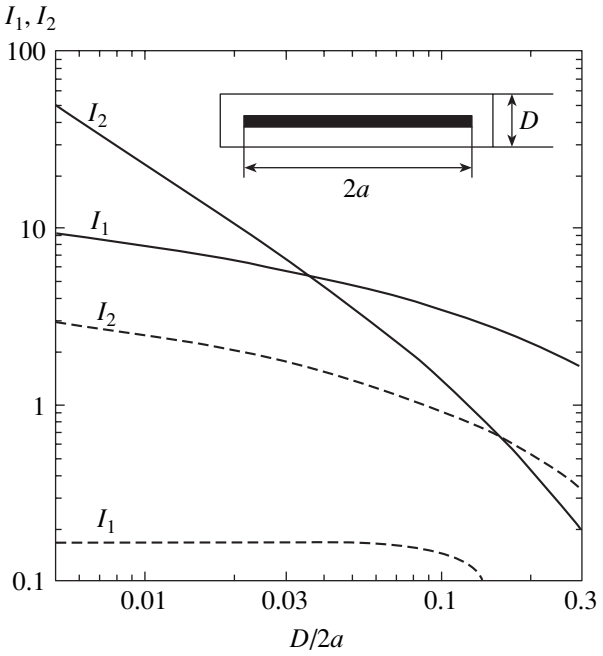

Fig. 3. Dependences of parameters I_1 and I_2 determining the values of H_j and σ (see formulas (18) and (21)) on the diameter-to-length ratio $D/2a$ of the grains. Dashed curves correspond to the case when the axes of the grains lie in the plane of the system, while solid curves correspond to the situation when the axes of the grains are perpendicular to this plane.

Parameters I_1 and I_2 for a 2D system have a finite value only provided that the grains do not touch one another.[4] Formally, this means that integration in relations (19) should be carried out over the domain in which points are separated from the surface of a rodlike grain by a distance longer than grain diameter D (see the inset to Fig. 3). The result of the integration naturally depends on the diameter-to-length ratio $D/2a$ of the grains.

Two cases should be distinguished: parallel axes of the grains (i) lie in the plane of the system or (ii) are perpendicular to this plane (this situation was analyzed in [6, 7]). In the latter case, all angles $\alpha = \pi/2$ and there is no need to integrate with respect to α. Figure 3 shows the corresponding dependences of parameters I_1 and I_2 on ratio $D/2a$.

[4] Otherwise, distribution function $F(j, H_3)$ loses its Gaussian shape and acquires long wings described by a power rather than the exponential law.

In the first case, numerical calculations yield $I_1 \lesssim 0.2 \ll 1$ (i.e., the Gaussian distribution (10) is almost symmetric relative to $H_3 = 0$) and $I_2 \lesssim 3$. The rodlike shape of the grains means that their length $2a$ is an order of magnitude (or more) larger than their diameter D, which gives $\Delta\Theta \lesssim 10^{-3}naD$. For this reason, $\Delta\Theta \lesssim 2 \times 10^{-4}$ even for a high grain concentration of $2naD \sim 0.5$ (the grains cover 50% of the surface). This means that the interaction between grains noticeably affects the magnetization relaxation in the system only at very low temperatures in this case.

In the second case, for $D/a \lesssim 0.02$, parameter $I_2 \gtrsim 10$ and is an order of magnitude larger than in the first case. This corresponds to a much stronger spread in random fields (a broader relaxation function $F(j, H_3)$) and a considerable elevation in the effective temperature in accordance with relation (21). Thus, the interaction of nanograins in a random 2D system considerably affects the relaxation of its magnetization, but only in a system of the second type (magnetic moments of the grains are perpendicular to the plane of the system).

3. CONCLUSIONS

In the framework of the generalized mean field approximation accounting for spatial fluctuations of the local magnetic field, it is shown that the collective effect of the dipole interaction in a random 3D system of identical (rodlike) magnetic nanoparticles with parallel easy magnetization axes leads to a displacement of the relaxation magnetization curves towards shorter times (i.e., it accelerates the relaxation process). The systems where the mean value of the local magnetic field differs from zero exhibit a negative feedback: relaxation is slowed down upon a decrease in the average magnetization. These conclusions agree with the results obtained in [6, 7] taking into account local field fluctuations in a regular system. At the same time, the results contradict the opinion that the interaction always increases the effective height of energy barriers (2) and, hence, slows down the relaxation.

As regards a random 2D system, the interaction of nanograins affects the relaxation of its magnetization only when the magnetic moments of the grains are perpendicular to the plane of the system, i.e., in the situation analyzed in [6, 7].

ACKNOWLEDGMENTS

This study was supported by the Russian Foundation for Basic Research (project nos. 03-02-17029 and 02-02-16974).

REFERENCES

1. J. L. Dormann, D. Fiorani, and E. Tronc, J. Magn. Magn. Mater. **202**, 251 (1999).
2. S. L. Ginzburg, *Irreversible Processes in Spin Glasses* (Nauka, Moscow, 1989).
3. E. Z. Meĭlikhov, Zh. Éksp. Teor. Fiz. **117**, 1136 (2000) [JETP **90**, 987 (2000)].
4. V. V. Rylkov, B. A. Aronzon, A. B. Davydov, *et al.*, Zh. Éksp. Teor. Fiz. **121**, 908 (2002) [JETP **94**, 779 (2002)].
5. D. K. Lottis, R. M. White, and E. Dan Dahlberg, Phys. Rev. Lett. **67**, 362 (1991).
6. S. I. Denisov and K. N. Trohidou, Phys. Rev. B **64**, 184433 (2001).
7. S. I. Denisov, T. V. Lyutyy, and K. N. Trohidou, Phys. Rev. B **67**, 014411 (2003).
8. H.-B. Braun, Phys. Rev. Lett. **71**, 3557 (1993).
9. M. Lederman, S. Shulz, and M. Ozaki, Phys. Rev. Lett. **73**, 1986 (1994).
10. L. Néel, Ann. Geophys. (C.N.R.S.) **5**, 99 (1949).
11. C. Kittel, *Introduction to Solid State Physics*, 7th ed. (Wiley, New York, 1996; Nauka, Moscow, 1978).
12. H. Mueller, Phys. Rev. **47**, 947 (1935).
13. H. Mueller, Phys. Rev. **50**, 547 (1936).
14. E. Z. Meĭlikhov and R. M. Farzetdinova, Zh. Éksp. Teor. Fiz. **122**, 1027 (2002) [JETP **95**, 886 (2002)].
15. E. Z. Meĭlikhov, Zh. Éksp. Teor. Fiz. **124**, 650 (2003) [JETP **97**, 587 (2003)].
16. E. Z. Meĭlikhov and R. M. Farzetdinova, Zh. Éksp. Teor. Fiz. **124**, 656 (2003) [JETP **97**, 593 (2003)].
17. A. Aharoni, IEEE Trans. Magn. **23**, 1853 (1987).
18. Vik. S. Dotsenko, Usp. Fiz. Nauk **165**, 481 (1995) [Phys. Usp. **38**, 457 (1995)].
19. R. G. Palmer, D. L. Stein, E. Abrahams, and P. W. Anderson, Phys. Rev. Lett. **53**, 958 (1984).

Translated by N. Wadhwa

Journal of Experimental and Theoretical Physics, Vol. 98, No. 6, 2004, pp. 1205–1213.
Translated from Zhurnal Éksperimental'noĭ i Teoreticheskoĭ Fiziki, Vol. 125, No. 6, 2004, pp. 1375–1384.

SOLIDS
Electronic Properties

Screening and Rearrangement of Excitonic States in Double Layer Systems

D. V. Kulakovskiĭ[a] and Yu. E. Lozovik[b]

[a]*Institute of Solid State Physics, Russian Academy of Sciences, Chernogolovka, Moscow oblast, 142432 Russia*
[b]*Institute of Spectroscopy, Russian Academy of Sciences, Troitsk, Moscow oblast, 142092 Russia*
e-mail: kulakovd@issp.ac.ru, lozovik@isan.troitsk.ru

Received September 23, 2003

Abstract—Screening and rearrangement of excitonic states in double layer systems were considered. Binding energy changes as a result of screening by spatially separated electrons were calculated for both direct and spatially indirect excitons. The critical electron concentrations at which screening effects cause a sharp decrease in the exciton binding energy and an increase in the exciton radius depending on the interlayer distance were determined. For a spatially indirect exciton, this dependence had a maximum caused by the competition of two effects as the interlayer distance grew, namely, a decrease in the seed interaction between electrons and holes and a weakening of the effect of hole screening by spatially separated electrons. The effect of spatially separated electron–exciton drag in a double layer system was studied in the Debye–Hückel approximation taking into account screening of interlayer electron–exciton interaction. © *2004 MAIK "Nauka/Interperiodica".*

1. INTRODUCTION

Advances in the technology for growing semiconducting heterostructures allowed high-quality samples with closely spaced parallel electron and (or) hole two-dimensional channels to be prepared. One of the examples of such structures is double quantum wells, in which two interacting electron–electron or electron–hole layers are separated by a barrier of width D. Currently, double quantum well systems attract much attention of researchers [1–10], in particular, in view of predicted superfluidity in such systems [11], quasi-Josephson phenomena [11, 12], and unusual properties in strong magnetic fields (see [13] and the references therein). It has also been predicted that interlayer electron–electron interaction should strongly influence the energy spectrum of electrons in both integer and fractional quantum Hall effects [14, 15], cause the appearance of fractions with even denominators [16], and increase the stability of the Wigner crystal state [17]. Moreover, spatially separated electrons and holes can form bound states, or indirect excitons. Such a system was found to have a fairly rich phase diagram (e.g., see [18]). Excitons with spatially separated electrons and holes can experience the transition to the liquid phase in a certain region of parameters, and the crystallization of indirect electrons could occur in a certain intermediate region of lower electron and hole concentrations [18]. Accordingly, the spectrum of collective excitations of double quantum wells is modified compared with the spectrum of collective excitations of a single quantum well.

An important feature of the "two-component" system that we are considering is the screening of excitons by electrons and/or holes, which causes a decrease in their binding energy and an increase in their radius. As follows from experimental data and theoretical calculations, the exciton luminescence line sharply disappears at some critical electron gas concentration [19, 20]. As the disappearance of the excitonic line is also observed for a very rarefied excitonic system, the problem actually reduces to studying the "jump" disappearance of an isolated excitonic state as the concentration of electrons grows (as distinct from the Mott dielectric–metal transition in a purely excitonic system that occurs when the density of the system increases). We address this problem in Sections 2 and 3.

Systems of quasi-two-dimensional excitons that coexist with electrons in the same [19] or a spatially separated layer (see [2, 6, 7] and the references therein) are of interest because of possible observation of drag effects. These effects could be used, first, to analyze excitonic systems by measuring the transport properties of electrons and, secondly, to control excitons by means of electron transport [21]. For this reason, one of the problems considered in Section 4 is that of the drag coefficient of spatially separated excitons and electrons.

2. THE REARRANGEMENT OF A DIRECT EXCITON IN A SYSTEM OF SPATIALLY SEPARATED EXCITONS AND ELECTRONS

Let there by two quantum wells of equal widths l_0 with infinitely high walls spaced D apart. One of these contains excitons whose concentration is N_{exc}, and the

other, electron gas with concentration N_s. We ignore tunneling between the two wells. The effect of screening by the electron gas will be included in the approximation of chaotic phases. Suppose that $N_{exc} \ll N_s$; we can then formulate the problem of screening of a single exciton. In order to study this effect, let us calculate the exciton binding energy as a function of the concentration N_s of the quasi-two-dimensional electron gas at various distances between the quantum wells. We will use the variational method for self-consistently calculating the energy of the exciton ground state in the quantum well.

Below, we consider GaAs/AlGaAs quantum wells. In the region of low momenta (low momenta give the major contribution to the effects under study), the splitting of the energy levels that correspond to light and heavy holes in a quantum well is fairly large, and we can therefore restrict ourselves to a consideration of a bound state on a heavy hole; the dispersion of a heavy hole in the region of low momenta of interest to us is quadratic. Bound electron states on light holes lie substantially higher in energy, and their binding energy is substantially lower; these states are for this reason of no interest to us. Calculations will be performed for the effective mass of the electron in the quantum well plane $m_e = 0.067m_0$, the effective mass of the hole in the quantum well plane $m_h = 0.26m_0$ (here, m_0 is the mass of the free electron), and static permittivity $\epsilon = 12.86$ [22]. Consider an exciton situated in the first quantum well. After separating the coordinates of the center of gravity, which describe motion over the plane of quantum wells, the Hamiltonian takes the form

$$H = -\frac{\hbar^2}{2\mu^*}\Delta + U(r, z_e, z_h), \tag{1}$$

where

$$U(r, z_e, z_h) = -\frac{e^2}{\epsilon\sqrt{r^2 + (z_e - z_h)^2}} + u(z_e, z_h). \tag{2}$$

Here, $\mu^* = m_e m_h/(m_e + m_h)$ is the reduced mass of the exciton; $u(z_e, z_h) = u(z_e) + u(z_h)$; $u(z_i)$ is the quantum well confining potential,

$$u(z_i) = 0, \quad z_i \le |l_0/2|,$$
$$u(z_i) = \infty, \quad z_i > |l_0/2|;$$

r is the coordinate of relative motion over the plane of quantum wells; and z_e and z_h are the coordinates of the motions of the electron and hole in the direction of quantum well growth.

As has been mentioned, the ground state energy will be determined by the variational method with the trial wave function (also see [20])

$$\Psi(r, z_e, z_h) = N\cos\left(\frac{\pi z_e}{l_0}\right)\cos\left(\frac{\pi z_h}{l_0}\right) \times \exp\left(-\frac{\sqrt{r^2 + \gamma^2(z_e - z_h)^2}}{r_0}\right), \tag{3}$$

where γ and r_0 are the variational parameters.

The condition that the distance between excitonic levels should be much smaller than the characteristic energy $\pi^2\hbar^2/2m_{e(h)}l_0^2$ of the dimensional quantization of the electron (hole) in the quantum well is sufficient for the adiabatic approximation to be applicable to this problem. For this reason, averaging the interaction potential along the direction of quantum well growth yields the effective potential

$$U_{eff}(r) = \int |\Psi(r, z_e, z_h)|^2 U(r, z_e, z_h) dz_e dz_h. \tag{4}$$

The Fourier transform of this potential is

$$U_{eff}(q) = \iint e^{i\mathbf{q}\cdot\mathbf{r}} U_{eff}(r) d\mathbf{r} = 2\pi\int J_0(qr) U_{eff}(r) r dr, \tag{5}$$

where $J_0(x)$ is the Bessel function of the first kind. Consider the screening of the effective interaction potential between an electron and a hole in one layer by spatially separated quasi-two-dimensional electrons. The corresponding equation written in the momentum representation has the form

$$U_{eff}^{scr}(q) = U_{eff}(q) + U_{12}(q)(\Pi + \Pi U_{22}(q)\Pi + \ldots)U_{12}(q) = U_{eff}(q) + \frac{U_{12}(q)\Pi U_{12}(q)}{1 - U_{22}(q)\Pi}, \tag{6}$$

where $U_{22}(q)$ is the Fourier transform[1] of the electron–electron interaction potential in the second layer,

$$U_{22}(r) = \left\langle \phi_e(z + D)\left|e^2/\sqrt{r^2 + (z + D)^2}\right|\phi_e(z + D)\right\rangle;$$

$U_{12}(q)$ is the Fourier transform of the interlayer electron–hole interaction potential,

$$U_{12}(r) = \left\langle \phi_h(z)\left|-e^2/\sqrt{r^2 + (z + D)^2}\right|\phi_e(z + D)\right\rangle;$$

[1] As in (5), $f(q) = 2\pi\int J_0(qr) f(r) r dr$.

Π is the polarization operator in the approximation of chaotic phases at $T = 0$ [23, 24],

$$\Pi = -\frac{m_e}{\pi\hbar^2}\left[1 - \Theta(q - 2k_F)\sqrt{1 - \frac{(2k_F)^2}{q^2}}\right];$$

$k_F = \sqrt{2\pi N_s}$ is the Fermi wave vector; and

$$\phi_e(z) = \phi_h(z) = \sqrt{\frac{2}{l_0}}\cos\left(\frac{\pi z}{l_0}\right)$$

represents the wave functions of the free electron and hole in the z direction. The second term in (6) describes the change in effective interaction $U_{\text{eff}}^{\text{scr}}(q)$ caused by static Lindhard screening by the electron gas contained in the second quantum well. Note that the potential $U_{12}(q)$ tends to zero and $U_{\text{eff}}^{\text{scr}}(q) \longrightarrow U_{\text{eff}}(q)$ as the distance between the quantum wells increases.

The ground state energy of the quasi-two-dimensional exciton is the minimum of the functional

$$F = \left\langle \Psi(r, z_e, z_h)\left|-\frac{\hbar^2}{2\mu}\Delta\right|\Psi(r, z_e, z_h)\right\rangle + \langle U_{\text{eff}}^{\text{scr}}(r)\rangle \quad (7)$$

with respect to the variational parameters r_0 and γ.

Subsequent calculations of the ground state energy and thence the exciton binding energy were performed numerically. The calculations for $l_0 = 300$ Å gave the critical parameters r_s^c at which the binding energy decreased e times (as in [20]) at various distances between the quantum wells. The corresponding dependence is shown in Fig. 1. For $D \longrightarrow 0$, when the two-dimensional electron gas is closest to the exciton, the threshold concentration is on the order of 2×10^{10} cm^{-2}. This value is much larger than that obtained for a single quantum well in [20]. The substantial difference in the threshold concentrations arises because the problem should be solved taking into account a nonlinear system response for a single well and a linear response for double wells. Let us clarify this point.

In a single well, the interaction between the screening quasi-two-dimensional electron gas and the hole equals the interaction between the hole and the electron that forms the exciton. As a result, we have an integral equation with respect to the screened effective potential. If the exciton and electron gas are spatially separated, a change in the interaction between the bound hole and electron does not cause a change in the interaction potential between the screening quasi-two-dimensional electron gas in one quantum well and the hole in the other.[2] It follows that we deal with a linear problem, which is similar to that considered in [25] when $D \longrightarrow 0$.

[2] Recall that we ignore tunneling in the system.

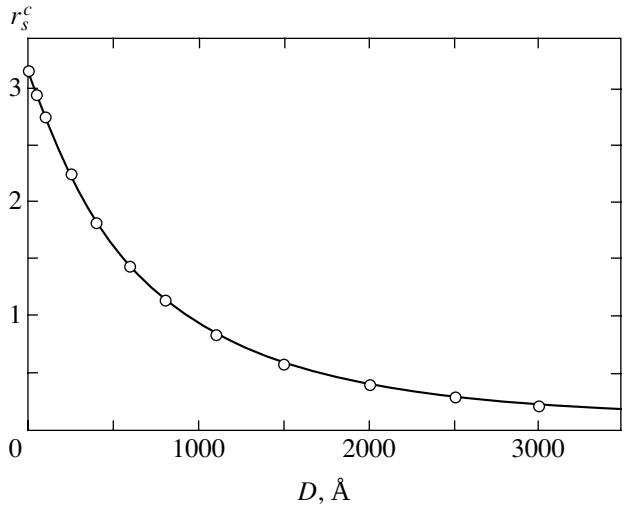

Fig. 1. Dependence of critical parameter r_s^c at which the collapse of the excitonic state in a GaAs/AlGaAs quantum well of width 300 Å occurs on distance D between quantum wells.

As has been mentioned above, the screening effect weakens as the distance between the quantum wells grows and disappears as $D \longrightarrow \infty$.

The problem of the finiteness of the quantum well barrier should be considered separately. In real GaAs/AlGaAs systems, the barrier height is about 360 meV. This value is several orders of magnitude higher than the exciton binding energy. The corresponding effect is therefore of importance for very narrow quantum wells, when the size of the exciton[3] is much larger than the quantum well width. The exciton can then be outside the well most of the time (e.g., see [26]). The screening effects and bound state rearrangement should then be studied taking into account the penetration of the wave function below the barrier. If $l_0 \geq 200$ Å, the influence of the barrier on the excitonic wave function is insignificant, and taking into account a finite barrier height yields energy corrections less than 5%. This shows that the model under consideration is a good approximation for studies of this kind.

3. SCREENING OF INTERLAYER EXCITONS

Let us turn to the problem of spatially indirect excitons. Let two layers[4] be situated at distance D from each other. One layer contains a hole gas of concentration N_h, and the other, an electron gas. Tunneling between the layers is ignored. Suppose that $N_h \ll N_s$ and $N_h a_B^2 \ll 1$, where a_B is the exciton Bohr radius. For these conditions, we can formulate the problem of

[3] The Bohr radius of the exciton is on the order of 100 Å.

[4] To simplify numerical calculations, we consider a purely two-dimensional case, because the small layer thickness is of no significance for the effect under consideration.

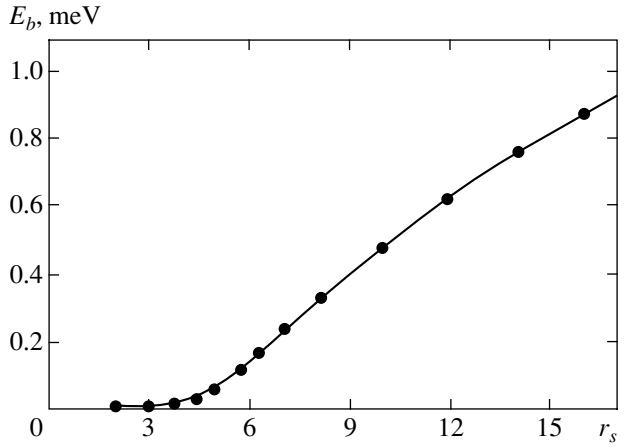

Fig. 2. Binding energy E_b of a spatially indirect exciton in a double layer system based on GaAs/AlGaAs with a 200 Å interlayer distance as a function of dimensionless parameter r_s in the approximation of chaotic phases (T = 0 K).

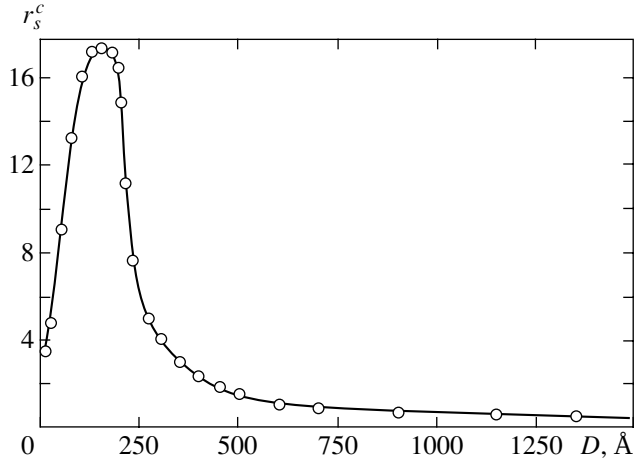

Fig. 3. Dependence of critical parameter r_s^c at which the collapse of a spatially indirect excitonic state occurs on interlayer distance D: $r_0 \longrightarrow a_B = \hbar^2\epsilon/2\mu e^2$, $\gamma = \text{const}/D$ ($D < r_0$), $r_0 = \text{const} \cdot D$, and $\gamma \longrightarrow 1$ at large D.

screening of a single spatially indirect exciton. The effect of screening by the electron gas will as previously be included in the approximation of chaotic phases. The screened interaction potential can then be written in the momentum representation in the form (e.g., see [24])

$$U^{\text{scr}}(q) = \frac{U_{12}(q)}{1 - U_{22}(q)\Pi}, \tag{8}$$

where

$$U_{22}(q) = \frac{2\pi e^2}{\epsilon q}, \quad U_{12}(q) = -\frac{2\pi e^2}{\epsilon q} e^{-qD}.$$

The Hamiltonian of the spatially indirect exciton has the form

$$\hat{H} = -\frac{\hbar^2}{2\mu}\Delta + U^{\text{scr}}(r), \tag{9}$$

where $U^{\text{scr}}(r)$ is the Fourier transform of the $U^{\text{scr}}(q)$ potential (see Footnote 1). The ground state energy of the spatially indirect exciton is found by minimizing the energy functional for the wave function

$$\Psi_{\text{ind}}(r) = N\exp\left(-\frac{\sqrt{r^2 + \gamma^2 D^2}}{r_0}\right) \tag{10}$$

with respect to the r_0 and γ parameters.

The binding energy of a spatially indirect exciton calculated for D = 200 Å as a function of dimensionless parameter r_s is shown in Fig. 2. The r_s parameter describes the mean distance between the electrons in the gas in Bohr radius a_B units, $r_s = (a_B\sqrt{2\pi N_s})^{-1}$. The figure shows that the bound state experiences a rearrangement similar to that in a single quantum well. Note that the rearrangement under consideration is smoother, which, like the existence of bound states at arbitrary quasi-two-dimensional electron gas concentrations, is caused by the purely two-dimensional character of the interaction potential.

On the other hand, because of the existence of many experimental works performed for structures with different interlayer distances [1, 2, 6, 7], the behavior of the bound state depending on distance D is of interest. The dependence of the critical parameter r_s^c on the distance between spatially separated electrons and holes is shown in Fig. 3. An unexpected and very intriguing behavior related to a change in the wave function of the spatially indirect exciton even when it is not screened is observed. For instance, the equations for the variational parameters in the region of small D values ($D < r_0$) take the form

$$r_0 \longrightarrow a_B = \frac{\hbar^2\epsilon}{2\mu e^2}, \quad \gamma = \frac{\text{const}}{D}$$

as $N_s \longrightarrow 0$. In the absence of screening, the binding energy of the spatially indirect exciton tends to the binding energy of the two-dimensional direct exciton as $D \longrightarrow 0$. Nevertheless, the presence of a growing γ parameter is indicative of different behaviors of the spatially indirect and two-dimensional direct excitons, and this difference is responsible for substantial differences in the effectiveness of screening of these bound states. At large D, the variational parameters behave as (see Fig. 3)

$$r_0 = \text{const} \cdot D, \quad \gamma \longrightarrow 1,$$

and the $r_s^c = r_s^c(D)$ dependence has a maximum at $r_0^{scr} \approx D$, where the transition from one region to the other occurs.[5]

Another question that we considered in detail was the influence of finite layer thicknesses in the z direction. Calculations by the numerical relaxation method (e.g., see [27]) show that this complication of the problem only results in the renormalization of the distance between spatially separated electrons and holes,

$$D_{\text{eff}} = D + \frac{\langle z_e \rangle}{2} + \frac{\langle z_h \rangle}{2}$$

($\langle z_{e,h} \rangle$ is the coordinates of the electron and hole averaged over the wave function), and does not give new physical effects. This result is, however, important for comparatively estimating experimental data on the binding energy of spatially indirect excitons and the effectiveness of indirect Coulomb interaction.

4. EXCITON-ELECTRON DRAG IN A DOUBLE LAYER SYSTEM

In this and the next sections, we discuss drag effects. Let us consider a double layer structure in which, in one of the layers indexed 1, excitons with density inhomogeneity are created by a laser (for instance, by using a mask opaque to laser radiation, focusing, etc.). The other layer indexed 2 contains electron gas of density n_2. Tunneling is ignored. Our goal is to calculate the response of the system of excitons to an external electric field applied to the system of electrons.

The exciton mass flux $\mathbf{i} = m_1 n_1 \mathbf{v}_1$ and the electron charge flux $\mathbf{j} = -en_2\mathbf{v}_2$ in the double layer system of electrons and excitons can be written via the exciton concentration gradient ∇n_1 and external electric field $\mathbf{E}_2$ applied to the electronic subsystem as

$$\mathbf{J} = \hat{K}\mathbf{S}, \tag{11}$$

where

$$\mathbf{J} = \begin{pmatrix} \mathbf{i}_1 \\ \mathbf{j}_2 \end{pmatrix}, \quad \hat{K} = \begin{pmatrix} -m_1 D_{11} & -n_1 m_1 \mu_{12} \\ e m_1 D_{21}/m_2 & e n_2 \mu_{22} \end{pmatrix},$$

$$\mathbf{S} = \begin{pmatrix} \nabla n_1 \\ \mathbf{E}_2 \end{pmatrix},$$

D_{11} is the exciton diffusion coefficient, D_{21} is the interdiffusion coefficient of excitons and electrons, μ_{12} is the mutual mobility (drag) coefficient of excitons and electrons, and μ_{22} is the coefficient of mobility of electrons.

Note that the D_{11} and μ_{22} coefficients (like D_{21} and μ_{12}) in the double layer system that we are considering take into account the interaction between electrons and excitons.

If $\nabla n_1 = 0$, the exciton flux is

$$\mathbf{i}_1 = -n_1 m_1 \mu_{12} \mathbf{E}_2. \tag{12}$$

As follows from (12), the velocity of excitons is then

$$\mathbf{v}_1 = -\mu_{12}\mathbf{E}_2. \tag{13}$$

Let us calculate the velocity that excitons acquire as a result of their interaction with electrons. The kinetic equations then take the form

$$\frac{\partial f_1}{\partial \mathbf{r}_1}\mathbf{v}_1 = I_1 + I_{12}, \tag{14}$$

$$\frac{\partial f_2}{\partial \mathbf{r}_2}\mathbf{v}_2 + \frac{\partial f_2}{\partial \mathbf{p}_2}\dot{\mathbf{p}}_2 = I_2 + I_{21}, \tag{15}$$

where I_1 is the collision integral that takes into account all exciton scattering processes, including exciton scattering by electrons; $\mathbf{p}_2$ is the momentum of electrons; and I_{12} is the collision integral that takes into account exciton scattering by electrons. As macroscopic forces do not act on excitons, the term $(\partial f_1/\partial \mathbf{p}_1)\dot{\mathbf{p}}_1$ in (14) is zero ($\mathbf{p}_1$ is the momentum of excitons).

To simplify (14) and (15), we assume that the current of electrons is uniform and the collision integral I_{21} is a small addition to I_2 and can be ignored in (15). In addition, our only interest is the drag velocity v_{drag}, which is assumed to predominate over the velocity of diffusion v_{diff}. We can then omit the term containing the derivative of f_1 with respect to the coordinate in (14). These simplifications yield

$$I_1 + I_{12} = 0, \tag{16}$$

$$\frac{\partial f_2}{\partial \mathbf{p}_2}\dot{\mathbf{p}}_2 = I_2. \tag{17}$$

As usual, (17) is linearized by representing f_2 in the form

$$f_2 = f_2^0 + f_2^0(1 - f_2^0)\psi_2, \tag{18}$$

where f_2^0 is the Fermi function satisfying the normalization condition

$$n_2 = 2\int f_2^0 \frac{d\mathbf{p}_2}{(2\pi\hbar)^2}. \tag{19}$$

[5] Here, r_0^{scr} is the radius of the screened spatially indirect exciton at the quasi-two-dimensional electron gas concentration that corresponds to the critical r_s^c parameter at given D.

Using the τ-approximation to I_2, we obtain

$$\psi_2 = -\frac{\tau_2}{m_2 k_B T} e\mathbf{E}_2 \cdot \mathbf{p}_2. \quad (20)$$

Here, $\mathbf{E}_2 = \{E_2, 0\}$ is the external electric field strength and τ_2 is the relaxation time of electrons.

Let us write (16) in more detail,

$$I_1 = -\sum_{\sigma_2, \sigma_{2'}} \int w\{ f_{1'}, f_{2'}(1 + f_1)(1 - f_2) - f_1 f_2 (1 + f_{1'})(1 - f_{2'})\} \times \delta(\varepsilon_1 + \varepsilon_2 - \varepsilon_{1'} - \varepsilon_{2'}) \frac{d\mathbf{p}_{1'}}{(2\pi\hbar)^2} \frac{d\mathbf{p}_2}{(2\pi\hbar)^2}, \quad (21)$$

where $w(\mathbf{p}_1\mathbf{p}_2; \mathbf{p}_{1'}\mathbf{p}_{2'}) = (2\pi/\hbar)|W(q)|^2$ is the probability of exciton scattering by an electron in the Born approximation ($\mathbf{q} = \mathbf{p}_{2'} - \mathbf{p}_2$) and $W(q)$ is the Fourier transform of the effective exciton–electron interaction energy (see Section 5). We will use f_1 in the form

$$f_1 = f_1^0 + f_1^0(1 + f_1^0)\psi_1, \quad (22)$$

where f_1^0 is the Bose function with the chemical potential $\mu = \mu(n_{10}) = \mu_0$ normalized as

$$n_{10} = \int f_1^0 \frac{d\mathbf{p}_1}{(2\pi\hbar)^2}. \quad (23)$$

Substituting f_1 given by (22), f_2 given by (18), and $I_1 = -(f_1 - f_1^0)/\tau_1$ (τ_1 is the relaxation time of excitons) into (21) yields the linearized equation

$$f_1^0(1 + f_1^0)\psi_1 = 2\tau_1 \int w\{ f_1^0 f_2^0 (1 + f_{1'}^0)(1 - f_{2'}^0)\} \times (\psi_{1'} + \psi_{2'} - \psi_1 - \psi_2) \times \delta(\varepsilon_1 + \varepsilon_2 - \varepsilon_{1'} - \varepsilon_{2'}) \frac{d\mathbf{p}_{1'}}{(2\pi\hbar)^2} \frac{d\mathbf{p}_2}{(2\pi\hbar)^2}. \quad (24)$$

The condition $v_{\text{diff}} \ll v_{\text{drag}}$ allows the ψ_1 and $\psi_{1'}$ terms in the integrand in (24) to be ignored.

The equation for the drag velocity takes the form

$$v_{\text{drag}} = \frac{1}{m_1 n_{10}} \int p_{1x} f_1^0 (1 + f_1^0)\psi_1 \frac{d\mathbf{p}_1}{(2\pi\hbar)^2}. \quad (25)$$

Let us write the equation for v_{drag} [see (13)] in the form

$$v_{\text{drag}} = -\mu_{12} E_2. \quad (26)$$

Taking into account equalities (24) and (25) yields μ_{12} in the form

$$\mu_{12} = \frac{2e\tau_1\tau_2}{m_1 m_2 n_{10} k_B T} \times \int w f_1^0 f_2^0 (1 + f_{1'}^0)(1 - f_{2'}^0) p_{1x}(p_{2'x} - p_{2x}) \times \delta(\varepsilon_1 + \varepsilon_2 - \varepsilon_{1'} - \varepsilon_{2'}) \frac{d\mathbf{p}_1}{(2\pi\hbar)^2} \frac{d\mathbf{p}_{1'}}{(2\pi\hbar)^2} \frac{d\mathbf{p}_2}{(2\pi\hbar)^2}. \quad (27)$$

After certain transformations of (27), the coefficient of mutual mobility μ_{12} can be written as

$$\mu_{12} = \frac{1}{8\pi^2} \frac{\tau_1\tau_2}{m_1 m_2 n_{10} \hbar^2} \frac{e}{k_B T} \times \int_0^\infty dq \int_{-\infty}^\infty d\omega W^2(q) q^3 \frac{\text{Im}\chi^B(q, \omega)\text{Im}\chi^F(q, \omega)}{\sinh^2(\hbar\omega/2k_B T)}, \quad (28)$$

where

$$\chi^B(q, \omega) = -\int \frac{f^0(\varepsilon_1) - f^0(\varepsilon_{1'})}{\varepsilon_1 - \varepsilon_{1'} + \hbar\omega + i\delta} \frac{d\mathbf{p}_1}{(2\pi\hbar)^2}, \quad (29)$$

$$\chi^F(q, \omega) = -\int \frac{f^0(\varepsilon_2) - f^0(\varepsilon_{2'})}{\varepsilon_2 - \varepsilon_{2'} + \hbar\omega + i\delta} \frac{d\mathbf{p}_2}{(2\pi\hbar)^2}. \quad (30)$$

If the parameters of the system are such that the distribution of excitons and electrons is Boltzmann (the classical case), a simpler equation for μ_{12} follows from (28), namely,

$$\mu_{12} = \frac{\tau_1\tau_2}{4\sqrt{2\pi}} \frac{e n_2}{m_1 m_2} \sqrt{\mu} (k_B T)^{-3/2} \times \int_0^\infty W^2(q) q^2 \exp\left(-\frac{q^2\hbar^2}{8\mu k_B T}\right) dq. \quad (31)$$

5. THE SCREENING OF THE DRAG EFFECT

Lastly, we turn to calculations of the screening of two-dimensional polarization (electron–dipole) interaction, which causes the drag of two-dimensional excitons by spatially separated electron gas. The effective interaction energy in the double layer system will be calculated using the self-consistent approximation. If

the exciton radius is much smaller than the distance between the electron and exciton, the interaction energy between the isolated electron and exciton has the form (see [21])

$$V_{\text{e-ex}}(\mathbf{r}_1 - \mathbf{r}_2, D) = -\frac{\gamma}{[(\mathbf{r}_1 - \mathbf{r}_2)^2 + D^2]^2},$$

where $\gamma = \alpha e^2/2\epsilon$, α is the polarizability of the two-dimensional exciton in the ground state, D is the distance between layers, $|\mathbf{r}_1 - \mathbf{r}_2|$ is the distance between the exciton and electron along layers, and ϵ is the medium permittivity. The equation for the effective interaction energy in a many-particle electron–exciton system will be derived on the assumption that exciton–exciton interaction is negligibly weak compared with electron–exciton interaction and can therefore be ignored. Let us place trial charge $-e$ into the electronic subsystem at the origin. The linearized kinetic equations for the distribution functions of excitons and electrons have the form

$$\frac{\partial f_1}{\partial \mathbf{r}_1}\mathbf{v}_1 + \frac{\partial f_1^0}{\partial \mathbf{p}_1}\dot{\mathbf{p}}_1 = 0, \tag{32}$$

$$\frac{\partial f_2}{\partial \mathbf{r}_2}\mathbf{v}_2 + \frac{\partial f_2^0}{\partial \mathbf{p}_2}\dot{\mathbf{p}}_2 = 0, \tag{33}$$

where

$$\dot{\mathbf{p}}_1 = -\frac{\partial}{\partial \mathbf{r}_1}W(\mathbf{r}_1, D), \quad \dot{\mathbf{p}}_2 = -\frac{\partial}{\partial \mathbf{r}_2}W(\mathbf{r}_2, 0).$$

The interaction energies $W(\mathbf{r}, 0)$ and $W(\mathbf{r}, D)$ obey the equations

$$W(\mathbf{r}, 0) = \int \frac{e^2\rho_2(\mathbf{r}')}{\epsilon|\mathbf{r} - \mathbf{r}'|}d\mathbf{r}' - \int \frac{\gamma\rho_1(\mathbf{r}')}{[(\mathbf{r} - \mathbf{r}')^2 + D^2]^2}d\mathbf{r}' + \frac{e^2}{\epsilon r}, \tag{34}$$

$$W(\mathbf{r}, D) = -\int \frac{\gamma\rho_2(\mathbf{r}')}{[(\mathbf{r} - \mathbf{r}')^2 + D^2]^2}d\mathbf{r}' - \frac{\gamma}{(r^2 + D^2)^2}, \tag{35}$$

where

$$\rho_1(\mathbf{r}) = \int f_1(\mathbf{r}, \mathbf{p})\frac{d\mathbf{p}}{(2\pi\hbar)^2},$$

$$\rho_2(\mathbf{r}) = 2\int f_2(\mathbf{r}, \mathbf{p})\frac{d\mathbf{p}}{(2\pi\hbar)^2}.$$

Passing to Fourier components in (32)–(35) (we assume that $\mathbf{k} = \{k, 0\}$) yields

$$f_1(\mathbf{k}, \mathbf{p}) = \frac{1}{v_{1x}}\frac{\partial f_1^0}{\partial p_{1x}}W(\mathbf{k}, D), \tag{36}$$

$$f_2(\boldsymbol{k}, \mathbf{p}) = \frac{1}{v_{2x}}\frac{\partial f_2^0}{\partial p_{2x}}W(\mathbf{k}, 0), \tag{37}$$

where f_1^0 is the Bose function, f_2^0 is the Fermi function,

$$W(\mathbf{k}, 0) = \frac{4\pi e^2}{\epsilon k}\int f_2(\mathbf{k}, \mathbf{p})\frac{d\mathbf{p}}{(2\pi\hbar)^2} - \gamma F(\mathbf{k}, D)\int f_1(\mathbf{k}, \mathbf{p})\frac{d\mathbf{p}}{(2\pi\hbar)^2} + \frac{2\pi e^2}{\epsilon k}, \tag{38}$$

$$W(\mathbf{k}, D) = -2\gamma F(\mathbf{k}, D)\int f_2(\mathbf{k}, \mathbf{p})\frac{d\mathbf{p}}{(2\pi\hbar)^2} - \gamma F(\mathbf{k}, D), \tag{39}$$

$F(\mathbf{k}, D) = (\pi k/D)K_1(kD)$, and $K_1(z)$ is the Macdonald function.

Using (36)–(39), we obtain a system of two algebraic equations for determining $W(k, 0)$ and $W(k, D)$,

$$W(k, 0) = \frac{2\pi e^2}{\epsilon k}\beta_2 W(k, 0) - \gamma\beta_1 F(k, d)W(k, D) + \frac{2\pi e^2}{\epsilon k}, \tag{40}$$

$$W(k, D) = -\gamma\beta_2 F(k, D)W(k, 0) - \gamma F(k, D), \tag{41}$$

where

$$\beta_1 = \int \frac{\partial f_1^0}{\partial p_x}\frac{1}{v_x}\frac{d\mathbf{p}}{(2\pi\hbar)^2},$$

$$\beta_2 = 2\int \frac{\partial f_2^0}{\partial p_x}\frac{1}{v_x}\frac{d\mathbf{p}}{(2\pi\hbar)^2}. \tag{42}$$

If f_1^0 and f_2^0 are Boltzmann distributions, then

$$\beta_1 = -\frac{n_{10}}{k_B T}, \quad \beta_2 = -\frac{n_2}{k_B T}, \tag{43}$$

and if f_2^0 is a Fermi step, then

$$\beta_2 = -\frac{m_2}{\pi\hbar^2}. \tag{44}$$

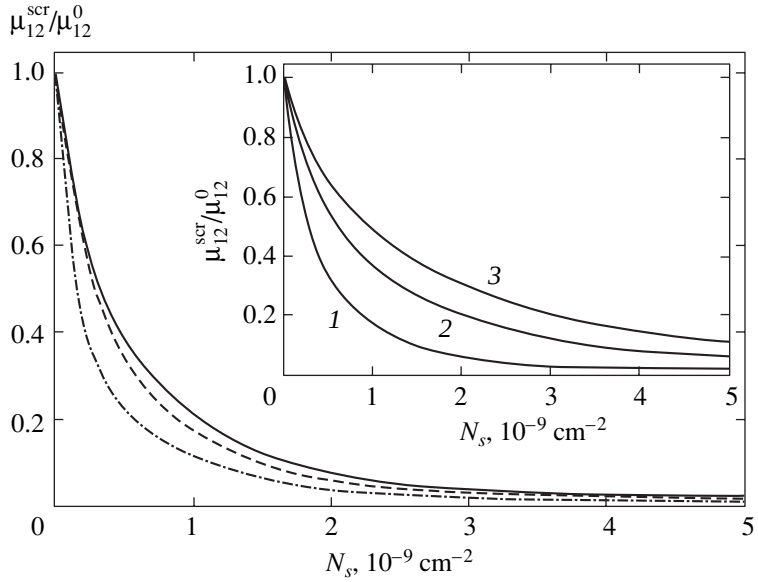

Fig. 4. Ratio $\mu_{12}^{scr}/\mu_{12}^{0}$ (μ_{12} is the exciton–electron drag coefficient) as a function of concentration N_s of a quasi-two-dimensional electron gas in a GaAs/AlGaAs quantum well at $T = 10$ K at various interlayer distances: $D = 150$ (solid line), 250 (dashed line), and 500 Å (dot-and-dash line). Shown in the inset is the $\mu_{12}^{scr}/\mu_{12}^{0}$ ratio as a function of N_s at $D = 250$ Å and $T = 10$ (*1*), 20 (*2*), and 30 K (*3*).

As a result, the equation for the effective interaction energy in a many-particle electron–exciton system takes the form

$$W(k, D) = -\frac{\gamma F(k, D)}{1 - 2\pi e^2 \beta_2/\epsilon k - \gamma^2 \beta_1 \beta_2 F^2}. \quad (45)$$

The effective interaction energy for a two-component system of interacting electrons and excitons with a low density of the latter ($N_{exc} a_B^2 \ll 1$) has the form

$$W(k, D) = -\frac{\gamma F(k, D)}{1 - 2\pi e^2 \Pi_{DH}/\epsilon k}, \quad (46)$$

where $\Pi_{DH} = \beta_2$ is the polarization operator in the classical Debye–Hückel approximation at $T \sim E_F$ [28, 29]. The polarizability of a two-dimensional exciton in the ground state is given by (e.g., see [18, 21])

$$\alpha = \frac{21}{16} a_B^2.$$

Taking this into account, we can write the $\gamma = \alpha e^2/2\epsilon$ parameter in (46) in the form

$$\gamma = \frac{21}{32} \frac{e^2 a_B^3}{\epsilon}. \quad (47)$$

Next, consider the influence of screening on the drag coefficient μ_{12}. Let us first fix the temperature of the system ($T = 10$ K) and construct the dependence of $\mu_{12}^{scr}/\mu_{12}^{0}$ on the concentration of the two-dimensional electron gas (Fig. 4); here, μ_{12}^{scr} is the screened drag coefficient calculated by (31) with potential (46) and μ_{12}^{0} is the drag coefficient for a system of noninteracting electrons and excitons. One can see that the exciton–electron drag coefficient decreases exponentially as n_2 increases. It follows that the drag effect in a strongly correlated electron–exciton system is less manifest than the drag effect in a rarefied electron–exciton or electron–electron system. This circumstance complicates experimental observations of this effect in systems of spatially separated electrons and excitons. On the other hand, the effectiveness of screening by a two-dimensional electron gas decreases as the temperature increases, and the exciton–electron drag coefficient increases, the interlayer distance being the same (Fig. 3, inset). We may therefore hope that this effect will be observed in high-quality structures at low electron gas concentrations.

6. CONCLUSIONS

In this work, we solved two problems for double layer systems. First, we considered a system with spatially separated excitons and electrons, studied spatially indirect screening effects, and obtained a dependence of the critical parameter r_s^c on distance D between quantum wells. It was found that, in such a system, the solution is found in the linear response approximation. In the limit $D \longrightarrow 0$, the results are in agreement with

those obtained by Kleinman [25], who considered a single quantum well in this approximation. In the second problem, the screening of a spatially indirect exciton was considered. We obtained the dependence of the binding energy of a spatially indirect exciton on the concentration of the quasi-two-dimensional electron gas to show that the bound state experienced rearrangement and constructed a dependence of the critical parameter r_s^c on distance D between the layers. This dependence was used to show how a given bound state was modified as D changed and how this change influenced the effectiveness of the screening properties of the quasi-two-dimensional electron gas. It was found that taking into account the thickness of layers caused the renormalization of the distance between the spatially separated electron and hole. Coulomb interaction in such systems with an interlayer distance on the order of 50–300 Å was shown to be substantial. In addition to the rearrangement of the excitonic state, we studied the drag effect in the system of spatially separated excitons and electrons. It was shown that the drag coefficient, which appeared because of screening by spatially separated electrons, decreased exponentially as the concentration of the electrons increased. On the other hand, the effectiveness of screening decreased and the drag coefficient μ_{12} therefore increased as the temperature grew. To summarize, the collective effects that we discussed in this work and that are mainly determined by electron–hole interlayer interactions (crystallization, superfluidity, drag effects, and quasi–Josephson phenomena) can be studied experimentally.

ACKNOWLEDGMENTS

This work was financially supported by the Russian Foundation for Basic Research and INTAS.

REFERENCES

1. S. V. Tovstonog, I. V. Kukushkin, L. V. Kulik, and V. E. Kirpichev, Pis'ma Zh. Éksp. Teor. Fiz. **76**, 592 (2002) [JETP Lett. **76**, 511 (2002)].
2. J. P. Cheng, J. Kono, B. D. McCombe, *et al.*, Phys. Rev. Lett. **74**, 450 (1995).
3. G. R. Aizin, B. Laikhtman, and G. Gumbs, Phys. Rev. B **64**, 125317 (2001).
4. J. Kolorenc, L. Smrcka, and P. Streda, Phys. Rev. B **66**, 085301 (2002).
5. Yu. E. Lozovik, O. L. Berman, and M. Willander, J. Phys. C **14**, 12457 (2002).
6. Yu. B. Vasilyev, V. A. Solov'ev, B. Ya. Mel'ster, *et al.*, Solid State Commun. **124**, 323 (2002).
7. A. V. Larionov, V. B. Timofeev, J. Hvam, and K. Soerensen, Pis'ma Zh. Éksp. Teor. Fiz. **75**, 233 (2002) [JETP Lett. **75**, 200 (2002)].
8. D. W. Snoke, Phys. Status Solidi B **238**, 389 (2003); Science **298**, 1368 (2002).
9. D. W. Snoke, S. Denev, Y. Liu, *et al.*, Nature **418**, 754 (2002).
10. V. V. Krivolapchuk, E. S. Moskalenko, and A. L. Zhmodikov, Phys. Rev. B **64**, 045313 (2001).
11. Yu. E. Lozovik and V. I. Yudson, Pis'ma Zh. Éksp. Teor. Fiz. **22**, 26 (1975) [JETP Lett. **22**, 11 (1975)]; Zh. Éksp. Teor. Fiz. **71**, 738 (1976) [Sov. Phys. JETP **44**, 389 (1976)]; L. V. Keldysh and Yu. V. Kopaev, Fiz. Tverd. Tela (Leningrad) **6**, 2791 (1964) [Sov. Phys. Solid State **6**, 2219 (1964)]; L. V. Keldysh and A. N. Kozlov, Zh. Éksp. Teor. Fiz. **54**, 978 (1968) [Sov. Phys. JETP **27**, 521 (1968)].
12. A. V. Klyuchnik and Yu. E. Lozovik, Zh. Éksp. Teor. Fiz. **76**, 670 (1979) [Sov. Phys. JETP **49**, 335 (1979)]; Yu. E. Lozovik and V. I. Yudson, Pis'ma Zh. Éksp. Teor. Fiz. **25**, 18 (1977) [JETP Lett. **25**, 14 (1977)]; Yu. E. Lozovik and M. Willander, Appl. Phys. A **71**, 379 (2000).
13. Yu. E. Lozovik and A. M. Ruvinskiĭ, Zh. Éksp. Teor. Fiz. **112**, 1791 (1997) [JETP **85**, 979 (1997)].
14. K. von Klitzing, G. Dorda, and M. Pepper, Phys. Rev. Lett. **45**, 494 (1980).
15. D. C. Tsui, H. L. Stormer, and A. C. Gossard, Phys. Rev. Lett. **48**, 1559 (1982).
16. Y. W. Suen, H. C. Manoharan, X. Ying, *et al.*, Phys. Rev. Lett. **72**, 3405 (1994).
17. H. C. A. Oji, A. H. MacDonald, and S. M. Girvin, Phys. Rev. Lett. **58**, 824 (1987).
18. Yu. E. Lozovik and O. L. Berman, Zh. Éksp. Teor. Fiz. **111**, 1879 (1997) [JETP **84**, 1027 (1997)]; Fiz. Tverd. Tela (St. Petersburg) **40**, 1350 (1998) [Phys. Solid State **40**, 1228 (1998)].
19. S. I. Gubarev, I. V. Kukushkin, S. V. Tovstonog, *et al.*, Pis'ma Zh. Éksp. Teor. Fiz. **72**, 469 (2000) [JETP Lett. **72**, 324 (2000)].
20. D. V. Kulakovskiĭ, S. I. Gubarev, and Yu. E. Lozovik, Pis'ma Zh. Éksp. Teor. Fiz. **74**, 123 (2001) [JETP Lett. **74**, 118 (2001)]; Zh. Éksp. Teor. Fiz. **121**, 915 (2002) [JETP **94**, 785 (2002)].
21. Yu. E. Lozovik and M. V. Nikitkov, Zh. Éksp. Teor. Fiz. **116**, 1440 (1999) [JETP **89**, 775 (1999)]; Zh. Éksp. Teor. Fiz. **111**, 1107 (1997) [JETP **84**, 612 (1997)].
22. M. Yu. Akimov, I. V. Kukushkin, S. I. Gubarev, *et al.*, Pis'ma Zh. Éksp. Teor. Fiz. **72**, 662 (2000) [JETP Lett. **72**, 460 (2000)].
23. F. Stern, Phys. Rev. Lett. **18**, 546 (1967).
24. Lian Zheng and A. H. MacDonald, Phys. Rev. B **49**, 5522 (1994).
25. D. A. Kleinman, Phys. Rev. B **32**, 3766 (1985).
26. A. V. Filinov, M. Bonitz, and Yu. E. Lozovik, Phys. Status Solidi B (in press).
27. S. I. Gubarev, O. V. Volkov, V. A. Koval'skiĭ, *et al.*, Pis'ma Zh. Éksp. Teor. Fiz. **76**, 673 (2002) [JETP Lett. **76**, 575 (2002)].
28. A. L. Fetter, Phys. Rev. B **10**, 3739 (1974).
29. J. M. Ziman, *Principles of the Theory of Solids*, 2nd ed. (Cambridge Univ. Press, London, 1972; Mir, Moscow, 1974).

Translated by V. Sipachev

Journal of Experimental and Theoretical Physics, Vol. 98, No. 6, 2004, pp. 1214–1221.
Translated from Zhurnal Éksperimental'noĭ i Teoreticheskoĭ Fiziki, Vol. 125, No. 6, 2004, pp. 1385–1392.

SOLIDS
Electronic Properties

Two Interacting Particles in an External Potential

Yu. N. Ovchinnikov

Max-Planck Institute für Physik Komplexer Systeme, D-01187, Dresden, Germany
Landau Institute for Theoretical Physics, Russian Academy of Sciences,
Chernogolovka, Moscow oblast, 142432 Russia
e-mail: yuri@fisica.cib.na.cnr.it

Received October 2, 2003

Abstract—The solution to the Schrödinger equation is analyzed for two particles interacting in an external potential. It is assumed that a shallow level exists for one of the particles in the external potential. It is shown that repulsion leads to a transfer of one of the particles to the continuous spectrum after attainment of the interaction threshold. For the shallow level, the threshold value of the interaction is independent of level depth.

1. INTRODUCTION

The interaction of particles in a solid cannot be exactly taken into account; various approximations used for this purpose make it possible to single out the "principal terms" with a subsequent allowance for the remainder [1–3]. The introduction of an impurity into a metal leads to a redistribution of the electron density and, hence, necessitates the inclusion of the electroneutrality condition. New physical phenomena are observed if the impurity is strong enough to lead to the formation of a localized state. As the first stage of investigation of this effect, we consider the problem of motion of two interacting particles in an external potential such that a shallow level exists for one of the particles. We assume that the interaction is repulsive. In the absence of interaction, the level can be filled with two particles (electrons) with opposite spins.

As a result of the interaction, one of the particles is separated from the center by a larger distance than the other. In this case, a difference emerges between the exact solution and the Hartree–Fock approximation. The Hartree–Fock equations are symmetric relative to the substitution $1 \longleftrightarrow 2$ and perturbation theory in the interaction generates two identical one-particle functions. For this reason, the Hartree–Fock equations acquire a bifurcation point above which two different functions of the one-particle approximation exist, and the energy of such a state is lower than the solution composed of identical one-particle functions. Above a certain critical value of the interaction, the level is occupied by only one particle, while the other particle goes to the continuum. This critical value can be determined in the Hartree–Fock approximation. Near the threshold, the correction terms to the Hartree–Fock approximation are small and can be found in perturbation theory.

2. SCATTERING FUNCTIONS IN A POTENTIAL WITH A SHALLOW LEVEL

We assume that $U(\mathbf{r})$ is a short-range potential in which a shallow level with energy $E_0 < 0$ exists. We set

$$\sqrt{2m|E_0|} = \kappa. \tag{1}$$

Since the level is shallow, the radius of the localized state κ^{-1} is much larger than the effective radius a of the potential $U(\mathbf{r})$. The results are independent of the explicit form of potential $U(\mathbf{r})$ as long as the localized level can be treated as shallow. For simplicity, we will demonstrate our conclusions for the simplest form of potential $U(\mathbf{r})$:

$$U(r) = \begin{cases} -U_0 \text{ for } |\mathbf{r}| < a, \\ 0 \text{ for } |\mathbf{r}| > a. \end{cases} \tag{2}$$

The localized (ground) state ψ_0 of the Schrödinger equation can be represented in the form

$$\psi_0 = \frac{1}{\sqrt{4\pi}}\frac{\chi_0}{\rho}, \tag{3}$$

where

$$|\mathbf{r}| = \rho,$$

$$\chi_0 = B\begin{cases} \exp(-\kappa\rho), & \rho > a, \\ e^{-\kappa a}\dfrac{\sin(\sqrt{2m(U_0 - |E_0|)}\rho)}{\sin(\sqrt{2m(U_0 - |E_0|)}a)}, & \rho < a. \end{cases} \tag{4}$$

The normalization coefficient B is given by

$$B^{-2} = e^{-2\kappa a}\left\{\frac{1}{2\kappa} + \frac{a}{2\sin^2(\sqrt{2m(U_0-|E_0|)}a)} - \frac{\cot(\sqrt{2m(U_0-|E_0|)}a)}{2\sqrt{2m(U_0-|E_0|)}}\right\} \quad (5)$$

in the approximation we are dealing with (independent of the explicit form of the potential), we have

$$B = \sqrt{2\kappa}. \quad (6)$$

Energy E_0 of the localized state is the solution to the equation

$$\tan(\sqrt{2m(U_0-|E_0|)}a) = -\frac{1}{\kappa}\sqrt{2m(U_0-|E_0|)}. \quad (7)$$

Under the condition $\kappa a \ll 1$, Eq. (7) leads to the important relation

$$\sqrt{2mU_0}a = \frac{\pi}{2} + \frac{2\kappa a}{\pi} + \ldots. \quad (8)$$

The wave function of the continuous spectrum in state s can be written in the form

$$\psi_E = \frac{1}{\sqrt{4\pi}}\frac{1}{\rho}\chi_E, \quad (9)$$

where

$$\chi_E = \sqrt{\frac{2}{L}} \times \begin{cases} \sin(\sqrt{2m(U_0+E)}\rho)\dfrac{\sin(\sqrt{2mE}a+\delta_E)}{\sin(\sqrt{2m(U_0+E)}a)}, & \rho < a, \\ \sin(\sqrt{2mE}\rho+\delta_E), & \rho > a, \end{cases} \quad (10)$$

L being the size of the sphere (at the boundary of this sphere, the boundary condition is set) and δ_E the scattering phase. The scattering phase satisfies the equation

$$\tan(\sqrt{2mE}a+\delta_E) = \sqrt{\frac{E}{U_0+E}}\tan(\sqrt{2m(U_0+E)}a). \quad (11)$$

It follows from Eqs. (8) and (11) that in the range of low energies ($E \ll U_0$), phase δ_E satisfies the equation

$$\sin\delta_E = \left(\frac{2mE}{2mE+\kappa^2}\right)^{1/2}, \quad \delta_{E=0} = \pi. \quad (12)$$

Expression (12) for the scattering phase at low energies is universal and independent of the explicit form of short-range potential $U(r)$ [4].

For a nonzero value of angular momentum, scattering functions $\psi^{(l,M)}$ can be chosen in the form

$$\psi_E^{(l,M)} = Y_l^M\chi_l(\rho)/\rho. \quad (13)$$

In the region $\rho > a$, function $\chi_l(\rho)$ satisfies the condition

$$\chi_l(\rho) \sim \sqrt{\rho}\left\{J_{l+1/2}\left(\sqrt{2mE}\rho\right) + (-1)^l\tan\delta_E^{(l)}J_{-(l+1/2)}\left(\sqrt{2mE}\rho\right)\right\}, \quad (14)$$

where $\delta_E^{(l)}$ is the scattering phase with angular momentum l and energy E, and J_ν is the Bessel function. For low energies, all scattering phases with $l \neq 0$ are small and can be neglected. In this case, we have

$$\chi_l(\rho) = \sqrt{\frac{\pi}{L}}\left(\sqrt{2mE}\rho\right)^{1/2}J_{l+1/2}\left(\sqrt{2mE}\rho\right), \quad l > 0. \quad (15)$$

In the absence of interaction, two particles with opposite spins can occupy the same level. The interaction leads to the emergence of correlation between the particles. The problem is to determine the threshold value of interaction potential $V(r_1 - r_2)$, for which the energy minimum is attained in the state with one of the particles in the continuous spectrum. To reveal the significant moments in the problem, we will use perturbation theory in interaction potential $V(r_1 - r_2)$. After this, we will use perturbation theory in the deviation of the potential from the threshold value. As the zero-order approximation, we will use the Hartree–Fock equations in this case.

3. PERTURBATION THEORY IN INTERACTION POTENTIAL

We write the operator $\hat{L}$ of the system of two interacting particles in the form

$$\hat{L} = \hat{H}_0 + V(r_1 - r_2) + 2|E_0|, \quad (16)$$

where $\hat{H}_0$ is the zeroth-approximation Hamiltonian

$$\hat{H}_0 = -\frac{1}{2m}(\Delta_{r_1} + \Delta_{r_2}) + U(r_1) + U(r_2), \quad (17)$$

$$\hat{L}_0 = \hat{H}_0 + 2|E_0|,$$

and Δ_{r_1} is the Laplacian.

The function

$$\tilde{\psi}_0(r_1, r_2) = \psi_0(r_1)\psi_0(r_2) \tag{18}$$

is the zeroth mode of operator $\hat{L}_0$,

$$\hat{L}_0\tilde{\psi}_0 = 0. \tag{19}$$

In perturbation theory, the function $\tilde{\psi}$ of the ground state of two particles and energy E can be represented in the form of a power series in interaction potential $V(r_1 - r_2)$:

$$\begin{aligned} \tilde{\psi} &= \tilde{\psi}_0 + \tilde{\psi}_1 + \tilde{\psi}_2 + \tilde{\psi}_3 + \ldots, \\ E &= -2|E_0| + E_1 + E_2 + E_3 + \ldots. \end{aligned} \tag{20}$$

From formulas (16) and (20), we obtain

$$\begin{aligned} \hat{L}_0\tilde{\psi}_1 + V\tilde{\psi}_0 - E_1\tilde{\psi}_0 &= 0, \\ \hat{L}_0\tilde{\psi}_2 + (V - E_1)\tilde{\psi}_1 - E_2\tilde{\psi}_0 &= 0, \\ \hat{L}_0\tilde{\psi}_3 + (V - E_1)\tilde{\psi}_2 - E_2\tilde{\psi}_1 - E_3\tilde{\psi}_0 &= 0, \\ \hat{L}_0\tilde{\psi}_4 + (V - E_1)\tilde{\psi}_3 - E_2\tilde{\psi}_2 - E_3\tilde{\psi}_1 - E_4\tilde{\psi}_0 &= 0, \end{aligned} \tag{21}$$

and so on.

The solvability condition for system of equations (21) determines the value of energy E_i:

$$\begin{aligned} E_1 &= \int d^3r_1 d^3r_2 \tilde{\psi}_0 V \tilde{\psi}_0, \\ E_2 &= \int d^3r_1 d^3r_2 \tilde{\psi}_0 V \tilde{\psi}_1, \\ E_3 &= \int d^3r_1 d^3r_2 \tilde{\psi}_0 V \tilde{\psi}_2, \\ &\ldots\ldots\ldots\ldots\ldots\ldots\ldots \end{aligned} \tag{22}$$

On the subspace orthogonal to the zeroth mode, operator $\hat{L}_0$ has the inverse operator $(\hat{L}_0^p)^{-1}$, which can be represented in the form

$$\begin{aligned} (\hat{L}_0^p)^{-1} &= \frac{\psi_0(r_1)\psi_0(r_1')\psi_\nu(r_2)\psi_\nu^*(r_2')}{E_\nu + |E_0|} \\ &+ \frac{\psi_\nu(r_1)\psi_\nu^*(r_1')\psi_0(r_2)\psi_0(r_2')}{E_\nu + |E_0|} \\ &+ \frac{\psi_\nu(r_1)\psi_\nu^*(r_1')\psi_\mu(r_2)\psi_\mu^*(r_2')}{E_\nu + E_\mu + 2|E_0|}. \end{aligned} \tag{23}$$

In this expression, indices ν and μ denote three variables: energy E and indices of angular momentum l, M,

$$\nu = \{E, l, M\}, \tag{24}$$

where energies $E_{\nu,\mu} \geq 0$. The sum over the states of the continuous spectrum is replaced by the integral with respect to energy,

$$\sum \longrightarrow \frac{L}{\pi} d\sqrt{2mE}, \tag{25}$$

and summation is carried out over indices l and M. In formula (20), partial summation can be carried out. This gives

$$\tilde{\psi} = \tilde{\psi}_0 - (\hat{L}_0^p)^{-1}\hat{R}\tilde{\psi}_0, \tag{26}$$

where operator $\hat{R}$ is defined by the expression

$$\begin{aligned} \hat{R} &= V - V[1 + (\hat{L}_0^p)^{-1}(V - E_1)]^{-1}(\hat{L}_0^p)^{-1}V \\ &- E_2V(\hat{L}_0^p)^{-1}\{1 - [(V - E_1)(\hat{L}_0^p)^{-1} + (\hat{L}_0^p)^{-1}(V - E_1)] \\ &+ [(V - E_1)(\hat{L}_0^p)^{-1}(V - E_1)(\hat{L}_0^p)^{-1} \\ &+ (V - E_1)(\hat{L}_0^p)^{-2}(V - E_1) \\ &+ (\hat{L}_0^p)^{-1}(V - E_1)(\hat{L}_0^p)^{-1}(V - E_1)] \\ &- [(V - E_1)(\hat{L}_0^p)^{-1}(V - E_1)(\hat{L}_0^p)^{-1}(V - E_1)(\hat{L}_0^p)^{-1} \\ &+ (V - E_1)(\hat{L}_0^p)^{-1}(V - E_1)(\hat{L}_0^p)^{-2}(V - E_1) \\ &+ (V - E_1)(\hat{L}_0^p)^{-2}(V - E_1)(\hat{L}_0^p)^{-1}(V - E_1) \\ &+ (\hat{L}_0^p)^{-1}(V - E_1)(\hat{L}_0^p)^{-1}(V - E_1) \\ &\times (\hat{L}_0^p)^{-1}(V - E_1)]\}(\hat{L}_0^p)^{-1}V + \ldots. \end{aligned} \tag{27}$$

It should be noted that operator $(\hat{L}_0^p)^{-1}(V - E_1)$ is not positive. It has negative eigenvalues E_- such that

$$|E_-| \geq E_1/|E_0|. \tag{28}$$

For this reason, perturbation theory in the interaction potential can be used in any case under the condition

$$E_1 < |E_0|. \tag{29}$$

The general formula for the solution for the ground state $\tilde{\psi}$ can be written in the form

$$\tilde{\psi}(\mathbf{r}_1, \mathbf{r}_2) = \tilde{\psi}(\rho_1, \rho_2, z), \tag{30}$$

where

$$|\mathbf{r}_{1,2}| = \rho_{1,2}, \quad z = \frac{\mathbf{r}_1 \cdot \mathbf{r}_2}{\rho_1\rho_2}. \tag{31}$$

For large values of quantities $\rho_{1,2}$, the number of significant harmonics is large. However, in the range of $\rho_{1,2} \gg \kappa^{-1}$, only one harmonic with angular momentum $l = 0$ survives since the asymptotic form at large dis-

tances is associated with singularities in the scattering phase. Nevertheless, in the general case, the approximation that takes into account only the states with $l = 0$ in the continuous spectrum cannot be used for calculating the energy corrections in formula (22). The energy of state can be reconstructed from the asymptotic expansion of the wave function.

4. SECOND-ORDER PERTURBATION THEORY FOR THE WAVE FUNCTION IN THE ASYMPTOTIC REGION

In the asymptotic region $\rho_{1,2} \geq \kappa^{-1}$, we can use for the extreme left operator the approximation that takes into account only the states with $l = 0$. In this approximation, the first-order correction $\tilde{\psi}_1$ is given by

$$\begin{aligned}\tilde{\psi}_1 = -\frac{2\pi}{\kappa}E_1\Bigg\{&\frac{\kappa e^{-\kappa\rho_1}}{4\pi^3\rho_1\rho_2}\int_0^\infty\frac{d\sqrt{2mE}}{E+|E_0|}\\ &\times\sin\delta_E\sin(\sqrt{2mE}\rho_2+\delta_E)\\ &+\frac{\kappa e^{-\kappa\rho_2}}{4\pi^3\rho_1\rho_2}\int_0^\infty\frac{d\sqrt{2mE}}{E+|E_0|}\sin\delta_E\\ &\times\sin(\sqrt{2mE}\rho_1+\delta_E)+\frac{1}{4\pi^4\rho_1\rho_2}\end{aligned} \tag{32}$$

$$\times\int_0^\infty\frac{d\sqrt{2mE_\nu}d\sqrt{2mE_\mu}}{E_\nu+E_\mu+2|E_0|}\sin\delta_{E_\nu}\sin\delta_{E_\mu}$$

$$\times\sin(\sqrt{2mE_\nu}\rho_1+\delta_{E_\nu})\sin(\sqrt{2mE_\mu}\rho_2+\delta_{E_\mu})\Bigg\}.$$

Phases δ_E in this equation are defined by formula (12). The first two integrals in formula (32) can be calculated comparatively easily for arbitrary values of $\rho_{1,2}$. In the asymptotic region, we obtain from Eq. (32)

$$\tilde{\psi}_1 = -\frac{mE_1}{2\pi\kappa}\frac{e^{-\kappa(\rho_1+\rho_2)}}{\rho_1\rho_2}\left[\frac{1}{2}-\kappa\max(\rho_1,\rho_2)\right]. \tag{33}$$

Formula (21) leads to the second-order correction to the wave function,

$$\tilde{\psi}_2 = -E_1(\hat{L}_0^p)^{-2}V\tilde{\psi}_0+(\hat{L}_0^p)^{-1}V(\hat{L}_0^p)^{-1}V\psi_0. \tag{34}$$

It should be noted that operator $(\hat{L}_0^p)^{-2}$ produces terms of the form $(\kappa\rho_{1,2})^2\exp(-\kappa(\rho_1+\rho_2))$ for large values of ρ. These terms determine the renormalization of quantity κ. Formulas (23) and (34) lead to

$$\begin{aligned}\tilde{\psi}_2 = &-\frac{\kappa e^{-\kappa(\rho_1+\rho_2)}}{2\pi\rho_1\rho_2}\frac{m^2E_1^2}{2\kappa^4}\left(\frac{1}{2}-\kappa^2\max(\rho_1^2,\rho_2^2)\right)-\frac{2\pi}{\kappa}E_2\Bigg\{\frac{\kappa e^{-\kappa\rho_1}}{4\pi^3\rho_1\rho_2}\int_0^\infty d\sqrt{2mE}\frac{\sin\delta_E\sin(\sqrt{2mE}\rho_2+\delta_E)}{E+|E_0|}\\ &+\frac{\kappa e^{-\kappa\rho_2}}{4\pi^3\rho_1\rho_2}\int_0^\infty d\sqrt{2mE}\frac{\sin\delta_E\sin(\sqrt{2mE}\rho_1+\delta_E)}{E+|E_0|}+\frac{1}{4\pi^4\rho_1\rho_2}\int_0^\infty\int d\sqrt{2mE_\mu}d\sqrt{2mE_\mu}\\ &\times\frac{\sin\delta_{E_\nu}\sin\delta_{E_\mu}\sin(\sqrt{2mE_\nu}\rho_1+\delta_{E_\nu})\sin(\sqrt{2mE_\mu}\rho_2+\delta_{E_\mu})}{E_\nu+E_\mu+2|E_0|}\Bigg\}.\end{aligned} \tag{35}$$

In formulas (32) and (35), quantities E_1 and E_2 are exact first- and second-order corrections to energy that take into account all harmonics. In the asymptotic region $\rho_{1,2} \gg \kappa^{-1}$, we obtain from Eq. (35) the correction $\tilde{\psi}_2$ to the wave function,

$$\begin{aligned}\tilde{\psi}_2 = \frac{\kappa e^{-\kappa(\rho_1+\rho_2)}}{2\pi\rho_1\rho_2}\Bigg\{&-\frac{m^2E_1^2}{2\kappa^4}\left(\frac{1}{2}-\kappa^2\max(\rho_1^2,\rho_2^2)\right)\\ &-\frac{mE_2}{\kappa^2}(1-\kappa\max(\rho_1,\rho_2))\Bigg\}.\end{aligned} \tag{36}$$

Thus, in the second order of perturbation theory, wave function $\tilde{\psi}$ in the asymptotic region $\rho_{1,2} \gg \kappa^{-1}$ is defined by the formula

$$\begin{aligned}\tilde{\psi} = \frac{\kappa e^{-\kappa(\rho_1+\rho_2)}}{2\pi\rho_1\rho_2}\Bigg\{&1-\frac{mE_1}{2\kappa^2}-\frac{m^2E_1^2}{4\kappa^4}-\frac{mE_2}{\kappa^2}\\ &+\Bigg(\frac{mE_1}{\kappa^2}\kappa\max(\rho_1,\rho_2)\\ &+\frac{mE_2}{\kappa^2}\kappa\max(\rho_1,\rho_2)+\frac{m^2E_1^2}{2\kappa^4}\kappa^2\max(\rho_1^2,\rho_2^2)\Bigg)\Bigg\}.\end{aligned} \tag{37}$$

This equation implies that value of κ for the particle closest to the center remains unchanged, while the value of κ for the particle at a larger distance from the center is renormalized and becomes equal to $\tilde{\kappa}$. The value of $\tilde{\kappa}$ can be determined from Eq. (37) and is given by

$$\tilde{\kappa} = \kappa\left\{1 - \frac{mE_1}{\kappa^2} - \frac{mE_2}{\kappa^2} - \frac{m^2E_1^2}{2\kappa^4}\right\}. \quad (38)$$

At large distances, the particles do not interact and, hence, the following relation holds:

$$E_1 + E_2 + E_3 + \ldots = \frac{1}{2m}(\kappa^2 - \tilde{\kappa}^2). \quad (39)$$

The first-order correction to energy E_1 is defined by formulas (3), (4), and (22) and is given by

$$E_1 = \pi^2\kappa^2 I_0, \quad (40)$$

where

$$I_0 = \int_0^\infty d\rho\rho V(\rho). \quad (41)$$

To obtain the second-order correction to energy E_2, the wave function $\tilde{\psi}_1$ must be determined at distances $\rho_{1,2} \sim R_{\text{int}}$, where R_{int} is the range of the interaction potential $V(r)$. At distances $\rho_{1,2} \geq R_{\text{int}}$, the function $\tilde{\psi}_1$ taking into account only the states with $l = 0$ is given by

$$\tilde{\psi}_1 = -\frac{\pi m\kappa I_0}{2\rho_1\rho_2}\left\{\exp(-\kappa(\rho_1 + \rho_2))(1 - \kappa(\rho_1 + \rho_2))\right.$$
$$+ \frac{1}{2\pi^2}\int\int_{-\infty}^{\infty}\frac{dxdyxy(-1 + xy + ix + iy)}{(x^2+1)(y^2+1)(x^2+y^2+2)} \quad (42)$$
$$\left.\times \exp(i\kappa x\rho_1 + i\kappa y\rho_2)\right\}.$$

At large distances $\rho_{1,2} \gg \kappa^{-1}$, Eq. (42) reproduces formula (33). In region $R_{\text{int}} < \rho_{1,2} \ll \kappa^{-1}$, the last term on the right-hand side of formula (42) has a logarithmic singularity. In this region, we obtain

$$\int\int_{-\infty}^{\infty}\frac{dxdy(-1 + xy + ix + iy)}{(x^2+1)(y^2+1)(x^2+y^2+2)}$$
$$\times \exp(i\kappa(x\rho_1 + y\rho_2)) \quad (43)$$
$$= -\pi - \frac{\pi^2}{2} + \pi K_0(\kappa\sqrt{2(\rho_1^2 + \rho_2^2)}),$$

where K_0 is the Bessel function. Finally, function $\tilde{\psi}_1$ in region $R_{\text{int}} < \rho_{1,2} \ll \kappa^{-1}$ is defined as

$$\tilde{\psi}_1 = -\frac{m\kappa I_0}{4\rho_1\rho_2}\left\{\frac{3\pi}{2} - 1 + K_0(\kappa\sqrt{2(\rho_1^2 + \rho_2^2)})\right\}. \quad (44)$$

The coefficient of the logarithmic singularity is numerically small; consequently, formula (44) enables us to obtain the second-order correction to energy to a high degree of accuracy,

$$E_2 = -\frac{\pi^3 m\kappa^2 I_0^2}{2}\left\{\left(\frac{3\pi}{2} - 1\right) + \ln\left(\frac{1}{\kappa R_{\text{int}}}\right)\right.$$
$$+ \frac{2}{\pi^2 I_0}\int\int_0^\infty d\rho_1 d\rho_2 \int_{-1}^{1} dz V(\sqrt{\rho_1^2 + \rho_2^2 + 2\rho_1\rho_2 z}) \quad (45)$$
$$\left.\times \ln\left(\frac{\sqrt{2}R_{\text{int}}}{\sqrt{\rho_1^2 + \rho_2^2}}\right)\right\},$$

where R_{int} is the characteristic range of interaction of two particles.

The repulsion of particles leads to a decrease in parameter $\tilde{\kappa}$ in the wave function of the particle at a larger distance from the center than the other particle. This phenomenon is apparently preserved in all orders of perturbation theory. The theory has two scales. One of these scales is associated with the logarithmic singularity and can be defined as

$$mI_0^{(1)} \approx \frac{2}{\pi}\frac{1}{\ln(1/\kappa R_{\text{int}})}. \quad (46)$$

The second scale is defined by formula (28):

$$mI_0^{(2)} = \frac{1}{2\pi^2}. \quad (47)$$

The first scale is smaller than the second scale only under the stringent condition

$$\ln\left(\frac{1}{\kappa R_{\text{int}}}\right) > 4\pi. \quad (48)$$

The enhancement of the interaction leads to the expulsion of the second particle to a delocalized state. Near the threshold, the value of $\tilde{\kappa}$ tends to zero. As a result, the emerging perturbation theory starts from strongly asymmetric one-particle scale.

5. THRESHOLD VALUE OF INTERACTION FOR TRANSFERRING THE SECOND PARTICLE TO A DELOCALIZED STATE

As the zero-order approximation for determining the threshold value of the interaction, we will use the Hartree–Fock equations

$$\begin{aligned}\left\{-\frac{1}{2m}\Delta_{r_1}+U(r_1)+\int V(r_1-r_3)\hat{\psi}_2^2(r_3)d^3r_3\right\}\\ \times\hat{\psi}_1(r_1)=-|E_1|\hat{\psi}_1(r_1),\\ \left\{-\frac{1}{2m}\Delta_{r_2}+U(r_2)+\int V(r_2-r_3)\hat{\psi}_1^2(r_3)d^3r_3\right\}\\ \times\hat{\psi}_2(r_2)=-|E_2|\hat{\psi}_2(r_2).\end{aligned}\tag{49}$$

This system of equations is symmetric relative to the substitution $\hat{\psi}_1 \longleftrightarrow \hat{\psi}_2$. Consequently, there exists a solution such that

$$\hat{\psi}_1=\hat{\psi}_2.\tag{50}$$

According to perturbation theory, this is the only solution that can be obtained. In this respect, the Hartree–Fock approximation differs from the exact solution, in which parameter κ of only one particle changes in the first two orders of perturbation theory. This means that the Hartree–Fock equations have a bifurcation point, above which a nonsymmetrical solution appears. The energy corresponding to this solution is lower than that for the symmetric solution.

We will confine our analysis to the range of interaction in which $|E_2| \longrightarrow 0$. In the Hartree–Fock approximation, operator $\hat{L}_0$ is given by

$$\begin{aligned}\hat{L}_0=-\frac{1}{2m}(\Delta_{r_1}+\Delta_{r_2})+U(r_1)+U(r_2)\\ +\int V(r_1-r_3)\hat{\psi}_2^2(r_3)d^3r_3\\ +\int V(r_2-r_3)\hat{\psi}_1^2(r_3)d^3r_3+|E_1|+|E_2|.\end{aligned}\tag{51}$$

The exact solution to the Schrödinger equation can be written in the form

$$\begin{aligned}\{\hat{L}_0+[V(r_1-r_2)-\int V(r_1-r_3)\hat{\psi}_2^2(r_3)d^3r_3\\ -\int V(r_2-r_3)\hat{\psi}_1^2(r_3)d^3r_3]\}\psi-\delta E\psi=0,\end{aligned}\tag{52}$$

where

$$\begin{aligned}\psi=\psi_1(r_1)\psi_2(r_2)+\delta\psi,\\ E=-|E_1|-|E_2|+\delta E.\end{aligned}\tag{53}$$

In the subspace orthogonal to function $\{\psi_1(r_1)\psi_2(r_2)\}$, operator $\hat{L}_0^p$ has the inverse operator

$$\begin{aligned}(\hat{L}_0^p)^{-1}=\frac{\hat{\psi}_1(r_1)\hat{\psi}_1(r_1')\hat{\tilde{\psi}}_\nu(r_2)\hat{\tilde{\psi}}_\nu^*(r_2')}{E_\nu+|E_2|}\\ +\frac{\hat{\psi}_\nu(r_1)\hat{\psi}_\nu^*(r_1')\hat{\psi}_2(r_2)\hat{\psi}_2(r_2')}{E_\nu+|E_1|}\\ +\frac{\psi_\nu(r_1)\psi_\nu^*(r_1')\hat{\tilde{\psi}}_\mu(r_2)\hat{\tilde{\psi}}_\mu^*(r_2')}{E_\nu+E_\mu+|E_1|+|E_2|}.\end{aligned}\tag{54}$$

In this expression, functions $\hat{\psi}_1$ and $\hat{\psi}_2$ are solutions of system of equations (49). Functions $\hat{\psi}_\nu(r_1)$ and $\hat{\psi}_\mu(r_2)$ of the continuous spectrum are the solutions of the same system of equations after the substitution $-|E_1| \longrightarrow E_\nu$ and $-|E_2| \longrightarrow E_\mu$ and the replacement of functions $\hat{\psi}_1$ and $\hat{\psi}_2$ in the braces by $\hat{\psi}_\nu(r_1)$ and $\hat{\tilde{\psi}}_\mu(r_1)$, respectively.

Since $|E_2| \longrightarrow 0$, we can use the zero-order approximation for function $\hat{\psi}_1$ and energy E_1 and set

$$\hat{\psi}_1(r_1)=\psi_0(r_1),\quad E_1=E_0,\tag{55}$$

where function ψ_0 is defined by formulas (3) and (4) and energy E_0 is defined by formula (7).

Potential $\hat{V}(\rho_2)$ for the second particle in the same approximation is given by

$$\begin{aligned}\hat{V}(\rho_2)=U_0(\rho_2)+\frac{B^2e^{-2\kappa\rho_2}}{4\rho_2}\\ \times\int_0^\infty d\rho_1\rho_1V(\rho_1)\ln\left(\frac{\rho_1+\rho_2}{\rho_1-\rho_2}\right)^2.\end{aligned}\tag{56}$$

As before, we set

$$\hat{\tilde{\psi}}(r_2)=\frac{\hat{\tilde{\chi}}^{(l)}(\rho_2)}{\rho_2}Y_l^M.\tag{57}$$

Function $\hat{\tilde{\chi}}^{(l)}(\rho_2)$ is the solution to the equation

$$\hat{\tilde{\chi}}''+2m\left[-\hat{V}(\rho_2)-\frac{l(l+1)}{\rho_2^2}+E\right]\hat{\tilde{\chi}}=0.\tag{58}$$

In the vicinity of the threshold, energy E_2 of the localized state tends to zero. In this case, Eq. (58) is

reduced to the simple equation

$$\hat{\tilde{\chi}}_2'' + 2m\left[-U_0(\rho_2) - |E_2| - \frac{\pi^2 B^2}{4} I_0 \delta(\rho - a)\right]\hat{\tilde{\chi}}_2 = 0. \quad (59)$$

This equation can easily be solved, which gives

$$\sqrt{2m|E_2|} = \kappa_2,$$

$$\sqrt{2m|E_2|} = \kappa - \frac{\pi^2 m B^2 I_0}{2}, \quad (60)$$

$$\hat{\tilde{\chi}}_2 = \sqrt{2\kappa_2}\exp(-\kappa_2\rho_2), \quad \rho_2 > a.$$

Equation (60) leads to the threshold value of interaction,

$$\pi^2 m I_0 = 1. \quad (61)$$

It should be noted that scattering amplitude f in perturbation theory for small energies is defined by the formula [4]

$$f = -\frac{2m}{\hbar^2}\int V(r) r^2 dr;$$

therefore, there exists a margin in interaction in determining the expulsion threshold before the Born approximation must be replaced by the exact scattering amplitude.

For low energies in the continuous spectrum (for $l = 0$), the solution to Eq. (58) is given by

$$\hat{\tilde{\chi}} = \sqrt{\frac{2}{L}}\sin(\sqrt{2mE}\rho_2 + \tilde{\delta}_E), \quad (62)$$

where scattering phase δ_E is the solution to the equation

$$\tan(\sqrt{2mE}a + \tilde{\delta}_E) = -\frac{\sqrt{2mE}}{ma(E + \kappa_a/ma)}, \quad (63)$$
$$\delta_{E=0} = \pi.$$

From Eq. (63), we obtain

$$\sin\tilde{\delta}_E = \left(\frac{mE}{m(E + \kappa_2^2/2)}\right)^{1/2}. \quad (64)$$

6. CORRECTION TO THE HARTREE–FOCK APPROXIMATION

The first-order correction $\delta E^{(1)}$ to the Hartree–Fock can be obtained with help of Eqs. (3), (4), (52), (55), and (60):

$$\delta E^{(1)} = -\int d^3 r_1 d^3 r_2 V(r_1 - r_2)\frac{\kappa\kappa_2}{4\pi^2 r_1^2 r_2^2} = -\pi^2 I_0 \kappa\kappa_2. \quad (65)$$

This correction is small, and we must now prove that, at large distances ($\rho_1 \gg \kappa^{-1}$, $\rho_2 \gg \kappa_2^{-1}$), the correction to the wave function is also small. The first order correction $\psi^{(1)}$ to the wave function is defined as

$$\psi^{(1)}(r_1, r_2) = -\int d^3 r_1' d^3 r_2' \frac{\psi_\nu(r_1)\psi_\nu^*(r_1')\hat{\tilde{\psi}}_\mu(r_2)\hat{\tilde{\psi}}_\mu^*(r_2')}{E_\nu + E_\mu + |E_1| + |E_2|} \times V(r_1' - r_2')\psi_0(r_1')\hat{\tilde{\psi}}_2(r_2'). \quad (66)$$

In the region $r_1 \gg \kappa^{-1}$, $r_2 \gg \kappa_2^{-1}$, only the states of continuous spectrum with $l = 0$ are significant. In this region, from Eq. (66), we obtain

$$\psi^{(1)}(r_1, r_2) = \frac{\delta E^{(1)}}{2\pi^3\sqrt{\kappa\kappa_2}\rho_1\rho_2} \times \int\int_0^\infty \frac{d\sqrt{2mE_\nu}\, d\sqrt{2mE_\mu}}{E_\nu + E_\mu + |E_1| + |E_2|} \times \sin\delta_{E\nu}\sin(\sqrt{2mE_\nu}\rho_1 + \delta_{E\nu})\sin\tilde{\delta}_{E\mu} \times \sin(\sqrt{2mE_\mu}\rho_2 + \tilde{\delta}_{E\mu}). \quad (67)$$

Using expressions (12) and (64) for phases $\delta_{E\nu}$ and $\tilde{\delta}_{E\mu}$. We can reduce expression (67) for function $\psi^{(1)}$ to the form

$$\psi^{(1)}(r_1, r_2) = \frac{m\delta E^{(1)}}{4\pi^2\rho_1\rho_2\sqrt{\kappa\kappa_2}} \times \int\int_{-\infty}^{\infty} \frac{dxdyxy(xy + i\kappa y + i\kappa_2 x - \kappa\kappa_2)}{(x^2 + \kappa^2)(y^2 + \kappa_2^2)(x^2 + y^2 + \kappa^2 + \kappa_2^2)} \times \exp(i\kappa\rho_1 + i\kappa_2\rho_2). \quad (68)$$

In the asymptotic region, $\rho_1 \gg \kappa^1$, $\rho_1 \gg \kappa_2^{-1}$, wave

function $\psi^{(1)}$ is given by the expression following from formula (68):

$$\psi^{(1)}(r_1, r_2) = \frac{m\delta E^{(1)} e^{-\kappa\rho_1 - \kappa_2\rho_2}}{2\pi\kappa\rho_1\rho_2}\left(\frac{\kappa_2}{\kappa}\right)^{1/2}\left(\kappa\rho_1 - \frac{1}{2}\right). \quad (69)$$

This formula shows that it is only quantity κ that is slightly renormalized in the given approximation. Quantity κ_2 remains unchanged and all corrections are small in parameter κ_2/κ tending to zero.

7. CONCLUSIONS

The Schrödinger equation is investigated for two interacting particles in an external potential. The external potential is assumed to be such that only a single shallow level exists for one of the particles. The repulsion between the particles leads to a transition of the other particle to the continuous spectrum, when the interaction attains the threshold value. The threshold value of the interaction is independent of the depth of the level as long as this level is shallow. In the vicinity of the threshold, one of the particles is separated from the center by much longer distances as compared to the other particle; in this case, the Hartree–Fock approximation can be used. The corrections to the Hartree–Fock approximation are determined. These corrections are small in parameter $\kappa_2/\kappa \longrightarrow 0$.

ACKNOWLEDGMENTS

This study was supported financially by the Russian Foundation for Basic Research and the Ministry of Science of the Russian Federation.

REFERENCES

1. J. M. Ziman, *Principles of the Theory of Solids* (Cambridge Univ. Press, Cambridge, 1964; Mir, Moscow, 1966).
2. A. A. Abrikosov, L. P. Gor'kov, and I. E. Dzyaloshinskiĭ, *Methods of Quantum Field Theory in Statistical Physics* (Fizmatgiz, Moscow, 1962; Prentice Hall, Englewood Cliffs, N.J., 1963).
3. A. A. Abrikosov, *Fundamentals of the Theory of Metals* (Nauka, Moscow, 1987; North-Holland, Amsterdam, 1988).
4. L. D. Landau and E. M. Lifshitz, *Course of Theoretical Physics*, Vol. 3: *Quantum Mechanics: Non-Relativistic Theory*, 2nd ed. (Fizmatgiz, Moscow, 1963; Pergamon, New York, 1977).

Translated by N. Wadhwa

Journal of Experimental and Theoretical Physics, Vol. 98, No. 6, 2004, pp. 1222–1230.
Translated from Zhurnal Éksperimental'noĭ i Teoreticheskoĭ Fiziki, Vol. 125, No. 6, 2004, pp. 1393–1402.

SOLIDS
Electronic Properties

Temperature Dependence of the Compressibility of Two-Dimensional Electron Systems with Long-Range Potential Fluctuations in the Quantum Hall Effect Regime

M. O. Dorokhova and S. I. Dorozhkin

Institute of Solid State Physics, Russian Academy of Sciences, Chernogolovka, Moscow oblast, 142432 Russia
e-mail: dorohova@issp.ac.ru

Received October 23, 2003

Abstract—The temperature dependence of the compressibility of two-dimensional electron systems (2DESs) in GaAs/AlGaAs heterostructures in the quantum Hall effect regime have been studied both experimentally and theoretically. The compressibility was determined using the capacitance spectroscopy technique and the measurements of a low-frequency electric field penetrating through the 2DES. The measured temperature dependences of the 2DES compressibility are quantitatively described using a model taking into account inhomogeneity of the electron density at a finite temperature. Changes in the chemical potential of the 2DES in the vicinity of even filling factors determined from the capacitive and transport measurements are mutually consistent and agree with the results of finite-temperature calculations. *© 2004 MAIK "Nauka/Interperiodica".*

1. INTRODUCTION

Since the discovery of the quantum Hall effect in 1980 [1], the thermodynamic density of systems (compressibility) of two-dimensional electron states (2DESs) in a quantizing magnetic field has been extensively studied [2–8]. The measurements of capacitance [2–4], heat capacity [5], magnetization [6], and magnetoresistance [4, 7, 8] showed unexpectedly high values of the density of states in the gap between the Landau levels, in sharp contrast with theoretical predictions [9, 10]. A possible explanation for this experimental fact, based on allowance for the electron density fluctuations caused by the long-range potential fluctuations in 2DESs, was suggested in [11, 12], but this idea was not provided with a reliable experimental basis. Additional difficulties were encountered in attempts to quantitatively explain the strong temperature dependence of the compressibility [4, 13].

This study is aimed at demonstrating that the model proposed in [11, 12] ensures a quantitative explanation for the whole body of data on the compressibility of 2DESs under the conditions of the integer quantum Hall effect. Such 2DESs are formed in selectively doped heterostructures characterized, according to the commonly accepted opinion, predominantly by the long-range potential fluctuations. Within the framework of the adopted model, an analytical expression for the temperature dependence of the compressibility of 2DESs in the regime of the integer quantum Hall effect have been obtained. In this model, the only parameter dependent on the properties of a sample (determining the width and the temperature-dependent amplitude of minima on the concentration dependence of the compressibility) is the dispersion of the electron density in the sample. This parameter determines the slope of the temperature dependence of the compressibility for even filling factors of the Landau levels in a broad range of magnetic fields and temperatures. We show that the broadening of the Landau levels due to a short-range random potential can be evaluated from the character of the temperature dependence of the compressibility. Such estimates have been obtained for the heterostructures studied.

As is known, the electron mobility in a 2DES is usually increased by means of an undoped spacer separating this system from the layer of donors supplying electrons. This spacer significantly decreases the amplitude of the short-range random potential. In this case, disorder in the 2DES is determined by a long-range random potential caused by fluctuations in the density of charged donors in the layers behind the spacer. For the following considerations, it is important to note that the influence of the random potential on the 2DES in a quantizing magnetic field H depends on the relationship between the potential correlation length δ and the magnetic length l_H. The short-range random potential with a correlation length $\delta \ll l_H$ leads to broadening of the Landau levels without violating the homogeneity of the electron density. In contrast, screening of the long-range potential by the 2DES in the case of $\delta \gg l_H$ is accompanied by redistribution of the electron density, leaving the Landau levels locally narrow. The Landau levels repeat the profile of the screened potential, while the electron density n varies along the sample.

1063-7761/04/9806-1222$26.00 © 2004 MAIK "Nauka/Interperiodica"

In an ideal sample without disorder in the absence of electron–electron interactions, the chemical potential μ in a quantizing magnetic field H at a zero temperature is a stepwise function of the electron density n (Fig. 1a). For $n = pn_L$, where $p = 1, 2, \ldots$ and $n_L = eH/hc$ is the number of electron states on the Landau level, the chemical potential exhibits jumps equal to the distance between the neighboring Landau levels and is independent of n in the intervals between jumps. The broadening of the Landau levels due to a short-range random potential is manifested primarily by an increase in the derivative $d\mu/dn$ for half-integer filling factors $\nu \equiv n/n_L = p + 1/2$ of the Landau levels and by a decrease in the magnitude of the chemical potential jumps for the integer ν values (Fig. 1b). Figure 1c shows the effect of a long-range random potential on the thermodynamic characteristics of a 2DES. In this case, the sample is characterized by the average electron density n_s and the average chemical potential μ_s. The adopted model with electron density dispersion σ independent of the filling factor ν unavoidably involves a situation (in the vicinity of integer ν) with two different Landau levels simultaneously filled in different regions of the sample. Such a pattern is observed in the case of nonlinear screening of long-range potential fluctuations [12, 14, 15].

Thus, the presence of long-range potential fluctuations leads primarily to the disappearance of jumps in $\mu_s(n_s)$ for integer values of the filling factor ν_s averaged over the sample leaving horizontal regions in the chemical potential. Figure 1 shows the behavior of the derivative $d\mu_s/dn_s$ in the three cases considered above. This quantity, inversely proportional to the compressibility of the 2DES, has been experimentally determined. Obviously, an inhomogeneous distribution of the electron density leads to a significant increase in the compressibility $dn_s/d\mu_s$ of the electron system for integer values of the filling factor ν_s averaged over the sample.

Following [11, 12], the experimental results were evaluated within the framework of a model assuming a Gaussian distribution of the electron density in the 2DES. To within the experimental accuracy, our experimental results are adequately described by calculations using the δ-shaped Landau levels without making allowance for an additional short-range random potential. It should be noted that the assumption concerning predominance of the long-range fluctuations in the electron density in our samples is based on the definite arrangement of layers in these heterostructures, where the δ-layer of donors is spaced from the 2DES by a distance (70 and 80 nm for the structures of two types studied) much greater than l_H, and the high electron mobilities (above 10^6 cm^2/(V s)). In our experiments, the derivative $d\mu_s/dn_s$ was determined by three different methods based on the measurements of (i) the capacitance of field-effect transistors in a magnetic field, (ii) the electric field penetrating through the 2DES [16]

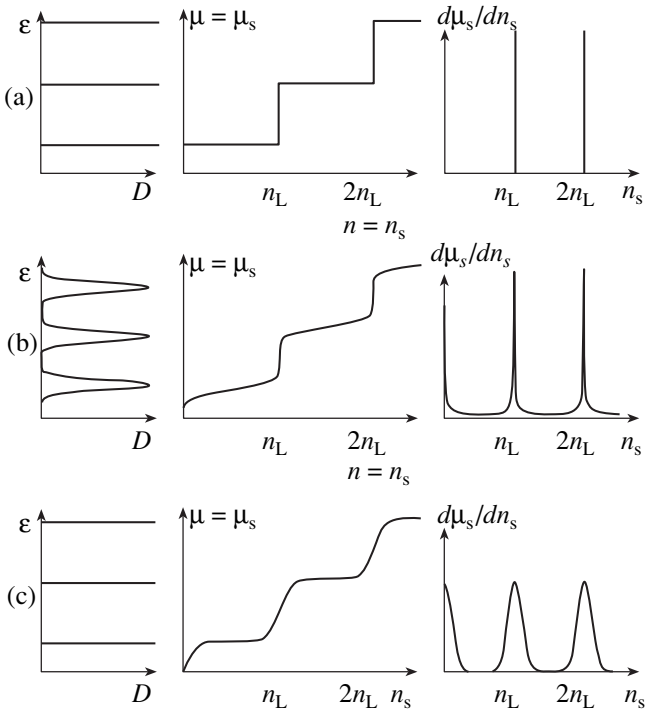

Fig. 1. The local density of states $D(\varepsilon) = dn/d\mu$ and the plots of μ_s and $d\mu_s/dn_s$ versus n_s for (a) the ideal 2DES and for the systems with only (b) a short-range and (c) a long-range random potential.

in transistors with two gates occurring on different sides of the 2DES, and (iii) the transport properties. The results obtained by the three methods were mutually consistent.

In the main part of this study, the analysis is carried out considering electrons as noninteracting. Evidence that the way used for the presentation of experimental data excludes to a considerable extent the effects of the electron–electron interaction will be given in the final part of the paper.

2. MAGNETOCAPACITANCE MEASUREMENTS

2.1. Sample Preparation

The samples for this study were based on GaAs/AlGaAs heterostructures grown by molecular beam epitaxy. The measurements of capacitance were performed on the samples of type I with a single gate electrode. These samples were grown with the following order of layers: GaAs–AlGaAs(70 nm)–Si(δ-layer)–AlGaAs(500 nm)–Si(δ-layer)–GaAs(10 nm). In this structure, a 2DES is formed in the GaAs layer near the lower GaAs/AlGaAs heterojunction. A rectangular metal gate electrode with an area of $S_g = 0.4 \times 2.3$ mm^2 was deposited onto the surface of the upper GaAs layer. As a result, a Schottky barrier is created between this electrode and the heterostructure.

The electron density n_s in the 2DES determined from the period of the Shubnikov–de Haas oscillations varies linearly with the voltage V_g between the 2DES and the gate. The coefficient of proportionality between the quantities $eS_g n_s$ and V_g coincides (with an accuracy of better than 1%) with the measured sample capacitance C = 165 pF, which indicates that the donors exhibit no recharge upon V_g variations. At a zero gate voltage, the electron density is $n_s = 1.4 \times 10^{11}$ cm^{-2} and their mobility is 1.2×10^6 cm^2/(V s). The type I samples had the form of a Hall bar with ohmic contacts to the 2DES, which allowed us to perform both the magnetocapacitance measurements and the investigation of transport properties of the 2DES.

The electric field penetrating through the 2DES was measured on the samples of type II, in which the lowest highly doped conducting GaAs layer performed the function of the back gate. This layer was followed by an AlAs/GaAs superlattice, which played the role of the barrier. The GaAs/AlGaAs heterojunction, at which the 2DES was formed, was spaced 608 nm from the back gate and 240 nm from the surface of the structure. The silicon δ-layer supplying electrons to the 2DES was separated from this system by a 80-nm-thick spacer (undoped AlGaAs layer). The type II samples also had the form of a Hall bar, in which the area of overlap with the back gate was S_{bg} = 3.24 mm^2. The front gate with an area of S_{fg} = 1 mm^2 occurred completely inside the region of overlap of the 2DES and the back gate. At a zero gate voltage, the electron mobility in samples II exceeded a level of 1×10^6 cm^2/(V s).

2.2. Experimental Techniques

Magnetocapacitance measurements consist in precise determination of the capacitance $C \equiv dQ/dV_g$ of a plane capacitor formed between the 2DES and the gate of the field-effect transistor, where Q is the charge and V_g is the voltage applied to this capacitor. Since there is a contact potential difference between the 2DES and the gate, the measured value includes a small correction δC proportional to the derivative $d\mu/dn$ [2, 17]:

$$\delta C \equiv C - C_g \approx -\frac{C^2}{S_g e^2}\frac{d\mu}{dn}, \tag{1}$$

where S_g is the 2DES area under the gate electrode, $C_g = \kappa S_g/4\pi d$ is the geometric capacitance of the sample, κ is the average permittivity of the insulator between the gate and the 2DES, and d is the thickness of this gate insulator. The correction δC is the only magnetic-field-dependent contribution to the capacitance, which accounts for all its specific features considered below. In the presence of electron density fluctuations in the 2DES, described by a Gaussian distribution with the dispersion σ, the correction to the capacitance acquires the following form [12]:

$$\begin{aligned}\delta C &\approx -\frac{C^2}{S_g e^2}\frac{d\mu_s}{dn_s} \\ &= -\frac{C^2}{\sqrt{2\pi}\sigma e^2 S_g}\int \frac{d\mu}{dn}\exp\left(-\frac{(n-n_s)^2}{2\sigma^2}\right)dn.\end{aligned} \tag{2}$$

For the measurement of $C(n_s)$, the gate voltage V_g determining the electron density n_s was modulated by the ac voltage with a frequency of 9.2 Hz and an amplitude of 20 mV. The ac current passing through the capacitor was measured using a current–voltage converter. Both components of the current were detected. The imaginary component is proportional to the sample capacitance. A decrease in the modulation amplitude by a factor of four did not change the shape of the experimental curves.

The electric field penetrating through the 2DES was measured on the samples of type II, with the 2DES confined between the two gates (front and back). When an ac voltage V_{fg} is applied between the 2DES and the front gate, the electric field partly penetrates through the electron system due to its finite compressibility and is screened by the back gate. The magnetic-field-dependent contribution to the current I_{bg} collected by the back gate is [16]

$$I_{bg} = \frac{d\mu_s}{dn_s}\frac{C_{bg}}{e^2 S_{bg}} I_{fg}, \tag{3}$$

where C_{bg} is the geometric capacitance between the back gate and the 2DES, S_{bg} is the area of overlap of the 2DES and the back gate electrode, and I_{fg} is the imaginary component of the current passing through the front gate.

The penetrating field was measured by applying an ac voltage with an amplitude of V_{fg} = 5 mV and a frequency of 9.2 Hz to the front gate. Two components of the response ac current I_{bg} from the back gate were measured using a current–voltage converter. The electron density in the 2DES was controlled by the voltage V_{bg} applied to the back gate, which could be varied from 250 to 450 mV. The corresponding electron density was proportional to V_{bg} with a coefficient of $\Delta n_s/\Delta V_{bg} = 1.24 \times 10^8$ cm^{-2} mV^{-1}.

Applicability of the above methods near the Hall plateaus is usually restricted to the region of not very small conductivity along the 2DES, otherwise the resistive effect [18] leads to a sharp increase in the real

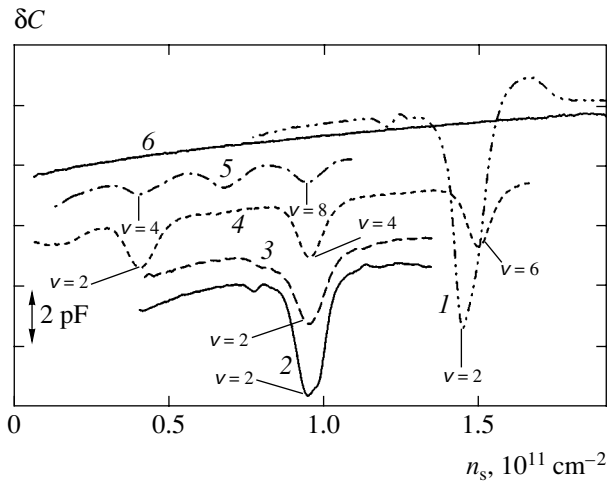

Fig. 2. The capacitance $C(n_s)$ measured in the quantum Hall effect regime in various magnetic field at various temperatures: (*1*) H = 3 T, T = 4.2 K; (*2*) H = 2 T, T = 3.1 K; (*3*) H = 2 T, T = 4.2 K; (*4*) H = 1 T, T = 1.2 K; (*5*) H = 0.5 T, T = 0.9 K; (*6*) $C(n_s, H = 0)$. The curves are shifted along the ordinate axis.

part of the measured signal accompanied by a decrease in the imaginary component. The results presented below were obtained in the absence of such resistive effects.

2.3. Capacitance in a Quantizing Magnetic Field

Using the techniques described above, we have studied the capacitance $C(n_s)$ of a plane capacitor formed between the 2DES and the gate of the field-effect transistor at various values of the quantizing magnetic field H and the temperature T. Figure 2 shows the typical plots of $C(n_s)$ measured in various magnetic fields. The minima in these curves reflect the jumps in the chemical potential at the values of filling factors corresponding to the quantum Hall effect states (see Eq. (1)). Note that minima corresponding to different states possess almost equal widths. This is illustrated in Fig. 3, where the minima of $C(n_s)$ observed in Fig. 2 are matched by shifting along the abscissa and ordinate axes and by the ordinate expansion. As can be seen from Fig. 3a showing the minima corresponding to the even filling factors in various magnetic fields (and different n_s), the width remains the same (to within 10%) upon an increase in the magnetic field strength (and, hence, in the cyclotron gap) by a factor of six. Figure 3b shows the minima matched by ordinate expansion for the filling factor $\nu_s = 2$ and the magnetic filed H = 2 T at various temperatures. The amplitude of these minima decreases with increasing temperature, but the width remains virtually unchanged up to a rather high temperature and then begins to grow. Figure 3c shows the matched minima for the even filling factors $\nu_s = 2$, 4, and 6 at a fixed magnetic field of H = 1 T. The widths of all these minima coincide to within 10%. The minima are well described by the Gaussians with dispersions $\sigma = (3.3 \pm 0.4) \times 10^9$ and $(5.2 \pm 0.5) \times 10^9$ cm^{-2} for the samples of types I and II, respectively.

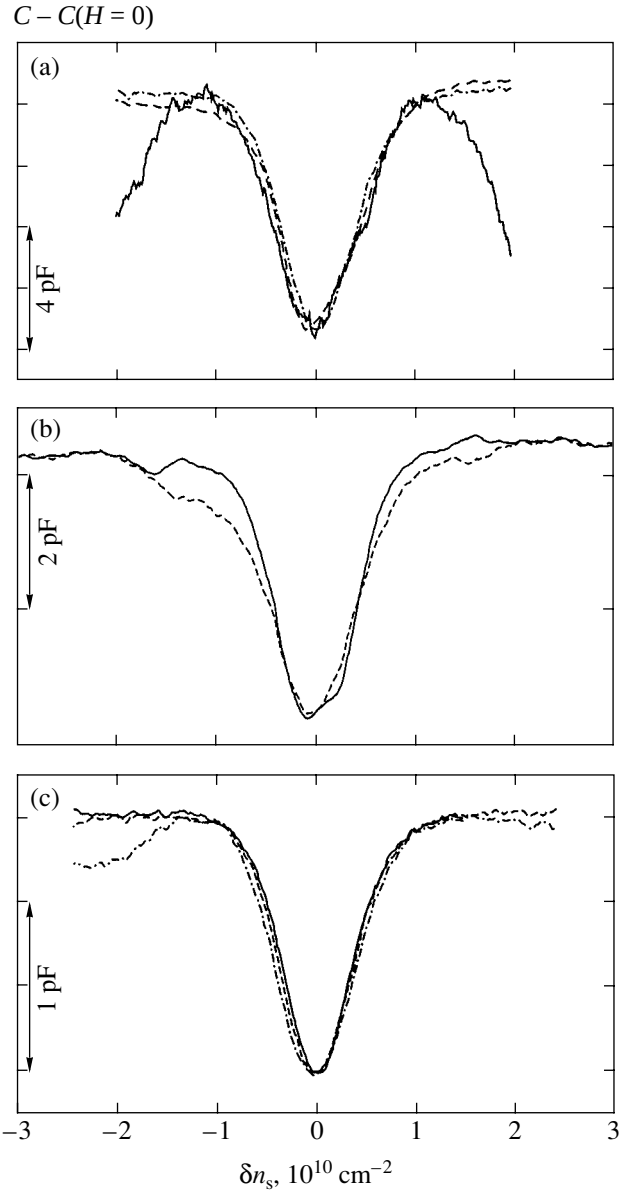

Fig. 3. Matched plots of the $C - C(H = 0)$ difference versus electron density variation δn_s from values corresponding to integer filling factors [the $C(n_s, H = 0)$ dependence was subtracted from the curves of Fig. 2 and the differences were matched by shifting along the ordinate and abscissa axes and multiplying the ordinate by various coefficients k]: (a) in a field of 0.5 T (dash-dot line, ν_s = 4, k = 12.5), 1 T (dashed line, ν_s = 2, k = 4.2), 3 T (solid line, ν_s = 2, k = 1); (b) for ν_s = 2 in a field of 2 T and T = 3.1 K (solid line, k = 1) and 4.2 K (dashed line, k = 1.6); (c) in a field of 1 T for ν_s = 2 (dash-dot line, k = 1.3), 4 (dashed line, k = 1.1), and 6 (solid line, k = 1).

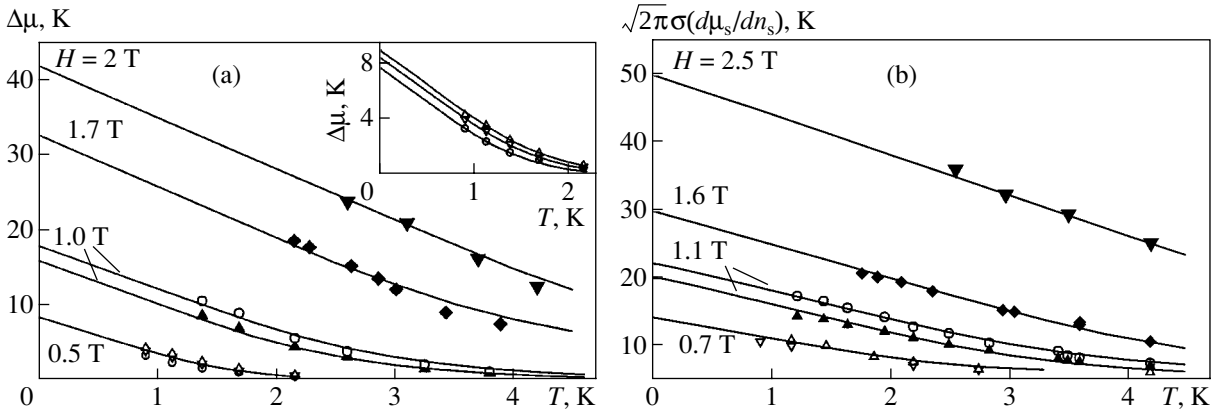

Fig. 4. The temperature dependence of (a) Δμ and (b) $\sqrt{2\pi}\,\sigma(d\mu_s/dn_s)$ determined from the magnetocapacitance and penetrating field measurements, respectively, for $\nu_s = 2$ (black symbols), 4 (○), 6 (▽), and 8 (△): solid lines show the results of numerical calculations (see the text); the inset shows the Δμ(*T*) curves for $\nu_s = 4, 6, 8$ measured at $H = 0.5$ T plotted on a greater scale.

Figure 4a shows the temperature dependence of the amplitude of Δ*C* minima (determined as the difference between the capacitance values for the integer and half-integer ν_s) recalculated to the chemical potential jumps:

$$\Delta\mu(T) \equiv -\sqrt{2\pi}\sigma\frac{\Delta C}{C^2}S_g e^2 = \sqrt{2\pi}\sigma\left(\left.\frac{d\mu_s}{dn_s}\right|_{\nu_s = 2p} - \left.\frac{d\mu_s}{dn_s}\right|_{\nu_s = 2p+1/2}\right). \quad (4)$$

Analogous data obtained from the measurements of field penetration in the samples of type II are presented in Figure 4b. In this case, the chemical potential jumps observed for the quantum Hall effect states correspond to maxima in the current I_{bg} to the back gate. This figure presents a quantity expressed as

$$\left.\frac{d\mu_s}{dn_s}\right|_{\nu_s = 2p} = [I_{bg}(H) - I_{bg}(H=0)]_{\nu_s = 2p}\frac{e^2 S_{bg}}{I_{fg}C_{bg}} + \frac{\pi\hbar^2}{m^*}, \quad (5)$$

under the assumption that the reciprocal thermodynamic density of states in the zero field is equal to the value corresponding to the case of noninteracting electrons:

$$\left.\frac{d\mu_s}{dn_s}\right|_{H=0} = \frac{\pi\hbar^2}{m^*}, \quad (6)$$

where m^* is the effective mass of electrons in GaAs. Note that both values exhibit nearly linear temperature dependences, especially in the region of large magnetic field strengths.

2.4. Discussion of Results

Let us firstly derive an analytical expression for the derivative $d\mu_s/dn_s$ and analyze the temperature dependence of this quantity. Consider a system comprising a set of narrow spin-split Landau levels. Denoting the cyclotron and spin splitting as Δ_c and Δ_s, respectively, the distance between levels can be expressed as $\Delta_c - \Delta_s$ and Δ_s. Below we assume that $\Delta_s \ll \Delta_c$, which is reliably valid for GaAs. Our experiments were performed under the condition $T \ll \Delta_c - \Delta_s$. In this case, the temperature dependence of the chemical potential can be calculated taking into account the occupation only of the four Zeeman sublevels closest to the Fermi level. First, let us consider the behavior of the chemical potential in the vicinity of the filling factor $\nu = 2$. Under the aforementioned condition on the temperature, the expressions given below will be valid for any even filling factors.

The energy and the chemical potential of the four-level system under consideration are measured from the center of the cyclotron gap. At a finite temperature, electrons are distributed over energy levels according to the Fermi function $f(E) = 1/[1 + \exp(E/T)]$, whereby

$$\nu = f\left(-\frac{\Delta_c + \Delta_s}{2} - \mu\right) + f\left(-\frac{\Delta_c - \Delta_s}{2} - \mu\right) + f\left(\frac{\Delta_c - \Delta_s}{2} - \mu\right) + f\left(\frac{\Delta_c + \Delta_s}{2} - \mu\right). \quad (7)$$

At a sufficiently low temperature, such that $T \ll (\Delta_c - \Delta_s)/2$, in the vicinity of the filling factor $\nu = 2$,

where $T \ll (\Delta_c - \Delta_s)/2 - |\mu|$, this expression can be reduced to

$$\nu = 2 + 4\sinh\frac{\mu}{T}\exp\left(-\frac{\Delta_c}{2T}\right)\cosh\frac{\Delta_s}{2T}. \quad (8)$$

From this we obtain

$$\frac{d\mu}{d\nu} = \frac{T}{2\sqrt{(\nu/2-1)^2 + b^2}}, \quad (9)$$

where $b = 2\exp(-\Delta_c/2T)\cosh(\Delta_s/2T)$. Relation (9) shows that the derivative $d\mu/d\nu|_{\nu=2}$ exponentially grows as $T \longrightarrow 0$.

For an inhomogeneous system, it is necessary to average expression (9) in accordance with formula (2), taking into account that $\nu_s = n_s/n_L$. Here, we present only the resulting analytical expression for $d\mu_s/dn_s$ at the maximum corresponding to $\nu_s = 2$,

$$\left.\frac{d\mu_s}{dn_s}\right|_{\nu_s=2} = \frac{T}{\sqrt{2\pi}\sigma}\exp\left(\frac{b^2 n_L^2}{\sigma^2}\right)K_0\left(\frac{b^2 n_L^2}{\sigma^2}\right), \quad (10)$$

where K_0 is the modified Bessel function of the second kind. At low temperatures, $T \ll \Delta_s$, the curve of $d\mu_s/dn_s(T)|_{\nu_s=2}$ takes the form

$$\left.\frac{d\mu_s}{dn_s}\right|_{\nu_s=2} = \frac{\Delta_c - \Delta_s}{\sqrt{2\pi}\sigma} - \frac{T}{\sqrt{2\pi}\sigma}\left[2\ln\frac{n_L}{\sigma} - \ln 2 + \gamma\right] + O\left(\frac{bn_L}{\sigma}\right), \quad (11)$$

where $\gamma = 0.577$ is the Euler constant.

Thus, for sufficiently low temperatures such that relation $bn_L/\sigma \ll 1$ is also satisfied, the dispersion of electron density leads to a change in the character of the temperature dependence from exponential to linear. Extrapolation of the linear temperature dependence to $T = 0$ in the limiting case under consideration determines the value of $\Delta_c - \Delta_s$. An expression for the case of $\Delta_s \ll T$, which is still closer to the experimental conditions, is as follows:

$$\left.\frac{d\mu_s}{dn_s}\right|_{\nu_s=2} = \frac{\Delta_c}{\sqrt{2\pi}\sigma} - \frac{T}{\sqrt{2\pi}\sigma}\left[2\ln\frac{2n_L}{\sigma} - \ln 2 + \gamma\right] + O\left(\frac{bn_L}{\sigma}\right). \quad (12)$$

This linear temperature dependence has a greater slope (corresponding to the double number of states $2n_L$ on the Landau level) and extrapolates to $\Delta_c/\sqrt{2\pi}\sigma$ for $T \longrightarrow 0$.

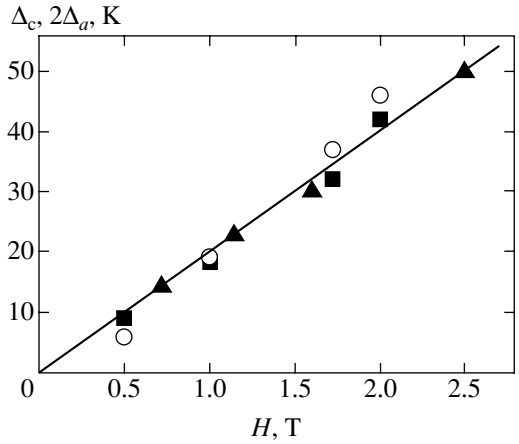

Fig. 5. The cyclotron gap versus magnetic field: (■) Δ_c values determined by approximation of the amplitude of the capacitance features at (H, ν) = (0.5 T, 8), (1 T, 4), (1.7 T, 2), and (2 T, 2); (▲) Δ_c values determined from the measurements of the penetrating field at (H, ν) = (0.7 T, 8), (1.1 T, 4), (1.6 T, 2), and (2.5 T, 2); (○) $2\Delta_a$ values determined from the activation measurements at features at (H, ν) = (0.5 T, 8), (1 T, 4), (1.7 T, 2), and (2 T, 2); solid bar shows the value of $\hbar\omega_c = He\hbar/m^*c$ for $m^* = 0.067m_0$.

For comparison with experiment, we numerically determined $\Delta\mu(T)$ using formula (4). Solid lines in Fig. 4a show the results of these calculations with a fitting parameter Δ_c (and the previously determined value of $\sigma = 3.3 \times 10^9$ cm^{-2} for all fields). A comparison of the slope of experimental plots with that of the calculated curves shows that the spin splitting is $\Delta_s \ll T$ in the entire temperature range studied. For this reason, calculations for the chemical potential at the center of the cyclotron gap were performed with nonenhanced spin gaps $\Delta_s = g\mu_B H$, where the g value is equal to the bulk value for GaAs ($g\mu_B = 0.3$ K/T).

The results of numerical calculations showed that $\Delta\mu(T)$ is a linear function in the same temperature region where $(d\mu_s/dn_s)_{\nu_s=2p}$ exhibits linear behavior, and

$$\Delta\mu(T=0) = \sqrt{2\pi}\sigma\left.\frac{d\mu_s}{dn_s}\right|_{\nu_s=2p} \quad (T=0).$$

Therefore, taking into account that $\Delta_s \ll T \ll \Delta_c$, the cyclotron gap Δ_c can be determined (to within Δ_s/Δ_c) by linear extrapolation of the experimental data for $\Delta\mu(T)$ to $T = 0$.

Figure 4b shows the results of numerical calculations of the quantity $\sqrt{2\pi}\sigma(d\mu_s/dn_s)_{\nu_s=2p}$ in comparison with the experimental data obtained for the field penetration. The value of $\sigma = 5.2 \times 10^9$ cm^{-2} was deter-

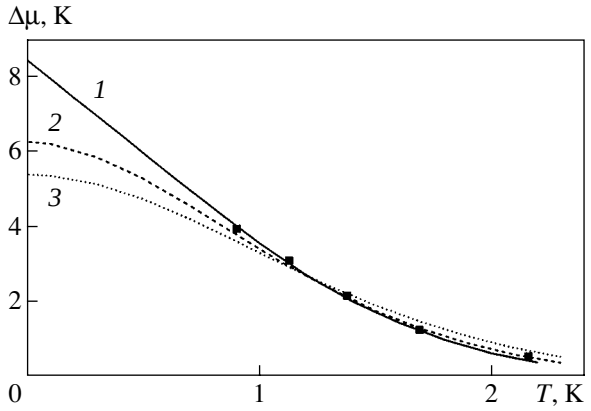

Fig. 6. The effect of the Landau level broadening due to the short-range potential calculated assuming a Gaussian distribution with the dispersion Γ for $\Delta_s = 0.15$ K, $\sigma/n_L = 0.26$, and (*1*) Γ = 0 K, $\Delta_c = 8.6$ K, (*2*) Γ = 1.0 K, $\Delta_c = 9.3$ K, and (*3*) Γ = 1.7 K, $\Delta_c = 10.5$ K in comparison to the results of capacitance measurements at $H = 0.5$ T and ν = 6 (squares).

mined previously, the spin splitting was taken equal to $\Delta_s = g\mu_B H$, and the only fitting parameter was the cyclotron gap determined by the intercept at $T = 0$. Thus, there is a good agreement between experimental data and the proposed model. The values of $\Delta_c(H)$ obtained by the two methods are compared in Fig. 5. These values are close to the cyclotron energy for GaAs.

When the concept of level broadening due to the short-range random potential is introduced into the model, the slope of the temperature dependences of $(d\mu_s/dn_s)_{\nu_s = 2p}$ and Δμ decreases as compared to the value for narrow levels in the entire temperature range and these temperature dependences exhibit saturation at low temperatures (Fig. 6). This behavior indicates that Δ_c obtained by extrapolating the measured curve of $\sqrt{2\pi}\sigma(d\mu_s/dn_s)_{\nu_s = 2p}$ to $T = 0$ does not exceed the real value. At the same time, Fig. 6 shows that determination of the spectral gap according to the "area of the minimum" [4, 13] at a finite temperature unavoidably leads to underestimated values even when the inverse compressibility $d\mu_s/dn_s$ exhibits saturation.

A comparison of the experimental data obtained for our samples at $H = 0.5$ T with the values calculated with allowance for the finite Γ value (Fig. 6) shows that $\Gamma/\Delta_c \le 0.15$ even in this case of a weak field. For greater values of Γ/Δ_c, the discrepancy between calculated and experimental values would exceed experimental uncertainty and cannot be compensated by selecting a different value of Δ_c. It should be noted that, for this estimate of the upper limit for the level width ($\Gamma/\Delta_c = 0.15$), the local density of states at the middle of the cyclotron gap does not exceed 2% of the density of states in a zero magnetic field.

3. COMPARISON OF THE RESULTS OF THERMOACTIVATION AND CAPACITANCE MEASUREMENTS

The gap in the energy spectrum of an electron system in the regime of the quantum Hall effect can be also determined by measuring the temperature dependence of the dissipative conductivity having an activation character:

$$\sigma_{xx}^{\min} = \sigma_0 \exp(-\Delta_a/T).$$

In the case of a screened long-range random potential, the activation energy Δ_a is equal to a distance from the Fermi level to the percolation level (coinciding with $\hbar\omega_c/2$ for a nonlinear screening and integer filling factor) [14].

The measured values of $2\Delta_a(H)$ are plotted in Fig. 5. The double activation energy is a linear function of the magnetic field strength, but the slope of this dependence ($2d\Delta_a/dH = 26$ K/T) is greater than that for the cyclotron splitting in GaAs ($e\hbar/m^*c = 19.5$ K/T). The same effect was observed in [19], where the corresponding value amounted to 26.5 K/T. In our experiments, the double activation energy exceeded the cyclotron splitting in the fields $H > 1$ T.

Using the results of transport measurements in the magnetic field and an expression for the conductivity [8],

$$\sigma_{xx}(n_s) = \sigma_0 \exp\left(-\frac{\Delta_a}{T}\right)\cosh\left(\frac{\mu_s(n_s)}{T}\right)$$

it is possible to determine $\mu_s(n_s)$. According to the results reported in [14], this formula (obtained in the model of homogeneously broadened Landau levels with electron activation to the mobility edge) is also applicable to the case of a screened long-range potential. Figure 7b shows the $\mu_s(n_s)$ curves calculated using the experimental plots of $\sigma_{xx}(n_s)/\sigma_{xx}^{\min}$ for various temperatures depicted in the inset to this figure.

The dependence $\mu_s(n_s)$ can be also determined from the results of capacitance measurements (see the inset to Fig. 7a). This is achieved by integrating the capacitance $C(n_s)$ relative to the curve

$$C_g(n_s) = C(n_s, H = 0) + \frac{\pi\hbar^2 C^2}{m^* S_g e^2}.$$

The results of such integration presented in Fig. 7a show that the $\mu_s(n_s)$ curves obtained using the capacitance and transport measurements are in good agree-

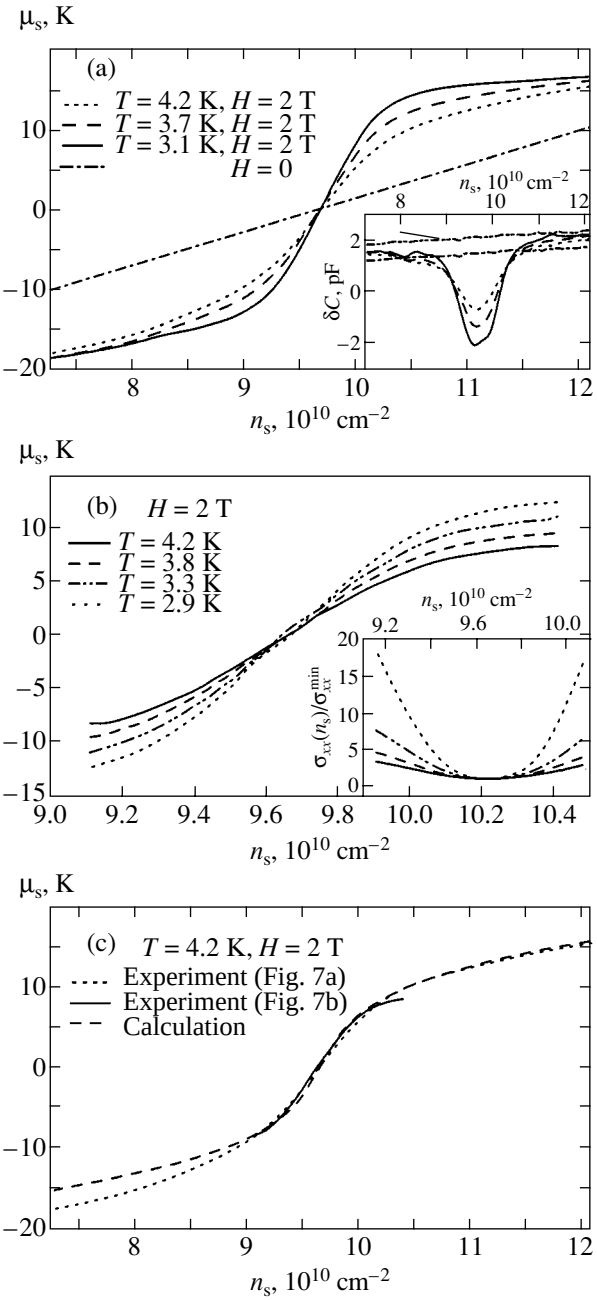

Fig. 7. Plots of $\mu_s(n_s)$: (a) determined by integrating $C(n_s)$ relative to the geometric capacitance $C_g(n_s)$ (the inset shows the temperature dependence of the capacitance measured in a field of $H = 2$ T); (b) determined from the results of the transport measurements (the inset shows the conductivity $\sigma_{xx}(n_s)/\sigma_{xx}^{min}$ measured at various temperatures); (c) comparison of the results of measurements and calculation for $T = 4.2$ K.

ment and coincide well with the theoretical calculations for the same temperature (Fig. 7c).

Now, let us consider the role of electron–electron interactions. It was demonstrated above that our experimental results could be described using the approximation of noninteracting electrons. The applicability of this approximation to description of the quantum Hall effect for even filling factors ν_s is probably related to the fact that the contribution of the electron–electron interaction to the thermodynamic density of states in a broad range of ν_s weakly depends on the magnetic field and is determined primarily by the electron density. This fact is reliably established, for example, in the case of $\nu_s = 1/2$ observed in strong magnetic fields [20]. Additional evidence is provided by zero value of the integral [21]

$$\int_{\nu}^{\nu+2} [C(n_s, H) - C(n_s, H = 0)]dn_s$$

in the case of weak fields, where the spin splitting is negligible. Being weakly dependent on the magnetic field, the electron–electron interaction does not influence the difference of capacitances for even filling factors and in a zero field and the difference of capacitances for the even and half-integer filling factors. In the latter case, a small difference in electron densities for the corresponding filling factors is apparently insignificant. Well-known cases of deviation from this behavior include the fractional quantum Hall effect states and enhanced values of splitting for small odd filling factors, which does not influence the results of this study.

Thus, we have demonstrated that nonzero $dn_s/d\mu_s$ values in the gap between the Landau levels observed for our samples are caused by the long-range fluctuations of the electron density. The experimental data obtained in a broad range of filling factors agree with the results of numerical calculations of $d\mu_s/dn_s$ in the case of narrow magnetic levels taking into account the temperature dependence of the chemical potential and its averaging with respect to the electron density. Our results imply a very small value of the local density of states in the gap between the levels. It was demonstrated that the capacitance and transport measurements give the same results for $d\mu_s/dn_s$ in the vicinity of $\nu = 2$.

ACKNOWLEDGMENTS

The authors are grateful to K. Ploog and V. Umanski for kindly providing the samples for investigation.

This study was supported by the Russian Foundation for Basic Research and by the INTAS Foundation.

REFERENCES

1. *The Quantum Hall Effect*, Ed. by R. Prange and S. M. Girvin (Springer, New York, 1987; Mir, Moscow, 1989).
2. T. P. Smith, B. B. Goldberg, P. J. Stiles, and M. Heiblum, Phys. Rev. B **32**, 2696 (1985).

3. V. M. Pudalov and S. G. Semenchinskiĭ, Pis'ma Zh. Éksp. Teor. Fiz. **44**, 526 (1986) [JETP Lett. **44**, 677 (1986)].
4. V. T. Dolgopolov, N. B. Zhitenev, and A. A. Shashkin, Zh. Éksp. Teor. Fiz. **94** (7), 307 (1988) [Sov. Phys. JETP **67**, 1471 (1988)].
5. E. Gornik, R. Lassing, G. Strasser, *et al.*, Phys. Rev. Lett. **54**, 1820 (1985).
6. J. P. Eisenstein, H. L. Stormer, V. Narayanamurti, *et al.*, Phys. Rev. Lett. **55**, 875 (1985).
7. E. Stahl, D. Weiss, G. Weinmann, and K. von Klitzing, J. Phys. C **18**, L783 (1985).
8. M. G. Gavrilov and I. V. Kukushkin, Pis'ma Zh. Éksp. Teor. Fiz. **43**, 79 (1986) [JETP Lett. **43**, 103 (1986)].
9. T. Ando, A. B. Fowler, and F. Stern, Rev. Mod. Phys. **54**, 437 (1982).
10. K. B. Efetov, *Supersymmetry in Disorder and Chaos* (Cambridge Univ. Press, New York, 1997).
11. R. R. Gerhardts and V. Gudmundsson, Phys. Rev. B **34**, 2999 (1986).
12. F. G. Pikus and A. L. Efros, Phys. Rev. B **47**, 16395 (1993).
13. V. S. Khrapai, A. A. Shashkin, and V. T. Dolgopolov, Phys. Rev. B **67**, 113305 (2003).
14. A. L. Efros, F. G. Pikus, and V. G. Burnett, Phys. Rev. B **47**, 2233 (1993).
15. D. B. Chklovskii, B. I. Shklovskii, and L. I. Glazman, Phys. Rev. B **46**, 4026 (1992).
16. J. P. Eisenstein, L. N. Pfeiffer, and K. W. West, Phys. Rev. B **50**, 1760 (1994).
17. T. Jungwirth and L. Smrčka, Phys. Rev. B **51**, 10181 (1995).
18. S. I. Dorozhkin, A. A. Shashkin, N. B. Zhitenev, and V. T. Dolgopolov, Pis'ma Zh. Éksp. Teor. Fiz. **44**, 189 (1986) [JETP Lett. **44**, 241 (1986)].
19. A. Usher, R. J. Nikolas, J. J. Harris, and C. T. Foxon, Phys. Rev. B **41**, 1129 (1990).
20. S. I. Dorozhkin, J. H. Smet, K. von Klitzing, *et al.*, Phys. Rev. B **63**, 121301 (2001).
21. M. O. Dorokhova, Candidate's Dissertation in Physics and Mathematics (Institute of Solid State Physics, Russian Academy of Sciences, Chernogolovka, 2000).

Translated by P. Pozdeev

Journal of Experimental and Theoretical Physics, Vol. 98, No. 6, 2004, pp. 1231–1236.
From Zhurnal Éksperimental'noĭ i Teoreticheskoĭ Fiziki, Vol. 125, No. 6, 2004, pp. 1403–1408.

SOLIDS
Electronic Properties

Fermi-Liquid Effects in Transresistivity in Quantum Hall Double Layers near ν = 1/2¶

N. A. Zimbovskaya

Department of Physics and Astronomy, St. Cloud State University, Cloud, MN, 56301 USA
Ural State Academy of Mining and Geology, Yekaterinburg, 620000 Russia
e-mail: nzimbov@physlab.sci.ccny.cuny.edu

Received November 24, 2003

Abstract—We present theoretical studies of the temperature and magnetic field dependences of the Coulomb drag transresistivity between two parallel layers of two-dimensional electron gases in the quantum Hall regime near half-filling of the lowest Landau level. It is shown that Fermi-liquid interactions between the relevant quasiparticles can significantly affect the transresistivity, providing its independence of the interlayer spacing for spacings that take values reported in the experiments. The obtained results agree with the experimental evidence. © *2004 MAIK "Nauka/Interperiodica".*

During the last decade, double-layer two-dimensional (2D) electron gas systems were of significant interest due to many remarkable phenomena that they exhibit, including the so-called Coulomb drag. In Coulomb drag experiments, two 2D electron gases are arranged close to each other, such that they can interact via Coulomb forces. A current I is applied to one layer of the system, and the voltage V_D in the other nearby layer is measured, with no current allowed to flow in that layer. The ratio $-V_D/I$ gives the transresistivity ρ_D, which characterizes the strength of the effect. The physical interpretation of the Coulomb drag is that momentum is transferred from the current-carrying layer to the nearby one due to interlayer interactions [1–3].

It was shown theoretically [4, 5] and confirmed with experiments [5] that the transresistivity between two 2D electron gases in the quantum Hall regime at half-filling of the lowest Landau level for both layers is proportional to $T^{4/3}$ (where T is the temperature of the system), which is quite different from the temperature dependence of ρ_D in the absence of the external magnetic field applied to 2D electron gases. This temperature dependence of the drag at $\nu = 1/2$ originates from the ballistic contribution to transresistivity. The latter reflects the response of the two-layer system to the driving disturbance of a finite wavevector $\mathbf{q}$ and finite frequency ω in the case where the relevant scales are smaller than the mean free path l of electrons ($ql \gg 1$) and times are shorter than their scattering time τ ($\omega\tau \gg 1$).[1]

In further experiments [7], the Coulomb drag was measured between 2D electron gases where the layer filling factor was varied around $\nu = 1/2$. The transresistivity was reported to be enhanced quadratically with $\Delta\nu = \nu - 1/2$. It was also reported that the curvature of the enhancement depended on temperature but was insensitive to both the sign of $\Delta\nu$ and the distance d between the layers. The present work is motivated with these experiments of [7]. We calculate the transresistivity between two layers of 2D electron gases subject to a strong magnetic field that provides ν close to 1/2 for both layers.

We start from the well-known expression [1, 3] that relates the Coulomb drag transresistivity to density–density components of the polarization in the layers $\Pi_{(1)}(\mathbf{q}, \omega)$ and $\Pi_{(2)}(\mathbf{q}, \omega)$,

$$\rho_D = \frac{1}{2(2\pi)^2}\frac{h}{e^2}\frac{1}{Tn^2}\int\frac{q^2 d\mathbf{q}}{(2\pi)^2}\int\frac{\hbar d\omega}{\sinh^2(\hbar\omega/2T)} \times |U(\mathbf{q}, \omega)|^2 \mathrm{Im}\Pi_{(1)}(\mathbf{q}, \omega)\mathrm{Im}\Pi_{(2)}(\mathbf{q}, \omega), \quad (1)$$

where $U(\mathbf{q}, \omega)$ is the screened interlayer Coulomb interaction, and electron densities in the layers are supposed to be equal ($n_1 = n_2 = n$).

Within the usual composite fermion approach [8], a single layer polarizability describes the part of the density–current electromagnetic response that is irreducible with respect to the Coulomb interaction. Adopting the random-phase approximation (RPA) for simplicity, we obtain the following expression for the 2×2 polarizability matrix:

$$\Pi^{-1} = (K^0)^{-1} + C^{-1}. \quad (2)$$

¶This article was submitted by author in English.

[1] When the external driving disturbance applied to one of the layers is of small $\mathbf{q}$, ω ($ql \ll 1$, $\omega\tau \ll 1$), the transresistivity is dominated by the diffusion contribution and new effects can emerge (see, e.g., [6] and references therein).

Here, the matrix K^0 gives the response of noninteracting composite fermions and C is the Chern–Simons interaction matrix. Assuming the wavevector $\mathbf{q}$ to lie in the x direction for definiteness, we have

$$C = \begin{pmatrix} 0 & \frac{iq}{4\pi\hbar} \\ -\frac{iq}{4\pi\hbar} & 0 \end{pmatrix}. \tag{3}$$

Starting from expression (2), we arrive at the following results for the density–density response function

$$\Pi_{00(i)}(\mathbf{q}, \omega) = \Pi_{(i)}(\mathbf{q}, \omega) = \frac{K^0_{00(i)}(\mathbf{q}, \omega)}{1 - \frac{8i\pi\hbar}{q}K^0_{01(i)}(\mathbf{q}, \omega) - \left(\frac{4\pi\hbar}{q}\right)^2 \Delta_{(i)}(\mathbf{q}, \omega)}. \tag{4}$$

Here,

$$\Delta_{(i)}(\mathbf{q}, \omega) = K^0_{00(i)}(\mathbf{q}, \omega)K^0_{11(i)}(\mathbf{q}, \omega) + (K^0_{01(i)}(\mathbf{q}, \omega))^2. \tag{5}$$

Within the RPA, the response functions included in Eqs. (4) and (5) are simply related to the components of the composite fermion conductivity tensor $\tilde{\sigma}$ [8],

$$\frac{1}{\tilde{\sigma}^{(i)}_{xx}(\mathbf{q}, \omega)} = \frac{iq^2}{\omega e^2}\left[\frac{1}{K^0_{00(i)}(\mathbf{q}, \omega)} - \frac{1}{K^0_{00(i)}(\mathbf{q}, 0)}\right],$$

$$\tilde{\sigma}^{(i)}_{yy}(\mathbf{q}, \omega) = -\frac{ie^2}{\omega}[K^0_{11(i)}(\mathbf{q}, \omega) - K^0_{11(i)}(\mathbf{q}, 0)], \tag{6}$$

$$\tilde{\sigma}^{(i)}_{xy} = -\tilde{\sigma}^{(i)}_{yx} = \frac{ie^2}{q}K^0_{01(i)}(\mathbf{q}, \omega).$$

To proceed, we calculate the components of the composite fermion conductivity at ν slightly away from 1/2. In this case, composite fermions experience a nonzero effective magnetic field

$$B_{\text{eff}} = B - B_{1/2}.$$

We concentrate on the ballistic contribution to the transresistivity, and we therefore need the asymptotics for the relevant conductivity components applicable in nonlocal ($ql \gg 1$) and high-frequency ($\omega\tau \gg 1$) regimes. The corresponding expressions for $\tilde{\sigma}_{ij}$ were obtained in earlier works [8]. However, these results are not appropriate for our analysis because they do not provide a smooth passage to the $B_{\text{eff}} \longrightarrow 0$ limit at finite $\mathbf{q}$. Therefore, we do not use them in further calculations. To obtain a suitable approximation for the composite fermion conductivity, we start from the standard solution of the Boltzmann transport equation for the composite fermion distribution function. This gives the following results for the composite fermion conductivity components for a single layer [9]:

$$\tilde{\sigma}_{\alpha\beta} = \frac{m^*e^2}{(2\pi\hbar)^2}\frac{1}{\Omega}\int_0^{2\pi} d\psi\, v_\alpha(\psi)\exp\left[-\frac{iq}{\Omega}\int_0^{\psi} v_x(\psi'')d\psi''\right] \times \int_{-\infty}^{\psi} v_\beta(\psi')\exp\left[\frac{iq}{\Omega}\int_0^{\psi'} v_x(\psi'')d\psi'' + \frac{1}{\Omega\tau}(\psi' - \psi)(1 - i\omega\tau)\right]d\psi'. \tag{7}$$

Here, m^* and Ω are the composite fermion effective mass and the cyclotron frequency at the effective magnetic field B_{eff}; ψ is the angular coordinate of the composite fermion cyclotron orbit. We now perform some formal transformations of this expression (7) following a way proposed before [9, 10]. First, we expand the composite fermion velocity components $v_\beta(\psi')$ in a Fourier series,

$$v_\beta(\psi') = \sum_k v_{k\beta}\exp(ik\psi'). \tag{8}$$

Substituting this expansion (8) in (7), we obtain

$$\tilde{\sigma} = \frac{m^*e^2}{(2\pi\hbar)^2}\sum_k v_{k\beta}\int_0^{2\pi} d\psi\, v_\alpha(\psi)\exp(ik\psi) \times \int_{-\infty}^{0}\exp\left[\left(ik\Omega - i\omega + \frac{1}{r} + iq\,v_x(\psi)\right)\theta + iq\int_0^{\infty}(v_x(\psi + \Omega\theta') - v_x(\psi))d\theta'\right]d\theta, \tag{9}$$

where

$$\theta = \frac{\psi' - \psi}{\Omega}.$$

Then, we introduce a new variable η related to the variable θ as

$$\eta = \left(ik\Omega - i\omega + \frac{1}{\tau} + iq\,v_x(\psi)\right)\theta + iq\int_0^{\theta}[v_x(\psi + \Omega\theta') - v_x(\psi)]d\theta'. \tag{10}$$

The result is

$$\tilde{\sigma}_{\alpha\beta} = \frac{im^*e^2}{(2\pi\hbar)^2}\sum_k v_{k\beta}\int_{-\infty}^{0} e^{\eta}d\eta \times \int_0^{2\pi}\frac{v_\alpha(\psi)\exp(ik\psi)}{\omega + i/\tau - k\Omega - qv_x(\psi+\Omega\theta)}d\psi. \quad (11)$$

Under the conditions of interest, $\omega\tau \gg 1$, $ql \gg 1$, and also assuming that the filling factor is close to $\nu = 1/2$, and, hence, $qv_F \gg \Omega$ (where v_F is the composite fermions Fermi velocity), the variable θ is approximately equal to

$$\eta\tau(1 + iql\cos\psi + ik\Omega\tau - i\omega\tau)^{-1}.$$

Taking this into account and expanding the last term in the denominator of (11) in powers of $\Omega\theta$, we obtain

$$qv_x(\psi+\Omega\theta) \approx qv_x(\psi) + \eta\Omega q\tau(1 + iql\cos\psi + ik\Omega\tau - i\omega\tau)^{-1}\frac{dv_x}{d\psi} + q\frac{\eta^2}{2}(\Omega\tau)^2(1 + iql\cos\psi + ik\Omega\tau - i\omega\tau)^{-2}\frac{d^2v_x}{d\psi^2}. \quad (12)$$

Substituting this asymptotic expression in (9), we can calculate the first terms of the expansions of relevant components of the composite fermion conductivity in powers of the small parameter $(qR)^{-1}$, where $R = v_F/\Omega$ is the composite fermion cyclotron radius. In the "collisionless" limit $1/\tau \longrightarrow 0$, we have

$$\tilde{\sigma}_{xx} = -N\frac{i\omega}{q^2}e^2\left\{1 + \frac{i\delta}{\sqrt{1-\delta^2}} + \frac{i\delta}{\sqrt{(1-\delta^2)^5}}\frac{1}{2(qR)^2}\left(1 - \frac{5}{4}\frac{1}{1-\delta^2}\right)\right\}, \quad (13)$$

$$\tilde{\sigma}_{yy} = N\frac{v_Fe^2}{q}\left\{\sqrt{1-\delta^2} + i\delta + \frac{1}{2(qR)^2}\left[\frac{7}{4}\frac{1}{\sqrt{(1-\delta^2)^5}} - \frac{1}{\sqrt{(1-\delta^2)^3}}\right]\right\}, \quad (14)$$

$$\tilde{\sigma}_{xy} = iN\frac{v_Fe^2}{q}\frac{\delta}{2qR}\left[\frac{1}{\sqrt{1-\delta^2}} + \frac{\delta^2}{\sqrt{(1-\delta^2)^3}}\right], \quad (15)$$

where $N = m^*/2\pi\hbar^2$ is the density of states at the composite fermion Fermi surface and $\delta = \omega/qv_F$. Using these results, we can easily obtain approximations for the functions $K^0_{\alpha\beta(i)}(\mathbf{q}, \omega)$ (α, β = 0.1) and, subsequently, the desired density–density response function given by (4). It was shown in [3] that the integral over ω in the expression (1) for ρ_D is dominated by $\omega \sim T$, and the major contribution to the integral over q in this expression comes from

$$q \sim k_F(T/T_0)^{1/3},$$

where k_F is the Fermi wavevector and the scaling temperature T_0 is defined below. Therefore, we obtain an estimate for δ, namely,

$$\delta \sim (T/\mu)(T_0/T)^{1/3},$$

where μ is the chemical potential of a single 2D electron gas included in the bilayer. For parameter T_0, taking values on the order of room temperature, δ is small compared to unity at low temperatures ($T \sim 1$ K).

Here, we limit ourselves to the case of two identical layers ($\Pi_{(1)} \equiv \Pi_{(2)} \equiv \Pi$). For $\delta \ll 1$, we obtain the approximation

$$\Pi_{00}(\mathbf{q}, \omega) = \frac{q^3}{q^3\left(\frac{dn}{d\mu}\right)^{-1} - 8\pi i\hbar\omega k_F\left(1 + 2(k_FR)^{-1} + \frac{3}{8}(qR)^{-2}\right)}, \quad (16)$$

where $dn/d\mu$ is the compressibility of the $\nu = 1/2$ state, which is defined as [3]

$$\frac{dn}{d\mu} \equiv \Pi_{00}(\mathbf{q} \longrightarrow 0;\ \omega \longrightarrow 0) = \frac{3m^*}{8\pi\hbar^2}. \quad (17)$$

This differs from the compressibility of the noninteracting 2D electron gas in the absence of the external magnetic field (the latter is equal to N). The difference in the compressibility values is a manifestation of the Chern–Simons interaction in strong magnetic fields.

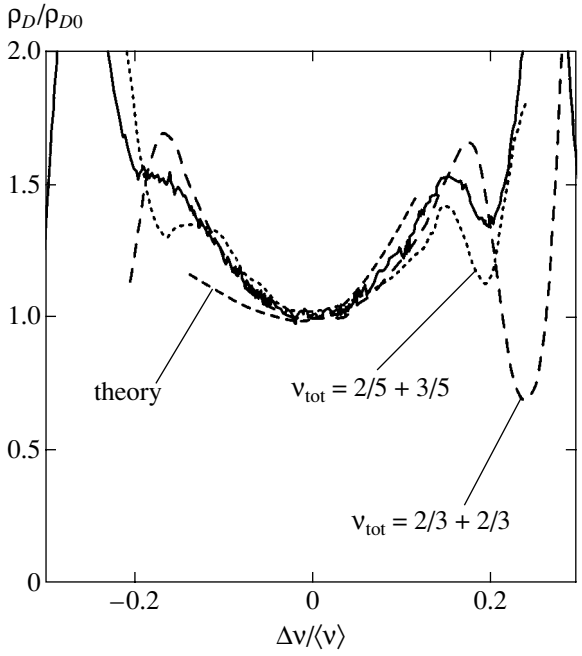

Fig. 1. Scaled drag resistivity versus $\Delta\nu$ at $T = 0.6$ K; the lowest dashed curve is the plot of Eq. (22) at $m^* = 4m_b$; $A_0 = 15$; and remaining curves represent the experimental data in [7].

In the following calculations, we adopt the expression used in [3] for the screened interlayer potential $U(\mathbf{q}, \omega)$,

$$U(\mathbf{q}, \omega) = \frac{1}{2}\frac{V_b + U_b}{1 + \Pi(\mathbf{q}, \omega)(V_b + U_b)} - \frac{1}{2}\frac{V_b - U_b}{1 + \Pi(\mathbf{q}, \omega)(V_b - U_b)}, \quad (18)$$

where

$$V_b(\mathbf{q}) = \frac{2\pi e^2}{\epsilon q}, \quad U_b(\mathbf{q}) = \frac{2\pi e^2}{\epsilon q}e^{-qd}$$

are the respective Fourier components of the bare Coulomb potentials for intralayer and interlayer interactions and ϵ is the dielectric constant. Substituting (18) in (1) and using our result (16) for $\Pi(\mathbf{q}, \omega)$, we can present the transresistivity in the "ballistic" regime as

$$\rho_D = \rho_{D0} + \delta\rho_D, \quad (19)$$

where the first term ρ_{D0} is the transresistivity at $\nu = 1/2$ when the effective magnetic field is zero and the second term gives a correction arising in a nonzero effective magnetic field (away from $\nu = 1/2$). As expected, our expression for ρ_{D0} coincides with the already known result [3],

$$\rho_{D0} = \frac{h}{e^2}\frac{\Gamma(7/3)\zeta(4/3)}{3\sqrt{3}}\left(\frac{T}{T_0}\right)^{4/3}, \quad (20)$$

where

$$T_0 = \frac{\pi e^2 n d}{\epsilon}(1 + \alpha),$$

and

$$\frac{1}{\alpha} = \frac{2\pi e^2 d}{\epsilon}\frac{dn}{d\mu}. \quad (21)$$

The leading term of the correction $\delta\rho_D$ at low temperatures,

$$T/T_0 \ll 1,$$

can be written as

$$\delta\rho_D = \frac{2}{3}\rho_{D0}\frac{1}{k_F R}\left(1 + \frac{3}{8}\frac{1}{k_F R}\right) + a^2\frac{h}{e^2}\left(\frac{2T_0}{T_0}\right)^{2/3}\frac{1}{(k_F R)^2} \quad (22)$$

$$\approx \frac{4}{3}\rho_{D0}\Delta\nu\left(1 + \frac{3}{4}\Delta\nu\right) + 4a^2\frac{h}{e^2}\left(\frac{2T}{T_0}\right)^{2/3}(\Delta\nu)^2,$$

where the dimensionless positive constant a^2 can be approximated as

$$a^2 = \frac{7}{24\sqrt{3}}\int_0^\infty\left(\frac{y^{2/3}}{\sinh^2 y} - \frac{1}{y^{4/3}\cosh^2 y}\right)dy. \quad (23)$$

We must remark that our result (23) cannot be used in the limit of $T \longrightarrow 0$. Actually, this expression provides a good asymptotic form for the coefficient a^2 when $(Tk_F l/\mu)^{1/3} \geq 1.5$. Assuming that the mean free path is on the order of 1.0 μm as in experiments [11] on dc magnetotransport in a single modulated 2D electron gas at ν close to 1/2, and using the estimate in [7] for the electron density $n = 1.4 \times 10^{15}$ m^{-2}, we find that expression (23) gives a good approximation for a^2 when T/μ is not less than 10^{-2}.

It follows from our results (19) and (22) that the transresistivity ρ_D is enhanced nearly quadratically with $\Delta\nu$ when the filling factor deviates from $\nu = 1/2$. The term linear in $\Delta\nu$ is also present in the expression for $\delta\rho_D$. This causes an asymmetric shape in the plot of Eq. (22) with respect to $\Delta\nu = 0$. However, this asymmetry is not very significant because the linear term is smaller than the last term in the right-hand side of (22). This difference in magnitude is due to the different temperature dependences of the terms considered. The first term, including the correction linear in $(k_F R)^{-1}$, is proportional to $(T/T_0)^{4/3}$, whereas the second one is proportional to $(T/T_0)^{2/3}$ and predominates at low temperatures. Therefore, the magnetic field dependence of the transresistivity near $\nu = 1/2$ matches that observed in the experiments (see Fig. 1).

Keeping only the largest term in (22), we can represent the ratio ρ_D/ρ_{D0} as

$$\frac{\rho_D}{\rho_{D0}} = 4\beta(\Delta\nu)^2 + 1 \tag{24}$$

with the coefficient

$$\beta = \frac{3\sqrt{3}a^2}{\Gamma(7/3)\zeta(4/3)}\left(\frac{2T_0}{T}\right)^{2/3}. \tag{25}$$

This coefficient is proportional to the curvature of the plot of Eq. (22) assuming that the first term is neglected. The curvature reveals a strong dependence on temperature; its character also agrees with experiments of [7], as shown in Fig. 2.

A striking feature of the experimental results is that they appear to be insensitive to the distance between the 2D electron gases. Sets of data corresponding to samples with different interlayer spacings $d_A = 10$ nm and $d_B = 22.5$ nm fall on the same curve. This concerns both the magnetic field dependence of the transresistivity and the temperature dependence of the parameter β. The results of the present analysis provide a possible explanation for this feature. It follows from (20)–(25) that the dependence of ρ_D on the interlayer spacing is completely included in the characteristic temperature T_0, which is defined with Eq. (21). The above quantity is nearly independent of the interlayer separation d when the parameter α takes values larger than unity. Estimating the parameter α given by Eq. (21), we find that the condition $\alpha > 1$ could be satisfied for small values of the compressibility of the $\nu = 1/2$ state. However, within the RPA, the effective mass of composite fermions coincides with the single electron band mass m_b, which takes the value $m_b \approx 0.07m_e$ for GaAs wells (m_e is the mass of a free electron). Using this value to estimate the compressibility introduced by Eq. (17), we obtain $\alpha \approx 0.44$. This is too small to provide insensitivity of the coefficient β determined by Eq. (25) to the interlayer distance for interlayer spacings reported in the experiments [3]. The above discrepancy could be removed by taking Fermi-liquid interactions among quasiparticles (composite fermions) into account. To include Fermi-liquid effects into consideration, we write the renormalized polarizability Π^* as [8]

$$\Pi^{*-1} = \Pi^{-1} + F_{(0)} + F_{(1)}, \tag{26}$$

where Π is the polarizability of noninteracting composite fermions defined with Eq. (2), and the remaining terms represent contributions arising due to the Fermi-liquid interaction in the composite fermion system. Only contributions from the first and greatest two terms in the expansion of the Fermi-liquid interaction function in Legendre polynomials (f_0 and f_1, respectively)

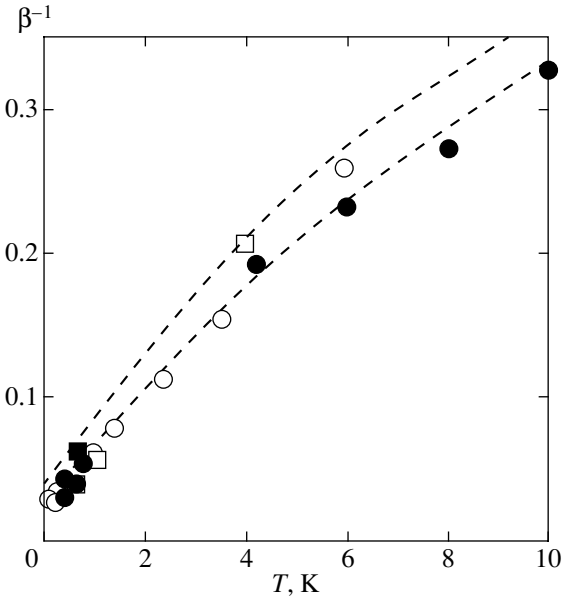

Fig. 2. Temperature dependence of the coefficient β^{-1} for interlayer distances $d = 10$ nm (upper curve) and $d = 22.5$ nm (lower curve) compared to the summary of experimental curvature at both spacings [7].

are kept in Eq. (26) to avoid too lengthy calculations. Matrix elements of the 2×2 matrices $F_{(0)}$ and $F_{(1)}$ are

$$F_{(0)} = \begin{pmatrix} f_0 & 0 \\ 0 & 0 \end{pmatrix},$$

$$F_{(1)} = \begin{pmatrix} \dfrac{m^* - m_b}{ne^2}\dfrac{\omega^2}{q^2} & 0 \\ 0 & -\dfrac{m^* - m_b}{ne^2} \end{pmatrix}. \tag{27}$$

Within the Fermi-liquid theory, the effective mass m^* is related to the "bare" mass m_b as

$$\frac{1}{m_b} = \frac{1}{m^*} + \frac{f_1}{2\pi\hbar^2} \equiv \frac{1 + A_1}{m^*}. \tag{28}$$

Using expressions (26)–(28) and performing calculations within the relevant limit $\delta \ll 1$, we obtain that the expression for the density–density response function for a single layer preserves the form given by Eq. (16), where the compressibility $dn/d\mu$ is replaced with the quantity $dn^*/d\mu$ renormalized due to the Fermi-liquid interaction,

$$\frac{dn^*}{d\mu} = \frac{3m^*}{8\pi\hbar^2}\left(1 + \frac{3m^*}{8\pi\hbar^2}f_0\right)^{-1} \equiv \frac{dn}{d\mu}\left(1 + \frac{dn}{d\mu}f_0\right)^{-1}. \tag{29}$$

For strongly correlated quasiparticles, this renormalization may significantly reduce the compressibility of the composite fermion liquid, and, consequently, increase the value of the parameter α. It is usually assumed [3, 8] that the Fermi-liquid renormalization of the effective mass significantly changes its value: $m^* \sim (5–10)m_b$. This gives values on the order of 10 for Fermi-liquid coefficient A_1. Using this estimate and substituting our renormalized compressibility (29) in expression (21), we arrive at the conclusion that $dn^*/d\mu$ is low enough for the condition $\alpha > 1$ to be satisfied when the Fermi-liquid parameter $A_0 = f_0/2\pi\hbar^2$ takes values on the order of 10–100. This conclusion does not seem unrealistic because it is reasonable to expect A_0 to be on the order of or greater than the next Fermi-liquid parameter A_1. We obtain a reasonably good agreement between the plot of our Eq. (22) and the experimental results using $A_0 = 15$ and $A_1 = 3$ ($m^* = 4m_b$) (Fig. 1).

Our results for the temperature dependence of β^{-1} also agree with the results of experiments [7]. The upper curve in Fig. 2 corresponds to the double-layer system with smaller interlayer spacing $d_A = 10$ nm, which gives $T_0 = 487$ K, and the lower curve exhibits the temperature dependence of β^{-1} for greater spacing $d_B = 22.5$ nm ($T_0 = 587$ K). The curves do not coincide, but they are arranged rather close to each other.

Finally, the results of the present analysis enable us to qualitatively describe all important features observed in the experiments in [7] on the Coulomb drag slightly away from half filling of the lowest Landau levels of both interacting 2D electron gases. They also give us grounds to treat these experimental results as one more piece of evidence for a strong Fermi-liquid interaction in the composite fermion system near half filling of the lowest Landau level. The above interaction provides a significant reduction of the compressibility of the composite fermion liquid and a consequent enhancement in the screening length in single layers. Essentially, the parameter α characterizes the ratio of the Thomas–Fermi screening length in a single 2D electron gas at $\nu = 1/2$ and the separation between the layers [3]. When $\alpha > 1$, intralayer interactions predominate those between the layers, which could be the reason for low sensitivity of the bilayer to changes in the interlayer spacing. It is likely that there is an explanation for the reported near-independence of the drag on the interlayer separation [7]. We believe that, at larger distances between the layers, the dependence of the transresistivity on d could be revealed in experiments. At the same time, the results in [7] give us a valuable opportunity to estimate the strength of Fermi-liquid interactions between quasiparticles at the $\nu = 1/2$ state, which is important for further studies of such systems.

ACKNOWLEDGMENTS

The author thanks K.L. Haglin and G.M. Zimbovsky for help with the manuscript.

REFERENCES

1. L. Zheng and A. H. MacDonald, Phys. Rev. B **48**, 8203 (1993).
2. A. Kamenev and Y. Oreg, Phys. Rev. B **52**, 7516 (1995).
3. I. Ussishkin and A. Stern, Phys. Rev. B **56**, 4013 (1997).
4. S. Sakhi, Phys. Rev. B **56**, 4098 (1997).
5. M. P. Lilly, J. P. Eisenstein, L. N. Pfeiffer, and K. W. West, Phys. Rev. Lett. **80**, 1714 (1998).
6. F. von Oppen, S. H. Simon, and A. Stern, Phys. Rev. Lett. **87**, 106803 (2001).
7. M. P. Lilly, J. P. Eisenstein, L. N. Pfeiffer, and K. W. West, cond-mat/9909231.
8. B. I. Halperin, P. A. Lee, and N. Read, Phys. Rev. B **47**, 7312 (1993); S. H. Simon and B. I. Halperin, Phys. Rev. B **48**, 17368 (1993).
9. N. A. Zimbovskaya and J. L. Birman, Phys. Rev. B **60**, 16762 (1999).
10. N. A. Zimbovskaya, *Local Geometry of the Fermi Surface and High-Frequency Phenomena in Metals* (Springer, New York, 2001).
11. R. L. Willett, K. W. West, and L. N. Pfeiffer, Phys. Rev. Lett. **83**, 2624 (1999).

Journal of Experimental and Theoretical Physics, Vol. 98, No. 6, 2004, pp. 1237–1249.
Translated from Zhurnal Éksperimental'noĭ i Teoreticheskoĭ Fiziki, Vol. 125, No. 6, 2004, pp. 1409–1422.

NONLINEAR PHYSICS

Diffraction Effects on Soliton Propagation

S. V. Sazonov
Kaliningrad State University, Kaliningrad, 236041 Russia
e-mail: nst@alg.kaliningrad.ru
Received December 29, 2003

Abstract—An averaged-Lagrangian method is used to analyze diffraction effects on propagation of solitons of various types in homogeneous media. It is shown that diffraction can counteract the self-focusing of dark and gray envelope solitons described by the nonlinear Schrödinger equation and solitons described by the Korteweg–de Vries equation when the soliton intensities do not exceed certain values. Conversely, diffraction enhances the self-focusing of dark and gray envelope solitons described by the modified Korteweg–de Vries equation, kinks described by the sine-Gordon equation, and domain walls in the u^4 model, which is explained by mutual correlation between transverse and longitudinal soliton dynamics. Critical parameters that determine soliton stability with respect to self-focusing are found for several models. *© 2004 MAIK "Nauka/Interperiodica".*

1. INTRODUCTION

Stability analysis of one-dimensional solitons described by various equations with respect to transverse perturbations (i.e., with respect to extension to additional dimensions) is important for experimental observation of solitons.

An averaged-Lagrangian method for analyzing problems of this kind was proposed in [1, 2]. This approach can be used to find approximate soliton-like solutions to various nonlinear wave equations and analyze their stability with respect to transverse perturbations, i.e., to extension to additional dimensions. The authors of [1, 2] developed a technique for detailed quantitative analysis of influence of long-wavelength perturbations, based on the use of "fast" and "slow" variables in trial soliton-like solutions. The nonlinear gas-dynamics equations for these variables obtained in [1, 2] were solved by the hodograph method. The formalism was applied to develop a soliton stability theory without assuming small perturbations. However, the hodograph method can be successfully applied only in the case of one-dimensional perturbations. Moreover, separation into fast and slow variables corresponds to the eikonal (geometric-optics) approximation for solitons [2, 3]. Diffraction effects, which play an essential role at the final stage of self-focusing, are left outside the scope of this approach.

Here, diffraction of solitons is interpreted as their self-diffraction in a homogeneous medium. Owing to the nonlinearity of solitons, certain properties of the medium exhibit transient variations in the regions occupied by solitons, and the solitons are diffracted by these inhomogeneities.

It is well known that self-focusing of a high-power continuous quasi-monochromatic beam is counteracted and, under certain conditions, can be compensated for by diffraction [4, 5]. As a result, the beam contracts to a certain diameter and propagates in a self-trapping regime in a nonlinear medium. Analogous behavior can be exhibited by envelope solitons with well-defined carrier frequencies.

Recently, optical and acoustic pulses with durations of about a period (or even a half-period) of the corresponding physical modes were generated in several laboratories around the world [6, 7]. In the standard terminology, they are called ultrashort or video pulses and, sometimes, video solitons. Most theoretical analyses of their propagation in nonlinear media are restricted to one-dimensional approximations. Their transverse dynamics were investigated without allowance for diffraction effects; i.e., only the eikonal approximation was applied. However, there is a difference in the dynamic behavior between envelope solitons and video pulses even in the geometric-optics approximation: the transverse dynamics are determined by the amplitude dependence of phase and group velocities in the former and latter cases, respectively. Therefore, there must also be some difference between diffraction effects on the transverse dynamics of envelope solitons and video pulses. These issues are addressed in the present study.

The paper is organized as follows. In Section 2, simple physical models are used to briefly derive nonlinear wave equations describing propagation of both envelope and video solitons in nonlinear media, including their transverse dynamics. In Section 3, diffraction effects on dark and gray envelope solitons are analyzed by an averaged-Lagrangian method. In Sections 4 and 5, analogous analyses are presented for video solitons in quadratic nonlinear media and for dark and gray video solitons in isotropic Kerr media, respectively. Effects of diffraction on the kinks described by the sine-Gordon equation and the domain walls predicted by the well-known u^4 model are considered in Section 6. In the Conclusions section, the results are summarized, diffi-

1063-7761/04/9806-1237$26.00 © 2004 MAIK "Nauka/Interperiodica"

culties and unsolved problems are outlined, and directions of further research in this field are sketched out.

2. NONLINEAR WAVE EQUATIONS

In this section, some three-dimensional nonlinear equations that admit soliton and soliton-like one-dimensional solutions are derived by invoking physical examples.

Consider the propagation of a linearly polarized high-power optical pulse in a nonlinear dielectric.

The Maxwell equation for the electric field E of the pulse is

$$\Delta E - \frac{1}{c^2}\frac{\partial^2 E}{\partial t^2} = \frac{4\pi}{c^2}\frac{\partial^2 P}{\partial t^2}, \tag{1}$$

where Δ is the Laplace operator, c is the speed of light in free space, and P is the polarization response of the medium.

As a first step, let us assume that the pulse spectrum (without any well-defined carrier in the general case) belongs to the transparent region of a dielectric. Suppose that the Fourier components of the pulse have frequencies satisfying a condition formulated in [8], which can be rewritten as

$$\mu_1 = (\omega_0\tau_p)^{-1} \ll 1, \tag{2}$$

where ω_0 is the characteristic optical-transition frequency and τ_p is the pulse time scale [9, 10].

Since the pulse spectrum does not contain any resonant Fourier components, the interaction between the field and the medium is relatively weak. Therefore, both dispersion and nonlinearity are sufficiently weak to be represented as additive effects by allowing for dispersion only in the linear part P_l of polarization response.

The contribution of ion polarization to the response of the medium is neglected. The optical electronic susceptibility $\chi(\omega)$ as a function of frequency is

$$\chi(\omega) = \frac{\omega_0^2\chi(0)}{\omega_0^2 - \omega^2},$$

where $\chi(0)$ is the static electron susceptibility.

Since dispersion is relatively weak, $\chi(\omega)$ can be represented as a power series in $(\omega/\omega_0)^2$:

$$\chi(\omega) = \chi(0)\left[1 + \left(\frac{\omega}{\omega_0}\right)^2\right] = \chi(0) + \frac{1}{2}\chi''(0)\omega^2.$$

Making the change $\omega \longrightarrow i\partial/\partial t$ in the expression for $\chi(\omega)$, we rewrite $P_l = \chi(\omega)E$ as

$$P_l = \chi(0)E - \frac{1}{2}\chi''(0)\frac{\partial^2 E}{\partial t^2}. \tag{3}$$

The nonlinear part of the response is represented as a power series in field strength restricted to cubic nonlinearity:

$$P_{non} = \chi_2 E^2 + \chi_3 E^3, \tag{4}$$

where χ_2 and χ_3 are, respectively, the second- and third-order inertia-free nonlinear susceptibilities.

The quadratic nonlinearity in (4) implies that the medium can be anisotropic, in which case χ_2 and χ_3 are third- and fourth-rank tensors, respectively. However, if the input pulse is polarized in the principal plane (defined by the optical axis and the input pulse propagation direction, i.e., the z axis), then the polarization of a pulse propagating perpendicularly to the extraordinary-wave polarization plane remains invariant [11]. In what follows, this condition is assumed to hold. Therefore, χ_2 and χ_3 can be treated as scalar quantities in (4). When $\chi_2 = 0$, the pulse propagates in an isotropic medium and χ_3 is a scalar without any additional condition.

Substituting (3) and (4) into (1), one obtains

$$\frac{\partial^2 E}{\partial z^2} - \frac{1}{v_0^2}\frac{\partial^2 E}{\partial t^2} = \frac{4\pi}{c^2}(\chi_2 E^2 + \chi_3 E^3) - \frac{2\pi}{c^2}\chi''(0)\frac{\partial^4 E}{\partial t^4} - \Delta_\perp E. \tag{5}$$

where $v_0 = c/n_0$ (n_0 is a linear inertia-free refractive index) and $\Delta_\perp$ is the transverse Laplace operator.

According to (3), weak dispersion and nonlinearity imply that the leading term in the expansion of P is $\chi(0)E$, which contributes to n_0. Other terms retained in (5) are of higher order in μ_1. The condition $\Delta_\perp E \ll \partial^2 E/\partial z^2$ of paraxial approximation is assumed to hold as well [1, 2]; i.e., the wavefront of a propagating pulse is weakly curved. This approximation is used in the theory of quasi-monochromatic beams [5]. Despite obvious limitations, the paraxial approximation can be used to obtain plausible results for transverse beam dynamics and to simplify analytical calculations taking into account diffraction.

In summary, the terms on the right-hand side of (5) are small as compared to each term on the left-hand side. In the zeroth approximation, the solutions to the linear wave equation describe waves propagating in both positive and negative directions along the z axis:

$$E = E_+\left(t - \frac{z}{v_0}\right) + E_-\left(t + \frac{z}{v_0}\right).$$

In the case of a forward-propagating wave E_+, the effects of the right-hand side of (5) are taken into account by introducing a "slow" coordinate $\zeta = \mu z$: $E = E(\tau, \zeta)$, where $\tau = t - z/v_0$. Dropping the terms of order μ_1^2, one has

$$\frac{\partial}{\partial t} = \frac{\partial}{\partial \tau}, \quad \frac{\partial^2}{\partial z^2} \approx \frac{1}{\partial v_0^2}\frac{\partial^2}{\partial \tau^2} - \frac{2\mu_1}{v_0}\frac{\partial^2}{\partial \tau \partial \zeta}.$$

Substituting this into (5), averaging the result over τ, and changing back to the variable z, one obtains

$$\frac{\partial E}{\partial z} - a_2 E\frac{\partial E}{\partial \tau} - a_3 E^2\frac{\partial E}{\partial \tau} - b\frac{\partial^3 E}{\partial \tau^3} = \frac{v_0}{2}\Delta_\perp \int_{-\infty}^{\tau} E d\tau', \tag{6}$$

where

$$a_2 = -\frac{4\pi v_0 \chi_2}{c^2}, \quad a_3 = -\frac{6\pi v_0 \chi_3}{c^2}, \quad b = \frac{\pi v_0 \chi''(0)}{c^2}.$$

Since the slowly varying envelope approximation is not employed in (6), this equation describes the dynamics of pulses containing an arbitrary number of modes. Thus, its scope is extended from video pulses to envelope pulses. It should be noted here a nonlinear Schrödinger (NLS) equation for the field envelope can be derived from (6) when $a_2 = 0$ by expressing the field as

$$E = \xi(z, \tau, \mathbf{r}_\perp)e^{i(\omega\tau - qz)} + \text{c.c.}. \tag{7}$$

Here, $\mathbf{r}_\perp$ is the transverse radius vector, q is the wave number in the coordinate system moving with the velocity v_0, and ξ is a slowly varying envelope satisfying the condition

$$\left|\frac{\partial \xi}{\partial \tau}\right| \ll \omega|\xi|.$$

Expression (7) entails

$$\frac{\partial E}{\partial z} = \left(\frac{\partial \xi}{\partial z} - iq\xi\right)e^{i(\omega\tau - qz)} + \text{c.c.},$$

$$\frac{\partial^2 E}{\partial \tau^3} \approx -\left(i\omega^3\xi + 3\omega^2\frac{\partial \xi}{\partial \tau} - 3i\omega\frac{\partial^2 \xi}{\partial \tau^2}\right)e^{i(\omega\tau - qz)} + \text{c.c.},$$

$$E^2\frac{\partial E}{\partial \tau} = \frac{1}{3}\frac{\partial}{\partial \tau}(E^3) \approx i\omega|\xi|^2\xi e^{i(\omega\tau - qz)} + \text{c.c.}, \tag{8}$$

$$\Delta_\perp \int_{-\infty}^{\tau} E d\tau' \approx -\frac{i}{\omega}\Delta_\perp \xi e^{i(\omega\tau - qz)} + \text{c.c.}$$

Here, the term of order $\partial^3\xi/\partial\tau^3$ in the second expression is neglected, because it represents dispersion of higher order as compared to the last term (proportional to $\partial^2\xi/\partial\tau^2$). In the third expression, both the fastest oscillating terms (proportional to $\exp[\pm 3i(\omega\tau - qz)]$) and the dispersive term of order $\partial(|\xi|^2\xi)/\partial\tau \ll \omega|\xi|^2\xi$ are dropped. In accordance with the paraxial and slowly varying envelope approximations, only the leading term is retained after integrating by parts in the last expression.

By substituting (8) into (6) and setting to zero the coefficients of terms proportional to ξ, it is found that $q = b\omega^3$. The resulting equation is

$$i\frac{\partial \xi}{\partial z} + \alpha|\xi|^2\xi + \beta\frac{\partial^2 \xi}{\partial \eta^2} = \frac{v_0}{2\omega}\Delta_\perp \xi, \tag{9}$$

where

$$\eta = \tau - 3\beta\omega^2 z = t - \frac{z}{v_g}.$$

The group velocity v_g is defined by the relation

$$\frac{1}{v_g} = \frac{\partial k}{\partial \omega} = \frac{1}{v_0} + 3b\omega^2,$$

where k is the wave number in the laboratory frame. The group-dispersion coefficient is

$$\beta = 3b\omega^2 = 0.5\frac{\partial^2 k}{\partial \omega^2}$$

and $\alpha = \omega a_3$.

Since $\alpha \propto -\chi_3$, defocusing behavior (see below) and normal group dispersion are observed when $\alpha, \beta > 0$. Vice versa, the case of self-focusing combined and anomalous dispersion corresponds to $\alpha, \beta < 0$. The combinations of defocusing behavior with anomalous group dispersion ($\alpha > 0$, $\beta < 0$) and self-focusing behavior with normal group dispersion ($\alpha < 0$, $\beta > 0$) are considered below in an analysis of the diffraction of dark solitons.

Now, consider the case of reverse inequality (2):

$$\mu_2 = \omega_0\tau_p \ll 1. \tag{10}$$

When (10) holds, the spectral pulse width, $\delta\omega \sim 1/\tau_p \gg \omega_0$, spans the corresponding range of quantum transition frequencies. Since this condition corresponds to strong interaction with the medium, dispersion and nonlinearity cannot be represented additively.

Condition (10) can be satisfied, in particular, for proton tunneling ($\omega_0 \sim 10^{13}$ s^{-1}) in the presence of a femtosecond optical pulse ($\tau_p \sim 10^{-14}$ s) [12]. Since interactions between optical electronic transitions characterized by $\omega_0 \sim 10^{15}$ s^{-1} and the field are weak in this

case, they can be taken into account by introducing an appropriate refractive index n_0.

It was shown in [9, 10, 12] that condition (10) entails

$$\frac{\partial P}{\partial t} = dN\omega_0 \sin\theta, \tag{11}$$

where d is the dipole moment for a tunneling transition, N is the number of transitions per unit second per unit volume,

$$\theta = \frac{2d}{\hbar}\int_{-\infty}^{t} E dt',$$

and $\hbar$ is Planck's constant.

Substituting (11) into (1) and averaging the result over t, one obtains the three-dimensional sine-Gordon equation

$$\Delta\theta - \frac{1}{v_0^2}\frac{\partial^2\theta}{\partial t^2} = g\sin\theta, \tag{12}$$

where

$$g = \frac{8\pi d^2 N\omega_0}{\hbar c^2}.$$

By changing to the variables $\tau = t - z/v_0$ and $\zeta = z + v_0 t$, Eq. (12) is rewritten as

$$\frac{\partial^2\theta}{\partial\tau\partial\zeta} = -a\sin\theta + \frac{v_0}{4}\Delta_\perp\theta, \tag{13}$$

where

$$a = \frac{v_0 g}{4} = \frac{2\pi d^2 N\omega_0 v_0}{\hbar c^2}.$$

Note that the paraxial approximation was not used in passing from (12) to (13). Therefore, Eq. (13) can be used to describe strongly curved wavefronts propagating in both directions along the z axis.

Finally, consider the Klein–Gordon–Fock equation frequently used to describe domain-wall dynamics in ferroelectrics, ferromagnets, and other solids below the critical temperature T_c of a second-order phase transition [13, 14]:

$$\Delta u - \frac{1}{v_0^2}\frac{\partial^2 u}{\partial t^2} = -g_0 u + b_0 u^3. \tag{14}$$

Here, v_0 is a characteristic velocity, u is an order parameter, and g_0 and b_0 are positive phenomenological parameters [$g_0 = a_1(T_c - T)$, where a_1 depends on the material, and b_0 is virtually independent of temperature]. In terms of $\tau = t - z/v_0$ and $\zeta = z + v_0 t$, this equation is rewritten as

$$\frac{\partial^2 u}{\partial\tau\partial\zeta} = a_0 u - s u^3 + \frac{v_0}{4}\Delta_\perp u, \tag{15}$$

where $a_0 = gv_0/4$ and $s = b_0 v_0/4$.

Again, the paraxial approximation is not employed here. The analysis that follows is focused on the effects of diffraction on the dynamics of solitons and domain walls described by Eqs. (6), (9), (13), and (15).

3. DIFFRACTION OF GRAY AND DARK ENVELOPE SOLITONS

When $\alpha\beta > 0$, Eq. (9) has a solution describing a one-dimensional gray soliton ($\Delta_\perp\xi = 0$):

$$\xi = \frac{1}{\tau_p}\sqrt{\frac{2\beta}{\alpha}}\exp\left(\frac{i\beta z}{\tau_p^2}\right)\operatorname{sech}\frac{\eta}{\tau_p}. \tag{16}$$

Henceforth, the Ritz–Whitham averaged-Lagrangian method is applied to allow for transverse dynamics [1, 2]. The Lagrangian associated with Eq. (9) is

$$\begin{aligned} L = {} & \frac{i}{2}\left(\xi^*\frac{\partial\xi}{\partial z} - \xi\frac{\partial\xi^*}{\partial z}\right) + \frac{\alpha}{2}|\xi|^4 \\ & - \beta\left|\frac{\partial\xi}{\partial\eta}\right|^2 + \frac{v_0}{2\omega}|\nabla_\perp\xi|^2. \end{aligned} \tag{17}$$

Following [2], let us use (16) as a template for a trial solution:

$$\xi = \sqrt{\frac{2\beta}{\alpha}}\rho e^{i\Phi}\operatorname{sech}(\rho\eta), \tag{18}$$

where ρ and Φ are functions of z and $\mathbf{r}_\perp$.

After substituting (18) into (17), an averaged Lagrangian is found by integration:

$$\begin{aligned} \Lambda \equiv \frac{\alpha}{4\beta}\int_{-\infty}^{\infty} L d\eta = {} & -\rho\frac{\partial\Phi}{\partial z} + \frac{\beta}{3}\rho^3 \\ & + \frac{v_0}{2\omega}\rho(\nabla_\perp\Phi)^2 + \frac{v_0}{6\omega}\left(\frac{\pi^2}{12} + 1\right)\frac{(\nabla_\perp\rho)^2}{\rho}. \end{aligned} \tag{19}$$

The Euler–Lagrange equations for Λ,

$$\frac{\partial}{\partial z}\frac{\partial\Lambda}{\partial(\partial\Phi/\partial z)} + \nabla_\perp\frac{\partial\Lambda}{\partial(\nabla_\perp\Phi)} = 0,$$

$$\frac{\partial\Lambda}{\partial\rho} - \nabla_\perp\frac{\partial\Lambda}{\partial(\nabla_\perp\rho)} = 0,$$

can be written as

$$\frac{\partial \rho}{\partial z} + \nabla_\perp(\rho \mathbf{V}_\perp) = 0,$$
$$\frac{\partial \varphi}{\partial z} + \frac{\mathbf{V}_\perp^2}{2} + \int \frac{dp}{\rho} = F(\rho, \nabla_\perp \rho, \Delta_\perp \rho), \tag{20}$$

where $\varphi = -v_0\Phi/\omega$, $\mathbf{V}_\perp = \nabla_\perp \varphi$,

$$F = \left(\frac{\pi^2}{12} + 1\right)\frac{v_0^2}{3\omega^2\rho}\left[2\Delta_\perp\rho - \frac{(\nabla_\perp\rho)^2}{\rho}\right], \tag{21}$$

and p is related to ρ by the equation

$$\frac{dp}{d\rho} = \frac{2v_0\beta}{\omega}\rho^2. \tag{22}$$

In the one-dimensional case ($\nabla_\perp = \Delta_\perp = 0$), Eq. (20) yields $\rho = \rho_0 = 1/\tau_p = \text{const}$ and $\Phi = -\omega\varphi/v_0 = \beta z/\tau_p^2$. Thus, trial solution (18) is found to be identical to the exact one-soliton solution given by (16). In what follows, equations analogous to (20) are used to validate trial solutions against exact one-dimensional one-soliton solutions.

System (20) is analogous to corresponding equations in the theory of nonlinear monochromatic beams [5].

The term on the right-hand side of the latter equation in (20) represents diffraction effects in transverse dynamics of a pulse. Neglecting it ($F = 0$), one obtains the eikonal approximation for solitons. In this case, system (20) is equivalent to the equations of inviscid fluid dynamics, where z, ρ, and p correspond to time, density, and pressure, respectively. The former equation in (20) is interpreted as the continuity equation; the latter, the Cauchy theorem for inviscid flows. Equation (22) describes an isentropic process associated with fluid motion. It is obvious that the criterion for soliton stability with respect to self-focusing in the eikonal approximation is identical to the stability condition of the "inviscid flow" described by Eqs. (20)–(22): $dp/d\rho > 0$ [11, 15, 16]. In view of (22), this implies that self-focusing and defocusing NLS solitons correspond to $\beta < 0$, $\alpha < 0$ [see (18)] and $\beta > 0$, $\alpha > 0$, respectively. These conditions admit an obvious physical interpretation. It follows from (7) and (16) that the wave number of a soliton in the laboratory frame is

$$k_s = \frac{\omega}{v_0} + q - \frac{\beta}{\tau_p^2} = k - \frac{\alpha\xi_m^2}{2},$$

where $k = \omega/v_0 + q$ is its linear part and ξ_m is the amplitude of soliton (16). The soliton refractive index is

$$n_s = \frac{ck_s}{\omega} = n_l - \frac{c\alpha\xi_m^2}{2\omega},$$

where $n_l = ck/\omega$ is its linear part.

By the Fermat principle, the wave normal bends in the direction of increasing refractive index. When $\alpha > 0$, the soliton refractive index is lower at the center of the soliton cross section, where its amplitude reaches its maximum. Therefore, the wavefront bulges forward, which leads to defocusing. When $\alpha < 0$, self-focusing (collapse) of a soliton is predicted in the eikonal approximation.

Now, let us examine effects due to diffraction. Following an approach developed in the theory of monochromatic beams [4, 5], consider an axially symmetric pulse. Rewriting (20) in a cylindrical coordinate system (z, r), let us seek a self-similar approximate solution for ρ [5]:

$$\rho(z, r) = \rho_0\frac{R_0^2}{R^2(z)}\exp\left[-\frac{r^2}{R^2(z)}\right], \tag{23}$$

where the constant R_0 is interpreted as the radius of the input pulse, $R(z)$ is its current radius, and ρ_0 is the inverse duration of the input pulse (proportional to its input amplitude).

The self-similar transverse dynamics of the soliton defined by (23) corresponds to an aberration-free approximation [4].

The analysis presented below focuses on the near-axis dynamics ($r^2/R^2 \ll 1$) [4, 5]. For this reason, the solution for φ is represented as the expansion

$$\varphi(z, r) = f_1(z) + \frac{r^2}{2}f_2(z) + \ldots. \tag{24}$$

It follows from the former equation in (20) combined with (23) and (24) that

$$f_2 = \frac{R'}{R}, \tag{25}$$

where the prime denotes a derivative with respect to z.

By substituting (23) and (24) into the latter equation in (20) and collecting the terms of degree zero and two in r, the following equations are obtained:

$$f_1' = -\frac{v_0\beta}{\omega}\rho_0^2\frac{R_0^4}{R^4} - \frac{8v_0^2}{3\omega^2}\left(\frac{\pi^2}{12} + 1\right)\frac{1}{R^2}, \tag{26}$$

$$f_2' + f_2^2 = \frac{2v_0\beta}{\omega}\rho_0^2\frac{R_0^4}{R^6} + \frac{4v_0^2}{3\omega^2}\left(\frac{\pi^2}{12} + 1\right)\frac{1}{R^4}. \tag{27}$$

According to (24), the value of f_2 characterizes the curvature of the constant-phase surfaces in the input

pulse. Indeed, the soliton phase can be represented as $\varphi_s = \omega t - \Phi_s$, where the total soliton phase eikonal is

$$\Phi_s = kz - \Phi = kx + \frac{\omega}{v_0}\varphi$$

$$= kz + \frac{\omega}{v_0}\left[f_1(z) + \frac{r^2}{2} f_2(z) + \ldots \right].$$

The eikonal curvature is positive and negative if $f_2 > 0$ and $f_2 < 0$, respectively.

The phase velocity v_{ph} is parallel to its normal, and its magnitude is defined by the relation

$$\frac{1}{v_{ph}} = \frac{1}{\omega}|\nabla\Phi| = \sqrt{\frac{1}{v_\parallel^2} + \frac{1}{v_\perp^2}},$$

where the longitudinal and transverse velocity components, $v_\parallel$ and $v_\perp$, are calculated as

$$\frac{1}{v_\parallel} = \frac{k}{\omega} + \frac{v_0}{\omega^2}\left(f_1' + \frac{r^2}{2} f_2' \right),$$

$$\frac{1}{v_\perp} = \frac{v_0}{\omega^2} r f_2.$$

It is obvious that the phase velocity on the soliton centerline (at $r = 0$) reduces to the longitudinal component, for which

$$\frac{1}{v_\parallel} = \frac{k}{\omega} + \frac{v_0 f'}{\omega^2}.$$

Thus, the value of f_1' determines the dispersive component of phase velocity on the centerline. Since the second term on the right-hand side in (26) characterizes the effect of diffraction on this component, it is clear that diffraction increases the near-axis phase velocity, i.e., reduces the effective refractive index. Thus, diffraction counteracts self-focusing, as in quasi-monochromatic beams.

The eikonal approximation corresponds to the limit $R_0, R \longrightarrow \infty$. In this limit, (26) yields $f_1' = -v_0\beta\rho_0^2/\omega$; i.e., defocusing by diffraction is eliminated. Hence,

$$\Phi = -\frac{\omega\varphi}{v_0} = \frac{\omega f_1}{v_0} = \beta\rho_0^2 z = \frac{\beta z}{\tau_p^2},$$

which is equal to Φ in exact solution (16).

The equation obtained by substituting (25) into (27) is formally equivalent to the equation of motion for a Newtonian particle of unit mass in the field with potential energy $U(R)$:

$$R'' = -\frac{\partial U}{\partial R}, \tag{28}$$

where

$$U = \frac{v_0\beta}{2\omega}\rho_0^2\frac{R_0^4}{R^4} + \frac{2v_0^2}{3\omega^2}\left(\frac{\pi^2}{12} + 1\right)\frac{1}{R^2}. \tag{29}$$

The parameters of the potential curve $U(R)$ defined by (29) are determined by properties of the medium and parameters of the input pulse. The first term on the right-hand side in (29) corresponds to the eikonal approximation, and the second one represents the effect of diffraction. Again, it is clear that diffraction has a defocusing effect.

To determine the function $R(z)$ describing soliton dynamics, Eq. (28) must be supplemented with boundary conditions: $R(0) = R_0$, $R'(0) = R_0'$. Suppose that the input pulse has a plane wavefront, i.e., $f_2(0) = 0$. Then, $R'(0) = 0$ by virtue of (25). In this case, defocusing is stronger than self-focusing if $R''(0) > 0$. According to (28), this condition entails

$$\left.\frac{\partial U}{\partial R}\right|_{R = R_0} < 0. \tag{30}$$

For a focusing medium ($\beta < 0$), it follows from (29) and (30) that

$$\rho_0^2 R_0^2 < \frac{\pi^2 + 12}{18}\frac{v_0}{|\beta|\omega} = 1.21\frac{v_0}{|\beta|\omega}. \tag{31}$$

The left-hand side of (31) is proportional to the input pulse intensity Q. Thus, as in the case of a high-power monochromatic beam [5], self-focusing is compensated for if the input soliton intensity does not exceed a certain critical value.

To analyze the effect of diffraction on propagation of dark envelope solitons, consider the solution to Eq. (9) when $\alpha\beta < 0$ [17]:

$$\xi = \frac{1}{\tau_p}\sqrt{\frac{2\beta}{\alpha}}\exp\left(-i\frac{2\beta z}{\tau_p^2}\right)\tanh\frac{\eta}{\tau_p}. \tag{32}$$

Note that the existence of dark solitons was supported by experiments [18].

Using (32) as a template, consider the trial solution

$$\xi = \sqrt{\frac{2\beta}{\alpha}}\rho e^{-i\Phi}\tanh(\rho\eta), \tag{33}$$

where the variables ρ and Φ are interpreted by analogy with their counterparts in (18).

Substitution of (33) into (17) and subsequent integration with respect to the "fast" variable η lead, among other things, to the divergent integrals

$$J_1 \equiv \int_{-\infty}^{\infty} \tanh^2(\rho\eta)d\eta, \quad J_2 \equiv \int_{-\infty}^{\infty} \tanh^4(\rho\eta)d\eta.$$

Note that these integrals arise from the quadratic and quartic terms in (17), respectively. As $\eta \longrightarrow \pm\infty$, the intensity of a dark soliton approaches a finite constant value corresponding to the classical "soliton vacuum" [19, 20]. The contributions of this "background" to the integrals result in divergent terms linear in η. A dark soliton can be treated as the deviation of $|\xi|^2$ from its "background" value $|\xi_\infty|^2 = 2\beta/(\alpha\tau_p^2)$ (see (32)), i.e., as a perturbation. By retaining the perturbation and discarding the "background" (i.e., ignoring the classical vacuum), the Lagrangian can be regularized by performing the following change in the divergent integrals:

$$\tanh^2(\rho\eta) = 1 - \operatorname{sech}^2(\rho\eta) \longrightarrow -\operatorname{sech}^2(\rho\eta). \quad (34)$$

An analogous procedure is used in quantum field theories when infinite terms corresponding to vacuum states are dropped and only deviations from vacuum are assumed to be observable [20]. Further argumentation supporting rule (34), including additional examples, is given below.

In summary, the regularized averaged Lagrangian is written as

$$\Lambda \equiv \frac{\alpha}{2\beta}\int_{-\infty}^{\infty} L_{\text{reg}}d\eta = -\rho\frac{\partial\Phi}{\partial z} - \frac{v_0}{2\omega}\rho(\nabla_\perp\Phi)^2 + \frac{2\beta}{3}\rho^3 + \frac{v_0}{6\omega}\left(\frac{\pi^2}{6}-1\right)\frac{(\nabla_\perp\rho)^2}{\rho}, \quad (35)$$

where L_{reg} is the regularized Lagrangian density obtained by substituting (32) into (17) and applying (34).

By varying (35) with respect to ρ and Φ, equations analogous to (20) are obtained, with $\varphi = v_0\Phi/\omega$,

$$F = \frac{v_0^2}{6\omega^2\rho}\left(\frac{\pi^2}{6}-1\right)\left[2\Delta_\perp\rho - \frac{(\nabla_\perp\rho)^2}{\rho}\right], \quad (36)$$

and

$$\int\frac{dp}{p} = -2\beta\rho^2$$

or

$$\frac{dp}{d\rho} = -\frac{4v_0\beta}{\omega}\rho^2. \quad (37)$$

In the one-dimensional case, $\rho = \rho_0 = 1/\tau_p$ and $\partial\Phi/\partial z = \beta\rho_0^2$, which yields $\Phi = 2\beta z/\tau_p^2$ in full agreement with (32) (see also (33)). Thus, regularization rule is validated by "one-dimensional testing."

In the eikonal approximation ($F = 0$), Eq. (37) shows that the dark NLS soliton is stable if $\beta < 0$ ($\alpha > 0$) and unstable with respect to self-focusing if $\beta > 0$ ($\alpha < 0$). The physical interpretation of this behavior is analogous to the case of a gray NLS soliton, i.e., associated with the dependence of the nonlinear soliton refractive index on the soliton intensity.

Introducing diffraction as in the scheme described above, one obtains Eq. (28) with

$$U = -\frac{v_0\beta}{\omega}\rho_0^2\frac{R_0^4}{R^4} + \frac{v_0^2}{3\omega^2}\left(\frac{\pi^2}{6}-1\right)\frac{1}{R^2}, \quad (38)$$

as well as (24) and (25). Furthermore,

$$f_1' = \frac{2v_0\beta}{\omega}\rho_0^2\frac{R_0^4}{R^4} - \frac{4v_0^2}{3\omega^2}\left(\frac{\pi^2}{6}-1\right)\frac{1}{R^2}.$$

The form of $U(R)$ is qualitatively similar to that of its counterpart for gray NLS solitons in both focusing ($\alpha < 0$, $\beta > 0$) and defocusing $\alpha > 0$, $\beta < 0$) media. If the an input soliton has a plane constant-phase wavefront ($R'(0) = 0$), then condition (30) for self-focusing compensation is

$$\rho_0^2R_0^2 < \frac{2v_0}{3\beta\omega}\left(\frac{\pi^2}{6}-1\right) = 0.43\frac{v_0}{\beta\omega}. \quad (39)$$

As in the case of a gray soliton, the intensity of a dark soliton must not exceed a certain critical value.

4. DIFFRACTION OF VIDEO SOLITONS IN A MEDIUM WITH QUADRATIC NONLINEARITY

If $a_3 = 0$ in (6), then the resulting Korteweg–de Vries (KdV) equation has the following one-dimensional soliton ($\Delta_\perp = 0$):

$$E = \frac{3b}{a_2\tau_p^2}\operatorname{sech}^2\frac{\tau - z/V}{2\tau_p}. \quad (40)$$

The parameter V is related to the soliton propagation velocity v in the laboratory frame:

$$\frac{1}{v} = \frac{1}{v_0} + \frac{1}{V} = \frac{1}{v_0} - \frac{b}{\tau_p^2}. \quad (41)$$

The Lagrangian density corresponding to (6) is

$$L = \frac{1}{2}\frac{\partial Q}{\partial z}\frac{\partial Q}{\partial \tau} - \frac{a_2}{6}\left(\frac{\partial Q}{\partial \tau}\right)^3 - \frac{a_3}{12}\left(\frac{\partial Q}{\partial \tau}\right)^4 + \frac{b}{2}\left(\frac{\partial^2 Q}{\partial \tau^2}\right)^2 - \frac{v_0}{4}(\nabla_\perp Q)^2. \quad (42)$$

The "potential" Q is related to the field E as follows:

$$E = \partial Q/\partial \tau.$$

Using (40) as a template, let us take the trial solution

$$Q = \frac{12b}{a_2}\gamma \tanh[\gamma(\tau - \Phi)], \quad (43)$$

where the dynamical variables γ and Φ depend on coordinates [1]. Note that a group eikonal is well defined in this case, rather than the phase eikonal associated with the NLS equation.

Substituting (43) into (42), setting $a_3 = 0$, averaging the result over τ, and applying (34) to a divergent integral analogous to J_1, one obtains

$$\Lambda \equiv \frac{a_2^2}{96b^2}\int_{-\infty}^{\infty} L d\tau = -\rho\frac{\partial \Phi}{\partial z} - \frac{12b}{5}\rho^{5/3} - \frac{v_0}{2}\rho(\nabla_\perp \Phi)^2 + \left(1 - \frac{\pi^2}{24}\right)\frac{v_0}{9}\frac{(\nabla_\perp \rho)^2}{\rho^{5/3}}, \quad (44)$$

where $\rho = \gamma^3$.

Variation of Λ with respect to ρ and Φ again leads to equations analogous to (20) with $\varphi = v_0\Phi$,

$$\frac{dp}{d\rho} = \frac{8v_0 b}{3}\rho^{2/3}, \quad (45)$$

$$F = \left(1 - \frac{\pi^2}{24}\right)\frac{v_0^2}{9\rho^{5/3}}\left[\frac{5(\nabla_\perp \rho)^2}{3\rho} - 2\Delta_\perp \rho\right]. \quad (46)$$

In the one-dimensional case, Eqs. (20) and (45) yield

$$\rho = \rho_0 = \gamma_0^3 = \text{const}, \quad \frac{\partial \Phi}{\partial z} = -b\rho_0^{2/3} = -4b\gamma_0^2.$$

Since $\gamma_0 = 1/2\tau_p$ (see (40) and (43)), it follows that $\Phi = -b/\tau_p^2$, in agreement with (40), (41), and (43).

"Process equation" (45) implies that the KdV soliton described in the eikonal approximation ($F = 0$) is stable if $b > 0$, i.e., in the case of normal dispersion. According to Eq. (40), $E > 0$ if $a_2 > 0$ and $E < 0$ if $a_2 < 0$. This result admits a simple physical interpretation. Indeed, (3) and (4) can be combined to define the effective susceptibility

$$\chi_{\text{eff}} = \chi_1 + \chi_2 E + \chi_3 E^2,$$

where χ_1 is the linear susceptibility (including dispersion), and the total refractive index is

$$n = \sqrt{1 + 4\pi\chi_{\text{eff}}} \approx 1 + 2\pi\chi_{\text{eff}} = 1 + 2\pi(\chi_1 + \chi_2 E + \chi_3 E^2) = 1 + 2\pi\chi_1 - \frac{c^2}{2v_0}a_2 E - \frac{c^2}{3v_0}a_3 E^2.$$

Since $a_3 = 0$, the refractive index on the centerline is reduced by nonlinearity when $a_2 E > 0$, i.e., defocusing is observed in accordance with the result obtained above.

This result can be derived directly from (40) and (41) if the group velocity v is expressed as

$$\frac{1}{v} = \frac{1}{v_0} - \frac{a_2 E_m}{3},$$

where E_m is the amplitude of soliton (40).

For the group refractive index defined as $n_g \equiv c/v$, it holds that

$$n_g = n_0 - \frac{c a_2 E_m}{3};$$

i.e., the group refractive index is minimal on the centerline if $a_2 E_m > 0$, whereas the group velocity reaches its maximum.

Introducing diffraction as in the scheme described above, one obtains Eq. (28) with

$$U = 4v_0 b\rho_0^{2/3}\left(\frac{R_0}{R}\right)^{4/3} + \frac{24 - \pi^2}{18}\frac{v_0^2}{\rho_0^{2/3}R_0^{4/3}R^{2/3}}. \quad (47)$$

Both expansion (24) and relation (25) hold, and $f_1(z)$ satisfies the equation

$$f_1' = -4v_0 b\rho_0^{2/3}\left(\frac{R_0}{R}\right)^{4/3} + \frac{24 - \pi^2}{27}\frac{v_0^2}{\rho_0^{2/3}R_0^{4/3}R^{2/3}}.$$

The form of $U(R)$ is qualitatively similar to that of its counterpart for the NLS soliton. Again, diffraction has a defocusing effect.

In the case of anomalous dispersion ($b < 0$), criterion (30) for compensation of self-focusing by diffraction leads to the condition

$$\gamma_0^4 R_0^2 < 0.10\frac{v_0}{|b|}, \quad (48)$$

where $\gamma_0 = \rho_0^{1/3} = 1/2\tau_{p0}$ is the inverse duration of an input KdV soliton. According to (40), its amplitude is estimated as $E_m \sim \gamma_0^2$. Therefore, inequality (48) provides an upper limit for the intensity of an input soliton.

The transverse length scale of the nonuniformity associated with a soliton is determined by its diameter (or radius). Therefore, the relative importance of diffraction as compared to effects described by geometric optics can be characterized by the dimensionless parameter

$$\delta \approx \frac{\lambda}{R}, \tag{49}$$

where λ is a typical soliton wavelength.

According to (23), self-focusing is accompanied by longitudinal self-compression of solitons. Since an envelope soliton spans a spectral range, the characteristic wavelength λ of its high-frequency components remains invariant under self-compression, while R decreases. Therefore, the parameter δ increases; i.e., the diffractive spread tends to increase. This explains criteria (31) and (39). In the case of a KdV video soliton, which has no carrier, the role of wavelength is played by its characteristic length:

$$\lambda \approx l \approx v_0\tau_p \approx \frac{v_0}{\gamma} = \frac{v_0}{\rho^{1/3}} \approx \frac{v_0}{\rho_0^{1/3}R_0^{2/3}}R^{2/3}$$

(see (23)).

Then,

$$\delta \approx \frac{v_0}{(\rho_0 R_0^2)^{1/3}}R^{-1/3}.$$

Similarly to the case of an envelope soliton, self-focusing is accompanied by an (albeit slower) increase in δ. Therefore, diffractive spread can suppress self-focusing, as expressed by condition (48).

5. DIFFRACTION OF VIDEO SOLITONS IN A MEDIUM WITH CUBIC NONLINEARITY

If $a_2 = 0$ in (6) and (42), then the resulting modified Korteweg–de Vries (MKdV) equation, which describes propagation of video solitons in an isotropic medium, has the one-dimensional one-solution solution

$$E = \frac{1}{\tau_p}\sqrt{\frac{6b}{a_3}}\operatorname{sech}\frac{\tau - z/V}{\tau_p}.$$

As in the case of a KdV soliton, the parameter V is related to the propagation velocity v in the laboratory frame by (41).

To allow for diffraction, the trial "potential" is defined as

$$Q = 2\sqrt{\frac{6b}{a_3}}\arctan e^{\rho(\tau-\Phi)}. \tag{50}$$

Substituting (50) into (42), setting $a_2 = 0$, and averaging the result over τ, a system similar to (20) is obtained, with $\mathbf{V}_\perp = \nabla_\perp\varphi$, $\varphi = v_0\Phi/2$,

$$F = \frac{\pi^2 v_0^2}{48\rho^3}\left[\Delta_\perp\rho - \frac{3}{2\rho}(\nabla_\perp\rho)^2\right], \tag{51}$$

and the "process equation"

$$\frac{dp}{d\rho} = \frac{b}{2}v_0\rho^2. \tag{52}$$

In the eikonal approximation ($F = 0$), the MKdV soliton is stable with respect to self-focusing if $b = 0$, i.e., in the case of normal dispersion. Both the one-soliton solution and (50) imply that $a_3 > 0$, or $\chi_3 < 0$ (see above), in this case; i.e., the medium is defocusing.

Introducing diffraction as in the scheme described above, one obtains Eq. (28) with

$$U = \frac{bv_0\rho_0^2R_0^4}{4R^4} + \frac{5\pi^2 v_0^2}{24\rho_0^2R_0^4}R^2. \tag{53}$$

Both (24) and (25) hold, and

$$f_1' = -\frac{bv_0}{4}\rho_0^2\frac{R_0^4}{R^4} - \frac{\pi^2 v_0^2}{12\rho_0^2R_0^4}R^2.$$

The first term on the right-hand side of (53) corresponds to the geometric-optics approximation, and the second one represents the influence of diffraction. It is clear that the diffraction part of "potential energy" is similar to the energy of harmonic oscillator, with the only exception that $R \geq 0$ here. In contrast to the examples discussed above, diffraction decreases the soliton radius. Accordingly, the function $U(R)$ has a minimum in a defocusing medium (b, $a_3 > 0$). In this case, diffraction counteracts transverse spread and can lead to self-trapping, in which case the soliton radius fluctuates about

$$R_m = R_0\left(\frac{12R_0^2}{5\pi^2 l_d l}\right)^{1/6},$$

where $l_d = (b\rho_0^3)^{-1} = \tau_{p0}^3/b$ is the characteristic length of dispersive spread and $l = v_0/\rho_0 = v_0\tau_{p0}$ is the length of an input soliton.

In a focusing medium (b, $a_3 < 0$), solitons are unstable and diffraction enhances self-focusing.

The unusual role played by diffraction in the dynamics of video solitons in isotropic media can be explained by analyzing the evolution of the parameter δ (see (49)). Indeed, assuming that

$$\lambda \sim v_0\tau_p \sim \frac{v_0}{\rho} \sim \frac{v_0 R^2}{\rho_0 R_0^2}$$

(see (23)) and using (49), one obtains

$$\delta \sim \frac{v_0}{\rho_0 R_0^2} R.$$

As $R \longrightarrow 0$ as a result of self-focusing, the parameter δ also tends to zero. In other words, the contribution of wave properties of the field decreases relative to those described by the eikonal approximation, and this makes it impossible to compensate for self-focusing of solitons by diffraction effects.

If b and a_3 in the MKdV equation have opposite signs, then its one-dimensional solution describes a dark video soliton:

$$E = \frac{1}{\tau_p}\sqrt{\frac{6b}{a_3}}\tanh\frac{\tau - z/V}{\tau_p}.$$

The parameter V is related to the soliton velocity v in the laboratory frame and its duration τ_p as follows:

$$\frac{1}{v} = \frac{1}{v_0} + \frac{1}{V} = \frac{1}{v_0} + \frac{2b}{\tau_p^2}. \tag{54}$$

Using the one-dimensional solution as a template, let us take

$$Q = \sqrt{\frac{6b}{a_3}}\ln\{\cosh[\rho(\tau - \Phi)]\}. \tag{55}$$

By substituting (55) into (42), setting $a_2 = 0$, averaging the result over τ, and applying regularization rule (34), an averaged Lagrangian is obtained. Variation with respect to ρ and group eikonal Φ leads to system (20) with $\mathbf{V}_\perp = \nabla_\perp\varphi$, $\varphi = v_0\Phi$,

$$\begin{aligned} F &= \frac{\pi^2 v_0^2}{12\rho^3}\left[\Delta_\perp\rho - \frac{3}{2\rho}(\nabla_\perp\rho)^2\right], \\ \frac{dp}{d\rho} &= -4bv_0\rho^2. \end{aligned} \tag{56}$$

Hence,

$$\int\frac{dp}{d\rho} = -2bv_0\rho^2.$$

In the one-dimensional case, $\rho = 1/\tau_p = \text{const}$ and $\varphi = 2bv_0 z/\tau_p^2$. Then, $\varphi = 2bz/\tau_p^2$ and the solution is identical with the one-dimensional dark soliton described by MKdV. As in the case of dark NLS solitons, it is clear that regularization rule (34) is physically correct.

In the eikonal approximation, the dark soliton is stable in a defocusing medium ($b < 0$, $a_3 > 0$) and exhibits self-focusing when $b > 0$ and $a_3 < 0$, which is obviously consistent with the nonlinear Fermat principle.

Allowance for diffraction leads to (24), (25), and (28) with

$$\begin{aligned} U &= -2bv_0\frac{\rho_0^2 R_0^4}{R^4} + \frac{5\pi^2 v_0^2}{6\rho_0^2 R_0^4}R^2, \\ f_1' &= 2bv_0\rho_0^2\frac{R_0^4}{R^4} - \frac{\pi^2 v_0^2}{3\rho_0^2 R_0^4}R^2. \end{aligned} \tag{57}$$

Again, diffraction enhances self-focusing. In the case of a defocusing medium with anomalous dispersion ($b < 0$, $a_3 > 0$), dark solitons can exhibit self-trapping behavior, in which case the soliton radius fluctuates about

$$R_m = R_0\left(\frac{24R_0^2}{5\pi^2 l_d l}\right)^{1/6}.$$

In a focusing medium, dark MKdV solitons are unstable with respect to transverse perturbations.

6. DIFFRACTION OF KINKS AND DOMAIN WALLS

Let us consider self-diffraction of solitons (kinks) described by the sine-Gordon equation and domain walls described by the Klein–Gordon–Fock equation.

Equation (13) has the one-soliton one-dimensional solution

$$\theta = 4\arctan\exp\left[\rho_0\left(\tau - \frac{\zeta}{V}\right)\right], \tag{58}$$

where ρ_0 and V are constant parameters such that $1/V = a/\rho_0^2$.

The argument in the exponential can be rewritten in the physical variables as $(t - z/v)/\tau_p$. In the laboratory frame, duration τ_p and velocity v are related to V as follows:

$$\frac{1}{\tau_p} = \sqrt{aV}\left(1 - \frac{v_0}{V}\right), \quad \frac{1}{v} = \left(\frac{1}{V} - \frac{1}{v_0}\right)\left(1 + \frac{v_0}{V}\right)^{-1}.$$

This implies a relation between v and τ_p:

$$\frac{1}{v^2} = \frac{1}{v_0^2} + g\tau_p^2. \tag{59}$$

The Lagrangian associated with (13) is

$$L = \frac{1}{2}\frac{\partial\theta}{\partial\zeta}\frac{\partial\theta}{\partial\tau} - 2a\sin^2\frac{\theta}{2} - \frac{v_0}{8}(\nabla_\perp\theta)^2. \quad (60)$$

In accordance with (55), the trial non-one-dimensional solution to (13) reducing to the one-soliton one when $\Delta_\perp\theta = 0$ is represented as

$$\theta = 4\arctan e^{\rho(\tau-\Phi)}, \quad (61)$$

where ρ and Φ are functions of $\zeta = z + at$ and transverse coordinates.

Substituting (61) into (60) and averaging the result over τ, one obtains the averaged Lagrangian

$$\Lambda \equiv \frac{1}{4}\int_{-\infty}^{\infty} L d\tau = -\rho\frac{\partial\Phi}{\partial\zeta} - \frac{v_0}{4}\rho(\nabla_\perp\Phi)^2 - \frac{a}{\rho} - \frac{\pi^2}{24\rho^3}(\nabla_\perp\rho)^2.$$

Its variation with respect to Φ and ρ leads to Eqs. (20) up to the change $z \longrightarrow \zeta = z + v_0 t$, where $\mathbf{V}_\perp = \nabla_\perp\varphi$, $\varphi = v_0\Phi/2$,

$$F = \frac{\pi^2 v_0^2}{24\rho^3}\left[\Delta_\perp\rho - \frac{3}{2\rho}(\nabla_\perp\rho)^2\right], \qquad \frac{dp}{d\rho} = \frac{v_0 a}{\rho^2}. \quad (62)$$

It is obvious that Eqs. (20) combined with (62) yield one-soliton solution (58) in the one-dimensional case.

The latter equation in (62) implies that the video soliton described by Eq. (13) is stable in the eikonal approximation with respect to self-focusing when $a \sim g > 0$.

Allowance for diffraction again leads to Eq. (28) with

$$U = -\frac{G}{4}R^4 + \frac{D}{2}R^2,$$
$$f_1'(\zeta) = \frac{v_0^2}{\rho_0^2 R_0^4}\left(\frac{gR^2}{5} - \frac{\pi^2}{3}\right)R^2, \quad (63)$$
$$G = \frac{v_0^2 g}{\rho_0^2 R_0^4}, \quad D = \frac{5\pi^2 v_0^2}{6\rho_0^2 R_0^4}.$$

Here, the prime denotes the second derivative with respect to $\zeta = z + v_0 t$. If the change $z \longrightarrow \zeta = z + v_0 t$ is made in (23), then R_0 can be interpreted as the soliton radius when $z = -v_0 t$. In particular, $R = R_0$ if $z = t = 0$; i.e., R_0 is the input soliton radius.

According to (63), diffraction (represented by the second term on its right-hand side) enhances self-focusing as in the case of a MKdV video soliton. When the input soliton has a plane wavefront ($R'(0) = 0$), Eq. (63) and condition (30) can be combined to obtain the defocusing criterion

$$R_0 > R_c \equiv \pi\sqrt{\frac{5}{6g}}, \quad (64)$$

which strengthens the corresponding condition derived in the eikonal approximation, $g > 0$. For this reason, the criterion for validity of the geometric-optics approximation for the soliton described by the sine-Gordon equation can be written as $R_0 \gg R_c$. If $R < R_c$, then solution (58) cannot exist. To estimate R_c for an electromagnetic video soliton propagating in a system with tunneling transitions, set $d \sim 10^{-18}$ CGSE units, $N \sim 10^{21}$ cm^{-3}, and $\omega_0 \sim 10^{13}$ s^{-1}. Then, $g \sim 10^3$ cm^{-2} and $R_c \sim 1$ mm.

Now, let us analyze the effect of transverse perturbations on a domain wall described by Eq. (14) (see also (15)). In the one-dimensional case,

$$u = \pm\sqrt{\frac{g_0}{b_0}}\tanh\frac{z - vt}{l}. \quad (65)$$

The transition layer thickness l is related to the domain-wall velocity v by the "relativistic" expression

$$l = l_0\sqrt{1 - \frac{v^2}{v_0^2}}, \quad (66)$$

where $l_0 = \sqrt{2/g_0}$.

As in the case of a soliton described by the sine-Gordon equation, it is convenient to use canonical variables in the non-one-dimensional case. Equation (15) is associated with the Lagrangian

$$L = \frac{1}{2}\frac{\partial u}{\partial\zeta}\frac{\partial u}{\partial\tau} + \frac{a_0}{2}u^2 - \frac{s}{4}u^4 + \frac{v_0}{4}\Delta_\perp u. \quad (67)$$

Let us take the following trial solution corresponding to (65):

$$u = \pm\sqrt{\frac{g_0}{b_0}}\tanh[\rho(\tau - \Phi)], \quad (68)$$

where ρ and Φ are functions of $\zeta = z + v_0 t$.

Substituting (68) into (67), averaging the result over τ, and applying (34), one obtains the averaged Lagrangian

$$\Lambda \equiv -\frac{b_0}{g_0}\int_{-\infty}^{\infty} L d\tau = \rho\frac{\partial\Phi}{\partial\zeta} + \frac{v_0}{4}\rho(\nabla_\perp\Phi)^2 + \frac{a_0}{2\rho} + \frac{v_0}{8}\left(\frac{\pi^2}{6} - 1\right)\frac{(\nabla_\perp\rho)^2}{\rho^3}. \quad (69)$$

By using (69) in the Euler–Lagrange equation for Φ and ρ, system (20) is obtained, where $\varphi = v_0\Phi/2$,

$$F = \frac{v_0^2}{\rho^3}\left(\frac{\pi^2}{6} - 1\right)\left[\Delta_\perp\rho - \frac{3(\nabla_\perp\rho)^2}{2\rho}\right]. \quad (70)$$

The corresponding "process equation" is

$$\frac{dp}{d\rho} = \frac{a_0 v_0}{2\rho^2}. \quad (71)$$

Thus, the eikonal approximation predicts the stability of solution (65) with respect to transverse perturbations. Moreover, it is clear that the trial solution given by (68), (20), and (71) reduces to (65), (66) in the one-dimensional case. This result provides additional support to the regularization procedure based on (34).

Allowance for diffraction ($F \neq 0$) leads to (24), (25), and (28) up to the change $z \longrightarrow \zeta$, where U is defined by (63) with

$$G = \frac{5}{2}\left(\frac{\pi^2}{6} - 1\right)\frac{v_0^2}{\rho_0^2 R_0^4}, \quad D = \frac{a_0 v_0^2}{4\rho_0^2 R_0^4},$$

while

$$f_1' = \frac{a_0 v_0}{2\rho_0^2 R_0^4}R^4 - 2v_0^2\left(\frac{\pi^2}{6} - 1\right)\frac{R^2}{\rho_0^2 R_0^4}.$$

By criterion (30), an axially symmetric domain wall is stable with respect to self-focusing described by (61), where

$$R_c = \sqrt{\frac{10}{g_0}\left(\frac{\pi^2}{6} - 1\right)}. \quad (72)$$

In the case of a second-order phase transition, $a \sim T_c - T$. Accordingly, condition (64) becomes more restrictive as the transition temperature is approached, while $R_c \sim 1/\sqrt{T_c - T}$. Thus, stable domains cannot form in the neighborhood of T_c as easily as far from the phase-transition temperature.

7. CONCLUSIONS

The present study reveals important trends in the behavior of transversely perturbed solitons of different types. It is shown that diffraction effects on transverse dynamics strongly depend on the soliton type. In particular, diffraction counteracts self-focusing of gray and dark NLS envelope solitons and KdV video solitons in media with quadratic nonlinearity if their intensities do not exceed certain critical values. The corresponding criteria are given by (31), (39), and (48). Conversely, diffraction enhances self-focusing of video solitons, kinks, and domain walls. The mechanism responsible for these effects is explained by correlation between the transverse and longitudinal soliton dynamics: transverse pulse compression is accompanied by longitudinal compression, amplitude growth, and a change in propagation velocity. This leads to the following question: what is the largest number of modes contained in a soliton for which defocusing by diffraction is overtaken by self-focusing? The change in diffraction effects may be associated with the essential role played by aberration. An answer to this question can be obtained, for example, by analyzing three-dimensional breather dynamics. The averaged-Lagrangian method can hardly be applied because of difficulties in analytical calculations of integrals. Either the method should be modified, or essentially different analytical approaches should be found.

These problems motivate the study of two-hump solitons propagating in the regime of synchronized long and short waves or Zakharov–Benney resonance [21, 22]. These solitons develop as bound states of envelope solitons and video solitons. They arise in plasma physics, optics, acoustics, solid-state physics, and the physics of macromolecules. One may expect competition between different diffraction effects on envelope and video solitons.

Furthermore, the effects considered here motivate analysis of diffraction effects on video solitons in media with combined quadratic and cubic nonlinearities.

By no means less important is the question about the effects of transverse perturbations on envelope and video solitons at the eikonal stage. According to Section 3, the transverse dynamics of envelope solitons are determined by the dependence of their phase velocity (or phase refractive index) on amplitude. This is clear from the fact that the group velocities of gray and dark NLS solitons are independent of their amplitudes, whereas the transverse dynamics of video solitons is determined by the amplitude dependence of their group velocities (or group refractive indices). This is made clear by comparing the stability criteria obtained in the eikonal approximation with the dependence of group velocities on soliton duration and noting that the amplitudes of video solitons increase with decreasing τ_p. The corresponding analyses presented in Sections 4 and 5 apply to the solitons described by the sine-Gordon equations as well. Basically, a nonlinear Fermat principle should be formulated for solitons to embrace these phenomena. Conditions should be determined under which transverse dynamics are determined by phase or group refractive indices (for envelope or video solitons, respectively) or by certain combinations of both in intermediate cases (for breathers).

The issues addressed here are of practical, as well as fundamental, importance in view of growing interest in the propagation of few-cycle nonlinear pulses in various media.

ACKNOWLEDGMENTS

This work was supported by the Russian Foundation for Basic Research, project no. 02-02-17710a.

REFERENCES

1. S. K. Zhdanov and B. A. Trubnikov, Zh. Éksp. Teor. Fiz. **92**, 1612 (1987) [Sov. Phys. JETP **65**, 904 (1987)].
2. S. K. Zhdanov and B. A. Trubnikov, *Quasi-Gaseous Unstable Media* (Nauka, Moscow, 1991).
3. B. B. Kadomtsev, *Collective Phenomena in a Plasma* (Nauka, Moscow, 1988).
4. S. A. Akhmanov, V. A. Vysloukh, and A. S. Chirkin, *The Optics of Femtosecond Laser Pulses* (Nauka, Moscow, 1988).
5. N. V. Karlov and N. A. Kirichenko, *Oscillations, Waves, and Structures* (Nauka, Moscow, 2001).
6. D. H. Auston, K. P. Cheung, J. A. Valdmanis, and D. A. Kleinman, Phys. Rev. Lett. **53**, 1555 (1984).
7. T. Brabec and F. Krausz, Rev. Mod. Phys. **72**, 545 (2000).
8. S. A. Kozlov and S. V. Sazonov, Zh. Éksp. Teor. Fiz. **111**, 404 (1997) [JETP **84**, 221 (1997)].
9. É. M. Belenov and A. V. Nazarkin, Pis'ma Zh. Éksp. Teor. Fiz. **51**, 252 (1990) [JETP Lett. **51**, 288 (1990)].
10. É. M. Belenov, A. V. Nazarkin, and V. A. Ushchapovskiĭ, Zh. Éksp. Teor. Fiz. **100**, 762 (1991) [Sov. Phys. JETP **73**, 422 (1991)].
11. S. V. Sazonov and A. F. Sobolevskiĭ, Zh. Éksp. Teor. Fiz. **123**, 1160 (2003) [JETP **96**, 1019 (2003)].
12. S. V. Nesterov and S. V. Sazonov, Fiz. Tverd. Tela (St. Petersburg) **45**, 303 (2003) [Phys. Solid State **45**, 319 (2003)].
13. A. D. Bruce and R. A. Cowley, *Structural Phase Transitions* (Taylor and Francis, Philadelphia, Pa., 1981; Mir, Moscow, 1984).
14. B. A. Strukov and A. P. Livanyuk, *Physical Principles of Ferroelectric Phenomena in Crystals* (Nauka, Moscow, 1995).
15. S. V. Sazonov, Zh. Éksp. Teor. Fiz. **119**, 419 (2001) [JETP **92**, 361 (2001)].
16. S. V. Sazonov, Usp. Fiz. Nauk **171**, 663 (2001) [Phys. Usp. **44**, 631 (2001)].
17. A. Hasegawa and F. Tappert, Appl. Phys. Lett. **23**, 171 (1973).
18. G. Agrawal, *Nonlinear Fiber Optics* (Academic, San Diego, 1995; Mir, Moscow, 1996).
19. R. Rajaraman, *Solitons and Instantons: An Introduction to Solitons and Instantons in Quantum Field Theory* (North-Holland, Amsterdam, 1982; Mir, Moscow, 1985).
20. A. M. Kosevich and A. S. Kovalev, *Introduction to the Nonlinear Physical Mechanics* (Naukova Dumka, Kiev, 1989).
21. R. K. Dodd, J. C. Eilbeck, J. Gibbon, and H. C. Morris, *Solitons and the Nonlinear Wave Equations* (Academic, New York, 1982; Mir, Moscow, 1988).
22. S. V. Sazonov and A. F. Sobolevskiĭ, Pis'ma Zh. Éksp. Teor. Fiz. **75**, 746 (2002) [JETP Lett. **75**, 621 (2002)].

Translated by A. Betev

Journal of Experimental and Theoretical Physics, Vol. 98, No. 6, 2004, pp. 1250–1261.
From Zhurnal Éksperimental'noĭ i Teoreticheskoĭ Fiziki, Vol. 125, No. 6, 2004, pp. 1423–1435.

MISCELLANEOUS

Josephson Charge-Phase Qubit with Radio Frequency Readout: Coupling and Decoherence¶

A. B. Zorin

Physikalisch-Technische Bundesanstalt 38116, Braunschweig, Germany
Institute for Nuclear Physics, Moscow State University, Moscow, 119992 Russia
e-mail: alexander.zorin@ptb.de

Received December 10, 2003

Abstract—The Josephson qubit based on a superconducting single charge transistor inserted in a low-inductance superconducting loop is considered. The loop is inductively coupled to a radio-frequency driven tank circuit enabling the readout of the qubit states by measuring the effective Josephson inductance of the transistor. The effect of qubit dephasing and relaxation due to electric and magnetic control lines, as well as the measuring system, is evaluated. Recommendations for qubit operation with minimum decoherence are given. © *2004 MAIK "Nauka/Interperiodica".*

1. INTRODUCTION

Superconducting quantum bit (qubit) circuits comprising mesoscopic Josephson tunnel junctions have recently demonstrated remarkable quantum coherence properties and are now considered as promising elements for a scalable quantum computer [1]. However, the readout of macroscopic quantum states of a single qubit or a system of coupled qubits with the minimum decoherence caused by the detector remains one of the most important engineering issues in this field.

The Josephson qubits are commonly subdivided into flux, phase, charge and charge-phase qubits. The design of charge and charge-phase qubits is based on a Cooper pair box [2] in which a small superconducting island with significant Coulomb energy is charged through a small Josephson junction (charge qubit) or a miniature double-junction SQUID (charge-phase). The distinct quantum states of the box generated by signals applied to a gate are associated with different observable charges on the island. This makes it possible to read out the qubit state by discriminating the island charge. Probing this charge can be done either by single quasiparticle tunneling across a small auxiliary tunnel junction attached to the island [3] or by a capacitively coupled electrometer [4]. In the charge-phase qubits, the quantum states of the box involve the phase coordinate of the SQUID loop and, hence, discriminating these states can also be done by measuring the persistent current circulating in the loop at an appropriate dc flux bias. Such a measurement was performed in the experiment of the Saclay group [5]. In their setup, nicknamed "Quantronium," the circulating current that passed through a larger auxiliary (third) junction was read out by measuring the switching current of this junction.

The persistent current is not the only phase-dependent quantity characterizing the quantum state of the charge-phase qubit. Another useful quantity is the Josephson inductance of the double junction, which can be probed by small radio-frequency (rf) oscillations induced in the qubit. Recently, we proposed a transistor configuration of the Cooper pair box (see Fig. 1) in which the macroscopic superconducting loop closing the transistor terminals is inductively coupled to a radio-frequency tank circuit [6]. Similar to the rf-SQUID-based method of measuring the Josephson junction impedance [7], this setup makes it possible to measure the rf impedance (more specifically, the Josephson inductance) of a system of two small tunnel junctions connected in series, and in doing so, to probe the macroscopic states of the qubit.

On the one hand, the advantage of this method consists in an effective decoupling between the qubit and a measurement device, which reduces the decoherence of the qubit. Moreover, the loop design of the qubit has the potential to perform data readout in a nondestructive way [8]. On the other hand, due to the selective characteristic of the tank, the bandwidth of this setup is rather narrow, and therefore the optimum relation between the relaxation time of the qubit and the time of measurement becomes an issue. Furthermore, the driving rf signal may induce appreciable frequency modulation and dephasing of the qubit during its evolution (performance of quantum operations). Switching the oscillations off and on is, however, possible only on a relatively long-time scale of a transient process in the tank.

In this paper, we address the problem of decoherence induced in the charge-flux qubit by the classical resonance tank circuit. In addition, we propose a mea-

¶This article was submitted by author in English.

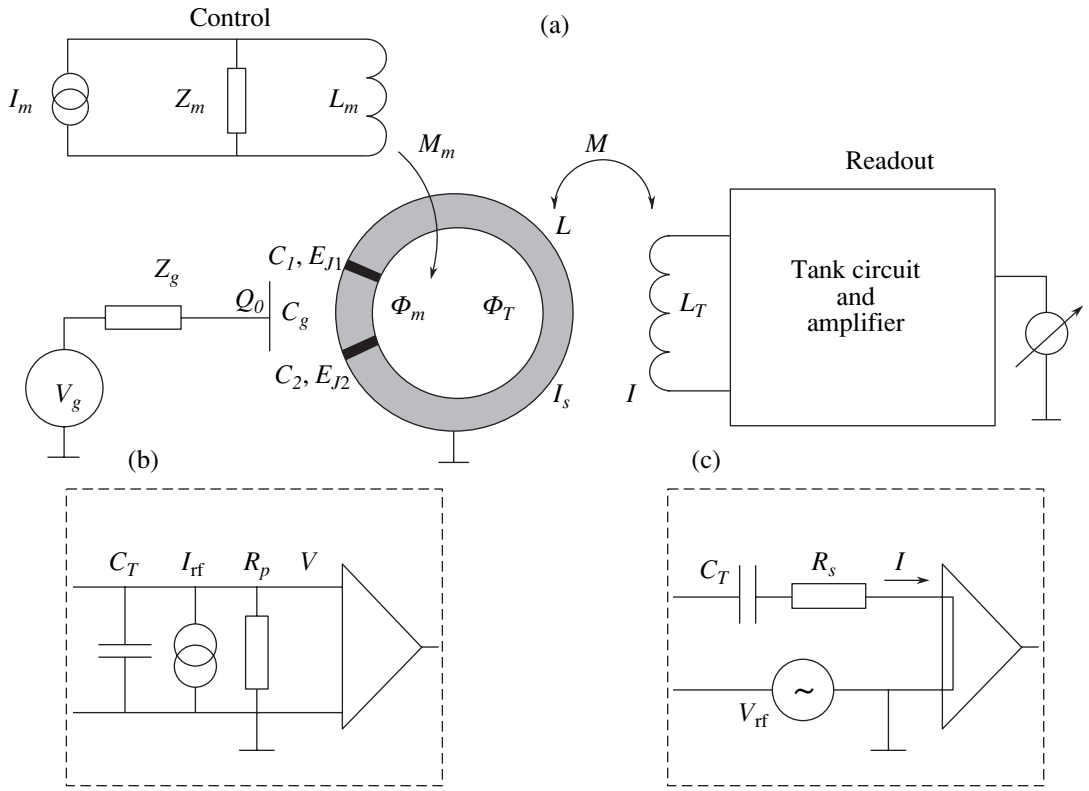

Fig. 1. (a) The electric circuit diagram of the charge-flux qubit inductively coupled to a tank circuit by the mutual inductance M. The macroscopic superconducting loop of inductance L is interrupted by two small Josephson tunnel junctions positioned close to each other and forming a single-charge transistor; the capacitively coupled gate polarizes the island of this transistor. The qubit is controlled by the charge Q_0 generated by the gate and the flux Φ_m induced by coil L_m. The tank circuit, which is either of a parallel (b) or a serial (c) type, is driven by a harmonic signal ($I_{\rm rf}$ or $V_{\rm rf}$, respectively) of the frequency $\omega_{\rm rf} \approx \omega_0$, the resonant frequency of the uncoupled tank circuit

surement strategy and optimize the regime of qubit operation for typical parameters of the circuit.

2. BACKGROUND

The small tunnel junctions of the charge-flux qubit are characterized by self-capacitances C_1 and C_2 and the Josephson coupling strengths E_{J1} and E_{J2}. These junctions with a small central island in-between and a capacitively coupled gate therefore form a single-charge transistor connected in our network as the Cooper pair box (see Fig. 1). The critical currents of the junctions are equal to

$$I_{c1,\,c2} = \frac{2\pi}{\Phi_0} E_{J1,\,J2},$$

where $\Phi_0 = h/2e$ is the flux quantum, and their mean value is

$$I_{c0} = \frac{1}{2}(I_{c1} + I_{c2}).$$

The design enables magnetic control of the Josephson coupling in the box in a dc SQUID manner. The system therefore has two parameters, the total Josephson phase across the two junctions $\phi = \varphi_1 + \varphi_2 = 2\pi\Phi/\Phi_0$ controlled by the flux Φ threading the loop and the gate charge Q_0 set by the gate voltage V_g. The geometrical inductance L of the loop is assumed to be much smaller than the Josephson inductance of the junctions $L_{J0} = \Phi_0/(2\pi I_{c0})$,

$$\beta_L = L/L_{J0} \ll 1. \tag{1}$$

Neglecting the magnetic energy term associated with the current through the small inductance L, we can express the Hamiltonian of the autonomous qubit circuit as

$$H_0 = \frac{(2en - Q_0)^2}{2C} - E_J(\phi)\cos\chi. \tag{2}$$

The second term in Eq. (2) originates from the total Josephson energy equal to $-E_{J1}\cos\varphi_1 - E_{J2}\cos\varphi_2$. The effective Josephson coupling strength is

$$E_J(\phi) = (E_{J1}^2 + E_{J2}^2 + 2E_{J1}E_{J2}\cos\phi)^{1/2},$$
$$|E_{J1} - E_{J2}| \le E_J(\phi) \le E_{J1} + E_{J2} \equiv 2E_{J0} = \frac{\Phi_0}{\pi} I_{c0}, \tag{3}$$

with the phase variable $\chi = \varphi + \gamma(\phi)$. The angle γ is

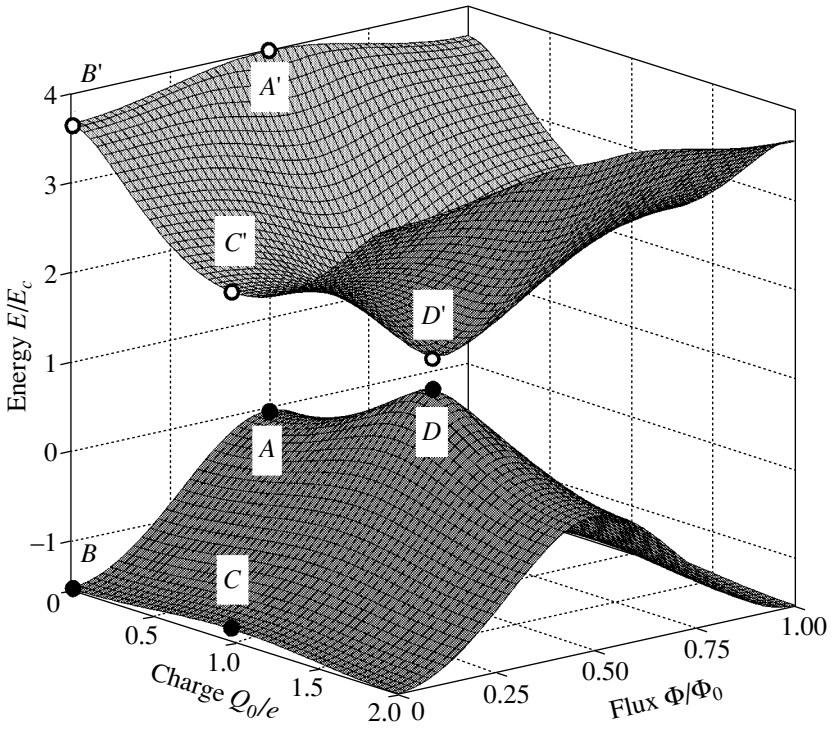

Fig. 2. Shape of the energy bands E_0 and E_1 in the charge-flux qubit calculated for the mean Josephson coupling $E_{J0} \equiv (E_{J1} + E_{J2})/2 = 2E_c$ and the Josephson coupling asymmetry parameter $|j_1 - j_2| = (E_{J1} - E_{J2})/(E_{J1} + E_{J2}) = 0.1$. Black (hollow) circles on the zero (excited) band surface mark the locations of magic points A (A'), B (B'), and C (C') and the avoided level crossing point D (D').

given by

$$\tan\gamma = (j_1 - j_2)\tan(\phi/2), \tag{4}$$

where the dimensionless Josephson energies are $j_{1,2} = E_{J1,J2}/(2E_{J0})$ with $j_1 + j_2 = 1$. The phase difference $\varphi = \frac{1}{2}(\varphi_1 - \varphi_2)$ is a variable conjugate to the island charge $2en = -2ei\frac{\partial}{\partial\varphi}$ and n is the operator of the number of excess Cooper pairs on the island. This charge enters the charging energy (first) term in Eq. (2), in which C is the total capacitance of the island, $C = C_1 + C_2 + C_g \approx C_1 + C_2$, and the gate capacitance $C_g \ll C_{1,2}$. The characteristic charging energy $E_c = e^2/2C$ is assumed to be of the order of the Josephson coupling energies $E_{J1} \sim E_{J2} \gg k_BT$.

The Schrödinger equation corresponding to the Hamiltonian in Eq. (2) is the Mathieu equation [9]. The eigenenergies form Bloch bands and the $|n, q\rangle$ are the Bloch wave functions of a particle in the periodic (Josephson) potential with "quasimomentum" (here, quasicharge) q. Its value is the charge induced by the gate source on the island, i.e., $q = Q_0 = C_gV_g$. Each of such eigenfunctions can be represented as a coherent superposition of plane waves,

$$|q, n\rangle = \sum_m C_m^{(n)} \exp\left[i\left(\frac{q}{2e} + m\right)\chi\right], \tag{5}$$

where $m = 0, \pm1, \pm2, \ldots$ is the number of the excess Cooper pairs on the island [10, 11]. The weights of these coherent contributions $\left|C_m^{(n)}\right|^2$ depend on q, the band index n, and the characteristic ratio

$$\lambda = E_J(\phi)/E_c. \tag{6}$$

The lowest two energy levels $E_n(q, \phi)$, i.e., $n = 0$ and 1 (see their dependences on q and ϕ in Fig. 2) form the basis $\{|0\rangle, |1\rangle\}$ suitable for qubit operation. In this basis, Hamiltonian (2) is diagonal,

$$H_0 = -\frac{1}{2}\epsilon\sigma_z, \tag{7}$$

where σ_i with $i = x, y, z$ is the Pauli spin operator. The general state of the qubit is

$$|\Psi\rangle = a|0\rangle + b|1\rangle, \tag{8}$$

with $|a|^2 + |b|^2 = 1$. It is remarkable that the level spacing $\epsilon(q, \phi) \equiv \hbar\Omega = E_1(q, \phi) - E_0(q, \phi)$, and therefore the transition frequency Ω are efficiently controlled by two knobs, i.e., by varying the parameters q and ϕ (or, equivalently, Q_0 and Φ).[1]

The idea underlying the measurement of this charge-flux qubit is based on inducing radio frequency oscillations in the tank circuit of frequency $\omega_{rf} \ll \Omega$ [6]. Due to inductive coupling M, these oscillations cause oscillations of the corresponding flux Φ_T (see Fig. 1a) and therefore of the total phase,

$$\phi = \frac{2\pi}{\Phi_0}(\Phi_T + \Phi_m) = \phi_a \sin(\omega_{rf} t + \theta) + \phi_0. \quad (9)$$

If the rf drive signal is sufficiently weak, the amplitude ϕ_a of these oscillations is relatively small, $\phi_a \ll \pi$. In this linear regime, the Josephson inductance is given by

$$L_J^{-1}(n, q, \phi) = \left(\frac{2\pi}{\Phi_0}\right)^2 \frac{\partial^2 E_n(q, \phi)}{\partial \phi^2}. \quad (10)$$

It is therefore determined by the local curvature of the energy surface E_n. For example, for $E_{J0} = 2E_c$ (see Fig. 2) at $q \approx 0$, the respective estimates within the zeroth and first bands are

$$L_J^{-1}(0, 0, \phi) \approx 0.4 L_{J0}^{-1} \cos\phi \quad (11)$$

and

$$L_J^{-1}(1, 0, \phi) \approx 0.1 L_{J0}^{-1} \cos\phi. \quad (12)$$

In the vicinity of the avoided crossing point, $q = e$ and $\phi = \pi$ (marked as D–D' in Fig. 2), the inverse inductances can increase significantly,

$$L_J^{-1}(n, 0, \pi) \approx \frac{(-1)^{n+1}}{4|j_1 - j_2|} L_{J0}^{-1}, \quad n = 0 \text{ and } 1, \quad (13)$$

because of a small asymmetry of the transistor parameters, $|j_1 - j_2| \ll 1$. For example, in the case presented in Fig. 2, $|j_1 - j_2| = 0.1$ and $L_J^{-1} = \mp 2.5 L_{J0}^{-1}$ for the zeroth and first band, respectively. At points C and C', the absolute values $|L_J^{-1}|$ are smaller, but the signs for $n = 0$ and 1 are still different.

Coupling to the qubit causes a shift in the resonance frequency $\omega_0 = (L_T C_T)^{-1/2}$ of the tank circuit, i.e., $\omega_0'(n) = \omega_0 + \delta\omega_0(n)$, where

$$\delta\omega_0(n) = \frac{1}{2} k^2 \beta_L \frac{L_{J0}}{L_J(n, q, \phi)} \omega_0. \quad (14)$$

Here,

$$k = \frac{M}{\sqrt{L_T L}} < 1 \quad (15)$$

is the dimensionless coupling coefficient. The resonance frequency shift $\delta\omega_0(n)$ carrying information about the qubit state $|n\rangle$ is found from the amplitude and/or phase of forced oscillations in the tank. For achieving sufficient resolution in such measurements, the quality factor of the tank circuit Q should be about or larger than the ratio $\omega_0/|\delta\omega_0(0) - \delta\omega_0(1)|$.

3. INHERENT AND EXTERNAL SOURCES OF DECOHERENCE

We neglected the quasiparticle tunneling that inevitably causes dissipation of energy. Even rare tunneling of individual quasiparticles across the tunnel junctions, i.e., on and from the island, can decohere the qubit and completely destroy the readout regime described above. These processes lead to a sudden change in the operation point, $q \longrightarrow q \pm e$ and, possibly, of the energy band index; i.e., they cause a relaxation of $1 \longrightarrow 0$.

The processes of single quasiparticle tunneling across a small Josephson junction have been studied by Averin and Likharev in [12, 13]. They generalized the orthodox theory of single electron tunneling to the case of a finite Josephson coupling, $E_J \neq 0$, taking into account the dynamics of the essential phase factors $\exp(\pm i\chi/2)$ in the electron tunneling terms added to a Hamiltonian of type (2). These factors are the operators of a single-electron transfer and their nonzero matrix elements in our basis are

$$e^{\pm}_{nn'} = \langle n, q | \exp(\pm i\chi/2) | q \pm e, n' \rangle. \quad (16)$$

The rates of transitions $|q, n\rangle \longrightarrow |q \pm e, n'\rangle$ are given by

$$\Gamma^{\pm}_{nn'} = |e^{\pm}_{nn'}|^2 \frac{I_{qp}(\epsilon^{\pm}_{nn'}/e)}{e} \left[1 - \exp\left(-\frac{\epsilon^{\pm}_{nn'}}{k_B T}\right)\right]^{-1}. \quad (17)$$

In our case, $I_{qp}(U)$ is the quasiparticle current-voltage dependence of the network of two tunnel junctions of the qubit connected in parallel. Because the energy surfaces are $2e$-periodic, the corresponding energy gains are identical,

$$\epsilon^{+}_{nn'} = \epsilon^{-}_{nn'} = E_n(q, \phi) - E_{n'}(q \pm e, \phi), \quad (18)$$

and their value depends on the operation point $\{Q_0, \Phi\}$ (see Fig. 2).

The relation between this energy and the superconductor energy gap Δ_{sc} is important for making the quasiparticle transitions infrequent or even eliminating them. First, if the voltage is $U = \epsilon^{\pm}_{nn'}/e \leq 2\Delta_{sc}/e$, the quasiparticle current $I_{qp}(U)$ entering Eq. (17) is exponen-

[1] In fact, the energy spectrum of this system is similar to that of Quantronium [5], having one additional large Josephson junction in the loop.

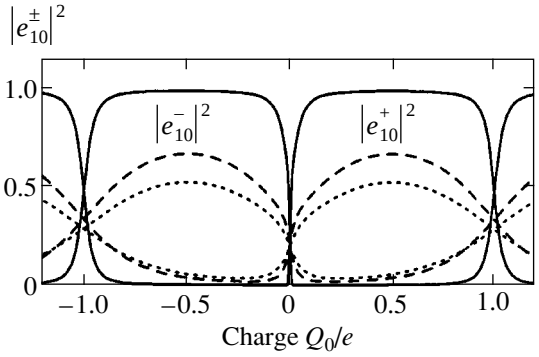

Fig. 3. Off-diagonal matrix elements of the single quasiparticle transfer operators $\exp(\pm i\chi/2)$ computed for different values of the equivalent Josephson coupling set by the flux $\Phi = \Phi_0/2$ (solid lines), $\Phi_0/4$ (dashed lines), and 0 (dotted lines). The qubit parameters are the same as in Fig. 2.

tially small, i.e., $\sim I_{c0}\exp(-\Delta_{sc}/k_BT)$.[2] At larger voltages, $U > 2\Delta_{sc}/e$, the current I_{qp} is enormously large, $\geq 2I_{c0}$. Therefore, in order to prevent, intensive tunneling of quasiparticles, the energy gain $\epsilon^{\pm}_{nn'}$ must never exceed $2\Delta_{sc}$. Second, if this gain is smaller than Δ_{sc}, then infrequent quasiparticle tunneling can, in principle, be blocked by the gap energy associated with one unpaired electron in the superconducting island (the so-called even-odd parity effect).[3]

Suppression of quasiparticle transitions within the zero energy band in superconducting Al single-charge transistors and Cooper pair boxes was extensively investigated experimentally. Depending on experimental skill and luck (see, e.g., [14–17]), the inspected devices often exhibited pure Cooper pair behavior when their charging energy E_c was not larger than $\sim 100\ \mu\text{eV} \approx 0.5\Delta_{\text{Al}}$, where Δ_{Al} is the superconductor energy gap of aluminum. Because the energy gain for transitions in the Cooper pair boxes and low-voltage-biased transistors, $\epsilon^{\pm}_{00}$, is less than E_c for any E_J, the condition $E_c < \Delta_{sc}$ can ensure suppression of quasiparticle tunneling in the ground state in a "good" qubit sample.

For quasiparticle transitions from the excited state, this condition is clearly insufficient. For example, for small E_J (corresponding to the flux value $\Phi = \Phi_0/2$, Eq. (3)), the energy gain values are between about E_c (for the process $D' \longrightarrow A$, see Fig. 2) and $4E_c$ (for the processes $A' \longrightarrow D'$ and $A' \longrightarrow D$). At larger E_J, both the minimum and maximum energy gain values are even larger. For example, for $E_J = 4E_c$ (i.e., $\Phi = 0$), the transitions $C' \longrightarrow B$ and $B' \longrightarrow C$ correspond to the respective energies $\approx 4E_c$ and $\approx 5E_c$. Because the first factor in the expression for the resulting relaxation rate,

$$[\tau_r^{(qp)}]^{-1} = \Gamma^{+}_{10} + \Gamma^{-}_{10} \approx (|e^{+}_{10}|^2 + |e^{-}_{10}|^2)\frac{I_{\text{qp}}(\epsilon^{\pm}_{10}/e)}{e}, \quad (19)$$

is nonzero for any Q_0 and Φ (see the plots of the two quantities in Fig. 3), only the condition $E_c \leq \Delta_{sc}/5$ can ensure suppression of these transitions at an arbitrary operation point of our qubit. An insufficiently small value of E_c was possibly the reason for the very short relaxation time (tens of nanoseconds) in the recent experiment with a charge qubit by Duty *et al.* [17]. Their Al Cooper pair box had $E_c \approx 08\Delta_{sc}$ and $E_J \approx 0.4E_c$, and therefore the energy gain in the chosen operation point ($Q_0 = 0.4e$) was too large, i.e., about $2.2E_c \approx 1.8\Delta_{sc} > \Delta_{sc}$ (this sample nicely showed the pure Cooper pair characteristic although in the ground state).

Moreover, there are several sources of decoherence due to coupling of the qubit to the environmental degrees of freedom. For evaluating the effect of these sources on the qubit, the coupling Hamiltonian term $H_{\text{coupl}} = H_c^{(e)} + H_c^{(m)}$ is included in the total Hamiltonian of the system,

$$H = H_0 + H_{\text{coupl}} + H_{\text{bath}}, \quad (20)$$

where H_{bath} is a bath operator, and $H_c^{(e)}$ and $H_c^{(m)}$ are the electric control line term and the magnetic coupling term respectively. The latter is associated with both the flux control line and the tank circuit. Fluctuations originating from the sources of gate- and flux-control lines can, in principle, lead to a significant decoherence of the qubit. As was shown in [18] and demonstrated in experiments [3–5], these effects can, however, be minimized by choosing the appropriate (minimum) coupling. On the other hand, the decoherence caused by the tank-circuit-based readout system requires special analysis, because weakening this coupling results in reducing the input signal. Below, we start with the sources of decoherence associated with the control lines and then analyze the effect of the tank circuit and amplifier.

4. COUPLING TO THE CHARGE CONTROL LINE

The coupling of the charge-phase qubit to the electric control line is actually similar to that of the gate coupling in the ordinary Cooper pair box [18]. However, we now assume that the Josephson coupling parameter λ is not necessarily small, as is usually assumed in the analysis of charge qubits. This general-

[2] See, for example, a simple approximation formula in S. Ramo, J. R. Whinnery and T. van Duzer, *Fields and Waves in Communication Electronics*, Wiley and Sons, New York (1965), p. 211.

[3] As follows from the entropy consideration, the threshold value is somewhat smaller than Δ_{sc} for finite volume of island and nonzero temperature; see for details M.T. Tuominen, J.M. Hergenrother, T.S. Tighe and M. Tinkham, Phys. Rev. Lett. **69**, 1997 (1992).

ization of the model is essential because the external flux Φ_m changes the effective Josephson energy (3) of the qubit over a wide range. The assumption that λ is not small implies that the eigenstates of our system, Eq. (5), are generally composed of several (not only two) plane-wave states.

The coupling term can be represented as

$$H_c^{(e)} = -2en\delta V_e, \tag{21}$$

where δV_e is the operator of voltage fluctuations on the island in the absence of Josephson coupling. The charge operator is equal to $2en = Q_0 - C\hat{V}$, and therefore the essential part of the coupling Hamiltonian is

$$H_c^{(e)} = C\hat{V}\delta V_e. \tag{22}$$

The voltage operator is given by

$$\hat{V} = \frac{\Phi_0}{2\pi}\dot{\varphi} = \frac{\Phi_0}{2\pi}\left(\dot{\chi} - \frac{\partial\gamma}{\partial\phi}\dot{\phi}\right) = \frac{\Phi_0}{2\pi}\dot{\chi}. \tag{23}$$

Here, we assume slow variation of the total phase ϕ, Eq. (9). The voltage operator $\hat{V}$ is similar to the velocity operator of an electron in the periodic electric potential of a crystal lattice [19], and its interband matrix elements are

$$V_{nn'} = \frac{\partial E_n}{\partial q}\delta_{n,n'} + i\frac{E_n - E_{n'}}{2e}\chi_{nn'}(1 - \delta_{n,n'}), \tag{24}$$

where $\delta_{n,n'}$ is the Kroneker delta and $\chi_{nn'}$ are the matrix elements of the phase operator χ [11].

Finally, the coupling Hamiltonian, Eq. (22), takes the form

$$H_c^{(e)} = (\sigma_x \sin\eta_e + \sigma_z \cos\eta_e)X_e, \tag{25}$$

where we introduce the operator

$$X_e = C\|V\|\delta V_e \tag{26}$$

with

$$\|V\| = \frac{1}{2}\sqrt{(V_{11} - V_{00})^2 + 4|V_{01}|^2} \tag{27}$$

and

$$\tan\eta_e = \frac{2|V_{01}|}{(V_{11} - V_{00})}. \tag{28}$$

(The plots of the terms entering Eqs. (27) and (28) obtained by numerical calculations are presented in Fig. 4.) Thus, $X_e = \sum_a C_a x_a$ can be considered as an operator of the bath [20] with the Hamiltonian

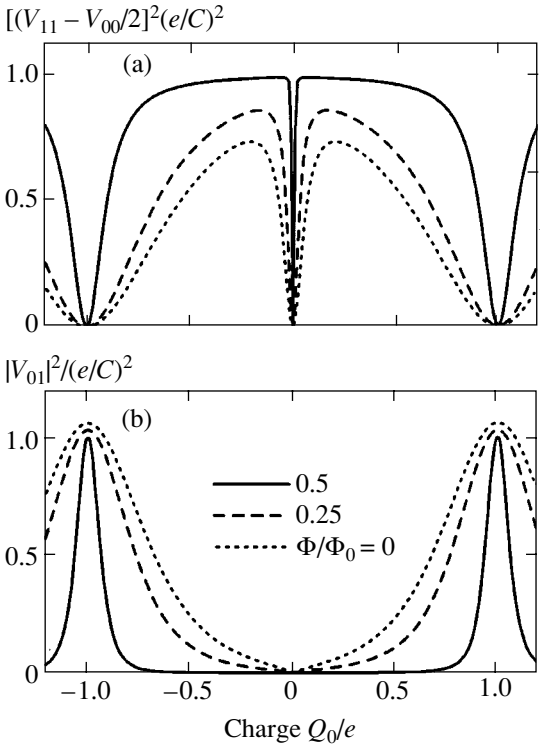

Fig. 4. Terms composed of diagonal (a) and off-diagonal (b) matrix elements of the operator $\hat{V}$ in Eqs. (27) and (28) for different values of the dimensionless flux Φ/Φ_0 for the given qubit parameters (see caption to Fig. 2)

$$H_b^{(e)} = \sum_a \left(\frac{p_a^2}{2m_a} + \frac{m_a\omega_a^2 x_a^2}{2}\right) \tag{29}$$

and the spectral density $S_X^{(e)}(\omega) = C^2\|V\|^2 S_V^{(e)}(\omega) = J_e(\omega)\Theta(\omega, T)/\omega$. Here, the oscillator energy function is

$$\Theta(\omega, T) = \frac{\hbar\omega}{2}\coth\frac{\hbar\omega}{2k_BT} \tag{30}$$

and

$$J_e(\omega) = \frac{\pi}{2}\sum_a \frac{C_a^2}{m_a\omega_a}\delta(\omega - \omega_a). \tag{31}$$

With C_g assumed to be small, the spectral density $S_V^{(e)}$ of the fluctuations of δV_e is given by

$$S_V^{(e)}(\omega) = \frac{2}{\pi}\left(\frac{C_g}{C}\right)^2 \mathrm{Re}Z_t(\omega)\Theta(\omega, T), \tag{32}$$

where $Z_t = (i\omega C_g + Z_g^{-1})^{-1}$ is determined by the parallel connection of the qubit capacitance $C_g C/(C_g + C) \approx C_g$ and the gate line impedance $Z_g(\omega) \sim R_{100} \equiv 100\Omega$. Therefore, for frequencies up to $\omega_g \equiv (R_{100}C_g)^{-1} \gg \epsilon/\hbar$, i.e., at all characteristic frequencies of the system, $\mathrm{Re}\, Z_t = R_{100}$. This is the case of linear damping in the Caldeira–Leggett model,

$$J_e(\omega) = \frac{\pi}{2}\alpha_e \hbar\omega, \tag{33}$$

with the dimensionless factor

$$\alpha_e(q, \phi) = \left(\frac{C_g\|V\|}{e}\right)^2 \frac{R_{100}}{R_Q} \lesssim \left(\frac{C_g}{C}\right)^2 \frac{R_{100}}{R_Q}, \tag{34}$$

where $R_Q = h/4e^2 \approx 6.45$ kΩ, the resistance quantum. The estimate similar to the last expression in Eq. (34) was given in [18] for small λ.

Relaxation and dephasing caused by the charge control line can therefore be described by the spin-boson model with linear damping [21]. The corresponding rates are given by the expressions

$$[\tau_r^{(e)}]^{-1} = \pi\alpha_e \sin^2\eta_e \Omega \coth\frac{\hbar\Omega}{2k_B T} \tag{35}$$

and

$$[\tau_\varphi^{(e)}]^{-1} = [2\tau_r^{(e)}]^{-1} + \pi\alpha_e \cos^2\eta_e \frac{2k_B T}{\hbar}. \tag{36}$$

One can see that in accordance with the conclusions made in [18, 22], reducing the coupling coefficient α_e by a small factor of $(C_g/C)^2 \ll 1$ can significantly depress the decoherence rates.

5. COUPLING TO THE FLUX CONTROL LINE

The inductive coupling of the qubit loop to the control and readout circuits is described by the Hamiltonian

$$H_c^{(m)} = -\hat{I}_s(\delta\Phi_m + \delta\Phi_T), \tag{37}$$

where $\hat{I}_s$ is the operator of the current circulating in the qubit loop, $\delta\Phi_m = M_m \delta I_m$ is the bath operator (proportional to fluctuations of the current δI_m in the control inductance L_m), and $\delta\Phi_T = M\delta I$ is the operator of the flux associated with current fluctuations in the tank circuit.

To specify the coupling, we represent operator $\hat{I}_s$ in eigenbasis (5); i.e., we find the matrix elements

$$\langle n|\hat{I}_s|n'\rangle, \quad n, n' = 0, 1. \tag{38}$$

In the general case, $\hat{I}_s$ is given by the expression

$$\hat{I}_s = \kappa_1 \dot{Q}_1 + \kappa_2 \dot{Q}_2, \tag{39}$$

with the dimensionless factors $\kappa_{1,2} = C_{2,1}/C$ such that $\kappa_1 + \kappa_2 = 1$. The quantities

$$Q_{1,2} = -2ei\frac{\partial}{\partial\varphi_{1,2}}$$

are the respective charges on the first and second junction, and their time derivatives are Josephson supercurrents,

$$\dot{Q}_{1,2} = \frac{i}{\hbar}[Q_{1,2}, H_0] = I_{c1,c2}\sin\varphi_{1,2}. \tag{40}$$

Using the identity

$$\varphi_{1,2} = \frac{\phi}{2} \pm \varphi = \frac{\phi}{2} \pm \chi \mp \gamma$$

and Eq. (4), we can represent the circulating current as

$$\hat{I}_s = I_1(\phi)\cos\chi + I_2(\phi)\sin\chi. \tag{41}$$

The respective amplitudes of these two components are

$$I_1 = \frac{2\pi}{\Phi_0}\frac{E_{J1}E_{J2}}{E_J(\phi)}\sin\phi \tag{42}$$

and

$$\begin{aligned} I_2 &= (j_1 - j_2)(\kappa_1 j_1 + \kappa_2 j_2)\frac{8\pi}{\Phi_0}\frac{E_{J0}^2}{E_J(\phi)} \\ &+ (\kappa_1 - \kappa_2)\frac{4\pi}{\Phi_0}\frac{E_{J1}E_{J2}}{E_J(\phi)}\cos^2\frac{\phi}{2}. \end{aligned} \tag{43}$$

Because the Hamiltonian in Eq. (2) is an even function of χ, the operators $\cos\chi$ and $\sin\chi$ entering Eq. (41) are diagonal and off-diagonal, respectively. The amplitude I_1 is merely the classical Josephson current across two large-capacitance junctions, expressed as a function of the overall phase difference ϕ, while the diagonal term $\cos\chi$ describes the suppression of this current due to the charging effect ($E_c \neq 0$) (see, e.g., [23]). The second, off-diagonal term in Eq. (41) is due to asymmetry of the transistor; it gives rise to the interband transitions $0 \longleftrightarrow 1$. Using the notation

$$c_{00} = \langle 0|\cos\chi|0\rangle, \quad c_{11} = \langle 1|\cos\chi|1\rangle \tag{44}$$

and

$$s_{01} = |\langle 0|\sin\chi|1\rangle| \tag{45}$$

for the nonzero values of the corresponding matrix elements, we obtain the coupling Hamiltonian in Eq. (37)

in the form

$$H_c^{(m)} = (\sigma_y \sin\eta_m + \sigma_z \cos\eta_m)(X_m + X_T), \quad (46)$$

where

$$X_{m,T} = -\|I\|\delta\Phi_{m,T}, \quad (47)$$

$$\|I\| = \frac{1}{2}\sqrt{[(c_{11}-c_{00})I_1]^2 + [2s_{01}I_2]^2}, \quad (48)$$

$$\tan\eta_m = \frac{2s_{01}I_2}{(c_{11}-c_{00})I_1} \quad (49)$$

(see the plots of the terms entering these expressions in Fig. 5).

We first omit the term X_T associated with fluctuations of the tank circuit in Eq. (46) and focus on the effect of fluctuations in the flux control line $\delta\Phi_m = M_m\delta I_m$. Assuming real impedance of the flux control line, $Z_m \sim R_{100}$, we obtain the spectral density of the operator $X_m \propto \delta I_m$ in the form $S_X^{(m)}(\omega) = M_m^2\|I\|^2 S_I^{(m)}(\omega) = J_m(\omega)\Theta(\omega, T)/\omega$. At frequencies below $\omega_m \equiv R_{100}/L_m$, the function J_m is linear,

$$J_m(\omega) = \frac{\pi}{2}\alpha_m\hbar\omega \quad (50)$$

with the dimensionless coupling factor

$$\alpha_m(q, \phi) = \left(\frac{2M_m\|I\|}{\Phi_0}\right)^2 \frac{R_Q}{R_{100}}. \quad (51)$$

At higher frequencies, $\omega > \omega_m$, the effective damping decays as $(\omega_m/\omega)^2$.

In fact, Eq. (51) describes the effect of coupling to the control flux in the general case. An estimate of the coupling factor based on the evaluation

$$\|I\| \approx \frac{1}{2}\left|\frac{\partial E_J}{\partial\Phi}\right|, \quad (52)$$

which is valid for a symmetric transistor ($I_2 = 0$) with small E_J, was made in [18]. Small mutual inductance M_m [18, 22] leads to small α_m and therefore causes significant depression of the corresponding relaxation rate,

$$[\tau_r^{(m)}]^{-1} = \pi\alpha_m \sin^2\eta_m \Omega \coth\frac{\hbar\Omega}{2k_BT}, \quad (53)$$

and dephasing rate,

$$[\tau_\phi^{(m)}]^{-1} = [2\tau_r^{(m)}]^{-1} + \pi\alpha_m \cos^2\eta_m \frac{2k_BT}{\hbar}. \quad (54)$$

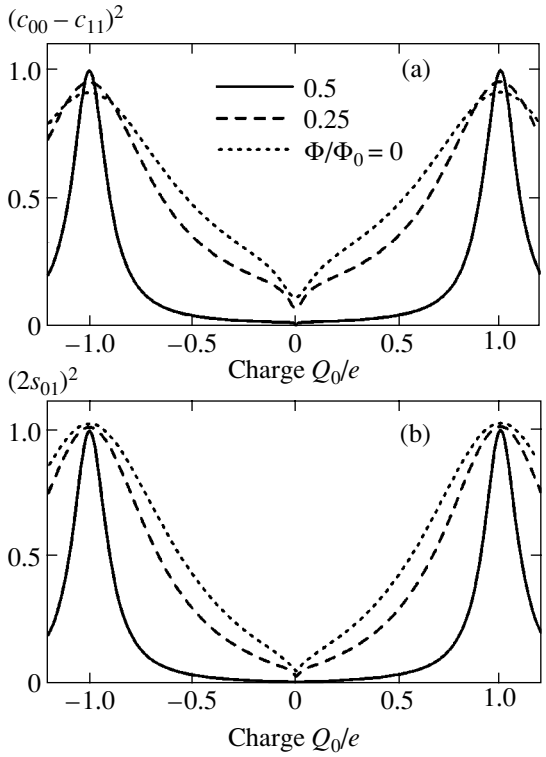

Fig. 5. Terms composed of diagonal (a) and off-diagonal (b) matrix elements of the operator $\cos\chi$ and $\sin\chi$, respectively, calculated for different values of the dimensionless flux Φ/Φ_0 for the given qubit parameters (see caption to Fig. 2).

So far, we have considered the effects of decoherence due to the charge and flux control lines as two independent effects. They must actually be described together using a multibath model [18]. If either of these decoherence effects is small, i.e., the so-called Hamiltonian-dominated regime is realized, the total rates due to contributions of the two control lines are given by

$$[\tau_r^{(c)}]^{-1} = [\tau_r^{(e)}]^{-1} + [\tau_r^{(m)}]^{-1}, \quad (55)$$

$$[\tau_\varphi^{(c)}]^{-1} = [2\tau_r^{(c)}]^{-1} + [\tau_\varphi^{(e)}]^{-1} + [\tau_\varphi^{(m)}]^{-1}. \quad (56)$$

In our model, we assume that such a regime is realized and, moreover, the resulting rates in Eqs. (55) and (56) can be made negligibly small. Below, we focus on the effect of the readout circuit, whose coupling strength has to be optimized.

6. DECOHERENCE DUE TO THE READOUT SYSTEM

In contrast to control lines, coupling to a readout device (in our case, the tank circuit with an amplifier) cannot be made arbitrarily small in order to reduce the decoherence. This coupling should ensure sufficiently strong signals at the amplifier input in order to perform

a measurement with a reasonable signal-to-noise ratio on a time scale shorter than that determined by other factors, namely, $\tau_r^{(c)}$. Moreover, without an efficient switch (see one possible design of such a switch, e.g., in [24]), such a coupling may cause significant dephasing of the qubit during quantum gate manipulation.

The inductive qubit coupling to the tank circuit is described by the Hamiltonian in Eq. (46). The spectral density of fluctuations of the corresponding variable $X_T \propto \delta\Phi_T = M\delta I$ is expressed as

$$S_X^{(T)}(\omega) = \frac{2}{\pi}M^2\|I\|^2 S_I^{(T)}(\omega) = J_T(\omega)\frac{\Theta(\omega, T^*)}{\omega}, \quad (57)$$

where $S_I^{(T)}(\omega)$ is the spectral density of the noise current δI across the inductance L_T. Because the cold (superconducting) tank circuit itself presumably has very low losses, a back-action noise δI of the amplifier is dominating. It is associated with the input real impedance, modeled by R_p or R_s for parallel and serial configurations, respectively (see Fig. 1). T^* is the effective temperature associated with this impedance.

The spectral density $S_I^{(T)}$ and the function $J_T(\omega)$ can be found from a network consideration. With the small detuning $\delta\omega_0 \ll \omega_0$ neglected, in the case of the parallel network (Fig. 1b), the spectral function J_T is given by the expression

$$J_T^{(p)}(\omega) = \frac{2}{\pi}\alpha_p\hbar\omega\frac{\omega_0^4}{(\omega^2-\omega_0^2)^2+\omega^2\omega_0^2Q^{-2}}, \quad (58)$$

with

$$\alpha_p = \left(\frac{2M\|I\|}{\Phi_0}\right)^2\frac{R_Q}{R_p} = \frac{k^2\beta_L}{\pi Q}\frac{\|I\|^2}{e\omega_0 I_{c0}} \quad (59)$$

and with the quality factor $Q = \omega_0 C_T R_p = R_p/\omega_0 L_T$. For the serial network shown in Fig. 1c, we have

$$J_T^{(s)}(\omega) = \frac{2}{\pi}\alpha_s\hbar\omega\frac{\omega^2\omega_0^2}{(\omega^2-\omega_0^2)^2+\omega^2\omega_0^2Q^{-2}}, \quad (60)$$

with

$$\alpha_s = \left(\frac{2M\|I\|}{\Phi_0}\right)^2\frac{R_Q R_s}{(\omega_0 L)^2} \quad (61)$$

and $Q = (\omega_0 C_T R_s)^{-1} = \omega_0 L_T/R_s$.

In contrast to the linear spectral functions for the control lines, Eqs. (33) and (50), the functions given by Eqs. (58) and (60) describe a structured bath, i.e., they both are of a Lorentzian (resonance) shape. A similar situation emerges, for example, in the case of the flux qubit with readout using a *C*-shunted dc SQUID [22]. The spin-boson model with a structured bath was analyzed theoretically in [25] on the basis of the flow equations. If the coupling is weak, as in our case, then only the high frequency ($\omega \sim \Omega$) and low frequency ($\omega \longrightarrow 0$) behaviors of $J(\omega)$ account for relaxation and dephasing, respectively [22, 26, 27].

Because the frequency Ω is typically about tens of gigahertz and the distance between the qubit and the amplifier presumably exceeds the wavelength, the effective real admittance of the parallel circuit at these frequencies is equal to R_{100}^{-1} and the impedance of the serial circuit is $\approx R_{100}$. Therefore, the relaxation rates increase by respective factors of $g_p = R_p/R_{100} \gg 1$ and $g_s = R_{100}/R_s \gg 1$.

For the parallel tank circuit, the relaxation and dephasing rates (presumably, $\ll\omega_0$) are equal to

$$[\tau_r^{(p)}]^{-1} = \pi g_p\alpha_p\sin^2\eta_m\left(\frac{\omega_0}{\Omega}\right)^4\Omega\coth\frac{\hbar\Omega}{2k_BT^*} \quad (62)$$

and

$$[\tau_\varphi^{(p)}]^{-1} = [2\tau_r^{(p)}]^{-1} + \pi\alpha_p\cos^2\eta_m\frac{k_BT^*}{\hbar}, \quad (63)$$

respectively. The relaxation rate is dramatically suppressed due to the small frequency ratio, $(\omega_0/\Omega) \ll 1$. For the serial configuration, the corresponding rates are

$$[\tau_r^{(s)}]^{-1} = \pi g_s\alpha_s\sin^2\eta_n\left(\frac{\omega_0}{\Omega}\right)^2\Omega\coth\frac{\hbar\Omega}{2k_BT^*}, \quad (64)$$

$$[\tau_\varphi^{(s)}]^{-1} = [2\tau_r^{(s)}]^{-1}. \quad (65)$$

The dephasing rate is determined by the rate of relaxation, because at low frequency, $\omega \ll \omega_0$, it follows that $J_T^{(s)}(\omega) \propto \omega^3$ [21]. Due to weaker decay of the serial circuit impedance at high frequencies, $\omega \gg \omega_0$, the relaxation rate is, however, substantially higher than in the case of the parallel circuit configuration. We therefore focus further consideration only on the parallel tank circuit as the more favorable (allowing longer measuring time).

7. MAGIC POINTS AND SOME ESTIMATIONS

Analysis of the coupling between the qubit and the tank circuit, Eqs. (46–49) and Fig. 5, shows that its strength $X_T \propto \|I\|$ and mixing angle η_m can be significantly varied by choosing an appropriate operation point. For example, as can be seen from Eq. (42), the diagonal component of X_T ($\propto I_1$), which essentially causes pure dephasing of the qubit, is zero, i.e., the mixing angle $\eta_m = \pi/2$, at the phase values $\phi = 0$ and π. The

derivatives $\partial E_{0,1}/\partial\phi$ and therefore the circulating supercurrent are zero. Moreover, as illustrated in Fig. 5b, if the gate charge $Q_0 \approx 0$ (i.e., derivatives $\partial E_{0,1}/\partial Q_0 = 0$), then $|s_{01}|$ and hence X_T are minimum. In particular, at the bias flux $\Phi_m = \Phi_0/2$ or, equivalently, $\phi = \pi$ (this point is marked in Fig. 2 as *A*), $E_J(\phi) = |E_{J1} - E_{J2}| \ll E_c$, and we can therefore use the explicit expressions for the wave functions, Eqs. (A.11) and (A.12) in [11], and obtain

$$|s_{01}| = \frac{1}{16\sqrt{2}}\frac{E_J(\phi)}{E_c} = \frac{|j_1 - j_2|}{8\sqrt{2}}\frac{E_{J0}}{E_c}. \quad (66)$$

Then the value of $\|I\|$ given by (48) is

$$\|I\|_A = |s_{01}|I_2 \approx \frac{|j_1 - j_2|}{8\sqrt{2}}\frac{E_{J0}}{E_c}I_{c0}, \quad (67)$$

where we have taken into account that $\kappa_1 \sim \kappa_2 \sim 0.5$ and the second term in Eq. (43), $\propto(\kappa_1 - \kappa_2)$, vanishes because $\cos(\phi/2) = 0$. At the point $Q_0 = 0$, $\phi = 0$ (marked as *B* in Fig. 2), the Josephson energy $E_J(\phi) = 2E_{J0}$ and $2|s_{01}|$ is approximately equal to $(1/8\sqrt{2})E_{J0}/E_c$ and therefore

$$\|I\|_B \approx \frac{|j_1 - j_2 + \kappa_1 - \kappa_2|}{8\sqrt{2}}\frac{E_{J0}}{E_c}I_{c0}, \quad (68)$$

while for $Q_0 = e$ (point *C* in Fig. 2), $|s_{01}| \approx 0.5$ and

$$\|I\|_C \approx |j_1 - j_2 + \kappa_1 - \kappa_2|I_{c0}. \quad (69)$$

It is remarkable that the effect of asymmetry in critical currents and capacitances of the junctions can, in principle, cancel if $(j_1 - j_2) = -(\kappa_1 - \kappa_2)$. In practice, however, the signs of $(j_1 - j_2)$ and $(\kappa_1 - \kappa_2)$ are normally similar because the critical current and capacitance are both proportional to the junction area and such cancelling does not occur.

Comparing Eqs. (67), (68), and (69), we can see that under the assumption of small asymmetry of the transistor, $j_1 \approx j_2 \approx \kappa_1 \approx \kappa_2 \approx 0.5$, the coupling strength α_p at the points $A(Q_0 = 0, \phi = \pi)$, $B(Q_0 = 0, \phi = 0)$, and $C(Q_0 = e, \phi = 0)$ is rather small, but it is significant at the point $D(Q_0 = e, \phi = \pi)$, where the parameter $|s_{01}| \approx 0.5$ and

$$\|I\|_D \approx I_{c0}. \quad (70)$$

To illustrate this behavior, the coupling strength evaluated for typical parameters of the system is presented in the table.

From the standpoint of operation with a minimum dephasing rate, the "magic" points *A*, *B*, and *C* at which $I_1 = 0$ (see Eq. (42)) are clearly preferable to other points in the Q_0–Φ plane. Therefore, manipulation of the qubit can, in principle, be performed at any of these points. The estimated values of the corresponding fidelity factor for quantum manipulation, $Q_\varphi \equiv \Omega\tau_\varphi^{(p)}$, given in the table, are sufficiently high. For example, in the case of preparation of the qubit at point *A*, the manipulation can be performed by means of a dc pulse applied to the transistor gate [3, 4, 17]. This pulse (with short rise and fall times) can rapidly switch the qubit, for example, to point *D* and back to *A* causing its evolution (although with significant dephasing) during the pulse span. Our qubit prepared in the ground state at point *A* or *B* or *C* can be (preferably) manipulated by a pulse of microwave frequency, $\sim\Omega$, applied to the gate. For example, the Quantronium qubit in the experiment by Vion *et al.* [5] was manipulated by microwave pulses at point *C*.

Evaluated qubit parameters derived under the assumption that $E_{J0} = 2E_c = 80$ μeV (i.e., $I_{c0} \approx 40$ nA and $5E_c = \Delta_{Al} \approx 200$ μeV, the energy gap of Al) and $j_1 - j_2 = \kappa_1 - \kappa_2 = 0.1$. The tank circuit quality factor $Q = 100$, frequency $\omega_0 = 2\pi \times 100$ MHz, $(L_T/C_T)^{1/2} = 100\Omega$, $k^2Q\beta_L = 20$ and temperature $T^* = 1$ K $\gg T \sim 20$ mK. As long as the dephasing rate at the magic points is nominally zero, a 0.1% inaccuracy of the adjustment of the values $\phi = \pi$ and 0 was assumed

Operation point:	*A*–*A*'	*B*–*B*'	*C*–*C*'	*D*–*D*'
Frequency $\Omega/2\pi$, GHz	39	50	36	4
Coupling strength α_p	2×10^{-2}	10^{-2}	4×10^{-2}	1
Qubit fidelity factor Q_φ	3×10^4	2×10^5	10^4	<30
Relaxation time $\tau_r^{(p)}$, s	8×10^{-2}	10^{-1}	6×10^{-3}	10^{-7}

For reading out the final state, the qubit dephasing is of minor importance, while the requirement of a sufficiently long relaxation time is decisive. Moreover, the relaxation rate may somewhat increase due to oscillations in the tank induced by a drive pulse (see Fig. 6), which leads to the development of oscillations around a magic point along the ϕ axis, Eq. (9). If the frequency of these oscillations is sufficiently low, $\omega_{rf} \ll \Omega$, they result only in a slow modulation of the transition frequency Ω. The increase in the amplitude of steady oscillations up to $\phi_a \approx \pi/2$ (determined by the amplitude of the drive pulse and detuning) yields a large output signal and still ensures the required resolution in the measurement provided the product $k^2Q\beta_L$ is sufficiently large. (At larger amplitudes ϕ_a, the circuit operates in a nonlinear regime probing the averaged reverse inductance of the qubit whose value, as well as the produced frequency shift $\delta\omega_0$, is smaller [28].) Because points *A* and *B* lie on the axis $Q_0 = 0$ and are both characterized by a sufficiently long relaxation time, a readout of the qubit state with the rf oscillation span $\pm\pi/2$ is preferable at either point. In the case of operation point *C*, the limited amplitude of the oscillations does not significantly reduce the relaxation time either. Significant reduction

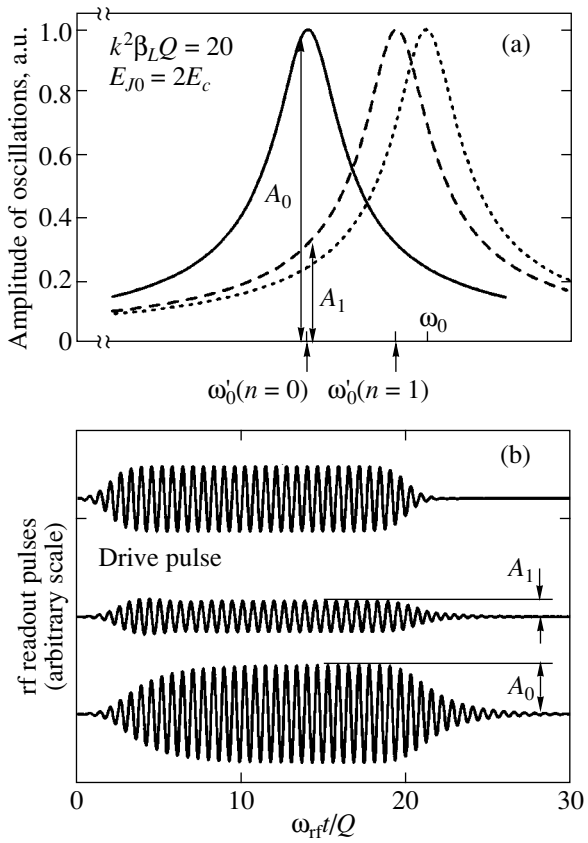

Fig. 6. Principle of narrow-band radio-frequency readout of the qubit. (a) The resonance curves of the uncoupled tank circuit (dotted line) and the tank circuit coupled to the qubit biased at operation point A in the excited state (dashed line) and in the ground state (solid line). (b) Driving rf pulse of frequency $\omega_{rf} = \omega_0'$ $(n = 0)$ applied to the tank circuit (top curve) and the response signal of the tank in resonance (the ground qubit state, bottom curve) and out of resonance (excited state, middle curve). A smooth envelope of the driving pulse is used to suppress transient oscillations and has a small effect on the rise time of the response signal. For clarity, the curves are shifted vertically.

of the relaxation time occurs in the vicinity of point D. Because of this property, which is due to the dependence of the transversal coupling strength on ϕ, Eqs. (43–49), the measurement of the Quantronium state using a switching current technique was possible in the middle of segment CD (see Fig. 2), where the (maximum) values of the circulating current in the excited and ground states were of different signs [5].

In the vicinity of level crossing point D, in which the gap between the zeroth and the first excited states is minimum, $\hbar\Omega = 2|j_1 - j_2|E_{J0}$, oscillations of ϕ may cause the Landau–Zener transitions $|0\rangle \longleftrightarrow |1\rangle$ [29]. The probability of a such transition per single sweep,

$$p_{LZ} = \exp\left[-2\pi\frac{(j_1 - j_2)^2 E_{J0}}{\phi_a \hbar\omega_{rf}}\right], \qquad (71)$$

can be appreciable in a sufficiently symmetric transistor and/or at a high driving frequency ω_{rf}, i.e., when $|j_1 - j_2| \lesssim (\hbar\omega_{rf}/E_{J0})^{1/2}$. These transitions lead to unwanted mixing of the qubit states [30]. In the vicinity of point A', where the gap between the first and the second (not shown in Fig. 2) energy bands is smaller [9], $\hbar\Omega_{12} = (j_1 - j_2)^2 E_{J0}^2/2E_c$, the Landau–Zener transitions $|1\rangle \longleftrightarrow |2\rangle$ are more probable. Fortunately, the second energy band has a positive curvature, $\partial^2 E_2(0, \phi = \pi)/\partial\phi^2 > 0$, and therefore the mixing of these states might even improve the distinguishability of signals from the ground and excited states. More rigorous analysis of this effect on operation of the qubit at point A is needed, however.

We finally evaluate the time of measurement required for the resolution of the states $n = 0$ and $n = 1$ at the most favorable magic points A and B. As schematically shown in Fig. 6, an rf drive pulse is applied to the tank circuit just after manipulation of the qubit $(t = 0)$ and induces growing oscillations in the tank. The amplitude of the oscillations of voltage V approaches a steady value A_0 (A_1) for $n = 0$ $(n = 1)$ after the time $t_{rise} \approx 2\pi Q/\omega_0$. Assuming a corresponding amplitude of oscillations of the phase $\phi_a = \pi/2$, we obtain the amplitudes

$$A_0 = \phi_a \frac{\Phi_0}{2\pi}\frac{\omega L_T}{M} = \left(\frac{\pi\Phi_0\omega R_p I_{c0}}{8k^2 Q\beta_L}\right)^{1/2} \approx 3\ \mu\text{V} \qquad (72)$$

and $A_1 \approx 1\ \mu$V for the parameters in the table.

Assuming that the equivalent noise of a semiconductor-based amplifier referred to the input is of the order of the Johnson voltage noise across $R_p \approx 10\ \text{k}\Omega$ at ambient temperature $T^* \sim 2$ K, i.e., $S_V^{1/2} \approx 1\ \text{nV}/\sqrt{\text{Hz}}$, we can express the signal-to-noise ratio as

$$\text{SNR} = \frac{(A_0 - A_1)\sqrt{t_{meas}}}{S_V^{1/2}} \approx 2\times 10^3\sqrt{t_{meas}/1\ \text{s}}, \qquad (73)$$

where t_{meas} is the time of measurement. This time should clearly be much shorter than the relaxation time $\tau_r^{(p)}$ (evaluated as ≈0.1 s, see table) and exceed the rise time of the oscillations in the tank $t_{rise} \approx 1\ \mu$s (the latter condition nicely agrees with the requirement of an SNR > 1). Thus, a drive pulse duration of ~10 μs ensuring $t_{meas} \sim 10\ \mu$s seems to be a good choice because it yields a sufficiently high value of SNR ≈ 6. The latter (as well as the quantum fidelity factor Q_φ) can be substantially improved using a SQUID-based low-noise amplifier [31].

8. CONCLUSIONS

We have demonstrated that both manipulation and readout of the charge-phase qubit coupled to a tank circuit is, in principle, possible. More specifically, the

decoherence effect of the electric and magnetic control lines can seemingly be minimized by reducing coupling to the qubit. The readout system based on the parallel tank circuit and cold amplifier can ensure sufficiently weak dephasing in the regime without an rf drive. The dephasing rate strongly depends on the accuracy of adjusting the offset flux bias $\Phi_m = 0$ or $\Phi_m = \Phi_0/2$ corresponding to operation at the magic points. High symmetry of the Josephson junction parameters may further improve the coherence characteristics of the qubit. Because the *LC* resonance tank circuit introduces only small noise at the high transition frequency of the qubit, $\Omega \gg \omega_0$, the rate of relaxation can also be made sufficiently small. Applying an rf drive pulse of limited span allows a readout of the qubit state in the regimes of single and repeated measurements.

Other problems in engineering Josephson qubits with weak decoherence are the $1/f$ noise of critical currents of Josephson junctions [32] and the $1/f$ background noise coupled to the charge variable [33], which have not been addressed in this paper but are equally important. Hopefully, in the given system, these effects might not be as strong as in "traditional" tunnel-junction devices like dc SQUIDs and single electron transistors operating at nonzero voltage bias. Due to perfect decoupling of the superconducting loop with the single-charge transistor from dc bias lines and due to the coherent nature of the Josephson current in the zero voltage bias regime, one could expect a minor back-action effect of the zero-bias operating transistor on its critical current noise and charge noise, which dramatically depend on the current fed (see, for example, [34]).

ACKNOWLEDGMENTS

The author would like to thank Per Delsing, Tim Duty, Yuriĭ Makhlin, and Frank Wilhelm for stimulating discussions. This work was partially supported by the European Union through the SQUBIT-2 project.

REFERENCES

1. J. Clarke, Science **299**, 1850 (2003) and references therein.
2. V. Bouchiat, D. Vion, P. Joyez, *et al.*, Phys. Scr. T **76**, 165 (1998).
3. Y. Nakamura, Yu. A. Pashkin, and J. S. Tsai, Nature **398**, 768 (1999); Yu. A. Pashkin, T. Yamamoto, O. Astafiev, *et al.*, Nature **421**, 823 (2003).
4. K. Bladh, D. Gunnarson, G. Johansson, *et al.*, Phys. Scr. T **102**, 167 (2002).
5. D. Vion, A. Aassime, A. Cottet, *et al.*, Science **296**, 886 (2002).
6. A. B. Zorin, Physica C (Amsterdam) **368**, 284 (2002).
7. R. Rifkin and B. S. Deaver, Jr., Phys. Rev. B **13**, 3894 (1976).
8. D. V. Averin, Phys. Rev. Lett. **88**, 207901 (2002).
9. *Handbook of Mathematical Functions*, Ed. by M. Abramowitz and I. A. Stegun, 2nd ed. (U.S. GPO, Washington, D.C., 1972; Nauka, Moscow, 1979), Chap. 20.
10. D. V. Averin, A. B. Zorin, and K. K. Likharev, Zh. Éksp. Teor. Fiz. **88**, 697 (1985) [Sov. Phys. JETP **61**, 407 (1985)].
11. K. K. Likharev and A. B. Zorin, J. Low Temp. Phys. **59**, 347 (1985).
12. D. V. Averin, Fiz. Nizk. Temp. **13**, 364 (1987) [Sov. J. Low Temp. **13**, 208 (1987)].
13. D. V. Averin and K. K. Likharev, in *Mesoscopic Phenomena in Solids*, Ed. by B. L. Altshuler, P. A. Lee, and R. A. Webb (Elsevier, Amsterdam, 1991), p. 175.
14. P. Joyez, P. Lafarge, A. Filipe, *et al.*, Phys. Rev. Lett. **72**, 2458 (1994).
15. A. Amar, D. Song, C. J. Lobb, and F. C. Wellstood, Phys. Rev. Lett. **72**, 3234 (1994).
16. J. Männik and J. E. Lukens, Phys. Rev. Lett. **92**, 057004 (2004).
17. T. Duty, D. Gunnarsson, K. Bladh, *et al.*, cond-mat/0305433.
18. Yu. Makhlin, G. Schön, and A. Shnirman, Rev. Mod. Phys. **73**, 357 (2001).
19. E. M. Lifshitz and L. P. Pitaevskiĭ, *Course of Theoretical Physics*, Vol. 5: *Statistical Physics* (Nauka, Moscow, 1978; Pergamon, New York, 1980), Part 2.
20. A. O. Caldeira and A. J. Leggett, Ann. Phys. (San Diego) **149**, 374 (1983).
21. A. J. Leggett, S. Chakravarty, A. T. Dorsey, *et al.*, Rev. Mod. Phys. **59**, 1 (1987).
22. C. H. van der Wal, F. K. Wilhelm, C. J. P. M. Harmans, and J. E. Mooij, Eur. Phys. J. B **31**, 111 (2003).
23. A. B. Zorin, Phys. Rev. Lett. **76**, 4408 (1996).
24. J. Clarke, T. L. Robertson, B. L. T. Plourde, *et al.*, Phys. Scr. T **102**, 173 (2002).
25. S. Kleff, S. Kehrein, and J. von Delft, cond-mat/0304177.
26. M. Grifoni, E. Paladino, and U. Weiss, Eur. Phys. J. B **10**, 719 (1999).
27. L. Tian, S. Lloyd, and T. P. Orlando, Phys. Rev. B **65**, 144516 (2002).
28. A. B. Zorin, Phys. Rev. Lett. **86**, 3388 (2001).
29. L. D. Landau, Phys. Z. Sowjetunion **1**, 89 (1932); C. Zener, Proc. R. Soc. London, Ser. A **137**, 696 (1932).
30. A. V. Shytov, D. A. Ivanov, and M. V. Feigel'man, cond-mat/0110490.
31. M.-O. André, M. Mück, J. Clarke, *et al.*, Appl. Phys. Lett. **75**, 698 (1999).
32. D. J. van Harlingen, T. L. Robertson, B. L. T. Plourde, *et al.*, cond-mat/0404307.
33. E. Paladino, L. Faoro, G. Falci, and R. Fazio, Phys. Rev. Lett. **88**, 228304 (2002).
34. V. A. Krupenin, D. E. Presnov, M. N. Savvateev, *et al.*, J. Appl. Phys. **84**, 3212 (1998).